



# The sedimentary geochemistry and geochronology of the Proterozoic greater McArthur Basin, northern Australia

Darwinaji Subarkah

This thesis is submitted in fulfilment of the requirements for the degree of  
Doctor of Philosophy

School of Physical Sciences  
Department of Earth Science  
The University of Adelaide  
Australia

March 2023



# Table of Contents

Table of Contents .....	i
List of Figures and Tables.....	v
Signed Statement.....	vii
Acknowledgments .....	viii
Abstract .....	ix
<b>Chapter 1: Introduction.....</b>	<b>1</b>
<b>1.1 Thesis Aims and Rationale .....</b>	<b>1</b>
<b>1.2 Geological Background.....</b>	<b>3</b>
1.2.1 Redbank Package .....	6
1.2.2 Glyde Package .....	6
1.2.3 Wilton Package .....	6
<b>1.4 Thesis Outline .....</b>	<b>8</b>
1.4.1 Chapter 2 .....	8
1.4.2 Chapter 3 .....	8
1.4.3 Chapter 4 .....	9
1.4.4 Chapter 5 .....	9
1.4.5 Chapter 6 .....	9
<b>Chapter 2: Unravelling the histories of Proterozoic shales through <i>in situ</i> Rb–Sr dating and trace element laser ablation analysis.....</b>	<b>10</b>
2.1 Abstract.....	13
2.2 Introduction .....	13
2.3 Geological Background.....	14
2.3 Methods.....	16
2.4 Results.....	16
2.5 Discussions.....	17
2.6 Conclusions .....	19
2.7 Acknowledgements .....	20
<b>Chapter 3: Constraining the geothermal parameters of <i>in situ</i> Rb–Sr dating on Proterozoic shales and their subsequent applications.....</b>	<b>21</b>
3.1 Abstract.....	24
3.2 Introduction .....	24

<b>3.2 Geological Background</b> .....	27
<b>3.3 Methods</b> .....	29
<b>3.4 Results</b> .....	32
<b>3.4.1 Compilation of legacy data</b> .....	32
<b>3.4.2 Mineralogy of the Velkerri Formation</b> .....	33
<b>3.4.3 Laser Ablation Data</b> .....	35
<b>3.4.4 Thermal Modelling</b> .....	36
<b>3.5 Discussions</b> .....	36
<b>3.5.1 Thermal Maturity of the Velkerri Formation</b> .....	36
<b>3.5.2 Thermochronological History of the Velkerri Formation</b> .....	39
<b>3.5.3 Modelled Predictions of the Geothermal Aureole Induced by the Derim Derim Dolerite</b> .....	45
<b>3.6 Conclusions</b> .....	48
<b>3.7 Acknowledgments</b> .....	48
<b>Chapter 4: Reconstructing the palaeoenvironments of Proterozoic packages from the greater McArthur Basin, Australia using a multi-proxy approach</b> .....	49
<b>4.1 Abstract</b> .....	52
<b>4.2 Introduction</b> .....	53
<b>4.2.1 Organic and inorganic geochemical evidence for changes in palaeoproductivity and palaeoredox conditions</b> .....	54
<b>4.2.2 Isotopic signatures for determining changes in palaeoseawater chemistry</b> .....	56
<b>4.3 Geological Background</b> .....	57
<b>4.3.1 Tawallah Group</b> .....	58
<b>4.3.2 McArthur Group</b> .....	59
<b>4.4 Methods</b> .....	61
<b>4.4.1 Carbonate geochemical analysis</b> .....	61
<b>4.4.2 Shale geochemical analysis</b> .....	62
<b>4.5 Results</b> .....	62
<b>4.5.1 Screening of non-authigenic signals in the whole-rock chemistry of the Tawallah and McArthur Group</b> .....	63
<b>4.6 Discussions</b> .....	66
<b>4.6.1 Palaeoproductivity, palaeoredox, and depositional constraints of the Tawallah and McArthur Groups</b> .....	66
<b>4.6.2 Isotopic constraints on the palaeoenvironments of the Amelia Dolostone</b> .....	69
<b>4.6.3 The global palaeo-water during the Proterozoic</b> .....	71



4.7 Conclusions .....	73
4.8 Acknowledgements .....	74
<b>Chapter 5: Characterising the economic Proterozoic Glyde Package of the greater McArthur Basin, northern Australia .....</b>	<b>75</b>
5.1 Abstract .....	78
5.2 Introduction .....	79
5.3 Geological Background .....	80
5.3.1 McArthur Group in the McArthur Basin <i>sensu stricto</i> .....	81
5.3.2 Limbunya Group in the Birrindudu Basin .....	83
5.4 Methods .....	84
5.4.1 Shale geochemical analysis .....	84
5.4.2. Carbonate geochemical analysis .....	85
5.4.3 High resolution imaging and in situ Rb–Sr dating with trace element analysis of shales .....	85
5.5 Results .....	86
5.5.1 Whole-rock shale and carbonate geochemistry of the Glyde Package .....	88
5.5.2 High-resolution petrographic mapping of shales from the Barney Creek Formation and the Fraynes Formation .....	88
5.5.3 Rb–Sr geochronology of distal shale samples from the Glyde Package .....	89
5.6 Discussions .....	91
5.7 Conclusions .....	97
5.8 Acknowledgements .....	97
<b>Chapter 6: Conclusions .....</b>	<b>98</b>
6.1 Summary .....	99
6.2 Future studies .....	104
<b>7. Bibliography .....</b>	<b>105</b>
<b>8. Supplementary Material .....</b>	<b>145</b>
<b>Additional information for Chapter 2 .....</b>	<b>145</b>
<b>Sampling, Petrography and Mineralogy .....</b>	<b>149</b>
<b>Elemental Analyses .....</b>	<b>152</b>
<b>Additional information for Chapter 3 .....</b>	<b>186</b>
<b>Petrography and Mineralogy .....</b>	<b>190</b>
<b>One-Dimensional Thermal Modelling .....</b>	<b>191</b>
<b>Analytical Data .....</b>	<b>192</b>

<b>Additional information for Chapter 4</b> .....	234
<b>Carbonate Isotopic Analysis</b> .....	234
<b>Shale Geochemical Analysis</b> .....	236
<b>Analytical Data</b> .....	237
<b>Additional information for Chapter 5</b> .....	280
<b>Carbonate Elemental Analysis</b> .....	284
<b>Carbonate Isotopic Analysis</b> .....	285
<b>Shale Geochemical Analysis</b> .....	286
<b>High resolution Scanning Electron Microscope mapping of shale samples</b> .....	287
<b>Analytical Data</b> .....	289

# List of Figures

Figure 1.1. Regional map of the greater McArthur Basin, northern Australia .....	5
Figure 1.2. Basin-scale group level correlation charts of the greater McArthur Basin .....	7
Figure 2.1. Geological map of the McArthur Basin with localities of sampled wells and stratigraphic log of the Roper Group .....	15
Figure 2.2. Micro-scale energy dispersive x-ray spectroscopy mineral maps of shale samples in the lower Roper Group .....	17
Figure 2.3. Summary of Rb-Sr isotopic data and $^{87}\text{Sr}/^{86}\text{Sr}$ initial ratios of the samples in the lower Roper Group .....	19
Figure 3.1. Schematic stratigraphy and geochronological summary of the Roper Group and the sample locations in this section .....	28
Figure 3.2. Summary of reprocessed down-hole well log data for the Atree 2 well .....	31
Figure 3.3. Covariation between Tmax and illite crystallinity in the Velkerri Formation . ...	37
Figure 3.4. Calculated vitrinite reflectance in Atree 2 modelled from Tmax, MPR, MPDF, and bitumen reflectance data .....	38
Figure 3.5. Spectral reflectance MLA maps of samples overlain on top of their respective BSE images .....	41
Figure 3.6. Summary of Rb–Sr geochronological results from the Velkerri Formation .....	42
Figure 3.7. Statistical relationships between alteration proxies from the Velkerri Formation .....	44
Figure 3.8. Rb–Sr single-spot ages from samples in the Velkerri Formation compared to their depositional window .....	45
Figure 3.9. 1D thermal model for sill intrusion of 75 m thickness in the Atree 2 well.....	47
Figure 4.1. Geological map of the greater McArthur Basin showing the location of the studied drill cores along with the generalised stratigraphy of the upper Tawallah Group and lower McArthur Group.....	60
Figure 4.2. Screening geochemical proxies for diagenetic alteration and detrital influence in the MCDD003 and MCDD005 wells.....	64
Figure 4.3. Geochemical shifts in the Amelia Dolostone up-section mirrored by the changes in relative sea level.....	65
Figure 4.4. Palaeoredox and palaeoproductivity proxies from well MCDD005 plotted with the relative sea level changes.....	67

Figure 4.5. Palaeoredox and palaeoproductivity proxies from well MCDD003 plotted with the relative sea level changes .....	68
Figure 4.6. Redox-sensitive trace element enrichments with respect to TOC content in the Tawallah Group and the lower McArthur Group .....	69
Figure 4.7. Trace element redox models for the Tawallah Group and the lower McArthur Group based on changes in V, Mo and Ce concentrations .....	69
Figure 4.8. Isotopic and elemental relationships in the Amelia Dolostone.....	73
Figure 5.1. Geological map of the greater McArthur Basin with outcrop of the Glyde Package and the sample localities for the studied Limbunya Group and the McArthur Group .....	81
Figure 5.2. Stratigraphic correlation of the Glyde Package units from the McArthur Basin and the Birrindudu Basin .....	84
Figure 5.3. Geochemical proxies for detrital contamination and alteration for the Glyde Package .....	87
Figure 5.4. In situ Rb–Sr geochronological results from shales in the Barney Creek Formation and Fraynes Formation sourced from boreholes LV09001 and Manbulloo S1 .....	90
Figure 5.5. Redox-sensitive trace element enrichments with respect to total organic carbon content in the Glyde Package .....	92
Figure 5.6. V/Mo versus Mo palaeoredox plot showing the heterogeneous conditions evident in the Glyde Package .....	93
Figure 5.7 Isotopic correlations between the McArthur Group sampled from LV09001 and the Limbunya Group from Manbulloo S1 .....	95
Figure 6.1. Basin evolution and redox model of the greater McArthur Basin .....	101
Figure 6.2. Updated $^{87}\text{Sr}/^{86}\text{Sr}$ curve for the global Proterozoic palaeo-water.....	102
Figure 6.3. Global correlations of the greater McArthur Basin based on $\delta^{13}\text{C}$ excursions ...	103

## List of Tables

Table 3.1. Mineralogical abundance of the Velkerri Formation shales collected by bulk XRD analysis and spectral reflectance MLA mapping in the well Atree 2 .....	35
Table 4.1. Summary of organic geochemistry in the Tawallah and McArthur Groups .....	66
Table 5.1. Summary of the palaeoredox geochemical results in the Glyde Package .....	91

# Signed Statement

I certify that this work contains no material which has been accepted for the award of any other degree or diploma in my name, in any university or other tertiary institution and, to the best of my knowledge and belief, contains no material previously published or written by another person, except where due reference has been made in the text. In addition, I certify that no part of this work will, in the future, be used in a submission in my name, for any other degree or diploma in any university or other tertiary institution without the prior approval of the University of Adelaide and where applicable, any partner institution responsible for the joint award of this degree.

The author acknowledges that copyright of published works contained within the thesis resides with the copyright holder(s) of those works.

I give permission for the digital version of my thesis to be made available on the web, via the University's digital research repository, the Library Search and also through web search engines, unless permission has been granted by the University to restrict access for a period of time.

I acknowledge the support I have received for my research through the provision of the MinEx CRC and the Australian Research Council Linkage Projects LP160101353 and LP200301457 in collaboration with Santos Ltd, Empire Energy Group Ltd, Northern Territory Geological Survey, Teck Resources, BHP, and Origin.

24/11/2022

Signed: .....

Date: .....

# Acknowledgements

Firstly, I would like to thank my supervisors Alan Collins, Morgan Blades, Juraj Farkaš, and Amber Jarrett for their endless support and guidance. A PhD often feels like a wild adventure, weathering through stormy seas and overcoming the rough patches. But they have always been a beacon, reminding me that every ocean has a distant shore, and I will reach it. I am forever grateful for their wealth of knowledge, tireless advice, and confidence in me. Most importantly, I would like to thank them for their kindness, which absolutely knows no bounds. I could not have wished for a better supervisory panel and this work would not have been possible without them.

I must also extend this gratitude to the loved ones who have helped me throughout this endeavour. In particular, I would like to thank Nhã-Uyên for her constant care, warmth, and reassurance. I am also grateful for Georgie, Jarred, Monica, and Alex for putting up with my distinctly loud laughter during our shared tenure of office 125. All of you, along with the ever growing members of the Tectonics and Earth Systems group, have made the Mawson building a home away from home. I am extremely lucky to have shared this experience with you and the rest of this wonderful student cohort.

Lastly, I would like to dedicate this thesis to my family in Indonesia. My mother, my father, and my brothers. Your words of encouragement have always kept me afloat throughout this project. With the completion of this work, it would have been years since I have returned home. Know that I think about you all every day, and I hope I have made you proud.

# Abstract

The greater McArthur Basin is a Proterozoic sedimentary system deposited in northern Australia and has been widely used to reconstruct ancient global biogeochemical systems. Sections within the basin are economically prospective, hosting petroleum supersystems and world-class metal deposits. Consequently, the geochemistry of the basin also plays a crucial role in the formation of energy and mineral resources. Identifying units with similar age and geochemistry is pivotal for finding analogous targets elsewhere in the region. However, dating Proterozoic sedimentary rocks can be difficult, as they are devoid of a diverse fossil record for biostratigraphy to be applicable.

To better define these parameters, a new laser-based technique to date shales using *in situ* Rb–Sr geochronology was developed. Here, geochronological and geochemical information are collected concurrently. Triaging these datasets help differentiate between samples that record primary signatures versus those that were altered. Thermal constraints of the same samples can also be obtained using indicators used in petroleum research. The development of this method is the subject of the second and third chapters in this thesis. *In situ* Rb–Sr dating of mature, oil-prone shales from the Velkerri Formation gave ages ca. 1448–1421 Ma, agreeing with previous Re–Os geochronology. This is interpreted as a minimum age, recording the deposition of the formation. Oppositely, thermally overmature shales sourced from the unit were dated at ca. 1336–1322 Ma. This is younger than its expected age and instead overlaps with the Derim Derim-Galiwinku/Yanliao magmatic event. Geothermal modelling found that a Derim Dolerite sill would have enough influence on the surrounding shales to reset their chronometer and elevate their organic matter into overmaturity. This method was also applied to the lower formations of the greater McArthur Basin; establishing correlations between the McArthur Basin and the Birrindudu Basin in Chapters 4 and 5. We build on this framework by constraining their palaeo-water conditions using multiple proxies. Bioproductivity indices such as Ba, P, and total organic carbon content display a relationship with several redox-sensitive tracers in the Redbank and Glyde Packages. Further evidence from Ce,  $\delta^{13}\text{C}_{\text{carb}}$ , and  $^{87}\text{Sr}/^{86}\text{Sr}$  values suggest that more oxic and productive basin waters occur in open, marine settings as opposed to restricted palaeoenvironments. In addition,  $\delta^{88/86}\text{Sr}$  analysis show that these marine settings are more likely to source mantle-like provenance, elevating bioproductivity and producing a redox gradient in the water column. Comparatively, restricted basins experienced stunted bioproductivity and were largely oxygen-poor. These isotopic excursions were also used to chemostratigraphically correlate coeval units elsewhere in the basin and globally.

Altogether, the geochronology of the greater McArthur Basin and similarly aged systems can benefit from the innovative dating method developed here. The thermochronological history of a sedimentary unit can be defined by timing its deposition or subsequent alteration events. The geochemical signatures of the basin also show that surface environments in the Proterozoic were deeply complex. Palaeo-water heterogeneity is controlled by basin-scale tectonic processes and would influence where and how economic resources form within the sediment.

# Chapter 1: Introduction

## 1.1 Thesis Aims and Rationale

The world-wide transition from fossil fuels to low-carbon energy sources has raised the demand for certain minerals and metals substantially (Tsafos, 2022, Coulomb et al., 2015, Eggert, 2010, Kalantzakos, 2020, McLellan et al., 2016). This decarbonisation of the global economy is largely driven in response to the climate crisis, with the aim to reduce carbon emissions and mitigate catastrophic climate change (Kalantzakos, 2020, Eggert, 2011, Nakano, 2021). Furthermore, these minerals are also essential to the production of emerging high-technology innovations and products (Coulomb et al., 2015, Eggert, 2010, McLellan et al., 2016, Kalantzakos, 2020). Consequently, this shift in global demand, with the context of complex geopolitical alignments, have prompted the race to securing uninterrupted access to such critical raw materials (Vakulchuk et al., 2020, Kalantzakos, 2020, Tsafos, 2022, Hayes and McCullough, 2018).

However, it should be noted that an immediate global change to completely all-green and renewable energy prove to be near impossible, due to inadequate infrastructure and potential subsequent financial repercussions (Zhang et al., 2019, Abotah and Daim, 2017). As such, natural gas has been identified as a potential key resource to bridge the gap in this transition (Gürsan and de Gooyert, 2021, Mohammad et al., 2021). Natural gas is economically competitive with other fossil fuels such as coal and diesel, whilst being a much cleaner energy source (Moniz et al., 2011, Kuhns and Shaw, 2018). As a result, natural gas can directly support the eventual conversion to renewable technologies by providing an alternative to avoiding greenhouse gas emissions in the immediate future (Gürsan and de Gooyert, 2021).

The greater McArthur Basin presents an excellent opportunity to help supply these necessities. It is one of the most important base metal provinces in Australia, forming a significant section of the Carpentaria Zn Belt, the world's largest Zn-Pb province (Southgate, 2000). Mineral commodities found in the sedimentary system range from base metals (Zn, Pb, Ag, Cu), uranium, iron ore, manganese, barite, and phosphate (Ahmad and Munson, 2013). In particular, the super-giant McArthur River Zn-Pb-Ag deposit is world-class, with a pre-mining resource estimate at 227 million tonnes at 9.2% Zn, 4.1% Pb, 0.2% Cu, and 41 ppm Ag (Porter, 2017). The base metal mineralisation here and elsewhere in the basin commonly occur stratiform to pyritic, organic rich shale and siltstone, comprising of fine-grained pyrite, galena, and sphalerite (Large et al., 1998, Smith and Croxford, 1975, Large et al., 2005, Spinks et al., 2020).

In addition to the critical mineral potential of the sedimentary system, the greater McArthur Basin is also highly prospective for conventional natural gas, shale-gas, and oil (Jarrett et al., 2022, Summons et al., 1988, Henson et al., 2020, Jarrett et al., 2019). Notably, the Beetaloo Sub-basin contains the basin's premier shale hydrocarbon plays, with reported original hydrocarbons in place values of 772 MMbbl of oil and 8626 Bscf of gas in the Kyalla Formation alone (Revie and Normington, 2016, Revie, 2017, Jarrett et al., 2022). As a result, the region has been identified as an integral part of the Australian Government's gas-driven



future strategies, with significant resources allocated to accelerate its development and promote exploration from industry (Trotman, 2021, Bartholomew, 2022, Bernecker et al., 2022).

Moreover, the importance of the greater McArthur Basin extends beyond its economic potential. Its Palaeo-to-Mesoproterozoic units have been used as a notable geological archive for reconstructing earth system processes during this period (Gibson et al., 2012, Lindsay and Brasier, 2000, Mukherjee and Large, 2020, Rafiei and Kennedy, 2019, Shen et al., 2002, Shen et al., 2003, Spinks et al., 2016a, Yang et al., 2019, Zhang et al., 2018a, Zhang et al., 2012, Zhang et al., 2021, Zhang et al., 2017, Zhao et al., 2004, Chen et al., 2022, Ding et al., 2020, Gibson et al., 2018, Kirscher et al., 2020, Mitchell et al., 2020, Nordsvan et al., 2018, Lyons et al., 2021). Marine sedimentary rocks here have provided insight to the evolution of early biological life during the eon (Jarrett et al., 2019, Butterfield, 2015, Javaux and Lepot, 2018, Knoll and Carroll, 1999, Spinks et al., 2016a, Mukherjee et al., 2018). Furthermore, their elemental fingerprints were also used to reconstruct past ocean and atmospheric chemistries (Zhang et al., 2018a, Bellefroid et al., 2018, Farquhar et al., 2011, Liu et al., 2021, Lyons et al., 2014, Mukherjee and Large, 2020). Importantly, these successions are coeval with rocks found in north China, Laurentia, and Siberia, helping researchers piece together ancient supercontinent cycles (Ding et al., 2020, Gibson et al., 2018, Kirscher et al., 2020, Mitchell et al., 2020, Nordsvan et al., 2018, Wang et al., 2019, Zhang et al., 2017).

Therefore, providing an improved chronostratigraphic and geochemical framework for the greater McArthur Basin would be beneficial for several reasons. Explorers will be able to develop better predictions of resource potential in the province and researchers can improve their understanding of how the planet evolved during this understudied time interval. Improved geochronology for the sedimentary system will better correlate distal but coeval units, locating analogous targets, and help construct a paragenetic sequence for mineralisation and hydrocarbon formation. On the other hand, understanding the palaeoredox geochemistry and palaeoenvironment of these rocks will elucidate the complexity of Proterozoic surface environments. The heterogeneous conditions of the basin sediments here would also be an important control on where critical minerals, metals, and energy resources would be found.

Consequently, this thesis is split into two main themes structured to tackle these topics. The first theme is explored in Chapters 2 and 3, with the aim to develop a new method to date Proterozoic sedimentary rocks. It is notoriously difficult to directly date sedimentary rocks of this age, as the absence of a distinct and diverse fossil record limits the use of biostratigraphy. Dating tuffaceous layers within the sediment is the most precise method to obtain depositional ages, but they are a rarity in these sequences (Southgate et al., 2000, Page et al., 2000, Kositcin and Carson, 2017). Furthermore, the interplay between bioproductivity, environment, and water chemistry in these ancient settings are difficult to formulate without a multi-proxy approach (Katz, 2005, McManus et al., 1999, Müller and Suess, 1979, Pedersen and Calvert, 1990, Piper and Perkins, 2004, Tribouillard et al., 2006).

To address these challenges, I focus on an innovative approach that utilises a laser-based technique to date authigenic clays in siltstones *in situ* using the Rb–Sr isotopic system. Recent advancements in tandem laser ablation mass spectrometer technologies now allows for the separation of parent and daughter isotopes with the same mass online (Hogmalm et al., 2017, Hogmalm et al., 2019, Simpson et al., 2021, Zack and Hogmalm, 2016, Bevan et al., 2021, Gorjovsky and Alard, 2020, Redaa et al., 2021a). This technique is cheaper, faster, and easier to utilise in comparison to the traditional whole-rock method. This laser-based technique have been applied several beta-decay systems and can provide better geological accuracy by integrating the chronological results with petrology and geochemistry (Redaa et al., 2021b, Scheibelhofer et al., 2022, Şengün et al., 2019, Simpson et al., 2021, Simpson et al., 2022, Subarkah et al., 2021, Subarkah et al., 2022, Tamblyn et al., 2021, Tillberg et al., 2017, Tillberg et al., 2020, Hogmalm et al., 2019, Laureijs et al., 2021, Olierook et al., 2020). In Chapter 1 of this thesis, the use of this method for Proterozoic shales have shown to be able to distinguish between early burial processes vs. later-stage post-depositional events. These findings were published in Subarkah et al. (2021). Such secondary events are consequential for the formation, mobilisation, and preservation of hydrocarbon reservoirs and mineral deposits. As a result, an application of this method was further explored in Chapter 2 by combining the use of this technique with common thermal maturation proxies used in petroleum geology. This dual approach found that the Rb–Sr isotopic system in shale-hosted clays are reset at similar parameters in which kerogen becomes thermally overmature (Subarkah et al., 2022). Consequently, the method has the potential to be used a thermochronometer, when used in conjunction with traditional palaeotemperature indicators from the same samples.

I then build-upon this geochronological framework in the second theme of this thesis. Here, I look to constrain the palaeo-water conditions of key sections of the greater McArthur Basin using traditional and novel geochemical proxies in Chapter 4 and 5. Palaeoproductivity of the sedimentary rocks from the lower parts of the basin were tracked by variations in Ba, P, and total organic carbon content (Dymond et al., 1992, Francois et al., 1995, Katz, 2005, McManus et al., 1999, Pedersen and Calvert, 1990, Tribovillard et al., 2006). Furthermore, the palaeoredox chemistry of these successions were also defined by several redox-sensitive trace elements such as Ce, V, and Mo (Algeo and Maynard, 2004, German and Elderfield, 1990, Lyons et al., 2009, Tostevin et al., 2016, Tribovillard et al., 2006). Isotopic studies were also undertaken to illustrate changes in palaeoenvironment and basin-scale tectonic evolution (Knoll et al., 1986, Derry and Jacobsen, 1988, Krabbenhöft et al., 2010), as these variables are intrinsically linked to each other. In Chapter 4 and 5, spatially distant units that record similar isotopic excursions were correlated by chemostratigraphy. These parallel trends suggest that the complex evolution of the greater McArthur Basin is extensively recorded in its spatially distant sequences. Therefore, the economic targets within the sediment has the potential to be laterally extensive across the region.

## **1.2 Geological Background**

The greater McArthur Basin is an informal term for an intracontinental, multi-phase sedimentary system (Fig. 1.1) that includes the rocks of the McArthur Basin *sensu stricto*, the Birrindudu Basin, and the Tomkinson Province (Close, 2014). The sedimentary system

covers over 180,000 km<sup>2</sup> of the northern Australian surface (Fig 1.1), with the individual basins previously mentioned interpreted to connect underground based on geophysical and drill core data (Close, 2014, Ahmad and Munson, 2013, Jarrett et al., 2021, Munson et al., 2020, Munson, 2019, Yang et al., 2019, Nixon et al., 2021, Kunzmann et al., 2020, Kunzmann et al., 2022, Blaikie and Kunzmann, 2020, Blaikie and Kunzmann, 2019, Frogtech Geoscience, 2018, Page et al., 2000, Page and Sweet, 1998, Plumb and Wellman, 1987, Rawlings, 1999). The basement geology consists of Archean-to-Palaeoproterozoic rocks of the North Australian Craton, and the basin is subsequently unconformably overlain by Neoproterozoic-to-Cambrian cover (Ahmad and Munson, 2013, Frogtech Geoscience, 2018, Plumb and Wellman, 1987, Blaikie and Kunzmann, 2020, Close, 2014).

Palaeomagnetic findings from northern Australia, north China, and Laurentia suggests that the continents neighboured each other through much of the Proterozoic (Kirscher et al., 2020, Pisarevsky et al., 2014, Ding et al., 2020, Wang et al., 2019, Zhang et al., 2012). This is further corroborated by similarities in magmatic events (Nixon et al., 2021, Zhang et al., 2021, Zhang et al., 2018b, Zhang et al., 2017, Hamilton and Buchan, 2010, Medig et al., 2014), astrochronology (Mitchell et al., 2020), sedimentary geology (Ding et al., 2017, Furlanetto et al., 2016, Lu et al., 2008, Yang et al., 2019, Yang et al., 2020, Yang et al., 2018), petroleum reservoirs (Liu et al., 2011, Zhang et al., 2018b, Yang et al., 2020, Jarrett et al., 2022, Ghorri et al., 2009, Wenzhi et al., 2018), and sediment-hosted mineralisation (Gibson et al., 2017, Southgate et al., 2000, Wang et al., 2014, Burrett and Berry, 2000, Barley and Groves, 1992). Consequently, the northern margins of the greater McArthur Basin is currently undefined, as it may have extended across distant continents (Fig. 1.1). The sedimentary units of the greater McArthur Basin are categorised into five, basin-scale packages (Fig. 1.2) based on their age, lithostratigraphy, igneous composition, and basin-fill geometry (Ahmad and Munson, 2013, Close, 2014, Rawlings, 1999). In stratigraphic order, these are the: Redbank, Goyder, Glyde, Favenc, and Wilton Packages (Fig. 1.2). The Redbank, Glyde, and Wilton Packages hold the most potential for economic resources in the basin and forms the focus of this study.

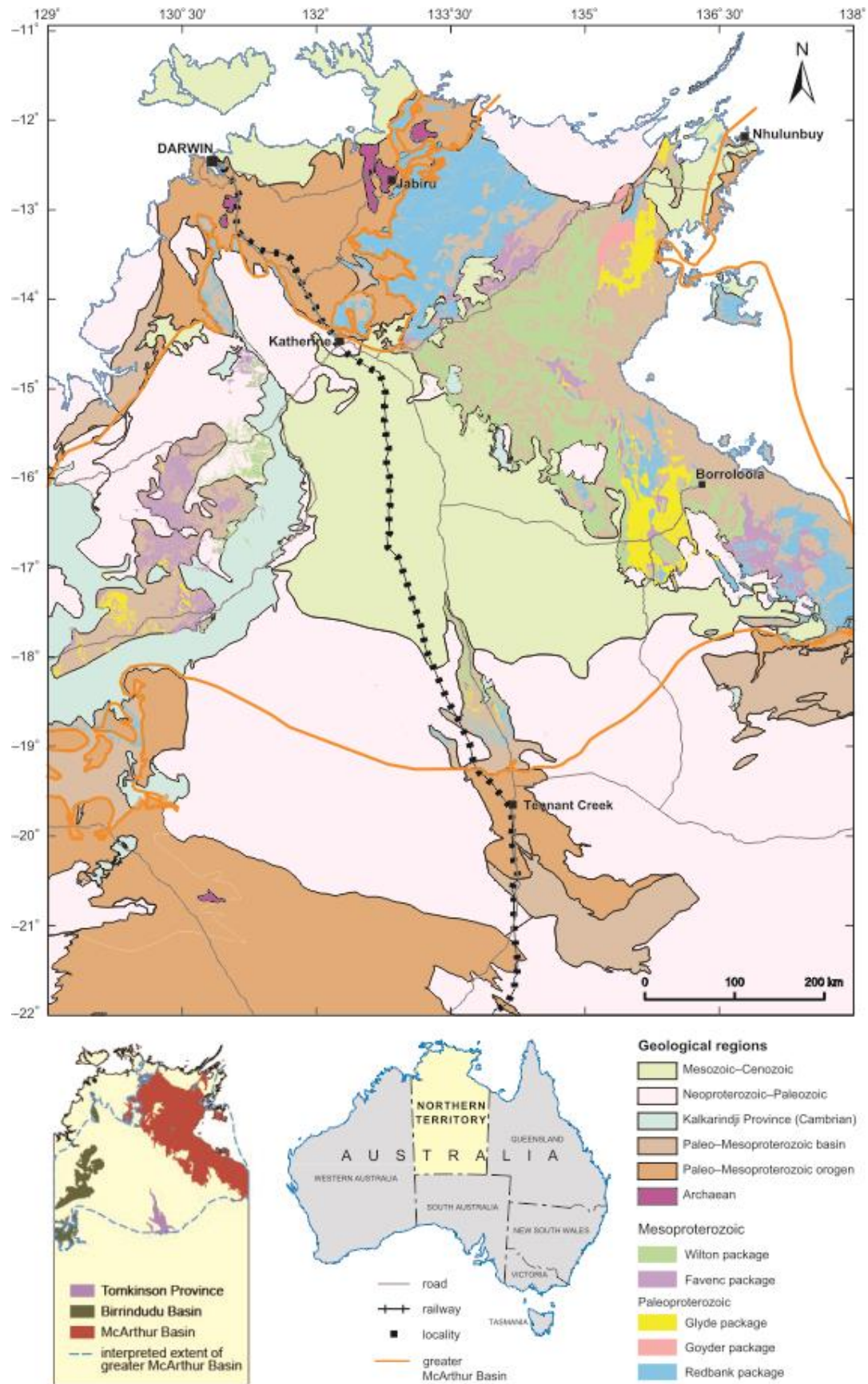


**Figure 1.1.** Regional map of the greater McArthur Basin adapted from Munson (2019), following the boundaries defined by Close (2014).

### 1.2.1 Redbank Package

The Redbank Package is the lowest stratigraphic division of the greater McArthur Basin (Fig. 1.2). It includes the Tawallah, Donydji, Spencer Creek, Groote Eylandt, and Katherine River Groups in the McArthur Basin *sensu stricto* (Rawlings, 1999, Rawlings, 2002). In addition, it also consists of the Tolmer and Birrindudu Groups in the Birrindudu Basin, and the Tomkinson Creek Group from the Tomkinson Province (Rawlings, 2002, Southgate et al., 2000). The lower sections of the Redbank Package are largely made of homogeneous successions of marginal marine-to-intertidal sandstone interlayered with a regionally extensive flood basalt unit (Ahmad and Munson, 2013, Rogers, 1996, Kunzmann et al., 2020). Further up stratigraphy, these units look to transition into a more marine palaeoenvironments, dominated by shale and carbonate units (Rogers, 1996, Kunzmann et al., 2020, Rawlings, 2002). The top of the package is represented by an assemblage of igneous and sedimentary rocks, associated with volcanic activity present in several parts of the basin concurrent with deposition (Rawlings, 2002, Kunzmann et al., 2020). Notably, the Redbank Package has seen a surge of recent interest as a frontier exploration basin, with potential for hosting hydrocarbon and mineral resources (Spinks et al., 2016b, Jarrett et al., 2022). The maximum and minimum depositional age of the Redbank Package have been constrained to be between 1815–1710 Ma (Ahmad and Munson, 2013, Rawlings, 1999).

### 1.2.2 Glyde Package

The McArthur, Vizard, and Habgood Groups make up the Glyde Package successions (Fig. 1.2) from the McArthur Basin *sensu stricto* (Rawlings, 1999). These are equivalent units to the Limbunya Group in the Birrindudu Basin and parts of the Namerinni Group in the Tomkinson Province (Rawlings, 1999, Ahmad and Munson, 2013, Close, 2014). The Glyde Package is largely made of carbonate rocks with interbedded mudstone and sandstone, interpreted to have deposited in a shallow-to-moderately deep marine environment (Ahmad and Munson, 2013, Kunzmann et al., 2022, Kunzmann et al., 2019, Schmid, 2015, Bull, 1998, Cutovinos et al., 2002, Haines, 1994). Evidence for syn-depositional faulting commonly occurs in the strata and have been proposed to control the local and regional hiatuses within the package (Ahmad and Munson, 2013, Rawlings, 1999, Haines, 1994). Importantly, the Barney Creek Formation in the McArthur Group hosts a super-giant base metal deposit within its sediment (Croxford et al., 1975). This Pb-Zn-Ag mineralisation is commonly stratabound to organic-rich, pyritic shales and is a substantial constituent of the Carpentaria Zn belt (Large and Wolf, 1981). Furthermore, this unit and its equivalents are also highly prospective for hydrocarbons, and makes up the McArthur Petroleum Supersystem (Jarrett et al., 2022). Tuffaceous layers from the Glyde Package are commonly present and have provided a depositional window between 1648–1609 Ma (Page et al., 2000, Page and Sweet, 1998, Munson et al., 2020, Kositcin and Carson, 2017).

### 1.2.3 Wilton Package

The Wilton Package is the youngest of the basin-scale sub-divisions and has also been known as the Roper Superbasin (Ahmad and Munson, 2013, Jackson et al., 1999, Rawlings, 1999, Close, 2014). It comprises of the laterally extensive Roper Group from the McArthur Basin *sensu stricto*, the Tijnuna Group in the Birrindudu Basin, and the Renner Group in the Tomkinson Province (Close, 2014, Rawlings, 1999). There is evidence for six large-scale,

upward-coarsening cycles in the Wilton Package, with the main lithologies comprising of marine mudstone and sandstone (Abbott and Sweet, 2000). Reconstruction of the palaeowater chemistry from this section suggests that the basin experienced periods of euxinia and redox stratification, suggesting that it was intermittently restricted and drawing comparisons to the modern Black Sea (Revie and MacDonald, 2017, Yang et al., 2018, Cox et al., 2016b, Cox et al., 2019). The Beetaloo Sub-basin have been interpreted to be the depocentre of these successions and holds the basin’s premier shale hydrocarbon plays (Jackson et al., 1986, Warren et al., 1998, Jarrett et al., 2022). The minimum age constraint for the Wilton Package is given by a U–Pb geochronology of a tuff layer from the underlying Favenc Package, dated at  $1589 \pm 3$  Ma (Page et al., 2000). This is bracketed by its maximum depositional age constrained from the crosscutting mafic Derim Derim dolerite intrusions dated at  $1313 \pm 1$  Ma (Yang et al., 2020).

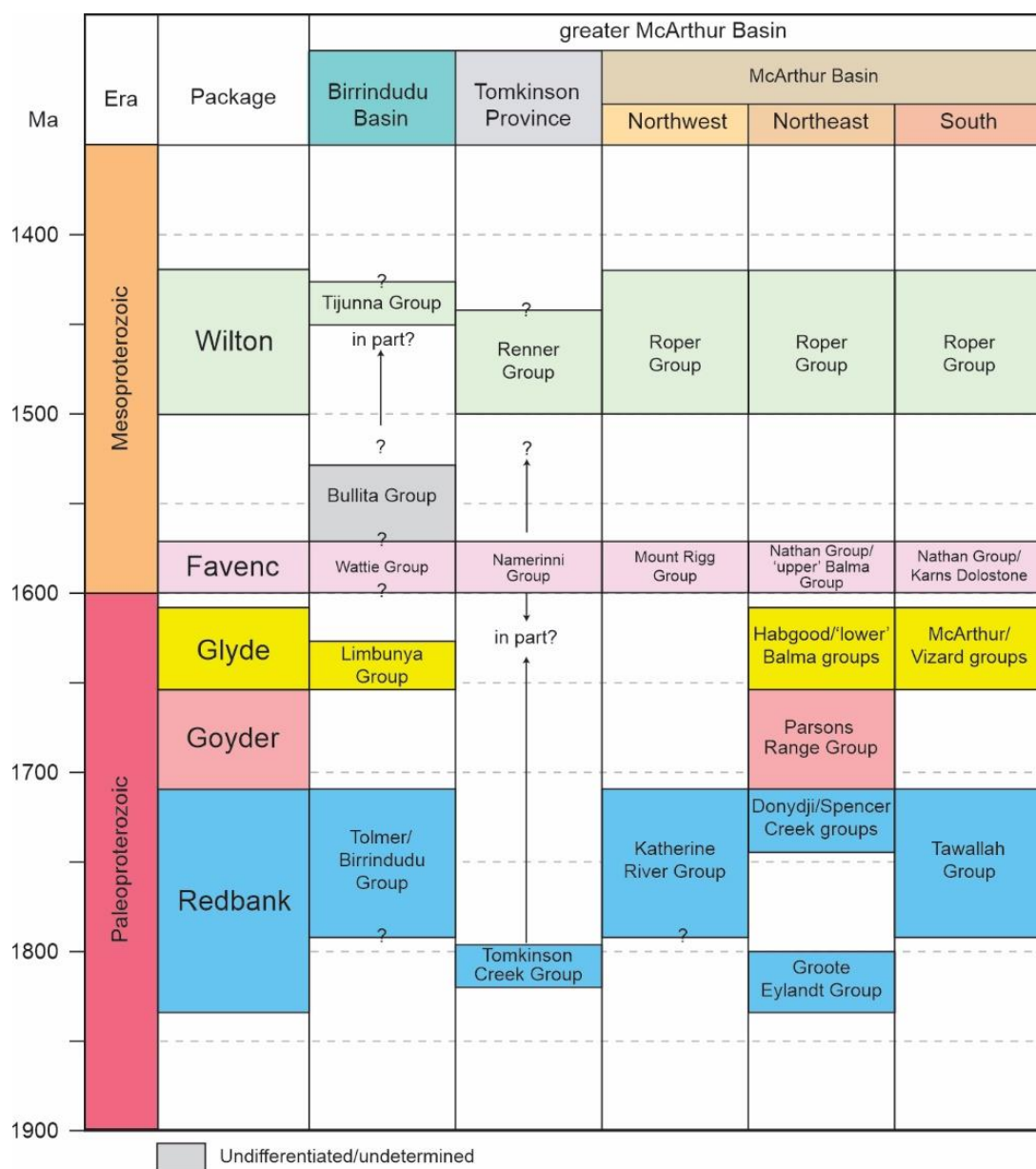


Figure 1.2. Basin-scale group level correlation charts of the greater McArthur Basin following Jarrett et al. (2022) with the interpreted coeval packages as defined by Rawlings (1999).



## 1.4 Thesis Outline

This thesis begins with an introductory chapter which looks to discuss the project aims and rationale as well as outline the regional geological setting. This is followed by two chapters focusing on the method development of *in situ* Rb–Sr dating on Proterozoic shales in the Roper Group and their applications for mineral and energy resources. These chapters are published as peer-reviewed journal articles. Chapter 4 and 5 looks to reconstruct the palaeoenvironment and palaeowater chemistry of the Redbank and Glyde Packages respectively using a multi-proxy approach. These indexes help elucidate the evolution of the redox conditions for these sedimentary rocks, which is an important control on organic matter preservation and entrapment of mobilised metals. Both chapters 4 and 5 are currently either in review for publication, or ready for submission. The final chapter concludes the thesis by summarising the findings in this study and proposing future research possibilities for the region.

### 1.4.1 Chapter 2

This chapter is published as: Subarkah, D., Blades, M.L., Collins, A.S., Farkaš, J., Gilbert, S., Löhr, S.C., Redaa, A., Cassidy, E., and Zack, T., 2022. Unravelling the histories of Proterozoic shales through *in situ* Rb–Sr dating and trace element laser ablation analysis. *Geology*, 50(1), pp.66–70. doi: <https://doi.org/10.1130/G49187.1>

Chapter 2 establishes the novel application of *in situ* Rb–Sr dating on Proterozoic shales, using sections from the lower Roper Group. This study provides a structured procedure for the use of this technique by first systematically mapping each sample with a high-resolution scanning electron microscope and petrographically confirming the origin of the targeted clay minerals. In addition, the geochemical information collected in conjunction with the Rb and Sr isotopes are also used to distinguish between two geological events recorded in the samples. Altogether, shales with clay minerals that look authigenic and have trace element signatures consistent with sea water of the time and gave Rb–Sr ages overlapping with the expected depositional age. On the other hand, samples with altered or replacement clay minerals yielded Rb–Sr dates and geochemistry more akin to the Derim Derim dolerite intrusion instead. Consequently, we show that this technique can be used to date the Proterozoic shale sections from the greater McArthur Basin and differentiate between early burial vs. secondary alteration events.

### 1.4.2 Chapter 3

This chapter is published as: Subarkah, D., Nixon, A.L., Jimenez, M., Collins, A.S., Blades, M.L., Farkaš, J., Gilbert, S.E., Holford, S. and Jarrett, A., 2022. Constraining the geothermal parameters of *in situ* Rb–Sr dating on Proterozoic shales and their subsequent applications. *Geochronology*, 4(2), pp.577–600. doi: <https://doi.org/10.5194/gchron-4-577-2022>

Chapter 3 continues to explore the method developed in the previous manuscript and now couples it with traditional palaeomaturity proxies commonly used for organic carbon content in petroleum geology. The combination of these techniques aims to constrain the geothermal sensitivity of the Rb–Sr system in Proterozoic shales. This case study shows that the chronometer can be reset at ca. 120°C in hydrothermal settings but can withstand higher temperatures (>190°C) in reactions not dominated by fluids. Importantly, these

constraints coincides with the temperatures needed to mature kerogen into the gas window as well as mobilise metals in sediment-exhalative deposits (Espitalié et al., 1977, Cooke et al., 2000).

### **1.4.3 Chapter 4**

This chapter is unpublished, but is prepared for submission to a peer-reviewed journal and written in manuscript style.

Chapter 4 provides a multi-proxy procedure to reconstruct the palaeoenvironment evolution of the greater McArthur Basin. This study focuses on the geochemistry of marine sedimentary rocks in the basal Redbank Package. Several alteration indicators are first analysed to verify that the samples here are still primary and not have been reset by post-depositional alteration events. Next, the palaeoproductivity and palaeoredox conditions of the units were defined using trace element indexes such as Ba, P, Mo, and V. Furthermore, the tectonic evolution of the basin and their subsequent effects on the C and Sr cycle were also investigated with isotopic proxies  $\delta^{13}\text{C}_{\text{carb}}$ ,  $^{87}\text{Sr}/^{86}\text{Sr}$ , and  $\delta^{88/86}\text{Sr}$ . Results from this study indicate that changes in palaeoenvironment becomes an important control on the nutrient supply of the basin. Consequently, these variables also play a major role in the efficiency of the biological redox pump in the water column. Sections that are interpreted to be more connected to the open ocean are relatively nutrient-rich, promoting biological productivity. In turn, these processes introduced more oxygen into the surrounding environments, which is recorded by several redox-sensitive trace element signatures. This redox gradient would be crucial for developing chemical traps for metallogenic fluids and accumulating hydrocarbons.

### **1.4.4 Chapter 5**

This chapter is submitted to the peer reviewed journal Ore Geology Reviews.

Chapter 5 integrates the use of geochronological and geochemical techniques applied in the previous chapters to characterise the economic Glyde Package. *In situ* Rb–Sr dating of the distal shales from the McArthur and Limbunya Groups show that the mineralised Barney Creek Formation and the Fraynes Formation are coeval units. In addition, they also display similarities in geochemical signatures, further corroborating the age data with chemostratigraphic correlations. Importantly, these spatially distant basins record similar changes in palaeoenvironment and palaeowater chemistry. As such, the Limbunya Group would also be potentially prospective for similar economic resources that are present in the McArthur Group.

### **1.4.5 Chapter 6**

Chapter 6 consists of a summary and discussions of the findings from this project, along with recommendations for future studies in the region to build upon this foundation.



## **Chapter 2: Unravelling the histories of Proterozoic shales through *in situ* Rb–Sr dating and trace element laser ablation analysis**

This chapter is published as:

Subarkah, D., Blades, M.L., Collins, A.S., Farkaš, J., Gilbert, S., Löhr, S.C., Redaa, A., Cassidy, E., and Zack, T., 2022. Unravelling the histories of Proterozoic shales through *in situ* Rb–Sr dating and trace element laser ablation analysis. *Geology*, 50(1), pp.66–70. doi: <https://doi.org/10.1130/G49187.1>

The Supplementary Files for this chapter can be found in:

<https://doi.org/10.1130/GEOL.S.16569531>

# Statement of Authorship

Title of Paper	Unravelling the histories of Proterozoic shales through in situ Rb–Sr dating and trace element laser ablation analysis
Publication Status	<input checked="" type="checkbox"/> Published <input type="checkbox"/> Accepted for Publication <input type="checkbox"/> Submitted for Publication <input type="checkbox"/> Unpublished and Unsubmitted work written in manuscript style
Publication Details	Subarkah, D., Blades, M.L., Collins, A.S., Farkaš, J., Gilbert, S., Löhr, S.C., Redaa, A., Cassidy, E. and Zack, T., 2022. Unravelling the histories of Proterozoic shales through in situ Rb–Sr dating and trace element laser ablation analysis. <i>Geology</i> , 50(1), pp.66–70. doi: <a href="https://doi.org/10.1130/G49187.1">https://doi.org/10.1130/G49187.1</a>

## Principal Author

Name of Principal Author (Candidate)	Darwinaji Subarkah		
Contribution to the Paper	Method development, analysis, data reduction and interpretation, manuscript drafting.		
Overall percentage (%)	80		
Certification:	This paper reports on original research I conducted during the period of my Higher Degree by Research candidature and is not subject to any obligations or contractual agreements with a third party that would constrain its inclusion in this thesis. I am the primary author of this paper.		
Signature		Date	12/10/2022

## Co-Author Contributions

By signing the Statement of Authorship, each author certifies that:

- i. the candidate's stated contribution to the publication is accurate (as detailed above);
- ii. permission is granted for the candidate to include the publication in the thesis; and
- iii. the sum of all co-author contributions is equal to 100% less the candidate's stated contribution.

Name of Co-Author	Morgan Blades		
Contribution to the Paper	Supervision, analysis, manuscript drafting.		
Signature		Date	12/10/2022

Name of Co-Author	Alan S. Collins		
Contribution to the Paper	Project funding, supervision, manuscript drafting.		
Signature		Date	12/10/2022

Name of Co-Author	Juraj Farkaš		
Contribution to the Paper	Project funding, supervision, manuscript drafting.		
Signature		Date	13th Oct, 2022
Name of Co-Author	Sarah Gilbert		
Contribution to the Paper	Method development, manuscript drafting.		
Signature		Date	12/10/2022
Name of Co-Author	Stefan Löhr		
Contribution to the Paper	Analysis, manuscript drafting.		
Signature		Date	12/10/2022
Name of Co-Author	Ahmad Redaa		
Contribution to the Paper	Method development, manuscript drafting.		
Signature		Date	12/10/2022
Name of Co-Author	Eilidh Cassidy		
Contribution to the Paper	Sample collection, analysis.		
Signature		Date	21/10/2022
Name of Co-Author	Thomas Zack		
Contribution to the Paper	Method development, manuscript drafting.		
Signature		Date	12/10/2022

## 2.1 Abstract

Authigenic components in marine sediments are important archives for past environment reconstructions. However, defining reliable age constraints and assessing the effects of post-depositional overprints in Precambrian sequences are challenging. We demonstrate a new laser-based analytical approach that has the potential to rapidly and accurately evaluate the depositional and alteration histories of Proterozoic shales. Our study employs a novel application of *in situ* Rb–Sr dating coupled with simultaneous trace-element analysis using reaction-cell laser ablation-inductively coupled plasma-tandem mass spectrometry (LA-ICP-MS/MS). We present results from shales sourced from two wells in the Proterozoic McArthur Basin, northern Australia. These rocks have been widely used by previous studies as a key section for ancient biogeochemical and palaeo-redox reconstructions. Shales from well UR5 yielded initial  $^{87}\text{Sr}/^{86}\text{Sr}$  ratios, Rb–Sr ages and rare earth element plus yttrium (REEY) patterns similar to those of a dolerite sampled from the same core. We propose that the UR5 samples chronicle hydrothermal alteration instigated by the dolerite intrusion. In contrast, a correlative shale from well UR6 yielded an age consistent with the expected depositional age ( $1577 \pm 56$  Ma) with REEY and initial  $^{87}\text{Sr}/^{86}\text{Sr}$  ratios similar to ca. 1.5 Ga seawater. We suggest that this sample records the minimum depositional age and early marine diagenetic history for this unit. This new technique can date Proterozoic shales quickly, cheaply and with minimum sample preparation. Importantly, ages are triaged to differentiate between those recording primary marine versus secondary processes. This novel approach provides a potentially powerful tool to date and fingerprint the vast array of ancient marine shales for further studies of Earth systems through deep time.

## 2.2 Introduction

Analyses of the sedimentary record have been integral in constraining how Earth systems have evolved over geological time. For example, geochemical proxies of seawater paleo-redox conditions reveal key periods of fluctuating oxygen levels that are intrinsically linked to the development of life (Lyons et al., 2014). Furthermore, the radiogenic  $^{87}\text{Sr}/^{86}\text{Sr}$  isotope record of seawater inferred from marine carbonates reflects the balance between Sr inputs from continental weathering versus that from submarine hydrothermal systems, reflecting global-scale tectonic changes (Kuznetsov et al., 2014, Planavsky et al., 2015b). However, these archives are only meaningful if one is able to accurately date and assess the primary compositions of the rocks investigated. These prerequisites are further complicated by the lack of diverse faunal record in the Proterozoic, restricting the use of biostratigraphy to constrain depositional ages. Consequently, an array of other chronological techniques has been developed to date Precambrian sedimentary rocks.

Shales are common throughout the Precambrian, but dating sedimentary packages dominated by shales has proven to be difficult. Re-Os dating of organic rich shales is a powerful technique for attaining depositional ages (Kendall et al., 2009, Ravizza and Turekian, 1989). However, this method has limitations. There is a low abundance of Re in natural environments, such that many shales are too Re-poor to date (Rainbird et al., 2020). In addition, the method is costly, time consuming, and yields hard-won, but limited data. Sample intervals also often represent deposition over tens to hundreds of centimeters

vertically and up to several kilometers laterally (Rainbird et al., 2020, Kendall et al., 2009). Detrital zircons are useful for analyzing provenance and establishing maximum depositional ages (Yang et al., 2019) where sand units are available. Dating volcanic beds in sedimentary units is the most precise method to obtain depositional ages (Southgate et al., 2000), but many sequences are devoid of such lithologies. Similarly, direct dating of intrusions in sedimentary rocks or early diagenetic minerals such as xenotime (Rasmussen et al., 2004) can provide minimum depositional ages of sediments.

Alternatively, the Rb-Sr isotopic system can date deposition (Compston and Pidgeon, 1962, Nebel, 2015), and early diagenetic illite formation in shales (Gorokhov et al., 2001). However, the past limitation of beta-decay-system chronometers such as  $^{87}\text{Rb}$ - $^{87}\text{Sr}$  was that daughter and parent isotopes could not be differentiated by traditional mass spectrometry. Instead, an arduous process of whole-rock digestion and column chromatography requiring large sample volumes was needed. This restricted the number of analyses undertaken and also prohibited effective identification and isolation of detrital or diagenetic phases, causing the technique to lose popularity. The development of tandem inductively coupled plasma-mass spectrometry (ICP-MS/MS) instruments allows for many of these challenges to be overcome (Zack and Hogmalm, 2016, Redaa et al., 2021a). Introduction of a reactive gas into a reaction cell between the two quadrupoles in a ICP MS/MS system, enables the online separation of  $^{87}\text{Sr}$  from  $^{87}\text{Rb}$  via measurement of the mass-shifted reaction product (Zack and Hogmalm, 2016, Hogmalm et al., 2017). This set-up allow for direct, *in situ* Rb-Sr dating of minerals and rocks when coupled to a laser ablation system. *In situ* Rb-Sr dating is capable of analyzing paragenetic phases while maintaining their micro-scale textural context (Armistead et al., 2020, Tamblyn et al., 2020). Precision in Rb-Sr age is primarily a function of a good spread in  $^{87}\text{Rb}/^{86}\text{Sr}$  ratios, the number of data points used to define the regression line, and the errors on each individual analysis (Nebel, 2015). We illustrate a novel application of *in situ* Rb-Sr dating coupled with trace elemental analysis from a set of Proterozoic shales from the McArthur Basin (north Australia, Fig. 2.1). A dolerite intrusion intersecting some of the studied shales was also analyzed. Geochemical and geochronological data collected simultaneously are used to distinguish the different depositional and alteration histories of these rocks.

### 2.3 Geological Background

The northern Australian Proterozoic McArthur Basin is intra-cratonic and consists of four unconformity-bound sedimentary packages (Ahmad and Munson, 2013). The Roper Group (ca. 1.6–1.3 Ga, Fig. 2.1B) is a sequence of marine shelf siliciclastic sedimentary (Yang et al., 2018) that forms the youngest part of the McArthur basin. The Collara Subgroup is dated by U-Pb zircon from a  $1492 \pm 4$  Ma tuff (Southgate et al., 2000). This subgroup is the focus of this study, and its maximum depositional age is defined by U-Pb geochronology of a tuffaceous layer in the stratigraphically lower Nathan Group, dated at  $1589 \pm 3$  Ma (Page et al., 2000). (Yang et al., 2020), respectively.

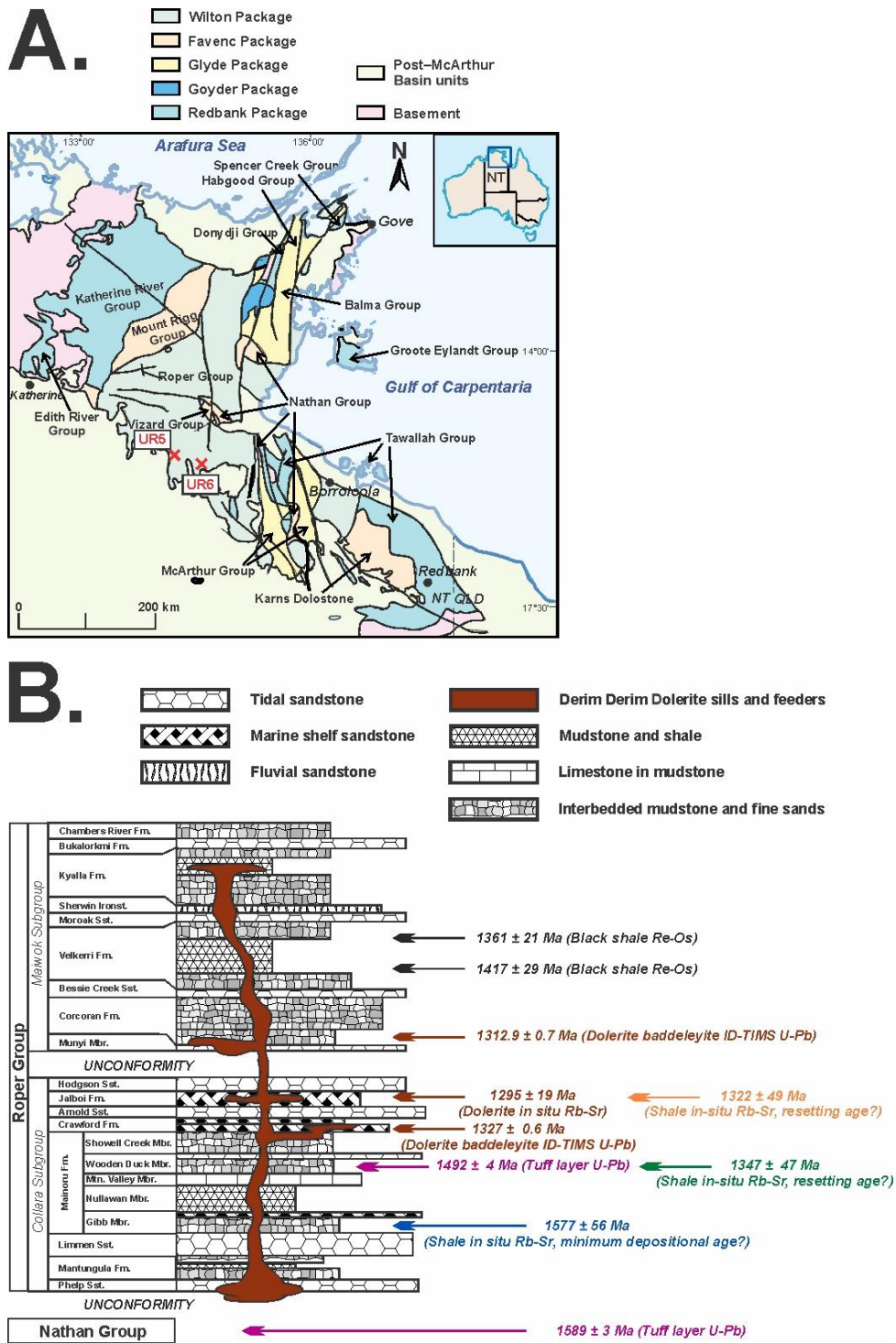


**Figure 2.1.** (A) Geological map of the McArthur Basin (northern Australia) with localities of sampled wells. NT—Northern Territory; QLD—Queensland. (B) Stratigraphic log of the Roper Group modified from Ahmad and Munson (2013) with summarized geochronological constraints. U-Pb tuff age in purple (Southgate et al., 2000, Page et al., 2000), U-Pb ages of sill cross-cutting Crawford and Corcoran Formations in brown (Bodorkos et al., 2022, Yang et al., 2020), Re-Os shale ages in black (Kendall et al., 2009), in situ Rb-Sr ages (orange, green, blue) from this study. Fm.—Formation; Ironst.—Ironstone; Sst.—Sandstone; Mbr.—Member; Mtn.—Mountain; ID-TIMS—isotope dilution–thermal ionization mass spectrometry.

We sampled the Derim Derim Dolerite (UR5\_229) that intrudes most formations of the Roper Group from well UR5 (Ahmad and Munson, 2013). U-Pb thermal ionization mass spectrometry (TIMS) analyses of the same suite sampled at locations >200 km apart yielded ages of  $1327.5 \pm 0.6$  Ma (Bodorkos et al., 2022) and  $1312.9 \pm 0.7$  Ma

We sampled the Collara Subgroup in two wells: UR5 and UR6 (Fig. 2.1A). Shale samples analyzed in this study are from the Gibb and Wooden Duck Members (Mainoru Formation; samples UR6\_269 and UR5\_578 respectively) and the Jalboi Formation (sample UR5\_139). Shales from UR5 were picked to constrain the alteration aureole of the Derim Derim intrusion based on the presence of high-temperature clay minerals evidenced in the HyLogger data (Smith, 2015).

### 2.3 Methods

The mineralogy and petrography of the shales were characterized by energy-dispersive X-ray spectroscopy (EDS) mapping with Nanomin software (Rafiei and Kennedy, 2019) at Macquarie University (Sydney, Australia) complemented with bulk powder X-ray diffraction (XRD). The dolerite was mapped for its petrographic textures and elemental composition using a scanning electron microscope at Adelaide Microscopy (Adelaide Australia; see the Supplemental Material). Laser analyses were performed at Adelaide Microscopy following Redaa et al. (2021a). Phlogopite nano-powder Mica-Mg as well as its natural mineral crystal (MDC) sourced from Bekily, Madagascar (Govindaraju et al., 1994) were used as standards for data normalization. In addition, an illite pressed powder pellet from Fithian, Illinois, USA (Kralik, 1984) was analyzed as a complementary in-house comparison to assess possible matrix differences between the phlogopite standards and the illite-rich shales analyzed in this study. Finally, the morphology and structure of laser craters in standards and samples were imaged using an Olympus FV3000 Confocal Microscope (Fig. S.2.5). Methodologies are extensively discussed in the Supplementary Material.

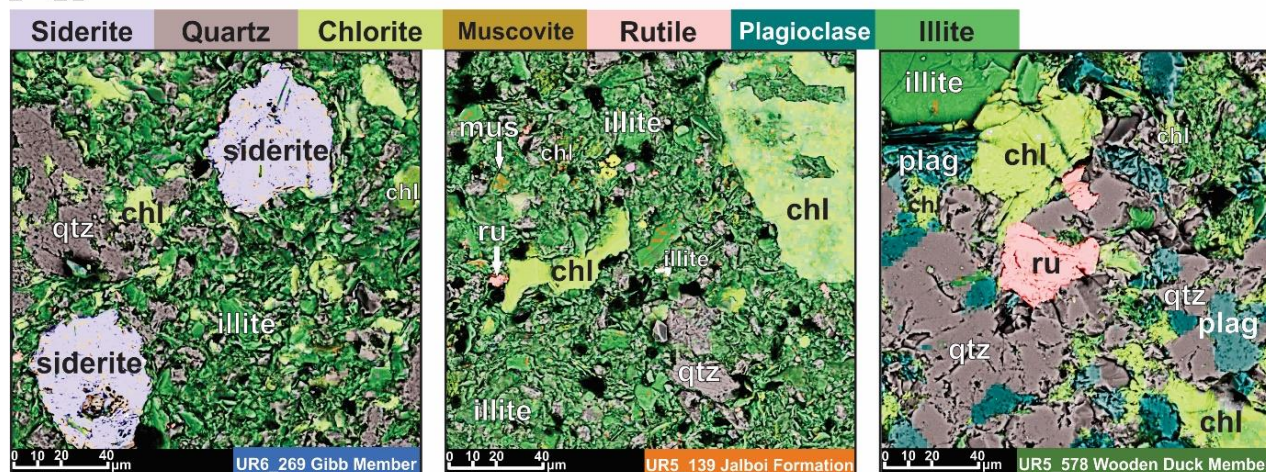
### 2.4 Results

The pit-depth profiles show that samples analyzed in this study have similar ablation characteristics to the Mica-Mg nano-powder standard and the Fithian illite pellet as opposed to the MDC mineral flake (Fig. S.2.5). Semi-quantitative and micro-scale identification of the studied shales are reported in Fig. 2.2. The Gibb Member shale (UR6\_269) gave an age of  $1577 \pm 56$  Ma with initial  $^{87}\text{Sr}/^{86}\text{Sr}$  ratio of  $0.7046 \pm 0.0073$ . The Derim Derim Dolerite (UR5\_229) yielded an age of  $1295 \pm 19$  Ma (initial  $^{87}\text{Sr}/^{86}\text{Sr}$  ratio:  $0.7314 \pm 0.010$ ). The Jalboi Formation shale (UR5\_139) gave an age of  $1322 \pm 49$  Ma (initial  $^{87}\text{Sr}/^{86}\text{Sr}$  ratio:  $0.7260 \pm 0.023$ ). Finally, the Wooden Duck Member shale (UR5\_578) had an age of  $1347 \pm 47$  Ma (initial  $^{87}\text{Sr}/^{86}\text{Sr}$  ratio:  $0.7339 \pm 0.015$ ). REEY values from all shale samples were normalized to those of sample UR\_269, as this is interpreted to be the best-preserved shale, with an initial  $^{87}\text{Sr}/^{86}\text{Sr}$  ratio reflective of ca. 1.5 Ga seawater (Fig. 2.3) and the least altered mineralogy (Fig. 2.2). All remaining samples show a normalized light rare



earth element (LREE) depletion (Fig. 2.3B). The Jalboi Formation shale is located closest to the dolerite intrusion and has REEY patterns most those of the dolerite.

**A.**



**B.**

Mineralogy	UR6_269 Gibb Member	UR5_139 Jalboi Formation	UR5_578 Wooden Duck Member
	Nanomin (wt %)	Nanomin (wt %)	Nanomin (wt %)
Illite	62%	67%	28%
Quartz	16%	23%	36%
Alkali feldspar	1.5%	3.3%	9.2%
Plagioclase	0.36%	0.75%	8.6%
Chlorite	5.7%	2.3%	14%
Muscovite	4.0%	1.9%	1.2%
Siderite	6.6%	0.0%	0.0%
Other	3.6%	1.4%	2.4%

**Figure 2.2.** (A) Micro-scale energy dispersive x-ray spectroscopy (EDS) mineral maps of all shale samples. Qtz— Quartz; Chl— Chlorite; Ru— Rutile; Plag— Plagioclase. (B) Semi-quantitative mineralogical data obtained by Nanomin software (Rafiei and Kennedy, 2019).

## 2.5 Discussions

The majority of illite in Proterozoic shales of the McArthur Basin are believed to have formed during early marine diagenesis via reverse weathering processes in equilibrium with paleo-seawater as opposed to being detrital products of continental weathering from soils like those commonly found in Phanerozoic shales (Rafiei and Kennedy, 2019). The widespread formation of authigenic marine clays have been proposed to be a major sink for Si during the Precambrian due to the absence of pelagic Si-mineralizing organisms (Isson and Planavsky, 2018). Therefore, these shales are prime candidates for *in situ* Rb–Sr dating to determine their depositional or early marine diagenetic histories. The dominance of cogenetic phases eases laser targeting and provides a good spread in  $^{87}\text{Rb}/^{86}\text{Sr}$  ratios. However, high resolution micro-scale mineral identification is important to confirm the authigenic mineral dominance and avoid detrital phase contamination (Supplementary Material).

The abundant clays in the Gibb Member shale UR6\_269 are dominantly illite and do not show typical irregular, detrital morphologies, supporting our interpretation of their



authigenic origin. Sample UR6\_269 is also the only sample to preserve siderite micro-nodules (Fig. 2.2A) which are intergrown with an illite and chlorite matrix, suggesting an early diagenetic origin. This is commonly found in marine shales precipitating under anoxic conditions with high levels of ferrous iron ( $\text{Fe}^{2+}$ ) and limited sulfur ( $\text{HS}^-$ ) availability (Mozley and Wersin, 1992). The Rb–Sr age of the Gibb Member shale is within its depositional window (Southgate et al., 2000, Page et al., 2000), suggesting that the analyzed bulk composition illite matrix of this sample formed authigenically during or soon after deposition. Furthermore, the initial  $^{87}\text{Sr}/^{86}\text{Sr}$  ratio of this shale (Fig. 2.3) is within error of estimates for coeval paleo-seawater (Kuznetsov et al., 2014), further confirming the marine origin of the dated assemblage. Although within error, the centroid value is slightly more radiogenic than that of paleo-seawater, which may reflect its shallow marine or semi-restricted depositional environment (El Meknassi et al., 2020). Nevertheless, we conclude that the geochronology, isotope geochemistry, and petrography of the Gibb Member shale reflect an early diagenetic signature, in equilibrium with contemporaneous ocean water as opposed to a late-stage non-marine alteration event.

Bulk XRD data and spectral reflectance analyses of the Derim Derim Dolerite (Smith, 2015) sample UR5\_229 (Supplementary Material) indicate its extensive alteration and chloritization. In addition, back scatter electron imaging and elemental mapping of UR5\_229 (Fig. S.2.2) reveals many K-rich (and by inference Rb-rich) phases. Rb-enriched secondary chlorite is a common product of hydrothermal alteration of mafic protoliths (Duane et al., 2004). The high initial  $^{87}\text{Sr}/^{86}\text{Sr}$  ratio of this sample (Fig. 2.3) suggests fluid-rock interaction processes involving substantial influx of radiogenic crustal fluids during the purported potassic alteration of the dolerite. The Rb–Sr age obtained from UR5\_229 dolerite is within error of the crystallization ages of Derim Derim intrusions obtained elsewhere in the McArthur Basin (Bodorkos et al., 2022, Yang et al., 2020), indicating that this fluid-infiltration event likely happened during, or soon after, dike intrusion.

Energy-dispersive X-ray spectroscopy screening of shales from the Jalboi Formation and Wooden Duck Member both show evidence for substantial post-depositional alteration (Fig. 2.2), likely caused by the Derim Derim Dolerite intrusion. Specifically, large chlorite aggregates in the Jalboi Formation replace other earlier clay constituents. In the Wooden Duck Member, illite aggregates display morphologies inconsistent with an early diagenetic origin; showing fissile and foliated matrices interlocking with quartz overgrowth. In addition, the presence of rutile in these rocks implies secondary redistribution of titanium. Ages and initial  $^{87}\text{Sr}/^{86}\text{Sr}$  ratios from the Jalboi Formation and Wooden Duck Member shales overlap with those from the Derim Derim Dolerite, yielding highly radiogenic and non-marine values (Fig. 2.3). Evidence for higher initial  $^{87}\text{Sr}/^{86}\text{Sr}$  ratios in marine carbonates and shales are commonly related to secondary processes such as (i) influence from late-stage diagenetic processes (Phan et al., 2019), (ii) the introduction of radiogenic Sr via later diagenetic fluid-rock interactions and metasomatism (Poitrasson et al., 1995), and (iii) inputs of radiogenic Sr sourced from detrital grains.

Fluid-rock interaction processes also have significant impact on REEY solubility and transport during later alteration. Both UR5 shales from well UR5 are depleted in LREE when

normalized to the Gibb Member shale. The Jalboi Formation shows extreme depletion, and has a similar REEY pattern to that of the dolerite intrusion (Fig. 2.3). Multiple factors and processes could have caused the relative LREE depletion observed in these shales. However, the increased LREE depletion with increased proximity of the shales to the intrusion suggest that intrusion-induced hydrothermal alteration is the most likely cause. Physical and chemical buffers have been shown to play a major role in fluid-rock interaction and alteration in marine sediments (Park et al., 2019).

Taken together, the resetting of the Rb-Sr chronometer with highly radiogenic initial  $^{87}\text{Sr}/^{86}\text{Sr}$  ratios, the observed depletions of LREEs as well as the petrography of the altered shales collected in vicinity of dolerite dike in UR5 clearly demonstrates that these rocks were altered during, or soon after, the dolerite emplacement. Previous studies have used the total Fe species measured in shales from UR5 to infer periods of anoxia during the Proterozoic (Shen et al., 2003). We argue these altered shales may not faithfully record primary paleo-redox conditions, as their bulk chemistry has likely been affected by the dolerite intrusion. Consequently, any interpretations made from these rocks to reconstruct past palaeoenvironments should be treated with caution.

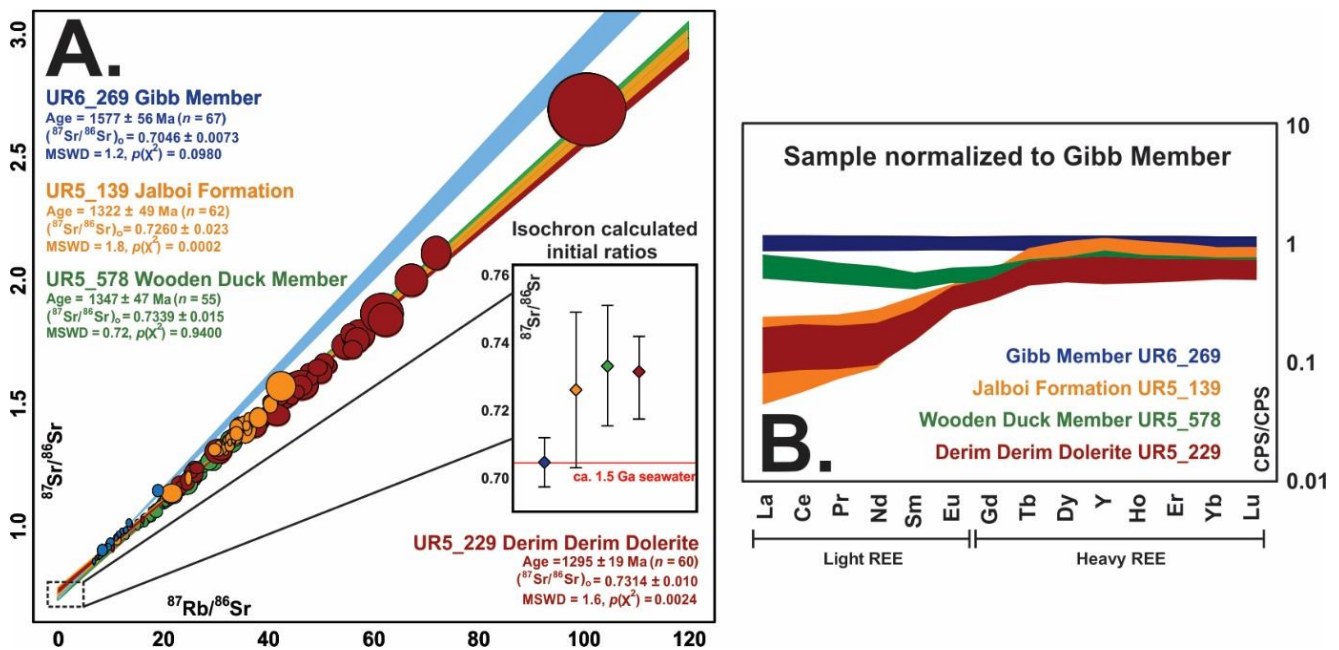


**Figure 2.3.** (A) Summary of Rb-Sr isotopic data and  $^{87}\text{Sr}/^{86}\text{Sr}$  initial ratios of the samples (see inset).  $^{87}\text{Sr}/^{86}\text{Sr}$  initial value of UR6\_269 overlaps with that of seawater ca. 1.5 Ga (Kuznetsov et al., 2014). MSWD—mean squared weighted deviation;  $(^{87}\text{Sr}/^{86}\text{Sr})_0$ —initial  $^{87}\text{Sr}/^{86}\text{Sr}$  ratio. (B) Average rare earth element plus yttrium (REEY) patterns of shale samples, normalized to REEY values of the Gibb Member shale. CPS—Count per second.

## 2.6 Conclusions

We present the first *in situ* Rb-Sr dating and elemental analyses of Proterozoic illite-rich shales as well as an altered dolerite intrusion. The Gibb Member shale from an intrusion-absent borehole was abundant in authigenic illite and yielded an Rb-Sr age consistent with the depositional age for the unit. In addition, the sample's initial  $^{87}\text{Sr}/^{86}\text{Sr}$  ratio overlaps with that of ca. 1.5 Ga seawater. In contrast, the Jalboi Formation and Wooden Duck Member shales were sourced from a well containing a dolerite intrusion. We demonstrated that their Rb-Sr isotopic systems were reset by the intrusion and their chemistry has affinities to the

altered dolerite. As such, we show that the chronological and geochemical data obtained together by this novel approach can be used to constrain the histories of Precambrian shales effectively, where authigenic phases make up the dominant Rb-Sr bearing constituents.

## **2.7 Acknowledgements**

This work was supported by the Australian Research Council Projects LP160101353 and DP210100462, forming MinEx CRC contribution #2021/47. Initial development of the *in situ* Rb-Sr dating technique at the University of Adelaide (Australia) was supported by Agilent Technologies Australia Ltd. We would like to thank Marissa Tremblay, Kai Rankenburg, Timothy Lyons, and an anonymous reviewer who all positively contributed to this thesis with their constructive inputs. We would also like to acknowledge and thank William Clyde for their valuable assessment of this work as the corresponding Science Editor.

# Chapter 3: Constraining the geothermal parameters of *in situ* Rb–Sr dating on Proterozoic shales and their subsequent applications

This chapter is published as:

Subarkah, D., Nixon, A.L., Jimenez, M., Collins, A.S., Blades, M.L., Farkaš, J., Gilbert, S.E., Holford, S. and Jarrett, A., 2022. Constraining the geothermal parameters of *in situ* Rb–Sr dating on Proterozoic shales and their subsequent applications. *Geochronology*, 4(2), pp.577-600. doi: <https://doi.org/10.5194/gchron-4-577-2022>

The Supplementary Files for this chapter can be found in:

<https://doi.org/10.25909/6315ea488cc5f>

# Statement of Authorship

Title of Paper	Constraining the geothermal parameters of in situ Rb–Sr dating on Proterozoic shales and their subsequent applications
Publication Status	<input checked="" type="checkbox"/> Published <input type="checkbox"/> Accepted for Publication <input type="checkbox"/> Submitted for Publication <input type="checkbox"/> Unpublished and Unsubmitted work written in manuscript style
Publication Details	Subarkah, D., Nixon, A.L., Jimenez, M., Collins, A.S., Blades, M.L., Farkaš, J., Gilbert, S.E., Holford, S. and Jarrett, A., 2022. Constraining the geothermal parameters of in situ Rb–Sr dating on Proterozoic shales and their subsequent applications. <i>Geochronology</i> , 4(2), pp.577-600. doi: <a href="https://doi.org/10.5194/gchron-4-577-2022">https://doi.org/10.5194/gchron-4-577-2022</a>

## Principal Author

Name of Principal Author (Candidate)	Darwinaji Subarkah		
Contribution to the Paper	Method development, analysis, data reduction and interpretation, manuscript drafting.		
Overall percentage (%)	75		
Certification:	This paper reports on original research I conducted during the period of my Higher Degree by Research candidature and is not subject to any obligations or contractual agreements with a third party that would constrain its inclusion in this thesis. I am the primary author of this paper.		
Signature		Date	26/10/2022

## Co-Author Contributions

By signing the Statement of Authorship, each author certifies that:

- i. the candidate's stated contribution to the publication is accurate (as detailed above);
- ii. permission is granted for the candidate to include the publication in the thesis; and
- iii. the sum of all co-author contributions is equal to 100% less the candidate's stated contribution.

Name of Co-Author	Angus L. Nixon		
Contribution to the Paper	Conceptualisation, computational modelling, manuscript drafting.		
Signature		Date	27/10/2022

Name of Co-Author	Monica Jimenez		
Contribution to the Paper	Conceptualisation, manuscript drafting.		
Signature		Date	27/10/2022

Name of Co-Author	Alan S. Collins		
Contribution to the Paper	Project funding, method development, supervision, manuscript drafting.		
Signature		Date	26/10/2022
Name of Co-Author	Morgan L. Blades		
Contribution to the Paper	Sampling, method development, supervision, manuscript drafting.		
Signature		Date	26/10/2022
Name of Co-Author	Juraj Farkaš		
Contribution to the Paper	Conceptualisation, method development, supervision, manuscript drafting.		
Signature		Date	28/10/2022
Name of Co-Author	Sarah E. Gilbert		
Contribution to the Paper	Metho development, experimentation, manuscript drafting.		
Signature		Date	26/10/2022
Name of Co-Author	Simon Holford		
Contribution to the Paper	Conceptualisation, manuscript drafting.		
Signature		Date	27/10/2022
Name of Co-Author	Amber Jarrett		
Contribution to the Paper	Data collection, manuscript drafting.		
Signature		Date	28/10/2022

### 3.1 Abstract

Recent developments in tandem laser ablation-mass spectrometer technology have demonstrated capacity for separating parent and daughter isotopes of the same mass online. As a result, beta decay chronometers can now be applied to the geological archive *in situ* as opposed to through traditional whole-rock digestions. One novel application of this technique is the *in situ* Rb–Sr dating of Proterozoic shales that are dominated by authigenic clays such as illite. This method can provide a depositional window for shales by differentiating signatures of early diagenetic processes versus late-stage secondary alteration. However, the hydrothermal sensitivity of the Rb–Sr isotopic system across geological timescales in shale-hosted clay minerals is not well understood. As such, we dated the Mesoproterozoic Velkerri Formation from the Atree 2 well in the Beetaloo Sub-basin (greater McArthur Basin), northern Australia, using this approach. We then constrained thermal history of these units using common hydrocarbon maturity indicators, and modelled effects of contact heating due to the intrusion of the Derim Derim Dolerite.

*In situ* Rb–Sr dating of mature, oil-prone shales in the diagenetic zone from the Velkerri Formation yielded ages of  $1448 \pm 81$  Ma,  $1434 \pm 19$  Ma, and  $1421 \pm 139$  Ma. These results agree with previous Re–Os dating of the unit and are interpreted as recording the timing of an early diagenetic event soon after deposition. Conversely, overmature, gas-prone shales in the anchizone sourced from deeper within the borehole were dated at  $1322 \pm 93$  Ma and  $1336 \pm 40$  Ma. These ages are younger than the expected depositional window for the Velkerri Formation. Instead, they are consistent with the age of the Derim Derim Dolerite mafic intrusion intersected 800 m below the Velkerri Formation. Thermal modelling suggests that a single intrusion of 75 m thickness would have been capable of producing a significant hydrothermal perturbation radiating from the sill top. The intrusion width proposed by this model is consistent with similar Derim Derim Dolerite sill thicknesses found elsewhere in the McArthur Basin. The extent of the hydrothermal aureole induced by this intrusion coincide with the window in which kerogen from the Velkerri Formation becomes overmature. As a result, the mafic intrusion intersected here is interpreted to have caused kerogen in these shales to enter the gas window, induced fluids that mobilise trace elements and reset the Rb–Sr chronometer. Consequently, we propose that the Rb–Sr chronometer in shales may be sensitive to temperatures of ca. 120°C in hydrothermal reactions but can withstand temperatures of more than 190°C in thermal systems not dominated by fluids. Importantly, this study demonstrates a framework for the combined use of *in situ* Rb–Sr dating and kerogen maturation indicators to help reveal the thermochronological history of Proterozoic sedimentary basins. As such, this approach can be a powerful tool for identifying the hydrocarbon potential of source rocks in similar geological settings.

### 3.2 Introduction

The Rb–Sr isotopic system has historically been one of the most powerful dating tools in Earth science. Rb is abundant in K-rich minerals such as micas, clays, and K-feldspar, and these minerals are commonly found in a wide range of geological settings (Simmons, 1998).

Therefore it is an effective technique to date processes such as igneous emplacement, metamorphism, sedimentation, clay authigenesis, and hydrothermal alteration when these phases can be differentiated (Nebel, 2015). Its long half-life also makes it applicable to date events as early as the infant stages of our solar system (Nebel et al., 2011, Minster et al., 1979, Papanastassiou and Wasserburg, 1970). Traditionally, the application of this method required an arduous process of column chromatography to chemically separate the parent ( $^{87}\text{Rb}$ ) and daughter ( $^{87}\text{Sr}$ ) isotopes and avoid isobaric interference between the two elements (Hahn et al., 1943, Hahn and Walling, 1938, Charlier et al., 2006, Faure, 1977, Yang et al., 2010, Dickin, 2018). Alas, this approach has historically been expensive, time consuming, and results in the loss of the genetic relationships between the minerals analysed, causing the technique to lose its popularity in recent years (Nebel, 2015).

Recent advancements in tandem laser ablation inductively coupled plasma mass spectrometry (LA-ICP-MS/MS) and similar instruments have revitalised the use of Rb–Sr by allowing them to be applied *in situ* (Zack and Hogmalm, 2016, Hogmalm et al., 2017, Bevan et al., 2021, Redaa et al., 2021a, Yim et al., 2021, Gorojovsky and Alard, 2020). Reactive gasses such as  $\text{N}_2\text{O}$  and  $\text{SF}_6$  can be introduced into a reaction cell between quadrupoles in an LA-ICP-MS/MS system, which permits the online separation of  $^{87}\text{Sr}$  from  $^{87}\text{Rb}$  through the measurement of the mass shifted Sr reaction product (Hogmalm et al., 2017, Zack and Hogmalm, 2016, Redaa et al., 2021a). This allows for a more rapid and economic analysis time, as well as the ability to preserve petrographic relationships during these analyses. Consequently, secondary input of Rb or Sr from inclusions, zonation, alteration, and detritus can be isolated, resulting in a better understanding of the geochronological results. However, it should be noted that nm or  $\mu\text{m}$  sized mineral intergrowths of different origins still provide challenges when large spot sizes are used. The application of similar setups with other beta-decay dating systems have also yielded promising results (Tamblyn et al., 2021, Simpson et al., 2021, Simpson et al., 2022, Ribeiro et al., 2021, Harrison et al., 2010, Hogmalm et al., 2019, Brown et al., 2022, Scheibelhofer et al., 2022, Rösel and Zack, 2022, Bevan et al., 2021).

Hence, the *in situ* Rb–Sr dating method can now be used very similarly to laser ablation U–Pb dating, where age information can be obtained reliably, rapidly, and cheaply. In addition, the initial  $^{87}\text{Sr}/^{86}\text{Sr}$  ratio from the calculated isochron and the elemental data concurrently collected with the Rb and Sr isotopes can fingerprint the geochemical nature of the samples analysed (Subarkah et al., 2021, Redaa et al., 2021b, Tamblyn et al., 2020, Li et al., 2020, Olierook et al., 2020, Şengün et al., 2019, Tillberg et al., 2020, Armistead et al., 2020, Laureijs et al., 2021). This approach has been shown to be capable of dating paragenetic sequences in deformation structures (Armistead et al., 2020, Tillberg et al., 2020), hydrothermal alteration assemblages (Laureijs et al., 2021), magmatic and metamorphic events (Li et al., 2020, Tamblyn et al., 2020), as well as metallogenic systems (Redaa et al., 2021b, Olierook et al., 2020, Şengün et al., 2019) whilst still preserving their micro-scale textural context.

Another novel use of this technique is to date Proterozoic shales in order to constrain their depositional window (Subarkah et al., 2021). Evidence suggests that clay minerals in



Proterozoic shales are dominated by authigenic products from reverse weathering processes during reactions in equilibrium with the formation waters (Rafiei and Kennedy, 2019, Rafiei et al., 2020, Isson and Planavsky, 2018, Mackenzie and Kump, 1995, Kennedy et al., 2006, Deepak et al., 2022). Conversely, clay assemblages in late Ediacaran and Phanerozoic shales are commonly dominated by detrital products from continental weathering and erosion of soils and unstable parent rocks (Baldermann et al., 2020, Galán, 2006, Singer, 1980, Rafiei et al., 2020, Chamley, 1989, Hillier, 1995, Wilson, 1999, Kennedy et al., 2006). Simple multicellular organisms such as fungi and lichen have been shown to dramatically influence the rate of chemical weathering in continental rocks (Kennedy et al., 2006, Rafiei et al., 2020, Mergelov et al., 2018, Lee and Parsons, 1999, Zambell et al., 2012, McMahon and Davies, 2018). Thus, the primarily authigenic nature of clay minerals in Proterozoic shales make them ideal targets for *in situ* Rb–Sr dating (Subarkah et al., 2021).

Despite the promising potential of the Rb–Sr isotopic system, the chronometer still holds some limitations. Rb and Sr are large ion lithophile elements that can sit in well-bound interstitial sites within a mineral lattice as well as adsorbed onto the surface where they are more susceptible to fluid mobilisation (Nebel, 2015, Villa, 1998, Li et al., 2019). In these environments, fluid-induced recrystallisation and alteration can drive element and isotopic exchange at lower effective closure temperatures than those empirically determined for classic thermal volume diffusion reactions (Dodson, 1973, Shepherd and Darbyshire, 1981, Tamblyn et al., 2020, Li et al., 2020, Subarkah et al., 2021, Redaa et al., 2021b). However, it should be noted that the Rb–Sr system in shale-hosted illite may also be affected during diagenesis via the transformation of smectite to illite-smectite mixed layer minerals.

In this study, we dated the Mesoproterozoic Velkerri Formation from the Roper Group of the McArthur Basin in northern Australia by *in situ* Rb–Sr geochronology and show that clay-mineral recrystallization in these shales occur at similar temperatures to kerogen catagenesis. The Roper Group is a good case study for *in situ* Rb–Sr shale dating, as it has been shown to be dominated by authigenic clays (Rafiei and Kennedy, 2019, Subarkah et al., 2021) and is chronologically well-constrained (Ahmad and Munson, 2013, Kendall et al., 2009, Southgate et al., 2000, Bodorkos et al., 2022, Yang et al., 2020, Subarkah et al., 2021, Cox et al., 2022). Furthermore, the resurgence of interest in the resource potential of the organic-rich Velkerri Formation has also yielded a framework of palaeotemperature data that aim to discern the maturation history of hydrocarbons within the unit (Ahmad and Munson, 2013, George and Ahmed, 2002, Jarrett et al., 2019, Jarrett et al., 2022, Crick et al., 1988, Taylor et al., 1994, Summons et al., 1994, Volk et al., 2005, Lemiux, 2011, Revie, 2014, Capogreco, 2017, Cox et al., 2016b).

Here, we targeted the Velkerri Formation (Fig. 3.1) from the thoroughly investigated well Atree 2 (Lemiux, 2011, NTGS., 1989, NTGS., 2009, NTGS., 2010, NTGS., 2012, Revie, 2014, George and Ahmed, 2002, Jarrett et al., 2019, Nguyen et al., 2019, Nixon et al., 2021, Sander et al., 2018, Yang et al., 2018, Capogreco, 2017, Cox et al., 2022, Cox et al., 2016b). We show that common hydrocarbon maturation proxies such as  $T_{max}$  data from Rock-Eval pyrolysis, aromatic hydrocarbons, bitumen reflectance, and illite crystallinity can help define the temperature sensitivity of the Rb–Sr isotopic system in organic-rich shales. In addition, we

have also modelled the geothermal aureole of a mafic intrusion that may have matured the kerogen into the gas window, altered trace elemental signatures and reset the Rb–Sr isotopic system within the unit. As a result, we demonstrate that combining this novel dating method with traditional kerogen maturation proxies can be a powerful tool for reconstructing the thermochronological evolution of Proterozoic basin systems. This approach can then be applied to aid in hydrocarbon exploration for similar settings.

### 3.2 Geological Background

The Palaeo-to-Mesoproterozoic greater McArthur Basin is an intra-cratonic sedimentary system exposed across 180,000 km<sup>2</sup> of northern Australia (Ahmad and Munson, 2013). The basin is sub-divided into five unconformity-bounded sedimentary packages characterized by similarities in age, lithology, and stratigraphic position (Rawlings, 1999, Jackson et al., 1999). The Roper Group is part of the Wilton Package which is the youngest of these sub-divisions (Rawlings, 1999, Jackson et al., 1999, Munson, 2016). The thickness of the Roper Group varies around 1 to 5 km across several different fault zones (Abbott and Sweet, 2000, Rawlings, 1999, Ahmad and Munson, 2013, Abbott et al., 2001). The Beetaloo Sub-basin (Fig. 3.1) is interpreted to be the main depocentre of the sedimentary system and preserves the thickest Roper Group sequences (Plumb and Wellman, 1987, Ahmad and Munson, 2013, Abbott et al., 2001, Jackson et al., 1987). Lithologically, the Roper Group comprises of a series of coarsening-up sequences dominated by marine mudstone and interbedded sandstone with minor successions of intraclastic limestone (Abbott and Sweet, 2000, Jackson et al., 1987, Yang et al., 2018, Munson, 2016). Records of water-column euxinia and redox stratification, as well as fluctuating salinity levels, suggests that the Roper Group formed in an intermittently restricted marine basin within an epicontinental setting similar to the modern Black Sea, or Baltic Sea (Revie and MacDonald, 2017, Yang et al., 2018, Ahmad and Munson, 2013, Mukherjee and Large, 2016, Cox et al., 2016b, Cox et al., 2022).

Age constraints of the Roper Group have been established through several geochronological methods (Page et al., 2000, Ahmad and Munson, 2013, Subarkah et al., 2021, Kendall et al., 2009, Yang et al., 2019, Yang et al., 2020, Yang et al., 2018, Jackson et al., 1999, Nixon et al., 2021, Southgate et al., 2000). The beginning of the group's genesis is bracketed by a SHRIMP U–Pb zircon study from a tuff within the underlying Nathan Group as well as minimum depositional age from an *in situ* Rb–Sr analysis in the lower Roper Group that yielded ages of  $1589 \pm 3$  Ma and  $1577 \pm 56$  Ma, respectively (Subarkah et al., 2021, Page et al., 2000). The unconformity between the Roper Group and the immediately underlying Nathan Group is likely related to the Isan Orogeny ca. 1.58 Ga (Jackson et al., 1999, Ahmad and Munson, 2013). Absolute dating of the Roper Group has been obtained through two SHRIMP U–Pb zircon studies from tuff layers in the Mainoru Formation resulting in ages of  $1492 \pm 4$  Ma and  $1493 \pm 4$  Ma (Jackson et al., 1999, Southgate et al., 2000). On the other hand, the Kyalla Formation at the top of the Roper Group is constrained to being deposited between the U–Pb age of its youngest detrital zircon at  $1313 \pm 47$  Ma (Yang et al., 2018) and the age of crosscutting Derim Derim dolerite intrusions at  $1313 \pm 1$  Ma,  $1324 \pm 4$  Ma, and  $1327.5 \pm 0.6$  Ma (Yang et al., 2020, Bodorkos et al., 2022).

A.

B.

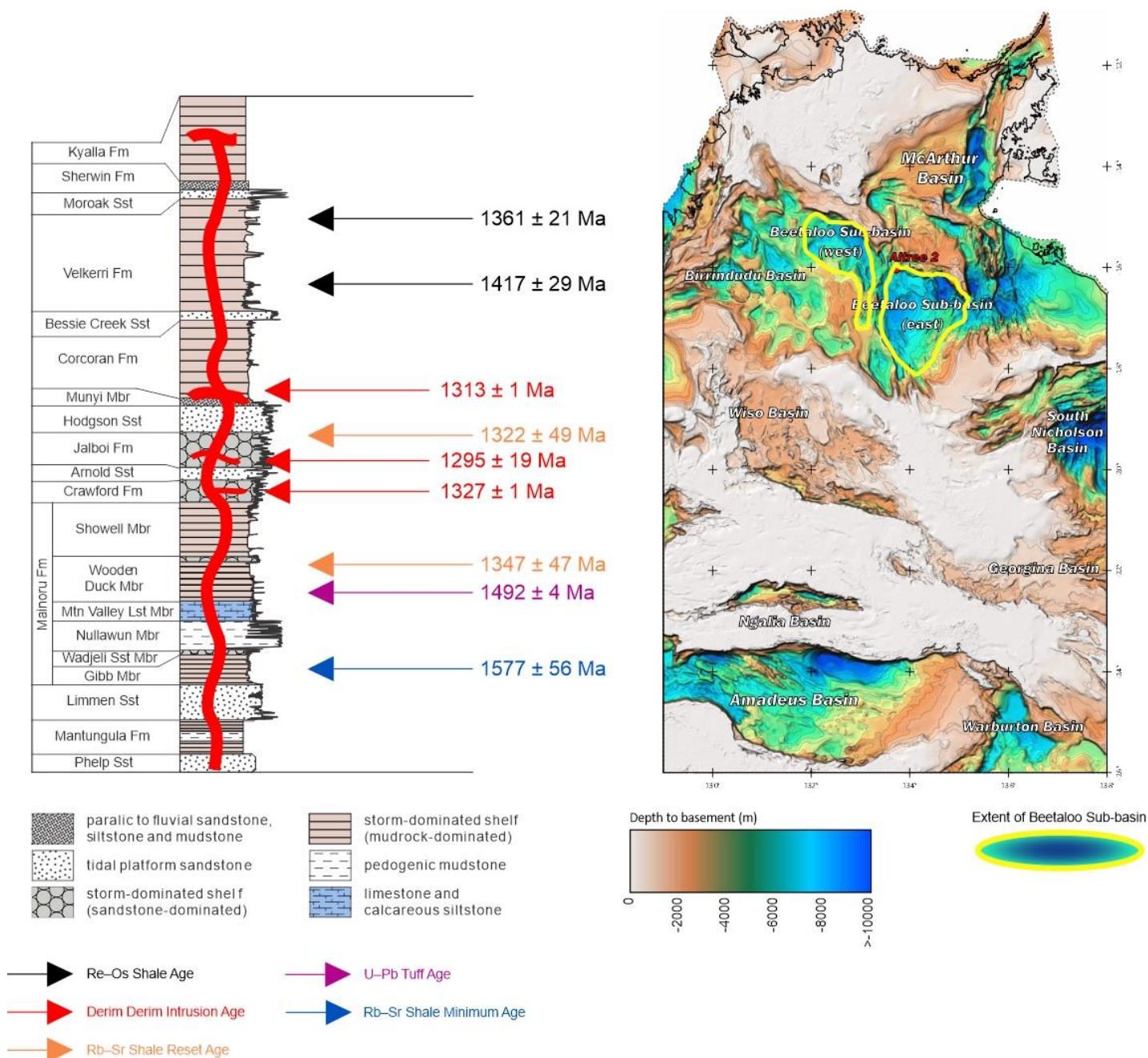


**Figure 3.1.** (A) Schematic stratigraphy and geochronological summary of the Roper Group (Abbott et al., 2001, Subarkah et al., 2021, Jackson et al., 1999, Southgate et al., 2000, Yang et al., 2020, Kendall et al., 2009). (B) Sample location and depth to basement map for the McArthur Basin adapted from Frogtech Geoscience (2018).

Mature organic-rich shales from the Velkerri Formation have been dated by Re–Os analysis at  $1417 \pm 29$  Ma and  $1361 \pm 21$  Ma (Kendall et al., 2009). These ages have been interpreted to be the depositional age of the formation. The geochronological constraints of the Roper Group are summarised in Figure 3.1. The Velkerri Formation is dominated by deep-basinal lithologies such as mudstones and siltstones that coarsens-up into the cross-bedded Moroak Sandstone and Sherwin Ironstone (Abbott et al., 2001). The Velkerri Formation is

interpreted to represent a deep-water, high-stand systems tract within a marine environment (Abbott et al., 2001, Warren et al., 1998). The Velkerri Formation is commonly sub-divided into three distinct members (from bottom to top, the Kalala, Amungee, and Wyworrie Members) based on variations in total organic carbon (TOC) content, gamma ray response, geochemistry, sedimentology and mineralogy (Cox et al., 2016b, Cox et al., 2019, Warren et al., 1998, Revie, 2016, Ahmad and Munson, 2013, Jarrett et al., 2019).

Importantly, the McArthur Basin experienced a complex thermal history following the deposition of the Roper Group Mafic sills of the Derim Derim Dolerite widely intrude all units in the Roper Group at ca. 1330–1300 Ma, with the oldest intrusions likely contemporaneous with the end of sedimentation in the basin (Yang et al., 2020, Bodorkos et al., 2022, Nixon et al., 2021, Subarkah et al., 2021, Ahmad and Munson, 2013). Little evidence of subsequent tectono-thermal perturbation is present within the basin until much of the region was overlain by subaerial basaltic lavas of the Kalkarindji Large Igneous Province (LIP) extruded at ca. 510 Ma (Evins et al., 2009, Glass and Phillips, 2006, Jourdan et al., 2014, Nixon et al., 2022). Following the Cambrian eruption of the Kalkarindji lavas, no significant (> 110°C) heating has been detected within the shallow parts of the basin (Duddy et al., 2004, Nixon et al., 2022).

The Atree 2 well drilled in the Beetaloo Sub-basin was chosen for this study as it intersects the entirety of the Velkerri Formation (Fig. 3.2). In addition, the well also intersected lavas of the Kalkarindji LIP directly overlying the Proterozoic sedimentary rocks and terminated at an intrusion of the Derim Derim Dolerite. Importantly, this well has also been the focus of numerous geochronological, geochemical and geobiological investigations from academia, private explorers as well as the Northern Territory Geological Survey (NTGS) which provide important complementary data to supplement this study (Cox et al., 2016b, Cox et al., 2019, Jarrett et al., 2019, Yang et al., 2018, Nixon et al., 2021, Warren et al., 1998, George and Ahmed, 2002, Nguyen et al., 2019, Sander et al., 2018, Lemiux, 2011, NTGS., 2009, NTGS., 2010, NTGS., 2012, Bodorkos et al., 2022, Cox et al., 2022).

### 3.3 Methods

Rock-Eval pyrolysis, aromatic hydrocarbon results, bitumen reflectance values, bulk x-ray diffraction (XRD) mineralogical compositions, and well log data were collated from several sources and compiled together in this study (NTGS., 2009, NTGS., 2010, NTGS., 1989, Cox et al., 2016b, Lemiux, 2011, Revie, 2014, NTGS., 2012, Revie et al., 2022, Jarrett et al., 2019). As such, their corresponding methodologies can be found in the references therein. The lithology of the Velkerri Formation was interpreted in detail (Fig. 3.2) using the electrical logs Gamma-Ray (GR), Neutron (NRS) and Density (RHOB) of the Atree-2 well (NTGS., 1989). Four lithologies were defined after applying cut-offs at each electrical log. They are then correlated along depth. Sandstone units corresponds to a GR < 130 API, NRS < 0.20 % and RHOB of around 2.5 g/cm<sup>3</sup>. This relates to a cross over between the RHOB and NRS logs and competent material at the GR. Interbedded shale and sands are defined by a GR > 130 and < 250 API, NRS > 0.20 and < 0.25 m<sup>3</sup>/m<sup>3</sup> and RHOB between 2.5 and 2.53 g/cm<sup>3</sup>. This lithology reflected a smaller breach between the density and neutron logs in comparison to the previous sandstone lithology. Shale units were constrained by a GR > 250 API, Neutron >

0.25 m<sup>3</sup>/m<sup>3</sup> and RHOB > 2.53 g/cm<sup>3</sup> and a minimum to no separation between the porosity logs. On the other hand, dolomitic siltstones have a GR response similar to the sandstone, with NRS ranging between 0.25 to 0.27 and RHOB > 2.62 g/cm<sup>3</sup>. This indicates a competent lithology in the GR with a gap between the neutron and density curves. In addition, T<sub>max</sub> data were also collated to discriminate the hydrocarbon maturation levels downhole. From this, a shift in hydrocarbon potential and T<sub>max</sub> gradients were identified at around 900 m (Fig. 3.2), where kerogen enters the gas window and becomes overmature. Five shale chips were then sampled from the Velkerri Formation in Atree 2 at depths of 415 m, 520 m, 696 m, 938 m, and 1220 m for further characterisation.

Samples were first imaged for their mineral composition and petrographic relationships. Back Scatter Electron (BSE) imaging and Mineral Liberation Analysis (MLA) maps of samples were collected using a Hitachi SU3800 Automated Mineralogy Scanning Electron Microscope at Adelaide Microscopy. BSE image tiles were done at 10 mm working distance and 20kV acceleration voltage with MLA maps were completed using a raster analysis with spectra collected at 0.35 µm/pixel resolution. Minerals previously categorised by bulk XRD analysis of the Velkerri Formation from Cox et al. (2016b) were used to develop a 'library' to help identify phases found by spectral reflectance MLA mapping. *In situ* Rb–Sr geochronology and trace element analysis were undertaken at Adelaide Microscopy using a laser ablation (RESOLUTION-LR ArF 193nm excimer laser) inductively coupled plasma tandem mass spectrometer (Agilent 8900x ICP-MS/MS) with the analytical parameters and tuning conditions following Redaa et al. (2021a). The laser set-up used in this study is provided in the Supplementary Material. Laser ablation data and error correlations were processed using the LADR software package (Norris and Danyushevsky, 2018, Schmitz and Schoene, 2007). During the data-processing step, Zr, Si, Ti, and rare earth element signatures were monitored to filter the detrital component of each analysis. Non-stable isotopic and elemental signatures were also culled or cropped during the processing of each analysis to aid in ensuring spot homogeneity. The <sup>87</sup>Rb decay constant used was 0.000013972 ± 4.5e-7 Myr<sup>-1</sup> following Villa et al. (2015). Isochron and single-spot ages were calculated with ISOPLOT (Vermeesch, 2018). Single-spot ages were calculated using the isochron intercept as their initial <sup>87</sup>Sr/<sup>86</sup>Sr ratios (Vermeesch, 2018, Nebel, 2015, Rösel and Zack, 2022). In addition, kernel density estimation (KDE) graphs (Vermeesch, 2012), cumulative age distributions (CAD) plots (Vermeesch, 2007), and multidimensional scaling (MDS) graphs (Vermeesch, 2013) were also constructed using ISOPLOT (Vermeesch, 2018) to differentiate between the population of single-spot ages from each sample.

The phlogopite nano-powder Mica-Mg (Govindaraju et al., 1994) was used as the primary reference material and its natural mineral equivalent MDC from the Ampandrandava Mine in Madagascar (Hogmalm et al., 2017, Armistead et al., 2020, Redaa et al., 2021a, Li et al., 2020) as well as glauconite reference material GL-O (Derkowski et al., 2009, Charbit et al., 1998) were used secondary age standards. As previously discussed in Subarkah et al. (2021), nano-powdered reference materials have similar ablation characteristics to fine-grained shales, with analogous matrix effects. As such, they are ideal standards for *in situ* analyses of these samples.



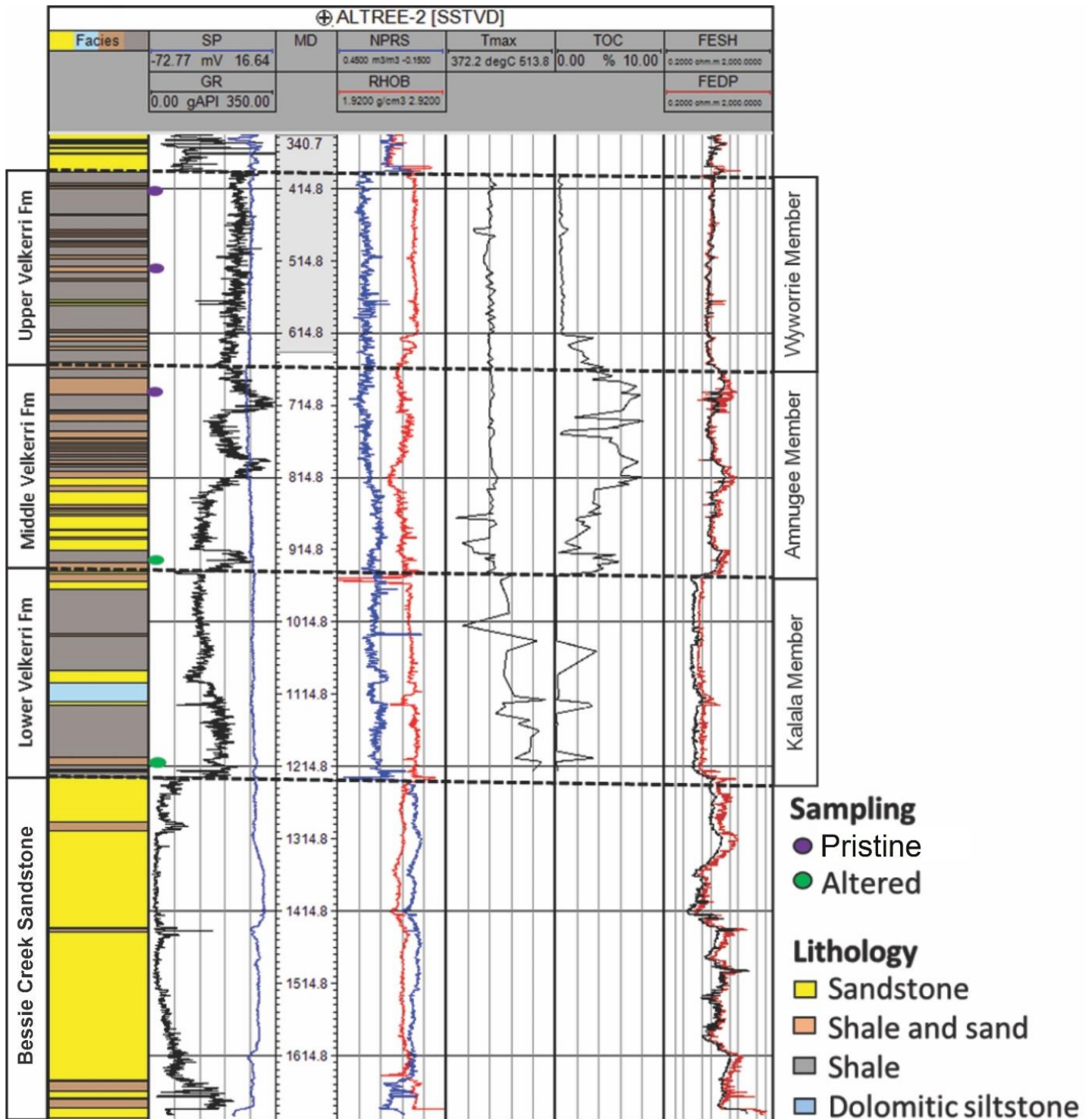


Figure 3.2. Summary of reprocessed down-hole well log data for Atree 2.

When anchored to an  $^{87}\text{Sr}/^{86}\text{Sr}$  initial ratio =  $0.72607 \pm 0.00363$  as reported by Hogmalm et al. (2017), MDC yielded an age of  $524 \pm 7$  Ma. This is within error of the published mean age of Mica-Mg at  $519 \pm 7$  Ma (Hogmalm et al., 2017). In addition, the independent reference material GL-O gave an age of  $96 \pm 4$  Ma, accurate to its published K–Ar age of  $95 \pm 1.5$  Ma (Charbit et al., 1998, Derkowski et al., 2009). It should be noted that this age is younger than the tuff-horizon age of the GL-O host rock, dated at  $113 \pm 0.3$  Ma (Selby, 2009).

Consequently, the ages yielded from GL-O have instead been proposed to be indicative of

the formation of glauconite occurring early after the deposition of the host rock (Selby, 2009). Glass standard NIST SRM 610 was used as a primary standard for elemental quantification in this study. Analysis of secondary standard BCR-2G yielded major, trace and rare earth element composition that were in good agreement (Pearson  $R > 0.999$ , Pearson  $R^2 > 0.999$ , and P Value  $< 0.0001$ ) with their published values as compiled in the GeoREM database (Jochum et al., 2005, Pearce et al., 1997, Jochum et al., 2011, Jochum and Stoll, 2008).

One-dimensional thermal modelling of the Atree 2 well was conducted using the SILLi 1.0 numerical model, which is designed for simulating thermal perturbation associated with sill emplacement within sedimentary basins (Iyer et al., 2018). First, palaeotemperatures were estimated from the compiled thermal maturity data (Disnar, 1994, Waliczek et al., 2021) following equations based on similar sedimentary systems that experienced a heating event due to burial and a subsequent igneous intrusion (Piedad-Sánchez et al., 2004). Forward modelling was then conducted to replicate maximum thermal conditions calculated in the well from the thermal maturity data, where palaeotemperatures suggest that the Wyworrie and Amungee Members experienced significant additional sedimentary cover in the Mesoproterozoic. During modelling, an additional 1.5 km of sedimentary rocks were added above the erosional unconformity now present above the McArthur Basin fill (Hall et al., 2021), while all post-Mesoproterozoic units were excluded. The upper contact of a sill with an initial temperature of 1150°C (Wang et al., 2012) was set at 2868 m, in accordance with adjusted burial depths during the Mesoproterozoic. As sill thickness is unconstrained within the Atree 2 well, multiple iterations were run with different thicknesses in order to establish the scenario able to best satisfy the thermal aureole extent observed in this well. From this, a sill thickness of 75 m was considered most appropriate, and is consistent with Derim Derim sill thicknesses of 10–100 m commonly observed across the basin (Lanigan and Torkington, 1991, Lanigan and Ledlie, 1990, Ledlie and Maim, 1989, NTGS., 2014, NTGS., 2015a, NTGS., 2016). Full modelling parameters and petrophysical properties are provided in the Supplementary Material.

### **3.4 Results**

#### **3.4.1 Compilation of legacy data**

All legacy data are compiled in the Supplementary Material and were checked for quality before interpretation as several factors such as contamination of cuttings due to drilling fluid or poor organic content can make results unreliable (Carvajal-Ortiz and Gentzis, 2015, Dembicki Jr, 2009, Peters, 1986). Rock-Eval pyrolysis values were screened using the thresholds described by Hall et al. (2016). Data were subsequently excluded from interpretation if these criteria were not met. More than 90% of the data yielded  $S_2 > 0.1$  mg HC/g, indicating that they were sufficiently abundant in organic content to provide well-defined peaks for characterising  $T_{max}$  and Hydrogen Index. Importantly, compilation of Rock-Eval pyrolysis values were all internally consistent (e.g., Hydrogen Index =  $S_2/TOC \times 100$ ). Next, there was no evidence of anomalously low  $T_{max}$  values ( $< 380^\circ\text{C}$ ) present. Extremely low  $T_{max}$  values are commonly a product of incorrect selection of the  $S_2$  peak by the program or the widening of the  $S_1$  peak from non-indigenous free hydrocarbons.  $T_{max}$  results

compiled in this study ranges between 384°C to 502°C with a mean of 433°C (st. dev. = 17). TOC content in the Velkerri Formation varies from 0.07% to 8.07%, averaging at 2.25% (st. dev. = 2.26). Clay mineral crystallinity and size data sourced for this compilation were standardised for interlaboratory comparisons (Warr and Rice, 1994, Warr and Mählmann, 2015). Full width at half maximum values from Atree 2 shale samples were computationally remeasured as a secondary check (Capogreco, 2017, NTGS., 2012, NTGS., 2010). Thirteen samples from the Velkerri Formation were analysed for their illite crystallinity. The Kübler Index (KI) for these shales range between 0.88 to 0.36, with decreasing values at depth and the lowest data originating from the Kalala Member. Methylphenanthrene distribution factor (MPDF), methylphenanthrene ratios (MPR), and bitumen reflectance data collated from Jarrett et al. (2019) and Revie et al. (2022) also displays an increasing trend down-hole.

### **3.4.2 Mineralogy of the Velkerri Formation**

Eleven mineral phases were identified by bulk XRD analysis of the Velkerri Formation from Cox et al. (2016b). The major mineral phases were quartz, kaolinite, illite, and orthoclase, which on average make up 90% of the total composition of the samples. Trace minerals include glauconite, montmorillonite, pyrite, magnetite, siderite, dolomite, and plagioclase. Our MLA mapping also identified these assemblages. Importantly, the two different methods categorised these minerals at similar abundances. However, results from MLA mapping also found other mineral assemblages not identified by bulk XRD analysis, including biotite, chlorite, clinocllore, apatite, and zircon. These differences could be due to the slightly different sub-intervals from which samples were analysed. Bulk XRD is a destructive procedure and therefore, the same section cannot be reused for *in situ* analysis. As a result, samples spaced 1–2 cm apart may yield different results. In addition, the targeted areas for MLA are often spatially localised and only based on 2D information. As such, they may not be representative for the bulk rock, making the comparison with XRD datasets difficult. The complete mineralogical abundance and correlations between results bulk XRD and MLA mapping are summarised in Table 3.1. Extensive petrographic descriptions of all samples can be found in the Supplementary Material.



Depth	Method	Apatite	Biotite	Chlorite	Dolomite	Glauconite	Illite	Kaolinite	Magnetite	Montmo rillonite	Orthoclase	Pyrite	Quartz	Siderite	Zircon	Plagioclase
415 m	Bulk XRD	0.00	0.00	0.00	0.25	0.82	34.05	21.25	0.36	1.79	13.33	0.28	26.13	1.76	0.00	0.00
	MLA Map	0.00	1.22	1.33	0.00	0.00	35.52	7.45	0.89	9.05	11.48	0.40	23.93	0.00	0.02	4.39
520 m	Bulk XRD	0.00	0.00	0.00	0.37	2.35	43.28	17.14	0.38	2.01	10.01	0.74	23.67	0.05	0.00	0.00
	MLA Map	0.00	0.07	0.08	0.00	0.00	36.51	7.11	0.00	0.04	4.08	0.24	47.94	0.00	0.00	0.85
696 m	Bulk XRD	0.00	0.00	0.00	0.21	1.53	27.59	2.07	0.00	1.49	13.40	4.11	45.02	0.00	0.00	4.57
	MLA Map	0.31	0.93	0.06	0.00	0.00	18.48	0.00	0.00	4.00	8.27	4.47	60.88	0.00	0.00	1.41
938 m	Bulk XRD	0.00	0.00	0.00	0.53	1.36	27.03	6.99	0.33	1.16	11.32	1.49	43.28	0.01	0.00	6.50
	MLA Map	1.2	0.00	0.06	0.00	0.00	22.13	5.46	0.00	0.00	3.37	1.60	57.79	0.00	0.00	6.90
1220 m	Bulk XRD	0.00	0.00	0.00	0.43	1.04	39.36	13.99	0.42	1.66	7.32	0.26	33.56	0.10	0.00	1.86
	MLA Map	0.00	0.01	0.01	0.05	0.00	38.18	20.21	0.00	0.00	4.45	0.01	35.25	0.00	0.01	1.63

Depth (m)	Pearson R	Pearson R 95% C.I.	Pearson R <sup>2</sup>	P Value
415	0.922	0.784–0.973	0.850	< 0.0001
520	0.866	0.648–0.953	0.750	<0.0001
696	0.953	0.868–0.984	0.910	<0.0001
938	0.965	0.898–0.988	0.930	<0.0001
1220	0.989	0.969–0.996	0.979	<0.0001

**Table 3.1.** Mineralogical abundance of the Velkerri Formation shales collected by bulk XRD analysis from Cox et al. (2016b) and spectral reflectance MLA mapping in this study. All values are in weight percent. B. Covariation between the mineral phases categorised by both methods.

### 3.4.3 Laser Ablation Data

Geochronological results yielded by samples from the Wyworrie and Amungee Members gave ages within error of each other. The sample from 415 m depth was dated at  $1448 \pm 81$  Ma. Next, the mudstone analysed from 520 m depth yielded an age of  $1434 \pm 19$  Ma. Thirdly, the shale sample studied from 696 m depth resulted in an age of  $1411 \pm 139$  Ma. A Kalala Member shale chip from 938 m at depth was dated at  $1322 \pm 93$  Ma. Another sample from this member, towards the boundary with the underlying Bessie Creek Sandstone at depth 1220 m resulted in an age of  $1336 \pm 40$  Ma. The range of precision from these Rb–Sr ages are primarily constrained by a substantial spread in  $^{87}\text{Rb}/^{86}\text{Sr}$  ratios, the number of data points defining the regression line as well as errors on each individual analysis (Nebel, 2015). The most precisely dated samples, extracted from 520 m and 1220 m depth, had the widest range of  $^{87}\text{Rb}/^{86}\text{Sr}$  ratios (0–50) whilst the other two samples preserved a range of  $^{87}\text{Rb}/^{86}\text{Sr}$  values less than 10 (Fig. 3.6). The variability in these values could be a subject of future studies in order to improve the success of this dating method. Single-spot ages were calculated for all spot analyses in each sample, and their populations categorically differ (Fig. 3.8).

Elemental concentrations of each sample were concurrently collected during the *in situ* Rb–Sr laser ablation investigation and they are in good agreement with data collected by bulk geochemical analysis from Cox et al. (2016b). Samples from depth 415 m, 520 m, and 696 m do not show any covariation between their total REEY concentrations and Sm/Nd ratios (Fig. 3.7). On the other hand, sample 938 m showed a statistically significant relationship between these two parameters (Pearson R = 0.58, Pearson R<sup>2</sup> = 0.336, P Value < 0.0001). In addition, Velkerri Formation shale sourced from depth 1220 m also showed a strong covariation between total REEY values and Sm/Nd (Pearson R = -0.545, Pearson R<sup>2</sup> = 0.297, P Value < 0.0001). These associations were also identified in the whole-rock geochemical data collected from Cox et al. (2016b). Figure 3.7B shows that samples between 390 – 900 m depth hold no statistically significant relationships between the two factors. However,

samples from deeper than 900 m display a strong relationship between the two variables (Pearson  $R = -0.559$ , Pearson  $R^2 = 0.312$ ,  $P$  Value = 0.003). The full geochronological and inorganic geochemical dataset for samples in this study can be found in the Supplementary Material.

#### **3.4.4 Thermal Modelling**

One-dimensional thermal modelling of the emplacement of a 75 m thick Derim Derim Dolerite sill at the base of the Atree 2 well is sufficient to produce a thermal aureole reaching temperatures  $> 110^\circ\text{C}$ , ca. 800 m above the top contact of the sill (Fig. 3.9A). Maximum palaeotemperatures recorded in the Wyworrie Members exceed those predicted in this simulation, however, this may be attributed to elevated temperatures in the shallow basin during eruption of the Kalkarindji LIP in the Cambrian (Nixon et al., 2022). The resultant maximum thermal profile is consistent with  $T_{\text{max}}$  derived palaeotemperature estimates and is thus considered a plausible model for the observed data from the well. Post-intrusion temperatures at depths that match the samples with reset Rb–Sr ages are much lower than observed in comparable isotopic systems for thermally induced diffusion (Dodson, 1973, Tillberg et al., 2020, Torgersen et al., 2015, Yoder and Eugster, 1955), with the shallowest reset sample peaking at ca.  $120^\circ\text{C}$ . Furthermore, elevated temperatures predicted by the modelling are geologically short lived, with temperatures returning to steady-state conditions by approximately half a million years following sill intrusion (Fig. 3.9B).

### **3.5 Discussions**

#### **3.5.1 Thermal Maturity of the Velkerri Formation**

Geochemical and mineralogical-based thermal maturity indicators collected via Rock-Eval studies and bulk XRD analyses were compiled in this study in order to establish a vertical profile of the Velkerri Formation and assess the local palaeo-thermal structure. The  $T_{\text{max}}$  parameter is the temperature at which the maximum rate of hydrocarbon generation occurs during pyrolysis analysis and is a common method used to reconstruct thermal histories of basin systems (Espitalié, 1986, Espitalié et al., 1977, Peters and Cassa, 1994, Tissot et al., 1987). Consequently, these thermal indicators need to be treated with caution when applied independently and are more suitable as qualitative discriminators as opposed to absolute quantitative parameters. However, such proxies can be more confidently used to estimate palaeotemperatures in sedimentary successions if they show a strong relationship with each other (Dellisanti et al., 2010, Ola et al., 2018, Waliczek et al., 2021, Burtner and Warner, 1986, Velde and Espitalié, 1989). Ultimately, both organic and inorganic indicators are essential for a robust understanding of the thermal histories of sedimentary sequences through time.

In this study, we examine the covariation between the  $T_{\text{max}}$  values and KI to reconstruct the thermal history of the Velkerri Formation in the Atree 2 well (Fig. 3.3). In our compilation, samples with immature kerogen ( $T_{\text{max}} < 435^\circ\text{C}$ ) correspond to rocks in the diagenetic zone (Kubler Index  $\text{KI} > 0.45^\circ\Delta 2\theta$ ). This relationship is true in similar studies and generally translates to palaeotemperatures of ca.  $100^\circ\text{C}$  (Dellisanti et al., 2010, Espitalié et al., 1977, Kosakowski et al., 1999, Kubler, 1967, Abad and Nieto, 2007).

Interestingly, the samples within the mature oil window ( $435^{\circ}\text{C} < T_{\text{max}} < 465^{\circ}\text{C}$ ) show a wide range of KI values between 0.39 and  $0.65^{\circ}\Delta 2\theta$  (Fig.3.3). This is possibly due to the delay between thermal reactions in clay minerals as opposed to organic matter (Ola et al., 2018). Although the maturation of organic matter and the morphology of clay minerals both largely depend on temperature, other processes such as the kinetics of the thermal reaction and geochemical composition of the sample can make these relationships non-linear (Ola et al., 2018, Velde and Vasseur, 1992, Pollastro, 1993, Varajao and Meunier, 1995, Meunier et al., 2004). The disparity between kerogen evolution and the equilibrium stage of illitisation at these temperatures may also play a role in this variability (Dellisanti et al., 2010). Nevertheless, an increase in  $T_{\text{max}}$  pyrolysis results from these samples still appears to correlate with a decrease in KI values. These thermometers would approximately equate to palaeotemperatures between 100 and  $150^{\circ}\text{C}$  (Kosakowski et al., 1999, Welte and Tissot, 1984, Árkai et al., 2002).

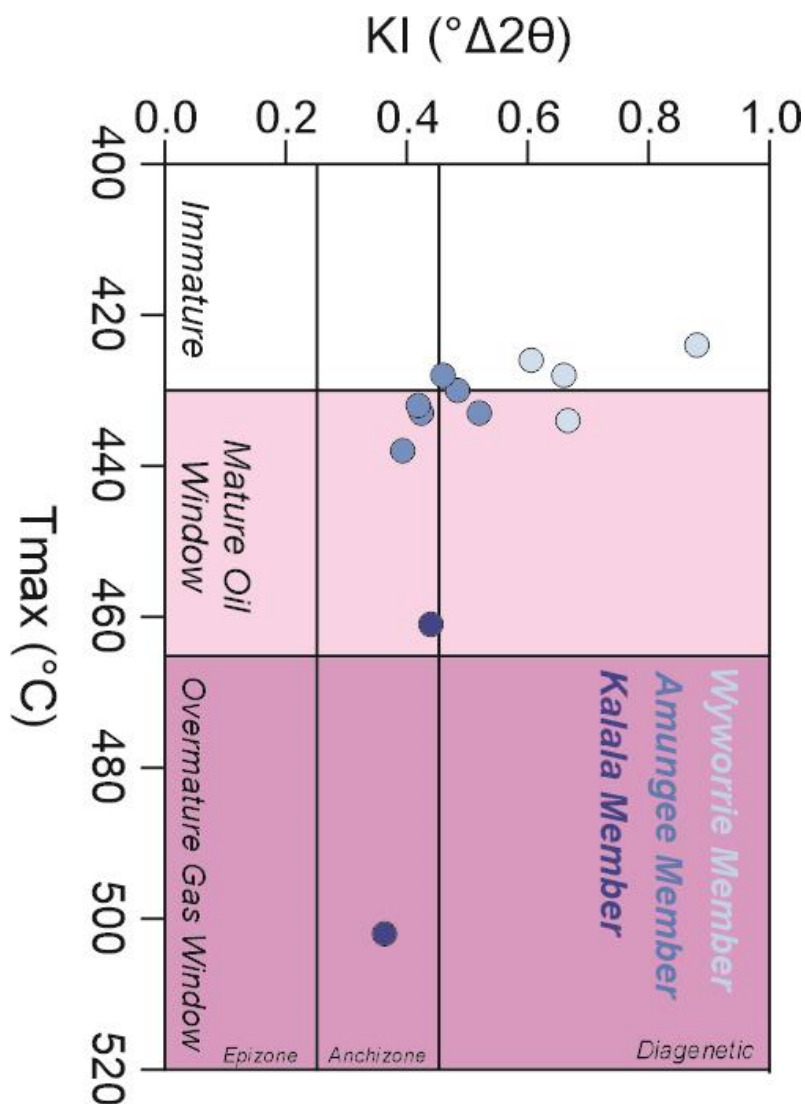


**Figure 3.3.** Covariation between  $T_{\text{max}}$  values from pyrolysis analysis and illite crystallinity KI in the Velkerri Formation. An increase in  $T_{\text{max}}$  coincide with a decrease in KI, suggesting that these proxies are both mainly sensitive to changes in palaeotemperature.

On the other hand, the sample displaying over-mature kerogen ( $T_{max} > 465^{\circ}\text{C}$ ) corresponds to the smallest KI value (Fig. 3.3) of  $0.36^{\circ}\Delta 2\theta$  (Dellisanti et al., 2010). These values commonly define the gas window and the anchizone, corresponding to palaeotemperatures of ca.  $200^{\circ}\text{C}$  (Kosakowski et al., 1999, Árkai et al., 2002, Dellisanti et al., 2010). Overall, a trend between increasing  $T_{max}$  and decreasing KI values (Fig. 3.3) confirms the feasibility of these parameters as thermal maturation proxies (Dellisanti et al., 2010).

Lastly, the thermal parameters for the Velkerri Formation can be further examined by inspecting the changes in MPDF (Kvalheim et al., 1987, Boreham et al., 1988), MPR (Wilhelms et al., 1998, Radke et al., 1982), and bitumen reflectance (Riediger, 1993). Previous studies have shown that aromatic hydrocarbons were effective in providing thermal constraints for the Velkerri Formation (George and Ahmed, 2002, Jarrett et al., 2019). These proxies were similarly sensitive to maturity variations from thermally immature to late oil window. As such, we normalise the thermal indicators used in this study by converting them all (Jarvie et al., 2001, Revie et al., 2022, Jarrett et al., 2019) to calculated vitrinite reflectance values ( $VR_{CALC}$ ; Fig. 3.4). The  $VR_{CALC}$  from four different thermal indicators show that the Velkerri Formation quickly elevated in maturity and enters the gas window at ca. 900 m depths (Fig. 3.4). The agreement of all proxies add further confidence in the temperature constrains used in this study.

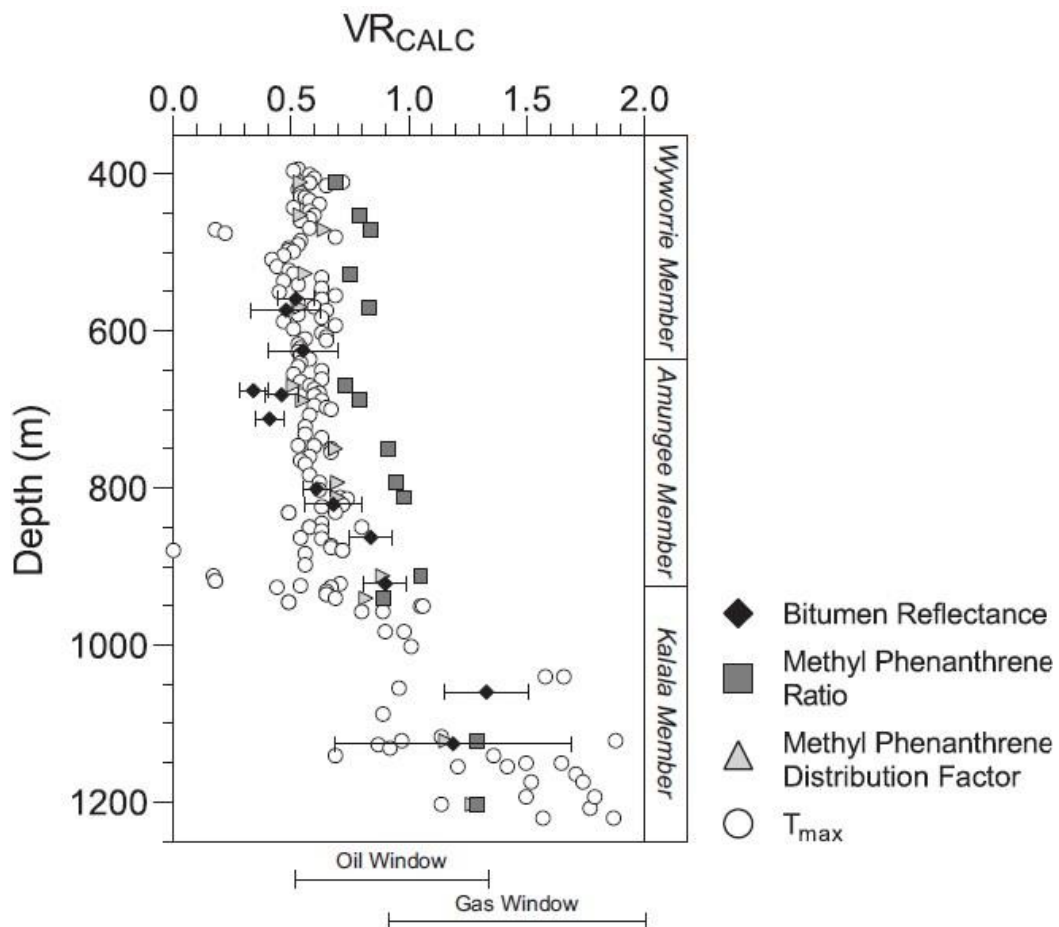


**Figure 3.4.** Calculated vitrinite reflectance ( $VR_{CALC}$ ) data down-hole modelled from  $T_{Max}$ , MPR, MPDF, and bitumen reflectance data compiled in this study (NTGS., 1989, NTGS., 2009, NTGS., 2010, NTGS., 2012, Lemiux, 2011, Revie, 2014, Revie et al., 2022, Jarrett et al., 2019, Capogreco, 2017).  $VR_{CALC}$  from all proxies all indicate an elevation in thermal maturity into the gas window at depths ca. 900 m.

Multiple geochemical and mineralogical thermal parameters from our compiled data-set demonstrate strong correlation between them, suggesting that the proxies used in this study primarily recorded changes in palaeotemperature as opposed to other possible variables. Notably, five different, independent, source-rock maturation proxies statistically agree and recorded similar step-wise increase in thermal history down-hole. As such, we investigated five samples approaching the geothermal anomaly in the Kalala Member for *in situ* Rb–Sr and trace element analysis. The changes in thermal maturation indexes throughout the well are used to help constrain the parameters of the Rb–Sr isotopic system in Proterozoic shales.

### 3.5.2 Thermochronological History of the Velkerri Formation

Although some of the geochronological results of these samples may overlap due to their errors (Fig. 3.6), they are still categorically different down-hole (Fig. 3.8). We display these differences by plotting the population of single-spot ages from each sample against each other. Kernel Distribution Estimate (KDE) plots of these results show that the distribution of single-spot ages from samples shallower than 900 m largely overlaps with the Re–Os age constraint (Fig. 3.8A; light pink) for the Velkerri Formation (Kendall et al., 2009). On the other hand, the population of single-spot ages from shales deeper than 900 m instead agree with the age for the Derim Derim Dolerite (Fig. 3.8A; dark pink) intrusion ca. 1330–1300 Ma (Bodorkos et al., 2022, Yang et al., 2020, Nixon et al., 2021, Ahmad and Munson, 2013).

Importantly, these sample-sets are statistically different from each other. This is graphically shown by their cumulative age distribution (CAD, Fig. 3.8B) and Multidimensional Scaling (MDS, Fig. 3.8C) plots. The second of these techniques statistically measures the dissimilarity between different age distributions through the Kolmogorov-Smirnov test (Vermeesch, 2013). In short, similar age distributions will plot closely to each other whilst distributions that are increasingly dissimilar will plot further away (Vermeesch, 2012, Vermeesch, 2013). Figure 3.8B and 3.8C show that samples shallower than 900 m had age distributions that are similar to each other (Fig. 3.8). Overall, these ages are statistically similar to the Re–Os constraint of the Velkerri Formation (Kendall et al., 2009), suggesting that they likely represent an early diagenetic/burial age soon after deposition. On the other hand, the single-age distributions of samples deeper than 900 m are statistically different to the previous sample set. They form their own cluster, which in turn coincides with the age of the Derim Derim Dolerites (Bodorkos et al., 2022, Yang et al., 2020, Nixon et al., 2021, Ahmad and Munson, 2013). Consequently, the Rb–Sr shales ages from this section are unlikely to date the deposition of the Velkerri Formation, but instead reflect a late-stage hydrothermal resetting induced by the intrusion.

The petrographic characteristics of assemblages in these samples are further evidence that the shales in the Velkerri Formation recorded two distinct thermochronological events. The abundant clays in samples from depth 415 m, 520 m, and 696 m are predominantly illite, with trace amounts of chlorite, kaolinite, and montmorillonite (Table 3.1). However, they do not show typical irregular, angular detrital morphologies (Fig. 3.5, Fig. S.3.2A-C). Instead, clay minerals in these samples form a matrix cement, filling in porous spaces, wrapping

around detrital grains and suggesting that they formed within the sediment during burial diagenesis (Rafiei and Kennedy, 2019, Rafiei et al., 2020, Subarkah et al., 2021). Primary sedimentary structures such as compaction of clays along the bedding plane can also still be identified in these samples (Fig. 3.5, Fig. S.3.2A-C, and Supplementary Material). These petrographic relationships are further discussed in the Supplementary Material and were similarly found in Roper Group shales elsewhere, indicating an early-diagenetic origin (Subarkah et al., 2021, Rafiei and Kennedy, 2019). Moreover, the ages from these samples are all in agreement with the deposition of the Velkerri Formation dated at  $1417 \pm 29$  Ma by Re–Os geochronology (Kendall et al., 2009), suggesting that the majority of illite formed relatively soon after sediment deposition.

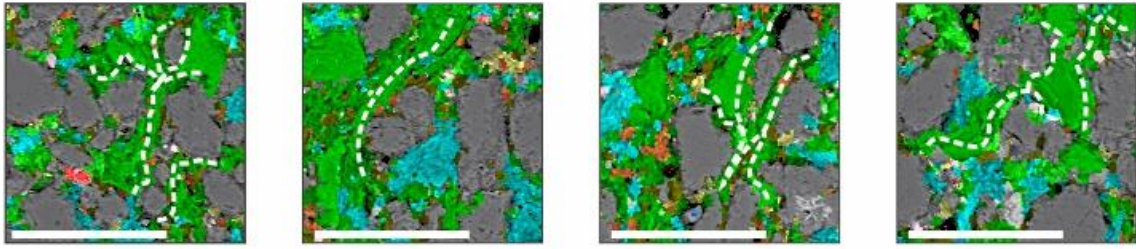
Nevertheless, we also sought to identify any potential secondary alteration of these shales by analysing their geochemical signatures. Sm/Nd ratios are common geochemical proxies for screening alteration in shales as Nd is preferentially lost relative to Sm during post-depositional processes (Awwiller and Mack, 1989, Awwiller and Mack, 1991). In addition, fluid-rock reactions also have a significant impact on rare earth element and yttrium solubility and transportation during hydrothermal events (Williams-Jones et al., 2012, Lev et al., 1999). Therefore, these parameters can be an effective tool for highlighting fingerprints of post-depositional geochemical mobilisation (Fig. 3.7).

Samples from depths shallower than 900 m show no significant relationships between their total rare earth elements and yttrium (REEY) concentrations and Sm/Nd ratios collected by laser ablation analysis or through traditional bulk trace element geochemistry (Cox et al., 2016b). These support an interpretation that these ages form a minimum depositional age for the unit, recording an early diagenetic event as opposed to a late-stage secondary overprint. Furthermore, temperature constraints for the Velkerri Formation at depths 390 – 900 m suggest that they are well-within the oil window (Fig. 3.3 and 3.4). As a result, we propose that this temperature window is not sufficient to disturb the Rb–Sr and trace element systems in these shales.

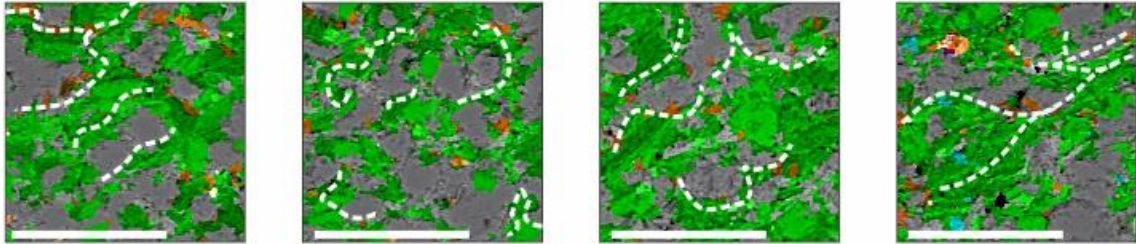
Conversely, shales collected from depths >900 m showed petrographic evidence of post-depositional alteration (Fig. 3.5 and Fig. S.3.2D-E). Clay minerals in the 938 m sample are fissile and foliated (Fig. 3.5). In addition, pyrite and apatite can be observed overgrowing illite and chlorite. Moreover, illite grains from the Kalala Member shale at 1220 m depth are notably larger and crystalline (Fig. 3.5 and Fig. S.3.2D-E), with features inconsistent with an early diagenetic origin (Fig. S.3.2D-E). Clay minerals were also found interlocking with quartz overgrowth and appear to replace earlier assemblages (Fig. 3.5 and Fig. S.3.2D-E).



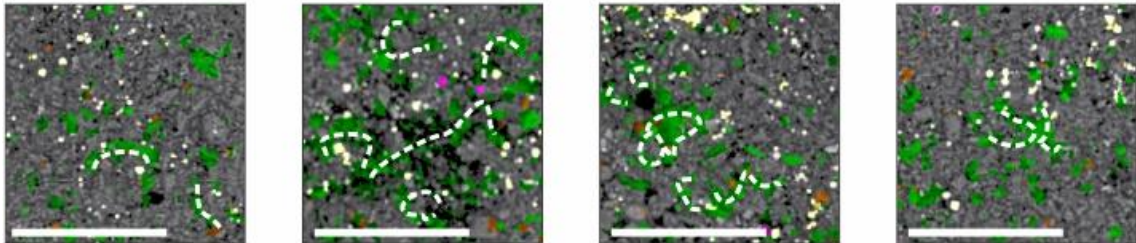
**Depth: 415 m.**



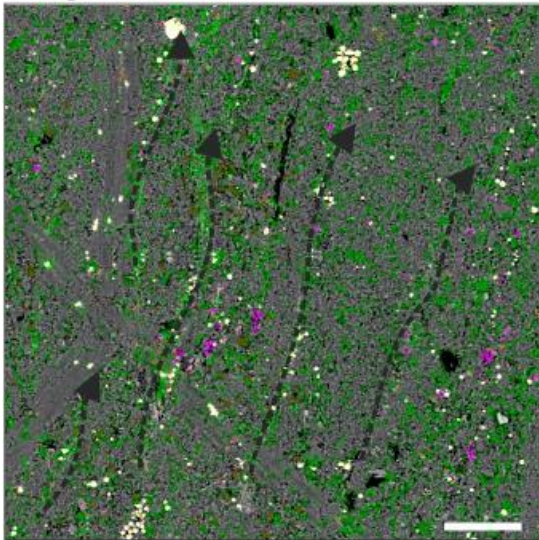
**Depth: 520 m.**



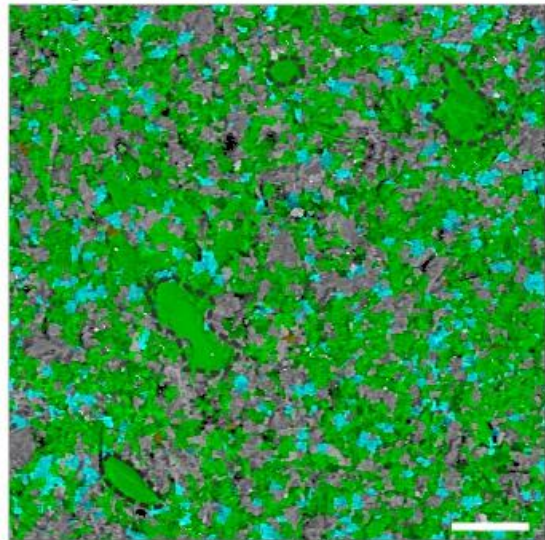
**Depth: 696 m.**



**Depth: 938 m.**



**Depth: 1220 m.**



**Albite**      **Apatite**      **Chalcopyrite**      **Glaucosite**      **Magnetite**  
**Illite**      **Kaolinite**      **Organic Matter**      **Pyrite**      **Quartz**      **Zircon**

**Figure 3.5.** Spectral reflectance MLA maps of samples selected for in situ laser ablation analysis in this study overlain on top of their respective BSE images. White dash lines show illite assemblages wrapping around detrital grains and forming cements. Black, dashed arrow lines show foliation in illite crystals. Black dashed lines show large illite crystals replacing previous clay assemblages. Solid white lines are 100 µm scale bars.



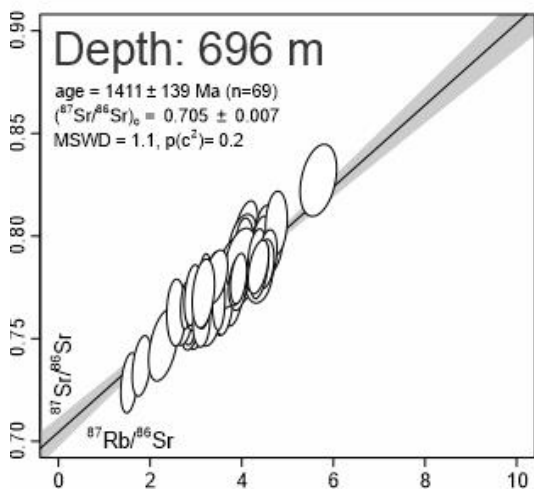
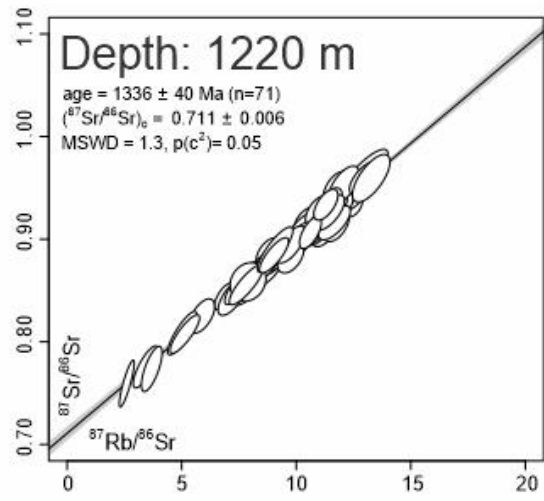
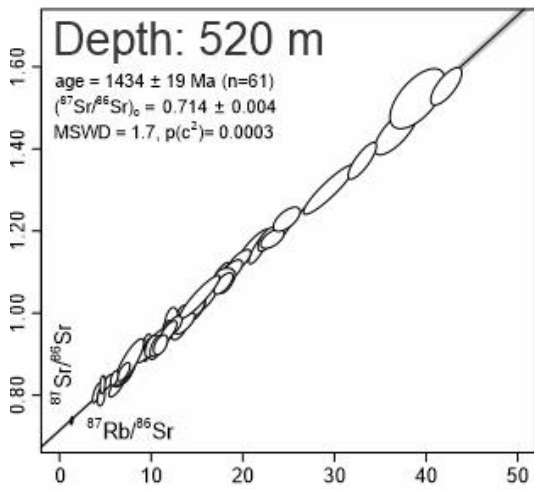
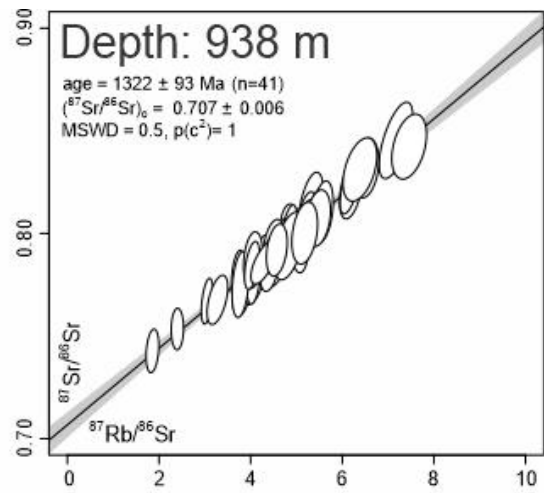
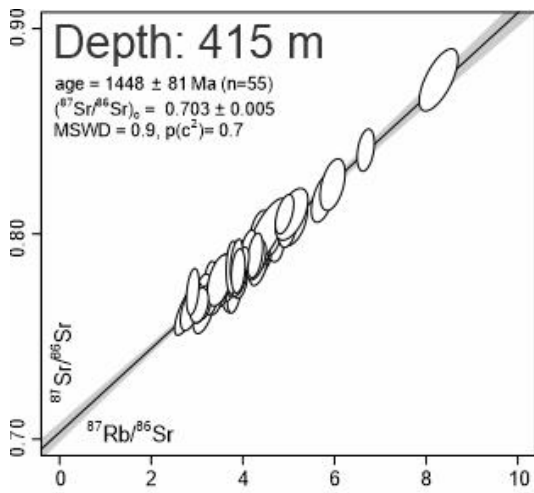


**Figure 3.6.** Summary of in situ Rb–Sr geochronological results from this study.

In addition to petrographic and geochronological disparities, samples from depths below 900 m display statistically significant relationships between total REEY concentrations and Sm/Nd ratios (Fig. 3.7). The shale chip analysed from 938 m had a positive relationship between an increase in Sm/Nd ratio and total REEY concentration (Pearson  $r$ : 0.580, R-squared: 0.336), while the sample collected from depth 1220 m preserved a negative relationship between Sm/Nd ratio and total REEY values (Pearson  $r$ : -0.545, R-squared: 0.297). These associations are similarly reflected in the bulk trace element data collated from Cox et al. (2016b). In the compiled data, shales from deeper than 900 m demonstrate a strong affinity between these controls (Pearson  $r$ : -0.559, R-squared: 0.312). These alteration indicators are further evidence that the Kalala Member at depths below 900 m experienced a late-stage secondary heating event, as trace elements are more readily mobilised in hydrothermal reactions (Williams-Jones et al., 2012, Poitrasson et al., 1995, Condie, 1991, Lev et al., 1999, Awwiller and Mack, 1989, Awwiller and Mack, 1991).

Importantly, thermal indicators from this interval suggest that kerogen in these shales are thermally overmature (Fig. 3.3 and 3.4). Previous studies have shown that the source rocks in the Velkerri Formation became overmature only when affected by magmatic events (Crick et al., 1988, George and Ahmed, 2002). As such, it is plausible that the Derim Derim Dolerite intersected in this well has imposed a hydrothermal alteration footprint onto the surrounding sediments via conductive heat loss and/or heat-transfer fluids. This magmatic pulse would have recrystallised the former mineral assemblages or induced a second mineralisation of clays, mobilised trace elements, and heated the kerogen within the Kalala Member to overmaturity. Thermal indicators (Fig. 3.4 and 3.9) suggest that source-rocks within this interval may have experienced palaeotemperatures of at least 150°C (Dellisanti et al., 2010, Hunt, 1995, Welte and Tissot, 1984). This is in good agreement with evidence from aqueous fluid inclusions in quartz veins within the Derim Derim Dolerite elsewhere, which have suggested that hydrocarbons from the Velkerri Formation migrated in the cooling sill at similar temperatures (Dutkiewicz et al., 2004). Importantly, such hydrothermal systems seem to be sufficient for disturbing the Rb–Sr isotopic system of these samples.

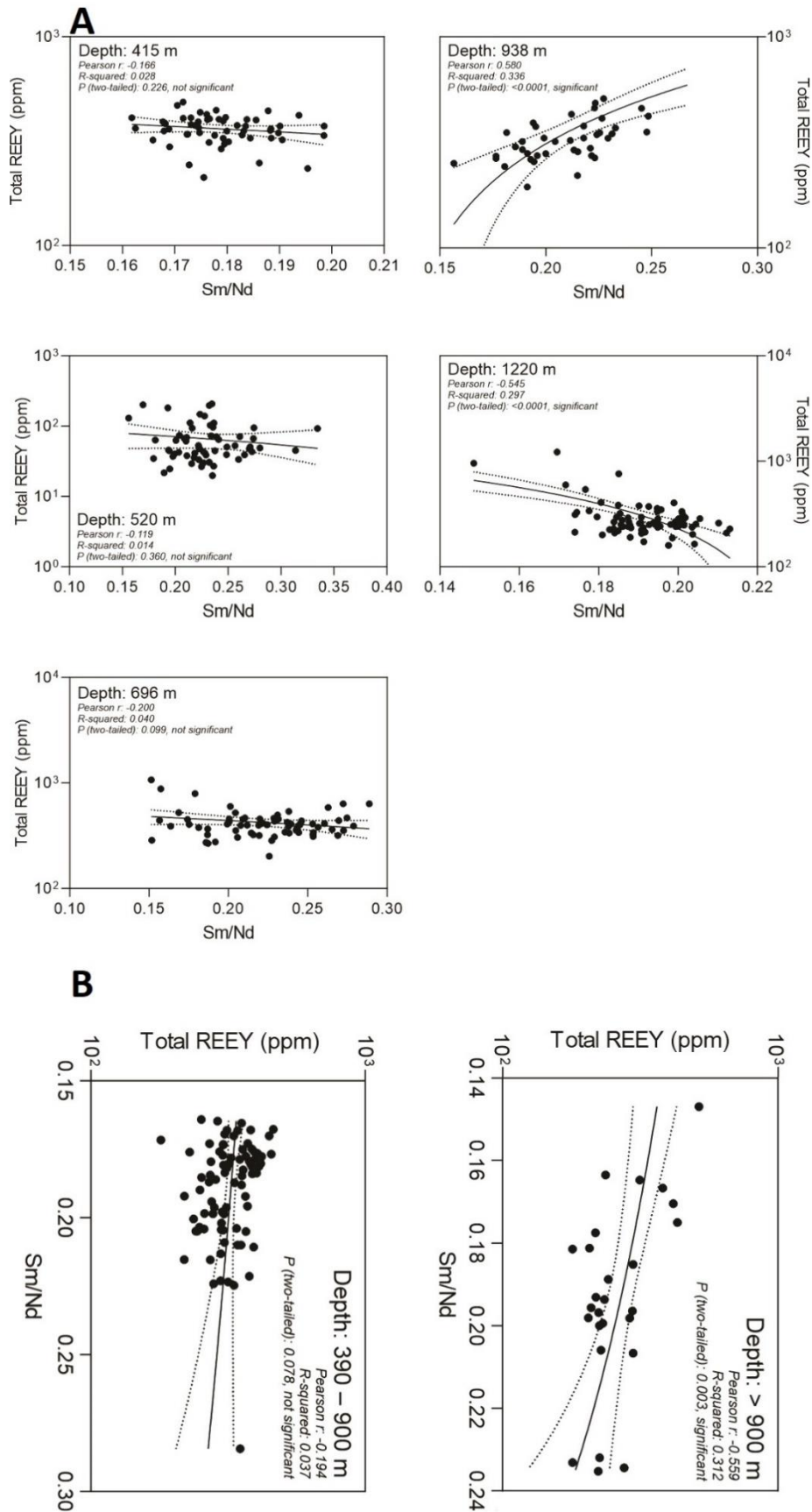


**Figure 3.7.** Statistical relationships between alteration proxies obtained from this study through laser ablation analysis (A) and whole-rock geochemical data (B) compiled from (Cox et al., 2016b).

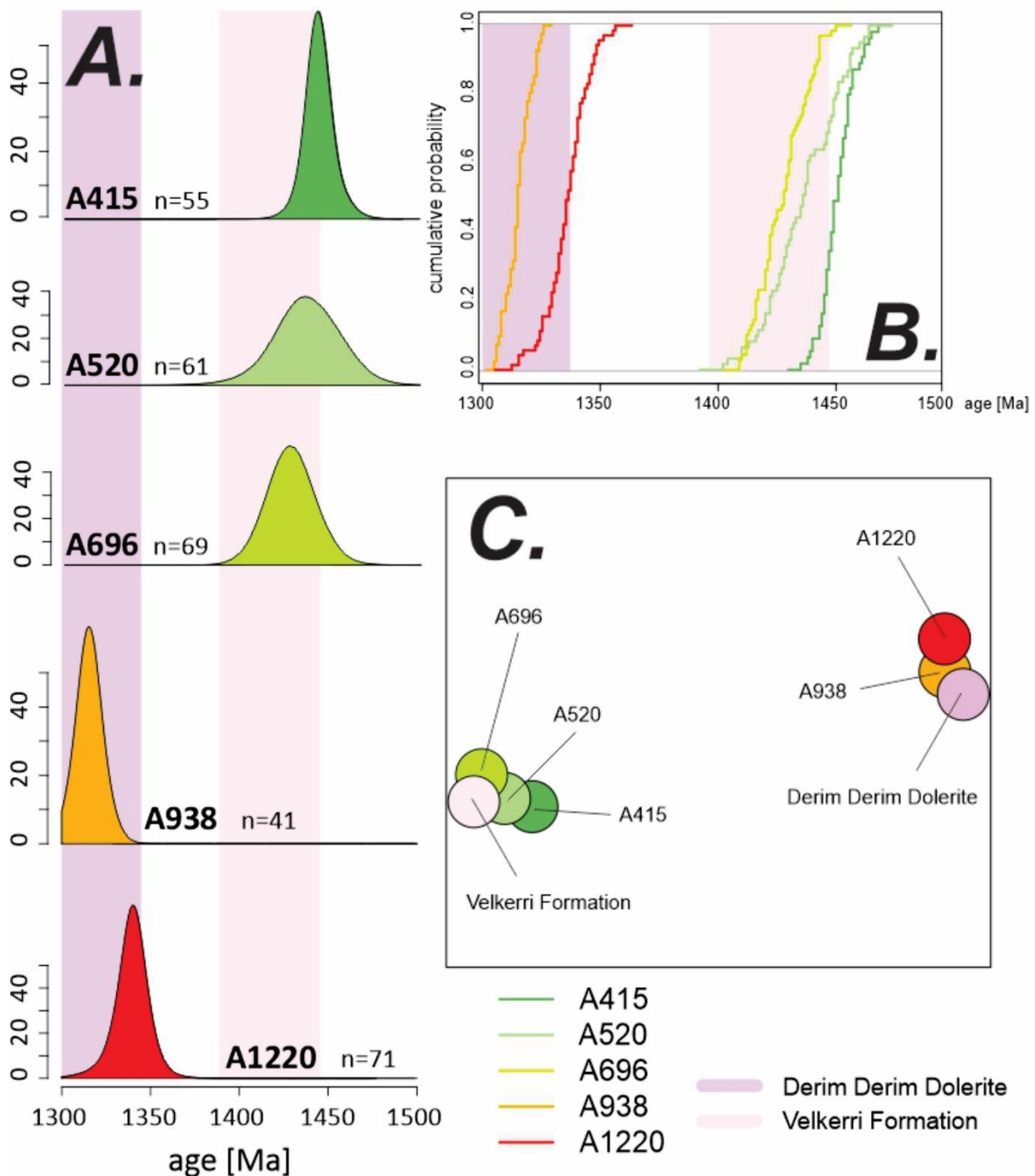


**Figure 3.8.** Single-spot ages from samples in this study illustrated by KDE (A), CAD (B), and MDS (C) plots. Note that the population of single-spot ages for samples at depths 415 m, 520 m, and 696 m all overlap with previous Velkerri Formation Re–Os age constraints shown in light pink (Kendall et al., 2009).

### 3.5.3 Modelled Predictions of the Geothermal Aureole Induced by the Derim Derim Dolerite

Resetting of Rb–Sr geochronology and overmaturation of hydrocarbons in the Kalala Member within the Atree 2 well implies the presence of a secondary hydrothermal aureole extending ca. 800 m away from the Derim Derim Dolerite sill, which is intersected at present day depth 1696 m. One-dimensional thermal modelling for a sill thickness of 75 m in the

Mesoproterozoic suggests temperatures exceeding the oil window over 120°C (Tissot et al., 1974, Waples, 1980) only extended ca. 700 m from the intrusion (Fig. 3.9A).

Samples at present day depths of 938 m and 1220 m yield Rb–Sr ages corresponding to emplacement timing of the Derim Derim Dolerite (Nixon et al., 2021, Yang et al., 2020), which suggests that the intrusion caused the chronometer to reset or induced a second mineralisation of clay phases. Predicted temperatures experienced by the shallowest reset sample, however, are lower than the inferred closure temperatures for observed K–Ar and Rb–Sr in sheet silicates (Dodson, 1973, Tillberg et al., 2020, Torgersen et al., 2015, Yoder and Eugster, 1955). In a scenario in which a sill of thickness 75 m was intruded below samples, rocks from present day depth of 938 m are only predicted to have experienced maximum heating to ca. 110°C (Fig. 3.9C), with temperatures exceeding 100°C for a duration of only ca. 150 ka (Fig. 3.9B).

Additionally, the eruption of lavas from the Kalkarindji LIP (Evins et al., 2009, Glass and Phillips, 2006, Jourdan et al., 2014) are preserved above Proterozoic sedimentary rocks in the Atree 2 well. Furthermore, regional apatite fission track data suggest that the thermal pulse induced during this LIP extrusion were short-lived but sufficient (> 190°C) to anneal tracks in the upper ~500 m of the basin (Nixon et al., 2022). However, the shallowest samples taken in this study (at depths 415 m, 520 m, and 696 m) did not have their Rb–Sr isotopic system disturbed despite experiencing such temperatures from this reheating event. Consequently, the thermal profile for the sample at 415 m depth provides a minimum closure temperature constraint for short-lived conditions which have not reset the Rb–Sr chronometer in these (presumably) dry shales over 800 million years after the Derim Derim dolerite intrusion. Interestingly, the Cambrian palaeotemperatures imposed by the Kalkarindji lavas (Nixon et al., 2022) are notably higher (> 190°C) than Mesoproterozoic palaeotemperatures reached by samples with Rb–Sr ages reset by the Derim Derim Dolerite (ca. 120°C; Fig. 3.9A-B).

Such disparity suggests that the presence of fluid (either connate, or sourced from the intrusion), rather than just temperature, is likely to play a critical role in determining whether the Rb–Sr record in a shale is reset. As such, the geochemical system in shales within the aureole may be disturbed at lower temperatures, as trace and rare earth elements are more easily mobilised in hydrothermal fluid systems (Villa, 1998, Nebel, 2015, Poitrasson et al., 1995, Williams-Jones et al., 2012, Li et al., 2019).

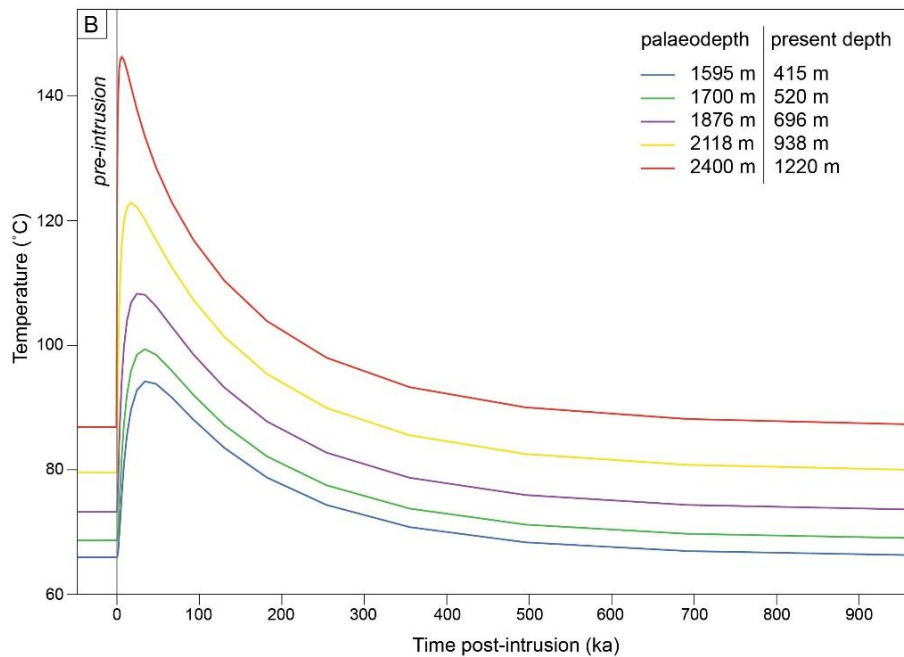
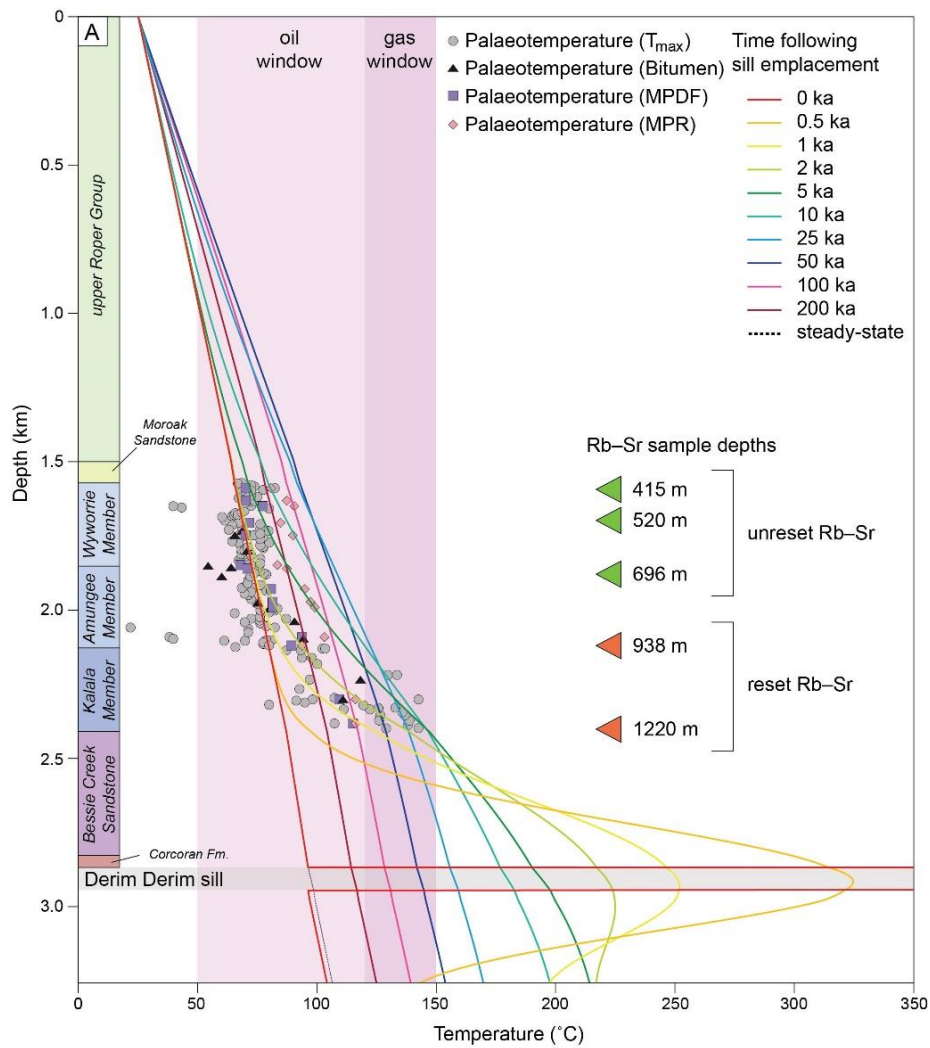


**Figure 3.9.** (A) One-dimensional thermal model for sill intrusion of 75 m thickness within the Atree 2 well depicting time steps following emplacement at 0 ka. Sill intrusion and Rb–Sr sample depths have been normalised to palaeodepths with 1.5 km of additional Mesoproterozoic sediments (Hall et al., 2021). Palaeotemperature estimates from  $VR_{CALC}$  data from the Atree 2 well have been included for comparison to modelled temperatures. B. Time-temperature profile for sample intervals within the Atree 2 well following intrusions of a sill of 75 m thick.

### 3.6 Conclusions

We show that the Velkerri Formation shales intersected by the Atree 2 well preserve evidence of an elevated Mesoproterozoic thermal gradient through an ~800 m thick section away from the intrusion of a Derim Derim Dolerite sill (Fig. 3.3, 3.4, and 3.9). *In situ* Rb–Sr isotopic ages from the Wyworrie and Amungee Members above this hydrothermal aureole yielded ages (Fig. 3.6 and 3.8) within error of their depositional age (Kendall et al., 2009). In addition, unaltered trace element compositions (Fig. 3.7) and petrographic relationships indicate that the shales preserve an early-diagenetic origin (Fig. 3.5 and Supplementary Material). However, the older Kalala Member that lies within the hydrothermal aureole yielded younger Rb–Sr ages (Fig. 3.6 and 3.8) consistent with the age of the Derim Derim Dolerite (Bodorkos et al., 2022, Ahmad and Munson, 2013, Nixon et al., 2021, Yang et al., 2020). Samples from this subset also recorded perturbed trace element signatures (Fig. 3.7) as well as fissile, foliated, and crystalline illite morphologies (Fig. 3.5 and Supplementary Material). This interval corresponds with disturbed thermal maturity indicators (Fig. 3.2, 3.3, and 3.4), suggesting that the Rb–Sr system is stable up to the maturation oil window and reset when the kerogen is overmature. Thermal modelling of the Derim Derim Dolerite suggests that a 75 m thick intrusion at the base of the Atree 2 well would have significantly elevated temperatures within 800 m of the sill, driving kerogen into the gas window, mobilising trace elements and resetting the Rb–Sr isotopic system in the Kalala Member.

In conclusion, we show that the *in situ* Rb–Sr dating of the Velkerri Formation combined with common hydrocarbon maturity proxies can help reveal the thermochronological history of Proterozoic argillaceous rocks. When used in tandem, these methods can constrain the age of deposition as well as subsequent secondary, late-stage geological events. Importantly, we demonstrate that this technique can aid sedimentary-hosted resource exploration, as hydrothermal overprints can be identified and dated as previously demonstrated in Subarkah et al. (2021). Specifically, for hydrocarbon exploration, we show that the thermo-kinetic parameters of shale-hosted Rb–Sr isotopic system in hydrothermal settings can coincide with the maturation of kerogen into the gas window (Dodson, 1973, Espitalié, 1986, Kubler, 1967).

### 3.7 Acknowledgments


This work was supported by the Australian Research Council Projects LP160101353 and LP200301457 with Santos Ltd, Empire Energy Group Ltd, Northern Territory Geological Survey, Teck Resources, BHP, and Origin as partners. The initial development and validation of *in situ* Rb–Sr dating technique at the University of Adelaide was also supported by Agilent Technologies Australia Ltd. This manuscript forms MinEx CRC contribution #2022/60. Aoife McFadden is thanked for their assistance in the MLA mapping of the samples in this study. Jarred Lloyd is thanked for his help in the laser data processing. Jarred Lloyd's code to process error correlations on LADR can be found in [https://github.com/jarredclloyd/PowerShell\\_LADR\\_errorcorrelation\\_workaround](https://github.com/jarredclloyd/PowerShell_LADR_errorcorrelation_workaround).

# **Chapter 4: Reconstructing the palaeoenvironments of Proterozoic packages from the greater McArthur Basin, Australia using a multi-proxy approach**

This chapter is unpublished and unsubmitted work written in manuscript style.



# Statement of Authorship

Title of Paper	Reconstructing the palaeoenvironments of Proterozoic packages from the greater McArthur Basin, Australia using a multi-proxy approach
Publication Status	<input type="checkbox"/> Published <input type="checkbox"/> Accepted for Publication <input checked="" type="checkbox"/> Submitted for Publication  Unpublished and Unsubmitted work written in manuscript style
Publication Details	Subarkah, D., Farkaš, J., Collins, A.S., Blades, M.L., Virgo, G., and Shao, Y. In Prep. Reconstructing the palaeoenvironments of Proterozoic packages from the greater McArthur Basin, Australia, using a multi-proxy approach.

## Principal Author

Name of Principal Author (Candidate)	Darwinaji Subarkah			
Contribution to the Paper	Method development, analysis, data reduction and interpretation, manuscript drafting.			
Overall percentage (%)	70			
Certification:	This paper reports on original research I conducted during the period of my Higher Degree by Research candidature and is not subject to any obligations or contractual agreements with a third party that would constrain its inclusion in this thesis. I am the primary author of this paper.			
Signature	<table border="1" style="width: 100%;"> <tr> <td style="width: 80%;"></td> <td style="width: 10%;">Date</td> <td style="width: 10%;">26/10/2022</td> </tr> </table>		Date	26/10/2022
	Date	26/10/2022		

## Co-Author Contributions

By signing the Statement of Authorship, each author certifies that:

- i. the candidate's stated contribution to the publication is accurate (as detailed above);
- ii. permission is granted for the candidate to include the publication in the thesis; and
- iii. the sum of all co-author contributions is equal to 100% less the candidate's stated contribution.

Name of Co-Author	Juraj Farkaš			
Contribution to the Paper	Conceptualisation, method development, supervision, manuscript drafting			
Signature	<table border="1" style="width: 100%;"> <tr> <td style="width: 80%;"></td> <td style="width: 10%;">Date</td> <td style="width: 10%;">28/10/2022</td> </tr> </table>		Date	28/10/2022
	Date	28/10/2022		

Name of Co-Author	Alan S. Collins			
Contribution to the Paper	Funding, supervision, manuscript drafting			
Signature	<table border="1" style="width: 100%;"> <tr> <td style="width: 80%;"></td> <td style="width: 10%;">Date</td> <td style="width: 10%;">28/10/2022</td> </tr> </table>		Date	28/10/2022
	Date	28/10/2022		

Name of Co-Author	Morgan L. Blades		
Contribution to the Paper	Supervision, data collection, manuscript drafting		
Signature		Date	28/10/2022
Name of Co-Author	Georgina Virgo		
Contribution to the Paper	Data interpretation, manuscript drafting		
Signature		Date	26/10/2022
Name of Co-Author	Yuxiao Shao		
Contribution to the Paper	Method development, manuscript drafting		
Signature		Date	28/10/2022

## 4.1 Abstract

Appreciable amounts of free oxygen ( $O_2$ ) in the Earth's surface environments first occurred between 2.4 to 2.1 billion years ago, in a turning point known as the Great Oxidation Event (GOE). The step-wise increase and fall in atmospheric  $O_2$  is intrinsically linked to the emergence of complex life and the tectonic history of our planet. However, these complex relationships are poorly understood in the Proterozoic. As such, we look to constrain past biological productivity and basin water geochemistry of a major continental seaway during this interval by investigating the 1.75 – 1.60 Ga sedimentary packages of the greater McArthur Basin in northern Australia. Furthermore,  $\delta^{18}O$ ,  $\delta^{13}C_{carb}$  and  $^{87}Sr/^{86}Sr$  isotopes were analysed and used as proxies to highlight post-depositional alteration, the dissolved inorganic carbon pool, and relative input between continental and marine/hydrothermal sources into the basin system, respectively. Importantly, our study also provides the first attempt to combine these proxies with the novel stable  $\delta^{88/86}Sr$  tracer for Proterozoic sedimentary packages.

Several alteration proxies from our samples such as  $\delta^{18}O$ , Mn/Sr, Sm/Nd, and La/Sm ratios indicate that the rocks analysed in this study have not experienced significant post-depositional secondary perturbations and are likely to record primary palaeoseawater signatures. This is further corroborated by the consistent trends in C and Sr isotopic data from spatially distant wells, thus presumably recording basin-scale trends. Notably, shifts in geochemical signatures also closely mirror changes in relative sea level, further suggesting the unaltered nature of these rocks.

Bioproductivity proxies from these packages such as total organic carbon (TOC) content, as well as Ba, and P enrichments display strong relationships with redox-sensitive trace elements; namely cerium, vanadium, and molybdenum. The changes in these geochemical signatures also closely mirror the regional transgressive-regressive cycles in the basin system. In addition, heavier  $\delta^{13}C_{carb}$  values here also coincide with more marine-like  $^{87}Sr/^{86}Sr$  signatures, and more positive  $\delta^{88/86}Sr$  data. These patterns also occur with prominent negative Ce anomalies, and by inference, more oxic redox conditions. Consequently, we suggest that increased biological productivity demonstrated by  $\delta^{13}C_{carb}$  were driven by more mafic inputs and increase in marine influence, evinced by the radiogenic and stable Sr isotopes. Input from hydrothermal activity are commonly associated with more marine environments, introducing an increasingly mantle-like source of nutrients. Alternatively, such nutrients can also be derived from an influx of oxygenated marine waters flooding the previously restricted domains of the basin system. In contrast, restricted basin conditions occur during relatively lower sea-levels. These episodes would likely be sourcing more felsic, continental, and relatively nutrient-poor river runoff. Such environments could limit biological productivity of photosynthetic organisms and hinder oxygen production. Overall, results from this study highlight how heterogeneous the oceans and continental seaways were during the Proterozoic. Consequently, generalised interpretations for the global biogeochemical system during this interval should be treated with caution.

## 4.2 Introduction

The Proterozoic is usually associated with a period of general stability within the Earth system. The eon is marked by relatively low atmospheric oxygen levels, (Lyons et al., 2014, Planavsky et al., 2014, Reinhard et al., 2013, Stüeken et al., 2016), a constant and warm climate inferred by an absence of glacial deposits (Kasting and Ono, 2006), as well as anoxic deep oceans (Scott et al., 2008, Holland, 2006). Consequently, this interval makes up the core of what previous investigators unfortunately entitled the ‘boring billion’ ca. 1.8 – 0.8 Ga (Buick et al., 1995). However, this eon of supposed biogeochemical constancy was also the backdrop for several key geological events in Earth’s history. These includes a series of worldwide orogenic events between ca. 1.8 – 1.3 Ga that involved the duration of the Nuna/Columbia supercontinent (Furlanetto et al., 2016, Gibson et al., 2018, Kirscher et al., 2020, Pisarevsky et al., 2014, Pourteau et al., 2018, Spence et al., 2021). Furthermore, key biological events such as the emergence and diversification of eukaryotes also occurred during this period (Bengtson et al., 2017, Butterfield, 2015, Katz, 2012, Love and Zumberge, 2021, Planavsky et al., 2015b, Sperling et al., 2022).

Importantly, a number of recent studies have suggested that atmospheric oxygen levels may have fluctuated variably during the Proterozoic (Bellefroid et al., 2018, Mukherjee and Large, 2016, Zhang et al., 2018a). This is contrary to the popular believe that such systems were stagnant during the era (Buick et al., 1995, Lyons et al., 2014, Reinhard et al., 2013). Furthermore, new investigations have also proposed that geographically distant sedimentary basins throughout the Proterozoic accommodated periods of deep oxidic waters within them. Both Sperling et al. (2014) and Zhang et al. (2016) provided evidence that ca. 1.4 Ga bottom basinal waters had enough dissolved oxygen for animal respiration in locations now found in parts of Russia and North China, respectively. If true, these results would have significant implications on the timing and spatial distribution of oxygen in Proterozoic marine systems. Constraints on atmospheric oxygen through this era are still poorly understood, as estimates vary in orders of magnitude between 0.1–10% of the present atmospheric level (Canfield et al., 2018, Crockford et al., 2018, Daines et al., 2017, Liu et al., 2015, Lyons et al., 2021, Planavsky et al., 2014, Wang et al., 2022).

In order to try and better understand the apparent heterogeneity of redox conditions in the Palaeoproterozoic surface environments, we have undertaken a multi-proxy investigation of the Proterozoic marine sedimentary archives from the ca. 1.8–1.6 Ga Tawallah and McArthur Groups within the greater McArthur Basin, northern Australia (Ahmad and Munson, 2013, Rawlings, 1999). The basin overlies the North Australian Craton (NAC) and records a billion years history of the Earth’s surface environment (Abbott and Sweet, 2000). The sedimentary rocks within the system are exceptionally thick and are relatively unmetamorphosed, which is important for preserving primary palaeo-seawater signature (Ahmad and Munson, 2013). Notably, the greater McArthur Basin has historically been used as a key section for unravelling biogeochemical cycles in the Proterozoic (Cox et al., 2022, Cox et al., 2016b, Cox et al., 2019, Jarrett et al., 2019, Johnston et al., 2008, Kunzmann et al., 2019, Mukherjee and Large, 2016, Mukherjee et al., 2019, Mukherjee et al., 2018, Shen et al., 2002, Shen et al., 2003, Spinks et al., 2016a, Vinnichenko et al., 2020, Yang et al., 2020). We build upon this foundation using a combination of organic and inorganic geochemical

data, as well as traditional ( $\delta^{13}\text{C}$  and  $^{87}\text{Sr}/^{86}\text{Sr}$ ) and novel ( $\delta^{88/86}\text{Sr}$ ) isotopic tracers. The geochemical proxies used here can help determine the past biological productivity, water-column oxygenation conditions and changes in depositional settings for these Proterozoic units (Farquhar et al., 2011, Laakso and Schrag, 2017, Pedersen and Calvert, 1990, Piper and Perkins, 2004, Tribovillard et al., 2006). The multi-proxy approach undertaken in this study and their possible consequences are briefly described here.

#### **4.2.1 Organic and inorganic geochemical evidence for changes in palaeoproductivity and palaeoredox conditions**

High total organic carbon (TOC) content in marine sediments can provide an insight for past biological productivity (Canfield, 1994, Pedersen and Calvert, 1990, Schoepfer et al., 2015). In addition, barium (Ba) and phosphorus (P) are elemental proxies that are also commonly used to constrain palaeoproductivity in marine environments (Algeo and Ingall, 2007, Brumsack, 1989, Calvert and Pedersen, 2007, Mackenzie et al., 1993, Schoepfer et al., 2015, Trappe, 2006, Tribovillard et al., 2006, Von Breyman et al., 1992). Authigenic barite forms in water columns due to biologically induced processes (Tribovillard et al., 2006). Live microorganisms incorporate Ba and releases it during decay, where it may precipitate as barite in waters which Ba-sulfate reaches its saturation point (Dehairs et al., 1980, Dehairs et al., 1991, Dymond et al., 1992, Falkner et al., 1993). As a result, relationships between authigenic barite and organic matter have historically been interpreted to reflect bio-activity and thus primary productivity in ancient basins (Francois et al., 1995, McManus et al., 1999, Sanchez-Vidal et al., 2005). Furthermore, P is essential to all life forms on our planet as it is critical for any metabolic processes. Its increase in abundance is linked to an increase in organic matter and high productivity (Benitez-Nelson, 2000, Filippelli, 1997, Föllmi, 1996, Ingall and Jahnke, 1997, Tribovillard et al., 2006). The authigenic precipitation of P in the form of phosphates, such as apatite, is conditioned by several factors such as pH, redox, bacterial activity and the availability of dissolved Ca and P (Benitez-Nelson, 2000, Filippelli, 1997, Ingall et al., 1993, Schoepfer et al., 2015).

However, these proxies can be susceptible to several different factors. These vary from an increase in nutrient fluxes (Condie et al., 2001, Meyer and Kump, 2008), clastic to biogenic sedimentation rates (Müller and Suess, 1979, Tyson, 2005), as well as preservation of organic matter (Canfield, 1994, Ingall et al., 1993, Müller and Suess, 1979, Tyson, 2005). Basin-scale anoxia or euxinia can also reduce the oxidation of organic matter and thus induce its preservation in marine sedimentary rocks (Hartnett et al., 1998, Kennedy et al., 2002, Mayer, 1994). Exposing organic matter to  $\text{H}_2\text{S}$  in oxygen-poor pore waters can form compounds that are more resistant to deterioration (Tribovillard et al., 2004, Zonneveld et al., 2010). Consequently, organic matter is better preserved during periods of water column euxinia as opposed to more oxic conditions. Additionally, Ba has also been shown to fluctuate under different redox conditions, as its reactivity can be linked to the availability of sulphate ions (Schoepfer et al., 2015). Barite may dissolve when reacted with anoxic pore waters (McManus et al., 1998, Torres et al., 1996, Von Breyman et al., 1992), which could limit the use of Ba as a palaeoproductivity proxy in the Proterozoic, where marine environments were considerably depleted in oxygen (Wei et al., 2021). The enrichment of P may also occur in low-productivity areas where they are affected by the redox cycling of

iron, as P may be adsorbed onto Fe oxyhydroxide compounds (Jarvis et al., 1994, Kraal et al., 2015, Piper and Perkins, 2004). As a result, P accumulated in reducing conditions can potentially diffuse back into the overlying water column (Diaz et al., 2008, Ingall et al., 2005). Nevertheless, the agreement between these three indicators can be used to confirm that they all confidently reflect changes in past biological productivity as opposed to other processes (Schoepfer et al., 2015).

To address these intricate relationships, we have used a number of redox-sensitive trace elements (TEs) to assess the transition between oxic, anoxic and euxinic conditions of the water-column during the deposition of the Tawallah and McArthur Group units (Algeo and Maynard, 2004, Cheng et al., 2015, Cox et al., 2016b, Li et al., 2015, Lyons et al., 2009, Lyons et al., 2003, Reinhard et al., 2013, Scott et al., 2008, Sperling et al., 2014, Spinks et al., 2016a, Tribovillard et al., 2006, Zhang et al., 2018a). For example, molybdenum (Mo) is a common elemental redox proxy and is the most abundant trace metal in the modern ocean (Millero, 1996, Wright, 1995). Mo concentrations in shales are enriched under anoxic conditions when it is incorporated during the deposition and preservation of organo-metallic complexes to form thiomolybdates (Helz et al., 1996, Scott and Lyons, 2012, Vorlicek and Helz, 2002) or during euxinia when it is sequestered in authigenic sulphides (Berrang and Grill, 1974, Morse and Luther III, 1999). Vanadium (V) is also abundant in the modern ocean water (Millero, 1996, Wright, 1995). Under oxygen-poor water columns  $V^{5+}$  is reduced to  $V^{4+}$  by organic compounds and hydrogen sulphide (Breit and Wanty, 1991), enriching the element at the oxic-anoxic and anoxic-euxinic boundaries and producing a similar relationship with TOC to that of Mo (Algeo and Maynard, 2004, Tribovillard et al., 2006). Further reduction of  $V^{4+}$  to  $V^{3+}$  also occurs during high sulphide conditions, resulting in a hyper enrichment of V (Breit and Wanty, 1991, Wanty and Goldhaber, 1992). In short, Mo and V shows a strong linear covariation with TOC under anoxia as they form chemical bonds with organic matter under oxygen-poor settings. However, both elements undergo nonlinear enrichment during euxinic conditions when sulphides become a major sink, and/or when the element undergoes further reduction to its lowest valence state (Algeo and Maynard, 2004, Tribovillard et al., 2006). On the other hand, under relatively more oxic conditions, both TEs are deposited in the detrital phase and will display no covariation with TOC (Algeo and Maynard, 2004, Tribovillard et al., 2006).

Cerium is another redox-sensitive trace element, and its concentrations in marine sediments has also widely been applied to interpret palaeoredox conditions (Bau and Dulski, 1996, Cullers, 2002, German and Elderfield, 1990, German et al., 1991). Ce exists in two different oxidation states, as  $Ce^{+3}$  where it is more soluble and as  $Ce^{+4}$  where it is insoluble. In oxygen-rich environments,  $Ce^{+3}$  is oxidised to  $Ce^{+4}$  and is incorporated onto the surface of ferromanganese oxides, removing it from the residual seawater (Elderfield and Greaves, 1981, German and Elderfield, 1990, Nath et al., 1994). Therefore, the depletion or abundance of Ce (i.e. the Ce anomaly) relative to its neighbouring REEs should reflect the redox changes or state of the water column during the deposition or accumulation of a sediment. A negative Ce anomaly is characteristic of well-oxygenated oceans but can vary in and between basins (Cullers, 2002, De Baar, 1991, De Baar et al., 1985). Furthermore, stratified water columns can develop negative Ce anomaly in oxic surface waters that

evolves into more positive values (equal to or more than 1) in deeper, anoxic waters (German et al., 1991). In particular, positive Ce anomalies can be found developing beneath the Mn redoxcline as Mn-oxides/oxyhydroxides are the main carrier of Ce in marine systems (Bau et al., 1997, de Baar et al., 1988, De Baar, 1991, Ohta and Kawabe, 2001). The Ce and Eu anomalies in this study were calculated following Lawrence and Kamber (2006). Overall, the variability in these redox-sensitive elements may provide insights into how heterogenetic oxygen-levels were during the formation of the Proterozoic Tawallah and McArthur Groups.

#### **4.2.2 Isotopic signatures for determining changes in palaeoseawater chemistry**

Further to the changes in organic and inorganic geochemistry of these units, we have also investigated their isotopic signatures. It has been shown that the  $\delta^{13}\text{C}_{\text{carb}}$  isotope values of unaltered marine carbonates reflects the composition of the dissolved inorganic carbon (DIC) pool for that coeval water-column (Knoll et al., 1986, Schidlowski, 1988). Primary productivity plays a critical role in the DIC pool, as biological processes like photosynthesis preferentially assimilate lighter  $^{12}\text{C}$ , leaving the DIC reservoir isotopically heavier (Kump and Arthur, 1999). On the other hand, remineralization of organic matter can increase the input of  $^{12}\text{C}$  into the water column (Sarmiento et al., 2007), shifting the DIC reservoir to isotopically lighter values. As a result, these processes can induce a variability in C isotope signature across water-depths. However, given that the residence time of C in oceans is orders of magnitude longer than the typical mixing time of seawater, contemporary marine carbonates that precipitated in separate locations are likely to retain still retain the same  $\delta^{13}\text{C}_{\text{carb}}$  isotope composition (Kump and Arthur, 1999, Shields and Veizer, 2002, Halverson et al., 2009). This means that, temporal shifts in  $\delta^{13}\text{C}_{\text{carb}}$  are a useful chemostratigraphic tool in a local, regional, and global scale through deep time. It should be noted that significant and systematic excursions throughout the stratigraphy are more important than absolute values when interpreting carbon isotope chemostratigraphy (Kump and Arthur, 1999, Shields and Veizer, 2002). Consequently, the long-term secular evolution of  $\delta^{13}\text{C}_{\text{carb}}$  can be used to record past changes in the global C cycle (Hayes et al., 1999).

The Sr composition of marine carbonates that precipitate from the global ocean or coeval basin waters can also be used for chemostratigraphic applications (Chen et al., 2022, DePaolo and Ingram, 1985, Kuznetsov et al., 2018, Veizer et al., 1999). Radiogenic  $^{87}\text{Sr}/^{86}\text{Sr}$  isotope excursions in marine carbonates have widely been applied as a powerful tool to track provenance, relative inputs between hydrothermal and riverine sources, as well as silicate weathering fluxes from continental erosion (Banner, 2004, Kuznetsov et al., 2018, McLennan et al., 1990). Shifts in the palaeoseawater  $^{87}\text{Sr}/^{86}\text{Sr}$  isotopic record of often coincide with the break up and amalgamation of super continents as well as periods of extensive glaciations (Chen et al., 2022, Halverson et al., 2010, Kuznetsov et al., 2018, Och and Shields-Zhou, 2012, Prokoph et al., 2004). Generally, more radiogenic  $^{87}\text{Sr}/^{86}\text{Sr}$  signatures of palaeoseawater correlate with an increase in orogenesis derived from super-continent amalgamation and continental-scale collision margins (Och and Shields-Zhou, 2012). Conversely, a decrease in marine  $^{87}\text{Sr}/^{86}\text{Sr}$  values are often associated with an influx of mantle/oceanic crust derived Sr sourced from rifts and mid-ocean ridges related to super-continent break-up (Semikhatov et al., 2002). An increase in the abundance of large igneous

provinces and activation of mantle plumes can also lower  $^{87}\text{Sr}/^{86}\text{Sr}$  values of the palaeoseawater (Prokoph et al., 2004).

However, the changes in marine  $^{87}\text{Sr}/^{86}\text{Sr}$  isotopic ratios do not track fluctuations linked to the carbonate cycle or the removal of Sr via the deposition of  $\text{CaCO}_3$  (Krabbenhöft et al., 2010, Vollstaedt et al., 2014). Instead, this process of marine carbonate formation versus dissolution can be tracked by mass-dependent fractionations of stable  $\delta^{88/86}\text{Sr}$ . These values change according to the different inputs and outputs in the ocean's Sr budget (Shao et al., 2021, Vollstaedt et al., 2014). The formation of marine carbonates preferentially takes up lighter Sr isotopes, with an average  $\delta^{88/86}\text{Sr}$  offset of -0.18‰ to -0.21‰ (Shao et al., 2021, Vollstaedt et al., 2014). Consequently, this reaction drives the palaeoseawater isotopically heavier by the same magnitude. Furthermore, igneous differentiation can also result in Sr isotopic fractionation. This reaction can result in felsic rocks having lighter  $\delta^{88/86}\text{Sr}$  ratios compared to mafic rocks (Amsellem et al., 2018, Charlier et al., 2012). As a result, riverine or continental weathering input of Sr into the ocean will have higher  $^{87}\text{Sr}/^{86}\text{Sr}$  ratios and lower  $\delta^{88/86}\text{Sr}$  values (Charlier et al., 2012, de Souza et al., 2010, Krabbenhöft et al., 2010, Vollstaedt et al., 2014). On the other hand, the flux of more mafic materials will have a characteristically lower  $^{87}\text{Sr}/^{86}\text{Sr}$  ratio but higher  $\delta^{88/86}\text{Sr}$  values (Amsellem et al., 2018, Charlier et al., 2012).

Overall, the combination of the trace element and isotopic record from this study will give us new insights on what processes can influence the chemistry of the palaeoseawater during the Proterozoic. The Tawallah and McArthur Group shales and carbonates here were sampled from wells MCDD003, and MCDD005 (Fig. 1). Samples were collected at 2 metre intervals depending on key lithological boundaries, organic-rich zones, and proximity to any obvious late-stage secondary alteration or veining.

### 4.3 Geological Background

The greater McArthur Basin is an informal name for a supracontinental Palaeo-to-Mesoproterozoic multi-phase sedimentary system extending over 180,000 km<sup>2</sup> of northern Australia (Ahmad and Munson, 2013, Close, 2014). This system includes rocks of the McArthur Basin in the northeast, Birrindudu Basin in the northwest and the Tomkinson Province in the south (Close, 2014). These individual basins are interpreted to be connected within the subsurface based on geophysical and drill core data (Ahmad and Munson, 2013). The greater McArthur Basin overlies Archean and Palaeoproterozoic basement rocks of the North Australian Craton (NAC) and unconformably underlie Neoproterozoic and Cambrian cover (Fig. 4.1).

Palaeomagnetic results from northern Australia and northern China suggests that these continents bordered each other throughout much of the Proterozoic (Kirscher et al., 2020, Pisarevsky et al., 2014, Zhang et al., 2012). The Yanshan Basin of the North China Craton has also been proposed to be contiguous with the region at the time of deposition (Nixon et al., 2021, Zhang et al., 2021). This is further supported by similarities in lithostratigraphy, provenance sources, ca. 1.3 Ga igneous activity, biogeochemistry, astrochronological constraints and sediment-hosted mineralisation (Mitchell et al., 2020, Nixon et al., 2021, Wang et al., 2019, Yang et al., 2019, Zhang et al., 2021, Zhang et al., 2018b, Zhang et al.,



2017). In addition, further palaeomagnetic results suggest that the continent was likely adjacent to Laurentia after collision at ca. 1.6 Ga until at least 1.3 Ga (Kirscher et al., 2020, Medig et al., 2014, Pourceau et al., 2018, Volante et al., 2020). This continental amalgamation forms a core part of the supercontinent Nuna, which lasted for ca. 600 Mya until its breakup ca. 1.2 Ga (Ding et al., 2020, Kirscher et al., 2020, Pisarevsky et al., 2014).

The greater McArthur Basin have also attracted renewed interest due to hosting promising economic energy and mineral resources. Large and proven hydrocarbon reserves are widespread throughout its stratigraphy and across the depositional system (Delle Piane et al., 2020, George et al., 1994, Henson et al., 2020, Jackson et al., 1988, Jackson et al., 1986, Jarrett et al., 2022, Summons et al., 1988, Yang et al., 2020). The basin is also a part of a prominent base metal province in Australia, forming a portion of the Carpentaria Zinc Belt (Southgate, 2000). The most significant mineral exploration activity occurs where base metal Zn-Pb-Ag deposits are hosted within organic rich siltstone of otherwise carbonate dominated sequences (Eldridge et al., 1993, Gianfriddo et al., 2022, Large et al., 1998, Large et al., 2000, Large et al., 2001, Li et al., 2022, Smith and Croxford, 1975, Spinks et al., 2020, Spinks et al., 2016b, Williford et al., 2011). These prospects are focussed within the two oldest of the region's five coherent, basin-scale, lithologically distinct depositional packages—the Tawallah Group and the McArthur Group (Rawlings, 1999). The Wuraliwuntya Member and the Wollogorang Formation of the Tawallah Group as well as the Mallapunyah Formation and the Amelia Dolostone from the McArthur Group are the focus of this study (Fig. 4.1 inset).

#### **4.3.1 Tawallah Group**

The Tawallah Group (Fig. 4.1) is the oldest coherent sequence in the greater McArthur Basin and includes several correlated but spatially distant groups (Rawlings, 1999). The Tawallah Group occurs in the McArthur Basin *sensu stricto*, which crops out in a broad region along the north and northeast of the Northern Territory (Ahmad and Munson, 2013, Blaikie and Kunzmann, 2020). This group overlies basement rocks of the Scrutton Inlier, the Pine Creek Orogen, and the Murphy Province (Rawlings, 1999). U–Pb zircon dates of volcanic rocks throughout the succession chronologically constrain deposition of the group to between 1820–1708 Ma (Ahmad and Munson, 2013, Page and Sweet, 1998, Rawlings, 1999). Detailed description of the sequence stratigraphy and interpreted depositional environments of the upper Tawallah Group, that forms the focus of this study, can be found in Kunzmann et al. (2020). The Tawallah Group is the southern McArthur Basin representative of the Redbank Package, and is correlated with the Katharine River Group, the Donydji Group, and the Groote Eylandt Group elsewhere in the McArthur Basin (Rawlings, 1999).

The Wuraliwuntya Member of the Wunumantyalu Sandstone is the oldest sedimentary unit of the Tawallah Group sampled in this study (Rawlings, 1999). It consists of a medium-grained basal sandstone followed by alternating layers of dolostone and siltstone. This sequence is interpreted to have been deposited in a storm-dominated subtidal, shallow marine environment which occasional periods of aerial exposure (Ahmad and Munson, 2013). Although the depositional age of the Wuraliwuntya Member is poorly understood, the maximum and minimum ages are constrained by the underlying ca. 1780 Ma Seigal

Volcanics (Rawlings, 1999) and the overlying ca. 1730 Ma Wollogorang Formation (Page et al., 2000) respectively.

The overlying Wollogorang Formation (Fig. 4.1) is laterally extensive and is interpreted to have been deposited in an intra-continental, shallow-marine environment coarsening up into more clastic-dominated near-shore settings (Ahmad and Munson, 2013). The unit is made of primarily mudstone and carbonaceous shales with interbeds of dolomitic sandstones, stromatolitic dolostones, cherts and evaporates (Jackson et al., 1986, Spinks et al., 2016a). Facies analysis of the upper Tawallah Group suggests that these successions formed an epeiric platform spanning hundreds of kms, which was deepening eastwards (Kunzmann et al., 2020, Rawlings, 1999). The U–Pb ages of the Nyanantu Formation at the top of the group provides a minimum depositional age of  $1708 \pm 5$  Ma for the top of the Redbank Package (Page et al., 2000).

#### **4.3.2 McArthur Group**

The ca. 1670–1600 Ma McArthur Group unconformably overlies the Tawallah Group over most of the McArthur Basin (Fig. 4.1). It correlates with the Habgood, Balma, and Vizard Groups elsewhere in the McArthur Basin, forming the Glyde Package of the greater McArthur Basin (Rawlings, 1999). The intervening Goyder Package is only locally preserved (Rawlings, 1999). The Glyde Package mainly comprises of evaporitic carbonate, mudstone and sandstone up 5 km-thick (Ahmad and Munson, 2013). Compared to the sandier Tawallah Group, the younger McArthur Group encompasses more shore-platform dolomitic lithologies with abundant stromatolites and pyritic, organic-rich siltstones (Kunzmann et al., 2022, Winefield, 1999). Tuff layers are common and have been obtained from the central and upper sections of the Glyde Package, resulting in U–Pb ages of 1650–1600 Ma (Ahmad and Munson, 2013, Rawlings, 1999). Extended facies analysis and sequence stratigraphy of the McArthur Group can be found in Kunzmann et al. (2019) and Schmid (2015). The oldest unit of the McArthur Group sampled in this study is the Mallapunyah Formation of the Umbolooga Subgroup. It is mainly recessive, and consists of red-purple dolomitic and cross-bedded sands interbedded with stromatolitic dolostone with common chert nodules, ripples, desiccation cracks, gypsum, and halite casts towards the top formation (Kunzmann et al., 2019, Winefield, 1999). This succession is interpreted to have been deposited in a continental, shallow-marine or sabkha environment (Ahmad and Munson, 2013, Kunzmann et al., 2019, Schmid, 2015). This broad marginal marine setting continues into the overlying Amelia Dolostone which comprises of interbedded stromatolitic dolostone with local beds of siderite-bearing dololomite (Jackson et al., 1987, Kunzmann et al., 2019).

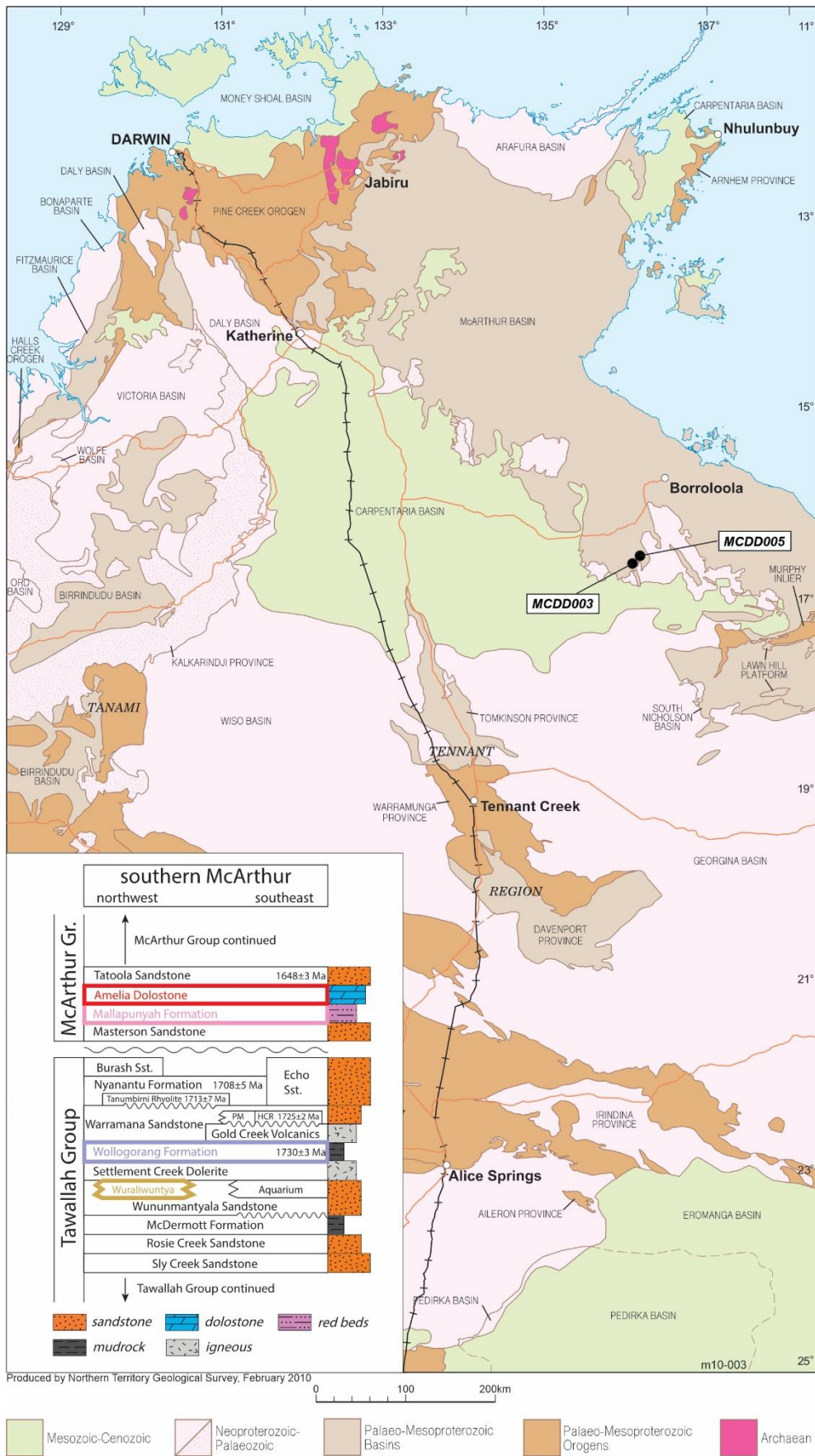


**Figure 4.1.** Simplified geological map of the greater McArthur Basin showing the location of the studied drill cores along with the generalised stratigraphy, lithology and geochronological constraints of the upper Tawallah Group and lower McArthur Groups from Page et al. (2000).

## 4.4 Methods

The methods and subsequent reference materials used in this study are summarised here and discussed further in the Supplementary Material (Subarkah, 2022a). Tawallah and McArthur Group shales and carbonates were sampled from wells MCDD003, and MCDD005 (Fig. 4.1). Samples were collected at 2 metre intervals depending on key lithological boundaries, organic-rich zones and proximity to any obvious late-stage secondary alteration. All of the data from the Amelia Dolostone are carbonate leachates while samples from the Wuraliwuntya Member, Wollogorang Formation, and Mallapunyah Formation are whole-rock geochemistry of organic shales and calcareous siltstones. Both wells are housed at the Northern Territory Geological Survey core facility in Darwin and their localities are provided within the Supplementary Material. Extensive descriptions of the sedimentary lithologies, features and characteristics of the formations as well as their interpreted depositional environments with their correlative units elsewhere in the region can be found in Kunzmann et al. (2020).

### 4.4.1 Carbonate geochemical analysis

The approach to determine elemental concentrations from carbonate rocks were adopted and modified from Kuznetsov et al. (2010) to minimise non-marine, secondary phases from the bulk sediment. Carbonates were micro-drilled along homogeneous bedding planes with the following rock powder washed with ammonium acetate to remove loosely bound cations. Further leaching followed using dilute ammonium acetate and acetic acid to extract the primary carbonate phase. The final solutions were used to determine elemental concentrations using an Agilent 8900 ICP-MS/MS operated in solution mode.

An aliquot of the sample solution prepared for elemental geochemistry of bulk carbonates were also measured for radiogenic and stable Sr isotopic analyses. Briefly, coupled  $^{87}\text{Sr}/^{86}\text{Sr}$  and  $\delta^{88/86}\text{Sr}$  analyses were performed on leached samples following a double-spiking approach developed at the Metal Isotope Group, University of Adelaide and described by Shao et al. (2018) and (2021). This was collected by thermal ionisation mass spectrometry (TIMS) Phoenix Isotopx instrument at the University of Adelaide. To determine  $\delta^{88/86}\text{Sr}$  values in carbonates, two aliquots (i.e., spiked and unspiked) were taken from a sample solution. One aliquot was spiked using an  $^{87}\text{Sr}$ - $^{84}\text{Sr}$  double spike solution, and the resulting Sr fraction of each sample was purified via ion chromatography using Sr-Spec micro-columns. Pure Sr fractions were then loaded on single non-zone-refined rhenium filaments before the TIMS analysis. For radiogenic  $^{87}\text{Sr}/^{86}\text{Sr}$  ratios, the unspiked aliquots were purified using the same approach and re-run on the same instrument using a multi-dynamic peak-hopping method (Shao et al., 2021). This approach allows for a typical  $^{88}\text{Sr}$  beam of about 6 volts to be attained and the following isotopic ratios were collected:  $^{87}\text{Sr}/^{86}\text{Sr}$ ,  $^{86}\text{Sr}/^{88}\text{Sr}$  and  $^{84}\text{Sr}/^{86}\text{Sr}$ . Calculation of corrected  $^{87}\text{Sr}/^{86}\text{Sr}$  ratios were based on internal normalisation of instrumental mass-dependent fractionation effects and assuming  $^{86}\text{Sr}/^{88}\text{Sr}$  value of 0.1194 as a normalising ratio (Nier, 1938). The standard reference materials 987 and JCP-1 were used for this procedure (Balcaen et al., 2005, Krabbenhöft et al., 2009, Shao et al., 2021).

Isotopic analysis of  $\delta^{13}\text{C}$  and  $\delta^{18}\text{O}$  in carbonates followed Spötl and Vennemann (2003). In short, micro-drilled rock powder samples were placed into glass vials and purged with

phosphoric acid and injected with helium. The ratio of the isotopic composition from the resultant gas was measured using a Dual Inlet Isotope Ratio Mass Spectrometer (DI-IRMS) with attached Fissions Isocarb Carbonate Preparation System at the University of Adelaide. These isotopic ratios were expressed as relative to Pee Dee Belemnite values using internal working standards.

#### 4.4.2 Shale geochemical analysis

Shale intervals were washed to be free of surface contamination and finely powdered using a tungsten carbide mill. Organic geochemistry were collected via pyrolysis using raw sample powder by a Weatherford's Source Rock Analyser following the method described by Cox et al. (2019). In short, the pyrolysis oven was first held at 300°C for 5 minutes and ramped at 25°C per minute up to 650°C. Subsequently the oven was reduced to 220°C and held for 5 minutes with the carrier gas converted to inert air (CO & CO<sub>2</sub> free) and purged, ramped at maximum heating to 580°C and held for 20 minutes. The flame ionisation detector (FID) was calibrated by running Weatherford Laboratories Instruments Division Standard 533. The IR Analysers were calibrated against standard gas with known concentration of CO<sub>2</sub> and CO. An analysis blank was run as 'blank' mode with the sample batch and the blank data was automatically subtracted from all analyses. An external check standard was also run first with each batch to ensure the instrument status with additional check standards every 10 samples. The results were processed with Optkin 3.0 software, where peak heights and geochemical indices such as total organic carbon (TOC), Oxygen Index (OI), Hydrogen Index (HI), and Production Index (PI) are automatically calculated. The resulting data were then screened using the criteria defined by Hall et al. (2016). Major, trace, and rare earth element (REE) analyses were analysed at Bureau Veritas using an Agilent 7900 Series ICP-MS. Laboratory investigations were performed on 0.15g of rock powder that were dissolved using a multi-step acid digestion (HNO<sub>3</sub>, HClO<sub>4</sub>, HNO<sub>3</sub>, and HF) following Cox et al. (2016b).

#### 4.5 Results

The reference materials JCP-1 and SRM 987 were used as isotopic standards for this study and can be found in Subarkah (2022a). Three runs of JCP-1 yielded a mean value of  $0.190 \pm 0.012$  and  $0.709157 \pm 0.000005$  for stable  $\delta^{88/86}\text{Sr}$  and radiogenic  $^{87}\text{Sr}/^{86}\text{Sr}$  isotopes respectively. This is accurate to the published values ( $\delta^{88/86}\text{Sr}$ :  $0.197 \pm 0.013$ ,  $^{87}\text{Sr}/^{86}\text{Sr}$ :  $0.709164 \pm 0.000006$ ) of the standard (Krabbenhöft et al., 2009). The standard SRM 987 gave a mean  $\delta^{88/86}\text{Sr}$  value of  $0.028 \pm 0.050$  and  $^{87}\text{Sr}/^{86}\text{Sr}$  value of  $0.710253 \pm 0.000003$ . This is also in good agreement with their respective data ( $\delta^{88/86}\text{Sr}$ :  $0.012 \pm 0.044$ ,  $^{87}\text{Sr}/^{86}\text{Sr}$ :  $0.710250 \pm 0.000010$ ) found in literature (Balcaen et al., 2005, Krabbenhöft et al., 2009).

Trace-element and organic carbon content of both wells are displayed in Fig 4.4 and 4.5. Redox-sensitive Ce anomalies in both wells range between 0.8 to 1.2. Samples from well MCDD005 show a larger variability in Mo/Al and V/Al contents, often differing in orders of magnitude from 0.01 to 100. On the other hand, Mo/Al and V/Al ratios in well MCDD003 is constrained to a maximum of 9 and 54, respectively. Notably, shale samples in MCDD003 can contain TOC content of more than 8 wt. %. This is significantly higher than that in MCDD005, where organic-rich shales has a maximum TOC content of 4 wt. % instead. Ba/Al ratios of MCDD005 also differs relatively in MCDD005, with a minimum of 0.01. On the

other hand, Ba/Al ratios in MCDD003 is consistently above 10 up stratigraphy. However, P/Al ratios for both wells are constrained to be between 0.001 and 1.

Isotopic data for the Amelia Dolostone carbonate samples are plotted in Fig. 4.3. Here, the lower sections of the Amelia Dolostone has  $^{87}\text{Sr}/^{86}\text{Sr}$  values most like the palaeoseawater signature ca. 1.65 Ga (Kuznetsov et al., 2018) and trends towards higher values up stratigraphy. This trend is broadly inversely mirrored by the  $\delta^{88/86}\text{Sr}$  ratios, with a general decreasing pattern from 0.5 to 0.0. This negative pattern can also be found in the  $\delta^{13}\text{C}_{\text{carb}}$  data, with an approximately -2.5 ‰ excursion up stratigraphy. The  $\delta^{18}\text{O}_{\text{carb}}$  data for the Amelia Dolostone range between -10 to -2.

#### **4.5.1 Screening of non-authigenic signals in the whole-rock chemistry of the Tawallah and McArthur Group**

Ce and Eu anomalies were calculated from REE data following Lawrence and Kamber (2006) as well as Liu et al. (2021). However, they may have been influenced by post-depositional processes after the formation of these samples. As such, geochemical overprinting and subsequent alteration of samples here were assessed through their Sm/Nd ratios, as Nd is preferentially lost relative to Sm during diagenesis (Awwiller and Mack, 1991, Mack and Awwiller, 1990). All samples show no correlation between Sm/Nd ratios and trace element proxies used in this study (Fig. 4.2C), suggesting that the geochemistry of these samples were not affected by secondary processes. LREE mobility is also commonly affected during diagenesis in black shales (Lev et al., 1999). However, they show a weak and negligible relationship with the geochemical indicators used in this study (Fig. 4.2D), further indicating that the trace elements within these samples have not been mobilised after deposition. Overall, these chemical screening indicators suggest that shale samples analysed here are likely to preserve their primary compositions and have not been altered by later events.

The elemental composition of the Amelia Dolostone carbonate samples from MCDD005 were further screened for possible alteration as they are investigated for isotopic analyses. The Mn/Sr ratio has widely been applied as an indicator of post-depositional alteration of marine carbonates by diagenetic or meteoric fluids, as Sr is expelled and Mn is incorporated during meteoric diagenesis of marine carbonates (Brand and Veizer, 1980). Consequently, low Mn/Sr ratios are commonly associated with well-preserved carbonate rocks and vice versa. Although the samples in this study have relatively high Mn/Sr ratios (mean = 29.3), they do not display any significant correlations with other geochemical proxies used (Fig. 4.2B). This may indicate that the elevated Mn or depleted Sr content in these samples may not directly reflect any alteration events. Instead, such elevated Mn content can be linked to the relatively reduced redox state of the Proterozoic water column or sediment-seawater interface, where Mn would be more readily available to be incorporated into marine carbonates under the redox cline (Huang et al., 2011, van Smeerdijk Hood and Wallace, 2015).

Another possible non-authigenic input that may influence the trace element budget of these samples are detrital components within them. As a result, Zirconium (Zr) is commonly used as a discriminant or index element to fingerprint increasing detritus in marine sedimentary rocks. This is important, detrital zircons are enriched in trace elements and can dominate

the REE budget of samples. Strong covariations between Zr and REEs in shales and carbonates have been shown to suggest significant input of trace elements from the detrital mineral (Garcia et al., 1991, Goodarzi et al., 2019, Schier et al., 2021, Tardy, 1975, Tostevin et al., 2016). In this study (Fig. 4.2E), Zr content displays a statistically weak and negligible relationship with Eu anomalies and V concentrations ( $R^2$  value = 0.033 and 0.17 respectively). Nevertheless, they show no correlations with any other REEY anomalies or trace and rare earth elemental concentrations in all of the samples studied. Overall, detrital contamination seems to not play a critical role in the results observed in this study.

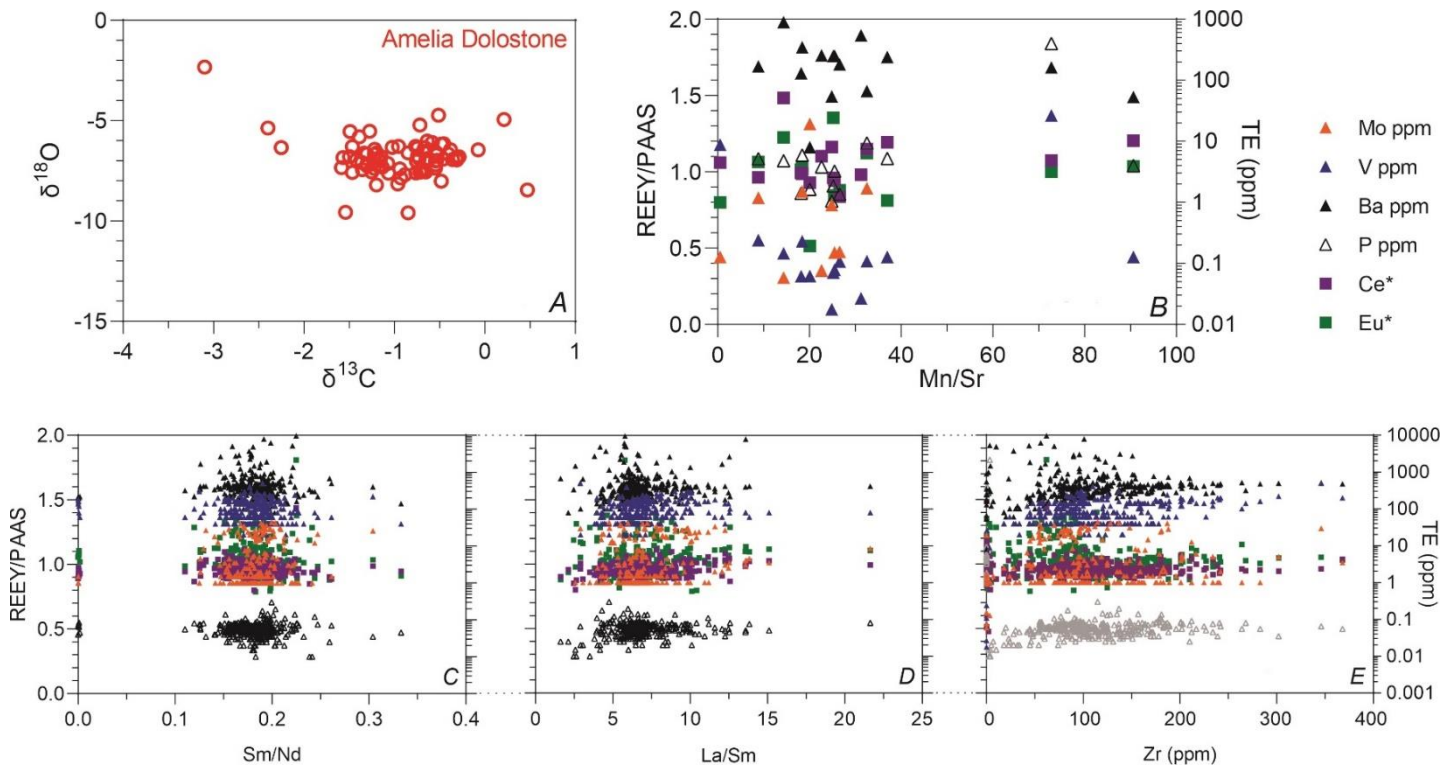
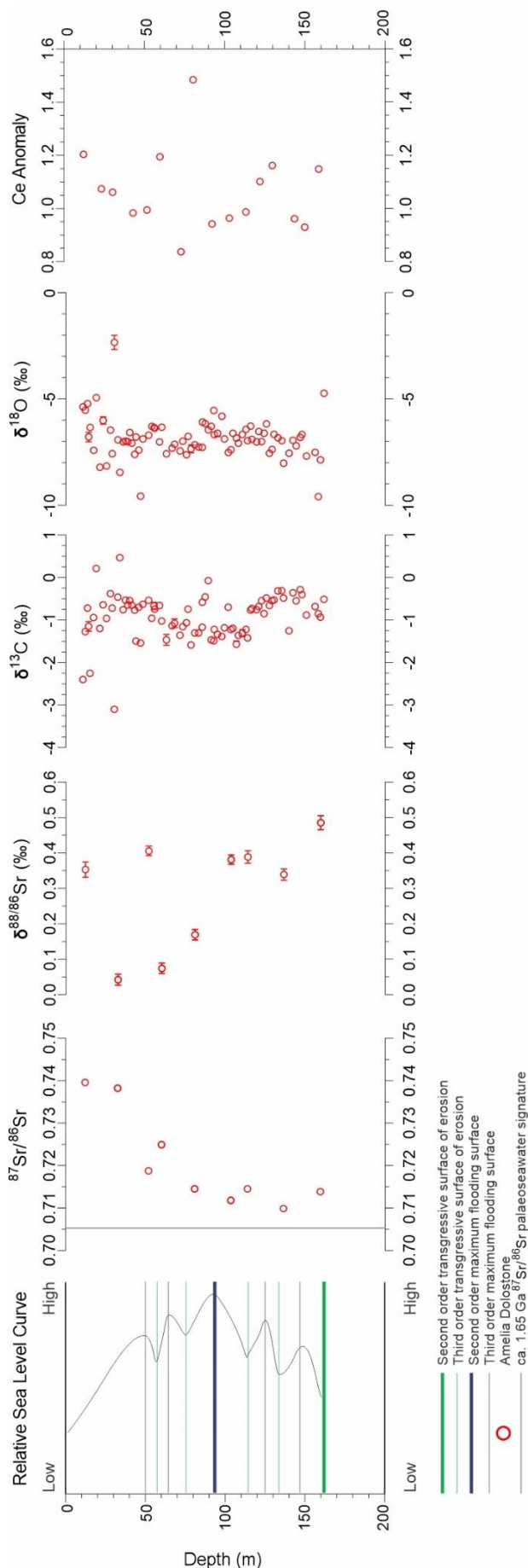


**Figure 4.2.** Screening geochemical proxies for diagenetic alteration and detrital influence. A. Covariation of carbon vs oxygen isotopic compositions in the Amelia Dolostone. Carbonates that has experienced secondary fluids will display a relationship between the two isotopic systems (Banner and Hanson, 1990). B-D. Covariation between diagenetic tracers in carbonates and shales and trace elements (Awwiller and Mack, 1989, Brand and Veizer, 1980, Lev et al., 1999, Mack and Awwiller, 1990). Covariation between detrital input and trace elements (Garcia et al., 1991, Tardy, 1975, Tostevin et al., 2016).

A  $\delta^{13}\text{C}_{\text{carb}}$  isotopic record profile through the Amelia Dolostone is established by analysing 82 samples (Fig. 4.3). All samples were of carbonate lithofacies with more inorganic than organic carbon content. The formation had no significant correlation ( $R^2$  coefficient = 0.056) identified between  $\delta^{13}\text{C}_{\text{carb}}$  and  $\delta^{18}\text{O}_{\text{carb}}$  (Fig. 4.2A), suggesting that these isotopic signatures have not been affected by secondary diagenetic alteration (Allan and Matthews, 1982, Banner and Hanson, 1990). In addition, no samples yielded anomalously light  $\delta^{18}\text{O}_{\text{carb}}$  (<-10‰ PDB, Fig. 4.2A), which also suggests that the formation has not experienced geochemical overprints from meteoric waters or elevated temperatures (Degens and Epstein, 1962, Killingley, 1983, Land, 1995). Consequently, the high-resolution C isotopic records presented here are interpreted to reflect primary signals imparted during the formation or deposition of carbonates (Fig 4.3). As such, they can be used for





chemostratigraphic correlations as well as help reconstruct the local/global carbon isotope curve during the Proterozoic.

Source Rock Analyser investigations of organic-rich shales in the Tawallah group were also assessed for possible contamination as they may impact the interpretation of data in this study. These factors can vary from samples tainted by drilling fluids or the lack of organic-content, yielding unreliable values (Carvajal-Ortiz and Gentzis, 2015, Dembicki Jr, 2009, Peters, 1986). Consequently, results in this study were screened using the criteria described by Hall et al. (2016) and any values that do not meet these thresholds were excluded from any further discussions. To ensure that well-defined peaks were available for characterising organic  $T_{max}$  and Hydrogen Index, samples needed to yield S2 values of at least 0.01 mg HC/g. Furthermore, the data were shown to be internally consistent (e.g., Hydrogen Index =  $S2/TOC \times 100$ ). Mean TOC of the same formation from spatially distant wells largely overlap within their corresponding standard deviations. The Wuraliwuntya Member has the lowest average TOC content out of all shale formations analysed in this study at 0.11%, followed by the Mallapunyah Formation with 0.27%. The  $T_{max}$  values for these units are also indicative of low thermal maturity (Espitalié, 1986). The Wollogorang Formation have relatively higher average TOC content between 1.29–1.77%. The mean  $T_{max}$  values from the two wells slightly differ, with the unit being thermally more mature in MCDD003. A summary of all shale rock pyrolysis results are displayed in Table 4.1.

**Figure 4.3.** Geochemical shifts in the Amelia Dolostone up-section mirrored by the changes in relative sea level interpreted from sedimentological logging by Kunzmann et al. (2020).



Well	Formation	TOC (%)				T <sub>max</sub> (°C)			
		Min.	Max.	Mean	Std. Dev.	Min.	Max.	Mean	Std. Dev.
MCDD005	Mallapunyah Formation	0.05	0.74	0.27	0.17	309	609	406	107
	Wollogorang Formation	0.21	3.74	1.77	1.07	308	451	413	40
MCDD003	Wollogorang Formation	0.10	8.31	1.29	1.80	302	609	476	85
	Wuraliwuntya Member	0.00	0.47	0.11	0.09	307	542	344	44

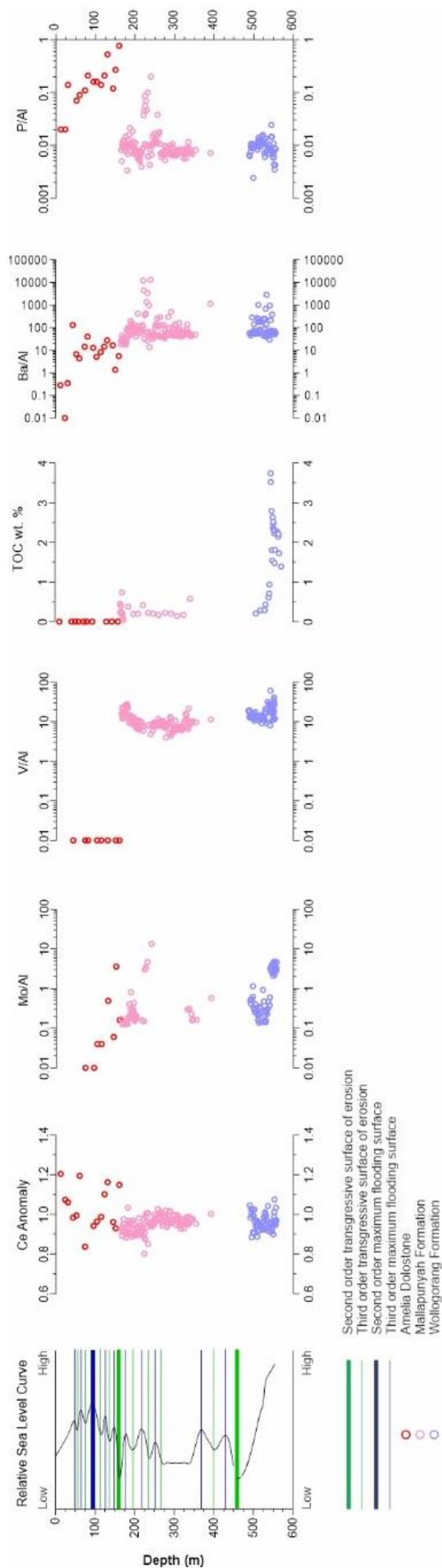
**Table 4.1:** Summary of Source Rock Analyser data in this study.

## 4.6 Discussions

### 4.6.1 Palaeoproductivity, palaeoredox, and depositional constraints of the Tawallah and McArthur Groups

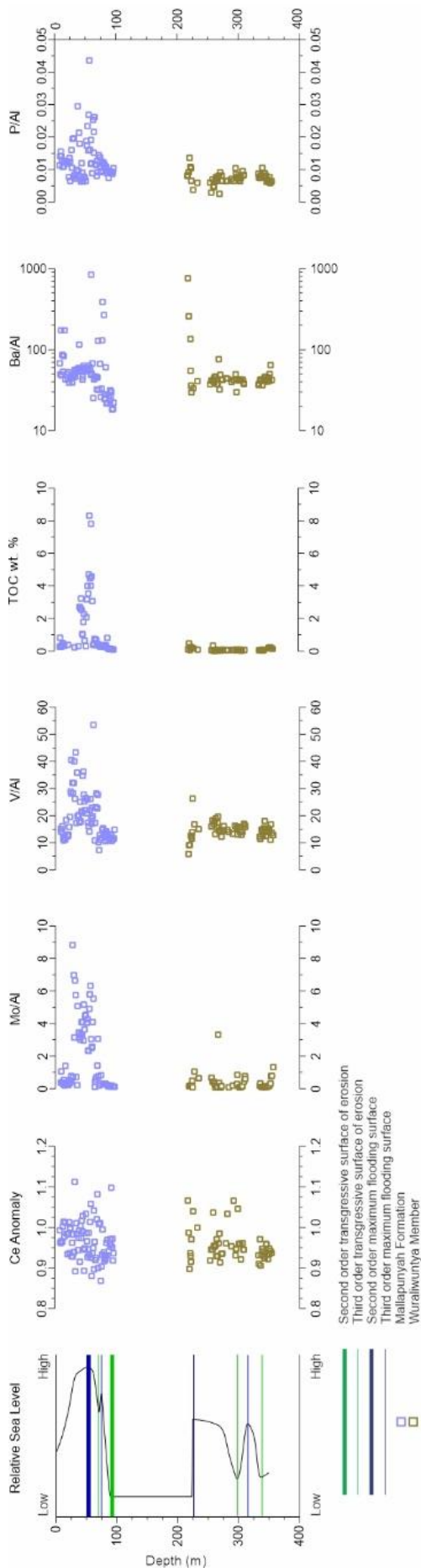
Elevated levels of TOC, Ba/Al, and P/Al generally occur concurrently in all samples analysed from both wells (Fig. 4.4 and 4.5). This should not be true if water-column redox conditions were the main driver in the accumulation of these proxies, as TOC accrues more-readily under anoxia whilst Ba and P are concentrated preferentially in oxic environments (Schoepfer et al., 2015). Consequently, if redox conditions were the primary drivers of the system, TOC, Ba, and P should have an opposing relationship (Falkner et al., 1993, Francois et al., 1995, Schoepfer et al., 2015). Therefore, it is possible that enhanced productivity is instead the dominant control of the palaeoenvironment during the deposition of the Tawallah and McArthur Group units here. Elevated biological and photosynthetic activity would induce a redox-stratified water column as oxygen is consumed at different rates (Cox et al., 2016b, Pedersen and Calvert, 1990, Schoepfer et al., 2015, Tribovillard et al., 2006, Yang et al., 2020). This may explain why trends in redox proxies Mo/Al and V/Al also roughly follow palaeoproductivity indicators up section. However, the Ce anomalies from these units do not follow this pattern as strongly.

The intricate relationship between palaeoproductivity and palaeoredox conditions are further illustrated in Figure 4.6. Here, higher TOC content show a positive relationship with elevated Mo/Al and V/Al ratios. Figure 4.6 shows that these relationships break down at both low (TOC < 1.5 wt. %) and high (TOC > 5 wt. %) organic richness, and are likely related to the different controls of trace element (TE) accumulation (Algeo and Lyons, 2006, Scott and Lyons, 2012). The low organic content interval likely reflects a more oxic water column, as TOC would be poorly preserved and TE would only be hosted in the detrital silicate phase (Algeo and Maynard, 2004, Tribovillard et al., 2006). This pattern is largely reflected by samples from the Wuraliwuntya Member, Mallapunyah Formation, and the Amelia Dolostone (Fig. 4.6). On the other hand, a strong positive relationship between TE and TOC occur during sub-oxic to anoxic conditions, as organo-metallic complexes become the principal sink for TEs (Algeo and Maynard, 2004, Scott and Lyons, 2012). This signature is recorded in the Wollogorang Formation samples with TOC between 1.5–5 wt. %. The redox



heterogeneity of the Wollogorang Formation is also highlighted by samples with TOC > 5 wt. %. In this interval, the relationship between TE and TOC breaks down, as the water column experiences euxinic conditions (Algeo and Maynard, 2004, Scott and Lyons, 2012). However, heterogeneous redox conditions of the different units here may have been masked by their largely poor organic content. As such, different redox models (Fig. 4.7) were also plotted to try to differentiate between changes in water-column oxygen availability in these units (Bau and Dulski, 1996, Piper and Calvert, 2009, Xu et al., 2012). In short, low V/Mo ratios with high Mo concentrations have been suggested to reflect euxinia, whereas high V/Mo ratios with low Mo concentrations indicate suboxic-anoxic environments (Piper and Calvert, 2009, Xu et al., 2012). Furthermore, negative Ce anomalies are commonly indicative of oxic water conditions, anoxic environments either form negligible or positive Ce anomalies (Bau and Dulski, 1996, Tostevin et al., 2016). Here, the Amelia Dolostone seems to again display the most oxic palaeoredox signature, with low V/Mo ratios and Mo content as well as negative Ce anomalies. In contrast, the Wuraliwuntya Member and the Mallapunyah Formation display a slight heterogenetic redox history, with some spread in V and Mo data as well as a weak negative Ce anomaly. Lastly, the Wollogorang Formation again displays the most complex palaeoredox chemistry. This unit records a wide spread in V and Mo values as well as variable Ce anomalies (Fig. 4.7). Notably, this signature is reflected in the Wollogorang Formation sourced from both wells, suggesting that this palaeoredox history is not a local. Importantly, these models consistently show that the oxygenation conditions of this large Proterozoic seaway commonly fluctuates up-stratigraphy.

**Figure 4.4:** Geochemical proxies from well MCDD005 plotted with the relative sea level changes interpreted from sedimentological logging by Kunzmann et al. (2020).



It should be noted that these palaeoredox and palaeoproductivity signatures closely mirrors the third-order transgressive-regressive cycles (Fig. 4.4 and 5) interpreted from Kunzmann et al. (2020). For example, TOC, Ba/Al, and P/Al content are typically enriched in periods of transgressions and depleted in regressive system tracts (Fig. 4.4 and 4.5). This eustatic control is similarly paralleled by redox-sensitive trace elements Mo/Al, V/Al, and Ce anomalies (Virgo et al., 2021). Previous studies have shown that palaeoproductivity and palaeoredox conditions can be influenced by changes in relative sea level (Dong et al., 2017, Katz, 2005, Rimmer et al., 2004, Tyson and Pearson, 1991). Such fluxes can impact the accumulation of organic matter and trace elements by controlling the sedimentation rate, sediment input, as well as the water column redoxcline (Demaison and Moore, 1980, Jackson and Raiswell, 1991, Katz, 2005, Tyson and Pearson, 1991). As a result, these parameters can also be regulated by the tectonic regimes of the basin system (Dong et al., 2017, Hemmesch et al., 2014, Hofer et al., 2013, Lash and Blood, 2014, Schieber et al., 2000). As the basin becomes more connected to the open ocean, palaeoproductivity can be amplified by increasing nutrient-rich supply from nutrient cycling across water columns and upwelling zones (Algeo and Ingall, 2007, Demaison and Moore, 1980, Dong et al., 2017, Pedersen and Calvert, 1990). A relatively higher base level can also induce this feedback by flooding a previously restricted environment with more oxygenated, marine waters as well as introducing a more nutrient-rich input from juvenile hydrothermal vents (Condie et al., 2001, Horton, 2015, Piper and Perkins, 2004, Shen et al., 2000, Spinks et al., 2016a, Tyson and Pearson, 1991, Yang et al., 2020). These conditions may be important for preserving or facilitating early biological life, as palaeoenvironments become more nourished, and wide-spread euxinia is banished (Spinks et al., 2016a).

**Figure 4.5.** Palaeoredox and palaeoproductivity proxies from well MCDD003 plotted with the relative sea level changes interpreted from Kunzmann et al. (2020).

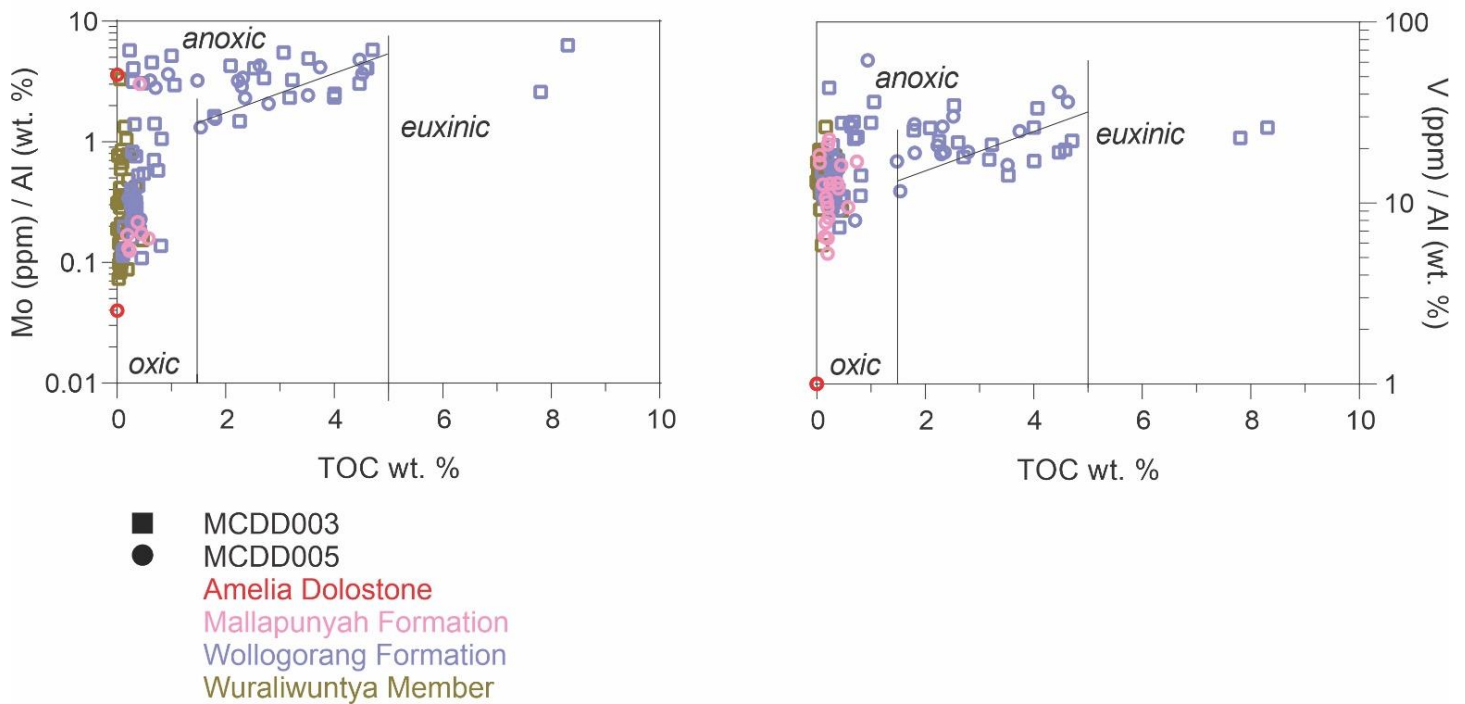


**Figure 4.6.** Redox-sensitive trace element enrichments with respect to TOC content. Mo and V both display similar relationships with TOC up to 5 weight percent. This linear covariation breaks down past this point, consistent with the onset of intermittent euxinia (Algeo and Lyons, 2006, Cox et al., 2016b, Lyons et al., 2009). Al normalisation is applied to correct for trace element dilutions associated with incorporation into secondary phases (Calvert and Pedersen, 1993, Tribouillard et al., 2006).

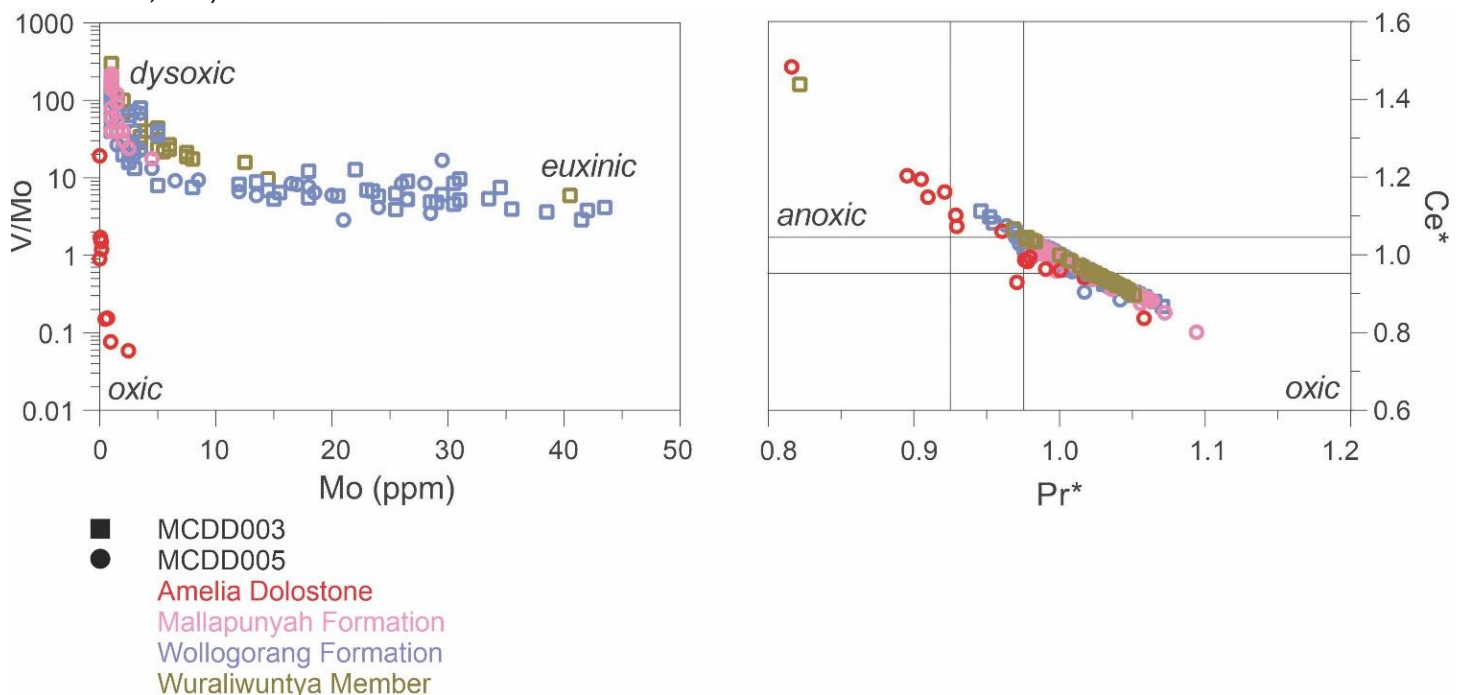


**Figure 4.7.** Trace element redox models based on changes in V, Mo and Ce concentrations (Bau and Dulski, 1996, Piper and Calvert, 2009, Xu et al., 2012).

#### 4.6.2 Isotopic constraints on the palaeoenvironments of the Amelia Dolostone

To better understand how this palaeoenvironment could have evolved during the evolution of the basin, we aim to investigate the Amelia Dolostone using several different isotopic tracers. Isotopic excursions would not be sensitive to changes in sedimentation rate and will more faithfully record palaeowater chemistries (Brand and Veizer, 1980, Derry and

Jacobsen, 1988). Relatively positive  $\delta^{13}\text{C}_{\text{carb}}$  excursions in the lower section of the Amelia Dolostone (160–120 m depth) are paralleled by less radiogenic  $^{87}\text{Sr}/^{86}\text{Sr}$  ratios (Fig. 4.3). The similar patterns between geochemical signatures and transgressive and regressive cycles shown here suggest that changes in depositional environment and eustasy play an important role in how these proxies vary temporally. A more marine environment is expected to source juvenile, mantle-derived Sr from the oceanic crust or hydrothermal vents, resulting in lower  $^{87}\text{Sr}/^{86}\text{Sr}$  ratios (Chen et al., 2022, Derry and Jacobsen, 1988, El Meknassi et al., 2020, Kuznetsov et al., 2018, Shields and Veizer, 2002). This is similarly recorded in the more positive  $\delta^{88/86}\text{Sr}$  values of ca. 0.3, which overlap with the average  $\delta^{88/86}\text{Sr}$  signatures of mafic materials (Amsellem et al., 2018, Charlier et al., 2012). Such mafic input is expected to be more nutrient rich, enhancing local bioproductivity which in turn generates more oxygen into the surrounding environments. This mechanism may have been reflected here by the heavier  $\delta^{13}\text{C}_{\text{carb}}$  values and negative Ce anomalies (Cox et al., 2016a, 2016b, Tribovillard et al., 2006, Yang et al., 2020, Young, 2013, Zerkle et al., 2017, Zhang et al., 2018a). The Settlement Creek Dolerite and Gold Creek Volcanics were emplaced during the deposition Wollogorang Formation (Ahmad and Munson, 2013, Cooke et al., 1998, Rawlings, 2002, Rogers, 1996). These mafic rocks seem to have been derived from an enriched mantle source (Cooke et al., 1998, Rawlings, 2002, Rogers, 1996) and would be a proximal nutrient-rich source, fuelling the local or regional biological productivity in the basin system.

Further up stratigraphy between 120–50 m depth,  $\delta^{13}\text{C}_{\text{carb}}$  excursions shifted ca.  $-0.50\text{‰}$ . However,  $^{87}\text{Sr}/^{86}\text{Sr}$  data in this section seems to stay relatively constant (Fig. 4.3) whilst  $\delta^{88/86}\text{Sr}$  trends towards relatively lighter values. This could suggest that there was an appreciable change in the marine Sr output flux linked to the carbonate cycle which was not recorded by the radiogenic  $^{87}\text{Sr}/^{86}\text{Sr}$  isotopes (Krabbenhöft et al., 2010, Ohno et al., 2008, Vollstaedt et al., 2014). As such, it is likely that the marine carbonate output was gradually decreasing, which would shift to lighter  $\delta^{88/86}\text{Sr}$  values (Ohno et al., 2008, Vollstaedt et al., 2014). The declining rate of marine carbonate formation would diminish the preferential uptake of lighter Sr isotopes from seawater into carbonates, but would have little impact on the  $^{87}\text{Sr}/^{86}\text{Sr}$  values (Vollstaedt et al., 2014). The precipitation of Precambrian marine carbonates commonly occur in shallower environments along the neritic zone and is sensitive to even minor changes in sea level due to its steeper slope and smaller areal extent (Ridgwell et al., 2003). Such settings would also promote early diagenetic carbonate cement formation in the sediment pile, which have been shown to preserve negative  $\delta^{13}\text{C}_{\text{carb}}$  values (Jiang et al., 2019, Kump and Arthur, 1999). In addition, exposure of organic carbon to the surface may also limit its burial efficiency and stimulate the remineralisation of bio-matter into the dissolved organic carbon pool, further saturating the carbon reservoir with  $^{12}\text{C}$  (Betts and Holland, 1991, Emerson, 1985, Hartnett et al., 1998, Jahnke, 1990). This input will increase the flux of lighter carbon isotopes and can also induce the negative  $\delta^{13}\text{C}_{\text{carb}}$  excursion seen in this section of the Amelia Dolostone (Kump and Arthur, 1999, Sarmiento et al., 2007).

Conversely, negative excursions, like seen at the top of the Amelia Dolostone (Fig. 4.3), may also occur under non-steady-state conditions during an increase in  $^{13}\text{C}$ -depleted carbon



from reduced reservoirs (Halverson et al., 2010, Rothman et al., 2003). This is commonly seen during the desiccation and aeration of organic-rich sediments in extensive, epeiric seaways (Higgins and Schrag, 2006), which notably coincides with the recessive nature of the studied unit (Ahmad and Munson, 2013, Kunzmann et al., 2020). This is further supported by the increase to more radiogenic, continental-like  $^{87}\text{Sr}/^{86}\text{Sr}$  signatures present at the top of the section that coincide with the fall in relative sea level (Fig. 4.3). This suggests that the carbonates in this interval have possibly experienced restriction from the open ocean and thus incorporated more evolved, felsic Sr fluxes through riverine flux (Halverson et al., 2010, Kuznetsov et al., 2018, Shields and Veizer, 2002, Veizer et al., 1992). Interestingly, there is also a general shift to lower  $\delta^{88/86}\text{Sr}$  isotopes towards the top of the unit (Fig. 4.3), further supporting an enhanced riverine flux or inputs of continent-derived Sr into the semi-restricted environment (Charlier et al., 2012, de Souza et al., 2010, Krabbenhöft et al., 2010, Shao et al., 2021, Vollstaedt et al., 2014).

The interplay between the three different isotopic systems and shallow water column redox conditions measured in the studied carbonates are summarised in Figure 4.8. These geochemical signatures show complex relationships between them and reveal temporal changes in the geochemistry of the basin waters from the Amelia Dolostone. More oxic conditions that are recorded within the Amelia Dolostone tend to be associated with more marine settings, recorded in the more positive  $\delta^{88/86}\text{Sr}$  and less radiogenic  $^{87}\text{Sr}/^{86}\text{Sr}$  isotopic values. These intervals also largely coincide with a more positive  $\delta^{13}\text{C}_{\text{carb}}$  signature, and thus presumably higher biological productivity (Kump and Arthur, 1999). Enhanced bioproductivity and organic C formation have been linked to more mafic and nutrient-rich inputs likely derived from the oceanic crust, LIPs, or hydrothermal vent systems (Anbar and Knoll, 2002, Cox et al., 2019, Horton, 2015, Rooney et al., 2014). Consequently, local or regional organic blooms in the basin can start to drive the redox cycle in the surrounding palaeoenvironment (Anbar and Knoll, 2002, Cox et al., 2016b, Laakso and Schrag, 2017, Love and Zumberge, 2021). This is reflected in the redox sensitive trace elements shown in this study. Such processes would be partly controlled by the basin's tectonic regime, changes in base level and relative connectivity versus restriction with respect to the open ocean and surrounding provenance source regions in the hinterlands (Cox et al., 2016a, Derry and Jacobsen, 1988, Dessert et al., 2003, Halverson et al., 2010, Kuznetsov et al., 2018, McLennan et al., 1993). The intermittent periods of marine transgression and nutrient/oxygen-rich influx may be integral for microorganisms to thrive in marine or coastal settings during the Proterozoic.

#### **4.6.3 The global palaeo-water during the Proterozoic**

Previous investigators have proposed that the Yanshan Basin on the North China Craton is equivalent to the greater McArthur Basin (Mitchell et al., 2020, Nixon et al., 2021, Wang et al., 2019, Yang et al., 2019, Zhang et al., 2017). Although these correlations have largely focussed on the younger Velkerri Formation and the Xiamaling Formation, more recent work has started to better constrain correlative units within the stratigraphically older sections of these basin systems. In particular, rocks from ca. 1.6 Ga Changcheng and Nankou Groups have similar tuff ages, lithology and interpreted depositional environments compared to the McArthur and Limbunya Group in northern Australia (Ahmad and Munson,

2013, Chu et al., 2007, Ding et al., 2017, Lu et al., 2008, Page et al., 2000, Page and Sweet, 1998). Notably, Kunzmann et al. (2019) have noted similar trends in  $\delta^{13}\text{C}_{\text{carb}}$  excursions between the McArthur Group and the Changcheng and Nankou Groups (Chu et al., 2007). Hence, we believe that this study can be used to further extend and reconstruct a global palaeoseawater carbon and strontium isotope curve for the Proterozoic. The  $\delta^{13}\text{C}_{\text{carb}}$  value most appropriate for this reconstruction should be that with the least radiogenic  $^{87}\text{Sr}/^{86}\text{Sr}$  ratio and  $\delta^{88/86}\text{Sr}$  value most akin to hydrothermal sources, indicating that the unit was most connected to the coeval Proterozoic open ocean within this particular time interval (Derry and Jacobsen, 1988, El Meknassi et al., 2020, Kuznetsov et al., 2018, Ohno et al., 2008, Vollstaedt et al., 2014). In addition, results from this study can also be used for regional chemostratigraphic applications, as a  $-1\text{‰}$   $\delta^{13}\text{C}_{\text{carb}}$  excursion have been reported in Amelia Dolostone elsewhere in the greater McArthur Basin (Lindsay and Brasier, 2000).

As such, our results here will be beneficial for providing a more robust reconstruction of the  $\delta^{13}\text{C}_{\text{carb}}$  and  $^{87}\text{Sr}/^{86}\text{Sr}$  isotopic curve ca. 1.65 Ga. Furthermore, we also provide the first step in constraining the palaeoseawater  $\delta^{88/86}\text{Sr}$  composition during this period. Accordingly, the possible Proterozoic seawater composition was plotted in Figure 4.8 using published datasets of global  $\delta^{13}\text{C}_{\text{carb}}$  excursion (Saltzman and Thomas, 2012),  $^{87}\text{Sr}/^{86}\text{Sr}$  ratio (Chen et al., 2022, Kuznetsov et al., 2018), modelled Ce average (Liu et al., 2021), and inferred  $\delta^{88/86}\text{Sr}$  composition of palaeo-seawater based on the offset of  $-0.18\text{‰}$  between marine carbonate and basin waters (Shao et al., 2021, Vollstaedt et al., 2014). From this fractionation factor, we estimate the Proterozoic palaeoseawater had a  $\delta^{88/86}\text{Sr}$  value of ca.  $0.7\text{‰}$ . This is relatively more positive than the value observed for modern seawater (Vollstaedt et al., 2014), and implies that the  $\delta^{88/86}\text{Sr}$  of palaeoseawater is becoming lighter over time.

Importantly, our results across the Tawallah and McArthur Groups (Fig. 4.6 and 4.7) further demonstrate that marine euxinia was not globally ubiquitous during the Proterozoic (Planavsky et al., 2011, Poulton and Canfield, 2011, Poulton et al., 2010). Sedimentary pyrite is a major sink for elements (e.g. Fe, Zn, P) that are essential for biological processes in prokaryotes and eukaryotes (Anbar and Knoll, 2002). Non-euxinic periods would prevent the formation of sedimentary pyrite in Proterozoic seawater or basin waters (Knoll et al., 2006, Spinks et al., 2016a, Zhang et al., 2016, Zhang et al., 2018a). As such, the delay of widespread marine euxinia has been proposed to play a critical role in the survival of early life during the Proterozoic (Spinks et al., 2016a). Furthermore, recent studies have highlighted the presence of regionally bio-productive, relatively more oxic basin systems in the Proterozoic (Bellefroid et al., 2018, Cox et al., 2016b, Gilleaudeau et al., 2016, Hua et al., 2013, Mukherjee and Large, 2020, Spinks et al., 2022, Zhang et al., 2016, Zhang et al., 2018a). The presence of these oxygenated environments were not limited to surface water settings like previously thought (Lyons et al., 2014, Planavsky et al., 2011, Poulton et al., 2010, Shen et al., 2003). Instead, they were dynamically driven by biological activity, susceptible to nutrient fluxes, as well as changes in their local palaeoenvironment. Overall,

these particular environments may be key in how life persevered during the largely nutrient-poor Proterozoic (Mukherjee and Large, 2020).

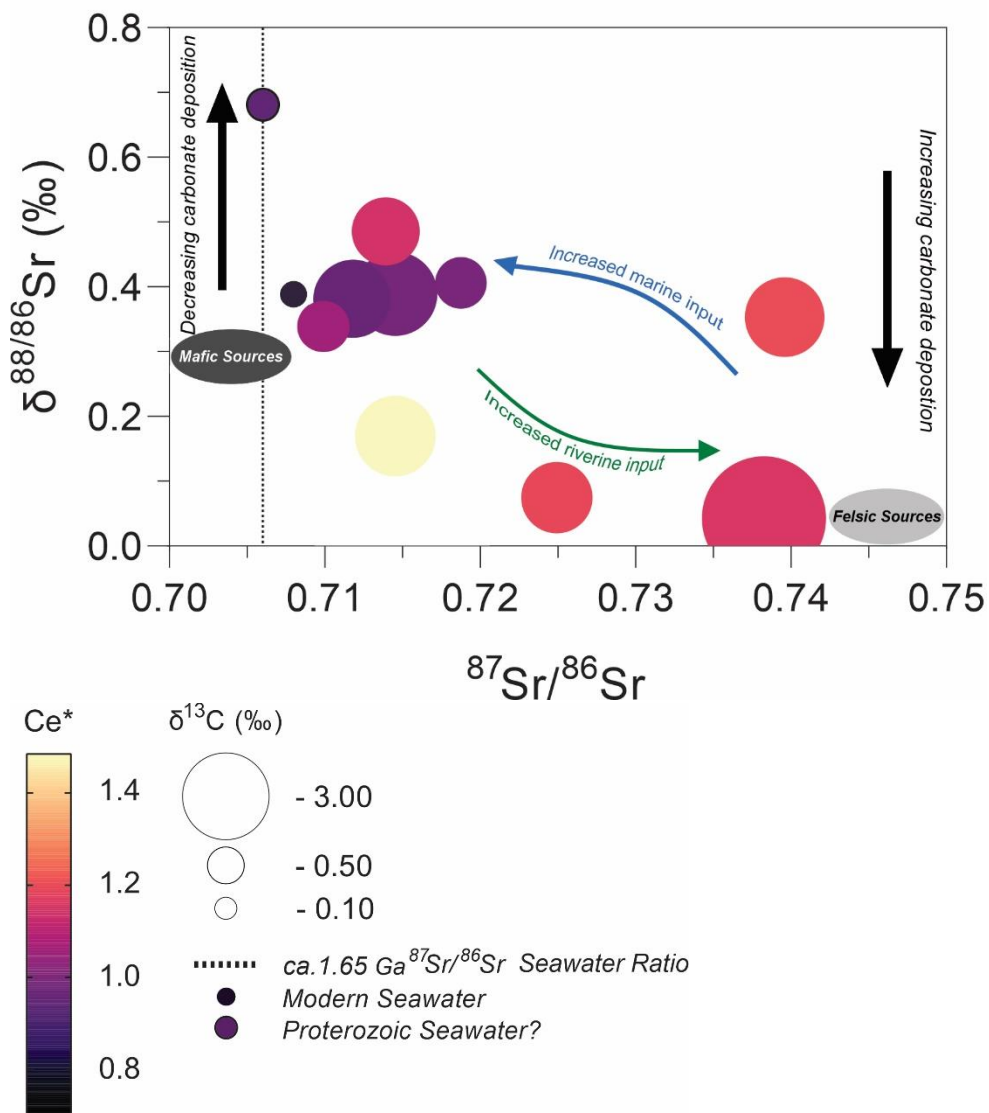


**Figure 4.8.** Isotopic and elemental relationships in the Amelia Dolostone. The increasing size of data points correspond to a more negative  $\delta^{13}C_{carb}$  signature. The changing colour scheme tracks the difference in Ce anomalies. The vertical and horizontal axis plot changes in  $\delta^{88/86}Sr$  and  $^{87}Sr/^{86}Sr$  respectively. Average values of mafic and felsic Sr fluxes were also plotted as reference, along with the different drivers that may fractionate the stable and radiogenic Sr isotopic system (de Souza et al., 2010, Krabbenhöft et al., 2010, Ohno et al., 2008, Paytan et al., 2021). Possible Proterozoic seawater composition was plotted based on known  $\delta^{13}C_{carb}$  excursion (Saltzman and Thomas, 2012),  $^{87}Sr/^{86}Sr$  isotopic value (Kuznetsov et al., 2018), statistically calculated global Ce anomaly average (Liu et al., 2021) and predicted  $\delta^{88/86}Sr$  isotopic offset of -0.18‰ between marine carbonates and the water column (Vollstaedt et al., 2014). Modern seawater values were plotted using known constraints of the same parameters (Kuznetsov et al., 2018, Liu et al., 2021, Saltzman and Thomas, 2012, Vollstaedt et al., 2014).

## 4.7 Conclusions

In conclusion, geochemical results from this study show strong evidence that Earth systems were much more dynamic during the Proterozoic than previous investigators have suggested. Constraints that would hinder and amplify nutrient fluxes such as changes in sea level, source inputs and water chemistry are integral for effective bioproductivity in systems such as the greater McArthur Basin. Relative connectivity to the open ocean can introduce



nutrient-rich, mantle-derived sources or oxic waters into a previously restricted basin. This can be recorded through high-resolution sedimentological analysis, as well as radiogenic and stable Sr isotopic investigations. Fluctuating efficacy of bioproductivity in the Proterozoic Tawallah and McArthur Groups were reflected in the Ba/Al, P/Al, and  $\delta^{13}\text{C}$  data. In addition, Ce, Mo, and V also recorded the changes in the redox-conditions of the water-column. Throughout the Proterozoic section of the greater McArthur Basin, palaeoenvironments that were more connected to the open ocean sourced more marine and/or mantle-like influx. Such inputs are likely nutrient-rich, and will enhance the local or regional bioproductivity. In turn, enhanced productivity of photosynthetic life can induce more oxic conditions to its surrounding environments. On the other hand, restricted settings in this study were dominated by continentally derived influx. This would be relatively nutrient-poor and limit bioproductivity. As a result, such changes would develop a more anoxic palaeoenvironment. This dynamic interplay should be tested in similarly aged sedimentary worldwide. These settings could be important refuge for early biological life to survive during the planet's mid-life crisis.

#### **4.8 Acknowledgements**

This work was supported by the Australian Research Council Projects LP160101353 and LP200301457 with Santos Ltd, Empire Energy Group Ltd, Northern Territory Geological Survey, Teck Resources, BHP and Origin as partners. The initial development and validation of in situ Rb–Sr dating technique at the University of Adelaide was also supported by Agilent Technologies Australia Ltd. This forms MinEx CRC contribution #2022/XX. Robert Klæbe, Tony Hall, and Aoife McFadden are thanked for their assistance in the laboratory proceedings done in this study.

# **Chapter 5: Characterising the economic Proterozoic Glyde Package of the greater McArthur Basin, northern Australia**

This chapter is submitted for publication in the peer-reviewed journal Ore Geology Reviews.

The Supplementary Files for this chapter can be found in:

<https://doi.org/10.25909/21424875.v1>

# Statement of Authorship

Title of Paper	Characterising the economic Proterozoic Glyde Package of the greater McArthur Basin, northern Australia
Publication Status	<input type="checkbox"/> Published <input type="checkbox"/> Accepted for Publication <input checked="" type="checkbox"/> Submitted for Publication <input type="checkbox"/> Unpublished and Unsubmitted work written in manuscript style
Publication Details	This manuscript was submitted for publication in the peer-reviewed journal Ore Geology Reviews.

## Principal Author

Name of Principal Author (Candidate)	Darwinaji Subarkah		
Contribution to the Paper	Conceptualisation, method development, analysis, data reduction and interpretation, manuscript drafting.		
Overall percentage (%)	70		
Certification:	This paper reports on original research I conducted during the period of my Higher Degree by Research candidature and is not subject to any obligations or contractual agreements with a third party that would constrain its inclusion in this thesis. I am the primary author of this paper.		
Signature		Date	28/10/2022

## Co-Author Contributions

By signing the Statement of Authorship, each author certifies that:

- i. the candidate's stated contribution to the publication is accurate (as detailed above);
- ii. permission is granted for the candidate to include the publication in the thesis; and
- iii. the sum of all co-author contributions is equal to 100% less the candidate's stated contribution.

Name of Co-Author	Alan S. Collins		
Contribution to the Paper	Project funding, supervision, manuscript drafting.		
Signature		Date	28/10/2022

Name of Co-Author	Morgan L. Blades		
Contribution to the Paper	Supervision, sample collection, manuscript drafting.		
Signature		Date	28/10/2022

Name of Co-Author	Juraj Farkaš		
Contribution to the Paper	Supervision, manuscript drafting.		
Signature		Date	28/10/2022
Name of Co-Author	Sarah Gilbert		
Contribution to the Paper	Method development, manuscript drafting.		
Signature		Date	28-Oct-2022
Name of Co-Author	Amber Jarrett		
Contribution to the Paper	Supervision, manuscript drafting		
Signature		Date	28/10/2022
Name of Co-Author	Maxwell Bullen		
Contribution to the Paper	Sample collection, data curation		
Signature		Date	02/11/2022
Name of Co-Author	William Giuliano		
Contribution to the Paper	Sample collection, data curation		
Signature		Date	03/11/2022

## 5.1 Abstract

The greater McArthur Basin is an informal term for a Palaeo-to-Mesoproterozoic sedimentary system which consists of terranes from the McArthur Basin, Birrindudu Basin, and the Tomkinson Province. These spatially distant basins have been interpreted to connect within the subsurface based on geophysical, lithological, and geochronological evidence. The coeval sedimentary units of the greater McArthur Basin were subdivided into non-genetic depositional ‘packages’ bookended by regional unconformities. In ascending order, these packages are called the: Redbank, Goyder, Glyde, Favenc, and Wilton Packages. The ca. 1660–1610 Ma Glyde Package is the focus of this study and hosts the economically important Barney Creek Formation, found in the McArthur Basin. The Barney Creek Formation of the McArthur Group holds the sediment-hosted, world-class, Zn-Pb-Ag McArthur River deposit. Importantly, it is also a key petroleum source rock and unconventional hydrocarbon reservoir, containing Australia’s geologically oldest oil and gas discoveries and forming a part of the McArthur Petroleum Supersystem. Consequently, identifying chronostratigraphically similar units elsewhere in the greater McArthur Basin would be key for explorers in finding analogous economic resources.

*In situ* Rb–Sr geochronological results of the Barney Creek Formation shales sourced from borehole LV09001 yielded ages of  $1634 \pm 59$  Ma and  $1635 \pm 67$  Ma. Shale samples from Fraynes Formation in borehole Manbulloo S1 were dated at  $1630 \pm 57$  Ma and  $1636 \pm 42$  Ma using the same approach. These ages are in good agreement with U–Pb dating of tuffaceous layers from each respective unit, suggesting that they represent their early burial histories and not secondary, post-depositional events. Consequently, these results indicate that the Fraynes Formation and the Barney Creek Formation here are direct chronostratigraphic equivalents.

In addition to the geochronological similarities, the  $\delta^{13}\text{C}_{\text{carb}}$ ,  $^{87}\text{Sr}/^{86}\text{Sr}$ , and  $\delta^{88/86}\text{Sr}$  isotopic constraints from both units also display parallel geochemical fingerprints up-section. These includes a positive  $\delta^{13}\text{C}_{\text{carb}}$  excursion of  $\sim 2.0$  ‰, a trend towards more crustal-dominated  $^{87}\text{Sr}/^{86}\text{Sr}$  ratios, and a negative  $\delta^{88/86}\text{Sr}$  excursion of  $\sim 2.5$  ‰. These findings further supports the application of isotopic chemostratigraphy as a powerful tool to correlate distal carbonaceous rocks in the basin system. Importantly, these geochemical fingerprints also show that the McArthur Group and the Limbunya Group experienced similar changes in palaeoenvironments during the evolution of the basin system. These changes include notable periods of basin restriction, which would influence the palaeo-water chemistry of the Glyde Package. However, trace element data collated in this study indicate that the sections may have recorded slightly different, heterogeneous palaeoredox histories. Geochemical models based on redox-sensitive trace elements V and Mo suggests that the Fraynes Formation sustained a much more euxinic water column as opposed to the Barney Creek Formation. Consequently, these differences will have implications for the accumulation and preservation of base metals and hydrocarbons within the sediment.

## 5.2 Introduction

The informally named Palaeoproterozoic to Mesoproterozoic greater McArthur Basin (Fig. 5.1) is a supracontinental sedimentary system unconformably overlying the deformed metamorphosed rocks of the North Australian Craton (Ahmad and Munson, 2013, Close, 2014, Page and Sweet, 1998, Rawlings, 1999). The system extends over 180,000 km<sup>2</sup> across northern Australia (Ahmad and Munson, 2013, Page and Sweet, 1998, Rawlings, 1999), from the borders of Western Australia into northwestern Queensland (Fig. 5.1). The greater McArthur Basin consists of sedimentary rocks of the McArthur Basin *sensu stricto*, the Birrindudu Basin, and the Tomkinson Province (Close, 2014). These far-separated successions have been interpreted to be continuous in the subsurface based on seismic (Blaikie and Kunzmann, 2017, Blaikie and Kunzmann, 2019, Blaikie and Kunzmann, 2020, Debacker et al., 2021, Frogtech Geoscience, 2018, Hoffman, 2014, Plumb and Wellman, 1987, Sheldon et al., 2021), sedimentological (Jarrett et al., 2022, Kunzmann et al., 2022, Kunzmann et al., 2020, Kunzmann et al., 2019, Page et al., 2000, Rawlings, 2002, Rawlings, 1999, Schmid, 2015, Smith, 2016), and geochronological findings (Bodorkos et al., 2022, Munson, 2019, Nixon et al., 2021, Page et al., 2000, Page and Sweet, 1998). The sedimentary units of the greater McArthur Basin were categorised into five, basin-scale, non-depositional packages based on their lithostratigraphy, age, composition of volcanism, and basin-fill geometry (Ahmad and Munson, 2013, Close, 2014, Rawlings, 1999). In stratigraphic order, these are the Redbank, Goyder, Glyde, Favenc, and Wilton Packages.

The Glyde Package hosts a super-giant base metal deposit that forms part of the Carpentaria Zn belt in northern Australia (Huston et al., 2006, Large et al., 2005, Leach et al., 2005, Porter, 2017). The HYC deposit is impressively well preserved, showing little evidence of deformation or metamorphism (Large et al., 2005). In addition, the Barney Creek Formation and their equivalent units also constitutes the prospective McArthur Petroleum Supersystem (Bradshaw, 1994, Jarrett et al., 2022). The McArthur Petroleum Supersystem contains Australia's geologically oldest conventional and unconventional oil and gas discoveries (Croon et al., 2015, Jackson et al., 1986). The region continues to be promising, with wells intersecting the province exhibiting both oil bleeds and gas shows (Crick et al., 1988, Croon et al., 2015, Jackson et al., 1988, Jackson et al., 1986, Jarrett et al., 2022, Kovac et al., 2014). Fourteen potential source rocks have been identified within the McArthur Petroleum Supersystem, many with very good to excellent organic richness (Jarrett et al., 2022). Many of the shales within this division are thermally mature, in the zone of oil and gas formation (Jarvie and Breyer, 2011). As such, establishing a chronological framework of equivalent units to the Barney Creek Formation would be essential for explorers in finding similar plays. Furthermore, understanding how the Barney Creek Formation and its coeval units evolve would also be key in understanding the formation, accumulation, and preservation of other potential base-metal mineralisation and hydrocarbon reservoirs.

Notably, previous investigators have also shown that the greater McArthur Basin was potentially part of a large, inter-continental seaway (Cox et al., 2022, Gibson et al., 2018, Kirscher et al., 2020, Pisarevsky et al., 2014, Wang et al., 2019, Zhang et al., 2012). Palaeomagnetic findings have suggested that northern Australia bordered other continents such as North China (Wang et al., 2019, Zhang et al., 2012), Baltica (Hamilton and Buchan,

2010, Karlstrom et al., 2001, Zhao et al., 2004), and Laurentia (Karlstrom et al., 2001, Kirscher et al., 2020, Medig et al., 2014) during the Proterozoic. This palaeogeographical link is further corroborated by the similarities in lithostratigraphy (Kunzmann et al., 2019, Yang et al., 2019, Zhang et al., 2021) basin provenance (Ding et al., 2017, Lu et al., 2008, Yang et al., 2018, Zhang et al., 2022), igneous activity (Bodorkos et al., 2022, Nixon et al., 2021, Zhang et al., 2018a, Zhang et al., 2017), astrochronological constraints (Mitchell et al., 2020), sediment-hosted mineralisation (Gianfriddo et al., 2022, Gibson et al., 2017, Gu et al., 2012, Southgate, 2000, Wang et al., 2014), and petroleum plays (Cox et al., 2022, Craig et al., 2013, Jarrett et al., 2022, Liu et al., 2021, Wenzhi et al., 2018, Yang et al., 2020). As such, this sedimentary system may be critical for global scale palaeoenvironment reconstructions during the Palaeoproterozoic (Cox et al., 2022, Cox et al., 2016b, Craig et al., 2013, Jarrett et al., 2022, Johnston et al., 2008, Lyons et al., 2014, Mukherjee and Large, 2020, Shen et al., 2002, Vinnichenko et al., 2020). In particular, the Glyde Package have historically been studied as a key section for understanding early biological life, palaeowater, and atmospheric chemistry ca. 1.6 Ga (Brocks et al., 2005, French et al., 2020, Kunzmann et al., 2019, Mukherjee et al., 2019, Oehler, 1977, Stüeken et al., 2021). Consequently, the findings from this study could also be used to help expand upon how surface environments evolved during this period.

In order to help characterise the extent of the economic Glyde Package, we look to establish a chronological framework and chemostratigraphic correlations between distal successions in the sedimentary system. In particular, this study focuses on the McArthur Group sourced from well LV09001 in the McArthur Basin *sensu stricto*, and the Limbunya Group from well Manbulloo S1 in the Birrindudu Basin. Shale-hosted clay minerals from both groups were dated using *in situ* Rb–Sr geochronology to bracket the depositional window of the units. Furthermore, chemical signatures of marine sedimentary rocks here were investigated using a multi-proxy approach to understand how the palaeoenvironment and palaeoredox history of the Glyde Package have evolved. Correlating these excursions would suggest that the complex tectonic regime of the sedimentary system is extensively recorded in both the McArthur Basin and the Birrindudu Basin. As a result, this would suggest that the under-explored Birrindudu Basin can also potentially host analogous economic potential that is present in the McArthur Basin.

### 5.3 Geological Background

The McArthur Group units from the southern McArthur Basin along with the Vizard and Habgood Groups from the northern McArthur Basin forms the McArthur Basin *sensu stricto* successions (Fig. 5.1) of the Glyde Package (Ahmad and Munson, 2013, Close, 2014, Rawlings, 1999). A maximum depositional constraint for the lower McArthur Group is defined by a green tuffaceous siltstone from the Mallapunyah Formation which gave an age of  $1653 \pm 17$  Ma (Ahmad and Munson, 2013, Page et al., 2000). Direct sensitive high-resolution ion microprobe (SHRIMP) U–Pb dating of volcanic zircons from tuffites in the Barney Creek Formation has yielded ages of  $1640 \pm 4$ ,  $1639 \pm 3$ , and  $1638 \pm 7$  Ma (Page et al., 2000, Page and Sweet, 1998). These results are interpreted to be the absolute depositional age of the unit (Munson, 2019). Lastly, another tuff layer from the unconformably overlying Balbirini Dolosotone gave a SHRIMP U–Pb age of  $1589 \pm 3$  Ma

(Page et al., 2000), bookending the depositional window for the McArthur Group. These ages are well correlated with those from the Limbunya Group, which forms the Birrindudu Basin successions of the Glyde Package (Close, 2014, Cutovinos et al., 2002, Munson, 2019, Munson et al., 2020, Smith, 2001). A detrital zircon analysis from the Farquharson Sandstone resulted in a maximum depositional age of  $1654 \pm 12$  Ma for the lower Limbunya Group (Kositcin and Carson, 2017). In addition, recent dating of tuff layers from the Fraynes Formation gave an age of  $1642 \pm 4$  Ma, suggesting that this unit is directly correlative to the Barney Creek Formation (Munson et al., 2020). These correlations and age constraints are summarised in Figure 5.2.

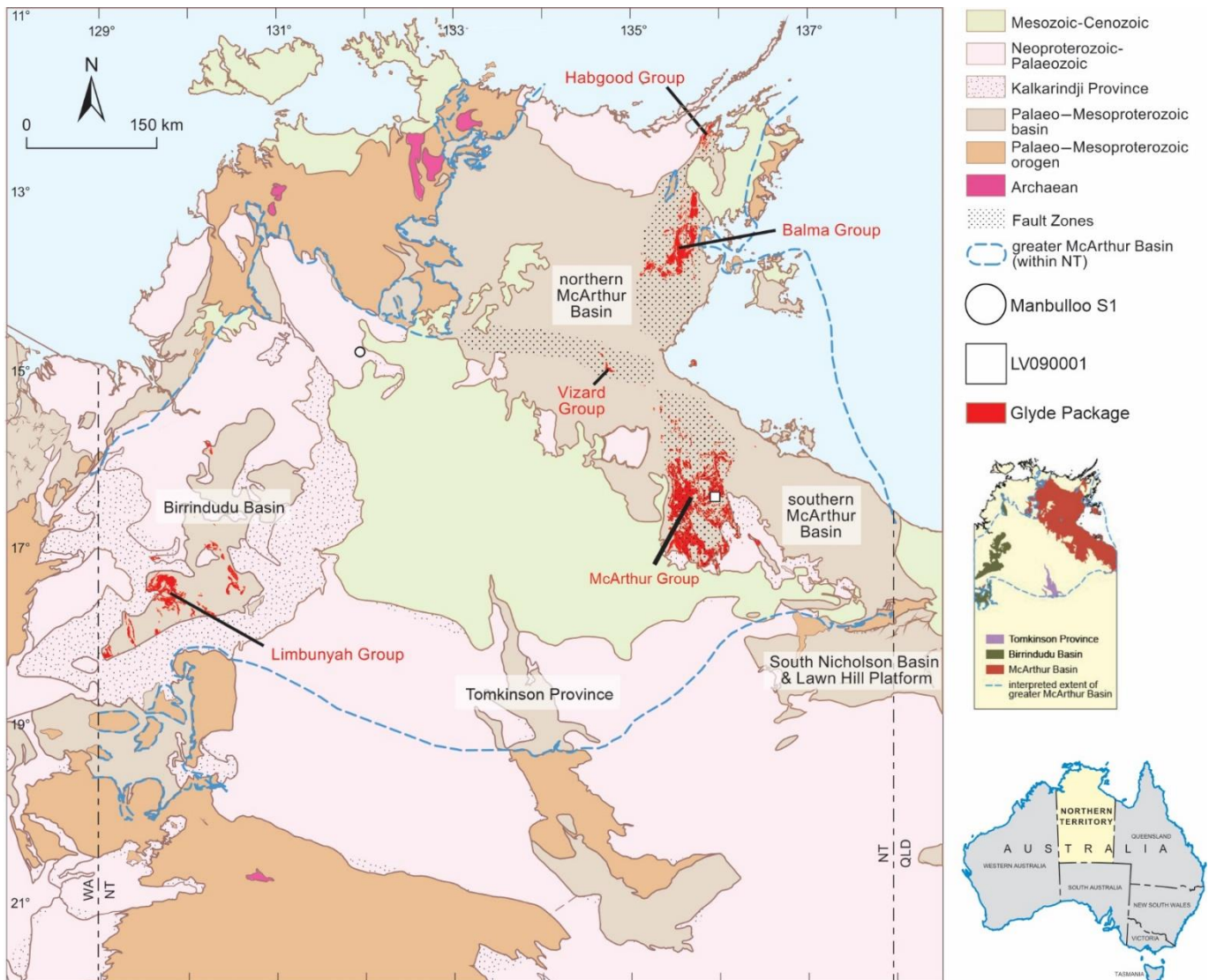


**Figure 5.1.** Geological map of the greater McArthur Basin as defined by Close (2014) with the outcropping components of the Glyde Package (Munson, 2019) and the localities of boreholes used in this study. The Northern Territory geological regions are sourced from the Northern Territory Geological Survey's 1:2.5M Geographic Information System dataset and can be found in <https://geoscience.nt.gov.au/gemis/ntqsgispu/> and <http://strike.nt.gov.au/wss.html>.

### 5.3.1 McArthur Group in the McArthur Basin *sensu stricto*

The McArthur Group is categorised into two sub-groups (Jackson et al., 1987, Plumb and Wellman, 1987): the older Umbolooga Subgroup and the overlying Batten Subgroup (Fig. 5.2). The Emmerugga Dolostone from the Umbolooga Subgroup is the oldest unit of the McArthur Group in this study. The formation is divided into two members: the Mara



Dolostone Member and the Mitchell Yard Dolostone Member (Pietsch, 1991, Winefield, 1999). The Mara Dolostone Member is primarily a stromatolitic dolarenite, with common occurrences of columnar, domal, and conical stromatolites (Ahmad and Munson, 2013). The Mitchell Yard Dolostone Member conformably overlies the Mara Dolostone Member and is instead more massive and featureless (Ahmad and Munson, 2013). These sections thicken up-section and were interpreted to have been deposited in a tidal to deep marine environment on an intracratonic carbonate platform (Ahmad and Munson, 2013, Winefield, 1999). The Teena Dolostone is younger than the Emmeruga Dolostone, and tuff layers within the unit have been dated at  $1639 \pm 6$  Ma (Page et al., 2000). The unit recorded a shallowing cycle up stratigraphy, with the youngest sections containing oolitic grainstone, rippled and laminated dolarenite, and thin beds of carbonaceous shale (Ahmad and Munson, 2013). Notably, the radiating fans of vertical dolomite crystals called the 'Coxco Needles' regularly occur in the Teena Dolostone (Jackson et al., 1987, Walker et al., 1977, Winefield, 2000). Similar pseudomorphs in coeval units from the greater McArthur Basin and other Palaeoproterozoic basins in northern Australia have also been observed, and they are used as a key feature to correlate units that are spatially apart (Ahmad and Munson, 2013). The Barney Creek Formation unconformably overlies the Teena Dolostone and is largely a recessive unit (Ahmad and Munson, 2013, Jackson et al., 1987, Kunzmann et al., 2022, Rawlings, 1999). The succession comprises of finely laminated to thinly bedded carbonaceous and pyritic siltstone, dololomite, and locally abundant tuff beds. The HYC Pyritic Shale Member here is continuously recessive and hosts the world-class Zn-Pb-Ag deposit (Eldridge et al., 1993, Large et al., 1998, Pietsch, 1991). The Barney Creek Formation has been interpreted to represent deep-water shaley carbonates deposited during the maximum flooding of a sea-level transgression (Bull, 1998, Kunzmann et al., 2019, Winefield, 1999). However, it should be noted that the Barney Creek Formation records significant differences in lateral facies and thicknesses across the McArthur Basin (Kunzmann et al., 2022). These differences are likely induced by a geographic shift in the depocentre that occurred during the structural re-organisation of the basin (Kunzmann et al., 2022). The overlying Reward Dolostone represents an upward-shallowing cycle after the deposition of the Barney Creek Formation (Ahmad and Munson, 2013, Kunzmann et al., 2022, Kunzmann et al., 2019). The depositional environment for the unit is likely to be locally high-energy to peritidal, with sections of stromatolitic dololomite to massive, cross-bedded sandstone (Haines, 1994, Pietsch, 1991). The lower contact with the Barney Creek Formation is commonly conformable and gradational, but locally disconformable where palaeo-regolith develops (Pietsch, 1991).

The Batten Subgroup (Fig. 5.2) unconformably overlies the Reward Dolostone (Jackson et al., 1987, Plumb and Wellman, 1987) and largely consists of shallower sequences than the Umbolooga Subgroup (Ahmad and Munson, 2013). The Lynott Formation is evaporitic, consisting of dolomitic siltstone, stromatolitic dolostone, and sandstone (Jackson et al., 1987). The uppermost section of the unit comprises of abundant cauliflower chert, suggesting that it was deposited in a supratidal to sabkha setting (Pietsch, 1991). A tuff-layer from the top of the Lynott Formation returned an age of  $1636 \pm 4$  Ma overlapping with the Barney Creek Formation (Page et al., 2000), suggesting that the unconformity with the

Batten Subgroup represents a short time gap. The following Yalco Formation is the youngest unit from the McArthur Group investigated in this study. The succession is commonly interbedded with stromatolitic dolarenite and rippled sandstone (Ahmad and Munson, 2013). Sedimentary structures such as ripple marks, desiccation cracks, and casts of evaporitic minerals further suggests that the unit was deposited in a shallow-marine environment that experienced intermittent emergence (Jackson et al., 1987, Pietsch, 1991). The McArthur Group samples here were sourced from the LV09001 drill hole (Fig. 5.1).

### **5.3.2 Limbunya Group in the Birrindudu Basin**

The Mallabah Dolostone is the oldest unit from the Limbunya Group (Fig. 5.2) that is assessed in this study. It comprises of laminated, stromatolitic dolostone fining upwards into dolomitic mudstone (Ahmad and Munson, 2013, Cutovinos et al., 2002). Sequences from the Mallabah Dolostone suggests a transition from shallow-marine conditions towards more lower-energy, deeper marine environments potentially below the wave base (Cutovinos et al., 2002). This marine environment is further reflected by the sedimentology of the overlying Kunja Siltstone which is dominated by laminated mudstone and fissile silts (Cutovinos et al., 2002). Consequently, the Kunja Siltstone has been interpreted to represent a maximum flooding surface (Ahmad and Munson, 2013). Tuff layers from this formation have yielded a U–Pb zircon age of  $1635 \pm 19$  Ma (Fanning, 1991). Previous investigators have also noted elevated organic carbon content and concentrations of Pb and Zn within the formation (Cutovinos et al., 2002), with a maximum TOC of 2.1 wt.% (Jarrett et al., 2022). The conformably overlying Farquharson Sandstone mainly consists of blocky, massive sandstone and depicts a change back into shallower environments (Ahmad and Munson, 2013) but is not sampled here.

The following Blue Hole Formation and Campbell Springs Dolostone are lithologically similar, comprising of dolomitic mudstone and siltstone as well as stromatolitic dolostone (Cutovinos et al., 2002, Dunster, 1998). However, they are separated by a distinctive purple interbed with hemispherical, bioherms of digitate stromatolites (Ahmad and Munson, 2013). Importantly, acicular crystal pseudomorphs identical to the Coxco Needles found in the Teena Dolostone are commonly abundant in the Blue Hole Formation and the Campbell Springs Dolostone (Sweet et al., 1974). Furthermore, a tuff zircon from the Campbell Springs Dolostone yielded a U–Pb age of  $1638 \pm 9$  Ma (Cutovinos et al., 2002). This is in good agreement with an age from the Teena Dolostone in the McArthur Basin (Page et al., 2000), suggesting that they are directly correlative units. These correlations are further supported by the overlying Fraynes Formation, which consists of micaceous siltstone with more carbonate interbeds up-section (Sweet et al., 1974). The Fraynes Formation is correlated with the Barney Creek Formation of the McArthur basin and is interpreted to have been deposited in a nearshore shallow-marine environment with intermittent periods of deeper-marine phase (Cutovinos et al., 2002). The Limbunya Group samples here were sourced from the Manbulloo S1 drill hole (Fig. 5.1).

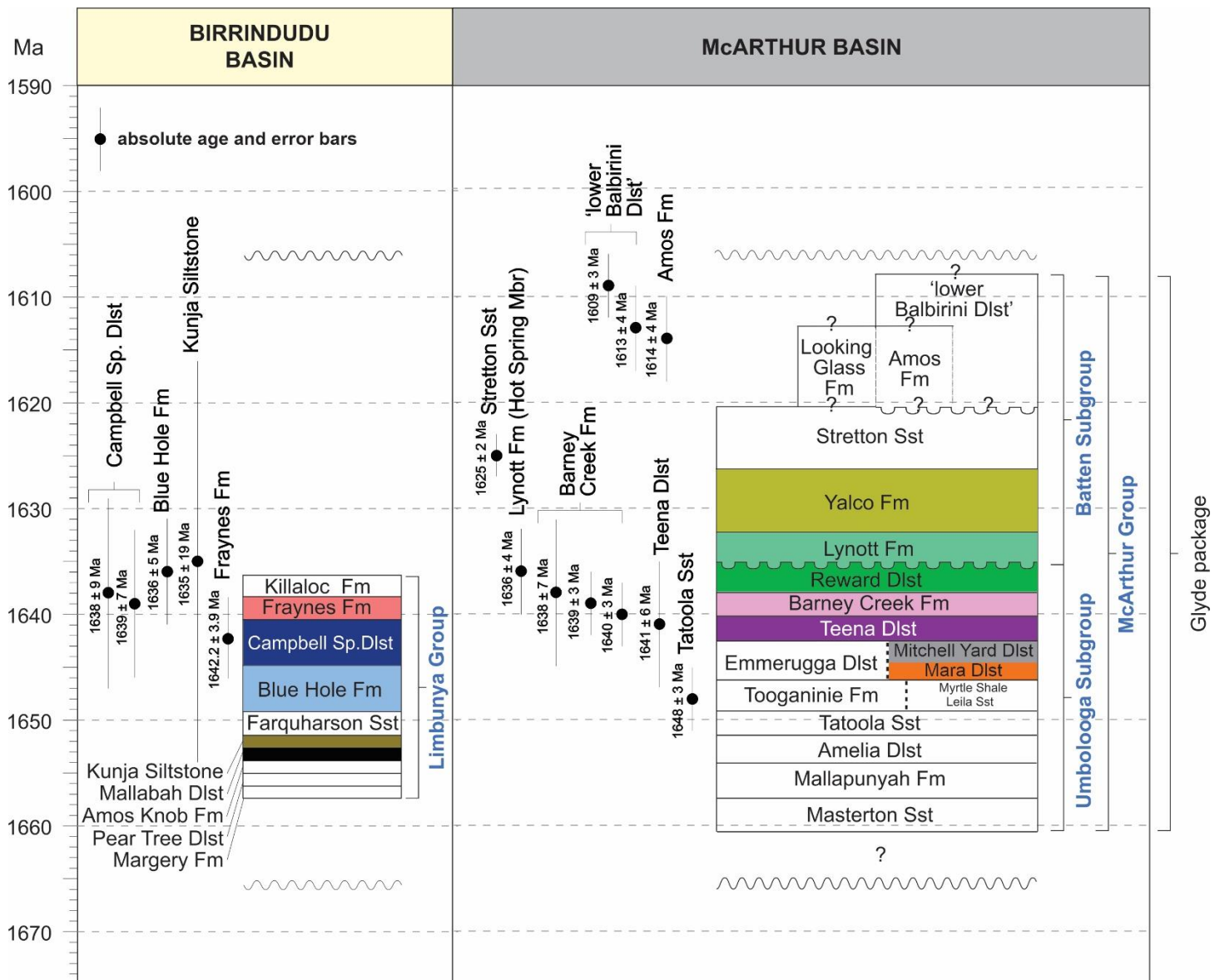


**Figure 5.2.** Stratigraphic correlation of the Glyde Package units from the McArthur Basin and the Birrindudu Basin adapted from Munson (2019) based on U–Pb dating of tuff layers in the corresponding formations (Kositcin and Carson, 2017, Munson et al., 2020, Page et al., 2000, Page and Sweet, 1998).

## 5.4 Methods

The methods and subsequent reference materials used in this study are summarised here and discussed further in the Supplementary Material. Geochemical data from literature were also compiled in this study and their methodologies can be found in the references therein (Bruisten and Brocks, 2015, Jarrett et al., 2018, Jarrett et al., 2021, NTGS., 2015b, Vinnichenko and Brocks, 2019, Vinnichenko et al., 2021).

### 5.4.1 Shale geochemical analysis

Shale samples were washed to rid of surface contaminants and were finely powdered using a tungsten carbide mill at the University of Adelaide. Organic geochemical data were collected by pyrolysis analysis of raw powdered samples by a Weatherford's Source Rock Analyser following Cox et al. (2016b). The flame ionisation detector (FID) was calibrated with a Weatherford Laboratories Instruments Division Standard 533 and analysers were

regulated against a standard gas with known concentration of CO<sub>2</sub> and CO. Results were processed with Optkin 3.0 software, where peaks and geochemical indices such as total organic carbon (TOC), Oxygen Index (OI), Hydrogen Index, and Production Index (PI) are automatically calculated. They were then screen using the criteria defined by Hall et al. (2016). Major, trace, and rare earth and yttrium element (REEY) analyses were collected at Bureau Veritas using an Agilent 7900 Series Inductively Coupled Plasma-Mass Spectrometer (ICP-MS).

#### **5.4.2. Carbonate geochemical analysis**

Major, trace, and REEY concentrations from carbonate rocks here were determined following Kuznetsov et al. (2010) to minimise non-authigenic, secondary phases from the bulk sediment. Homogeneous carbonate laminations were micro-drilled and their following rock powder washed with ammonium acetate to remove loosely bounded cations. Further leaching was then done using dilute ammonium acetate and acetic acid to extract the primary carbonate phase. Elemental concentrations were then analysed on the final solutions using an Agilent 8900 ICP-MS/MS operated in solution mode at Adelaide Microscopy.

Radiogenic and stable Sr isotopic analyses were undertaken on an aliquot of the sample solution prepared for elemental geochemistry of bulk carbonates. The coupled  $^{87}\text{Sr}/^{86}\text{Sr}$  and  $\delta^{88/86}\text{Sr}$  determinations were completed at the University of Adelaide using a Phoenix Isotopx thermal ionisation mass spectrometry (TIMS) instrument following Shao et al. (2021). Briefly, two aliquots (i.e., spiked and unspiked) were taken from a sample solution to define the  $\delta^{88/86}\text{Sr}$  values in samples. One of the aliquots was spiked using an  $^{87}\text{Sr}$ - $^{84}\text{Sr}$  double spike solution, with the resulting Sr fraction separated via ion chromatography using Sr-Spec micro-columns. Pure Sr fractions were then loaded on single non-zone-refined rhenium filaments for TIMS analysis. The unspiked aliquots were purified using the same approach and ran on the same instrument using a multi-dynamic peak-hopping method (Shao et al., 2021) for radiogenic  $^{87}\text{Sr}/^{86}\text{Sr}$  ratios. The standard reference materials 987 and JCP-1 were used for this procedure (Balcaen et al., 2005, Krabbenhöft et al., 2009, Shao et al., 2021). On the other hand,  $\delta^{13}\text{C}$  and  $\delta^{18}\text{O}$  in carbonates were collected following Spötl and Vennemann (2003). In short, micro-drilled rock powder samples were placed into glass vials, purged with phosphoric acid, and injected with helium. The ratio of the isotopic composition from the resultant gas was measured using a Dual Inlet Isotope Ratio Mass Spectrometer (DI-IRMS) with attached Fissions Isocarb Carbonate Preparation System at the University of Adelaide. These values are expressed as relative to Pee Dee Belemnite values using internal working standards.

#### **5.4.3 High resolution imaging and in situ Rb–Sr dating with trace element analysis of shales**

Shale samples prepared for *in situ* Rb–Sr dating and trace element analysis were first mapped for their petrographic textures and elemental composition. This was done using an FEI Quanta 450 Scanning Electron Microscope (SEM) with attached Oxford Ultima Max Large Area SDD EDS detector at Adelaide Microscopy following Subarkah et al. (2021) and (2022). The images were processed using the Oxford Aztec EDS software. Detrital, replacement, and

non-K-bearing minerals were avoided for *in situ* Rb–Sr analysis to avoid incorporating non-authigenic phases.

*In situ* Rb–Sr analyses were performed at Adelaide Microscopy following the approach described by Redaa et al. (2021a) using an Agilent 8900 ICP-MS/MS instrument coupled to a RESOLUTION ArF 193nm excimer laser ablation system. Each spot analysis consisted of 20 seconds of gas background collected while the laser was not firing, followed by 40 seconds of ablation time. A reaction gas N<sub>2</sub>O was introduced in the reaction chamber that to react with Sr forming <sup>87</sup>Sr<sup>16</sup>O. This allows the reaction product to be measured without mass interference with <sup>87</sup>Rb. Laser and mass spectrometer parameters used here are summarised in the Supplementary Information. All samples were analysed using a 67 μm laser beam, 5 Hz repetition rate and a fluence of 3.5 J/cm<sup>2</sup>. Targeting a mixture of several clay-sized, cogenetic minerals in one ablation spot using the same approach have proven to yield robust isochrons and ages (Subarkah et al., 2021, Subarkah et al., 2022, Tillberg et al., 2020). Phlogopite nano-powder Mica-Mg was used as the primary reference material for Rb/Sr (Govindaraju et al., 1994) and the synthetic reference glass NIST610 (Hogmalm et al., 2017, Woodhead and Hergt, 2001) for normalisation of Sr/Sr ratios and trace elements. The natural phlogopite mineral crystal MDC sourced from the same location as Mica-Mg (Govindaraju et al., 1994) and glauconite sample GL-O of known Cretaceous age from Bagnols-sur-Cèze, France were also analysed as secondary age standards during the same run (Rousset et al., 2004). In addition, basalt standard BCR-2G was also used as a secondary standard to cross-check elemental quantification (Jochum et al., 2005, Wilson, 1997). Laser ablation data and error correlations were processed using the LADR software package (Norris and Danyushevsky, 2018, Schmitz and Schoene, 2007). During the data-processing, Zr, Si, Ti, and REEY signals were monitored to filter the non-authigenic component in each ablation analysis (Subarkah et al., 2022). Non-stable isotopic and elemental signatures were also screened during the process to ensure spot homogeneity. Isochron ages and initial <sup>87</sup>Sr/<sup>86</sup>Sr ratios were calculated using IsoplotR (Vermeesch, 2018). Geochronological errors reported in this study are 2σ.

## 5.5 Results

Three runs of JCP-1 yielded a mean value of  $0.190 \pm 0.012$  for stable  $\delta^{88/86}\text{Sr}$  ratios and  $0.709157 \pm 0.000005$  for <sup>87</sup>Sr/<sup>86</sup>Sr isotopes respectively. These results are accurate to the published values ( $\delta^{88/86}\text{Sr}$ :  $0.197 \pm 0.013$ , <sup>87</sup>Sr/<sup>86</sup>Sr:  $0.709164 \pm 0.000006$ ) of the standard (Krabbenhöft et al., 2009). Next, the SRM 987 gave a mean  $\delta^{88/86}\text{Sr}$  value of  $0.028 \pm 0.050$  and <sup>87</sup>Sr/<sup>86</sup>Sr value of  $0.710253 \pm 0.000003$ . This is also in good agreement with their respective data ( $\delta^{88/86}\text{Sr}$ :  $0.012 \pm 0.044$ , <sup>87</sup>Sr/<sup>86</sup>Sr:  $0.710250 \pm 0.000010$ ) found in literature (Balcaen et al., 2005, Krabbenhöft et al., 2009). Mean values of major, trace and REEY in BCR-2G here are also within error and positively correlates (Pearson R > 0.999, Pearson R<sup>2</sup> > 0.999, and P Value < 0.0001) with their published record (Jochum et al., 2016, Jochum et al., 2005, Wilson, 1997).

Reference material Mica-Mg (Govindaraju et al., 1994) prepared here as a nano-powder pellet and a phlogopite sample MDC sourced from the same location were used as primary and secondary standards for *in situ* Rb–Sr geochronology respectively (Hogmalm et al.,

2017, Jegal et al., 2022, Redaa et al., 2021a). These standards have been used jointly and are assumed to be of the same age (Armistead et al., 2020, Hogmalm et al., 2017, Li et al., 2020, Redaa et al., 2021a, Redaa et al., 2021b, Subarkah et al., 2022, Tamblyn et al., 2020). The standards Mica-Mg and MDC were anchored to its reported  $^{87}\text{Sr}/^{86}\text{Sr}$  value of  $0.72607 \pm 0.00363$  (Hogmalm et al., 2017) and gave an age of  $522 \pm 4$  and  $529 \pm 6$  Ma, respectively. This is within error of the average age of the source rocks at  $519 \pm 7$  Ma (Hogmalm et al., 2017). The glauconite GL-O secondary standard (Rousset et al., 2004) analysed here gave an age of  $94 \pm 3$  Ma, accurate to its published K–Ar age of  $95 \pm 1.5$  Ma (Derkowski et al., 2009). It should be noted that the age of GL-O is consistently younger than the age of the rock ( $113 \pm 0.3$  Ma) it is hosted in (Selby, 2009). Consequently, the ages yielded from GL-O have been interpreted to instead time the glauconite formation after the deposition of its host rock (Selby, 2009). Further discussions of the results used in this study can be found in the Supplementary Material (Subarkah, 2022b).

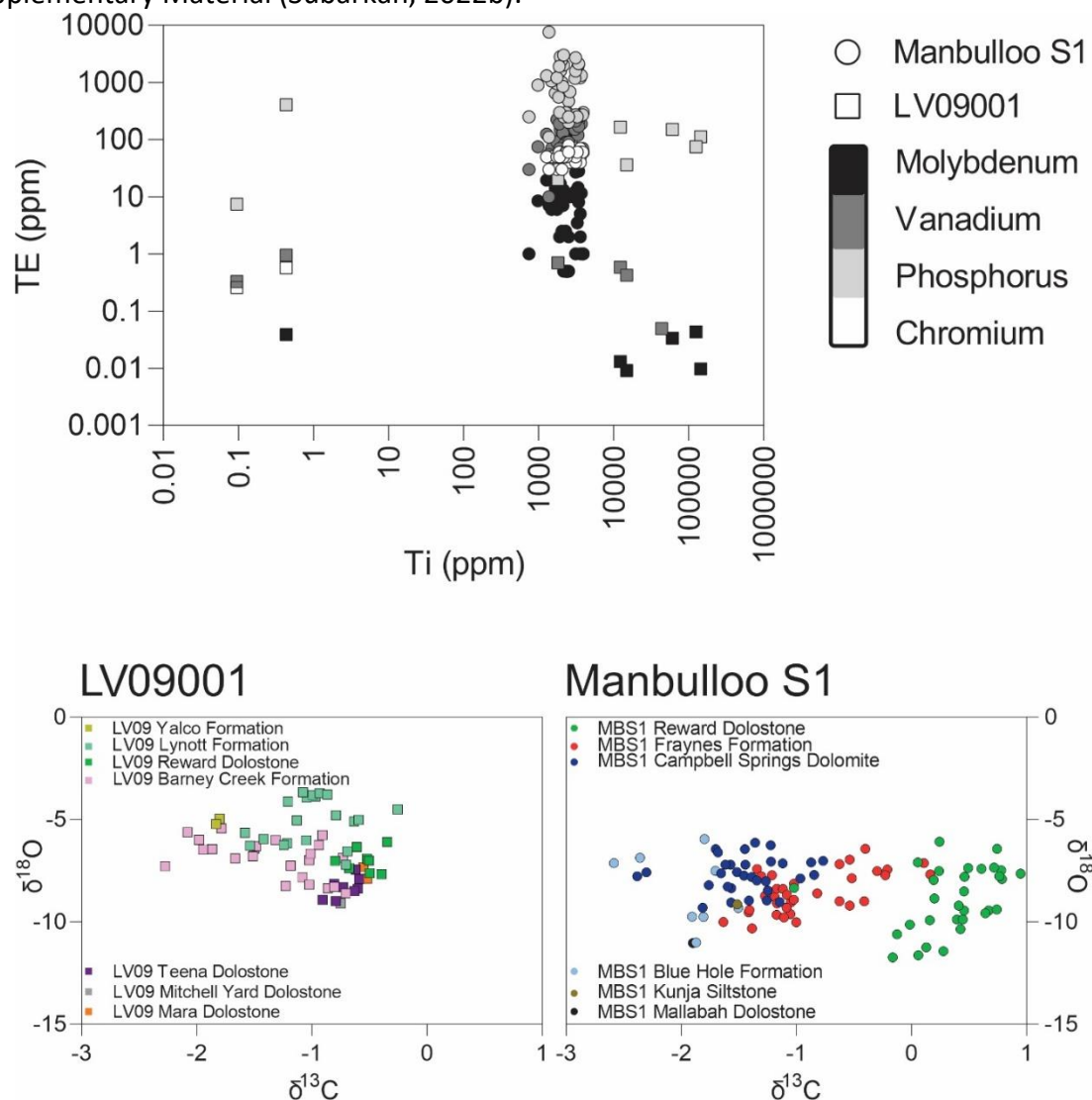


**Figure 5.3.** Geochemical proxies for detrital contamination (Reinhard et al., 2013) and alteration (Banner and Hanson, 1990) in this study show that the trace element proxies used here can be used for palaeoenvironment reconstructions.

### 5.5.1 Whole-rock shale and carbonate geochemistry of the Glyde Package

The chemical signatures of marine sedimentary rocks have been applied to help elucidate past earth systems processes interacting on our planet's surface. However, it is crucial to show that the chemical fingerprints used for further interpretations represent the authigenic component of these rocks. For example, the geochemical composition of whole-rock samples in this study may be influenced by detrital input, and its trace element budget may be dominated by this detrital component. As such, Titanium (Ti) is used here (Fig. 5.3) and elsewhere (Reinhard et al., 2013) as an index element to fingerprint increasing detrital flux into marine sedimentary rocks. Consequently, relationships between Ti and trace elements may suggest a significant influence on the geochemical signature of these samples (Goodarzi et al., 2019, Reinhard et al., 2013, Schier et al., 2021, Tostevin et al., 2016). However, Ti content and trace element composition display no statistically significant covariations (Fig. 5.3). As such, detrital contamination is considered to be minimal in the results observed in this study.

Furthermore, these geochemical signatures may also be affected by post-depositional diagenetic alteration (Allan and Matthews, 1982, Banner and Hanson, 1990, Degens and Epstein, 1962, Killingley, 1983, Land, 1995). Such secondary reactions are commonly screened by identifying relationships (Fig. 5.3) between the  $\delta^{13}\text{C}$  and  $\delta^{18}\text{O}$  isotopic systems (Allan and Matthews, 1982, Banner and Hanson, 1990). Samples from both wells show no significant correlations between these two isotopes (Fig. 5.3). In addition, anomalously light  $\delta^{18}\text{O}$  values have been suggested to be caused by geochemical overprinting from meteoric waters or elevated temperatures (Degens and Epstein, 1962, Killingley, 1983, Land, 1995). All of the  $\delta^{18}\text{O}$  isotopic results here are heavier than  $-15\text{‰}$  (Fig. 5.3). Together, the lack of detrital input and the evidence for diagenetic overprint suggest that the geochemistry of these samples reflect the coeval basin water composition during their formation in the Proterozoic. The isotopic signatures from the Fraynes Formation and the Barney Creek Formation display the best correlations with each other (Fig. 5.7). This includes a positive  $\delta^{13}\text{C}_{\text{carb}}$  excursion of  $2.0\text{‰}$ , fluctuations in  $^{87}\text{Sr}/^{86}\text{Sr}$  up-section, and a negative  $\delta^{88/86}\text{Sr}$  excursion of  $-2.5\text{‰}$ .

The Fraynes Formation here yielded the most variable TOC and redox-sensitive proxies (Fig. 5.5 and 5.6). This heterogeneity similarly mirrored by findings from the Barney Creek Formation. On the other hand, the trace element indicators from Campbell Springs Dolostone and the Teena Dolostone looks to be relatively more homogeneous (Fig. 5.6). Notably, samples from the Reward Dolostone, and the Lynott Formation consistently had lower average redox index element concentrations in comparison to the other units studied here (Fig. 5.6). The whole-rock geochemical data collected is summarised in Table 5.1.

### 5.5.2 High-resolution petrographic mapping of shales from the Barney Creek Formation and the Fraynes Formation

Prior to *in situ* laser analysis, samples were mapped for their petrographic relationships and discussed in the Supplementary Material (Subarkah, 2022b). The finest-grained, homogeneous, black laminations of each sample were targeted to avoid detrital contamination, obvious alteration assemblages, and veining. Clay minerals from the Barney

Creek Formation in well LV09001 and the Fraynes Formation from Manbulloo S1 had similar morphologies. These minerals do not exhibit characteristics commonly found in detrital clays such as angular, fragmented boundaries, large grain sizes, and textural immaturity (Deepak et al., 2022, Rafiei and Kennedy, 2019, Rafiei et al., 2020). Instead, they look to form in the sediment as an authigenic assemblage along with quartz minerals. A Barney Creek Formation shale sample from depth 463.60 m shows fine illite flakes concentrated in mottled domains, with sections where individual flakes cannot be distinguished (Subarkah, 2022b). Concentrations of illite commonly preserve their compaction structures, wrapping around detrital quartz grains. A sample of the same unit from depth 469.50 m still displays primary bedding structures. Illite minerals here are interconnected, filling pore spaces and grow together with quartz cement. These clay morphologies are similarly displayed in the Fraynes Formation shale samples from Manbulloo S1. Furthermore, early diagenetic pyrite can be observed growing together with siderite. This is often an important indicator of anoxic water columns with varying availability of sulphur (Mozley and Wersin, 1992). Altogether, these petrographic relationships suggest the authigenic formation of clay minerals in the shales. Such morphologies have been identified elsewhere in the Proterozoic marine sedimentary rocks and have been interpreted to be a result of reverse weathering processes (Deepak et al., 2022, Kennedy et al., 2006, Kennedy et al., 2002, Rafiei and Kennedy, 2019, Rafiei et al., 2020, Subarkah et al., 2021).

### **5.5.3 Rb–Sr geochronology of distal shale samples from the Glyde Package**

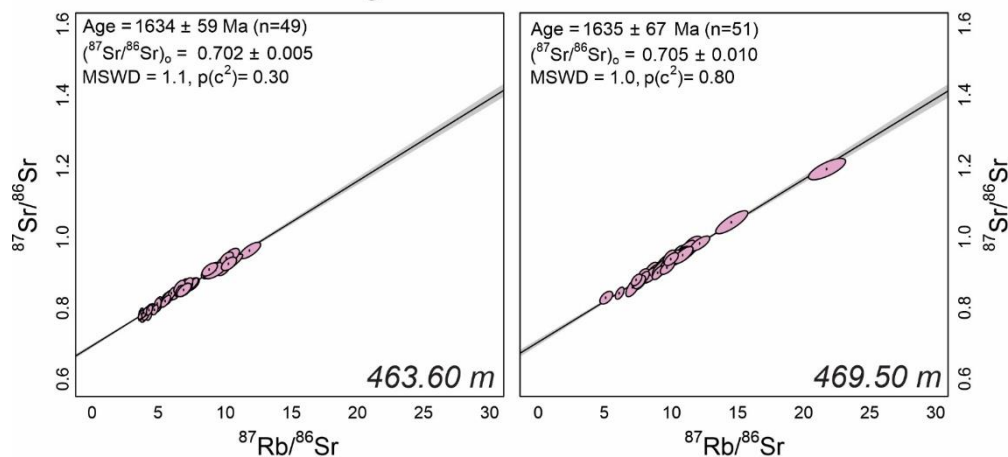
*In situ* Rb–Sr geochronology of shale samples from the Glyde Package gave ages and  $^{87}\text{Sr}/^{86}\text{Sr}$  initial ratios (denoted as  $^{87}\text{Sr}/^{86}\text{Sr}_0$ ) in good agreement with each other. Two samples from the Barney Creek Formation sourced from depths 463.60 and 469.50 m depths in the well LV09001 were dated at  $1634 \pm 59$  ( $^{87}\text{Sr}/^{86}\text{Sr}_0$ :  $0.702 \pm 0.005$ ) and  $1635 \pm 67$  Ma ( $^{87}\text{Sr}/^{86}\text{Sr}_0$ :  $0.705 \pm 0.010$ ), respectively (Fig. 5.4). Analysis of shales from the Fraynes Formation from depths 785.24 and 868.75 m in Manbulloo S1 (Fig. 5.4) yielded ages of  $1630 \pm 57$  ( $^{87}\text{Sr}/^{86}\text{Sr}_0$ :  $0.700 \pm 0.010$ ) and  $1636 \pm 42$  Ma ( $^{87}\text{Sr}/^{86}\text{Sr}_0$ :  $0.690 \pm 0.010$ ). Notably, these Rb–Sr ages are within error of the expected ages for each unit (Fig. 5.2), derived from dating tuff layers within the corresponding formations in other localities (Kositcin and Carson, 2017, Munson et al., 2020, Page et al., 2000, Page and Sweet, 1998). Furthermore, the  $^{87}\text{Sr}/^{86}\text{Sr}$  initial ratios calculated from their respective isochrons (Fig. 5.4) also overlapped with the expected  $^{87}\text{Sr}/^{86}\text{Sr}$  signature of Proterozoic seawater 0.705–0.706 (Chen et al., 2022, Kuznetsov et al., 2018, Shields and Veizer, 2002).



Unit	TOC (wt. %)			Mo (ppm)			V (ppm)		
	Min.	Mean	Max.	Min.	Mean	Max.	Min.	Mean	Max.
Lynott Formation	0.13	0.19	0.25	0.48	0.50	0.51	0.05	17.65	26.57
Reward Dolostone	1.08	1.59	2.08	0.27	0.71	1.23	25.37	26.25	27.18
Barney Creek Formation	0.11	2.06	4.71	0.29	3.37	8.30	24.61	33.62	51.10
Fraynes Formation	0.04	2.09	8.39	1.00	18.77	101.00	30.00	147.33	250.00
Teena Dolostone	0.14	1.86	5.01	2.47	4.50	6.38	8.07	27.46	44.40
Campbell Springs Dolostone	0.19	1.52	2.63	0.50	1.63	7.00	10.0	71.88	90.0

**Table 5.1.** Summary of the palaeoredox geochemical results in this study.

### LV09001 Barney Creek Formation



### Manbulloo S1 Fraynes Formation

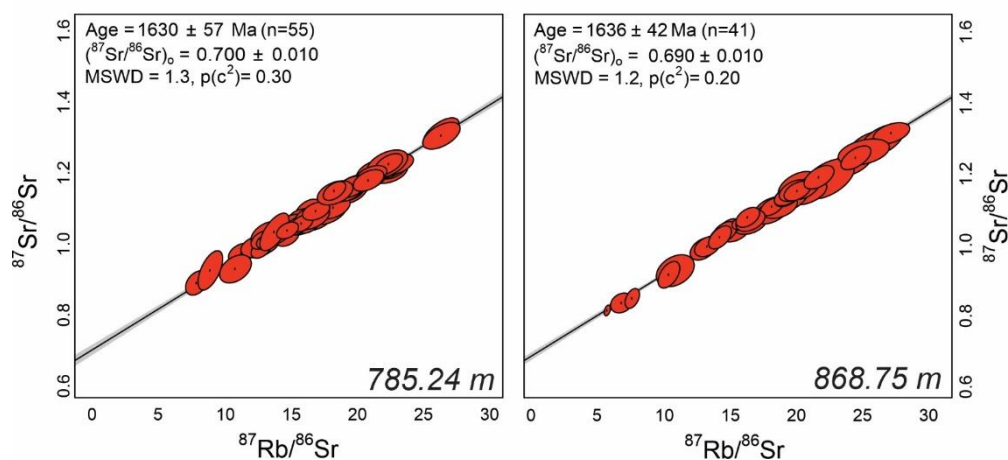


**Figure 5.4.** In situ Rb–Sr geochronological results from shales in the Barney Creek Formation and Fraynes Formation sourced from boreholes LV09001 and Manbulloo S1, respectively.

## 5.6 Discussions

The Rb–Sr ages and isotopic fingerprints from shale samples here (Fig. 5.4) overlaps with their expected depositional ages (Kositcin and Carson, 2017, Munson et al., 2020, Page et al., 2000, Page and Sweet, 1998) as well as the coeval palaeowater  $^{87}\text{Sr}/^{86}\text{Sr}$  chemistry (Chen et al., 2022, Kuznetsov et al., 2018, Shields and Veizer, 2002). Consequently, these results are interpreted as minimum age constraints for the two respective units, recording an early diagenetic event in equilibrium with the surrounding formation waters during or soon after deposition (Subarkah et al., 2021). Importantly, these signatures seems to have not been disturbed by a late-stage alteration event (Subarkah et al., 2022). As such, they provide a conservative depositional window for the Barney Creek Formation and the Fraynes Formation, and directly correlate these distal units.

In addition to the geochronological data, geochemical signatures from this study also show that the samples still retains their primary composition and have not experienced significant post-depositional perturbations (Fig. 5.3). As a result, they can be used for palaeoenvironment investigations as well as correlating distal sequences. Samples here were analysed for several redox-sensitive trace elements to assess the oxygenation conditions of the formation waters during the deposition of the respective units. The two main palaeoredox proxies used in this study are enrichments in molybdenum (Mo) and vanadium (V). Mo is a commonly used trace element redox proxy as it is the most abundant trace metal in the modern ocean (Millero, 1996, Wright, 1995). In anoxic conditions, Mo is enriched within the sediment as it forms thiomolybdates and preserves organo-metallic complexes (Helz et al., 1996, Vorlicek and Helz, 2002). As such, Mo concentrations will have a strong, positive relationship with total organic carbon (TOC) content (Fig. 5.5) under oxygen-poor water columns (Scott and Lyons, 2012). This relationship is similarly mirrored by abundance in V (Fig. 5.5), where in the presence of anoxia,  $\text{V}^{5+}$  is reduced to  $\text{V}^{4+}$  by organic compounds (Breit and Wanty, 1991). Notably, Mo experiences hyper enrichment during euxinia, where it is sequestered in solid solution with authigenic sulphides (Berrang and Grill, 1974, Morse and Luther III, 1999). Similarly,  $\text{V}^{4+}$  also undergoes further reduction to  $\text{V}^{3+}$  by reactions with hydrogen sulphide (Wanty and Goldhaber, 1992). As a result, the relationships between both elements and TOC content breaks down in euxinic water columns (Fig. 5.5), as sulphides become a competing sink for Mo and V against organic compounds (Algeo and Maynard, 2004, Tribovillard et al., 2006). Importantly, under oxic conditions, both elements will be deposited in the detrital phase, displaying no relationships with TOC content and depleted in the sediment (Algeo and Maynard, 2004, Piper and Calvert, 2009, Tribovillard et al., 2006). The fact that V accumulates more readily under suboxic to anoxic conditions, relative to euxinic environments (Emerson and Husted, 1991, Wanty and Goldhaber, 1992) allows these two redox sensitive trace elements can be used together to distinguish complex bottom water heterogeneity (Fig. 5.6). Low V/Mo ratios are more reflective of euxinia, and in contrast, high V/Mo ratios suggests anoxic water columns (Piper and Calvert, 2009, Spinks et al., 2016a).

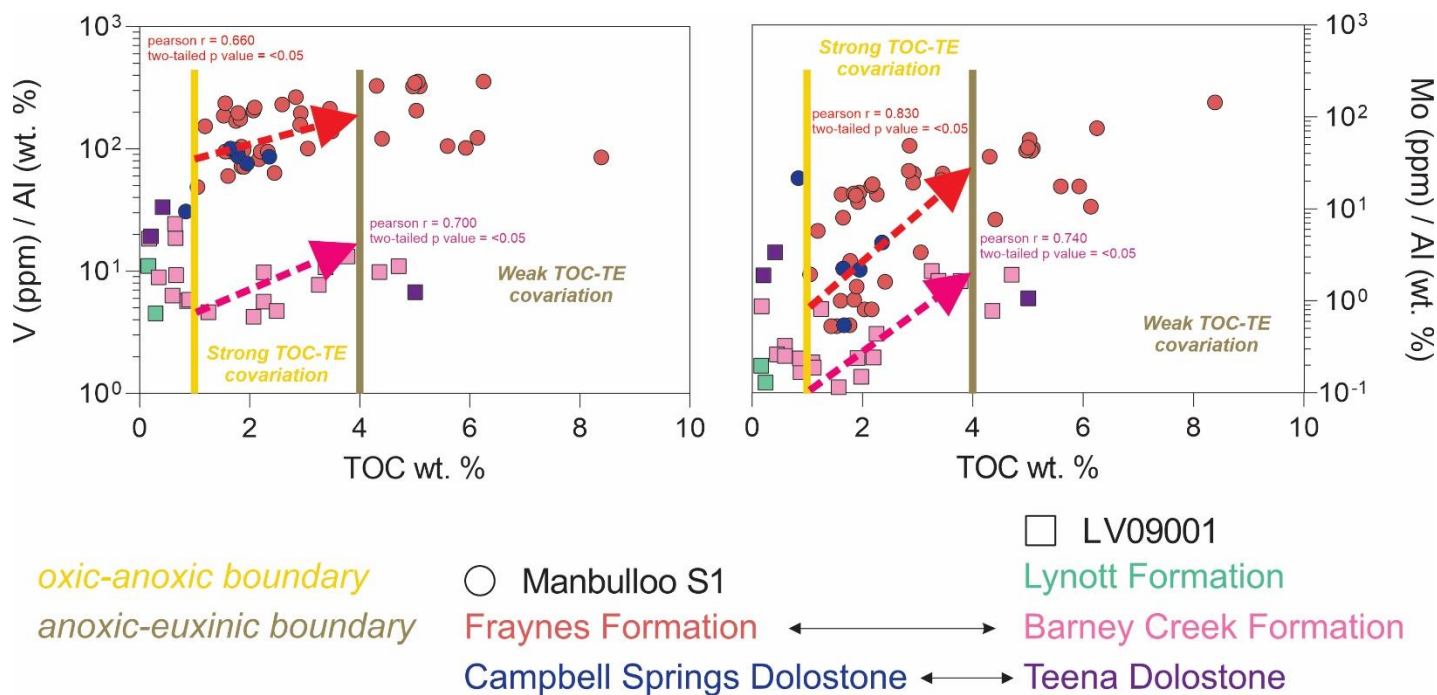


**Figure 5.5.** Redox-sensitive trace element enrichments with respect to total organic carbon (TOC) content. Note that V and Mo both show similar patterns, with strong linear relationships with TOC between 1–4 wt. %. These thresholds are similarly found elsewhere in sections of the greater McArthur Basin with excellent hydrocarbon reservoir potential (Cox et al., 2016b). This positive covariation and its subsequent breakdown at TOC content above 4 wt. % is consistent with the onset of anoxia followed by intermittent euxinia (Algeo and Maynard, 2004, Scott and Lyons, 2012). Note that the Fraynes Formation show a stronger affinity for euxinic conditions compared to the Barney Creek Formation.

Trace element proxies in this study show that the Teena Dolostone from the McArthur Group and the Campbell Springs Dolostone from the Limbunya Group do not exhibit any significant relationships between TEs and TOC content (Fig. 5.5). As such, we suggest that these units were deposited beneath a relatively suboxic to anoxic water column (Scott and Lyons, 2012). This is similarly indicated by the high V/Mo ratios (Fig. 5.6) of these units (Piper and Calvert, 2009). Further up in stratigraphy, the Barney Creek Formation and the Fraynes Formation both displays a more complex redox history (Fig. 5.5 and 5.6). Here, V and Mo exhibits a strong, positive relationship with TOC content between 1–4 wt. % (Figure 5.5), indicating an anoxic system, and consistent with organic matter being the dominant sink for TEs (Algeo and Maynard, 2004, Scott and Lyons, 2012). Notably, this linear covariation breaks down above a TOC content of 4 wt. %. At these elevated TOC values, V and Mo experiences are interpreted to be enriched in the sediment as it is scavenged by precipitating sulfides during water column euxinia (Algeo and Maynard, 2004, Scott and Lyons, 2012). This threshold have been similarly recorded in the Velkerri Formation, where bioproductivity have been suggested to drive redox-heterogeneity in the water column (Cox et al., 2016b). However, the results from the Fraynes Formation does suggest that it has experienced a more intense sulfidic environment in comparison to the Barney Creek Formation. Here, the relationship between redox-sensitive trace elements and TOC breaks down more readily, and the sediment is hyper-enriched in Mo (Fig. 5.5 and 5.6). Such conditions would make the Fraynes Formation highly prospective for hosting base-metal mineralisation as well as hydrocarbon resources; as euxinic sediments are excellent traps for

metallogenic fluids and preserving organic matter (Calvert and Pedersen, 1993, Degens and Mopper, 1975, Demaison and Moore, 1980, Large and Wolf, 1981, Lyons et al., 2006, Spinks et al., 2016b, Walters, 2006). This extensive euxinic period in the Fraynes Formation is further supported by the low V/Mo ratios with high Mo content (Fig. 5.6), implying that the unit experienced hyper enrichment in Mo and not V (Piper and Calvert, 2009). Prior to the deposition of the Barney Creek Formation and the Fraynes Formation, the package seems to be relatively more oxygen-rich (Fig. 5.6). This transient period of oxic environments seems to be extensive, as correlative sections from the Teena Dolostone and the Campbell Springs Dolostone records similar signatures. After the deposition of the Barney Creek Formation and the Fraynes Formation, the package transitioned back into relatively more oxygen-rich basin waters, reflected by the Reward Dolostone and the Lynott Formation (Fig. 5.6).

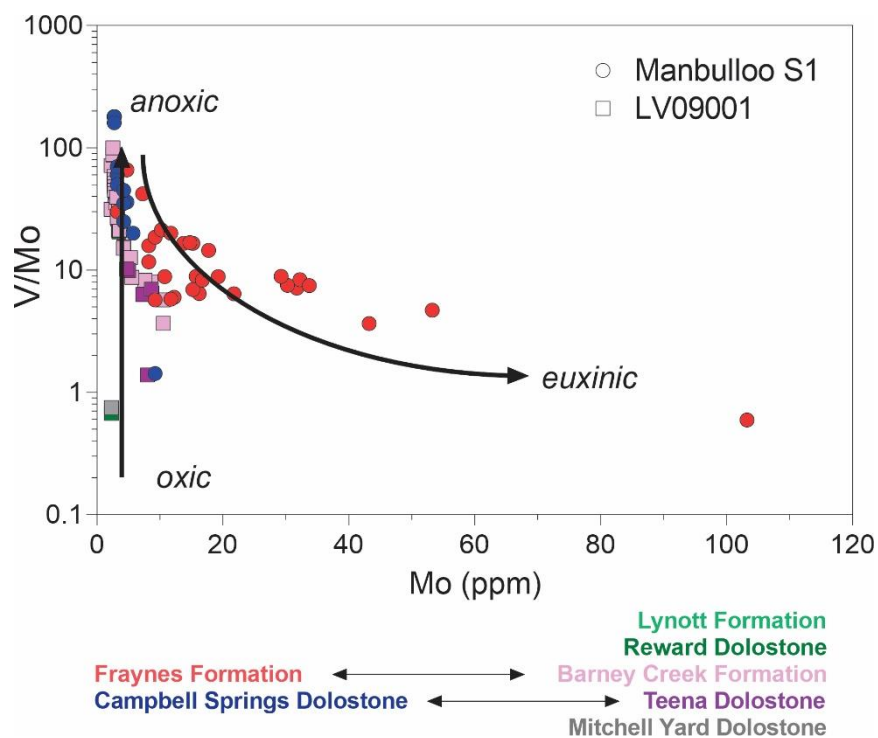


**Figure 5.6.** V/Mo versus Mo palaeoredox plot showing the heterogeneous conditions evident in the Glyde Package. High V/Mo ratios with low concentrations of Mo indicate suboxic-to-anoxic environments whereas low V/Mo ratios with high concentrations of Mo highlight periods of euxinia (Piper and Calvert, 2009, Xu et al., 2012). Similar to Figure 5.5, this plot also shows that the Fraynes Formation is more euxinic than the Barney Creek Formation.

However, it is possible that this redox variability also occurs laterally, as the basin undergoes a change in palaeogeography and the same formations record different facies (Kunzmann et al., 2022). If this is true, the geochemical signatures here may not be totally representative of their respective units. Nevertheless, this redox heterogeneity hints at how complex this Proterozoic continental seaway was during its formation. Consequently, the delay of widespread anoxia or euxinia during here could be important for the survival of early biological life in this period (Spinks et al., 2016a).

The palaeoenvironment and tectonic evolution of the basin have been shown to be an important control on its coeval water chemistry (Benitez-Nelson, 2000, Calvert and

Pedersen, 1993, Chen et al., 2022, Condie et al., 2001, Derry and Jacobsen, 1988, El Meknassi et al., 2020, Tostevin et al., 2016). Such variability can be tracked by several isotopic proxies. For example, the  $\delta^{13}\text{C}_{\text{carb}}$  isotope values of unaltered marine carbonates have been used to deduce the composition of the dissolved inorganic carbon (DIC) pool for its coeval water-column (Knoll et al., 1986, Schidlowski, 1988). Biological activity plays a key role in the DIC reservoir, as processes like photosynthesis preferentially remove lighter  $^{12}\text{C}$  from the water mass, resulting in the DIC pool being isotopically heavier (Kump and Arthur, 1999). In contrast, organic matter remineralisation can reintroduce  $^{12}\text{C}$  into the water column, consequently leaving the DIC pool isotopically lighter (Sarmiento et al., 2007). As a result, the changes in the  $\delta^{13}\text{C}_{\text{carb}}$  record can fingerprint the interplay between these processes. Furthermore, cogenetic marine carbonates that precipitated distally can also retain the same  $\delta^{13}\text{C}_{\text{carb}}$  excursions, as the residence time of C in oceans is orders of magnitude longer than the typical mixing time of seawater (Kump and Arthur, 1999, Shields and Veizer, 2002). As such, shifts in  $\delta^{13}\text{C}_{\text{carb}}$  can record changes in bioproductivity and be applied for chemostratigraphic studies in a local, regional, and global scale (Hayes and Waldbauer, 2006, Shields-Zhou and Mills, 2017, Shields and Veizer, 2002, Veizer et al., 1999, Veizer et al., 1992).

In addition to the  $\delta^{13}\text{C}_{\text{carb}}$  isotope excursions, the Sr composition of marine carbonates can also be used to unravel the evolution of the basin. In particular, the  $^{87}\text{Sr}/^{86}\text{Sr}$  signatures from authigenic marine carbonates can reflect the provenance into the sedimentary system, relative input of Sr between hydrothermal/marine and riverine sources, as well as silicate weathering from continental erosion (Banner, 2004, Chen et al., 2022, Derry and Jacobsen, 1988, El Meknassi et al., 2020, Kuznetsov et al., 2018, Veizer et al., 1999). Higher ratios in the global palaeoseawater  $^{87}\text{Sr}/^{86}\text{Sr}$  archive reflect increased erosion of ancient rocks, often caused by an escalation in global mountain belt development that appears to reflect supercontinent amalgamation and continent-continent collisions (Kuznetsov et al., 2018). Conversely, lower ratios are usually explained by an influx of mantle/oceanic crust derived Sr from rift boundaries in relation to supercontinent break-up (Semikhatov et al., 2002). Furthermore, the presence of large igneous provinces and mantle plumes can also drive the  $^{87}\text{Sr}/^{86}\text{Sr}$  values of palaeoseawater lower (Prokoph et al., 2004).

However, it should be noted that the changes in the palaeoseawater  $^{87}\text{Sr}/^{86}\text{Sr}$  record do not track fluctuations linked to the carbonate cycle or the removal of Sr via deposition of carbonates (Krabbenhöft et al., 2010, Vollstaedt et al., 2014). The input and outputs of the ocean's Sr budget can instead be traced by mass-dependent fractionation processes of stable  $\delta^{88/86}\text{Sr}$  through carbonate formation or dissolution (Andrews et al., 2016, Krabbenhöft et al., 2010, Shalev et al., 2017, Shao et al., 2021). During the precipitation of carbonates in marine settings, lighter Sr isotopes are preferentially removed from seawater, with an average  $\delta^{88/86}\text{Sr}$  offset of -0.18‰ to -0.21‰ (Shao et al., 2021, Vollstaedt et al., 2014). As such, this mechanism drives the palaeoseawater isotopically heavier by the same magnitude. Additionally, igneous differentiation can also drive fractionation of Sr isotopes. The influx of Sr from felsic, or granitic detritus transported by rivers from the weathering of continental crust will induce lighter  $\delta^{88/86}\text{Sr}$  values but higher  $^{87}\text{Sr}/^{86}\text{Sr}$  ratios (Amsellem et al., 2018, Charlier et al., 2012, de Souza et al., 2010, Krabbenhöft et al., 2010, Vollstaedt et

al., 2014). On the contrary, basins sourcing more mafic materials from the mantle or hydrothermal input will characteristically have higher  $\delta^{88/86}\text{Sr}$  values but lower  $^{87}\text{Sr}/^{86}\text{Sr}$  ratios (Amsellem et al., 2018, Charlier et al., 2012).

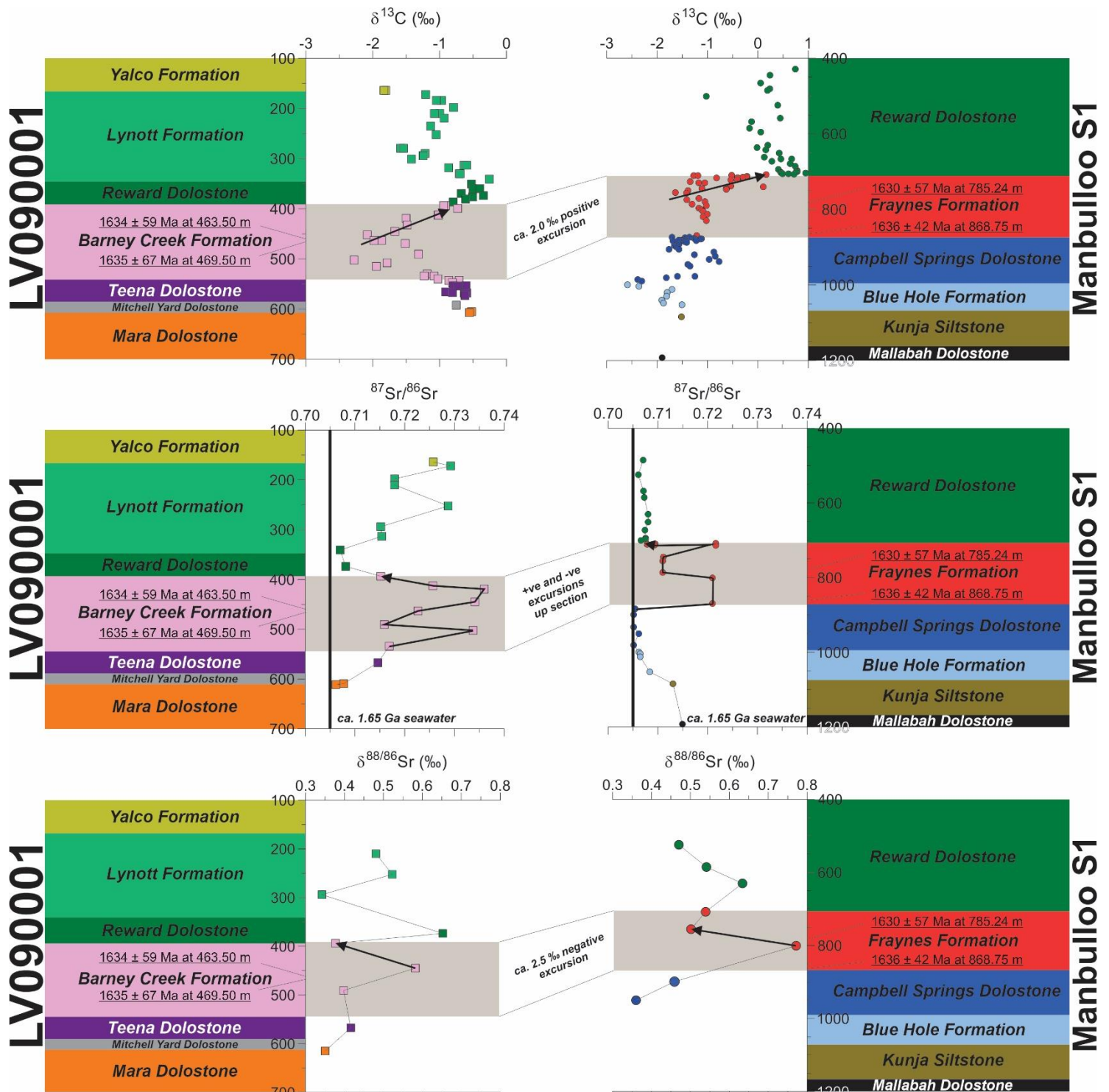


**Figure 5.7.** Chemostratigraphic correlations between the McArthur Group sampled from LV090001 and the Limbunya Group from Manbulloo S1. Similar patterns in  $\delta^{13}\text{C}_{\text{carb}}$ ,  $^{87}\text{Sr}/^{86}\text{Sr}$ , and  $\delta^{88/86}\text{Sr}$  isotopic signatures from carbonate lithologies further suggests that the Barney Creek Formation and the Fraynes Formation are contemporaneous units. This includes a  $\delta^{13}\text{C}_{\text{carb}}$  excursion of  $\sim 2.0$  ‰, a trend towards lower  $^{87}\text{Sr}/^{86}\text{Sr}$  ratios up-section, and a  $\delta^{88/86}\text{Sr}$  excursion of  $\sim 2.5$  ‰ (relative to NIST987). These similarities also suggests that basin-scale evolution of the Glyde Package can be recorded by distal sequences in the McArthur Basin and the Birrindudu Basin.



The combination of these isotopic proxies can be used to investigate the evolution of the basin system across distal locations, as they would be less susceptible to localised changes such as sedimentation rate, accumulation, or preservation (Canfield, 1994, Ingall et al., 1993, Müller and Suess, 1979, Tyson, 2005). Figure 5.7 shows that the bottom of the McArthur Group, in this study sampled from the Mara Dolostone, Mitchell Yard Dolostone, and the Teena Dolostone, all recorded a steady  $\delta^{13}\text{C}_{\text{carb}}$  value of -1.0 ‰. This constancy is similarly reflected by the  $\delta^{88/86}\text{Sr}$  results from this section, which hover at 0.35–0.4‰ (Fig. 5.7). However, the  $^{87}\text{Sr}/^{86}\text{Sr}$  signatures here notably vary (Fig. 5.7), with a transition from palaeoseawater-like  $^{87}\text{Sr}/^{86}\text{Sr}$  ratios (0.705–0.706) in the Mara Dolostone to that more reflective of a restricted setting in the Teena Dolostone (Chen et al., 2022, El Meknassi et al., 2020). Notably, these trends are similarly shown by the Campbell Springs Dolostone in the Limbunya Group (Fig. 5.7). The chemostratigraphic evidence here, along with correlations in lithostratigraphy (Cutovinos et al., 2002, Dunster, 1998, Sweet et al., 1974) and geochronology (Cutovinos et al., 2002, Page et al., 2000) further corroborates that they are coeval units. Consequently, these results may indicate that the DIC reservoir and the carbonate precipitation/dissolution mechanism remains relatively constant during the deposition of these formations. On the other hand, the sedimentary system seems to evolve and become progressively more restricted. The analogous palaeoenvironments recorded in these formations could explain why they recorded similar palaeoredox conditions (Fig. 5.5 and 5.6).

Further up stratigraphy, the Barney Creek Formation and the Fraynes Formation continue to mirror the changes in isotope geochemistry. In this interval, both preserve a  $\delta^{13}\text{C}_{\text{carb}}$  excursion of ca. +2.0 ‰, with an initial trend towards higher  $^{87}\text{Sr}/^{86}\text{Sr}$  ratios followed by lower values at the top, and a negative  $\delta^{88/86}\text{Sr}$  -2.5 ‰ shift. This complex period is also reflected in the heterogeneous redox history of these units, as both formations fluctuate between euxinic-to-sub-oxic conditions (Fig. 5.5 and 5.6). Here, heavier  $\delta^{13}\text{C}_{\text{carb}}$  values at the termination of the Barney Creek Formation and the Fraynes Formation coincide with lower  $^{87}\text{Sr}/^{86}\text{Sr}$  ratios and lighter  $\delta^{88/86}\text{Sr}$  results (Fig. 5.7). Such relationships can suggest that biological productivity thrived better as the restricted basin reconnects to more marine waters. These trends may be induced by the introduction of more nutrient-rich, oxic waters or up-welling zones flooding a previously restricted palaeoenvironment (Condie et al., 2001, Piper and Perkins, 2004, Shen et al., 2000, Tyson and Pearson, 1991). These intermittent periods of basin connectivity and restriction would also have had a profound effect on salinity and carbonate saturation, subsequently controlling the precipitation and dissolution of  $\text{CaCO}_3$  (Diloreto et al., 2021, Shao et al., 2021). The McArthur Basin and the Birrindudu Basin continue to display analogous geochemical results after the deposition of the previous units. Here, the Reward Dolostone is recorded in both boreholes LV090001 (Schmid, 2015) and Manbulloo S1 (NTGS., 2015b), with both yielding a  $\delta^{13}\text{C}_{\text{carb}}$  values of -0.5 ‰, and  $^{87}\text{Sr}/^{86}\text{Sr}$  ratios close to palaeoseawater (Chen et al., 2022). Although these results are comparable to the older Mara Dolostone and their equivalents (Fig. 5.7), the Reward Dolostone noticeably gave a much heavier  $\delta^{88/86}\text{Sr}$  signature of ca. 0.6 ‰. This discrepancy could be explained by differences in rate of carbonate deposition (Krabbenhöft et al., 2010, Vollstaedt et al., 2014), as hypersaturation of  $\text{CaCO}_3$  directly relates to an increasing trend of

$\delta^{88/86}\text{Sr}$  (Shao et al., 2021). The Lynott Formation and the Yalco Formation in the McArthur Basin have no proposed correlative sequences in the Birrindudu Basin (Ahmad and Munson, 2013, Munson, 2019, Page et al., 2000). However, these units revert back to a more restricted setting reflected by higher  $^{87}\text{Sr}/^{86}\text{Sr}$  ratios (Fig. 5.7). This interpretation is further supported by the shift into lower  $\delta^{88/86}\text{Sr}$  ratios, which suggests an increase in flux of continent-derived Sr into the semi-restricted environment (Amsellem et al., 2018, Charlier et al., 2012, Krabbenhöft et al., 2010, Paytan et al., 2021, Vollstaedt et al., 2014). These sources would be relatively nutrient-poor, and consequently inhibits biological activity. This delimiting factor looks to be recorded by further negative excursions in  $\delta^{13}\text{C}_{\text{carb}}$  of the units.

Altogether, the Glyde Package sections in this study records similar changes in palaeoenvironments during the evolution of the basin system. Consequently, this dynamic period may be characteristic for the Glyde Package and could be reflected in coeval units elsewhere in the greater McArthur Basin.

## 5.7 Conclusions

The *in situ* Rb–Sr dating of Barney Creek Formation and Fraynes Formation shales in this study provides the depositional window of these units and directly correlates them (Figure 5.4). In addition, several isotopic proxies such as  $\delta^{13}\text{C}_{\text{carb}}$ ,  $^{87}\text{Sr}/^{86}\text{Sr}$ , and  $\delta^{88/86}\text{Sr}$  show that the basin's tectonic regime plays a critical part in what detritus or nutrient flux is being sourced into the system (Figure 5.7). In turn, these processes are the main driver of bioproductivity and redox conditions (Figure 5.5 and 5.6) in the palaeo-waters (Anbar and Knoll, 2002, Cox et al., 2016b, Dessert et al., 2003, Horton, 2015, Yang et al., 2020). The heterogeneity in oxygenation conditions indicated by redox-sensitive trace elements V and Mo relate to the changing palaeoenvironments, and are integral in forming potential source rocks for base-metal mineralisation and hydrocarbon reservoirs (Calvert and Pedersen, 1993, Degens and Mopper, 1975, Demaison and Moore, 1980, Large and Wolf, 1981, Lyons et al., 2006, Spinks et al., 2016a, Walters, 2006). Importantly, our study shows that the complex basin evolution of the Glyde Package is extensively recorded in the distal sequences of the McArthur Basin and the Birrindudu Basin. As such, the Birrindudu Basin would be primed for hosting similar economic targets that are present in the McArthur Basin.

## 5.8 Acknowledgements

This work was supported by the Australian Research Council Projects LP160101353 and LP200301457 with Santos Ltd, Empire Energy Group Ltd, Northern Territory Geological Survey, Teck Resources, BHP, and Origin as partners. The initial development and validation of *in situ* Rb–Sr dating technique at the University of Adelaide was also supported by Agilent Technologies Australia Ltd. This manuscript forms MinEx CRC contribution #2022/xx. Aoife McFadden is thanked for their assistance in the SEM mapping of the samples in this study. Robert Klæbe and Yuexiao Shao are thanked for their support in the laboratory analysis. Jarred Lloyd is thanked for his help in the laser data processing. Jarred Lloyd's code to process error correlations on LADR can be found in [https://github.com/jarredclloyd/PowerShell\\_LADR\\_errorcorrelation\\_workaround](https://github.com/jarredclloyd/PowerShell_LADR_errorcorrelation_workaround).



## **Chapter 6: Conclusions**

This chapter concludes the thesis by summarising the outcomes from chapters 2–5 and provides suggestions for possible future work to complement the findings in this thesis.

## 6.1 Summary

In conclusion, Chapters 2 and 3 explore the first theme of this thesis and provides a systematic procedure for *in situ* Rb–Sr dating of Proterozoic shales. This was then applied to improve on the existing chronological framework for the greater McArthur Basin (Subarkah et al., 2021, Subarkah et al., 2022). The development of this technique first involves characterising primary authigenic clays from detrital or replacement products (Deepak et al., 2022, Rafiei and Kennedy, 2019, Rafiei et al., 2020). Next, the geochronological information obtained is used in combination with the trace element data collected concurrently to fingerprint primary signatures vs. secondary alteration events (Subarkah et al., 2021). Common palaeotemperature proxies used in petroleum geology such as  $T_{\max}$ , Kubler Index, bitumen reflectance, and aromatic hydrocarbons were also analysed to better constrain the sensitivity of the Rb–Sr system in shale-hosted clay minerals (Subarkah et al., 2022). Findings from this study suggests that the chronometer can be reset in a similar temperature window in which metals mobilise in sediment-exhalative mineralisation and kerogen matures into the gas window (Subarkah et al., 2022, Kubler, 1967, Espitalié et al., 1977, Cooke et al., 2000).

In Chapter 2, *in situ* Rb–Sr dating of authigenic shales from the Mainoru Formation gave an age of  $1577 \pm 56$  Ma (Subarkah et al., 2021). On the other hand, altered shales from the same sub-group gave ages of  $1322 \pm 49$  Ma and  $1347 \pm 47$  Ma, as they were reset by the Derim Derim-Galiwinku/Yanliao large igneous province (Subarkah et al., 2021, Nixon et al., 2021, Bodorkos et al., 2022, Yang et al., 2020). These ages provide a chronological window for the wider Roper Group, with the beginning of deposition starting prior to  $1577 \pm 56$  Ma and then terminating at the maximum age of  $1322 \pm 49$  Ma. These ages parallel the previous constraints of the Roper Group; provided by a U–Pb date of a tuff layer from the underlying Nathan Group at  $1589 \pm 3$  Ma and the cross-cutting Derim Derim Dolerite at  $1313 \pm 1$  Ma (Yang et al., 2020, Page et al., 2000).

The geothermal sensitivity of the Rb–Sr system in shale-hosted clays is further investigated in Chapter 3. Here, the method was used in conjunction with traditional thermal sensitivity parameters for organic rich shales (Subarkah et al., 2022, Jarrett et al., 2022). Oil-prone shales in the gas window sampled from the Velkerri Formation were dated using *in situ* Rb–Sr geochronology at  $1448 \pm 81$  Ma,  $1434 \pm 19$  Ma, and  $1411 \pm 139$  Ma. These results were in good agreement with previous Re–Os geochronology for the unit and have been interpreted to time the deposition of the Velkerri Formation (Kendall et al., 2009, Subarkah et al., 2022). Importantly, these findings suggest that the temperatures at which kerogen matures in the oil-window would not be sufficient to reset the Rb–Sr system in the Velkerri Formation shales (Subarkah et al., 2022). In contrast, gas-prone shales from deeper in the succession were dated using the same method, yet gave younger ages at  $1322 \pm 93$  Ma and  $1336 \pm 40$  Ma. Similar to the reset samples in Chapter 2, these ages do not date deposition, but instead records a hydrothermal overprint induced by the Derim Derim sill present at the bottom of the well (Fig. 3.8 and 3.9). Geothermal modelling of this overprint found that a 75 m thick sill would have enough influence on the overlying sediments to drive the kerogen into the gas window and reset their isotopic chronometer (Subarkah et al., 2022).

These parameters can be used as an advantage and help constrain post-depositional processes that would affect the hydrocarbon maturation in the Velkerri Formation. *In situ* Rb–Sr geochronology of Proterozoic shales have the potential to be a powerful thermochronological tool when used in tandem with common palaeotemperature indexes. Notably, this approach would directly time the targeted source rock. This is a fundamental advantage against other geochronological tools that can only constrain the surrounding rock package (i.e. U–Pb zircon, apatite). Furthermore, findings from Chapter 3 indicates that the geothermal sensitivity of the Rb–Sr system in shale-hosted clays overlaps with the gas window (Subarkah et al., 2022, Jarrett et al., 2022, Kubler, 1967, Espitalié, 1986). Consequently, the technique has the potential to pinpoint what processes control the accumulation of gas reservoirs in the petroleum supersystems of the greater McArthur Basin. It should be noted that these temperatures are also sufficient for mobilising metals in sediment-exhalative metallogenic processes (Cooke et al., 2000).

This method was also used to define the depositional window for the Glyde and Wilton Packages in Chapter 5. In this example, successions of the Glyde Package from the McArthur and Limbunya Group look to correlate chronologically with each other (Fig. 5.4). Shales from the Barney Creek Formation were dated at  $1634 \pm 59$  Ma and  $1635 \pm 67$  Ma using this approach. Similarly, *in situ* Rb–Sr geochronology of shales from the Fraynes Formation resulted in age of  $1630 \pm 57$  Ma and  $1636 \pm 42$  Ma, suggesting that these two units are direct equivalents.

The second theme of this thesis focuses on reconstructing the palaeoenvironment and paleo-water changes in the greater McArthur Basin. These geochemical trends are defined using a multi-proxy approach and is the focus Chapters 4 and 5. Bioproductivity and redox conditions of the sedimentary system are reconstructed using a number of indicator trace elements such as Ba, P, Mo, and V (Cox et al., 2016b, Dymond et al., 1992, Francois et al., 1995, Pedersen and Calvert, 1990, Schoepfer et al., 2015, Tribovillard et al., 2006). Ba and P are essential elements needed by biological organisms and have been used to reflect productivity in ancient settings (Dymond et al., 1992, Föllmi, 1996, McManus et al., 1998, Filippelli, 1997). Furthermore, Mo and V are abundant trace elements in the current ocean and accumulates at different rates under variable redox conditions (Algeo and Maynard, 2004, Tribovillard et al., 2006). Bioproductivity and redox conditions are intrinsically linked (Tribovillard et al., 2006, Cox et al., 2016b, Poulton et al., 2010, Reinhard et al., 2013), which emphasises the need for a multi-proxy approach. This is then further supported by isotopic studies to better understand the tectonic evolution of the sedimentary system (Bartley and Kah, 2004, Condie et al., 2001, Emerson, 1985, Hayes and Waldbauer, 2006, Krabbenhöft et al., 2010, Kuznetsov et al., 2018, Shao et al., 2021, Shields-Zhou and Mills, 2017). The C isotope evolution of the sediments provide insight on the efficiency of organic activity and carbon burial (Lindsay and Brasier, 2000, Saltzman and Thomas, 2012, Shields and Veizer, 2002). Additionally, the  $^{87}\text{Sr}/^{86}\text{Sr}$  signatures from these rocks can also help track the basin's relative connectivity or restriction to the open ocean (Derry and Jacobsen, 1988, El Meknassi et al., 2020). Restricted basins are more likely to source Sr from fluxes of crustal weathering, which results in higher  $^{87}\text{Sr}/^{86}\text{Sr}$  ratios (El Meknassi et al., 2020, Kuznetsov et al., 2018, Veizer et al., 1992, Derry and Jacobsen, 1988). On the contrary, basins connected to

the open ocean derive Sr from mafic sources such as hydrothermal vents or mid-ocean ridges, reflected by their lower  $^{87}\text{Sr}/^{86}\text{Sr}$  values (El Meknassi et al., 2020, Kuznetsov et al., 2018, Veizer et al., 1992).

Results from Chapter 4 and 5 indicate that changes in palaeogeography looks to play an important control for what is being sourced into the basin (Fig. 6.1). Elevated productivity in the Redbank Package occurs when the basin influx is dominated by nutrient-rich detritus (Figure 4.9 and 6.1), and consequently drives the efficacy of the biological redox pump (Cox et al., 2016b, Cox et al., 2016a, Dessert et al., 2003, Yang et al., 2020, Anbar and Knoll, 2002). Such nutrient-rich influx is likely sourced from mantle-like provenance or upwelling zones during intervals where the basin is more connected (Fig. 6.1) to the open ocean (Horton, 2015, Yang et al., 2020, Cox et al., 2016b, Shen et al., 2000). This redox heterogeneity is similarly recorded in the overlying Glyde Package (Fig. 5.5 and 5.6) and is crucial for the accumulation of hydrocarbons and the entrapment of redox-sensitive base metals (Walters, 2006, Lyons et al., 2006, Cooke et al., 2000). Importantly, these intricate relationships are recorded in spatially distant rocks from the Redbank and Glyde Package (Fig. 5.7). As such, they provide further evidence that mineralisation and petroleum plays in the greater McArthur Basin are likely to be spatially extensive, and not mutually restricted to particular sub-basins (Jarrett et al., 2022, Large et al., 2005, Gibson et al., 2017, Southgate et al., 2000, Close, 2014).

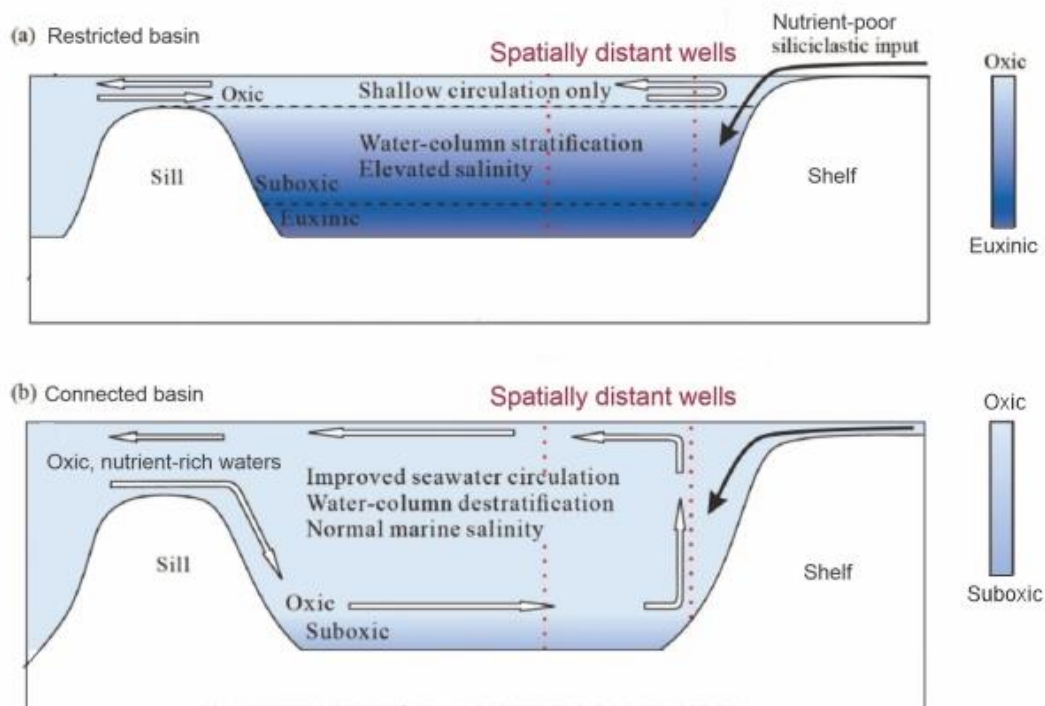


**Figure 6.1.** Basin evolution redox model of the greater McArthur Basin in this study modified from Peng (2022). Spatially distant units can potentially record the similar geochemical changes in the sedimentary system.

Additionally, the geochemical signatures of the greater McArthur Basin could also be used to help illustrate the global Proterozoic surface environments. These inferences are applicable for periods in which these rocks were connected to their contemporaneous oceans (Chen et al., 2022, Saltzman and Thomas, 2012, Kuznetsov et al., 2018, Shields-Zhou and Mills, 2017). These sections are reflected by samples with the lowest  $^{87}\text{Sr}/^{86}\text{Sr}$  ratios,

overlapping with the seawater curve for their particular time intervals (El Meknassi et al., 2020, Chen et al., 2022, Kuznetsov et al., 2018). In this study, several samples (Fig. 6.2) from the Glyde Package had  $^{87}\text{Sr}/^{86}\text{Sr}$  values with overlapping with expected palaeo-seawater at ca. 1650-1630 Ma (Chen et al., 2022). Notably, the Campbell Springs Dolostone provided  $^{87}\text{Sr}/^{86}\text{Sr}$  ratios lower than the expected palaeo-seawater curve from literature (Chen et al., 2022). As such, they can be added to the compilation and help better constrain the Sr cycle for this section in earth's history (Fig. 6.2). From this, a rapid drop in global palaeo-seawater  $^{87}\text{Sr}/^{86}\text{Sr}$  signal of  $\sim -0.001$  was projected between 1650-1630 Ma. This trend towards lower  $^{87}\text{Sr}/^{86}\text{Sr}$  beginning at ca. 1650 Ma has been interpreted to reflect the break-up of supercontinent Nuna, and subsequent influx of more juvenile material (Anderson, 1983, Kuznetsov et al., 2018, Gibson et al., 2018, Chen et al., 2022). My data helps fills the gap in knowledge (Fig. 6.2) for this relatively understudied interval in Earth's history (Chen et al., 2022, Saltzman and Thomas, 2012, Shields and Veizer, 2002). This is further validated by providing direct chronological constraints for the units in Chapters 4 and 5, as well as validating their geochemical signatures using the multi-proxy approach in this study.

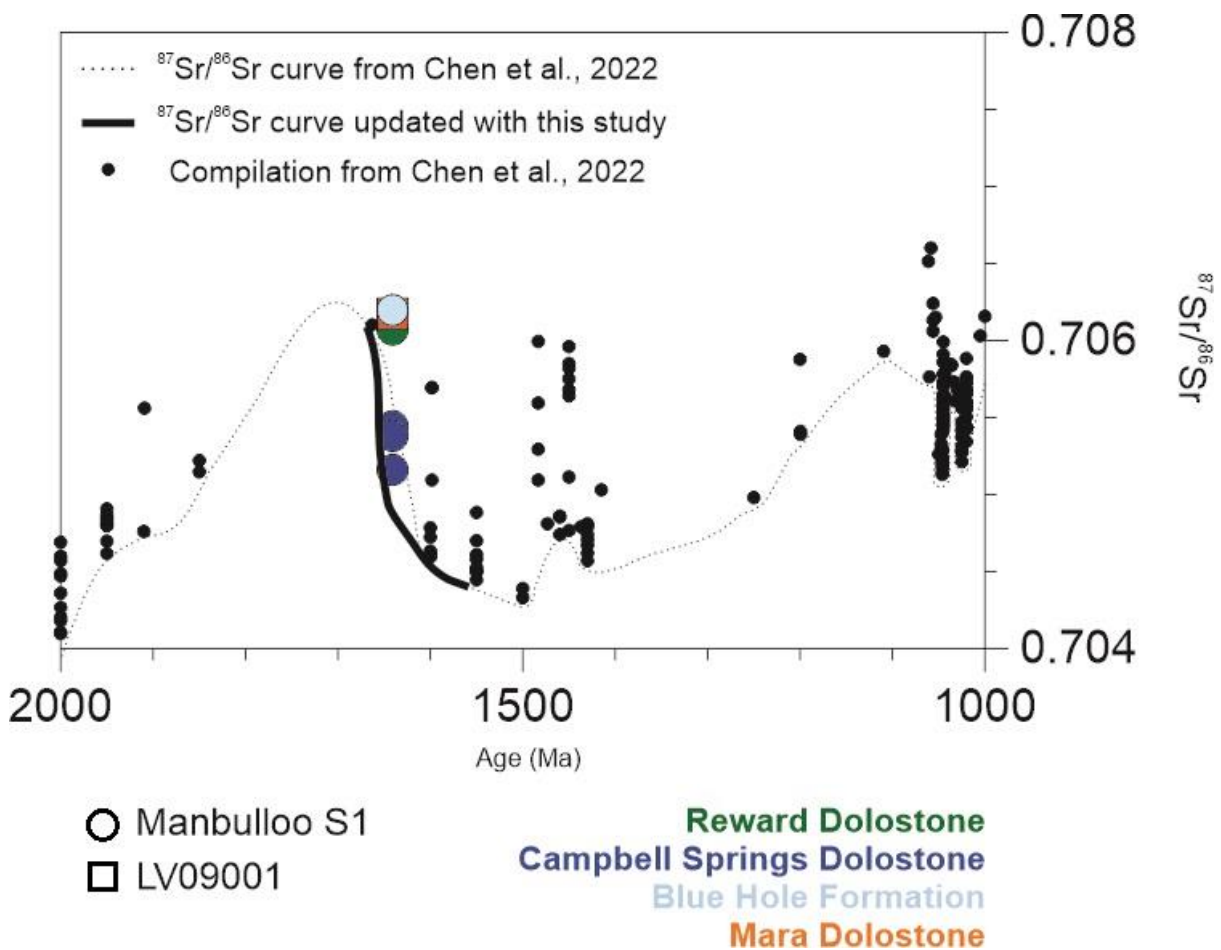


**Figure 6.2.** Updated global palaeo-water  $^{87}\text{Sr}/^{86}\text{Sr}$  curve (Chen et al., 2022) from the lowest values in this study. Note that this curve is poorly constrained for this interval in earth's history.

After confirming the basin's connectivity to the open ocean using their  $^{87}\text{Sr}/^{86}\text{Sr}$  ratios, we also aim to use its  $\delta^{13}\text{C}$  signatures to reconstruct the global marine C cycle in the Proterozoic (Shields and Veizer, 2002, Shields-Zhou and Mills, 2017, Bartley and Kah, 2004, Emerson, 1985, Kump and Arthur, 1999, Miyazaki et al., 2018). Our findings in Chapter 5 establish that

the  $\delta^{13}\text{C}$  in the Glyde Package of the greater McArthur Basin is at least a regional signal, recorded in coeval units that were spatially apart from each other (Fig. 5.7). Notably, these excursions have also been recorded by other sections of the Glyde Package and time-equivalent successions in the Mount Isa Basin (Lindsay and Brasier, 2000, Kunzmann et al., 2019). As such, the positive  $\delta^{13}\text{C}$  excursions highlighted in this project might be extensively recorded in Proterozoic basins throughout northern Australia. Recently, Kunzmann et al. (2019) correlated similar  $\delta^{13}\text{C}$  isotopic shifts between the McArthur Group in the southern McArthur Basin with the similar-aged Changcheng Group in the Yanshan Basin, north China (Chu et al., 2007). Given that the north Australian and the north China cratons were thought to have bordered each other throughout much of the Proterozoic (Gibson et al., 2018, Mitchell et al., 2020, Ding et al., 2020, Nixon et al., 2021), it is possible that the positive  $\delta^{13}\text{C}$  excursions identified here recorded the signal of a seaway that would have connected continents (Cox et al., 2016b).

If this is true, these signatures might also be expressed in Proterozoic basins across Laurentia and Baltica (Burrett and Berry, 2000, Furlanetto et al., 2016, Karlstrom et al., 2001, Kirscher et al., 2020, Nordsvan et al., 2018, Hamilton and Buchan, 2010). Interestingly, a similar  $\sim 2.0\text{‰}$  positive excursion (Fig. 6.3) is also recorded in the similar-aged Proterozoic Semri Group from the Vindhyan Basin, India (Ray et al., 2003, Kumar et al., 2002). This similar excursion can have important implications for the reconstruction of the global palaeo-seawater C isotopic record, as India is not thought to be proximal to the aforementioned continents during the late Palaeoproterozoic (Burrett and Berry, 2000, Furlanetto et al., 2016, Karlstrom et al., 2001, Kirscher et al., 2020, Nordsvan et al., 2018, Hamilton and Buchan, 2010). A global positive  $\delta^{13}\text{C}$  excursion may be driven by processes such as efficacy of organic carbon burial, increased nutrient delivery, and elevated levels of  $\text{CO}_2$  in the atmosphere (Kump and Arthur, 1999, Miyazaki et al., 2018, Shields-Zhou and Mills, 2017). Improved chronological and chemostratigraphic constraints on these sections would be crucial for confirming whether or not this excursion was a global phenomenon.

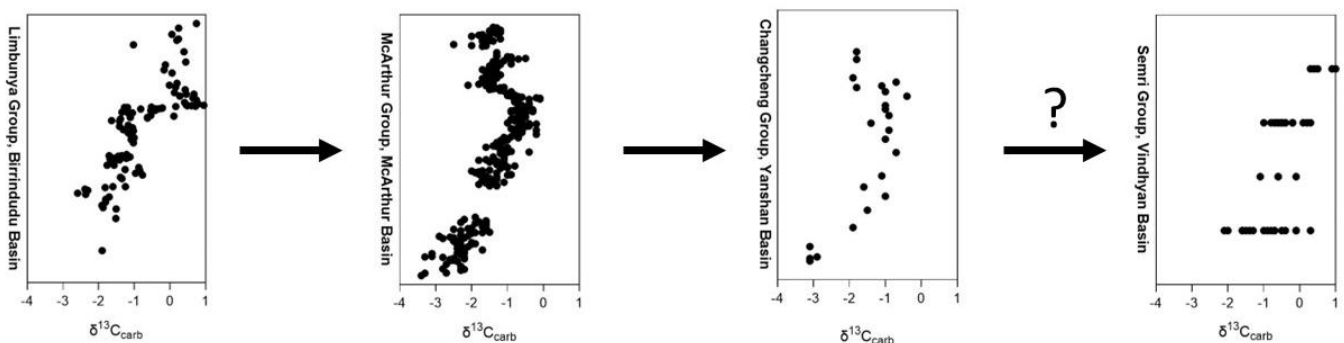


**Figure 6.3.** Possible global correlations of the greater McArthur Basin based on  $\delta^{13}\text{C}$  excursions in this study and similar-aged sediments deposited elsewhere during the Proterozoic (Kunzmann et al., 2019, Chu et al., 2007, Ray et al., 2003).

Nevertheless, these findings directly show that biogeochemical systems in the planet's surface were far from stagnant and boring during the Proterozoic. These processes were dynamic, influencing the survival of early life, regulating oxygen in the ocean and atmosphere, and accumulating energy and mineral resources (Spinks et al., 2016a, Sperling et al., 2022, Bellefroid et al., 2018, Gilleaudeau et al., 2016, Lyons et al., 2021, Planavsky et

al., 2015a, Spinks et al., 2022, Zhang et al., 2016, Gibson et al., 2017, Large et al., 2017, Lyons et al., 2006). Altogether, they may be a systematically fundamental step that set the stage for the evolutionary growth and diversification of life in the Cambrian (Mukherjee et al., 2018, Young, 2013).

## **6.2 Future studies**

Altogether, this project has formed a new foundation to approach and investigate the greater McArthur Basin and similar Proterozoic sedimentary systems. The novel dating method developed here can be applied to other stratigraphic units within the basin that are still poorly constrained. These findings can then be used to form chronostratigraphic correlations between spatially separated units. It can also be used to date other Proterozoic basin systems that prove difficult to geochronologically determine. Furthermore, this method can also be applied to time post-depositional processes that could control the formation of energy and mineral resources. The geothermal sensitivity of the chronometer largely overlaps with the temperature of the oil-gas window and metallogenic fluids in sedimentary systems (Subarkah et al., 2022, Espitalié et al., 1977, Cooke et al., 2000). It should be noted that recent studies suggest the base metal mineralisation in the greater McArthur Basin is not syn-depositional (Large et al., 1998, Large et al., 2001) and instead occurs through diagenetic processes after burial (Spinks et al., 2020, Gianfriddo et al., 2022). As such, this technique can potentially be used to directly time the paragenesis of sediment-hosted mineralisation.

In addition to the geochronological advancements in this study, we also show that the isotopic record of spatially distant but coeval successions from the greater McArthur Basin looks to display similar excursions up stratigraphy. This has been useful for chemostratigraphic applications and supporting the chronological correlations between these successions. Another impactful use of this information would be to compare these excursions with similarly aged strata in other continents to show whether these changes are globally recorded (Chen et al., 2022, Shields and Veizer, 2002, Kuznetsov et al., 2018). Comparable units to the greater McArthur Basin can be found in Proterozoic sedimentary systems in north China, Laurentia, and Baltica (Chu et al., 2007, Ding et al., 2020, Furlanetto et al., 2016, Liu et al., 2011, Nixon et al., 2021). If these excursions are seen elsewhere, they can then be used to infer the global secular evolution of the C and Sr cycle (Chen et al., 2022, Kuznetsov et al., 2018, Shields-Zhou and Mills, 2017).

## 7. Bibliography

- ABAD, I. & NIETO, F. 2007. Physical meaning and applications of the illite Kübler index: measuring reaction progress in low-grade metamorphism. *Diagenesis and Low-Temperature Metamorphism, Theory, Methods and Regional Aspects, Seminarios. Sociedad Espanola: Sociedad Espanola Mineralogia*, 53-64. From <http://hdl.handle.net/10261/32515>.
- ABBOTT, S. T. & SWEET, I. P. 2000. Tectonic control on third-order sequences in a siliciclastic ramp-style basin: an example from the Roper Superbasin (Mesoproterozoic), northern Australia. *Australian Journal of Earth Sciences*, 47, 637-657. DOI: <https://doi.org/10.1046/j.1440-0952.2000.00795.x>.
- ABBOTT, S. T., SWEET, I. P., PLUMB, K. A., YOUNG, D. N., CUTOVINOS, A., FERENCZI, P. A. & PIETSCH, B. A. 2001. Roper Region: Urapunga and Roper River Special, Northern Territory (Second Edition). 1:250000 geological map series explanatory notes, SD 53-10, 11. *National Geoscience Mapping Accord*. Darwin: Northern Territory Geological Survey and Geoscience Australia. From <https://geoscience.nt.gov.au/gemis/ntgsjspui/handle/1/81859>.
- ABOTAH, R. & DAIM, T. U. 2017. Towards building a multi perspective policy development framework for transition into renewable energy. *Sustainable Energy Technologies and Assessments*, 21, 67-88. DOI: <https://doi.org/10.1016/j.seta.2017.04.004>.
- AHMAD, A. & MUNSON, T. J. 2013. *Geology and mineral resources of the Northern Territory*, Northern Territory Geological Survey. From <https://geoscience.nt.gov.au/gemis/ntgsjspui/handle/1/81446>.
- ALGEO, T. J. & INGALL, E. 2007. Sedimentary Corg: P ratios, paleocean ventilation, and Phanerozoic atmospheric pO<sub>2</sub>. *Palaeogeography, Palaeoclimatology, Palaeoecology*, 256, 130-155. DOI: <https://doi.org/10.1016/j.palaeo.2007.02.029>.
- ALGEO, T. J. & LYONS, T. W. 2006. Mo-total organic carbon covariation in modern anoxic marine environments: Implications for analysis of paleoredox and paleohydrographic conditions. *Paleoceanography*, 21, 1. DOI: <https://doi.org/10.1029/2004PA001112>.
- ALGEO, T. J. & MAYNARD, J. B. 2004. Trace-element behavior and redox facies in core shales of Upper Pennsylvanian Kansas-type cyclothems. *Chemical Geology*, 206, 289-318.
- ALLAN, J. R. & MATTHEWS, R. K. 1982. Isotope signatures associated with early meteoric diagenesis. *Sedimentology*, 29, 797-817. DOI: <https://doi.org/10.1002/9781444304510.ch16>.
- AMSELLEM, E., MOYNIER, F., DAY, J. M. D., MOREIRA, M., PUCHTEL, I. S. & TENG, F.-Z. 2018. The stable strontium isotopic composition of ocean island basalts, mid-ocean ridge basalts, and komatiites. *Chemical Geology*, 483, 595-602.
- ANBAR, A. D. & KNOLL, A. H. 2002. Proterozoic ocean chemistry and evolution: a bioinorganic bridge? *Science*, 297, 1137-42. DOI: <https://doi.org/10.1126/science.1069651>.
- ANDERSON, J. L. 1983. Proterozoic anorogenic granite plutonism of North America. DOI: <https://doi.org/10.1130/MEM161-p133>
- ANDREWS, M. G., JACOBSON, A. D., LEHN, G. O., HORTON, T. W. & CRAW, D. 2016. Radiogenic and stable Sr isotope ratios (<sup>87</sup>Sr/<sup>86</sup>Sr,  $\delta^{88}$ /<sup>86</sup>Sr) as tracers of riverine cation sources and biogeochemical cycling in the Milford Sound region of Fiordland, New Zealand. *Geochimica et Cosmochimica Acta*, 173, 284-303. DOI: <https://doi.org/10.1016/j.gca.2015.10.005>.



- ÁRKAI, P., SASSI, F. & DESMONS, J. 2002. Towards a unified nomenclature in metamorphic petrology. *Very low-to low-grade metamorphic rocks. A proposal on behalf of the IUGS Subcommittee on the Systematics of Metamorphic Rocks*. From [http://www.tetrapods.co.uk/scmr/docs/papers/paper\\_5.pdf](http://www.tetrapods.co.uk/scmr/docs/papers/paper_5.pdf).
- ARMISTEAD, S. E., COLLINS, A. S., REDAA, A., JEPSON, G., GILLESPIE, J., GILBERT, S., BLADES, M. L., FODEN, J. D. & RAZAKAMANANA, T. 2020. Structural evolution and medium-temperature thermochronology of central Madagascar: implications for Gondwana amalgamation. *Journal of the Geological Society*, 177, 784-798. DOI: <https://doi.org/10.1144/jgs2019-132>.
- AWWILLER, D. N. & MACK, L. E. 1989. Diagenetic Resetting of Sm-Nd Isotope Systematics in Wilcox Group Sandstones and Shales, San Marcos Arch, South-Central Texas. *AAPG Bulletin*, 39, 321-330. From <https://archives.datapages.com/data/gcags/data/039/039001/0321.htm>.
- AWWILLER, D. N. & MACK, L. E. 1991. Diagenetic modification of Sm-Nd model ages in Tertiary sandstones and shales, Texas Gulf Coast. *Geology*, 19, 311-314. DOI: [https://doi.org/10.1130/0091-7613\(1991\)019%3C0311:DMOSNM%3E2.3.CO;2](https://doi.org/10.1130/0091-7613(1991)019%3C0311:DMOSNM%3E2.3.CO;2).
- BALCAEN, L., SCHRIJVER, I. D., MOENS, L. & VANHAECKE, F. 2005. Determination of the  $^{87}\text{Sr}/^{86}\text{Sr}$  isotope ratio in USGS silicate reference materials by multi-collector ICP–mass spectrometry. *International Journal of Mass Spectrometry*, 242, 251-255. DOI: <https://doi.org/10.1016/j.ijms.2004.10.025>.
- BALDERMANN, A., ABDULLAYEV, E., TAGHIYEVA, Y., ALASGAROV, A. & JAVAD-ZADA, Z. 2020. Sediment petrography, mineralogy and geochemistry of the Miocene Islam Dağ Section (Eastern Azerbaijan): Implications for the evolution of sediment provenance, palaeo-environment and (post-) depositional alteration patterns. *Sedimentology*, 67, 152-172. DOI: <https://doi.org/10.1111/sed.12638>.
- BANNER, J. L. 2004. Radiogenic isotopes: systematics and applications to earth surface processes and chemical stratigraphy. *Earth-Science Reviews*, 65, 141-194. DOI: [https://doi.org/10.1016/S0012-8252\(03\)00086-2](https://doi.org/10.1016/S0012-8252(03)00086-2).
- BANNER, J. L. & HANSON, G. N. 1990. Calculation of simultaneous isotopic and trace element variations during water-rock interaction with applications to carbonate diagenesis. *Geochimica et Cosmochimica Acta*, 54, 3123-3137. DOI: [https://doi.org/10.1016/0016-7037\(90\)90128-8](https://doi.org/10.1016/0016-7037(90)90128-8).
- BARLEY, M. & GROVES, D. 1992. Supercontinent cycles and the distribution of metal deposits through time. *Geology*, 20, 291-294. DOI: [https://doi.org/10.1130/0091-7613\(1992\)020%3C0291:SCATDO%3E2.3.CO;2](https://doi.org/10.1130/0091-7613(1992)020%3C0291:SCATDO%3E2.3.CO;2).
- BARTHOLOMEW, L. 2022. Australian onshore petroleum acreage and releases. *The APPEA Journal*, 62, S544-S554. From <https://www.publish.csiro.au/aj/aj21219>.
- BARTLEY, J. K. & KAH, L. C. 2004. Marine carbon reservoir, Corg-Ccarb coupling, and the evolution of the Proterozoic carbon cycle. *Geology*, 32, 129-132. DOI: <https://doi.org/10.1130/G19939.1>.
- BAU, M. & DULSKI, P. 1996. Distribution of yttrium and rare-earth elements in the Penge and Kuruman iron-formations, Transvaal Supergroup, South Africa. *Precambrian Research*, 79, 37-55. DOI: [https://doi.org/10.1016/0301-9268\(95\)00087-9](https://doi.org/10.1016/0301-9268(95)00087-9).
- BAU, M., MÖLLER, P. & DULSKI, P. 1997. Yttrium and lanthanides in eastern Mediterranean seawater and their fractionation during redox-cycling. *Marine Chemistry*, 56, 123-131. DOI: [https://doi.org/10.1016/S0304-4203\(96\)00091-6](https://doi.org/10.1016/S0304-4203(96)00091-6).

- BELLEFRÖID, E. J., HOOD, A. V. S., HOFFMAN, P. F., THOMAS, M. D., REINHARD, C. T. & PLANAVSKY, N. J. 2018. Constraints on Paleoproterozoic atmospheric oxygen levels. *Proceedings of the National Academy of Sciences*, 115, 8104. DOI: <https://doi.org/10.1073/pnas.1806216115>.
- BENGTSON, S., SALLSTEDT, T., BELIVANOVA, V. & WHITEHOUSE, M. 2017. Three-dimensional preservation of cellular and subcellular structures suggests 1.6 billion-year-old crown-group red algae. *PLOS Biology*, 15, e2000735. DOI: <https://doi.org/10.1371/journal.pbio.2000735>.
- BENITEZ-NELSON, C. R. 2000. The biogeochemical cycling of phosphorus in marine systems. *Earth-Science Reviews*, 51, 109-135. DOI: [https://doi.org/10.1016/S0012-8252\(00\)00018-0](https://doi.org/10.1016/S0012-8252(00)00018-0).
- BERNECKER, T., BRADSHAW, B. E., FEITZ, A. J. & KALINOWSKI, A. A. 2022. Evaluating Australia's energy commodity resources potential for a net-zero emission future. *The APPEA Journal*, 62, S555-S561. From <https://www.publish.csiro.au/aj/AJ21091>.
- BERRANG, P. & GRILL, E. 1974. The effect of manganese oxide scavenging on molybdenum in Saanich Inlet, British Columbia. *Marine Chemistry*, 2, 125-148. DOI: [https://doi.org/10.1016/0304-4203\(74\)90033-4](https://doi.org/10.1016/0304-4203(74)90033-4).
- BETTS, J. & HOLLAND, H. 1991. The oxygen content of ocean bottom waters, the burial efficiency of organic carbon, and the regulation of atmospheric oxygen. *Palaeogeography, Palaeoclimatology, Palaeoecology*, 97, 5-18. DOI: [https://doi.org/10.1016/0031-0182\(91\)90178-T](https://doi.org/10.1016/0031-0182(91)90178-T).
- BEVAN, D., COATH, C. D., LEWIS, J., SCHWIETERS, J., LLOYD, N., CRAIG, G., WEHRS, H. & ELLIOTT, T. 2021. In situ Rb–Sr dating by collision cell, multicollection inductively-coupled plasma mass-spectrometry with pre-cell mass-filter (CC-MC-ICPMS/MS). *Journal of analytical atomic spectrometry*, 36, 917-931. DOI: <https://doi.org/10.1039/D1JA00006C>
- BLAIKIE, T. & KUNZMANN, M. Towards an improved understanding of the 3D structural architecture of the greater McArthur Basin through geophysical interpretation and modelling. Annual Geoscience Exploration Seminar (AGES) Proceedings, Alice Springs, Northern Territory 28 - 29 March 2017. From <https://geoscience.nt.gov.au/gemis/ntgsjspui/handle/1/85111>.
- BLAIKIE, T. & KUNZMANN, M. 2019. Sub-basin architecture of the Proterozoic McArthur Group, southern McArthur Basin. *ASEG Extended Abstracts*, 2019, 1-4. DOI: <https://doi.org/10.1080/22020586.2019.12073083>.
- BLAIKIE, T. N. & KUNZMANN, M. 2020. Geophysical interpretation and tectonic synthesis of the Proterozoic southern McArthur Basin, northern Australia. *Precambrian Research*, 343, 105728. DOI: <https://doi.org/10.1016/j.precamres.2020.105728>.
- BODORKOS, S., CROWLEY, J. L., CLAOUÉ-LONG, J. C., ANDERSON, J. R. & MAGEE, C. W. 2022. Precise U–Pb baddeleyite dating of the Derim Derim Dolerite, McArthur Basin, Northern Territory: old and new SHRIMP and ID-TIMS constraints. *Australian Journal of Earth Sciences*, 1-15. DOI: <https://doi.org/10.1080/08120099.2020.1749929>.
- BOREHAM, C., CRICK, I. & POWELL, T. 1988. Alternative calibration of the Methylphenanthrene Index against vitrinite reflectance: Application to maturity measurements on oils and sediments. *Organic Geochemistry*, 12, 289-294. DOI: [https://doi.org/10.1016/0146-6380\(88\)90266-5](https://doi.org/10.1016/0146-6380(88)90266-5).

- BRADSHAW, M. 1994. Petroleum systems in West Australian basins. *Proceedings of Petroleum Exploration Society of Australian Symposium*, 93-118. From [https://pesa.com.au/the\\_sedimentary\\_basins\\_of\\_wa\\_p93-118-pdf/](https://pesa.com.au/the_sedimentary_basins_of_wa_p93-118-pdf/).
- BRAND, U. & VEIZER, J. 1980. Chemical diagenesis of a multicomponent carbonate system; 1, Trace elements. *Journal of Sedimentary Research*, 50, 1219-1236. DOI: <https://doi.org/10.1306/212F7BB7-2B24-11D7-8648000102C1865D>.
- BREIT, G. N. & WANTY, R. B. 1991. Vanadium accumulation in carbonaceous rocks: A review of geochemical controls during deposition and diagenesis. *Chemical Geology*, 91, 83-97. DOI: [https://doi.org/10.1016/0009-2541\(91\)90083-4](https://doi.org/10.1016/0009-2541(91)90083-4).
- BROCKS, J. J., LOVE, G. D., SUMMONS, R. E., KNOLL, A. H., LOGAN, G. A. & BOWDEN, S. A. 2005. Biomarker evidence for green and purple sulphur bacteria in a stratified Palaeoproterozoic sea. *Nature*, 437, 866-870. DOI: <https://doi.org/10.1038/nature04068>.
- BROWN, D. A., SIMPSON, A., HAND, M., MORRISSEY, L. J., GILBERT, S., TAMBLYN, R. & GLORIE, S. 2022. Laser-ablation Lu-Hf dating reveals Laurentian garnet in subducted rocks from southern Australia. *Geology*, 50, 837-842. DOI: <https://doi.org/10.1130/G49784.1>.
- BRUISTEN, B. & BROCKS, J. J. 2015. Organic and inorganic geochemical analyses of the Barney Creek Formation, McArthur Basin, Australia. *Postgraduate in Geology, Australian National University*. DOI: <https://doi.org/10.25911/5d5145163fd80>.
- BRUMSACK, H. J. 1989. Geochemistry of recent TOC-rich sediments from the Gulf of California and the Black Sea. *Geologische Rundschau*, 78, 851-882. DOI: <https://doi.org/10.1007/BF01829327>.
- BUICK, R., DES MARAIS, D. J. & KNOLL, A. H. 1995. Stable isotopic compositions of carbonates from the Mesoproterozoic Bangemall group, northwestern Australia. *Chemical Geology*, 123, 153-171. DOI: [https://doi.org/10.1016/0009-2541\(95\)00049-R](https://doi.org/10.1016/0009-2541(95)00049-R).
- BULL, S. 1998. Sedimentology of the Palaeoproterozoic Barney Creek Formation in DDH BMR McArthur 2, southern McArthur basin, northern territory. *Australian Journal of Earth Sciences*, 45, 21-31. DOI: <https://doi.org/10.1080/08120099808728364>.
- BURRETT, C. & BERRY, R. 2000. Proterozoic Australia–Western United States (AUSWUS) fit between Laurentia and Australia. *Geology*, 28, 103-106. DOI: [https://doi.org/10.1130/0091-7613\(2000\)28%3C103:PAUSAF%3E2.0.CO;2](https://doi.org/10.1130/0091-7613(2000)28%3C103:PAUSAF%3E2.0.CO;2).
- BURTNER, R. L. & WARNER, M. A. 1986. Relationship between illite/smectite diagenesis and hydrocarbon generation in Lower Cretaceous Mowry and Skull Creek shales of the northern Rocky Mountain area. *Clays and Clay Minerals*, 34, 390-402. DOI: <https://doi.org/10.1346/CCMN.1986.0340406>.
- BUTTERFIELD, N. J. 2015. Early evolution of the Eukaryota. *Palaeontology*, 58, 5-17. DOI: <https://doi.org/10.1111/pala.12139>.
- CALVERT, S. E. & PEDERSEN, T. F. 1993. Geochemistry of Recent oxic and anoxic marine sediments: Implications for the geological record. *Marine Geology*, 113, 67-88. DOI: [https://doi.org/10.1016/0025-3227\(93\)90150-T](https://doi.org/10.1016/0025-3227(93)90150-T).
- CALVERT, S. E. & PEDERSEN, T. F. 2007. Chapter Fourteen Elemental Proxies for Palaeoclimatic and Palaeoceanographic Variability in Marine Sediments: Interpretation and Application. *Developments in Marine Geology*, 1, 567-644. [https://doi.org/10.1016/S1572-5480\(07\)01019-6](https://doi.org/10.1016/S1572-5480(07)01019-6).

- CANFIELD, D. E. 1994. Factors influencing organic carbon preservation in marine sediments. *Chemical geology*, 114, 315-329. [https://doi.org/10.1016/0009-2541\(94\)90061-2](https://doi.org/10.1016/0009-2541(94)90061-2).
- CANFIELD, D. E., ZHANG, S., FRANK, A. B., WANG, X., WANG, H., SU, J., YE, Y. & FREI, R. 2018. Highly fractionated chromium isotopes in Mesoproterozoic-aged shales and atmospheric oxygen. *Nat Commun*, 9, 2871. DOI: <https://doi.org/10.1038/s41467-018-05263-9>.
- CAPOGRECO, N. 2017. Provenance and thermal history of the Beetaloo Basin using illite crystallinity and zircon geochronology and trace element data. *Bachelor of Science (Honours), University of Adelaide*. From <https://hdl.handle.net/2440/126541>.
- CARVAJAL-ORTIZ, H. & GENTZIS, T. 2015. Critical considerations when assessing hydrocarbon plays using Rock-Eval pyrolysis and organic petrology data: Data quality revisited. 152, 113-122. DOI: <https://doi.org/10.1016/j.coal.2015.06.001>.
- CHAMLEY, H. 1989. Clay formation through weathering. *Clay sedimentology*. Springer. DOI: [https://doi.org/10.1007/978-3-642-85916-8\\_2](https://doi.org/10.1007/978-3-642-85916-8_2).
- CHARBIT, S., GUILLOU, H. & TURPIN, L. 1998. Cross calibration of K–Ar standard minerals using an unspiked Ar measurement technique. *Chemical Geology*, 150, 147-159. DOI: [https://doi.org/10.1016/S0009-2541\(98\)00049-7](https://doi.org/10.1016/S0009-2541(98)00049-7).
- CHARLIER, B. L., GINIBRE, C., MORGAN, D., NOWELL, G. M., PEARSON, D., DAVIDSON, J. P. & OTTLEY, C. 2006. Methods for the microsampling and high-precision analysis of strontium and rubidium isotopes at single crystal scale for petrological and geochronological applications. *Chemical Geology*, 232, 114-133. DOI: <https://doi.org/10.1016/j.chemgeo.2006.02.015>.
- CHARLIER, B. L. A., NOWELL, G. M., PARKINSON, I. J., KELLEY, S. P., PEARSON, D. G. & BURTON, K. W. 2012. High temperature strontium stable isotope behaviour in the early solar system and planetary bodies. *Earth and Planetary Science Letters*, 329-330, 31-40. DOI: <https://doi.org/10.1016/j.epsl.2012.02.008>.
- CHEN, X., ZHOU, Y. & SHIELDS, G. A. 2022. Progress towards an improved Precambrian seawater  $^{87}\text{Sr}/^{86}\text{Sr}$  curve. *Earth-Science Reviews*, 224, 103869. DOI: <https://doi.org/10.1016/j.earscirev.2021.103869>.
- CHENG, M., LI, C., ZHOU, L. & XIE, S. 2015. Mo marine geochemistry and reconstruction of ancient ocean redox states. *Science China Earth Sciences*, 58, 2123-2133. DOI: <https://doi.org/10.1007/s11430-015-5177-4>.
- CHU, X., ZHANG, T., ZHANG, Q. & LYONS, T. W. 2007. Sulfur and carbon isotope records from 1700 to 800Ma carbonates of the Jixian section, northern China: Implications for secular isotope variations in Proterozoic seawater and relationships to global supercontinental events. *Geochimica et Cosmochimica Acta*, 71, 4668-4692. DOI: <https://doi.org/10.1016/j.gca.2007.07.017>.
- CLOSE, D. 2014. The McArthur Basin: NTGS' approach to a frontier petroleum basin with known base metal prospectivity. Annual Geoscience Exploration Seminar (AGES) Proceedings, Alice Springs, Northern Territory Geological Survey. From <https://geoscience.nt.gov.au/gemis/ntgjsjpui/handle/1/82357>.
- COMPSTON, W. & PIDGEON, R. 1962. Rubidium-Strontium Dating of Shales by the Total-Rock Method. *Journal of Geophysical Research*, 67, 3493-3502. DOI: <https://doi.org/10.1029/JZ067i009p03493>.
- CONDIE, K. C. 1991. Another look at rare earth elements in shales. *Geochimica et Cosmochimica Acta*, 55, 2527-2531. DOI: [https://doi.org/10.1016/0016-7037\(91\)90370-K](https://doi.org/10.1016/0016-7037(91)90370-K).

- CONDIE, K. C., DES MARAIS, D. J. & ABBOTT, D. 2001. Precambrian superplumes and supercontinents: a record in black shales, carbon isotopes, and paleoclimates? *Precambrian Research*, 106, 239-260. DOI: [https://doi.org/10.1016/S0301-9268\(00\)00097-8](https://doi.org/10.1016/S0301-9268(00)00097-8).
- COOKE, D. R., BULL, S. W., DONOVAN, S. & ROGERS, J. R. 1998. K-metasomatism and base metal depletion in volcanic rocks from the McArthur Basin, Northern Territory; implications for base metal mineralization. *Economic Geology*, 93, 1237-1263. DOI: <https://doi.org/10.2113/gsecongeo.93.8.1237>.
- COOKE, D. R., BULL, S. W., LARGE, R. R. & MCGOLDRICK, P. J. 2000. The importance of oxidized brines for the formation of Australian Proterozoic stratiform sediment-hosted Pb-Zn (Sedex) deposits. *Economic Geology*, 95, 1-18. DOI: <https://doi.org/10.2113/gsecongeo.95.1.1>.
- COULOMB, R., DIETZ, S., GODUNOVA, M. & NIELSEN, T. B. 2015. Critical minerals today and in 2030: an analysis for OECD countries. *OECD Environment Working Papers*. DOI: <https://dx.doi.org/10.1787/5jrtknwm5hr5-en>.
- COX, G. M., COLLINS, A. S., JARRETT, A. J., BLADES, M. L., SHANNON, A. V., YANG, B., FARKAS, J., HALL, P. A., O'HARA, B. & CLOSE, D. J. A. B. 2022. A very unconventional hydrocarbon play: the Mesoproterozoic Velkerri Formation of northern Australia. *AAPG Bulletin* 2022; 106 (6): 1213–1237. DOI: <https://doi.org/10.1306/12162120148>.
- COX, G. M., HALVERSON, G. P., STEVENSON, R. K., VOKATY, M., POIRIER, A., KUNZMANN, M., LI, Z.-X., DENYSZYN, S. W., STRAUSS, J. V. & MACDONALD, F. A. 2016a. Continental flood basalt weathering as a trigger for Neoproterozoic Snowball Earth. *Earth and Planetary Science Letters*, 446, 89-99. DOI: <https://doi.org/10.1016/j.epsl.2016.04.016>.
- COX, G. M., JARRETT, A., EDWARDS, D., CROCKFORD, P. W., HALVERSON, G. P., COLLINS, A. S., POIRIER, A. & LI, Z.-X. 2016b. Basin redox and primary productivity within the Mesoproterozoic Roper Seaway. *Chemical Geology*, 440, 101-114. DOI: <https://doi.org/10.1016/j.chemgeo.2016.06.025>.
- COX, G. M., SANSJOFRE, P., BLADES, M. L., FARKAS, J. & COLLINS, A. S. 2019. Dynamic interaction between basin redox and the biogeochemical nitrogen cycle in an unconventional Proterozoic petroleum system. *Sci Rep*, 9, 5200. DOI: <https://doi.org/10.1038/s41598-019-40783-4>.
- CRAIG, J., BIFFI, U., GALIMBERTI, R., GHORI, K., GORTER, J., HAKHOO, N., LE HERON, D., THUROW, J. & VECOLI, M. 2013. The palaeobiology and geochemistry of Precambrian hydrocarbon source rocks. *Marine and Petroleum Geology*, 40, 1-47. DOI: <https://doi.org/10.1016/j.marpetgeo.2012.09.011>.
- CRICK, I., BOREHAM, C., COOK, A. & POWELL, T. 1988. Petroleum geology and geochemistry of Middle Proterozoic McArthur Basin, northern Australia II: Assessment of source rock potential. *AAPG Bulletin*, 72, 1495-1514. DOI: <https://doi.org/10.1306/703C99D8-1707-11D7-8645000102C1865D>.
- CROCKFORD, P. W., HAYLES, J. A., BAO, H., PLANAVSKY, N. J., BEKKER, A., FRALICK, P. W., HALVERSON, G. P., BUI, T. H., PENG, Y. & WING, B. A. 2018. Triple oxygen isotope evidence for limited mid-Proterozoic primary productivity. *Nature*, 559, 613-616. DOI: <https://doi.org/10.1038/s41586-018-0349-y>.

- CROON, M., BLUETT, J., TITUS, L. & JOHNSON, R. 2015. Formation evaluation case study: Glyde unconventional Middle Proterozoic play in the McArthur Basin, northern Australia. *The APPEA Journal*, 55, 429-429. DOI: <https://doi.org/10.1071/AJ14064>.
- CROXFORD, N., GULSON, B. & SMITH, J. 1975. The McArthur deposit: A review of the current situation. *Mineralium Deposita*, 10, 302-304.
- CULLERS, R. L. 2002. Implications of elemental concentrations for provenance, redox conditions, and metamorphic studies of shales and limestones near Pueblo, CO, USA. *Chemical Geology*, 191, 305-327. DOI: [https://doi.org/10.1016/S0009-2541\(02\)00133-X](https://doi.org/10.1016/S0009-2541(02)00133-X).
- CUTOVINOS, A., BEIER, P., KRUSE, P., ABBOTT, S., DUNSTER, J., BRESCIANINI, R., ABBOT, S., DUNSTER, J. & BRESCIANINI, R. 2002. Limbunya, Northern Territory, 1: 250 000 geological map series and explanatory notes, SE 52-07. *Northern Territory Geological Survey, Special Publications*, 3. From <https://geoscience.nt.gov.au/gemis/ntgsjspui/handle/1/87272>.
- DAINES, S. J., MILLS, B. J. W. & LENTON, T. M. 2017. Atmospheric oxygen regulation at low Proterozoic levels by incomplete oxidative weathering of sedimentary organic carbon. *Nature Communications*, 8, 14379. DOI: <https://doi.org/10.1038/ncomms14379>.
- DE BAAR, H. J. 1991. On cerium anomalies in the Sargasso Sea. *Geochimica et Cosmochimica Acta*, 55, 2981-2983. DOI: [https://doi.org/10.1016/0016-7037\(91\)90463-F](https://doi.org/10.1016/0016-7037(91)90463-F).
- DE BAAR, H. J., BACON, M. P., BREWER, P. G. & BRULAND, K. W. 1985. Rare earth elements in the Pacific and Atlantic Oceans. *Geochimica et Cosmochimica Acta*, 49, 1943-1959. DOI: [https://doi.org/10.1016/0016-7037\(85\)90089-4](https://doi.org/10.1016/0016-7037(85)90089-4).
- DE BAAR, H. J., GERMAN, C. R., ELDERFIELD, H. & VAN GAANS, P. 1988. Rare earth element distributions in anoxic waters of the Cariaco Trench. *Geochimica et Cosmochimica Acta*, 52, 1203-1219. DOI: [https://doi.org/10.1016/0016-7037\(88\)90275-X](https://doi.org/10.1016/0016-7037(88)90275-X).
- DE SOUZA, G. F., REYNOLDS, B. C., KICZKA, M. & BOURDON, B. 2010. Evidence for mass-dependent isotopic fractionation of strontium in a glaciated granitic watershed. *Geochimica et Cosmochimica Acta*, 74, 2596-2614. DOI: <https://doi.org/10.1016/j.gca.2010.02.012>.
- DEBACKER, T., CONNORS, K., PRYER, L., BLEVIN, J., HENLEY, P. & SHI, Z. 2021. The Northern Territory SEEBASE®: An updated, Territory-wide depth-to-basement model for explorers. *Northern Territory Geological Survey Digital Information Packages*. From <https://geoscience.nt.gov.au/gemis/ntgsjspui/handle/1/91173>.
- DEEPAK, A., LÖHR, S., ABBOTT, A. N., HAN, S., WHEELER, C. & SHARMA, M. 2022. Testing the Precambrian reverse weathering hypothesis using a 1-billion-year record of marine shales. *Goldschmidt Conference Proceedings*. From <https://conf.goldschmidt.info/goldschmidt/2022/meetingapp.cgi/Paper/10825>.
- DEGENS, E. & MOPPER, K. 1975. Factors Controlling the Distribution and Early Diagenesis. *Chemical oceanography*, 6, 59. DOI: <https://doi.org/10.1016/B978-0-12-588606-2.50012-6>.
- DEGENS, E. T. & EPSTEIN, S. 1962. Relationship between O18/O16 ratios in coexisting carbonates, cherts, and diatomites. *AAPG Bulletin*, 46, 534-542. DOI: <https://doi.org/10.1306/BC743841-16BE-11D7-8645000102C1865D>.
- DEHAIRS, F., CHESSELET, R. & JEDWAB, J. 1980. Discrete suspended particles of barite and the barium cycle in the open ocean. *Earth and Planetary Science Letters*, 49, 528-550. DOI: [https://doi.org/10.1016/0012-821X\(80\)90094-1](https://doi.org/10.1016/0012-821X(80)90094-1).

- DEHAIRS, F., STROOBANTS, N. & GOEYENS, L. 1991. Suspended barite as a tracer of biological activity in the Southern Ocean. *Marine Chemistry*, 35, 399-410. DOI: [https://doi.org/10.1016/S0304-4203\(09\)90032-9](https://doi.org/10.1016/S0304-4203(09)90032-9).
- DELLE PIANE, C., UYSAL, I. T., FAIZ, M., PAN, Z., BOURDET, J., LI, Z., RAVEN, M. D. & DEWHURST, D. N. 2020. Thermal maturity and reservoir quality of the Velkerri Formation, Beetaloo Sub-basin, Northern Territory. *The APPEA Journal*, 60, 697-702. DOI: <https://doi.org/10.1071/AJ19189>.
- DELLISANTI, F., PINI, G. A. & BAUDIN, F. 2010. Use of T max as a thermal maturity indicator in orogenic successions and comparison with clay mineral evolution. *Clay minerals*, 45, 115-130. DOI: doi:10.1180/claymin.2010.045.1.115.
- DEMAISON, G. J. & MOORE, G. T. 1980. Anoxic Environments and Oil Source Bed Genesis. *AAPG Bulletin*, 64, 1179-1209. DOI: <https://doi.org/10.1306/2F91945E-16CE-11D7-8645000102C1865D>.
- DEMBICKI JR, H. 2009. Three common source rock evaluation errors made by geologists during prospect or play appraisals. *AAPG bulletin*, 93, 341-356. DOI: <https://doi.org/10.1306/10230808076>.
- DEPAOLO, D. J. & INGRAM, B. L. 1985. High-resolution stratigraphy with strontium isotopes. *Science*, 227, 938-941. DOI: <https://doi.org/10.1126/science.227.4689.938>.
- DERKOWSKI, A., ŚRODOŃ, J., FRANUS, W., UHLÍK, P., BANAŚ, M., ZIELIŃSKI, G., ČAPLOVIČOVÁ, M. & FRANUS, M. 2009. Partial dissolution of glauconitic samples: Implications for the methodology of K-Ar and Rb-Sr dating. *Clays and Clay Minerals*, 57, 531-554. DOI <https://doi.org/10.1346/CCMN.2009.0570503>.
- DERRY, L. A. & JACOBSEN, S. B. 1988. The Nd and Sr isotopic evolution of Proterozoic seawater. *Geophysical Research Letters*, 15, 397-400. DOI: <https://doi.org/10.1029/GL015i004p00397>.
- DESSERT, C., DUPRÉ, B., GAILLARDET, J., FRANÇOIS, L. M. & ALLEGRE, C. J. 2003. Basalt weathering laws and the impact of basalt weathering on the global carbon cycle. *Chemical Geology*, 202, 257-273. DOI: <https://doi.org/10.1016/j.chemgeo.2002.10.001>.
- DIAZ, J., INGALL, E., BENITEZ-NELSON, C., PATERSON, D., DE JONGE, M. D., MCNULTY, I. & BRANDES, J. A. 2008. Marine polyphosphate: a key player in geologic phosphorus sequestration. *Science*, 320, 652-655.
- DICKIN, A. P. 2018. Radiogenic isotope geology. *Cambridge University Press*. ISBN: 9781107099449, 1107099447
- DILORETO, Z. A., GARG, S., BONTOGNALI, T. R. R. & DITTRICH, M. 2021. Modern dolomite formation caused by seasonal cycling of oxygenic phototrophs and anoxygenic phototrophs in a hypersaline sabkha. *Scientific Reports*, 11, 4170. DOI: <https://doi.org/10.1038/s41598-021-83676-1>.
- DING, J., SHI, Y., KRÖNER, A. & ANDERSON, J. 2017. Constraints on sedimentary ages of the Chuanlinggou Formation in the Ming Tombs, Beijing, North China Craton: LA-ICP-MS and SHRIMP U–Pb dating of detrital zircons. *Acta Geochimica*, 37, 1-24. DOI: <https://doi.org/10.1007/s11631-017-0211-1>.
- DING, J., ZHANG, S., ZHAO, H., XIAN, H., LI, H., YANG, T., WU, H. & WANG, W. 2020. A combined geochronological and paleomagnetic study on ~1220 Ma mafic dikes in the North China Craton and the implications for the breakup of Nuna and assembly of Rodinia. *American Journal of Science*, 320, 125. DOI: <https://doi.org/10.2475/02.2020.02>.

- DISNAR, J. R. 1994. Determination of maximum paleotemperatures of burial (MPTB) of sedimentary rocks from pyrolysis data on the associated organic matter: basic principles and practical application. *Chemical Geology*, 118, 289-299. DOI: [https://doi.org/10.1016/0009-2541\(94\)90182-1](https://doi.org/10.1016/0009-2541(94)90182-1).
- DODSON, M. H. 1973. Closure temperature in cooling geochronological and petrological systems. *Contributions to Mineralogy and Petrology*, 40, 259-274. DOI: <https://doi.org/10.1007/BF00373790>.
- DONG, T., HARRIS, N. B. & AYRANCI, K. 2017. Relative sea-level cycles and organic matter accumulation in shales of the Middle and Upper Devonian Horn River Group, northeastern British Columbia, Canada: Insights into sediment flux, redox conditions, and bioproductivity. *GSA Bulletin*, 130, 859-880. DOI: <https://doi.org/10.1130/B31851.1>.
- DUANE, M. J., KRUGER, F. J., TURNER, A. M., WHITELAW, H. T., COETZEE, H. & VERHAGEN, B. T. 2004. The timing and isotopic character of regional hydrothermal alteration and associated epigenetic mineralization in the western sector of the Kaapvaal Craton (South Africa). *Journal of African Earth Sciences*, 38, 461-476. DOI: <https://doi.org/10.1016/j.jafrearsci.2004.03.002>.
- DUDDY, I., GREEN, P., GIBSON, H. & HEGARTY, K. 2004. Regional Palaeothermal episodes in Northern Australia. *Timor Sea Petroleum Geoscience: Proceedings of the Timor Sea Symposium*. 19, 20. ISBN: 0-7245-7072-1
- DUNSTER, J. 1998. Reconnaissance of the Proterozoic rocks of the Victoria River Region. *Mineral Exploration Reports*. Darwin, Northern Territory, Australia: Northern Territory Geological Survey. From <https://geoscience.nt.gov.au/gemis/ntgsjspui/handle/1/69726>.
- DUTKIEWICZ, A., VOLK, H., RIDLEY, J. & GEORGE, S. C. 2004. Geochemistry of oil in fluid inclusions in a middle Proterozoic igneous intrusion: implications for the source of hydrocarbons in crystalline rocks. *Organic Geochemistry*, 35, 937-957. DOI: <https://doi.org/10.1016/j.orggeochem.2004.03.007>.
- DYMOND, J., SUESS, E. & LYLE, M. 1992. Barium in deep-sea sediment: A geochemical proxy for paleoproductivity. *Paleoceanography*, 7, 163-181. DOI: <https://doi.org/10.1029/92PA00181>.
- EGGERT, R. G. 2010. Critical minerals and emerging technologies. *Issues in Science and Technology*, 26, 49-58. From <https://www.jstor.org/stable/43315186>.
- EGGERT, R. G. 2011. Minerals go critical. *Nature chemistry*, 3, 688-691. DOI: <https://doi.org/10.1038/nchem.1116>.
- EL MEKNASSI, S., DERA, G., DE RAFÉLIS, M., BRAHMI, C., LARTAUD, F., HODEL, F., JEANDEL, C., MENJOT, L., MOUNIC, S., HENRY, M., BESSON, P. & CHAVAGNAC, V. 2020. Seawater  $^{87}\text{Sr}/^{86}\text{Sr}$  ratios along continental margins: Patterns and processes in open and restricted shelf domains. *Chemical Geology*, 558, 119874. DOI: <https://doi.org/10.1016/j.chemgeo.2020.119874>.
- ELDERFIELD, H. & GREAVES, M. 1981. Negative cerium anomalies in the rare earth element patterns of oceanic ferromanganese nodules. *Earth and Planetary Science Letters*, 55, 163-170. DOI: [https://doi.org/10.1016/0012-821X\(81\)90095-9](https://doi.org/10.1016/0012-821X(81)90095-9).
- ELDRIDGE, C. S., WILLIAMS, N. & WALSHE, J. L. 1993. Sulfur isotope variability in sediment-hosted massive sulfide deposits as determined using the ion microprobe SHRIMP; II, A study of the H.Y.C. Deposit at McArthur River, Northern Territory, Australia. *Economic Geology*, 88, 1-26. DOI: <https://doi.org/10.2113/gsecongeo.88.1.1>.



- EMERSON, S. 1985. The Carbon Cycle and Atmospheric CO<sub>2</sub>: Natural Variations, Archaean to Present. *Am. Geophys. Union*, 78-87. DOI: 10.1029/GM032.
- EMERSON, S. R. & HUESTED, S. S. 1991. Ocean anoxia and the concentrations of molybdenum and vanadium in seawater. *Marine Chemistry*, 34, 177-196. DOI: [https://doi.org/10.1016/0304-4203\(91\)90002-E](https://doi.org/10.1016/0304-4203(91)90002-E).
- ESPITALIÉ, J. 1986. Use of Tmax as a maturation index for different types of organic matter: comparison with vitrinite reflectance. *Collection colloques et séminaires-Institut français du pétrole*, 475-496. ISSN: 0073-8360.
- ESPITALIÉ, J., MADEC, M., TISSOT, B., MENNIG, J. & LEPLAT, P. 1977. Source rock characterization method for petroleum exploration. *Offshore Technology Conference*. DOI: <https://doi.org/10.4043/2935-MS>.
- EVINS, L. Z., JOURDAN, F. & PHILLIPS, D. J. L. 2009. The Cambrian Kalkarindji Large Igneous Province: Extent and characteristics based on new <sup>40</sup>Ar/<sup>39</sup>Ar and geochemical data. 110, 294-304. DOI: <https://doi.org/10.1016/j.lithos.2009.01.014>.
- FALKNER, K. K., BOWERS, T., TODD, J., LEWIS, B., LANDING, W. & EDMOND, J. 1993. The behavior of barium in anoxic marine waters. *Geochimica et Cosmochimica Acta*, 57, 537-554. DOI: [https://doi.org/10.1016/0016-7037\(93\)90366-5](https://doi.org/10.1016/0016-7037(93)90366-5).
- FANNING, C. 1991. Ion microprobe U–Pb zircon dating of a tuffaceous horizon within the Kunja Siltstone, Victoria River Basin, Northern Territory. *Report for Pacific Oil and Gas Pty Ltd. Canberra, ACT: Research School of Earth Sciences, Australian National University*.
- FARQUHAR, J., ZERKLE, A. L. & BEKKER, A. 2011. Geological constraints on the origin of oxygenic photosynthesis. *Photosynth Res*, 107, 11-36. DOI: <https://doi.org/10.1007/s11120-010-9594-0>.
- FAURE, G. 1977. Principles of isotope geology. Wiley. OSTI: 7100564.
- FILIPPELLI, G. M. 1997. Controls on phosphorus concentration and accumulation in oceanic sediments. *Marine Geology*, 139, 231-240. DOI: [https://doi.org/10.1016/S0025-3227\(96\)00113-2](https://doi.org/10.1016/S0025-3227(96)00113-2).
- FÖLLMI, K. 1996. The phosphorus cycle, phosphogenesis and marine phosphate-rich deposits. *Earth-Science Reviews*, 40, 55-124. DOI: [https://doi.org/10.1016/0012-8252\(95\)00049-6](https://doi.org/10.1016/0012-8252(95)00049-6).
- FRANCOIS, R., HONJO, S., MANGANINI, S. J. & RAVIZZA, G. E. 1995. Biogenic barium fluxes to the deep sea: Implications for paleoproductivity reconstruction. *Global Biogeochemical Cycles*, 9, 289-303. DOI: <https://doi.org/10.1029/95GB00021>.
- FRENCH, K. L., BIRDWELL, J. E. & BERG, M. V. 2020. Biomarker similarities between the saline lacustrine eocene green river and the paleoproterozoic barney creek formations. *Geochimica et Cosmochimica Acta*, 274, 228-245. DOI: <https://doi.org/10.1016/j.gca.2020.01.053>.
- FROGTECH GEOSCIENCE, N. T. G. S. 2018. SEEBASE® study and GIS for greater McArthur Basin. *Digital Information Package*. 017. From <https://geoscience.nt.gov.au/gemis/ntgjsjpui/handle/1/87064>.
- FURLANETTO, F., THORKELSON, D. J., RAINBIRD, R. H., DAVIS, W. J., GIBSON, H. D. & MARSHALL, D. D. 2016. The Paleoproterozoic Wernecke Supergroup of Yukon, Canada: Relationships to orogeny in northwestern Laurentia and basins in North America, East Australia, and China. *Gondwana Research*, 39, 14-40. DOI: <https://doi.org/10.1016/j.gr.2016.06.007>.

- GALÁN, E. 2006. Genesis of clay minerals. *Developments in clay science*, 1, 1129-1162. DOI: [https://doi.org/10.1016/S1572-4352\(05\)01042-1](https://doi.org/10.1016/S1572-4352(05)01042-1).
- GARCIA, D., COELHO, J. & PERRIN, M. 1991. Fractionation between TiO<sub>2</sub> and Zr as a measure of sorting within shale and sandstone series (northern Portugal). *European Journal of Mineralogy*, 3, 401-414. DOI: <https://doi.org/10.1127/ejm/3/2/0401>.
- GEORGE, S. & AHMED, M. Use of aromatic compound distributions to evaluate organic maturity of the Proterozoic middle Velkerri Formation, McArthur Basin, Australia. *Proceedings from The Sedimentary Basins of Western Australia*. 253-270. From [https://pesa.com.au/the\\_sedimentary\\_basins\\_of\\_wa\\_3\\_p253-270-pdf/](https://pesa.com.au/the_sedimentary_basins_of_wa_3_p253-270-pdf/).
- GEORGE, S. C., LLORCA, S. M. & HAMILTON, P. J. 1994. An integrated analytical approach for determining the origin of solid bitumens in the McArthur Basin, northern Australia. *Organic Geochemistry*, 21, 235-248. DOI: [https://doi.org/10.1016/0146-6380\(94\)90187-2](https://doi.org/10.1016/0146-6380(94)90187-2).
- GERMAN, C. R. & ELDERFIELD, H. 1990. Application of the Ce anomaly as a paleoredox indicator: The ground rules. *Paleoceanography*, 5, 823-833. DOI: <https://doi.org/10.1029/PA005i005p00823>.
- GERMAN, C. R., HOLLIDAY, B. P. & ELDERFIELD, H. 1991. Redox cycling of rare earth elements in the suboxic zone of the Black Sea. *Geochimica et Cosmochimica Acta*, 55, 3553-3558. DOI: [https://doi.org/10.1016/0016-7037\(91\)90055-A](https://doi.org/10.1016/0016-7037(91)90055-A).
- GHORI, K., CRAIG, J., THUSU, B., LÜNING, S. & GEIGER, M. 2009. Global Infracambrian petroleum systems: a review. *Geological Society, London, Special Publications*, 326, 109-136. DOI: <https://doi.org/10.1144/SP326.6>.
- GIANFRIDDO, C., BULL, S. W. & ANDREWS, T. M. 2022. The Rosie pyrite hydrothermal system in the McArthur Basin: tectono-sedimentary constraints on mineralization and alkali metasomatism in stratiform sediment-hosted sulfide deposits of northern Australia. *Mineralium Deposita*, 57, 377-398. DOI: <https://doi.org/10.1007/s00126-021-01069-w>.
- GIBSON, G. M., CHAMPION, D. C., WITHNALL, I. W., NEUMANN, N. L. & HUTTON, L. J. 2018. Assembly and breakup of the Nuna supercontinent: Geodynamic constraints from 1800 to 1600 Ma sedimentary basins and basaltic magmatism in northern Australia. *Precambrian Research*, 313, 148-169. DOI: <https://doi.org/10.1016/j.precamres.2018.05.013>.
- GIBSON, G. M., HENSON, P. A., NEUMANN, N. L., SOUTHGATE, P. N. & HUTTON, L. J. 2012. Paleoproterozoic–earliest Mesoproterozoic basin evolution in the Mount Isa region, northern Australia and implications for reconstructions of the Nuna and Rodinia supercontinents. *Episodes Journal of International Geoscience*, 35, 131-141. DOI: <https://doi.org/10.18814/epiiugs/2012/v35i1/012>.
- GIBSON, G. M., HUTTON, L. J. & HOLZSCHUH, J. 2017. Basin inversion and supercontinent assembly as drivers of sediment-hosted Pb–Zn mineralization in the Mount Isa region, northern Australia. *Journal of the Geological Society*, 174, 773-786. DOI: <https://doi.org/10.1144/jgs2016-105>.
- GILLEAUDEAU, G., FREI, R., KAUFMAN, A., KAH, L., AZMY, K., BARTLEY, J., CHERNYAVSKIY, P. & KNOLL, A. 2016. Oxygenation of the mid-Proterozoic atmosphere: clues from chromium isotopes in carbonates. *Geochemical Perspectives Letters*, 2, 178-187. DOI: [doi: 10.7185/geochemlet.1618](https://doi.org/10.7185/geochemlet.1618).

- GLASS, L. M. & PHILLIPS, D. 2006. The Kalkarindji continental flood basalt province: A new Cambrian large igneous province in Australia with possible links to faunal extinctions. *Geology*, 34, 461-464. DOI: <https://doi.org/10.1130/G22122.1>.
- GOODARZI, F., GENTZIS, T., SANEI, H. & PEDERSEN, P. K. 2019. Elemental Composition and Organic Petrology of a Lower Carboniferous-Age Freshwater Oil Shale in Nova Scotia, Canada. *ACS Omega*, 4, 20773-20786. DOI: <https://doi.org/10.1021/acsomega.9b03227>.
- GOROJOVSKY, L. & ALARD, O. 2020. Optimisation of laser and mass spectrometer parameters for the in situ analysis of Rb/Sr ratios by LA-ICP-MS/MS. *Journal of Analytical Atomic Spectrometry*, 35, 10, 2322-2336. DOI: <https://doi.org/10.1021/acsomega.9b03227>.
- GOROKHOV, I., SIEDLECKA, A., ROBERTS, D., MELNIKOV, N. & TURCHENKO, T. 2001. Rb–Sr dating of diagenetic illite in Neoproterozoic shales, Varanger Peninsula, northern Norway. *Geological Magazine*, 138, 541-562. DOI: <https://doi.org/10.1017/S001675680100574X>.
- GOVINDARAJU, K., RUBESKA, I. & PAUKERT, T. 1994. Report On Zinnwaldite Zw-C Analysed By Ninety-Two Git-lwg Member-Laboratories. *Geostandards Newsletter*, 18, 1-42. DOI: <https://doi.org/10.1111/j.1751-908X.1994.tb00502.x>.
- GU, X., ZHANG, Y., SCHULZ, O., VAVTAR, F., LIU, J., ZHENG, M. & ZHENG, L. 2012. The Woxi W–Sb–Au deposit in Hunan, South China: an example of late Proterozoic sedimentary exhalative (SEDEX) mineralization. *Journal of Asian Earth Sciences*, 57, 54-75. DOI: <https://doi.org/10.1016/j.jseaes.2012.06.006>.
- GÜRSAN, C. & DE GOOYERT, V. 2021. The systemic impact of a transition fuel: Does natural gas help or hinder the energy transition? *Renewable and Sustainable Energy Reviews*, 138, 110552. DOI: <https://doi.org/10.1016/j.rser.2020.110552>.
- HAHN, O., STRASSMAN, F., MATTAUCH, J. & EWALD, H. 1943. Geologische Altersbestimmungen mit der strontium methode. *Chem. Zeitung*, 67, 55-6.
- HAHN, O. & WALLING, E. 1938. Über die Möglichkeit geologischer Altersbestimmungen rubidiumhaltiger Mineralien und Gesteine. *Zeitschrift für anorganische und allgemeine Chemie*, 236, 78-82. DOI: <https://doi.org/10.1002/zaac.19382360109>.
- HAINES, P. 1994. The Balma and Habgood groups, northern McArthur Basin, Northern Territory; stratigraphy and correlations with the McArthur Group. *AusIMM Annual Conference, Australian Mining Looks North; the Challenges and Choices*. 147-152.
- HALL, L., BOREHAM, C. J., EDWARDS, D. S., PALU, T., BUCKLER, T., TROUP, A. & HILL, A. 2016. Cooper Basin Source Rock Geochemistry. *Geoscience Australia Record*. 2016, 06. DOI: <http://dx.doi.org/10.11636/Record.2016.006>.
- HALL, L. S., ORR, M. L., LECH, M. E., LEWIS, S., BAILEY, A. H. E., OWENS, R., BRADSHAW, B. E. & BERNARDEL, G. 2021. Geological and Bioregional Assessments: assessing the prospectivity for tight, shale and deep-coal resources in the Cooper Basin, Beetaloo Subbasin and Isa Superbasin. *The APPEA Journal*, 61, 477-484. DOI: <https://doi.org/10.1071/AJ20035>.
- HALVERSON, G. P., HURTGEN, M. T., PORTER, S. M. & COLLINS, A. S. 2009. Chapter 10 Neoproterozoic-Cambrian Biogeochemical Evolution. *Developments in Precambrian Geology*, 16, 351-365. DOI: [https://doi.org/10.1016/S0166-2635\(09\)01625-9](https://doi.org/10.1016/S0166-2635(09)01625-9).
- HALVERSON, G. P., WADE, B. P., HURTGEN, M. T. & BAROVICH, K. M. 2010. Neoproterozoic chemostratigraphy. *Precambrian Research*, 182, 337-350. DOI: <https://doi.org/10.1016/j.precamres.2010.04.007>.

- HAMILTON, M. A. & BUCHAN, K. L. 2010. U–Pb geochronology of the Western Channel Diabase, northwestern Laurentia: implications for a large 1.59 Ga magmatic province, Laurentia's APWP and paleocontinental reconstructions of Laurentia, Baltica and Gawler craton of southern Australia. *Precambrian Research*, 183, 463-473. DOI: <https://doi.org/10.1016/j.precamres.2010.06.009>.
- HARRISON, T. M., HEIZLER, M. T., MCKEEGAN, K. D. & SCHMITT, A. K. 2010. In situ 40K–40Ca 'double-plus' SIMS dating resolves Klokken feldspar 40K–40Ar paradox. *Earth and Planetary Science Letters*, 299, 426-433. DOI: <https://doi.org/10.1016/j.epsl.2010.09.023>.
- HARTNETT, H. E., KEIL, R. G., HEDGES, J. I. & DEVOL, A. H. 1998. Influence of oxygen exposure time on organic carbon preservation in continental margin sediments. *Nature*, 391, 572-575. DOI: <https://doi.org/10.1038/35351>.
- HAYES, J. M., STRAUSS, H. & KAUFMAN, A. J. 1999. The abundance of <sup>13</sup>C in marine organic matter and isotopic fractionation in the global biogeochemical cycle of carbon during the past 800 Ma. *Chemical Geology*, 161, 103-125. DOI: [https://doi.org/10.1016/S0009-2541\(99\)00083-2](https://doi.org/10.1016/S0009-2541(99)00083-2).
- HAYES, J. M. & WALDBAUER, J. R. 2006. The carbon cycle and associated redox processes through time. *Philos Trans R Soc Lond B Biol Sci*, 361, 931-50. DOI: <https://doi.org/10.1098/rstb.2006.1840>.
- HAYES, S. M. & MCCULLOUGH, E. A. 2018. Critical minerals: A review of elemental trends in comprehensive criticality studies. *Resources Policy*, 59, 192-199. DOI: <https://doi.org/10.1016/j.resourpol.2018.06.015>.
- HELZ, G., MILLER, C., CHARNOCK, J., MOSSELMANS, J., PATTRICK, R., GARNER, C. & VAUGHAN, D. 1996. Mechanism of molybdenum removal from the sea and its concentration in black shales: EXAFS evidence. *Geochimica et Cosmochimica Acta*, 60, 3631-3642. DOI: [https://doi.org/10.1016/0016-7037\(96\)00195-0](https://doi.org/10.1016/0016-7037(96)00195-0).
- HEMMESCH, N. T., HARRIS, N. B., MNICH, C. A. & SELBY, D. 2014. A sequence-stratigraphic framework for the Upper Devonian Woodford Shale, Permian Basin, west Texas. *AAPG Bulletin*, 98, 23-47. DOI: <https://doi.org/10.1306/05221312077>.
- HENSON, P., ROBINSON, D., CARR, L., EDWARDS, D. S., MACFARLANE, S. K., JARRETT, A. J. M. & BAILEY, A. H. E. 2020. Exploring for the Future—a new oil and gas frontier in northern Australia. *The APPEA Journal*, 60, 703-711. DOI: <https://doi.org/10.1071/AJ19080>.
- HIGGINS, J. & SCHRAG, D. 2006. Beyond methane: Towards a theory for the Paleocene–Eocene Thermal Maximum. *Earth and Planetary Science Letters*, 245, 523-537. DOI: <https://doi.org/10.1016/j.epsl.2006.03.009>.
- HILLIER, S. 1995. Erosion, sedimentation and sedimentary origin of clays. *Origin and mineralogy of clays*. Springer. DOI: [https://doi.org/10.1007/978-3-662-12648-6\\_4](https://doi.org/10.1007/978-3-662-12648-6_4).
- HOFER, G., WAGREICH, M. & NEUHUBER, S. 2013. Geochemistry of fine-grained sediments of the upper Cretaceous to Paleogene Gosau Group (Austria, Slovakia): Implications for paleoenvironmental and provenance studies. *Geoscience Frontiers*, 4, 449-468. DOI: <https://doi.org/10.1016/j.gsf.2012.11.009>.
- HOFFMAN, T. 2014. New insights into the expanse of the McArthur Superbasin. *Annual Geoscience Exploration Seminar (AGES) Record of Abstracts*. From <https://geoscience.nt.gov.au/gemis/ntgsjspui/handle/1/81540>.

- HOGMALM, K. J., DAHLGREN, I., FRIDOLFSSON, I. & ZACK, T. 2019. First in situ Re-Os dating of molybdenite by LA-ICP-MS/MS. *Mineralium Deposita*, 54, 821-828. DOI: <https://doi.org/10.1007/s00126-019-00889-1>.
- HOGMALM, K. J., ZACK, T., KARLSSON, A. K. O., SJÖQVIST, A. S. L. & GARBE-SCHÖNBERG, D. 2017. In situ Rb–Sr and K–Ca dating by LA-ICP-MS/MS: an evaluation of N<sub>2</sub>O and SF<sub>6</sub> as reaction gases. *Journal of Analytical Atomic Spectrometry*, 32, 305-313. DOI: <https://doi.org/10.1039/C6JA00362A>.
- HOLLAND, H. D. 2006. The oxygenation of the atmosphere and oceans. *Philosophical Transactions of the Royal Society B: Biological Sciences*, 361, 903-915. DOI: <https://doi.org/10.1098/rstb.2006.1838>.
- HORTON, F. 2015. Did phosphorus derived from the weathering of large igneous provinces fertilize the Neoproterozoic ocean? *Geochemistry, Geophysics, Geosystems*, 16, 1723-1738. DOI: <https://doi.org/10.1002/2015GC005792>.
- HUA, G., YUANSHEG, D., LIAN, Z., JIANGHAI, Y., HU, H., MIN, L. & YUAN, W. 2013. Trace and rare earth elemental geochemistry of carbonate succession in the Middle Gaoyuzhuang Formation, Pingquan Section: Implications for Early Mesoproterozoic ocean redox conditions. *Journal of Palaeogeography*, 2, 209-221. DOI: <https://doi.org/10.3724/SP.J.1261.2013.00027>.
- HUANG, J., CHU, X., JIANG, G., FENG, L. & CHANG, H. 2011. Hydrothermal origin of elevated iron, manganese and redox-sensitive trace elements in the c. 635 Ma Doushantuo cap carbonate. *Journal of the Geological Society*, 168, 805-816. DOI: <https://doi.org/10.1144/0016-76492010-132>.
- HUNT, J. M. 1995. Petroleum geochemistry and geology. W.H. Freeman. ISBN: 9780716724414, 0716724413.
- HUSTON, D. L., STEVENS, B., SOUTHGATE, P. N., MUHLING, P. & WYBORN, L. 2006. Australian Zn-Pb-Ag ore-forming systems: a review and analysis. *Economic Geology*, 101, 1117-1157. DOI: <https://doi.org/10.2113/gsecongeo.101.6.1117>.
- INGALL, E. & JAHNKE, R. 1997. Influence of water-column anoxia on the elemental fractionation of carbon and phosphorus during sediment diagenesis. *Marine Geology*, 139, 219-229. DOI: [https://doi.org/10.1016/S0025-3227\(96\)00112-0](https://doi.org/10.1016/S0025-3227(96)00112-0).
- INGALL, E., KOLOWITH, L., LYONS, T. & HURTGEM, M. 2005. Sediment carbon, nitrogen and phosphorus cycling in an anoxic fjord, Effingham Inlet, British Columbia. *American Journal of Science*, 305, 240-258. DOI: <https://doi.org/10.2475/ajs.305.3.240>.
- INGALL, E. D., BUSTIN, R. & VAN CAPPELLEN, P. 1993. Influence of water column anoxia on the burial and preservation of carbon and phosphorus in marine shales. *Geochimica et Cosmochimica Acta*, 57, 303-316. DOI: [https://doi.org/10.1016/0016-7037\(93\)90433-W](https://doi.org/10.1016/0016-7037(93)90433-W).
- ISSON, T. T. & PLANAVSKY, N. J. 2018. Reverse weathering as a long-term stabilizer of marine pH and planetary climate. *Nature*, 560, 471-475. DOI: <https://doi.org/10.1038/s41586-018-0408-4>.
- IYER, K., SVENSEN, H. & SCHMID, D. W. 2018. SILLi 1.0: a 1-D numerical tool quantifying the thermal effects of sill intrusions. *Geosci. Model Dev.*, 11, 43-60. DOI: <https://doi.org/10.5194/gmd-11-43-2018>.
- JACKSON, J., SWEET, I. P. & POWELL, T. G. 1988. Studies On Petroleum Geology And Geochemistry, Middle Proterozoic, McArthur Basin Northern Australia I: Petroleum Potential. *The APPEA Journal*, 28, 283-302. DOI: <https://doi.org/10.1071/AJ87022>

- JACKSON, M., SWEET, I., PAGE, R. & BRADSHAW, B. 1999. The South Nicholson and Roper Groups: evidence for the early Mesoproterozoic Roper Superbasin. *Integrated Basin Analysis of the Isa Superbasin using Seismic, Well-log, and Geopotential Data: An Evaluation of the Economic Potential of the Northern Lawn Hill Platform: Canberra, Australia, Australian Geological Survey Organisation Record*, 19.
- JACKSON, M. J., MUIR, M. D. & PLUMB, K. A. 1987. Geology of the Southern McArthur Basin, Northern Territory. *Australian Government Public Service Record*. 220. From <http://pid.geoscience.gov.au/dataset/ga/18>.
- JACKSON, M. J., POWELL, T. G., SUMMONS, R. E. & SWEET, I. P. 1986. Hydrocarbon shows and petroleum source rocks in sediments as old as  $1.7 \times 10^9$  years. *Nature*, 322, 727-729. DOI: <https://doi.org/10.1038/322727a0>.
- JACKSON, M. J. & RAISWELL, R. 1991. Sedimentology and carbon-sulphur geochemistry of the Velkerri Formation, a mid-Proterozoic potential oil source in northern Australia. *Precambrian Research*, 54, 81-108. DOI: [https://doi.org/10.1016/0301-9268\(91\)90070-Q](https://doi.org/10.1016/0301-9268(91)90070-Q).
- JAHNKE, R. A. 1990. Early diagenesis and recycling of biogenic debris at the seafloor, Santa Monica Basin, California. *Journal of marine research*, 48, 413-436. DOI: <https://doi.org/10.1357/002224090784988773>.
- JARRETT, A., COX, G., SOUTHBY, C., HONG, Z., PALATY, P., CARR, L. & HENSON, P. 2018. Source rock geochemistry of the McArthur Basin, Northern Australia. *Rock-Eval pyrolysis data release*. 2018/024. DOI: <http://dx.doi.org/10.11636/Record.2018.024>.
- JARRETT, A. J., BAILEY, A., CHEN, J. & MUNSON, T. J. 2021. Petroleum geology and geochemistry of the Birrindudu Basin, greater McArthur Basin. *Annual Geoscience Exploration Seminar (AGES) Proceedings*, 115. From <https://geoscience.nt.gov.au/gemis/ntgjsjpsui/handle/1/91413>.
- JARRETT, A. J., COX, G. M., BROCKS, J. J., GROSJEAN, E., BOREHAM, C. J. & EDWARDS, D. S. 2019. Microbial assemblage and palaeoenvironmental reconstruction of the 1.38 Ga Velkerri Formation, McArthur Basin, northern Australia. *Geobiology*, 17, 360-380. DOI: <https://doi.org/10.1111/gbi.12331>.
- JARRETT, A. J. M., MUNSON, T. J., WILLIAMS, B., BAILEY, A. H. E. & PALU, T. 2022. Petroleum supersystems in the greater McArthur Basin, Northern Territory, Australia: prospectivity of the world's oldest stacked systems with emphasis on the McArthur Supersystem. *The APPEA Journal*, 62, 245-262. DOI: <https://doi.org/10.1071/AJ21018>.
- JARVIE, D. & BREYER, J. 2011. Shale resource systems for oil and gas: Part 1–Shale gas resource systems; Part 2–Shale oil resource systems. *Shale reservoirs–Giant resources for the 21st century, AAPG Memoir*, 97, 1-31. DOI: <https://doi.org/10.1306/13321446M973489>.
- JARVIE, D. M., CLAXTON, B. L., HENK, F. & BREYER, J. T. 2001. Oil and shale gas from the Barnett Shale, Ft. Worth Basin, Texas. *AAPG Annual Meeting Program*. A100. From <https://www.searchanddiscovery.com/abstracts/html/2001/annual/abstracts/0386.htm>.
- JARVIS, I., BURNETT, W., NATHAN, Y., ALMBAYDIN, F., ATTIA, A., CASTRO, L., FLICOTEAUX, R., HILMY, M. E., HUSAIN, V. & QUTAWNAH, A. 1994. Phosphorite geochemistry: state-of-the-art and environmental concerns. *Eclogae Geologicae Helvetiae*, 87, 643-700. ISSN: 0967-0653

- JAVAUX, E. J. & LEPOT, K. 2018. The Paleoproterozoic fossil record: Implications for the evolution of the biosphere during Earth's middle-age. *Earth-Science Reviews*, 176, 68-86. DOI: <https://doi.org/10.1016/j.earscirev.2017.10.001>.
- JEGAL, Y., ZIMMERMANN, C., REISBERG, L., YEGHICHEYAN, D., CLOQUET, C., PEIFFERT, C., GERARDIN, M., DELOULE, E. & MERCADIER, J. 2022. Characterisation of Reference Materials for In Situ Rb-Sr Dating by LA-ICP-MS/MS. *Geostandards and Geoanalytical Research*. DOI: <https://doi.org/10.1111/ggr.12456>.
- JIANG, L., PLANAVSKY, N., ZHAO, M., LIU, W. & WANG, X. 2019. Authigenic origin for a massive negative carbon isotope excursion. *Geology*, 47, 115-118. DOI: <https://doi.org/10.1130/G45709.1>.
- JOCHUM, K. & STOLL, B. 2008. Reference materials for elemental and isotopic analyses by LA-(MC)-ICP-MS: Successes and outstanding needs. *Laser ablation ICP-MS in the Earth sciences: Current practices and outstanding issues*, 147-168, 40. From <https://hdl.handle.net/11858/00-001M-0000-0014-8633-5>.
- JOCHUM, K. P., WEIS, U., SCHWAGER, B., STOLL, B., WILSON, S. A., HAUG, G. H., ANDREA, M. O. & ENZWEILER, J. 2016. Reference Values Following ISO Guidelines for Frequently Requested Rock Reference Materials. *Geostandards and Geoanalytical Research*, 40, 333-350. DOI: <https://doi.org/10.1111/j.1751-908X.2015.00392.x>.
- JOCHUM, K. P., WEIS, U., STOLL, B., KUZMIN, D., YANG, Q., RACZEK, I., JACOB, D. E., STRACKE, A., BIRBAUM, K., FRICK, D. A., GÜNTHER, D. & ENZWEILER, J. 2011. Determination of Reference Values for NIST SRM 610–617 Glasses Following ISO Guidelines. *Geostandards and Geoanalytical Research*, 35, 397-429. DOI: <https://doi.org/10.1111/j.1751-908X.2011.00120.x>.
- JOCHUM, K. P., WILLBOLD, M., RACZEK, I., STOLL, B. & HERWIG, K. 2005. Chemical Characterisation of the USGS Reference Glasses GSA-1G, GSC-1G, GSD-1G, GSE-1G, BCR-2G, BHVO-2G and BIR-1G Using EPMA, ID-TIMS, ID-ICP-MS and LA-ICP-MS. *Geostandards and Geoanalytical Research*, 29, 285-302. DOI: <https://doi.org/10.1111/j.1751-908X.2005.tb00901.x>.
- JOHNSTON, D. T., FARQUHAR, J., SUMMONS, R. E., SHEN, Y., KAUFMAN, A. J., MASTERTON, A. L. & CANFIELD, D. E. 2008. Sulfur isotope biogeochemistry of the Proterozoic McArthur Basin. *Geochimica et Cosmochimica Acta*, 72, 4278-4290. DOI: <https://doi.org/10.1016/j.gca.2008.06.004>.
- JOURDAN, F., HODGES, K., SELL, B., SCHALTEGGER, U., WINGATE, M., EVINS, L., SÖDERLUND, U., HAINES, P., PHILLIPS, D. & BLENKINSOP, T. J. G. 2014. High-precision dating of the Kalkarindji large igneous province, Australia, and synchrony with the Early–Middle Cambrian (Stage 4–5) extinction. *Geology*, 42, 543-546. DOI: <https://doi.org/10.1130/G35434.1>.
- KALANTZAKOS, S. 2020. The race for critical minerals in an era of geopolitical realignments. *The International Spectator*, 55, 1-16. DOI: <https://doi.org/10.1080/03932729.2020.1786926>.
- KARLSTROM, K. E., ÅHÄLL, K.-I., HARLAN, S. S., WILLIAMS, M. L., MCLELLAND, J. & GEISSMAN, J. W. 2001. Long-lived (1.8–1.0 Ga) convergent orogen in southern Laurentia, its extensions to Australia and Baltica, and implications for refining Rodinia. *Precambrian Research*, 111, 5-30. DOI: [https://doi.org/10.1016/S0301-9268\(01\)00154-1](https://doi.org/10.1016/S0301-9268(01)00154-1).

- KASTING, J. & ONO, S. 2006. Palaeoclimates: The first two billion years. *Philosophical transactions of the Royal Society of London. Series B, Biological sciences*, 361, 917-29. DOI: <https://doi.org/10.1098/rstb.2006.1839>.
- KATZ, B. J. 2005. Controlling factors on source rock development—a review of productivity, preservation, and sedimentation rate. *SEPM Society for Sedimentary Geology*, 82. DOI: <https://doi.org/10.2110/pec.05.82>.
- KATZ, L. A. 2012. Origin and diversification of eukaryotes. *Annual review of microbiology*, 66, 411-427. DOI: <https://doi.org/10.1146/annurev-micro-090110-102808>.
- KENDALL, B., CREASER, R., GORDON, G. & ANBAR, A. 2009. Re-Os and Mo isotope systematics of black shales from the Middle Proterozoic Velkerri and Wollgorang Formations, McArthur Basin, northern Australia. *Geochimica et Cosmochimica Acta*, 73, 2534-2558. DOI: <https://doi.org/10.1016/j.gca.2009.02.013>.
- KENNEDY, M., DROSER, M., MAYER, L. M., PEVEAR, D. & MROFKA, D. 2006. Late Precambrian oxygenation; inception of the clay mineral factory. *Science*, 311, 1446-1449. DOI: <https://doi.org/10.1126/science.1118929>.
- KENNEDY, M. J., PEVEAR, D. R. & HILL, R. J. 2002. Mineral surface control of organic carbon in black shale. *Science*, 295, 657-660. DOI: <https://doi.org/10.1126/science.1066611>.
- KILLINGLEY, J. S. 1983. Effects of diagenetic recrystallization on 18O/16O values of deep-sea sediments. *Nature*, 301, 594-597. DOI: <https://doi.org/10.1038/301594a0>.
- KIRSCHER, U., MITCHELL, R. N., LIU, Y., NORDSVAN, A. R., COX, G. M., PISAREVSKY, S. A., WANG, C., WU, L., MURPHY, J. B. & LI, Z.-X. 2020. Paleomagnetic constraints on the duration of the Australia-Laurentia connection in the core of the Nuna supercontinent. *Geology*, 49, 174-179. DOI: <https://doi.org/10.1130/G47823.1>.
- KNOLL, A. H. & CARROLL, S. B. 1999. Early animal evolution: emerging views from comparative biology and geology. *Science*, 284, 2129-37. DOI: <https://doi.org/10.1126/science.284.5423.2129>.
- KNOLL, A. H., HAYES, J. M., KAUFMAN, A. J., SWETT, K. & LAMBERT, I. B. 1986. Secular variation in carbon isotope ratios from Upper Proterozoic successions of Svalbard and East Greenland. *Nature*, 321, 832-838. DOI: <https://doi.org/10.1038/321832a0>.
- KNOLL, A. H., JAVAUX, E. J., HEWITT, D. & COHEN, P. 2006. Eukaryotic organisms in Proterozoic oceans. *Philosophical Transactions of the Royal Society B: Biological Sciences*, 361, 1023-1038. DOI: <https://doi.org/10.1098/rstb.2006.1843>.
- KOSAKOWSKI, G., KUNERT, V., CLAUSER, C., FRANKE, W. & NEUGEBAUER, H. J. 1999. Hydrothermal transients in Variscan crust: paleo-temperature mapping and hydrothermal models. *Tectonophysics*, 306, 325-344. DOI: [https://doi.org/10.1016/S0040-1951\(99\)00064-5](https://doi.org/10.1016/S0040-1951(99)00064-5).
- KOSITCIN, N. & CARSON, C. 2017. New SHRIMP U-Pb Zircon Ages from the Birrindudu and Victoria Basins, Northern Territory: July 2016-June 2017, *Geoscience Australia Records*, 2017/016. DOI: <http://dx.doi.org/10.11636/Record.2017.016>.
- KOVAC, P., TITUS, L., CEVALLOS, C. & BLUETT, J. 2014. Exploring for unconventional hydrocarbon plays in the Glyde Basin, Northern Territory, using FALCON® airborne gravity gradiometry (AGG) data. *The APPEA Journal*, 54, 519-519. DOI: <https://doi.org/10.1071/AJ13092>.
- KRAAL, P., BURTON, E. D., ROSE, A. L., KOCAR, B. D., LOCKHART, R. S., GRICE, K., BUSH, R. T., TAN, E. & WEBB, S. M. 2015. Sedimentary iron–phosphorus cycling under contrasting redox conditions in a eutrophic estuary. *Chemical Geology*, 392, 19-31. DOI: <https://doi.org/10.1016/j.chemgeo.2014.11.006>.



- KRABBENHÖFT, A., EISENHAUER, A., BÖHM, F., VOLLSTAEDT, H., FIETZKE, J., LIEBETRAU, V., AUGUSTIN, N., PEUCKER-EHRENBRINK, B., MÜLLER, M. N., HORN, C., HANSEN, B. T., NOLTE, N. & WALLMANN, K. 2010. Constraining the marine strontium budget with natural strontium isotope fractionations ( $^{87}\text{Sr}/^{86}\text{Sr}$ ,  $\delta^{88}/^{86}\text{Sr}$ ) of carbonates, hydrothermal solutions and river waters. *Geochimica et Cosmochimica Acta*, 74, 4097-4109. DOI: <https://doi.org/10.1016/j.gca.2010.04.009>.
- KRABBENHÖFT, A., FIETZKE, J., EISENHAUER, A., LIEBETRAU, V., BÖHM, F. & VOLLSTAEDT, H. 2009. Determination of radiogenic and stable strontium isotope ratios ( $^{87}\text{Sr}/^{86}\text{Sr}$ ;  $\delta^{88}/^{86}\text{Sr}$ ) by thermal ionization mass spectrometry applying an  $^{87}\text{Sr}/^{84}\text{Sr}$  double spike. *Journal of Analytical Atomic Spectrometry*, 24, 1267-1271. DOI: <https://doi.org/10.1039/B906292K>.
- KRALIK, M. 1984. Effects of cation-exchange treatment and acid leaching on the Rb-Sr system of illite from Fithian, Illinois. *Geochimica et Cosmochimica Acta*, 48, 527-533. DOI: [https://doi.org/10.1016/0016-7037\(84\)90281-3](https://doi.org/10.1016/0016-7037(84)90281-3).
- KUBLER, B. 1967. La cristallinité de l'illite et les zones tout à fait supérieures du métamorphisme. *Etages tectoniques*, 105-121. From <https://cir.nii.ac.jp/crid/1574231875718999296>.
- KUHNS, R. J. & SHAW, G. H. 2018. Coal and natural gas. *Navigating the Energy Maze*. Springer. DOI: <https://doi.org/10.1007/978-3-319-22783-2>.
- KUMAR, B., SHARMA, S. D., SREENIVAS, B., DAYAL, A., RAO, M., DUBEY, N. & CHAWLA, B. 2002. Carbon, oxygen and strontium isotope geochemistry of Proterozoic carbonate rocks of the Vindhyan Basin, central India. *Precambrian Research*, 113, 43-63. DOI: [https://doi.org/10.1016/S0301-9268\(01\)00199-1](https://doi.org/10.1016/S0301-9268(01)00199-1).
- KUMP, L. R. & ARTHUR, M. A. 1999. Interpreting carbon-isotope excursions: carbonates and organic matter. *Chemical Geology*, 161, 181-198. DOI: [https://doi.org/10.1016/S0009-2541\(99\)00086-8](https://doi.org/10.1016/S0009-2541(99)00086-8).
- KUNZMANN, M., CROMBEZ, V., BLAIKIE, T. N., CATUNEANU, O., KING, R., HALVERSON, G. P., SCHMID, S. & SPINKS, S. C. 2022. Sequence stratigraphy of the ca 1640 Ma Barney Creek Formation, McArthur Basin, Australia. *Australian Journal of Earth Sciences*, 1-29. DOI: <https://doi.org/10.1080/08120099.2022.2095030>.
- KUNZMANN, M., CROMBEZ, V., CATUNEANU, O., BLAIKIE, T. N., BARTH, G. & COLLINS, A. S. 2020. Sequence stratigraphy of the ca. 1730 Ma Wollgorang Formation, McArthur Basin, Australia. *Marine and Petroleum Geology*, 116, 104297. DOI: <https://doi.org/10.1016/j.marpetgeo.2020.104297>.
- KUNZMANN, M., SCHMID, S., BLAIKIE, T. N. & HALVERSON, G. P. 2019. Facies analysis, sequence stratigraphy, and carbon isotope chemostratigraphy of a classic Zn-Pb host succession: The Proterozoic middle McArthur Group, McArthur Basin, Australia. *Ore Geology Reviews*, 106, 150-175. DOI: <https://doi.org/10.1016/j.oregeorev.2019.01.011>.
- KUZNETSOV, A. B., MELEZHNIK, V. A., GOROKHOV, I. M., MELNIKOVA, N. N., KONSTANTINOVA, G. V., KUTYAVIN, E. P. & TURCHENKO, T. L. 2010. Sr isotopic composition of Paleoproterozoic  $^{13}\text{C}$ -rich carbonate rocks: The Tulomozero Formation, SE Fennoscandian Shield. *Precambrian Research*, 182, 300-312. DOI: <https://doi.org/10.1016/j.precamres.2010.05.006>.
- KUZNETSOV, A. B., SEMIKHATOV, M. A. & GOROKHOV, I. M. 2014. The Sr isotope chemostratigraphy as a tool for solving stratigraphic problems of the Upper

- Proterozoic (Riphean and Vendian). *Stratigraphy and Geological Correlation*, 22, 553-575. DOI: <https://doi.org/10.1134/S0869593814060033>.
- KUZNETSOV, A. B., SEMIKHATOV, M. A. & GOROKHOV, I. M. 2018. Strontium Isotope Stratigraphy: Principles and State of the Art. *Stratigraphy and Geological Correlation*, 26, 367-386. DOI: <https://doi.org/10.1134/S0869593818040056>.
- KVALHEIM, O. M., CHRISTY, A. A., TELNÆS, N. & BJØRSETH, A. 1987. Maturity determination of organic matter in coals using the methylphenanthrene distribution. *Geochimica et Cosmochimica Acta*, 51, 1883-1888. DOI: [https://doi.org/10.1016/0016-7037\(87\)90179-7](https://doi.org/10.1016/0016-7037(87)90179-7).
- LAAKSO, T. A. & SCHRAG, D. P. 2017. A theory of atmospheric oxygen. *Geobiology*, 15, 366-384. DOI: <https://doi.org/10.1111/gbi.12230>.
- LAND, L. S. 1995. Comment on "Oxygen and carbon isotopic composition of Ordovician brachiopods: Implications for coeval seawater" by H. Qing and J. Veizer. *Geochimica et Cosmochimica Acta*, 59, 2843-2844. DOI: [https://doi.org/10.1016/0016-7037\(94\)90345-X](https://doi.org/10.1016/0016-7037(94)90345-X).
- LANIGAN, K. & LEDLIE, I. M. 1990. Walton-1,2 EP 24 McArthur Basin, Northern Territory Well Completion Report. Northern Territory, Australia: Pacific Oil and Gas. *Northern Territory Geological Survey Reports*, PR1989-0088. From <https://geoscience.nt.gov.au/gemis/ntgsjspui/handle/1/79422>.
- LANIGAN, K. & TORKINGTON, J. 1991. Well Completion Report EP19 - Sever 1, Daly Sub-basin of the McArthur Basin. Northern Territory, Australia: Pacific Oil and Gas. *Northern Territory Geological Survey Reports*, PR1990-0069. From <https://geoscience.nt.gov.au/gemis/ntgsjspui/handle/1/79258>.
- LARGE, D. E. & WOLF, K. H. 1981. Sediment-hosted submarine exhalative lead-zinc deposits—a review of their geological characteristics and genesis. *Handbook of strata-bound and stratiform ore deposits*, 9, 469-507. ISBN: 9780444597076, 0444597077.
- LARGE, R. R., BULL, S. W., COOKE, D. R. & MCGOLDRICK, P. J. 1998. A genetic model for the H.Y.C. Deposit, Australia; based on regional sedimentology, geochemistry, and sulfide-sediment relationships. *Economic Geology*, 93, 1345-1368. DOI: <https://doi.org/10.2113/gsecongeo.93.8.1345>.
- LARGE, R. R., BULL, S. W. & MCGOLDRICK, P. J. 2000. Lithochemical halos and geochemical vectors to stratiform sediment hosted Zn–Pb–Ag deposits: Part 2. H.Y.C deposit, McArthur River, Northern Territory. *Journal of Geochemical Exploration*, 68, 105-126. DOI: [https://doi.org/10.1016/S0375-6742\(99\)00084-9](https://doi.org/10.1016/S0375-6742(99)00084-9).
- LARGE, R. R., BULL, S. W., MCGOLDRICK, P. J., WALTERS, S., DERRICK, G. M. & CARR, G. R. 2005. Stratiform and strata-bound Zn-Pb-Ag deposits in Proterozoic sedimentary basins, northern Australia. *Economic Geology*, 100, 931-963. DOI: <https://doi.org/10.5382/AV100.28>.
- LARGE, R. R., BULL, S. W. & WINEFIELD, P. R. 2001. Carbon and Oxygen Isotope Halo in Carbonates Related to the McArthur River (HYC) Zn-Pb-Ag Deposit, North Australia: Implications for Sedimentation, Ore Genesis, and Mineral Exploration. *Economic Geology*, 96, 1567-1593. DOI: <https://doi.org/10.2113/gsecongeo.96.7.1567>.
- LARGE, R. R., MUKHERJEE, I., GREGORY, D. D., STEADMAN, J. A., MASLENNIKOV, V. V. & MEFFRE, S. 2017. Ocean and Atmosphere Geochemical Proxies Derived from Trace Elements in Marine Pyrite: Implications for Ore Genesis in Sedimentary Basins. *Economic Geology*, 112, 423-450. DOI: <https://doi.org/10.2113/econgeo.112.2.423>.

- LASH, G. G. & BLOOD, D. R. 2014. Organic matter accumulation, redox, and diagenetic history of the Marcellus Formation, southwestern Pennsylvania, Appalachian basin. *Marine and Petroleum Geology*, 57, 244-263. DOI: <https://doi.org/10.1016/j.marpetgeo.2014.06.001>.
- LAUREIJS, C. T., COOGAN, L. A. & SPENCE, J. 2021. In situ Rb-Sr dating of celadonite from altered upper oceanic crust using laser ablation ICP-MS/MS. *Chemical Geology*, 120339. DOI: <https://doi.org/10.1016/j.chemgeo.2021.120339>.
- LAWRENCE, M. G. & KAMBER, B. S. 2006. The behaviour of the rare earth elements during estuarine mixing—revisited. *Marine Chemistry*, 100, 147-161. DOI: <https://doi.org/10.1016/j.marchem.2005.11.007>.
- LEACH, D. L., SANGSTER, D. F., KELLEY, K. D., LARGE, R. R., GARVEN, G., ALLEN, C. R., GUTZMER, J. & WALTERS, S. 2005. Sediment-hosted lead-zinc deposits: A global perspective. Society of Economic Geologist. DOI: <https://doi.org/10.5382/AV100.18>.
- LEDLIE, I. M. & MAIM, K. 1989. Lawrence 1 EP 5 McArthur Basin, Northern Territory Well Completion Report. Northern Territory, Australia: Pacific Oil and Gas. *Northern Territory Geological Survey Reports*, PR1989-0005. From <https://geoscience.nt.gov.au/gemis/ntgjsjpui/handle/1/79504>.
- LEE, M. & PARSONS, I. 1999. Biomechanical and biochemical weathering of lichen-encrusted granite: textural controls on organic–mineral interactions and deposition of silica-rich layers. *Chemical Geology*, 161, 385-397. DOI: [https://doi.org/10.1016/S0009-2541\(99\)00117-5](https://doi.org/10.1016/S0009-2541(99)00117-5).
- LEMIUX, Y. 2011. Atree 2, Burdo 1, Chanin 1, Jamison 1, McManus 1, Shenandoah 1A, Walton 2, Balmain-1, Elliott-1 pyrolysis and tight rock analysis. Northern Territory, Australia: Talisman Energy, Advanced Well Technologies, *Northern Territory Geological Survey Reports*, PR2012-0011. From <https://geoscience.nt.gov.au/gemis/ntgjsjpui/handle/1/79502>.
- LEV, S. M., MCLENNAN, S. M. & HANSON, G. N. 1999. Mineralogic controls on REE mobility during black-shale diagenesis. *Journal of Sedimentary Research*, 69, 1071-1082. DOI: <https://doi.org/10.2110/jsr.69.1071>.
- LI, C., PLANAVSKY, N. J., LOVE, G. D., REINHARD, C. T., HARDISTY, D., FENG, L., BATES, S. M., HUANG, J., ZHANG, Q., CHU, X. & LYONS, T. W. 2015. Marine redox conditions in the middle Proterozoic ocean and isotopic constraints on authigenic carbonate formation: Insights from the Chuanlinggou Formation, Yanshan Basin, North China. *Geochimica et Cosmochimica Acta*, 150, 90-105. DOI: <https://doi.org/10.1016/j.gca.2014.12.005>.
- LI, S.-S., SANTOSH, M., FARKAŠ, J., REDAA, A., GANGULY, S., KIM, S. W., ZHANG, C., GILBERT, S. & ZACK, T. 2020. Coupled U-Pb and Rb-Sr laser ablation geochronology trace Archean to Proterozoic crustal evolution in the Dharwar Craton, India. *Precambrian Research*, 343, 105709. DOI: <https://doi.org/10.1016/j.precamres.2020.105709>.
- LI, S., WANG, X.-C., HU, S.-Y., GUAGLIARDO, P., KILBURN, M., GOLDING, S. D., RODRIGUES, S. & BOURDET, J. 2022. Recognition of a widespread Paleoproterozoic hydrothermal system in the southern McArthur Basin, northern Australia, by in-situ analysis of fine-grained pyrite and spatially-associated solid bitumen in the Lamont Pass palaeohigh. *Ore Geology Reviews*, 144, 104834. DOI: <https://doi.org/10.1016/j.oregeorev.2022.104834>.
- LI, S., WANG, X.-C., LI, C.-F., WILDE, S. A., ZHANG, Y., GOLDING, S. D., LIU, K. & ZHANG, Y. 2019. Direct Rubidium-Strontium Dating of Hydrocarbon Charge Using Small

- Authigenic Illitic Clay Aliquots from the Silurian Bituminous Sandstone in the Tarim Basin, NW China. *Scientific Reports*, 9, 1-13. DOI: <https://doi.org/10.1038/s41598-019-48988-3>.
- LINDSAY, J. F. & BRASIER, M. D. 2000. A carbon isotope reference curve for ca. 1700–1575 Ma, McArthur and Mount Isa Basins, Northern Australia. *Precambrian Research*, 99, 271-308. DOI: [https://doi.org/10.1016/S0301-9268\(99\)00062-5](https://doi.org/10.1016/S0301-9268(99)00062-5).
- LIU, X.-M., KAH, L. C., KNOLL, A. H., CUI, H., WANG, C., BEKKER, A. & HAZEN, R. M. 2021. A persistently low level of atmospheric oxygen in Earth's middle age. *Nature Communications*, 12, 351. DOI: <https://doi.org/10.1038/s41467-020-20484-7>.
- LIU, X. M., KAH, L. C., KNOLL, A. H., CUI, H., KAUFMAN, A. J., SHAHAR, A. & HAZEN, R. M. 2015. Tracing Earth's O<sub>2</sub> evolution using Zn/Fe ratios in marine carbonates. *Geochemical Perspectives Letters*, 2, 24-34. DOI: 10.7185/geochemlet.1603.
- LIU, Y., ZHONG, N., TIAN, Y., QI, W. & MU, G. 2011. The oldest oil accumulation in China: Meso-proterozoic Xiamaling Formation bituminous sandstone reservoirs. *Petroleum Exploration and Development*, 38, 503-512. DOI: [https://doi.org/10.1016/S1876-3804\(11\)60050-5](https://doi.org/10.1016/S1876-3804(11)60050-5).
- LOVE, G. D. & ZUMBERGE, J. A. 2021. Emerging Patterns in Proterozoic Lipid Biomarker Records. Cambridge University Press. DOI: <https://doi.org/10.1017/9781108847117>.
- LU, S., ZHAO, G., WANG, H. & HAO, G. 2008. Precambrian metamorphic basement and sedimentary cover of the North China Craton: A review. *Precambrian Research*, 160, 77-93. DOI: <https://doi.org/10.1016/j.precamres.2007.04.017>.
- LYONS, T. W., ANBAR, A. D., SEVERMANN, S., SCOTT, C. & GILL, B. C. 2009. Tracking Euxinia in the Ancient Ocean: A Multiproxy Perspective and Proterozoic Case Study. *Annual Review of Earth and Planetary Sciences*, 37, 507-534. DOI: 10.1146/annurev.earth.36.031207.124233.
- LYONS, T. W., DIAMOND, C. W., PLANAVSKY, N. J., REINHARD, C. T. & LI, C. 2021. Oxygenation, Life, and the Planetary System during Earth's Middle History: An Overview. *Astrobiology*, 21, 906-923. DOI: <https://doi.org/10.1089/ast.2020.2418>.
- LYONS, T. W., GELLATLY, A. M., MCGOLDRICK, P. J. & KAH, L. C. 2006. Proterozoic sedimentary exhalative (SEDEX) deposits and links to evolving global ocean chemistry. *Memoirs-Geological Society of America*, 198, 169. DOI: <https://doi.org/10.1130/MEM198>.
- LYONS, T. W., REINHARD, C. T. & PLANAVSKY, N. J. 2014. The rise of oxygen in Earth's early ocean and atmosphere. *Nature*, 506, 307-15. DOI: <https://doi.org/10.1038/nature13068>.
- LYONS, T. W., WERNE, J. P., HOLLANDER, D. J. & MURRAY, R. W. 2003. Contrasting sulfur geochemistry and Fe/Al and Mo/Al ratios across the last oxic-to-anoxic transition in the Cariaco Basin, Venezuela. *Chemical Geology*, 195, 131-157. DOI: [https://doi.org/10.1016/S0009-2541\(02\)00392-3](https://doi.org/10.1016/S0009-2541(02)00392-3).
- MACK, L. E. & AWWILLER, D. N. 1990. Sm/Nd ratio as a diagenetic tracer, Paleogene, Texas Gulf Coast. *AAPG Bulletin*, 74, 5. OSTI Identifier: 6985113.
- MACKENZIE, F. T. & KUMP, L. R. 1995. Reverse weathering, clay mineral formation, and oceanic element cycles. *Science*, 270, 586-586. DOI: <https://doi.org/10.1126/science.270.5236.586>.
- MACKENZIE, F. T., VER, L. M., SABINE, C., LANE, M. & LERMAN, A. 1993. Interactions of C, N, P and S Biogeochemical Cycles and Global Change. *NATO ASI Series*, 4. Springer. DOI: [https://doi.org/10.1007/978-3-642-76064-8\\_1](https://doi.org/10.1007/978-3-642-76064-8_1).

- MAYER, L. M. 1994. Surface area control of organic carbon accumulation in continental shelf sediments. *Geochimica et Cosmochimica Acta*, 58, 1271-1284. DOI: [https://doi.org/10.1016/0016-7037\(94\)90381-6](https://doi.org/10.1016/0016-7037(94)90381-6).
- MCLELLAN, B. C., YAMASUE, E., TEZUKA, T., CORDER, G., GOLEV, A. & GIURCO, D. 2016. Critical minerals and energy—impacts and limitations of moving to unconventional resources. *Resources*, 5, 19. DOI: <https://doi.org/10.3390/resources5020019>.
- MCLENNAN, S., HEMMING, S., MCDANIEL, D. & HANSON, G. 1993. Geochemical approaches to sedimentation, provenance, and tectonics. *Special Papers-Geological Society of America*, 21-21. DOI: <https://doi.org/10.1130/SPE284-p21>.
- MCLENNAN, S. M., TAYLOR, S. R., MCCULLOCH, M. T. & MAYNARD, J. B. 1990. Geochemical and Nd/Sr isotopic composition of deep-sea turbidites: Crustal evolution and plate tectonic associations. *Geochimica et Cosmochimica Acta*, 54, 2015-2050. DOI: [https://doi.org/10.1016/0016-7037\(90\)90269-Q](https://doi.org/10.1016/0016-7037(90)90269-Q).
- MCMAHON, W. J. & DAVIES, N. S. 2018. Evolution of alluvial mudrock forced by early land plants. *Science*, 359, 1022-1024. DOI: <https://doi.org/10.1126/science.aan4660>.
- MCMANUS, J., BERELSON, W. M., HAMMOND, D. E. & KLINKHAMMER, G. P. 1999. Barium cycling in the North Pacific: Implications for the utility of Ba as a paleoproductivity and paleoalkalinity proxy. *Paleoceanography*, 14, 53-61. DOI: <https://doi.org/10.1029/1998PA900007>.
- MCMANUS, J., BERELSON, W. M., KLINKHAMMER, G. P., JOHNSON, K. S., COALE, K. H., ANDERSON, R. F., KUMAR, N., BURDIGE, D. J., HAMMOND, D. E. & BRUMSACK, H. J. 1998. Geochemistry of barium in marine sediments: Implications for its use as a paleoproxy. *Geochimica et Cosmochimica Acta*, 62, 3453-3473. DOI: [https://doi.org/10.1016/S0016-7037\(98\)00248-8](https://doi.org/10.1016/S0016-7037(98)00248-8).
- MEDIG, K. P. R., THORKELESON, D. J., DAVIS, W. J., RAINBIRD, R. H., GIBSON, H. D., TURNER, E. C. & MARSHALL, D. D. 2014. Pinning northeastern Australia to northwestern Laurentia in the Mesoproterozoic. *Precambrian Research*, 249, 88-99. DOI: <https://doi.org/10.1016/j.precamres.2014.04.018>.
- MERGELOV, N., MUELLER, C. W., PRATER, I., SHORKUNOV, I., DOLGIKH, A., ZAZOVSKAYA, E., SHISHKOV, V., KRUPSKAYA, V., ABROSIMOV, K. & CHERKINSKY, A. 2018. Alteration of rocks by endolithic organisms is one of the pathways for the beginning of soils on Earth. *Scientific reports*, 8, 1-15. DOI: <https://doi.org/10.1038/s41598-018-21682-6>.
- MEUNIER, A., VELDE, B. & VELDE, B. 2004. Illite: Origins, evolution and metamorphism. *Springer Science & Business Media*. ISBN: 9783540204862, 3540204865.
- MEYER, K. M. & KUMP, L. R. 2008. Oceanic euxinia in Earth history: causes and consequences. *Annu. Rev. Earth Planet. Sci.*, 36, 251-288. DOI: [10.1146/annurev.earth.36.031207.124256](https://doi.org/10.1146/annurev.earth.36.031207.124256).
- MILLERO, F. J. 1996. Chemical oceanography. *CRC press*. ISBN: 9780849322808, 0849322804.
- MINSTER, J. F., RICARD, L. P. & ALLE`GRE, C. J. 1979. 87Rb-87Sr chronology of enstatite meteorites. *Earth and Planetary Science Letters*, 44, 420-440. DOI: [https://doi.org/10.1016/0012-821X\(79\)90081-5](https://doi.org/10.1016/0012-821X(79)90081-5).
- MITCHELL, R. N., KIRSCHER, U., KUNZMANN, M., LIU, Y. & COX, G. M. 2020. Gulf of Nuna: Astrochronologic correlation of a Mesoproterozoic oceanic euxinic event. *Geology*, 49, 25-29. DOI: <https://doi.org/10.1130/G47587.1>.
- MIYAZAKI, Y., PLANAVSKY, N. J., BOLTON, E. W. & REINHARD, C. T. 2018. Making Sense of Massive Carbon Isotope Excursions With an Inverse Carbon Cycle Model. *Journal of*

- Geophysical Research: Biogeosciences*, 123, 2485-2496. DOI: <https://doi.org/10.1029/2018JG004416>.
- MOHAMMAD, N., MOHAMAD ISHAK, W. W., MUSTAPA, S. I. & AYODELE, B. V. 2021. Natural Gas as a Key Alternative Energy Source in Sustainable Renewable Energy Transition: A Mini Review. *Frontiers in Energy Research*, 237. DOI: <https://doi.org/10.3389/fenrg.2021.625023>.
- MONIZ, E. J., JACOBY, H. D., MEGGS, A. J., ARMTRONG, R., COHN, D., CONNORS, S., DEUTCH, J., EJAZ, Q., HEZIR, J. & KAUFMAN, G. 2011. The future of natural gas. *Cambridge, MA: Massachusetts Institute of Technology*. From <https://energy.mit.edu/publication/future-natural-gas/>.
- MORSE, J. & LUTHER III, G. 1999. Chemical influences on trace metal-sulfide interactions in anoxic sediments. *Geochimica et Cosmochimica Acta*, 63, 3373-3378. DOI: [https://doi.org/10.1016/S0016-7037\(99\)00258-6](https://doi.org/10.1016/S0016-7037(99)00258-6).
- MOZLEY, P. S. & WERSIN, P. 1992. Isotopic composition of siderite as an indicator of depositional environment. *Geology*, 20, 817-820. DOI: [https://doi.org/10.1130/0091-7613\(1992\)020%3C0817:ICOSAA%3E2.3.CO;2](https://doi.org/10.1130/0091-7613(1992)020%3C0817:ICOSAA%3E2.3.CO;2).
- MUKHERJEE, I. & LARGE, R. R. 2016. Pyrite trace element chemistry of the Velkerri Formation, Roper Group, McArthur Basin: Evidence for atmospheric oxygenation during the Boring Billion. *Precambrian Research*, 281, 13-26. DOI: <https://doi.org/10.1016/j.precamres.2016.05.003>.
- MUKHERJEE, I. & LARGE, R. R. 2020. Co-evolution of trace elements and life in Precambrian oceans: The pyrite edition. *Geology*, 48, 1018-1022. DOI: <https://doi.org/10.1130/G47890.1>.
- MUKHERJEE, I., LARGE, R. R., BULL, S., GREGORY, D. G., STEPANOV, A. S., ÁVILA, J., IRELAND, T. R. & CORKREY, R. 2019. Pyrite trace-element and sulfur isotope geochemistry of paleo-mesoproterozoic McArthur Basin: Proxy for oxidative weathering. *American Mineralogist*, 104, 1256-1272. DOI: <https://doi.org/10.2138/am-2019-6873>.
- MUKHERJEE, I., LARGE, R. R., CORKREY, R. & DANYUSHEVSKY, L. V. 2018. The Boring Billion, a slingshot for Complex Life on Earth. *Scientific Reports*, 8, 4432. DOI: <https://doi.org/10.1038/s41598-018-22695-x>.
- MÜLLER, P. J. & SUESS, E. 1979. Productivity, sedimentation rate, and sedimentary organic matter in the oceans—I. Organic carbon preservation. *Deep Sea Research Part A. Oceanographic Research Papers*, 26, 1347-1362. DOI: [https://doi.org/10.1016/0198-0149\(79\)90003-7](https://doi.org/10.1016/0198-0149(79)90003-7).
- MUNSON, T. 2016. Sedimentary Characterisation of the Wilton Package, Greater MacArthur Basin, Northern Territory, *Northern Territory Geological Survey Record*, 2016-003. From <https://geoscience.nt.gov.au/gemis/ntgsjspui/handle/1/83806>.
- MUNSON, T. 2019. Detrital zircon geochronology investigations of the Glyde and Favenc packages: Implications for the geological framework of the greater McArthur Basin, Northern Territory, *Annual Geoscience Exploration Seminar (AGES) Proceedings*. From <https://geoscience.nt.gov.au/gemis/ntgsjspui/handle/1/88373>.
- MUNSON, T. J., DENYSZYN, S. W., SIMMONS, J. M. & KUNZMANN, M. 2020. A 1642 Ma age for the Fraynes Formation, Birrindudu Basin, confirms correlation with the economically significant Barney Creek Formation, McArthur Basin, Northern Territory. *Australian Journal of Earth Sciences*, 67, 321-330. DOI: <https://doi.org/10.1080/08120099.2020.1669708>.

- NAKANO, J. 2021. The Geopolitics of Critical Minerals Supply Chains, *Center for Strategic & International Studies*. From <https://www.jstor.org/stable/resrep30033.1>.
- NATH, B. N., ROELANDTS, I., SUDHAKAR, M., PLÜGER, W. & BALARAM, V. 1994. Cerium anomaly variations in ferromanganese nodules and crusts from the Indian Ocean. *Marine Geology*, 120, 385-400. DOI: [https://doi.org/10.1016/0025-3227\(94\)90069-8](https://doi.org/10.1016/0025-3227(94)90069-8).
- NEBEL, O. 2015. Rb–Sr Dating. *Encyclopedia of Scientific Dating Methods*. Dordrecht: Springer Netherlands. DOI: <https://doi.org/10.1007/978-94-007-6304-3>.
- NEBEL, O., SCHERER, E. E. & MEZGER, K. 2011. Evaluation of the  $^{87}\text{Rb}$  decay constant by age comparison against the U–Pb system. *Earth and Planetary Science Letters*, 301, 1-8. DOI: <https://doi.org/10.1016/j.epsl.2010.11.004>.
- NGUYEN, K., LOVE, G. D., ZUMBERGE, J. A., KELLY, A. E., OWENS, J. D., ROHRSEN, M. K., BATES, S. M., CAI, C. & LYONS, T. W. 2019. Absence of biomarker evidence for early eukaryotic life from the Mesoproterozoic Roper Group: Searching across a marine redox gradient in mid-Proterozoic habitability. *Geobiology*, 17, 247-260. DOI: <https://doi.org/10.1111/gbi.12329>.
- NIER, A. O. 1938. The isotopic constitution of strontium, barium, bismuth, thallium and mercury. *Physical Review*, 54, 275. DOI: <https://doi.org/10.1103/PhysRev.54.275>.
- NIXON, A. L., GLORIE, S., COLLINS, A. S., BLADES, M. L., SIMPSON, A. & WHELAN, J. A. 2021. Inter-cratonic geochronological and geochemical correlations of the Derim Derim–Galiwinku/Yanliao reconstructed Large Igneous Province across the North Australian and North China cratons. *Gondwana Research*, 103, 473-486. DOI: <https://doi.org/10.1016/j.gr.2021.10.027>.
- NIXON, A. L., GLORIE, S., HASTEROK, D., COLLINS, A. S., FERNIE, N. & FRASER, G. 2022. Low-temperature thermal history of the McArthur Basin: Influence of the Cambrian Kalkarindji Large Igneous Province on hydrocarbon maturation. *Basin Research*, 00, 1-24. DOI: <https://doi.org/10.1111/bre.12691>.
- NORDSVAN, A. R., COLLINS, W. J., LI, Z.-X., SPENCER, C. J., POURTEAU, A., WITHNALL, I. W., BETTS, P. G. & VOLANTE, S. 2018. Laurentian crust in northeast Australia: Implications for the assembly of the supercontinent Nuna. *Geology*, 46, 251-254. DOI: <https://doi.org/10.1130/G39980.1>.
- NORRIS, A. & DANYUSHEVSKY, L. 2018. Towards Estimating the Complete Uncertainty Budget of Quantified Results Measured by LA-ICP-MS. *Goldschmidt: Boston, MA, USA*. From <https://norsci.com/?p=ladr>.
- NTGS. 1989. Atree 1 and 2 EP 24 McArthur Basin, Northern Territory Well Completion Report, Pacific Oil and Gas. *Northern Territory Geological Survey Reports*, PR1989-0016. From <https://geoscience.nt.gov.au/gemis/ntgsjspui/handle/1/79405>.
- NTGS. 2009. Core Sample Analysis. Total Organic Carbon, Programmed Pyrolysis Data. Atree 2, Balmain 1, Elliott 1, Jamison 1. *Northern Territory Geological Survey Reports*, CSR0173. From <https://geoscience.nt.gov.au/gemis/ntgsjspui/handle/1/84880>.
- NTGS. 2010. EP24 Atree 2 Petrology and organic geochemistry. *Northern Territory Geological Survey Reports*, CSR0185. From <https://geoscience.nt.gov.au/gemis/ntgsjspui/handle/1/84887>.
- NTGS. 2012. Quantitative X-Ray Diffraction Analysis of 30 samples. *Northern Territory Geological Survey Reports*, CSR0181. From <https://geoscience.nt.gov.au/gemis/ntgsjspui/handle/1/84920>.

- NTGS. 2014. Basic Well Completion Report, NT EP167, Tarlee S3. *Northern Territory Geological Survey Reports*, PR2015- 0016. From <https://geoscience.nt.gov.au/gemis/ntgsjspui/handle/1/83524>.
- NTGS. 2015a. Basic Well Completion Report NT EP167 Birdum Creek 1. *Northern Territory Geological Survey Reports*, PR2016-W006. From <https://geoscience.nt.gov.au/gemis/ntgsjspui/handle/1/86120>.
- NTGS. 2015b. Final Well Completion Report, NT EP167, Manbulloo-S1. *Northern Territory Geological Survey Reports*, PR2015-0017. From <https://geoscience.nt.gov.au/gemis/ntgsjspui/handle/1/83412>.
- NTGS. 2016. Basic Well Completion Report NT - EP167 Wyworrie 1. *Northern Territory Geological Survey Reports*, PR2016-W025. From <https://geoscience.nt.gov.au/gemis/ntgsjspui/handle/1/91900>.
- OCH, L. M. & SHIELDS-ZHOU, G. A. 2012. The Neoproterozoic oxygenation event: environmental perturbations and biogeochemical cycling. *Earth-Science Reviews*, 110, 26-57. DOI: <https://doi.org/10.1016/j.earscirev.2011.09.004>.
- OEHLER, J. H. 1977. Microflora of the HYC pyritic shale member of the Barney Creek Formation (McArthur Group), middle Proterozoic of northern Australia. *Alcheringa*, 1, 315-349. DOI: <https://doi.org/10.1080/03115517708527768>.
- OHNO, T., KOMIYA, T., UENO, Y., HIRATA, T. & MARUYAMA, S. 2008. Determination of <sup>88</sup>Sr/<sup>86</sup>Sr mass-dependent isotopic fractionation and radiogenic isotope variation of <sup>87</sup>Sr/<sup>86</sup>Sr in the Neoproterozoic Doushantuo Formation. *Gondwana Research*, 14, 126-133. DOI: <https://doi.org/10.1016/j.gr.2007.10.007>.
- OHTA, A. & KAWABE, I. 2001. REE (III) adsorption onto Mn dioxide ( $\delta$ -MnO<sub>2</sub>) and Fe oxyhydroxide: Ce (III) oxidation by  $\delta$ -MnO<sub>2</sub>. *Geochimica et Cosmochimica Acta*, 65, 695-703. DOI: [https://doi.org/10.1016/S0016-7037\(00\)00578-0](https://doi.org/10.1016/S0016-7037(00)00578-0).
- OLA, P. S., AIDI, A. K. & BANKOLE, O. M. 2018. Clay mineral diagenesis and source rock assessment in the Bornu Basin, Nigeria: Implications for thermal maturity and source rock potential. *Marine and Petroleum Geology*, 89, 653-664. DOI: <https://doi.org/10.1016/j.marpetgeo.2017.10.031>.
- OLIEROOK, H. K., RANKENBURG, K., ULRICH, S., KIRKLAND, C. L., EVANS, N. J., BROWN, S., MCINNES, B. I., PRENT, A., GILLESPIE, J. & MCDONALD, B. 2020. Resolving multiple geological events using in situ Rb–Sr geochronology: implications for metallogenesis at Tropicana, Western Australia. *Geochronology*, 2, 283-303. DOI: <https://doi.org/10.5194/gchron-2-283-2020>.
- PAGE, R. W., JACKSON, M. J. & KRASSAY, A. A. 2000. Constraining sequence stratigraphy in north Australian basins: SHRIMP U–Pb zircon geochronology between Mt Isa and McArthur River. *Australian Journal of Earth Sciences*, 47, 431-459. DOI: <https://doi.org/10.1046/j.1440-0952.2000.00797.x>.
- PAGE, R. W. & SWEET, I. P. 1998. Geochronology of basin phases in the western Mt Isa Inlier, and correlation with the McArthur Basin. *Australian Journal of Earth Sciences*, 45, 219-232. DOI: <https://doi.org/10.1080/08120099808728383>.
- PAPANASTASSIOU, D. A. & WASSERBURG, G. J. 1970. RbSr ages from the ocean of storms. *Earth and Planetary Science Letters*, 8, 269-278.
- PARK, Y., SWANSON-HYSELL, N. L., MACLENNAN, S. A., MALOOF, A. C., GEBRESLASSIE, M., TREMBLAY, M. M., SCHOENE, B., ALENE, M., ANTTILA, E. S. C., TESEMA, T. & HAILEAB, B. 2019. The lead-up to the Sturtian Snowball Earth: Neoproterozoic



- chemostratigraphy time-calibrated by the Tambien Group of Ethiopia. *GSA Bulletin*, 132, 1119-1149. DOI: <https://doi.org/10.1130/B35178.1>.
- PAYTAN, A., GRIFFITH ELIZABETH, M., EISENHAUER, A., HAIN MATHIS, P., WALLMANN, K. & RIDGWELL, A. 2021. A 35-million-year record of seawater stable Sr isotopes reveals a fluctuating global carbon cycle. *Science*, 371, 1346-1350. DOI: <https://doi.org/10.1126/science.aaz9266>.
- PEARCE, N. J., PERKINS, W. T., WESTGATE, J. A., GORTON, M. P., JACKSON, S. E., NEAL, C. R. & CHENERY, S. P. 1997. A compilation of new and published major and trace element data for NIST SRM 610 and NIST SRM 612 glass reference materials. *Geostandards newsletter*, 21, 115-144. DOI: <https://doi.org/10.1111/j.1751-908X.1997.tb00538.x>.
- PEDERSEN, T. & CALVERT, S. 1990. Anoxia vs. productivity: what controls the formation of organic-carbon-rich sediments and sedimentary rocks? *AAPG bulletin*, 74, 454-466. DOI: <https://doi.org/10.1306/OC9B232B-1710-11D7-8645000102C1865D>.
- PENG, J. 2022. What besides redox conditions? Impact of sea-level fluctuations on redox-sensitive trace-element enrichment patterns in marine sediments. *Science China Earth Sciences*, 65, 1985-2004. DOI: <https://doi.org/10.1007/s11430-021-9959-8>.
- PETERS, K. 1986. Guidelines for Evaluating Petroleum Source Rock Using Programmed Pyrolysis. *AAPG Bulletin*, 70. DOI: <https://doi.org/10.1306/94885688-1704-11D7-8645000102C1865D>.
- PETERS, K. E. & CASSA, M. R. 1994. Applied source rock geochemistry: Chapter 5: Part II. Essential elements. *AAPG Special Volumes*, A077, 93-120. From <https://archives.datapages.com/data/specpubs/methodo2/images/a077/a0770001/0050/00930.pdf>.
- PHAN, T. T., HAKALA, J. A., LOPANO, C. L. & SHARMA, S. 2019. Rare earth elements and radiogenic strontium isotopes in carbonate minerals reveal diagenetic influence in shales and limestones in the Appalachian Basin. *Chemical Geology*, 509, 194-212. DOI: <https://doi.org/10.1016/j.chemgeo.2019.01.018>.
- PIEDAD-SÁNCHEZ, N., IZART, A., MARTÍNEZ, L., SUÁREZ-RUIZ, I., ELIE, M. & MENETRIER, C. 2004. Paleothermicity in the Central Asturian Coal Basin, North Spain. *International Journal of Coal Geology*, 58, 205-229. DOI: <https://doi.org/10.1016/j.coal.2004.02.001>.
- PIETSCH, B. 1991. 1: 2500000 Geological Map Series and Explanatory notes SE 53-03. *Northern Territory Geological Survey Special Publications*, 3. From <https://geoscience.nt.gov.au/gemis/ntgjsjpui/handle/1/87272>.
- PIPER, D. & PERKINS, R. 2004. A modern vs. Permian black shale—the hydrography, primary productivity, and water-column chemistry of deposition. *Chemical geology*, 206, 177-197. DOI: <https://doi.org/10.1016/j.chemgeo.2003.12.006>.
- PIPER, D. Z. & CALVERT, S. E. 2009. A marine biogeochemical perspective on black shale deposition. *Earth-Science Reviews*, 95, 63-96. DOI: <https://doi.org/10.1016/j.earscirev.2009.03.001>.
- PISAREVSKY, S. A., ELMING, S.-Å., PESONEN, L. J. & LI, Z.-X. 2014. Mesoproterozoic paleogeography: Supercontinent and beyond. *Precambrian Research*, 244, 207-225. DOI: <https://doi.org/10.1016/j.precamres.2013.05.014>.
- PLANAVSKY, N. J., MCGOLDRICK, P., SCOTT, C. T., LI, C., REINHARD, C. T., KELLY, A. E., CHU, X., BEKKER, A., LOVE, G. D. & LYONS, T. W. 2011. Widespread iron-rich conditions in the mid-Proterozoic ocean. *Nature*, 477, 448-451. DOI: <https://doi.org/10.1038/nature10327>.

- PLANAUSKY, N. J., REINHARD, C. T., WANG, X., THOMSON, D., MCGOLDRICK, P., RAINBIRD, R. H., JOHNSON, T., FISCHER, W. W. & LYONS, T. W. 2014. Low Mid-Proterozoic atmospheric oxygen levels and the delayed rise of animals. *Science*, 346, 635. DOI: <https://www.science.org/doi/10.1126/science.1258410>.
- PLANAUSKY, N. J., TARHAN, L., BELLEFROID, E., EVANS, D., REINHARD, C., LOVE, G. & LYONS, T. 2015a. Late Proterozoic transitions in climate, oxygen, and tectonics, and the rise of complex life. *Earth-Life Transitions: Paleobiology in the Context of Earth System Evolution*, 21. DOI: doi:10.1017/S108933260000303X.
- PLANAUSKY, N. J., TARHAN, L. G., BELLEFROID, E. J., EVANS, D. A. D., REINHARD, C. T., LOVE, G. D. & LYONS, T. W. 2015b. Late Proterozoic Transitions in Climate, Oxygen, and Tectonics, and the Rise of Complex Life. *The Paleontological Society Papers*, 21, 47-82. DOI: doi:10.1017/S1089332600002965.
- PLUMB, K. & WELLMAN, P. 1987. McArthur Basin, Northern Territory: mapping of deep troughs using gravity and magnetic anomalies. *BMR Journal of Australian Geology & Geophysics*, 10, 243-251. From [https://d28rz98at9flks.cloudfront.net/81221/Jou1987\\_v10\\_n3\\_p243.pdf](https://d28rz98at9flks.cloudfront.net/81221/Jou1987_v10_n3_p243.pdf).
- POITRASSON, F., PIN, C. & DUTHOU, J. L. 1995. Hydrothermal remobilization of rare earth elements and its effect on Nd isotopes in rhyolite and granite. *Earth and Planetary Science Letters*, 130, 1-11. DOI: [https://doi.org/10.1016/0012-821X\(94\)00257-Y](https://doi.org/10.1016/0012-821X(94)00257-Y).
- POLLASTRO, R. M. 1993. Considerations and applications of the illite/smectite geothermometer in hydrocarbon-bearing rocks of Miocene to Mississippian age. *Clays and Clay minerals*, 41, 119-119. DOI: <https://doi.org/10.1346/CCMN.1993.0410202>.
- PORTER, T. 2017. McArthur River Zn-Pb-Ag deposit: Australasian Institute of Mining and Metallurgy. *Monograph*, 32, 479-482. From <https://www.ausimm.com/publications/monograph/monograph-32---australian-ore-deposits>.
- POULTON, S. W. & CANFIELD, D. E. 2011. Ferruginous Conditions: A Dominant Feature of the Ocean through Earth's History. *Elements*, 7, 107-112. DOI: <https://doi.org/10.2113/gselements.7.2.107>.
- POULTON, S. W., FRALICK, P. W. & CANFIELD, D. E. 2010. Spatial variability in oceanic redox structure 1.8 billion years ago. *Nature Geoscience*, 3, 486-490. DOI: <https://doi.org/10.1038/ngeo889>.
- POURTEAU, A., SMIT, M. A., LI, Z. X., COLLINS, W. J., NORDSVAN, A. R., VOLANTE, S. & LI, J. 2018. 1.6 Ga crustal thickening along the final Nuna suture. *Geology*, 46, 959-962. DOI: <https://doi.org/10.1130/G45198.1>.
- PROKOPH, A., ERNST, R. E. & BUCHAN, K. L. 2004. Time-series analysis of large igneous provinces: 3500 Ma to present. *The Journal of Geology*, 112, 1-22. DOI: <https://www.journals.uchicago.edu/doi/abs/10.1086/379689>.
- RADKE, M., WILLSCH, H., LEYTHAEUSER, D. & TEICHMÜLLER, M. 1982. Aromatic components of coal: relation of distribution pattern to rank. *Geochimica et Cosmochimica Acta*, 46, 1831-1848. DOI: [https://doi.org/10.1016/0016-7037\(82\)90122-3](https://doi.org/10.1016/0016-7037(82)90122-3).
- RAFIEI, M. & KENNEDY, M. 2019. Weathering in a world without terrestrial life recorded in the Mesoproterozoic Velkerri Formation. *Nature Communications*, 10, 3448. DOI: <https://doi.org/10.1038/s41467-019-11421-4>.
- RAFIEI, M., LÖHR, S., BALDERMANN, A., WEBSTER, R. & KONG, C. 2020. Quantitative petrographic differentiation of detrital vs diagenetic clay minerals in marine

- sedimentary sequences: Implications for the rise of biotic soils. *Precambrian Research*, 350, 105948. DOI: <https://doi.org/10.1016/j.precamres.2020.105948>.
- RAINBIRD, R., ROONEY, A., CREASER, R. & SKULSKI, T. 2020. Shale and pyrite Re-Os ages from the Hornby Bay and Amundsen basins provide new chronological markers for Mesoproterozoic stratigraphic successions of northern Canada. *Earth and Planetary Science Letters*, 548. DOI: <https://doi.org/10.1016/j.epsl.2020.116492>.
- RASMUSSEN, B., FLETCHER, I. R., BENGTSON, S. & MCNAUGHTON, N. J. 2004. SHRIMP U–Pb dating of diagenetic xenotime in the Stirling Range Formation, Western Australia: 1.8 billion year minimum age for the Stirling biota. *Precambrian Research*, 133, 329-337. DOI: <https://doi.org/10.1016/j.precamres.2004.05.008>.
- RAVIZZA, G. & TUREKIAN, K. K. 1989. Application of the 187Re-187Os system to black shale geochronometry. *Geochimica et Cosmochimica Acta*, 53, 3257-3262. DOI: [https://doi.org/10.1016/0016-7037\(89\)90105-1](https://doi.org/10.1016/0016-7037(89)90105-1).
- RAWLINGS, D. 2002. Sedimentology, volcanology and geodynamics of the Redbank package, McArthur basin, northern Australia. *Phd Thesis from University of Tasmania*. From <https://eprints.utas.edu.au/11603>.
- RAWLINGS, D. J. 1999. Stratigraphic resolution of a multiphase intracratonic basin system: the McArthur Basin, northern Australia. *Australian Journal of Earth Sciences*, 46, 703-723. DOI: <https://doi.org/10.1046/j.1440-0952.1999.00739.x>.
- RAY, J. S., VEIZER, J. & DAVIS, W. J. 2003. C, O, Sr and Pb isotope systematics of carbonate sequences of the Vindhyan Supergroup, India: age, diagenesis, correlations and implications for global events. *Precambrian Research*, 121, 103-140. DOI: [https://doi.org/10.1016/S0301-9268\(02\)00223-1](https://doi.org/10.1016/S0301-9268(02)00223-1).
- REDAA, A., FARKAŠ, J., GILBERT, S., COLLINS, A. S., WADE, B., LÖHR, S., ZACK, T. & GARBE-SCHÖNBERG, D. 2021a. Assessment of elemental fractionation and matrix effects during in situ Rb–Sr dating of phlogopite by LA-ICP-MS/MS: implications for the accuracy and precision of mineral ages. *Journal of Analytical Atomic Spectrometry*, 36, 322-344. DOI: <https://doi.org/10.1039/DOJA00299B>.
- REDAA, A., FARKAŠ, J., HASSAN, A., COLLINS, A. S., GILBERT, S. & LÖHR, S. C. 2021b. Constraints from in-situ Rb-Sr dating on the timing of tectono-thermal events in the Umm Farwah shear zone and associated Cu-Au mineralisation in the Southern Arabian Shield, Saudi Arabia. *Journal of Asian Earth Sciences*, 105037. DOI: <https://doi.org/10.1016/j.jseaes.2021.105037>
- REINHARD, C. T., PLANAVSKY, N. J., ROBBINS, L. J., PARTIN, C. A., GILL, B. C., LALONDE, S. V., BEKKER, A., KONHAUSER, K. O. & LYONS, T. W. 2013. Proterozoic ocean redox and biogeochemical stasis. *Proc Natl Acad Sci U S A*, 110, 5357-62. DOI: <https://doi.org/10.1073/pnas.1208622110>
- REVIE, D. 2014. XRD analysis greater McArthur Basin. *Northern Territory Geological Survey Reports*, CSR0367. From <https://geoscience.nt.gov.au/gemis/ntgsjspui/handle/1/85053>.
- REVIE, D. 2016. Interpretive summary of integrated petroleum geochemistry of selected wells in the greater McArthur Basin, NT, Australia. *Northern Territory Geological Survey Reports*, CSR0413. From <https://geoscience.nt.gov.au/gemis/ntgsjspui/handle/1/85085>.
- REVIE, D. 2017. Unconventional petroleum resources of the Roper Group, McArthur Basin, *Northern Territory Geological Survey Reports*, 2017-002. From <https://geoscience.nt.gov.au/gemis/ntgsjspui/handle/1/85134>.

- REVIE, D. & MACDONALD, G. Volumetric resource assessment of the lower Kyalla and middle Velkerri formations of the McArthur Basin. *Annual Geoscience Exploration Seminar (AGES) Proceedings*, 29. From <https://geoscience.nt.gov.au/gemis/ntgsjspui/handle/1/85149>.
- REVIE, D. & NORMINGTON, V. 2016. Shale resource data from the greater McArthur Basin. *Northern Territory Geological Survey Digital Information Package* DIP014. From <https://geoscience.nt.gov.au/gemis/ntgsjspui/handle/1/82595>.
- REVIE, D., NORMINGTON, V. & JARRETT, A. 2022. Shale resource data from the greater McArthur Basin. *Northern Territory Geological Survey Digital Information Package*. From <https://geoscience.nt.gov.au/gemis/ntgsjspui/handle/1/82595>.
- RIBEIRO, B. V., FINCH, M. A., CAWOOD, P. A., FALEIROS, F. M., MURPHY, T. D., SIMPSON, A., GLORIE, S., TEDESCHI, M., ARMIT, R. & BARROTE, V. R. 2021. From microanalysis to supercontinents: Insights from the Rio Apa Terrane into the Mesoproterozoic SW Amazonian Craton evolution during Rodinia assembly. *Journal of Metamorphic Geology*, 40(4), 631-663. DOI: <https://doi.org/10.1111/jmg.12641>.
- RIDGWELL, A. J., KENNEDY, M. J. & CALDEIRA, K. 2003. Carbonate deposition, climate stability, and Neoproterozoic ice ages. *Science*, 302, 859-862. DOI: <https://doi.org/10.1126/science.1088342>.
- RIEDIGER, C. L. 1993. Solid bitumen reflectance and Rock-Eval Tmax as maturation indices: an example from the "Nordegg Member", Western Canada Sedimentary Basin. *International Journal of Coal Geology*, 22, 295-315. DOI: [https://doi.org/10.1016/0166-5162\(93\)90031-5](https://doi.org/10.1016/0166-5162(93)90031-5).
- RIMMER, S. M., THOMPSON, J. A., GOODNIGHT, S. A. & ROBL, T. L. 2004. Multiple controls on the preservation of organic matter in Devonian–Mississippian marine black shales: geochemical and petrographic evidence. *Palaeogeography, Palaeoclimatology, Palaeoecology*, 215, 125-154. DOI: <https://doi.org/10.1016/j.palaeo.2004.09.001>.
- ROGERS, J. 1996. Geology and tectonic setting of the Tawallah Group, southern McArthur basin, Northern Territory. *PhD Thesis from University of Tasmania*. DOI: [https://eprints.utas.edu.au/11608/1/front-Rogers\\_PhD\\_thesis\\_1996.pdf](https://eprints.utas.edu.au/11608/1/front-Rogers_PhD_thesis_1996.pdf).
- ROONEY, A. D., MACDONALD, F. A., STRAUSS, J. V., DUDÁS, F. Ö., HALLMANN, C. & SELBY, D. 2014. Re-Os geochronology and coupled Os-Sr isotope constraints on the Sturtian snowball Earth. *Proceedings of the National Academy of Sciences*, 111, 51-56. DOI: <https://doi.org/10.1073/pnas.1317266110>.
- RÖSEL, D. & ZACK, T. 2022. LA-ICP-MS/MS Single-Spot Rb-Sr Dating. *Geostandards and Geoanalytical Research*, 46, 143-168. DOI: <https://doi.org/10.1111/ggr.12414>.
- ROTHMAN, D. H., HAYES, J. M. & SUMMONS, R. E. 2003. Dynamics of the Neoproterozoic carbon cycle. *Proceedings of the National Academy of Sciences of the United States of America*, 100, 8124-8129. DOI: <https://doi.org/10.1073/pnas.0832439100>.
- ROUSSET, D., LECLERC, S., CLAUER, N., LANCELOT, J. L., CATHELIN, M. & ARANYOSSY, J. F. O. 2004. Age and Origin of Albian Glauconites and Associated Clay Minerals Inferred from a Detailed Geochemical Analysis. *Journal of Sedimentary Research*, 74, 631-642. DOI: <https://doi.org/10.1306/031104740631>.
- SALTZMAN, M. R. & THOMAS, E. 2012. Chapter 11 - Carbon Isotope Stratigraphy. In: GRADSTEIN, F. M., OGG, J. G., SCHMITZ, M. D. & OGG, G. M. (eds.) *The Geologic Time Scale*. Boston: Elsevier. ISBN: 9780444594488, 0444594485.

- SANCHEZ-VIDAL, A., COLLIER, R. W., CALAFAT, A., FABRES, J. & CANALS, M. 2005. Particulate barium fluxes on the continental margin: a study from the Alboran Sea (Western Mediterranean). *Marine chemistry*, 93, 105-117. DOI: <https://doi.org/10.1016/j.marchem.2004.07.004>.
- SANDER, R., PAN, Z., CONNELL, L. D., CAMILLERI, M., GRIGORE, M. & YANG, Y. 2018. Controls on methane sorption capacity of Mesoproterozoic gas shales from the Beetaloo Sub-basin, Australia and global shales. *International Journal of Coal Geology*, 199, 65-90. DOI: <https://doi.org/10.1016/j.coal.2018.09.018>.
- SARMIENTO, J., GRUBER, N. & MCELROY, M. 2007. Ocean Biogeochemical Dynamics. *Physics Today*, 60, 65. DOI: <https://doi.org/10.1515/9781400849079>.
- SCHEIBLHOFER, E., MOSER, U., LÖHR, S., WILMSEN, M., FARKAŠ, J., GALLHOFER, D., BÄCKSTRÖM, A. M., ZACK, T. & BALDERMANN, A. 2022. Revisiting Glauconite Geochronology: Lessons Learned from In Situ Radiometric Dating of a Glauconite-Rich Cretaceous Shelfal Sequence. *Minerals*, 12, 818. DOI: <https://doi.org/10.3390/min12070818>.
- SCHIDLOWSKI, M. 1988. A 3,800-million-year isotopic record of life from carbon in sedimentary rocks. *Nature*, 333, 313-318. DOI: <https://doi.org/10.1038/333313a0>.
- SCHIEBER, J., KRINSLEY, D. & RICIPUTI, L. 2000. Diagenetic origin of quartz silt in mudstones and implications for silica cycling. *Nature*, 406, 981-985. DOI: <https://doi.org/10.1038/35023143>.
- SCHIER, K., HIMMLER, T., LEPLAND, A., KRAEMER, D., SCHÖNENBERGER, J. & BAU, M. 2021. Insights into the REY inventory of seep carbonates from the Northern Norwegian margin using geochemical screening. *Chemical Geology*, 559, 119857. DOI: <https://doi.org/10.1016/j.chemgeo.2020.119857>.
- SCHMID, S. 2015. Sedimentological review of the Barney Creek Formation in drillholes LV09001, BJ2, McA5, McArthur Basin. *Northern Territory Geological Survey Reports*, 2015-006. From <https://geoscience.nt.gov.au/gemis/ntgsjspui/handle/1/82473>.
- SCHMITZ, M. D. & SCHOENE, B. 2007. Derivation of isotope ratios, errors, and error correlations for U-Pb geochronology using <sup>205</sup>Pb-<sup>235</sup>U-(<sup>233</sup>U)-spiked isotope dilution thermal ionization mass spectrometric data. *Geochemistry, Geophysics, Geosystems*, 8. DOI: <https://doi.org/10.1029/2006GC001492>.
- SCHOEPFER, S. D., SHEN, J., WEI, H., TYSON, R. V., INGALL, E. & ALGEO, T. J. 2015. Total organic carbon, organic phosphorus, and biogenic barium fluxes as proxies for paleomarine productivity. *Earth-Science Reviews*, 149, 23-52. DOI: <https://doi.org/10.1016/j.earscirev.2014.08.017>.
- SCOTT, C. & LYONS, T. W. 2012. Contrasting molybdenum cycling and isotopic properties in euxinic versus non-euxinic sediments and sedimentary rocks: Refining the paleoproxies. *Chemical Geology*, 324-325, 19-27. DOI: <https://doi.org/10.1016/j.chemgeo.2012.05.012>.
- SCOTT, C., LYONS, T. W., BEKKER, A., SHEN, Y., POULTON, S. W., CHU, X. & ANBAR, A. D. 2008. Tracing the stepwise oxygenation of the Proterozoic ocean. *Nature*, 452, 456-9. DOI: <https://doi.org/10.1038/nature06811>.
- SELBY, D. 2009. U-Pb zircon geochronology of the Aptian/Albian boundary implies that the GL-O international glauconite standard is anomalously young. *Cretaceous Research*, 30, 1263-1267. DOI: <https://doi.org/10.1016/j.cretres.2009.07.001>.
- SEMIKHATOV, M., KUZNETSOV, A., GOROKHOV, I., KONSTANTINOVA, G., MELNIKOV, N., PODKOVYROV, V. & KUTYAVIN, E. 2002. Low <sup>87</sup>Sr/<sup>86</sup>Sr ratios in seawater of the

- Grenville and post-Grenville time: determining factors. *Stratigraphy and Geological Correlation*, 10, 1-41. From [https://www.researchgate.net/publication/298586199\\_Low\\_Sr-87Sr-86\\_ratios\\_in\\_Seawater\\_of\\_the\\_Grenville\\_and\\_post-Grenville\\_time\\_Determining\\_factors](https://www.researchgate.net/publication/298586199_Low_Sr-87Sr-86_ratios_in_Seawater_of_the_Grenville_and_post-Grenville_time_Determining_factors).
- ŞENGÜN, F., BERTRANDSSON ERLANDSSON, V., HOGMALM, J. & ZACK, T. 2019. In situ Rb-Sr dating of K-bearing minerals from the orogenic Akçaabat gold deposit in the Menderes Massif, Western Anatolia, Turkey. *Journal of Asian Earth Sciences*, 185, 104048. DOI: <https://doi.org/10.1016/j.jseaes.2019.104048>.
- SHALEV, N., GAVRIELI, I., HALICZ, L., SANDLER, A., STEIN, M. & LAZAR, B. 2017. Enrichment of <sup>88</sup>Sr in continental waters due to calcium carbonate precipitation. *Earth and Planetary Science Letters*, 459, 381-393. DOI: <https://doi.org/10.1016/j.epsl.2016.11.042>.
- SHAO, Y., FARKAŠ, J., HOLMDEN, C., MOSLEY, L., KELL-DUIVESTEIN, I., IZZO, C., REIS-SANTOS, P., TYLER, J., TÖRBER, P., FRÝDA, J., TAYLOR, H., HAYNES, D., TIBBY, J. & GILLANDERS, B. M. 2018. Calcium and strontium isotope systematics in the lagoon-estuarine environments of South Australia: Implications for water source mixing, carbonate fluxes and fish migration. *Geochimica et Cosmochimica Acta*, 239, 90-108. DOI: <https://doi.org/10.1016/j.gca.2018.07.036>.
- SHAO, Y., FARKAŠ, J., MOSLEY, L., TYLER, J., WONG, H., CHAMBERLAYNE, B., RAVEN, M., SAMANTA, M., HOLMDEN, C., GILLANDERS, B. M., KOLEVICA, A. & EISENHAUER, A. 2021. Impact of salinity and carbonate saturation on stable Sr isotopes ( $\delta^{88}/^{86}\text{Sr}$ ) in a lagoon-estuarine system. *Geochimica et Cosmochimica Acta*, 293, 461-476. DOI: <https://doi.org/10.1016/j.gca.2020.11.014>.
- SHELDON, H. A., SCHAUBS, P. M., BLAIKIE, T. N., KUNZMANN, M., POULET, T. & SPINKS, S. C. 2021. 3D thermal convection in the Proterozoic McArthur River Zn-Pb-Ag mineral system, northern Australia. *Ore Geology Reviews*, 133, 104093. DOI: <https://doi.org/10.1016/j.oregeorev.2021.104093>.
- SHEN, Y., CANFIELD, D. E. & KNOLL, A. H. 2002. Middle Proterozoic ocean chemistry: Evidence from the McArthur Basin, northern Australia. *American Journal of Science*, 302, 81. DOI: <https://doi.org/10.2475/ajs.302.2.81>.
- SHEN, Y., KNOLL, A. & WALTER, M. 2003. Evidence for low sulphate and anoxia in a mid-Proterozoic marine basin. *Nature*, 423, 632-5. DOI: <https://doi.org/10.1038/nature01651>.
- SHEN, Y., SCHIDLOWSKI, M. & CHU, X. 2000. Biogeochemical approach to understanding phosphogenic events of the terminal Proterozoic to Cambrian. *Palaeogeography, Palaeoclimatology, Palaeoecology*, 158, 99-108. DOI: [https://doi.org/10.1016/S0031-0182\(00\)00033-X](https://doi.org/10.1016/S0031-0182(00)00033-X).
- SHEPHERD, T. J. & DARBYSHIRE, D. P. F. 1981. Fluid inclusion Rb–Sr isochrons for dating mineral deposits. *Nature*, 290, 578-579. DOI: <https://doi.org/10.1038/290578a0>.
- SHIELDS-ZHOU, G. & MILLS, B. 2017. Tectonic controls on the long-term carbon isotope mass balance. *Proceedings of the National Academy of Sciences of the United States of America*, 114. DOI: <https://doi.org/10.1073/pnas.1614506114>.
- SHIELDS, G. & VEIZER, J. 2002. Precambrian marine carbonate isotope database: Version 1.1. *Geochemistry, Geophysics, Geosystems*, 3, 1 of 12-12 of 12. DOI: <https://doi.org/10.1029/2001GC000266>.

- SIMMONS, E. C. 1998. Rubidium: Element and geochemistry. *Geochemistry*. Dordrecht: Springer Netherlands. DOI: [https://doi.org/10.1007/1-4020-4496-8\\_299](https://doi.org/10.1007/1-4020-4496-8_299).
- SIMPSON, A., GILBERT, S., TAMBLYN, R., HAND, M., SPANDLER, C., GILLESPIE, J., NIXON, A. & GLORIE, S. 2021. In-situ LuHf geochronology of garnet, apatite and xenotime by LA ICP MS/MS. *Chemical Geology*, 577, 120299. DOI: <https://doi.org/10.1016/j.chemgeo.2021.120299>.
- SIMPSON, A., GLORIE, S., HAND, M., SPANDLER, C., GILBERT, S. & CAVE, B. 2022. In situ Lu–Hf geochronology of calcite. *Geochronology*, 4, 353-372. DOI: <https://doi.org/10.5194/gchron-4-353-2022>.
- SINGER, A. 1980. The paleoclimatic interpretation of clay minerals in soils and weathering profiles. *Earth-Science Reviews*, 15, 303-326. DOI: [https://doi.org/10.1016/0012-8252\(80\)90113-0](https://doi.org/10.1016/0012-8252(80)90113-0).
- SMITH, B. R. 2015. HyLogger drillhole report for Urapunga 5, McArthur Basin, Northern Territory. *Northern Territory Geological Survey Reports*, HDP0042. From <https://geoscience.nt.gov.au/gemis/ntgsjspui/handle/1/81982>.
- SMITH, B. R. 2016. Stratigraphic analysis of the Mainoru Formation, Roper Group, McArthur Basin using HyLogger. *Northern Territory Geological Survey Technical Note*, 2016-001. From <https://geoscience.nt.gov.au/gemis/ntgsjspui/handle/1/84311>.
- SMITH, J. 2001. Summary of results - Joint NTGS - AGSO Age Determination Program 1999-2001. *Northern Territory Geological Survey Reports*, 2001-007. From <https://geoscience.nt.gov.au/gemis/ntgsjspui/handle/1/82409>.
- SMITH, J. W. & CROXFORD, N. J. W. 1975. An isotopic investigation of the environment of deposition of the McArthur mineralization. *Mineralium Deposita*, 10, 269-276. DOI: <https://doi.org/10.1007/BF00207885>
- SOUTHGATE, P. 2000. Carpentaria-Mt Isa Zinc Belt: Basement framework, chronostratigraphy and geodynamic evolution of Proterozoic successions. *Australian Journal of Earth Sciences*, 47, 337-340. DOI: <https://doi.org/10.1046/j.1440-0952.2000.00798.x>.
- SOUTHGATE, P. N., BRADSHAW, B. E., DOMAGALA, J., JACKSON, M. J., IDNURM, M., KRASSAY, A. A., PAGE, R. W., SAMI, T. T., SCOTT, D. L., LINDSAY, J. F., MCCONACHIE, B. A. & TARLOWSKI, C. 2000. Chronostratigraphic basin framework for Palaeoproterozoic rocks (1730–1575 Ma) in northern Australia and implications for base-metal mineralisation. *Australian Journal of Earth Sciences*, 47, 461-483. DOI: <https://doi.org/10.1046/j.1440-0952.2000.00787.x>.
- SPENCE, J. S., SANISLAV, I. V. & DIRKS, P. H. G. M. 2021. 1750–1710 Ma deformation along the eastern margin of the North Australia Craton. *Precambrian Research*, 353, 106019. DOI: <https://doi.org/10.1016/j.precamres.2020.106019>.
- SPERLING, E. A., BOAG, T. H., DUNCAN, M. I., ENDRIGA, C. R., MARQUEZ, J. A., MILLS, D. B., MONARREZ, P. M., SCLAFANI, J. A., STOCKEY, R. G. & PAYNE, J. L. 2022. Breathless through Time: Oxygen and Animals across Earth’s History. *The Biological Bulletin*, 243, 000-000. DOI: 10.1086/721754.
- SPERLING, E. A., ROONEY, A. D., HAYS, L., SERGEEV, V. N., VOROB'EVA, N. G., SERGEEVA, N. D., SELBY, D., JOHNSTON, D. T. & KNOLL, A. H. 2014. Redox heterogeneity of subsurface waters in the Mesoproterozoic ocean. *Geobiology*, 12, 373-386. DOI: <https://doi.org/10.1111/gbi.12091>.
- SPINKS, S. C., PEARCE, M. A., LIU, W., KUNZMANN, M., RYAN, C. G., MOORHEAD, G. F., KIRKHAM, R., BLAIKIE, T., SHELDON, H. A., SCHAUBS, P. M. & RICKARD, W. D. A. 2020.

- Carbonate Replacement as the Principal Ore Formation Process in the Proterozoic McArthur River (HYC) Sediment-Hosted Zn-Pb Deposit, Australia. *Economic Geology*. DOI: <https://doi.org/10.5382/econgeo.4793>.
- SPINKS, S. C., SCHMID, S. & PAGÈS, A. 2016a. Delayed euxinia in Paleoproterozoic intracontinental seas: Vital havens for the evolution of eukaryotes? *Precambrian Research*, 287, 108-114. DOI: <https://doi.org/10.1016/j.precamres.2016.11.002>.
- SPINKS, S. C., SCHMID, S., PAGÈS, A. & BLUETT, J. 2016b. Evidence for SEDEX-style mineralization in the 1.7 Ga Tawallah Group, McArthur Basin, Australia. *Ore Geology Reviews*, 76, 122-139. DOI: <https://doi.org/10.1016/j.oregeorev.2016.01.007>.
- SPINKS, S. C., SPERLING, E. A., THORNE, R. L., LAFOUNTAIN, F., WHITE, A. J., ARMSTRONG, J., WOLTERING, M. & TYLER, I. M. 2022. Mesoproterozoic surface oxygenation accompanied major sedimentary manganese deposition at 1.4 and 1.1 Ga. *Geobiology*. DOI: <https://doi.org/10.1111/gbi.12524>.
- SPÖTL, C. & VENNEMANN, T. W. 2003. Continuous-flow isotope ratio mass spectrometric analysis of carbonate minerals. *Rapid Communications in Mass Spectrometry*, 17, 1004-1006. DOI: <https://doi.org/10.1002/rcm.1010>.
- STÜEKEN, E. E., GREGORY, D. D., MUKHERJEE, I. & MCGOLDRICK, P. 2021. Sedimentary exhalative venting of bioavailable nitrogen into the early ocean. *Earth and Planetary Science Letters*, 565, 116963. DOI: <https://doi.org/10.1016/j.epsl.2021.116963>.
- STÜEKEN, E. E., KIPP, M. A., KOEHLER, M. C. & BUICK, R. 2016. The evolution of Earth's biogeochemical nitrogen cycle. *Earth-Science Reviews*, 160, 220-239. DOI: <https://doi.org/10.1016/j.earscirev.2016.07.007>.
- SUBARCAH, D. 2022a. *Geochemistry and geochronology of the Palaeoproterozoic Redbank Package, greater McArthur basin, northern Australia* [Online]. The University of Adelaide. Available: [https://adelaide.figshare.com/articles/online\\_resource/Geochemistry\\_and\\_geochronology\\_of\\_the\\_Palaeoproterozoic\\_Redbank\\_Package\\_greater\\_McArthur\\_basin\\_northern\\_Australia/21424941](https://adelaide.figshare.com/articles/online_resource/Geochemistry_and_geochronology_of_the_Palaeoproterozoic_Redbank_Package_greater_McArthur_basin_northern_Australia/21424941) [Accessed].
- SUBARCAH, D. 2022b. *Geochronology and geochemistry of the Glyde Package, greater McArthur Basin, northern Australia* [Online]. The University of Adelaide. Available: [https://adelaide.figshare.com/articles/online\\_resource/Geochronology\\_and\\_geochemistry\\_of\\_the\\_Glyde\\_Package\\_greater\\_McArthur\\_Basin\\_northern\\_Australia/21424875](https://adelaide.figshare.com/articles/online_resource/Geochronology_and_geochemistry_of_the_Glyde_Package_greater_McArthur_Basin_northern_Australia/21424875) [Accessed].
- SUBARCAH, D., BLADES, M. L., COLLINS, A. S., FARKAŠ, J., GILBERT, S., LÖHR, S. C., REDAA, A., CASSIDY, E. & ZACK, T. 2021. Unravelling the histories of Proterozoic shales through in situ Rb-Sr dating and trace element laser ablation analysis. *Geology*, 1, 66-70. DOI: <https://doi.org/10.1130/G49187.1>.
- SUBARCAH, D., NIXON, A. L., JIMENEZ, M., COLLINS, A. S., BLADES, M. L., FARKAŠ, J., GILBERT, S. E., HOLFORD, S. & JARRETT, A. 2022. Constraining the geothermal parameters of in situ Rb-Sr dating on Proterozoic shales and their subsequent applications. *Geochronology*, 4, 577-600. DOI: <https://doi.org/10.5194/gchron-4-577-2022>.
- SUMMONS, R. E., POWELL, T. G. & BOREHAM, C. J. 1988. Petroleum geology and geochemistry of the Middle Proterozoic McArthur Basin, Northern Australia: III. Composition of extractable hydrocarbons. *Geochimica et Cosmochimica Acta*, 52, 1747-1763. DOI: [https://doi.org/10.1016/0016-7037\(88\)90001-4](https://doi.org/10.1016/0016-7037(88)90001-4).



- SUMMONS, R. E., TAYLOR, D. & BOREHAM, C. J. 1994. Geochemical Tools For Evaluating Petroleum Generation In Middle Proterozoic Sediments Of The Mcarthur Basin, Northern Territory, Australia. *The APPEA Journal*, 34, 692-706. DOI: <https://doi.org/10.1071/AJ93051>.
- SWEET, I. P., MENDUM, J. R., BULTITUDE, R. J. & MORGAN, C. M. 1974. The geology of the southern Victoria River region, Northern Territory. *Bureau Of Mineral Resources*, 167. Persistent Identifier: <http://pid.geoscience.gov.au/dataset/ga/15079>.
- TAMBLYN, R., HAND, M., MORRISSEY, L., ZACK, T., PHILLIPS, G. & OCH, D. 2020. Resubduction of lawsonite eclogite within a serpentinite-filled subduction channel. *Contributions to Mineralogy and Petrology*, 175, 74. DOI: <https://doi.org/10.1007/s00410-020-01712-1>.
- TAMBLYN, R., HAND, M., SIMPSON, A., GILBERT, S., WADE, B. & GLORIE, S. 2021. In situ laser ablation Lu–Hf geochronology of garnet across the Western Gneiss Region: campaign-style dating of metamorphism. *Journal of the Geological Society*, 179, 4. DOI: <https://doi.org/10.1144/jgs2021-094>.
- TARDY, Y. 1975. Element partition ratios in some sedimentary environments. II. Studies on North-American black shales. *Sciences Géologiques, bulletins et mémoires*, 28, 75-95. From [https://www.persee.fr/doc/sgeol\\_0302-2692\\_1975\\_num\\_28\\_1\\_1468](https://www.persee.fr/doc/sgeol_0302-2692_1975_num_28_1_1468).
- TAYLOR, D., KONTOROVICH, A. E., LARICHEV, A. I. & GLIKSON, M. 1994. Petroleum Source Rocks In The Roper Group Of The Mcarthur Basin: Source Characterisation And Maturity Determinations Using Physical And Chemical Methods. *The APPEA Journal*, 34, 279-296. DOI: <https://doi.org/10.1071/AJ93026>.
- TILLBERG, M., DRAKE, H., ZACK, T., HOGMALM, J. & ÅSTRÖM, M. 2017. In Situ Rb-Sr Dating of Fine-grained Vein Mineralizations Using LA-ICP-MS. *Procedia Earth and Planetary Science*, 17, 464-467. DOI: <https://doi.org/10.1016/j.proeps.2016.12.117>.
- TILLBERG, M., DRAKE, H., ZACK, T., KOOIJMAN, E., WHITEHOUSE, M. J. & ÅSTRÖM, M. E. 2020. In situ Rb-Sr dating of slickenfibres in deep crystalline basement faults. *Scientific Reports*, 10, 562. DOI: <https://doi.org/10.1038/s41598-019-57262-5>.
- TISSOT, B., DURAND, B., ESPITALIE, J. & COMBAZ, A. 1974. Influence of nature and diagenesis of organic matter in formation of petroleum. *AAPG Bulletin*, 58, 499-506. DOI: <https://doi.org/10.1306/83D91425-16C7-11D7-8645000102C1865D>.
- TISSOT, B., PELET, R. & UNGERER, P. 1987. Thermal history of sedimentary basins, maturation indices, and kinetics of oil and gas generation. *AAPG Bulletin*, 71, 1445-1466. DOI: <https://doi.org/10.1306/703C80E7-1707-11D7-8645000102C1865D>.
- TORGERSEN, E., VIOLA, G., ZWINGMANN, H. & HARRIS, C. 2015. Structural and temporal evolution of a reactivated brittle–ductile fault – Part II: Timing of fault initiation and reactivation by K–Ar dating of synkinematic illite/muscovite. *Earth and Planetary Science Letters*, 410, 212-224. DOI: <https://doi.org/10.1016/j.epsl.2014.09.051>.
- TORRES, M., BRUMSACK, H., BOHRMANN, G. & EMEIS, K. 1996. Barite fronts in continental margin sediments: a new look at barium remobilization in the zone of sulfate reduction and formation of heavy barites in diagenetic fronts. *Chemical Geology*, 127, 125-139. DOI: [https://doi.org/10.1016/0009-2541\(95\)00090-9](https://doi.org/10.1016/0009-2541(95)00090-9).
- TOSTEVIN, R., SHIELDS, G. A., TARBUCK, G. M., HE, T., CLARKSON, M. O. & WOOD, R. A. 2016. Effective use of cerium anomalies as a redox proxy in carbonate-dominated marine settings. *Chemical Geology*, 438, 146-162. DOI: <https://doi.org/10.1016/j.chemgeo.2016.06.027>.

- TRAPPE, J. 2006. Phanerozoic phosphorite depositional systems: a dynamic model for a sedimentary resource system, *Lecture Notes in Earth Sciences*, 1, Springer. DOI: <https://doi.org/10.1007/BFb0009670>.
- TRIBOVILLARD, N., ALGEO, T. J., LYONS, T. & RIBOULLEAU, A. 2006. Trace metals as paleoredox and paleoproductivity proxies: An update. *Chemical Geology*, 232, 12-32. DOI: <https://doi.org/10.1016/j.chemgeo.2006.02.012>.
- TRIBOVILLARD, N., RIBOULLEAU, A., LYONS, T. & BAUDIN, F. 2004. Enhanced trapping of molybdenum by sulfurized marine organic matter of marine origin in Mesozoic limestones and shales. *Chemical Geology*, 213, 385-401. DOI: <https://doi.org/10.1016/j.chemgeo.2004.08.011>.
- TROTMAN, P. 2021. 2021 Offshore petroleum exploration acreage release. *The APPEA Journal*, 61, 291-293. From <https://www.publish.csiro.au/AJ/pdf/AJ20191>.
- TSAFOS, N. 2022. Safeguarding the Global Market for Critical Minerals. *Testimony to the Standing Committee on Industry and Technology of the Canadian Parliament*, 44-1. From <https://www.jstor.org/stable/pdf/resrep39857.pdf>.
- TYSON, R. 2005. The "productivity versus preservation" controversy: cause, flaws, and resolution. *Special Publication-SEPM*, 82, 17. From [https://archives.datapages.com/data/sepm\\_sp/SP82/The\\_productivity\\_Versus\\_Preservation\\_Controversy.pdf](https://archives.datapages.com/data/sepm_sp/SP82/The_productivity_Versus_Preservation_Controversy.pdf).
- TYSON, R. V. & PEARSON, T. H. 1991. Modern and ancient continental shelf anoxia: an overview. *Geological Society, London, Special Publications*, 58, 1-24. DOI: <https://doi.org/10.1144/GSL.SP.1991.058.01.01>.
- VAKULCHUK, R., OVERLAND, I. & SCHOLTEN, D. 2020. Renewable energy and geopolitics: A review. *Renewable and Sustainable Energy Reviews*, 122, 109547. DOI: <https://doi.org/10.1016/j.rser.2019.109547>.
- VAN SMEERDIJK HOOD, A. & WALLACE, M. W. 2015. Extreme ocean anoxia during the Late Cryogenian recorded in reefal carbonates of Southern Australia. *Precambrian Research*, 261, 96-111. DOI: <https://doi.org/10.1016/j.precamres.2015.02.008>.
- VARAJAO, A. & MEUNIER, A. 1995. Particle morphological evolution during the conversion of I/S to illite in Lower Cretaceous shales from Sergipe-Alagoas Basin, Brazil. *Clays and Clay minerals*, 43, 14-28. DOI: <https://doi.org/10.1346/CCMN.1995.0430103>.
- VEIZER, J., ALA, D., AZMY, K., BRUCKSCHEN, P., BUHL, D., BRUHN, F., CARDEN, G. A., DIENER, A., EBNETH, S. & GODDERIS, Y. 1999.  $^{87}\text{Sr}/^{86}\text{Sr}$ ,  $\delta^{13}\text{C}$  and  $\delta^{18}\text{O}$  evolution of Phanerozoic seawater. *Chemical geology*, 161, 59-88. DOI: [https://doi.org/10.1016/S0009-2541\(99\)00081-9](https://doi.org/10.1016/S0009-2541(99)00081-9).
- VEIZER, J., PLUMB, K. A., CLAYTON, R. N., HINTON, R. W. & GROTZINGER, J. P. 1992. Geochemistry of Precambrian carbonates: V. Late Paleoproterozoic seawater. *Geochimica et Cosmochimica Acta*, 56, 2487-2501. DOI: [https://doi.org/10.1016/0016-7037\(92\)90204-V](https://doi.org/10.1016/0016-7037(92)90204-V).
- VELDE, B. & ESPITALIÉ, J. 1989. Comparison of kerogen maturation and illite/smectite composition in diagenesis. *Journal of Petroleum Geology*, 12, 103-110. DOI: <https://doi.org/10.1111/j.1747-5457.1989.tb00223.x>.
- VELDE, B. & VASSEUR, G. 1992. Estimation of the diagenetic smectite to illite transformation in time-temperature space. *American Mineralogist*, 77, 967-976. From <https://pubs.geoscienceworld.org/msa/ammin/article/77/9-10/967/42710/Estimation-of-the-diagenetic-smectite-to-illite>.

- VERMEESCH, P. 2007. Quantitative geomorphology of the White Mountains (California) using detrital apatite fission track thermochronology. *Journal of Geophysical Research: Earth Surface*, 112. DOI: <https://doi.org/10.1029/2006JF000671>.
- VERMEESCH, P. 2012. On the visualisation of detrital age distributions. *Chemical Geology*, 312-313, 190-194. DOI: <https://doi.org/10.1016/j.chemgeo.2012.04.021>.
- VERMEESCH, P. 2013. Multi-sample comparison of detrital age distributions. *Chemical Geology*, 341, 140-146. DOI: <https://doi.org/10.1016/j.chemgeo.2013.01.010>.
- VERMEESCH, P. 2018. IsoplotR : A free and open toolbox for geochronology. *Geoscience Frontiers*, 9. DOI: <https://doi.org/10.1016/j.gsf.2018.04.001>.
- VILLA 1998. Isotopic closure. *Terra Nova*, 10, 42-47. DOI: <https://doi.org/10.1046/j.1365-3121.1998.00156.x>.
- VILLA, I. M., DE BIÈVRE, P., HOLDEN, N. & RENNE, P. 2015. IUPAC-IUGS recommendation on the half life of <sup>87</sup>Rb. *Geochimica et Cosmochimica Acta*, 164, 382-385. DOI: <https://doi.org/10.1016/j.gca.2015.05.025>.
- VINNICHENKO, G. & BROCKS, J. J. 2019. Results of a sampling study for LV09, MBXDD001, 14MCDDH001 and 14MCDDH002 drillcores. *Northern Territory Geological Survey Reports*, CSR0500. From <https://geoscience.nt.gov.au/gemis/ntgjsjpui/handle/1/91756>.
- VINNICHENKO, G., JARRETT, A. J., VAN MALDEGEM, L. M. & BROCKS, J. J. 2021. Substantial maturity influence on carbon and hydrogen isotopic composition of n-alkanes in sedimentary rocks. *Organic Geochemistry*, 152, 104171. DOI: <https://doi.org/10.1016/j.orggeochem.2020.104171>.
- VINNICHENKO, G., JARRETT, A. J. M., HOPE, J. M. & BROCKS, J. J. 2020. Discovery of the oldest known biomarkers provides evidence for phototrophic bacteria in the 1.73 Ga Wollogorang Formation, Australia. *Geobiology*, 18, 544-559. DOI: <https://doi.org/10.1111/gbi.12390>.
- VIRGO, G. M., COLLINS, A. S., AMOS, K. J., FARKAŠ, J., BLADES, M. L. & SUBARCAH, D. 2021. Descending into the “snowball”: High resolution sedimentological and geochemical analysis across the Tonian to Cryogenian boundary in South Australia. *Precambrian Research*, 367, 106449. DOI: <https://doi.org/10.1016/j.precamres.2021.106449>.
- VOLANTE, S., POURTEAU, A., COLLINS, W. J., BLEREAU, E., LI, Z. X., SMIT, M., EVANS, N. J., NORDSVAN, A. R., SPENCER, C. J. & MCDONALD, B. J. 2020. Multiple P–T–d–t paths reveal the evolution of the final Nuna assembly in northeast Australia. *Journal of Metamorphic Geology*, 38, 593-627. DOI: <https://doi.org/10.1111/jmg.12532>.
- VOLK, H., GEORGE, S. C., DUTKIEWICZ, A. & RIDLEY, J. 2005. Characterisation of fluid inclusion oil in a Mid-Proterozoic sandstone and dolerite (Roper Superbasin, Australia). *Chemical Geology*, 223, 109-135. DOI: <https://doi.org/10.1016/j.chemgeo.2004.12.024>.
- VOLLSTAEDT, H., EISENHAUER, A., WALLMANN, K., BÖHM, F., FIETZKE, J., LIEBETRAU, V., KRABBENHÖFT, A., FARKAŠ, J., TOMAŠOVÝCH, A., RADDATZ, J. & VEIZER, J. 2014. The Phanerozoic  $\delta^{88}/^{86}\text{Sr}$  record of seawater: New constraints on past changes in oceanic carbonate fluxes. *Geochimica et Cosmochimica Acta*, 128, 249-265. DOI: <https://doi.org/10.1016/j.gca.2013.10.006>.
- VON BREYMAN, M. T., EMEIS, K.-C. & SUESS, E. 1992. Water depth and diagenetic constraints on the use of barium as a palaeoproductivity indicator. *Geological Society, London, Special Publications*, 64, 273-284. DOI: <https://doi.org/10.1144/GSL.SP.1992.064.01.18>.

- VORLICEK, T. P. & HELZ, G. R. 2002. Catalysis by mineral surfaces: implications for Mo geochemistry in anoxic environments. *Geochimica et Cosmochimica Acta*, 66, 3679-3692. DOI: [https://doi.org/10.1016/S0016-7037\(01\)00837-7](https://doi.org/10.1016/S0016-7037(01)00837-7).
- WALICZEK, M., MACHOWSKI, G., POPRAWA, P., ŚWIERCZEWSKA, A. & WIĘCŁAW, D. 2021. A novel VRo, Tmax, and S indices conversion formulae on data from the fold-and-thrust belt of the Western Outer Carpathians (Poland). *International Journal of Coal Geology*, 234, 103672. DOI: <https://doi.org/10.1016/j.coal.2020.103672>.
- WALKER, R., MUIR, M., DIVER, W., WILLIAMS, N. & WILKINS, N. 1977. Evidence of major sulphate evaporite deposits in the Proterozoic McArthur Group, Northern Territory, Australia. *Nature*, 265, 526-529. DOI: <https://doi.org/10.1038/265526a0>.
- WALTERS, C. C. 2006. The Origin of Petroleum. *Practical Advances in Petroleum Processing*. Springer. DOI: [https://doi.org/10.1007/978-0-387-25789-1\\_2](https://doi.org/10.1007/978-0-387-25789-1_2).
- WANG, C., DENG, J., CARRANZA, E. J. M. & LAI, X. 2014. Nature, diversity and temporal-spatial distributions of sediment-hosted Pb—Zn deposits in China. *Ore Geology Reviews*, 56, 327-351. DOI: <https://doi.org/10.1016/j.oregeorev.2013.06.004>.
- WANG, C., LECHTE, M. A., REINHARD, C. T., ASael, D., COLE, D. B., HALVERSON, G. P., PORTER, S. M., GALILI, N., HALEVY, I., RAINBIRD, R. H., LYONS, T. W. & PLANAVSKY, N. J. 2022. Strong evidence for a weakly oxygenated ocean-atmosphere system during the Proterozoic. *Proceedings of the National Academy of Sciences*, 119, e2116101119. DOI: <https://doi.org/10.1073/pnas.2116101119>.
- WANG, C., LI, Z.-X., PENG, P., PISAREVSKY, S., LIU, Y., KIRSCHER, U. & NORDSVAN, A. 2019. Long-lived connection between the North China and North Australian cratons in supercontinent Nuna: paleomagnetic and geological constraints. *Science Bulletin*, 64, 873-876. DOI: <https://doi.org/10.1016/j.scib.2019.04.028>.
- WANG, X.-C., LI, Z.-X., LI, X.-H., LI, J., LIU, Y., LONG, W.-G., ZHOU, J.-B. & WANG, F. J. J. O. P. 2012. Temperature, pressure, and composition of the mantle source region of Late Cenozoic basalts in Hainan Island, SE Asia: a consequence of a young thermal mantle plume close to subduction zones?. *Journal of Petrology*, 53, 177-233. DOI: [10.1093/petrology/egr061](https://doi.org/10.1093/petrology/egr061).
- WANTY, R. B. & GOLDHABER, M. B. 1992. Thermodynamics and kinetics of reactions involving vanadium in natural systems: Accumulation of vanadium in sedimentary rocks. *Geochimica et Cosmochimica Acta*, 56, 1471-1483. DOI: [https://doi.org/10.1016/0016-7037\(92\)90217-7](https://doi.org/10.1016/0016-7037(92)90217-7).
- WAPLES, D. W. 1980. Time and temperature in petroleum formation: application of Lopatin's method to petroleum exploration. *AAPG bulletin*, 64, 916-926. DOI: <https://doi.org/10.1306/2F9193D2-16CE-11D7-8645000102C1865D>.
- WARR, L. & MÄHLMANN, R. F. 2015. Recommendations for Kübler index standardization. *Clay Minerals*, 50, 283-286. DOI: [10.1180/claymin.2015.050.3.02](https://doi.org/10.1180/claymin.2015.050.3.02)
- WARR, L. & RICE, A. 1994. Interlaboratory standardization and calibration of day mineral crystallinity and crystallite size data. *Journal of Metamorphic Geology*, 12, 141-152. DOI: <https://doi.org/10.1111/j.1525-1314.1994.tb00010.x>.
- WARREN, J. K., GEORGE, S. C., HAMILTON, P. J. & TINGATE, P. 1998. Proterozoic Source Rocks: Sedimentology and Organic Characteristics of the Velkerri Formation, Northern Territory, Australia. *AAPG Bulletin*, 82, 442-463. DOI: <https://doi.org/10.1306/1D9BC435-172D-11D7-8645000102C1865D>.

- WEI, G.-Y., LING, H.-F., SHIELDS, G. A., HOHL, S. V., YANG, T., LIN, Y.-B. & ZHANG, F. 2021. Revisiting stepwise ocean oxygenation with authigenic barium enrichments in marine mudrocks. *Geology*, 49, 1059-1063. DOI: <https://doi.org/10.1130/G48825.1>.
- WELTE, D. & TISSOT, P. 1984. Petroleum formation and occurrence. Springer. DOI: <https://doi.org/10.1007/978-3-642-87813-8>.
- WENZHI, Z., SUYUN, H., ZECHENG, W., ZHANG, S. & TONGSHAN, W. 2018. Petroleum geological conditions and exploration importance of Proterozoic to Cambrian in China. *Petroleum Exploration and Development*, 45, 1-14. DOI: [https://doi.org/10.1016/S1876-3804\(18\)30001-6](https://doi.org/10.1016/S1876-3804(18)30001-6).
- WILHELMS, A., TELNĪS, N., STEEN, A. & AUGUSTSON, J. 1998. A quantitative study of aromatic hydrocarbons in a natural maturity shale sequence—the 3-methylphenanthrene/retene ratio, a pragmatic maturity parameter. *Organic Geochemistry*, 29, 97-105. DOI: [https://doi.org/10.1016/S0146-6380\(98\)00112-0](https://doi.org/10.1016/S0146-6380(98)00112-0).
- WILLIAMS-JONES, A., MIGDISOV, A. & SAMSON, I. 2012. Hydrothermal Mobilisation of the Rare Earth Elements - a Tale of "Ceria" and "Yttria". *Elements*, 8, 355-360. DOI: <https://doi.org/10.2113/gselements.8.5.355>.
- WILLIFORD, K. H., GRICE, K., LOGAN, G. A., CHEN, J. & HUSTON, D. 2011. The molecular and isotopic effects of hydrothermal alteration of organic matter in the Paleoproterozoic McArthur River Pb/Zn/Ag ore deposit. *Earth and Planetary Science Letters*, 301, 382-392. DOI: <https://doi.org/10.1016/j.epsl.2010.11.029>.
- WILSON, M. J. 1999. The origin and formation of clay minerals in soils: past, present and future perspectives. *Clay minerals*, 34, 7-25. DOI: <https://doi.org/10.1180/000985599545957>.
- WILSON, S. A. 1997. United States Geological Survey Certificate of Analysis Basalt, Columbia River BCR-2. *U.S. Geological Survey Open-File Report*, 98-xxx. DOI: [https://emrlibrary.gov.yk.ca/ygs/open\\_files/2019/2019-1/Appendix%20C/C4\\_QAQC/BCR-2\\_StandardInformation\\_USGS.pdf](https://emrlibrary.gov.yk.ca/ygs/open_files/2019/2019-1/Appendix%20C/C4_QAQC/BCR-2_StandardInformation_USGS.pdf).
- WINEFIELD, P. 1999. Sedimentology and diagenesis of late palaeoproterozoic carbonates, Southern McArthur Basin, northern Australia. *PhD Thesis from University of Tasmania*. From [https://eprints.utas.edu.au/11692/2/Whole-Winefield\\_thesis\\_1999.pdf](https://eprints.utas.edu.au/11692/2/Whole-Winefield_thesis_1999.pdf).
- WINEFIELD, P. R. 2000. Development of late Paleoproterozoic aragonitic seafloor cements in the McArthur Group, northern Australia. *Special Publications of SEPM*, 67. ISBN: 1-56576-072-7.
- WOODHEAD, J. D. & HERGT, J. M. 2001. Strontium, Neodymium and Lead Isotope Analyses of NIST Glass Certified Reference Materials: SRM 610, 612, 614. *Geostandards Newsletter*, 25, 261-266. DOI: <https://doi.org/10.1111/j.1751-908X.2001.tb00601.x>.
- WRIGHT, J. 1995. *Seawater: its composition, properties, and behaviour*, Pergamon.
- XU, G., HANNAH, J. L., BINGEN, B., GEORGIEV, S. & STEIN, H. J. 2012. Digestion methods for trace element measurements in shales: Paleoredox proxies examined. *Chemical Geology*, 324-325, 132-147. DOI: <https://doi.org/10.1016/j.chemgeo.2012.01.029>.
- YANG, B., COLLINS, A., BLADES, M., CAPOGRECO, N., PAYNE, J., MUNSON, T., COX, G. & GLORIE, S. 2019. Middle-late Mesoproterozoic tectonic geography of the North Australia Craton: U–Pb and Hf isotopes of detrital zircon grains in the Beetaloo Sub-basin, Northern Territory, Australia. *Journal of the Geological Society*, 176, jgs2018-159. DOI: <https://doi.org/10.1144/jgs2018-159>.

- YANG, B., COLLINS, A. S., COX, G. M., JARRETT, A. J. M., DENYSZYN, S., BLADES, M. L., FARKAŠ, J. & GLORIE, S. 2020. Using Mesoproterozoic Sedimentary Geochemistry to Reconstruct Basin Tectonic Geography and Link Organic Carbon Productivity to Nutrient Flux from a Northern Australian Large Igneous Province. *Basin Research*, 32(6), 1734-1750. DOI: <https://doi.org/10.1111/bre.12450>.
- YANG, B., SMITH, T. M., COLLINS, A. S., MUNSON, T. J., SCHOEMAKER, B., NICHOLLS, D., COX, G., FARKAS, J. & GLORIE, S. 2018. Spatial and temporal variation in detrital zircon age provenance of the hydrocarbon-bearing upper Roper Group, Beetaloo Sub-basin, Northern Territory, Australia. *Precambrian Research*, 304, 140-155. DOI: <https://doi.org/10.1016/j.precamres.2017.10.025>.
- YANG, Y. H., ZHANG, H. F., CHU, Z. Y., XIE, L. W. & WU, F.-Y. 2010. Combined chemical separation of Lu, Hf, Rb, Sr, Sm and Nd from a single rock digest and precise and accurate isotope determinations of Lu–Hf, Rb–Sr and Sm–Nd isotope systems using Multi-Collector ICP-MS and TIMS. *International Journal of Mass Spectrometry*, 290, 120-126. DOI: <https://doi.org/10.1016/j.ijms.2009.12.011>.
- YIM, S.-G., JUNG, M.-J., JEONG, Y.-J., KIM, Y. & CHEONG, A. C.-S. 2021. Mass fractionation of Rb and Sr isotopes during laser ablation-multicollector-ICPMS: in situ observation and correction. *Journal of Analytical Science and Technology*, 12, 10. DOI: <https://doi.org/10.1186/s40543-021-00263-9>.
- YODER, H. S. & EUGSTER, H. P. 1955. Synthetic and natural muscovites. *Geochimica et Cosmochimica Acta*, 8, 225-280. DOI: [https://doi.org/10.1016/0016-7037\(55\)90001-6](https://doi.org/10.1016/0016-7037(55)90001-6).
- YOUNG, G. M. 2013. Precambrian supercontinents, glaciations, atmospheric oxygenation, metazoan evolution and an impact that may have changed the second half of Earth history. *Geoscience Frontiers*, 4, 247-261. DOI: <https://doi.org/10.1016/j.gsf.2012.07.003>.
- ZACK, T. & HOGMALM, K. J. 2016. Laser ablation Rb/Sr dating by online chemical separation of Rb and Sr in an oxygen-filled reaction cell. *Chemical Geology*, 437, 120-133. DOI: <https://doi.org/10.1016/j.chemgeo.2016.05.027>.
- ZAMBELL, C., ADAMS, J., GORRING, M. & SCHWARTZMAN, D. 2012. Effect of lichen colonization on chemical weathering of hornblende granite as estimated by aqueous elemental flux. *Chemical Geology*, 291, 166-174. DOI: <https://doi.org/10.1016/j.chemgeo.2011.10.009>.
- ZERKLE, A. L., POULTON, S. W., NEWTON, R. J., METTAM, C., CLAIRE, M. W., BEKKER, A. & JUNIUM, C. K. 2017. Onset of the aerobic nitrogen cycle during the Great Oxidation Event. *Nature*, 542, 465-467. DOI: <https://doi.org/10.1038/nature20826>.
- ZHANG, K., ZHU, X., WOOD, R. A., SHI, Y., GAO, Z. & POULTON, S. W. 2018a. Oxygenation of the Mesoproterozoic ocean and the evolution of complex eukaryotes. *Nature Geoscience*, 11, 345-350. DOI: <https://doi.org/10.1038/s41561-018-0111-y>.
- ZHANG, M., WANG, Q., ZHOU, D. & DING, H. 2019. Evaluating uncertain investment decisions in low-carbon transition toward renewable energy. *Applied Energy*, 240, 1049-1060. DOI: <https://doi.org/10.1016/j.apenergy.2019.01.205>.
- ZHANG, S.-H., ERNST, R. E., MUNSON, T. J., PEI, J., HU, G., LIU, J.-M., ZHANG, Q.-Q., CAI, Y.-H. & ZHAO, Y. 2021. Comparisons of the Paleo-Mesoproterozoic large igneous provinces and black shales in the North China and North Australian cratons. *Fundamental Research*. DOI: <https://doi.org/10.1016/j.fmre.2021.10.009>.

- ZHANG, S.-H., ERNST, R. E., PEI, J.-L., ZHAO, Y., ZHOU, M.-F. & HU, G.-H. 2018b. A temporal and causal link between ca. 1380 Ma large igneous provinces and black shales: Implications for the Mesoproterozoic time scale and paleoenvironment. *Geology*, 46, 963-966. DOI: <https://doi.org/10.1130/G45210.1>.
- ZHANG, S.-H., ZHAO, Y., LI, X.-H., ERNST, R. E. & YANG, Z.-Y. 2017. The 1.33–1.30 Ga Yanliao large igneous province in the North China Craton: Implications for reconstruction of the Nuna (Columbia) supercontinent, and specifically with the North Australian Craton. *Earth and Planetary Science Letters*, 465, 112-125. DOI: <https://doi.org/10.1016/j.epsl.2017.02.034>.
- ZHANG, S., LI, Z.-X., EVANS, D. A. D., WU, H., LI, H. & DONG, J. 2012. Pre-Rodinia supercontinent Nuna shaping up: A global synthesis with new paleomagnetic results from North China. *Earth and Planetary Science Letters*, 353-354, 145-155. DOI: <https://doi.org/10.1016/j.epsl.2012.07.034>.
- ZHANG, S., WANG, X., WANG, H., BJERRUM, C. J., HAMMARLUND, E. U., COSTA, M. M., CONNELLY, J. N., ZHANG, B., SU, J. & CANFIELD, D. E. 2016. Sufficient oxygen for animal respiration 1,400 million years ago. *Proceedings of the National Academy of Sciences*, 113, 1731. DOI: <https://doi.org/10.1073/pnas.1523449113>.
- ZHANG, W., XU, W., LIU, P., LIU, C. & LIU, F. 2022. Eastern North China Craton–North Australia Craton connection at 1.0 Ga through detrital zircon mixing modelling. *Terra Nova*, 34(6), 554-560. DOI: <https://doi.org/10.1111/ter.12622>.
- ZHAO, G., SUN, M., WILDE, S. A. & LI, S. 2004. A Paleo-Mesoproterozoic supercontinent: assembly, growth and breakup. *Earth-Science Reviews*, 67, 91-123. DOI: <https://doi.org/10.1016/j.earscirev.2004.02.003>.
- ZONNEVELD, K. A., VERSTEEGH, G. J., KASTEN, S., EGLINTON, T. I., EMEIS, K.-C., HUGUET, C., KOCH, B. P., DE LANGE, G. J., DE LEEUW, J. W. & MIDDELBURG, J. J. 2010. Selective preservation of organic matter in marine environments; processes and impact on the sedimentary record. *Biogeosciences*, 7, 483-511. DOI: <https://doi.org/10.5194/bg-7-483-2010>.

## 8. Supplementary Material

### Additional information for Chapter 2

Samples were comprehensively characterized by SEM-EDS mineral mapping in conjunction with bulk XRD data to confirm phase identifications. Backscatter electron (BSE) images and mineral maps were obtained with a FEI Teneo LoVac field emission scanning electron microscope (SEM) equipped with dual Bruker XFlash Series 6 energy dispersive X-ray spectroscopy (EDS) detectors. BSE images of the entire sample (100 nm pixel resolution) and EDS spectra (2  $\mu\text{m}$  step size, 8 ms acquisition time) for mineral mapping of smaller regions of interest were obtained using the FEI Maps Mineralogy software, followed by classification of the individual EDS spectra using the FEI Nanomin software (FEI Nanomin/Maps Mineralogy (Rafiei et al., 2020)). Nanomin deconvolves mixed EDS spectra and can assign up to three minerals per analysed single spot. Mineral concentrations (reported as wt. %) in the mapped areas are determined by converting the mineral area % to wt. % using published densities for all identified sample constituents, with accuracy and precision comparable to quantitative XRD analysis (Rafiei et al., 2020). Bulk XRD analyses were done at University of Adelaide as an independent crystallography based mineral identification of samples to confirm the phases characterized by Nanomin micro-imaging using a Bruker D8 Advance XRD (Fig. S.2.3).

Laser analyses on samples and standards were carried out at Adelaide Microscopy, University of Adelaide using a laser ablation (RESOLUTION-LR ArF 193nm excimer laser) inductively couple-mass spectrometer (Agilent 8900x ICP-MS/MS) with the analytical parameters and tuning conditions following (Redaa et al., 2021) summarised in Table S.2.1.

One spot analysis consisted of 20 seconds of gas background collected while the laser was not firing followed by 40 seconds of ablated signal. Strontium isotopes were measured in the oxidised molecule SrO. Strontium was oxidised with N<sub>2</sub>O gas in the reaction chamber (e.g. <sup>87</sup>Sr<sup>16</sup>O formed from <sup>87</sup>Sr at 103 amu) whilst the unreactive <sup>85</sup>Rb was measured on-mass. Dwell times for each Sr isotope were 50ms, 10ms for Rb and 5ms for all other masses totalling to 0.31 seconds. Average pit depths for each spot analysis are approximately 25  $\mu\text{m}$ . As such, each spot will comprise of an 'average' value from all the minerals within the crater. High resolution EDS mapping with Nanomin software of shales provides direct observations of crystallized, cogenetic K (Rb-bearing) clays (illite). These are the dominant mineralogy in each sample. Therefore, we conclude that the Rb–Sr data collected from each spot analysis are derived predominantly from these illites. In addition, we also identify an absence of detrital clays, as has been reported quite widely for Proterozoic shales (Rafiei and Kennedy, 2019), and instead recognize quartz to be the main detrital component. Quartz has negligible Rb and Sr, so does not influence our results. Ablating several clay-size minerals in one analysis have previously been done effectively using the same method to constrain fault reactivation histories in deep crystalline basements (Tillberg et al., 2020).



TABLE S.2.1. LA-ICP-MS/MS INSTRUMENTAL PARAMETERS

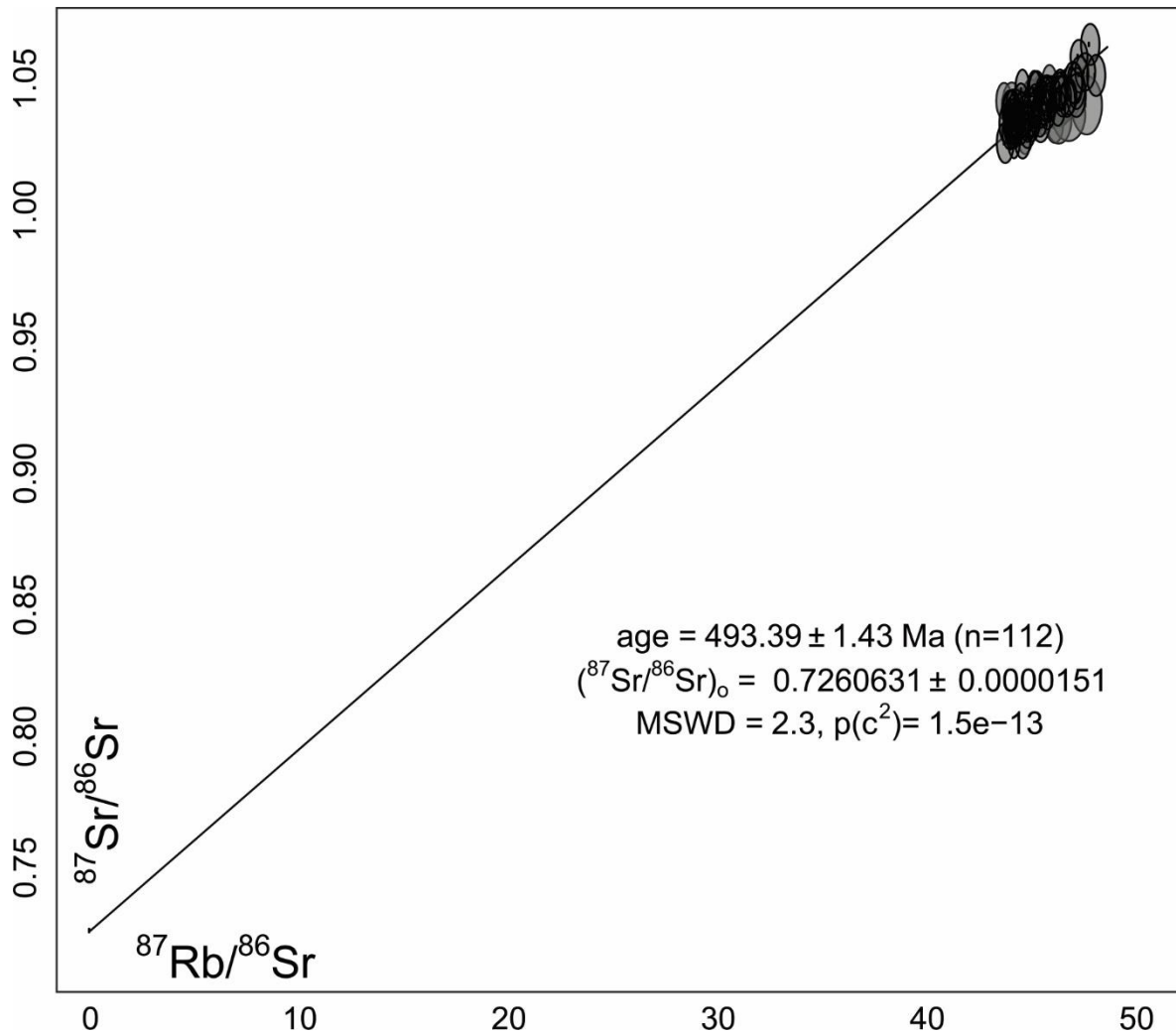
<i>Laser Parameters</i>	<i>Value</i>	<i>Unit</i>
Ar carrier gas	1050	ml/min
Fluence	3.5	J/cm <sup>2</sup>
He carrier gas	350	ml/min
N <sub>2</sub> addition	3.5	ml/min
Repetition rate	10	Hz
Spot size	74	μm
<i>ICP-MS/MS Plasma Parameters</i>	<i>Value</i>	<i>Unit</i>
RF plasma power	1350	W
<i>ICP-MS/MS Lens Parameters</i>	<i>Value</i>	<i>Unit</i>
Lens extract 1	-2.0	V
Lens extract 2	-150	V
Omega bias	75	V
Omega lens	7.0	V
Q1 entrance	2.0	V
Q1 exit	-1.0	V
Cell focus	-2.0	V
Cell entrance	-100	V
Cell exit	-150	V
Deflect	-10	V

Plate bias	-80	V
<b>ICP-MS/MS Q1 Parameters</b>		
Q1 bias	-2.0	V
Q1 prefilter bias	-9.0	V
Q1 postfilter bias	-10	V
<b>ICP-MS/MS Cell Parameters</b>		
N <sub>2</sub> O flow rate	0.37	mL/min
OctP bias	-23	V
Axial acceleration	2.0	V
OctP RF	180	V
Energy discrimination	-10	V
<b>ICP-MS/MS Q2 Parameters</b>		
Q2 bias	-33	V

In situ Rb–Sr dating of CRPG reference material Mica-MG (Govindaraju et al., 1994) prepared as a nano-powder pellet and a phlogopite mineral sample MDC sourced from the same quarry in Bekily, Madagascar were assumed to be of the same age (Armistead et al., 2020; Hogmalm et al., 2017; Li et al., 2020; Redaa et al., 2021) and were used as primary and secondary standards respectively. Furthermore, an independent illite pressed powdered pellet sample from Fithian, Illinois (Kralik, 1984) was also analyzed to determine whether the phlogopite nanopowder standard is suitable laser-ablation analysis of illite-rich granular shale samples. Glass standards NIST-610 and BCR-2G (Jochum et al., 2016; Wilson, 1997) were also analyzed as standards for element quantification. Isochron ages were calculated using IsoplotR software (Paton et al., 2011; Vermeesch, 2018) and a Rb decay constant of  $1.393 \times 10^{-11}$  (Nebel et al., 2011) was used.

The mineral standard MDC was anchored to  $^{87}\text{Rb}/^{86}\text{Sr} = 0.00001 \pm 0.000001$  and  $^{87}\text{Sr}/^{86}\text{Sr} = 0.72607 \pm 0.00363$  initial ratios as reported by Hogmalm et al. (2017), yielding an age of  $493.4 \pm 1.4$  Ma (Fig. S.2.1). This is approximately 4.4% younger than the published mean age of Mica-MG ( $519.4 \pm 6.5$  Ma; Hogmalm et al. 2017). A discussion of the categorical differences and deviations between Mica-MG and MDC can be found in length within Redaa

et al. (2021). To summarise, the observed differences in elemental Rb/Sr fractionation between the nano-powder and natural mineral flakes of the same phlogopite are likely due to their different ablation properties (Redaa et al., 2021). The granulated texture of the nano-powder material resulted in an irregular ablation characteristic that can be observed from the textures in the base of the laser-ablation pits (Fig. S.2.5). In contrast, the lasered craters of the natural mineral MDC showed a much more homogenous flat and shallower profile. These components will have effects on the down-hole fractionation patterns of the  $^{87}\text{Rb}/^{86}\text{Sr}$  ratios analysed and therefore can influence the resulting age.



**Figure S.2.1. A.** In situ Rb–Sr dating of MDC phlogopite anchored to  $^{87}\text{Sr}/^{86}\text{Sr}$  initial ratio of  $0.72607 \pm 0.00363$  reported by Hogmalm et al. (2017).

On the other hand, the Fithian Illite powdered sample yielded an age (Fig. S.2.2:  $305.7 \pm 26.9$  Ma) within error of its published age ( $284.0 \pm 8.0$  Ma) when anchored to reported initial  $^{87}\text{Sr}/^{86}\text{Sr}$  ratio of  $0.7109 \pm 0.0006$  from the same study (Kralik, 1984). This accurate independent age constraint, along with the similarities in laser-ablation crater profiles between the Fithian Illite powder and MicaMG, demonstrates that the two powdered samples have comparable ablation characteristics. Furthermore, the laser-pit textures of the analysed shales are also consistent with that of the Fithian Illite and MicaMG (Fig. S.2.5). As such, their corresponding matrix effects should also be similar, and therefore no correction

on the  $^{87}\text{Sr}/^{86}\text{Sr}$  or the  $^{87}\text{Rb}/^{86}\text{Sr}$  ratios analysed needs to be applied based on the MDC result.

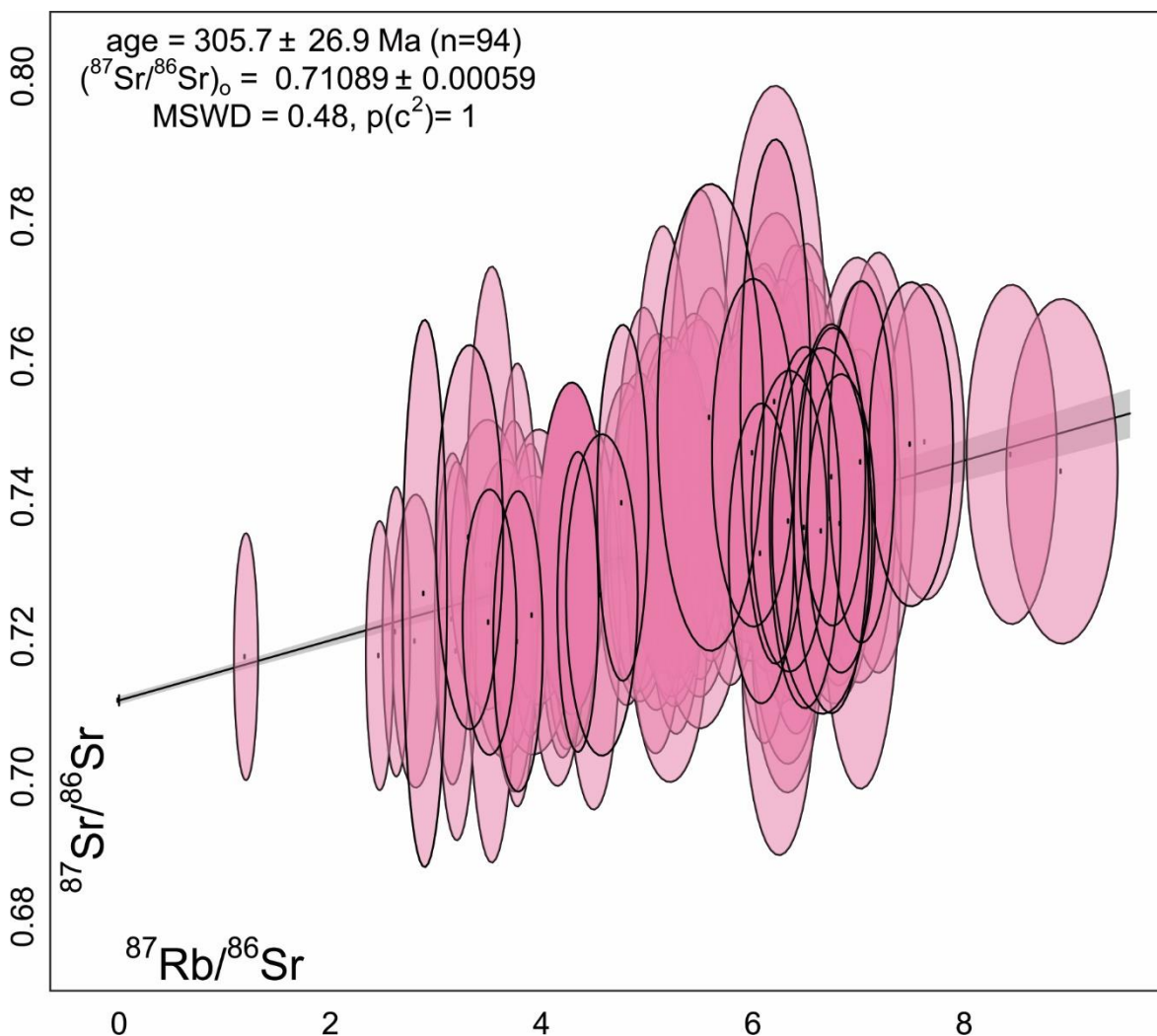


Figure S.2.2. In situ Rb–Sr dating of Fillian Illite powder anchored to  $^{87}\text{Sr}/^{86}\text{Sr}$  initial ratio of  $0.7109 \pm 0.0006$  (Kralik, 1984).

### Sampling, Petrography and Mineralogy

The Derim Derim Dolerite chip was sourced from the well Urapunga 5 (UR5) at 229 meters. Jalboi Formation and Wooden Duck Member shales were sampled from the same borehole at depths of 139 meters and 578 meters respectively to determine the alteration aureole of the intrusion. The Gibb Member shale was retrieved from Urapunga 6 borehole at 269 meters.

#### False colour composite and back scatter electron image for Derim Derim Dolerite U5\_229

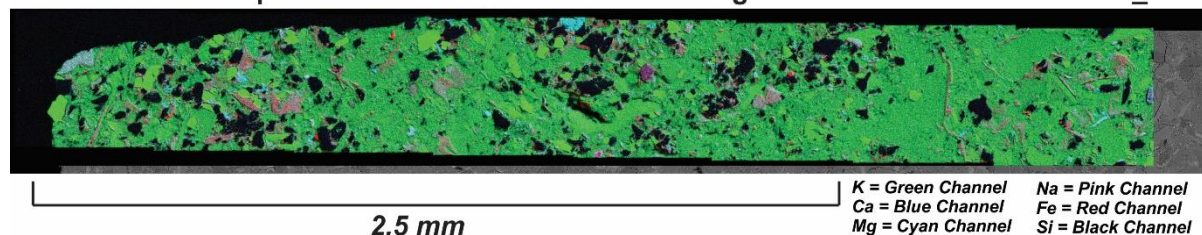
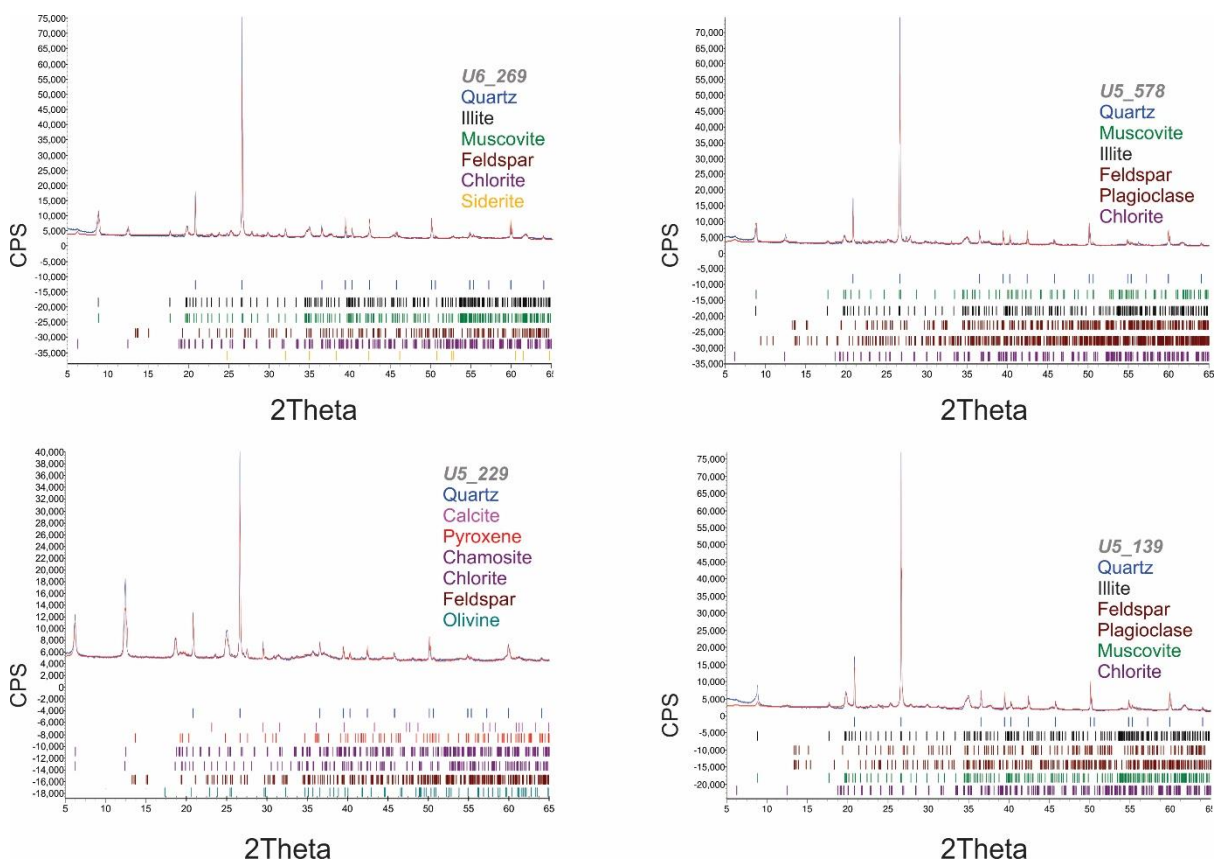


Figure S.2.3. False colour composite and back scatter electron image for Derim Derim Dolerite U5\_229.

Derim Derim dolerite sample U5\_229 was mapped for its petrographic textures and elemental composition using a Scanning Electron Microscope (SEM) FEI Quanta 450 with attached Oxford Ultima Max Large Area SDD EDS detector at Adelaide Microscopy. The resulting false colour composite and back scatter electron (BSE) image is shown in Fig. S.2.3. Si-rich grains, presumably quartz, form broken aggregates throughout the region of interest. Thin, Fe-rich slivers can be seen cross-cutting larger, K-Na-Mg grain boundaries. As a whole, the sample is non-crystalline, with brecciated textures and K-rich matrices indicating non-primary petrographic morphologies. Bulk XRD and spectral reflectance analyses of the dolerite (Fig. S.2.4 and Smith 2015) shows extensive chloritization in the sample. Together, the petrography and mineralogy of U5\_229 evince substantial potassic hydrothermal or epithermal alteration of the sample. Previous studies have dated Rb-rich chlorite-bearing rocks that indicate fluid flow and hydrothermally altered protoliths (Duane et al., 2004).



**Figure S.2.4.** Bulk XRD mineral composition of samples in this study. The order and colour of minerals listed correspond to the individual peaks identified in the samples.

Nanomin SEM-EDS mineral mapping and XRD analysis show the Gibb Member shale sample (U6\_267) to be a matrix-supported silty clay, with illite clay as the dominant phase (>60 wt. %). Silt to very fine sand-size quartz (detrital), chlorite (feldspar replacement) and siderite (concretions formed during earliest diagenesis) is dispersed through the clay matrix, along with trace quantities of < 5  $\mu\text{m}$  authigenic rutile grains. Illite is concentrated in mottled, elongate, interconnected domains up to 30  $\mu\text{m}$  in diameter. Illite comprising these domains is intergrown with authigenic quartz, commonly randomly oriented with respect to bedding and in some cases of nm size such that individual flakes cannot be distinguished. Together with the matrix supported nature of the sample and evidence for differential compaction of

illite domains around siderite concretions, these observations argue for an early, reverse weathering origin for the dominant proportion of illite (Rafiei & Kennedy, 2019; Rafiei et al., 2020). Rare exceptions to include large flakes of illite, interpreted to be physical weathering products of mica, and equant domains of pure illite with sharply delineated outlines and of similar size to chlorite grains, interpreted to be of feldspar alteration origin. Both occur only very rarely and are not expected to impact on in situ Rb-Sr analyses.

The Jalboi Formation shale (U5\_139) shows a similar mineral assemblage and mesoscale fabric to the Gibb Member shale, containing ~ 65 wt. % illite, but does not preserve siderite. The sample contains a higher abundance of detrital silt to fine sand size quartz and minor feldspar. The illite matrix shows a fissile and foliated fabric, not normally found in authigenic/early diagenetic shales. Large illite grains up to 100  $\mu\text{m}$  can also be found intergrown with this foliated matrix. Their grain morphologies are inconsistent with that of detrital origins, and instead are more likely products from the recrystallization of the finer-grained clay matrix. Trace quantities of rutile grains within the sample suggests a secondary redistribution of titanium. Detailed examination of the fine-grained matrix identifies an interlocking fabric reflecting the partial recrystallisation of clays as well as replacement by large chlorite domains.

The Wooden Duck Member shale sample (U5\_578) shows the lowest amount of illite compared to the previous two shale samples at < 30 wt. %. In addition, the sample has highest percentage of detrital quartz at 36 wt. %. Similar to the Jalboi Formation, chlorite is abundant and can be seen replacing other clays, forming a crystalline matrix with interlocking grain fabrics. The majority of clays within the sample also look to be recrystallized or of replacement phases. Furthermore, secondary rutile up to 40  $\mu\text{m}$  can also be found within the sample, suggesting similar fluid-rock interactions that were experienced by the Jalboi Formation shale.

Overall, the petrography of the Wooden Duck Member and the Jalboi Formations shales both suggest that they have experienced similar secondary fluid-rock interactions. The fissile and inter-grown matrices, recrystallization and replacement of majority clay phases, crystalline and interlocking grain fabrics as well as the remobilization of Ti were likely results of a late-stage alteration event instigated by the dolerite intrusion. The complete Nanomin SEM-EDS mineral maps of these samples can be provided upon request.

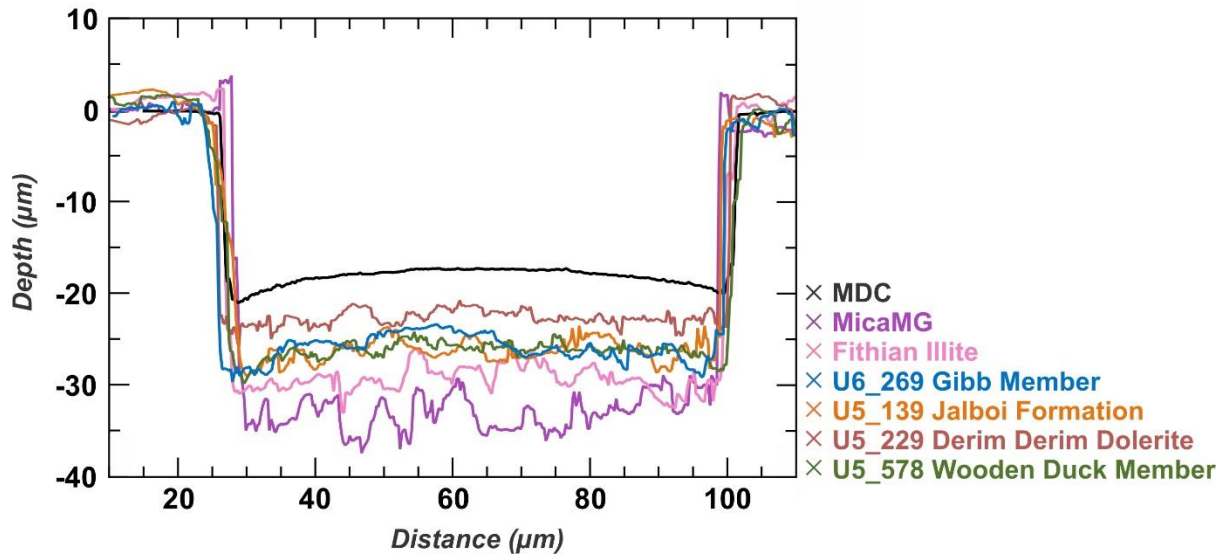


Figure S.2.5. Laser profilometry images of laser ablation craters and down-hole fractionation profiles of standards and samples analyzed. Note that the MDC natural mineral is the only analysis with a flat and homogeneous pit texture.

### Elemental Analyses

Elemental analyses of standards and their subsequent QAQC and secondary checks are reported below and cross-referenced with their respective published values (Woodhead et al., 2007). Major, trace and rare earth elements of analyses were normalized against NIST610 and basalt glass reference material BCR2G was used to check accuracy. REEY patterns of samples normalized to NIST610 are shown in Fig. S.2.6 Shales and dolerite from UR5 display a LREE depletion pattern relative to the Gibb Member shale from UR6.

### Samples normalised to NIST610

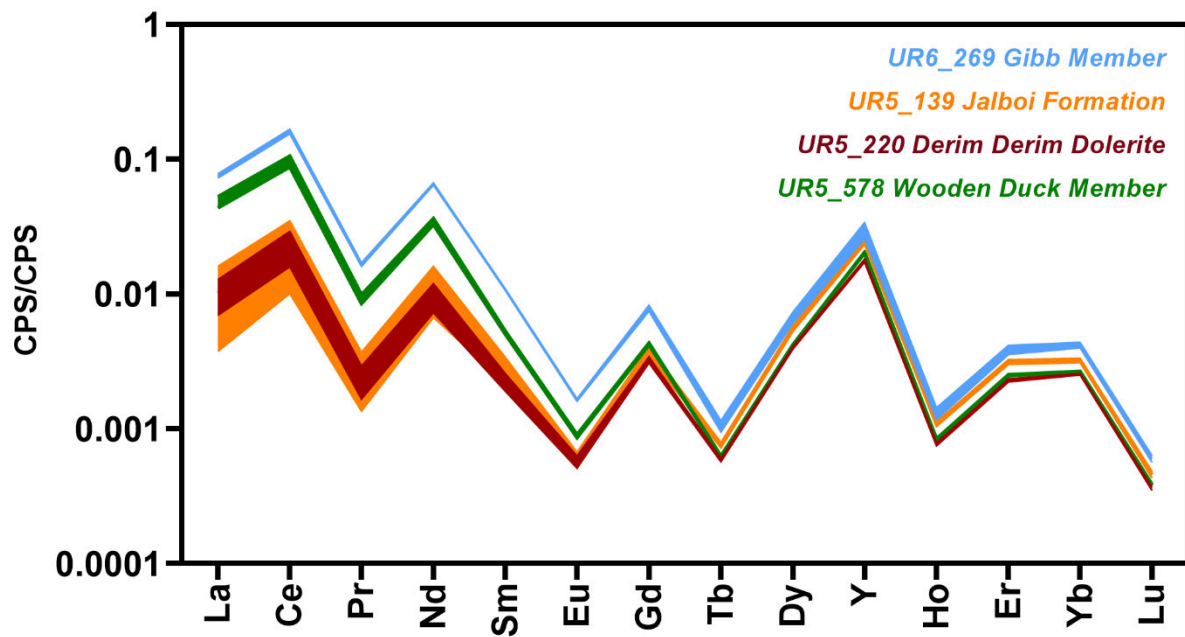


Figure S.2.6. REEY patterns of samples normalized to NIST610. Note that all U5 samples have a LREE depletion pattern relative to the U6 Gibb Member shale.



	La_C PS	Ce_C PS	Pr_CP S	Nd_ CPS	Sm_ CPS	Eu_C PS	Gd_C PS	Tb_C PS	Dy_C PS	Y_CP S	Ho_C PS	Er_C PS	Yb_C PS	Lu_CP S
<b>G_BCR2 G</b>														
bcr-2 - 1.d	6066 4	1211 80	1944 9	1514 4	3292	3470	3060	3088	4760	8198 5	3974	3619	2172	1478
bcr-2 - 10.d	2825 67	5670 11	8984 0	7035 6	1544 0	1636 4	1442 1	1505 3	2349 2	3875 82	1817 5	1783 9	9941	7014
bcr-2 - 11.d	2295 59	4401 29	7428 2	5699 9	1219 3	1274 4	1183 5	1215 5	1885 1	3136 96	1458 7	1431 0	7970	5735
bcr-2 - 12.d	2398 18	4671 06	7350 8	5974 5	1231 6	1352 4	1197 3	1277 4	2017 0	3329 55	1574 0	1505 6	8376	6267
bcr-2 - 2.d	5472 2	1092 97	1648 4	1368 0	2746	3177	2602	2790	4391	7763 3	3595	3267	1820	1405
bcr-2 - 3.d	5540 0	1086 81	1815 0	1370 1	2961	3230	2799	2855	4604	7719 6	3582	3419	1972	1361
bcr-2 - 4.d	5361 7	1052 68	1550 8	1343 1	2654	3024	2835	2930	4367	7551 5	3674	3463	1788	1421
bcr-2 - 5.d	2683 58	5164 42	8430 7	6601 8	1413 5	1465 7	1370 0	1408 4	2189 2	3692 88	1716 7	1675 6	9319	6733
bcr-2 - 6.d	2572 30	5047 39	8088 5	6339 8	1350 9	1427 8	1314 5	1362 7	2141 9	3521 95	1635 1	1603 4	9044	6520
bcr-2 - 7.d	2787 76	5394 68	8863 0	6842 5	1446 0	1529 6	1340 0	1418 9	2261 9	3760 36	1740 8	1664 8	9165	6521
bcr-2 - 8.d	2729 84	5431 84	8665 1	6792 6	1498 8	1538 6	1403 2	1454 4	2345 4	3782 98	1786 1	1739 9	9613	6608
bcr-2 - 9.d	2607 33	5075 50	8295 7	6503 0	1418 3	1438 3	1299 2	1346 9	2120 6	3596 83	1642 1	1574 8	8965	6295
bcr2 - 43.d	2447 60	4855 82	7854 4	6158 0	1270 5	1351 9	1204 2	1260 4	1955 7	3305 91	1512 1	1418 5	8194	5676
bcr2 - 44.d	2419 09	4855 73	7731 2	6017 0	1241 8	1331 0	1218 3	1233 8	1910 3	3283 27	1477 3	1429 7	8312	5689
bcr2 - 45.d	2488 82	4927 88	8019 6	6190 6	1269 9	1323 0	1221 6	1277 0	1942 4	3340 14	1496 2	1473 2	8153	5737
bcr2 - 47.d	2409 54	4822 18	7781 0	5987 2	1265 0	1347 3	1177 8	1192 6	1910 9	3239 85	1471 5	1384 8	8093	5544
bcr2 - 49.d	2414 03	4796 23	7795 8	5920 1	1244 0	1334 1	1191 2	1222 0	1887 9	3258 60	1479 8	1412 8	8001	5648
bcr2 - 50.d	2406 78	4776 52	7730 6	5939 2	1262 0	1312 0	1196 1	1223 0	1952 5	3244 29	1498 6	1424 9	7890	5657
bcr2 - 51.d	2444 24	4901 40	7863 3	6009 5	1257 9	1341 4	1185 0	1258 4	1918 0	3284 58	1490 2	1451 3	8051	5792
bcr2 - 52.d	2455 47	4903 70	7936 2	6106 3	1285 9	1374 1	1198 3	1236 0	1965 1	3303 44	1478 0	1417 0	7883	5839
bcr2 - 53.d	2314 25	4599 67	7517 1	5769 0	1206 8	1267 1	1130 5	1165 1	1829 5	3099 36	1403 5	1352 1	7607	5411
bcr2 - 54.d	2321 82	4689 04	7454 9	5808 3	1210 8	1259 2	1132 7	1162 0	1867 7	3135 97	1422 2	1408 7	7541	5528
bcr2 - 55.d	2353 57	4652 81	7479 0	5814 9	1185 0	1268 7	1122 8	1222 3	1854 7	3168 96	1400 0	1373 0	7604	5393
bcr2 - 56.d	2351 25	4729 88	7604 0	5815 8	1231 5	1282 4	1142 1	1177 8	1831 6	3144 86	1438 6	1373 0	7586	5461
bcr2 - 57.d	2014 80	3972 96	6480 9	4971 4	1059 7	1133 4	9874	1024	1605 4	2779 30	1255 0	1200 7	6736	4721
bcr2 - 58.d	2114 10	4099 86	6611 9	5154 9	1070 2	1132 6	9742	1067 6	1663 7	2826 79	1276 9	1234 6	6850	4823
bcr2 - 59.d	2155 14	4250 70	6903 1	5376 7	1130 6	1144 9	1072	1083 1	1695 8	2924 37	1334 9	1274 0	7331	5087
bcr2 - 60.d	2230 49	4475 78	7109 0	5509 6	1192 8	1233 8	1087	1137 3	1743 4	2997 19	1345 1	1319 4	7348	5403
bcr2 - 61.d	2264 24	4557 67	7338 8	5673 4	1148 8	1232 9	1080	1129 7	1778 2	3047 66	1381 2	1323 5	7444	5313
bcr2 - 62.d	2291 62	4587 12	7313 7	5696 3	1196 5	1251 4	1120	1188 0	1805 0	3069 35	1406 9	1354 9	7482	5405
bcr2 - 63.d	2271 79	4545 19	7274 8	5592 0	1161 5	1232 2	1085	1122 5	1822 3	3047 93	1378 4	1320 3	7502	5273
bcr2 - 64.d	2231 63	4489 30	7187 4	5595 4	1163 7	1218 0	1071	1130 5	1795 4	3026 51	1370 2	1295 2	7426	5216



bcr2 - 65.d	2336 55	4682 16	7630 7	5807 6	1200 4	1262 4	1143 2	1174 4	1832 2	3124 42	1402 0	1363 8	7618	5574
bcr2 - 66.d	2305 40	4642 74	7396 6	5708 0	1209 9	1298 8	1126 3	1166 4	1832 7	3084 39	1435 3	1373 9	7585	5671
bcr2 - 67.d	2239 45	4476 14	7160 0	5479 7	1138 9	1222 3	1079 8	1147 2	1798 9	3006 54	1379 3	1314 3	7458	5459
bcr2 - 68.d	2289 45	4589 68	7414 9	5671 1	1198 0	1246 9	1126 9	1169 8	1791 0	3069 85	1423 1	1333 7	7384	5257
bcr2 - 69.d	2286 46	4634 85	7363 3	5759 5	1195 0	1276 4	1132 3	1148 8	1803 1	3051 48	1381 5	1353 4	7522	5446
bcr2 - 70.d	2227 91	4445 45	7220 0	5488 1	1143 2	1235 6	1116 7	1151 0	1801 3	2993 86	1398 3	1291 4	7569	5414
bcr2 - 71.d	2334 29	4603 67	7539 5	5673 2	1191 0	1252 9	1116 9	1170 4	1795 4	3087 07	1426 6	1359 1	7839	5461
bcr2 - 72.d	2241 77	4554 68	7320 9	5628 1	1177 4	1249 4	1121 7	1183 8	1797 7	3062 41	1417 8	1350 0	7581	5358
bcr2 - 73.d	2279 26	4527 76	7307 8	5670 1	1181 9	1221 6	1104 0	1180 6	1779 2	3062 64	1366 6	1329 7	7510	5420
bcr2 - 74.d	2290 83	4608 71	7384 7	5655 9	1144 0	1280 9	1121 3	1151 0	1842 1	3052 46	1425 8	1343 6	7438	5441
<b>G_NIST 610</b>														
nist610 - 43.d	6548 116	6321 538	8085 145	1251 907	1197 528	4712 678	1116 187	8445 155	2014 697	7581 316	8036 680	2733 719	1582 212	8061 819
nist610 - 44.d	6570 995	6358 392	8098 317	1269 797	1201 013	4708 525	1120 395	8450 350	2026 679	7553 126	8018 958	2732 248	1587 360	8037 226
nist610 - 45.d	6613 108	6406 690	8160 659	1269 722	1207 784	4740 595	1121 074	8504 319	2026 480	7663 509	8046 039	2735 865	1584 168	8055 602
nist610 - 46.d	6599 334	6381 721	8149 165	1268 235	1208 200	4714 331	1126 470	8481 215	2027 825	7665 797	8045 285	2736 598	1584 666	8049 118
nist610 - 47.d	6621 808	6386 421	8117 837	1268 817	1209 946	4725 395	1118 369	8489 153	2036 089	7655 164	8071 389	2733 402	1584 793	8055 893
nist610 - 48.d	6525 043	6321 437	8034 368	1259 407	1194 731	4653 254	1112 369	8429 051	2008 572	7596 904	7972 905	2709 453	1581 239	8005 717
nist610 - 49.d	6372 546	6176 886	7899 525	1222 940	1175 652	4596 311	1092 497	8281 669	1956 090	7388 595	7841 830	2668 851	1538 612	7868 066
nist610 - 50.d	6407 006	6201 318	7921 084	1233 068	1179 685	4607 907	1096 866	8315 663	1968 446	7414 942	7902 162	2682 145	1557 704	7922 731
nist610 - 51.d	6518 594	6301 417	8068 840	1259 109	1200 834	4676 715	1116 920	8458 111	2011 115	7547 166	8018 908	2732 646	1586 060	8048 312
nist610 - 52.d	6528 522	6296 345	8041 171	1263 863	1202 750	4676 349	1114 067	8416 559	2010 206	7546 653	8002 366	2712 910	1581 454	8008 276
nist610 - 53.d	6378 712	6177 547	7888 138	1228 237	1174 294	4588 125	1092 661	8252 539	1963 123	7336 242	7837 591	2670 957	1553 652	7881 315
nist610 - 54.d	6452 909	6223 075	7948 364	1232 711	1182 856	4608 979	1105 640	8316 396	1986 901	7419 505	7904 330	2689 786	1554 664	7916 395
nist610 - 55.d	6462 891	6248 235	7968 155	1248 273	1186 822	4629 090	1104 292	8336 125	1989 779	7508 438	7873 325	2686 964	1555 778	7911 324
nist610 - 56.d	6457 712	6232 744	7921 394	1239 385	1184 700	4597 476	1101 025	8303 839	1975 140	7481 032	7908 666	2684 687	1556 686	7890 549
nist610 - 57.d	6427 846	6203 673	7938 054	1231 269	1188 177	4612 873	1103 451	8318 434	1977 881	7444 423	7890 362	2682 001	1556 930	7898 158
nist610 - 58.d	6363 912	6150 557	7879 009	1229 379	1179 307	4559 584	1092 058	8228 602	1955 633	7384 654	7797 897	2657 953	1531 779	7806 662
nist610 - 59.d	6257 476	6051 229	7731 238	1206 499	1160 171	4507 734	1081 417	8124 678	1926 862	7239 634	7706 306	2618 406	1511 542	7720 948
nist610 - 60.d	6304 271	6063 445	7761 692	1208 250	1161 333	4522 787	1078 138	8143 219	1929 768	7302 776	7719 580	2622 665	1523 707	7711 265
nist610 - 61.d	6404 604	6177 234	7880 101	1226 582	1176 910	4579 996	1095 330	8268 542	1956 537	7403 744	7849 067	2659 457	1546 950	7854 549
nist610 - 62.d	6366 641	6118 571	7798 843	1223 640	1167 637	4538 843	1097 291	8202 224	1947 272	7336 216	7757 624	2644 277	1523 491	7787 219
nist610 - 63.d	6254 817	6019 038	7711 138	1198 114	1152 899	4468 323	1075 432	8086 889	1911 057	7190 023	7681 470	2604 578	1495 176	7693 454
nist610 - 64.d	6169 631	5950 971	7639 648	1188 132	1143 354	4419 397	1063 359	7985 214	1889 822	7136 824	7573 754	2591 079	1489 569	7607 743
nist610 - 65.d	6247 992	6024 342	7701 870	1189 639	1151 051	4468 389	1073 462	8079 217	1908 941	7223 172	7654 601	2607 739	1505 725	7658 936

nist610 - 66.d	6183 572	5961 462	7622 092	1187 553	1141 979	4431 991	1065 413	8014 319	1896 628	7148 544	7592 473	2577 567	1488 040	7611 983
nist610 - 67.d	6211 888	6006 588	7675 963	1199 501	1146 877	4464 585	1071 342	8043 734	1893 764	7163 578	7621 113	2606 352	1500 878	7671 985
nist610 - 68.d	6203 922	5980 377	7634 497	1195 160	1145 670	4465 700	1072 843	8050 622	1895 703	7144 489	7646 075	2592 348	1497 326	7657 334
nist610 - 69.d	6114 126	5929 463	7556 413	1182 452	1136 896	4405 704	1059 734	7973 010	1870 592	7039 058	7594 796	2561 608	1482 362	7597 282
nist610 - 70.d	6106 968	5918 040	7565 356	1178 771	1135 569	4406 498	1060 793	7954 909	1878 125	7048 430	7566 249	2568 570	1477 320	7569 892
nist610 - 71.d	6110 774	5912 941	7555 588	1173 627	1134 351	4394 527	1062 562	7941 369	1873 082	7065 475	7543 315	2577 684	1466 211	7566 534
nist610 - 72.d	6093 834	5903 240	7517 084	1172 987	1131 618	4377 367	1053 719	7897 909	1858 102	7044 952	7492 783	2555 064	1477 221	7508 260
nist610 - 73.d	6163 889	5933 461	7591 977	1185 865	1134 317	4396 271	1058 697	7957 508	1884 075	7114 385	7573 617	2572 265	1473 981	7579 683
nist610 - 74.d	6144 331	5914 976	7580 179	1183 387	1141 050	4425 750	1062 047	7953 787	1883 492	7106 430	7580 182	2576 431	1483 723	7577 043
nist610 - 80.d	8621 469	8256 274	1068 3087	1836 269	1730 947	6238 390	1514 660	1136 3717	2759 178	9924 692	1074 9041	3664 492	2269 097	1077 4884
nist610 - 81.d	8671 559	8295 677	1073 6366	1859 803	1744 432	6263 012	1515 552	1135 8196	2766 556	9969 874	1078 4474	3665 238	2279 575	1083 9735
nist610 - 82.d	8876 428	8481 740	1097 3291	1886 773	1801 619	6393 895	1547 238	1157 5802	2815 070	1020 1608	1097 7770	3736 192	2307 879	1103 3083
nist610 - 83.d	8822 781	8484 397	1089 5303	1884 911	1787 564	6354 109	1544 930	1156 1530	2794 386	1018 0671	1094 1813	3722 821	2305 142	1102 5387
nist610 - 84.d	8763 191	8412 282	1087 4147	1881 298	1783 690	6321 434	1533 688	1152 0108	2795 080	1006 3895	1089 3147	3716 577	2300 648	1094 6397
nist610 - 85.d	8793 004	8437 692	1084 9442	1879 203	1773 583	6332 036	1535 674	1152 9885	2795 979	1012 3618	1090 0653	3729 098	2301 519	1097 0179
nist610 - 86.d	8673 694	8329 129	1073 3264	1856 905	1747 542	6268 560	1514 109	1142 4926	2772 962	9982 540	1078 7971	3676 564	2279 466	1088 9261
nist610 - 87.d	8629 378	8280 886	1064 6054	1842 142	1720 542	6212 815	1511 758	1136 3438	2755 316	9890 345	1072 6558	3662 156	2268 295	1082 6652

	StdCorr Rb87 Sr86s	StdCorr Rb87 Sr86s Int2SE	StdCorr Sr87s Sr86s	StdCorr Sr87s Sr86s Int2SE
M MicaMG 1	151.5000	1.1000	1.8530	0.0150
M MicaMG 2	156.8000	1.1000	1.8730	0.0130
M MicaMG 3	156.4000	1.1000	1.8580	0.0120
M MicaMG 4	158.2000	1.3000	1.8630	0.0120
M MicaMG 5	157.2000	1.3000	1.8520	0.0130
M MicaMG 6	159.9000	1.4000	1.8590	0.0130
M MicaMG 7	158.6000	1.3000	1.8640	0.0110
M MicaMG 8	160.8000	1.2000	1.8530	0.0130
M MicaMG 9	160.8000	1.3000	1.8480	0.0140
M MicaMG 10	157.6000	1.3000	1.8560	0.0120
M MicaMG 11	156.5000	1.5000	1.8410	0.0150
M MicaMG 12	159.2000	1.1000	1.8480	0.0130
M MicaMG 13	158.6000	1.4000	1.8460	0.0140
M MicaMG 14	157.7000	1.1000	1.8610	0.0110
M MicaMG 15	157.5000	1.1000	1.8510	0.0110
M MicaMG 16	154.9000	1.4000	1.8590	0.0140
M MicaMG 17	157.9000	1.1000	1.8550	0.0120
M MicaMG 18	155.9000	1.3000	1.8480	0.0120
M MicaMG 19	157.8000	1.5000	1.8520	0.0140
M MicaMG 20	157.7000	1.2000	1.8500	0.0140

M MicaMG 21	159.8000	1.5000	1.8560	0.0130
M MicaMG 22	157.5000	1.1000	1.8540	0.0140
M MicaMG 23	156.1000	1.4000	1.8580	0.0130
M MicaMG 24	156.1000	1.3000	1.8520	0.0130
M MicaMG 25	155.4000	1.5000	1.8440	0.0150
M MicaMG 26	155.0000	1.2000	1.8550	0.0140
M MicaMG 27	154.7000	1.2000	1.8550	0.0110
M MicaMG 28	154.8000	1.2000	1.8560	0.0130
M MicaMG 29	158.6000	1.2000	1.8660	0.0110
M MicaMG 30	157.4000	1.3000	1.8610	0.0120
M MicaMG 31	154.8000	1.1000	1.8500	0.0120
M MicaMG 32	153.9000	1.3000	1.8480	0.0120
M MicaMG 33	154.2000	1.2000	1.8620	0.0120
M MicaMG 34	153.4000	1.3000	1.8420	0.0130
M MicaMG 35	156.1000	1.1000	1.8700	0.0140
M MicaMG 36	152.7000	1.1000	1.8490	0.0120
M MicaMG 37	153.1000	1.2000	1.8430	0.0130
M MicaMG 38	153.9000	1.4000	1.8360	0.0110
M MicaMG 39	155.9000	1.3000	1.8510	0.0130
M MicaMG 40	157.7900	0.9900	1.8520	0.0110
M MicaMG 41	155.1000	1.1000	1.8470	0.0130
M MicaMG 42	155.2000	1.0000	1.8590	0.0130
M MicaMG 43	150.1000	1.4000	1.8280	0.0150
M MicaMG 44	148.6000	1.8000	1.8340	0.0190
M MicaMG 45	152.8000	1.3000	1.8440	0.0120
M MicaMG 46	152.6000	1.2000	1.8540	0.0130
M MicaMG 47	153.3000	1.4000	1.8430	0.0150
M MicaMG 48	155.7000	1.3000	1.8550	0.0120
M MicaMG 49	154.8000	1.5000	1.8590	0.0130
M MicaMG 50	155.7000	1.3000	1.8550	0.0120
M MicaMG 51	154.5000	1.1000	1.8520	0.0150
M MicaMG 52	153.2000	1.2000	1.8540	0.0130
M MicaMG 53	150.7000	1.6000	1.8500	0.0130
M MicaMG 54	154.1000	1.6000	1.8540	0.0130
M MicaMG 55	153.1000	1.3000	1.8540	0.0140
M MicaMG 56	153.0000	1.4000	1.8480	0.0130
M MicaMG 57	151.5000	1.0000	1.8570	0.0130
M MicaMG 58	154.7000	1.2000	1.8620	0.0120
M MicaMG 59	155.5000	1.4000	1.8550	0.0130
M MicaMG 60	153.3000	1.7000	1.8250	0.0190
M MicaMG 61	154.9000	1.5000	1.8570	0.0160
M MicaMG 62	154.7000	1.2000	1.8600	0.0150
M MicaMG 63	150.5000	1.2000	1.8500	0.0120
M MicaMG 64	153.6000	1.4000	1.8480	0.0130
M MicaMG 65	153.7000	1.3000	1.8410	0.0130

M MicaMG 66	153.1000	1.2000	1.8560	0.0120
M MicaMG 67	152.7000	1.5000	1.8390	0.0140
M MicaMG 68	154.5000	1.3000	1.8540	0.0120
M MicaMG 69	156.1000	0.9700	1.8600	0.0140
M MicaMG 70	158.1000	1.0000	1.8640	0.0130
M MicaMG 71	154.8000	1.3000	1.8410	0.0140
M MicaMG 72	155.0000	1.2000	1.8410	0.0130
M MicaMG 73	153.8000	1.0000	1.8640	0.0120
M MicaMG 74	152.8000	1.3000	1.8520	0.0130
M MicaMG 75	151.3000	1.3000	1.8560	0.0130
M MicaMG 76	155.7000	1.5000	1.8670	0.0120
M MicaMG 77	153.8000	1.0000	1.8620	0.0130
M MicaMG 78	154.3000	1.1000	1.8500	0.0120
M MicaMG 79	151.1000	1.7000	1.8570	0.0130
M MicaMG 80	158.1000	1.1000	1.8620	0.0110
M MicaMG 81	154.2000	1.0000	1.8450	0.0130
M MicaMG 82	152.5000	1.4000	1.8510	0.0140
M MicaMG 83	153.5000	1.0000	1.8460	0.0140
M MicaMG 84	153.8000	1.1000	1.8430	0.0140
M MicaMG 85	153.5000	1.2000	1.8420	0.0130
M MicaMG 86	152.6000	1.3000	1.8340	0.0120
M MicaMG 87	153.6000	1.1000	1.8660	0.0130
M MicaMG 88	152.8000	1.4000	1.8530	0.0150
M MicaMG 89	154.9000	1.1000	1.8540	0.0140
M MicaMG 90	152.6000	1.2000	1.8560	0.0140
M MicaMG 91	154.4800	0.9900	1.8530	0.0130
M MicaMG 92	153.5000	1.1000	1.8550	0.0120
M MicaMG 93	150.2000	1.1000	1.8440	0.0110
M MicaMG 94	152.8000	1.2000	1.8550	0.0120
M MicaMG 95	152.8000	1.2000	1.8420	0.0140
M MicaMG 96	153.0000	1.0000	1.8510	0.0130
M MicaMG 97	151.7000	1.1000	1.8420	0.0130
M MicaMG 98	152.1000	1.0000	1.8370	0.0120
M MicaMG 99	154.1000	1.2000	1.8630	0.0130
M MicaMG 100	153.6000	1.2000	1.8560	0.0150
M MicaMG 101	154.6000	1.1000	1.8620	0.0120
M MicaMG 102	152.6000	1.1000	1.8540	0.0120
M MicaMG 103	152.1000	1.0000	1.8540	0.0130
M MicaMG 104	152.9000	1.5000	1.8460	0.0120
M MicaMG 105	151.1000	1.2000	1.8600	0.0120
M MicaMG 106	152.7000	1.3000	1.8480	0.0150
M MicaMG 107	152.7000	1.2000	1.8620	0.0130
M MicaMG 108	154.4000	1.0000	1.8720	0.0140
M MicaMG 109	153.9000	1.3000	1.8500	0.0140
M MicaMG 110	153.7000	1.0000	1.8450	0.0130

M MicaMG 111	155.0000	1.2000	1.8660	0.0150
	0.0010	0.0001	0.7261	0.0000
M MDCmica 1	43.6600	0.3000	1.0417	0.0056
M MDCmica 2	44.0500	0.3100	1.0347	0.0064
M MDCmica 3	44.6300	0.3000	1.0374	0.0058
M MDCmica 4	44.6600	0.2900	1.0289	0.0060
M MDCmica 5	45.3300	0.3300	1.0398	0.0060
M MDCmica 6	45.7600	0.3600	1.0427	0.0071
M MDCmica 7	44.9500	0.2700	1.0334	0.0058
M MDCmica 8	45.0400	0.3000	1.0402	0.0055
M MDCmica 9	45.5000	0.2600	1.0372	0.0050
M MDCmica 10	44.7100	0.2900	1.0330	0.0058
M MDCmica 11	45.4200	0.3200	1.0446	0.0057
M MDCmica 12	45.0100	0.2900	1.0374	0.0052
M MDCmica 13	44.8200	0.2900	1.0362	0.0053
M MDCmica 14	44.7600	0.2600	1.0358	0.0060
M MDCmica 15	45.5100	0.3000	1.0369	0.0065
M MDCmica 16	44.2500	0.2800	1.0385	0.0065
M MDCmica 17	45.0400	0.3000	1.0404	0.0057
M MDCmica 18	44.0300	0.3800	1.0393	0.0077
M MDCmica 19	44.7500	0.3200	1.0388	0.0050
M MDCmica 20	46.2700	0.4900	1.0342	0.0071
M MDCmica 21	44.9400	0.3100	1.0434	0.0053
M MDCmica 22	46.7500	0.6400	1.0364	0.0081
M MDCmica 23	44.8800	0.3200	1.0392	0.0063
M MDCmica 24	47.6100	0.5900	1.0401	0.0091
M MDCmica 25	44.6700	0.3000	1.0383	0.0059
M MDCmica 26	46.8000	0.4500	1.0449	0.0078
M MDCmica 27	45.2100	0.3100	1.0363	0.0059
M MDCmica 28	45.5700	0.3400	1.0417	0.0064
M MDCmica 29	46.3600	0.3900	1.0402	0.0066
M MDCmica 30	46.0800	0.3200	1.0321	0.0051
M MDCmica 31	45.4800	0.3300	1.0405	0.0053
M MDCmica 32	46.5000	0.2900	1.0440	0.0066
M MDCmica 33	46.5600	0.3400	1.0420	0.0069
M MDCmica 34	45.6000	0.3100	1.0395	0.0052
M MDCmica 35	46.5200	0.3400	1.0419	0.0064
M MDCmica 36	46.7100	0.3100	1.0435	0.0063
M MDCmica 37	45.8300	0.3000	1.0479	0.0061
M MDCmica 38	46.3700	0.3100	1.0424	0.0057
M MDCmica 39	46.3700	0.2800	1.0456	0.0058
M MDCmica 40	45.9600	0.3400	1.0444	0.0055
M MDCmica 41	46.2400	0.3100	1.0455	0.0058
M MDCmica 42	47.1100	0.3700	1.0438	0.0067
M MDCmica 43	46.4500	0.3300	1.0434	0.0062

M MDCmica 44	46.6700	0.3100	1.0425	0.0056
M MDCmica 45	47.2400	0.3300	1.0586	0.0052
M MDCmica 46	46.7600	0.3000	1.0435	0.0057
M MDCmica 47	47.2800	0.3400	1.0518	0.0056
M MDCmica 48	46.9600	0.3500	1.0488	0.0064
M MDCmica 49	47.1200	0.3300	1.0465	0.0064
M MDCmica 50	47.5400	0.3900	1.0528	0.0058
M MDCmica 51	48.0600	0.3600	1.0514	0.0064
M MDCmica 52	47.0500	0.3000	1.0483	0.0064
M MDCmica 53	47.7800	0.3600	1.0632	0.0064
M MDCmica 54	43.9200	0.2800	1.0383	0.0060
M MDCmica 55	44.4700	0.2900	1.0415	0.0056
M MDCmica 56	45.1100	0.2700	1.0456	0.0062
M MDCmica 57	45.1300	0.2700	1.0402	0.0064
M MDCmica 58	45.1100	0.2700	1.0381	0.0056
M MDCmica 59	45.7300	0.3000	1.0385	0.0062
M MDCmica 60	45.7100	0.3400	1.0438	0.0063
M MDCmica 61	45.7200	0.2900	1.0441	0.0055
M MDCmica 62	45.7900	0.2600	1.0412	0.0059
M MDCmica 63	45.8100	0.3000	1.0411	0.0061
M MDCmica 64	45.6000	0.3100	1.0426	0.0066
M MDCmica 65	46.3400	0.2600	1.0446	0.0055
M MDCmica 66	46.3400	0.3000	1.0469	0.0055
M MDCmica 67	45.1400	0.3000	1.0461	0.0055
M MDCmica 68	45.3900	0.2800	1.0357	0.0062
M MDCmica 69	45.2300	0.3200	1.0456	0.0061
M MDCmica 70	44.9900	0.2900	1.0331	0.0055
M MDCmica 71	45.5100	0.3200	1.0396	0.0056
M MDCmica 72	46.2300	0.2900	1.0395	0.0059
M MDCmica 73	45.5400	0.3200	1.0441	0.0059
M MDCmica 74	45.4500	0.3100	1.0404	0.0072
M MDCmica 75	45.6600	0.2700	1.0408	0.0058
M MDCmica 76	45.3900	0.3200	1.0383	0.0056
M MDCmica 77	44.0100	0.2900	1.0326	0.0061
M MDCmica 78	44.4200	0.3400	1.0322	0.0058
M MDCmica 79	43.9500	0.2600	1.0336	0.0058
M MDCmica 80	44.5400	0.2800	1.0459	0.0063
M MDCmica 81	44.9200	0.3400	1.0400	0.0055
M MDCmica 82	44.2400	0.2700	1.0387	0.0060
M MDCmica 83	44.0400	0.2600	1.0293	0.0047
M MDCmica 84	44.2200	0.3000	1.0316	0.0057
M MDCmica 85	44.6400	0.3800	1.0361	0.0060
M MDCmica 86	44.4900	0.3600	1.0364	0.0069
M MDCmica 87	44.9300	0.3300	1.0363	0.0069
M MDCmica 88	44.0100	0.2700	1.0334	0.0062

M MDCmica 89	44.0100	0.3000	1.0349	0.0061
M MDCmica 90	44.2800	0.2600	1.0335	0.0059
M MDCmica 91	44.1700	0.3100	1.0336	0.0059
M MDCmica 92	44.7800	0.3000	1.0334	0.0059
M MDCmica 93	44.5500	0.3000	1.0268	0.0057
M MDCmica 94	43.9400	0.2900	1.0300	0.0055
M MDCmica 95	43.7600	0.2600	1.0331	0.0061
M MDCmica 96	44.2500	0.2600	1.0341	0.0060
M MDCmica 97	44.0800	0.2700	1.0386	0.0061
M MDCmica 98	44.1900	0.3200	1.0364	0.0052
M MDCmica 99	44.1500	0.2900	1.0315	0.0064
M MDCmica 100	43.7200	0.3300	1.0258	0.0063
M MDCmica 101	44.1500	0.3300	1.0351	0.0059
M MDCmica 102	44.5700	0.3500	1.0365	0.0070
M MDCmica 103	44.0100	0.3200	1.0381	0.0060
M MDCmica 104	44.1100	0.2800	1.0365	0.0061
M MDCmica 105	44.1400	0.2500	1.0281	0.0067
M MDCmica 106	44.3000	0.2800	1.0334	0.0058
M MDCmica 107	44.7200	0.3800	1.0344	0.0060
M MDCmica 108	44.7800	0.3100	1.0308	0.0057
M MDCmica 109	45.0300	0.3400	1.0358	0.0063
M MDCmica 110	45.4100	0.3700	1.0339	0.0064
M MDCmica 111	44.8200	0.2900	1.0344	0.0057
G NIST610 1	2.1533	0.0083	0.7100	0.0013
G NIST610 2	2.1549	0.0086	0.7106	0.0013
G NIST610 3	2.1686	0.0077	0.7110	0.0013
G NIST610 4	2.1706	0.0085	0.7104	0.0016
G NIST610 5	2.1823	0.0083	0.7106	0.0014
G NIST610 6	2.1824	0.0087	0.7098	0.0016
G NIST610 7	2.1899	0.0090	0.7098	0.0015
G NIST610 8	2.1916	0.0083	0.7100	0.0015
G NIST610 9	2.1854	0.0083	0.7099	0.0013
G NIST610 10	2.1743	0.0088	0.7111	0.0016
G NIST610 11	2.1908	0.0091	0.7093	0.0015
G NIST610 12	2.1865	0.0081	0.7098	0.0015
G NIST610 13	2.1912	0.0080	0.7105	0.0012
G NIST610 14	2.1809	0.0078	0.7120	0.0015
G NIST610 15	2.1900	0.0091	0.7101	0.0014
G NIST610 16	2.1826	0.0091	0.7088	0.0015
G NIST610 17	2.1863	0.0076	0.7090	0.0014
G NIST610 18	2.1776	0.0073	0.7093	0.0014
G NIST610 19	2.1866	0.0073	0.7096	0.0014
G NIST610 20	2.1893	0.0071	0.7104	0.0016
G NIST610 21	2.1863	0.0076	0.7106	0.0016

G NIST610 22	2.1764	0.0072	0.7094	0.0012
G NIST610 23	2.1959	0.0076	0.7098	0.0017
G NIST610 24	2.1868	0.0080	0.7099	0.0013
G NIST610 25	2.1810	0.0064	0.7100	0.0014
G NIST610 26	2.1808	0.0073	0.7116	0.0013
G NIST610 27	2.1902	0.0084	0.7112	0.0016
G NIST610 28	2.1879	0.0078	0.7098	0.0015
G NIST610 29	2.1853	0.0085	0.7097	0.0014
G NIST610 30	2.1754	0.0080	0.7097	0.0016
G NIST610 31	2.1864	0.0074	0.7083	0.0013
G NIST610 32	2.1823	0.0088	0.7094	0.0017
G NIST610 33	2.1871	0.0074	0.7095	0.0015
G NIST610 34	2.1822	0.0079	0.7109	0.0014
G NIST610 35	2.1818	0.0078	0.7106	0.0014
G NIST610 36	2.1764	0.0091	0.7102	0.0014
G NIST610 37	2.1900	0.0081	0.7104	0.0015
G NIST610 38	2.1850	0.0074	0.7108	0.0014
G NIST610 39	2.1889	0.0080	0.7109	0.0016
G NIST610 40	2.1846	0.0086	0.7104	0.0014
G NIST610 41	2.1924	0.0079	0.7093	0.0013
G NIST610 42	2.1803	0.0083	0.7108	0.0014
G NIST610 43	2.1964	0.0079	0.7101	0.0014
G NIST610 44	2.1840	0.0087	0.7099	0.0014
G NIST610 45	2.1947	0.0087	0.7098	0.0016
G NIST610 46	2.1803	0.0088	0.7104	0.0018
G NIST610 47	2.1856	0.0084	0.7089	0.0016
G NIST610 48	2.1871	0.0087	0.7089	0.0017
G NIST610 49	2.1846	0.0073	0.7116	0.0016
G NIST610 50	2.1825	0.0094	0.7096	0.0014
G NIST610 51	2.1827	0.0085	0.7101	0.0014
G NIST610 52	2.1804	0.0078	0.7095	0.0015
G NIST610 53	2.1710	0.0091	0.7085	0.0017
G NIST610 54	2.1753	0.0079	0.7118	0.0014
G NIST610 55	2.1736	0.0076	0.7098	0.0016
G NIST610 56	2.1701	0.0073	0.7089	0.0014
G NIST610 57	2.1743	0.0074	0.7091	0.0014
G NIST610 58	2.1757	0.0080	0.7110	0.0015
G NIST610 59	2.1696	0.0078	0.7094	0.0014
G NIST610 60	2.1658	0.0071	0.7106	0.0015
G NIST610 61	2.1621	0.0072	0.7102	0.0017
G NIST610 62	2.1635	0.0072	0.7103	0.0015
G NIST610 63	2.1746	0.0077	0.7110	0.0014
G NIST610 64	2.1552	0.0070	0.7100	0.0014
G NIST610 65	2.1686	0.0073	0.7103	0.0016
G NIST610 66	2.1580	0.0082	0.7093	0.0014



G NIST610 67	2.1592	0.0073	0.7097	0.0017
G NIST610 68	2.1548	0.0083	0.7098	0.0014
G NIST610 69	2.1601	0.0091	0.7100	0.0017
G NIST610 70	2.1511	0.0078	0.7117	0.0015
G NIST610 71	2.1647	0.0075	0.7098	0.0017
G NIST610 72	2.1496	0.0085	0.7100	0.0017
G NIST610 73	2.1555	0.0081	0.7087	0.0016
G NIST610 74	2.1617	0.0073	0.7099	0.0014
G BCR2G 1	0.3801	0.0023	0.7066	0.0018
G BCR2G 2	0.3736	0.0021	0.7054	0.0018
G BCR2G 3	0.3680	0.0020	0.7054	0.0023
G BCR2G 4	0.3678	0.0020	0.7055	0.0026
G BCR2G 5	0.3736	0.0021	0.7046	0.0026
G BCR2G 6	0.3719	0.0024	0.7049	0.0022
G BCR2G 7	0.3636	0.0021	0.7052	0.0026
G BCR2G 8	0.3769	0.0023	0.7074	0.0024
G BCR2G 9	0.3629	0.0020	0.7051	0.0024
G BCR2G 10	0.3666	0.0020	0.7046	0.0020
G BCR2G 11	0.3633	0.0023	0.7044	0.0022
G BCR2G 12	0.3607	0.0024	0.7059	0.0024
G BCR2G 13	0.3634	0.0022	0.7037	0.0025
G BCR2G 14	0.3694	0.0025	0.7076	0.0029
G BCR2G 15	0.3580	0.0023	0.7059	0.0028
G BCR2G 16	0.3759	0.0023	0.7053	0.0029
G BCR2G 17	0.3630	0.0022	0.7043	0.0024
G BCR2G 18	0.3639	0.0021	0.7053	0.0023
G BCR2G 19	0.3624	0.0019	0.7051	0.0020
G BCR2G 20	0.3623	0.0024	0.7061	0.0025
G BCR2G 21	0.3622	0.0022	0.7071	0.0023
G BCR2G 22	0.3664	0.0025	0.7045	0.0024
G BCR2G 23	0.3540	0.0028	0.7044	0.0026
G BCR2G 24	0.3676	0.0023	0.7059	0.0028
G BCR2G 25	0.3643	0.0022	0.7057	0.0022
G BCR2G 26	0.3666	0.0024	0.7051	0.0020
G BCR2G 27	0.3600	0.0020	0.7045	0.0023
G BCR2G 28	0.3624	0.0021	0.7031	0.0025
G BCR2G 29	0.3640	0.0019	0.7073	0.0022
G BCR2G 30	0.3676	0.0022	0.7049	0.0024
G BCR2G 31	0.3565	0.0022	0.7050	0.0028
G BCR2G 32	0.3537	0.0022	0.7042	0.0023
G BCR2G 33	0.3632	0.0021	0.7075	0.0022
G BCR2G 34	0.3645	0.0020	0.7045	0.0024
G BCR2G 35	0.3617	0.0020	0.7057	0.0020
G BCR2G 36	0.3608	0.0023	0.7062	0.0024

G BCR2G 37	0.3631	0.0024	0.7056	0.0026
G BCR2G 38	0.3660	0.0021	0.7055	0.0027
G BCR2G 39	0.3512	0.0024	0.7065	0.0025
G BCR2G 40	0.3620	0.0024	0.7055	0.0023
G BCR2G 41	0.3652	0.0025	0.7071	0.0023
G BCR2G 42	0.3627	0.0022	0.7069	0.0023
G BCR2G 43	0.3592	0.0021	0.7042	0.0026
G BCR2G 44	0.3629	0.0024	0.7057	0.0024
G BCR2G 45	0.3638	0.0024	0.7040	0.0021
G BCR2G 46	0.3635	0.0022	0.7061	0.0022
G BCR2G 47	0.3540	0.0024	0.7048	0.0022
G BCR2G 48	0.3709	0.0027	0.7059	0.0023
G BCR2G 49	0.3625	0.0028	0.7028	0.0026
G BCR2G 50	0.3632	0.0023	0.7069	0.0025
G BCR2G 51	0.3617	0.0024	0.7063	0.0020
G BCR2G 52	0.3618	0.0022	0.7039	0.0021
G BCR2G 53	0.3634	0.0021	0.7034	0.0022
G BCR2G 54	0.3731	0.0021	0.7062	0.0027
G BCR2G 55	0.3602	0.0022	0.7066	0.0021
G BCR2G 56	0.3700	0.0021	0.7071	0.0023
G BCR2G 57	0.3820	0.0018	0.7074	0.0019
G BCR2G 58	0.3770	0.0020	0.7067	0.0019
G BCR2G 59	0.3752	0.0022	0.7047	0.0021
G BCR2G 60	0.3639	0.0021	0.7062	0.0019
G BCR2G 61	0.3715	0.0023	0.7066	0.0025
G BCR2G 62	0.3721	0.0024	0.7053	0.0027
G BCR2G 63	0.3609	0.0027	0.7063	0.0025
G BCR2G 64	0.3729	0.0024	0.7054	0.0023
G BCR2G 65	0.3638	0.0024	0.7052	0.0025
G BCR2G 66	0.3611	0.0021	0.7050	0.0027
G BCR2G 67	0.3676	0.0022	0.7054	0.0025
G BCR2G 68	0.3622	0.0023	0.7039	0.0026
G BCR2G 69	0.3629	0.0024	0.7055	0.0025
G BCR2G 70	0.3719	0.0022	0.7058	0.0021
G BCR2G 71	0.3621	0.0025	0.7052	0.0021
G BCR2G 72	0.3675	0.0024	0.7071	0.0024
G BCR2G 73	0.3660	0.0022	0.7049	0.0024
G BCR2G 74	0.3638	0.0023	0.7076	0.0023
IlliteJF - 1.csv	4.2854	0.2570	0.7326	0.0194
IlliteJF - 10.csv	5.6070	0.2160	0.7431	0.0218
IlliteJF - 11.csv	4.4929	0.2028	0.7224	0.0222
IlliteJF - 11.csv	4.3103	0.1819	0.7267	0.0184
IlliteJF - 12.csv	7.5229	0.4041	0.7251	0.0247
IlliteJF - 12.csv	5.9830	0.3647	0.7405	0.0196

IlliteJF - 13.csv	6.4907	0.3337	0.7414	0.0243
IlliteJF - 13.csv	7.3991	0.3144	0.7681	0.0487
IlliteJF - 14.csv	6.1643	0.2494	0.7409	0.0184
IlliteJF - 15.csv	5.1490	0.2181	0.7467	0.0261
IlliteJF - 15.csv	6.4032	0.2484	0.7438	0.0262
IlliteJF - 16.csv	5.3786	0.2583	0.6412	0.0249
IlliteJF - 17.csv	5.7896	0.2246	0.7349	0.0178
IlliteJF - 18.csv	4.1977	0.1664	0.7251	0.0182
IlliteJF - 19.csv	4.1505	0.1962	0.7193	0.0169
IlliteJF - 19.csv	6.3418	0.2744	0.7417	0.0206
IlliteJF - 2.csv	6.3192	0.2794	0.7768	0.0427
IlliteJF - 2.csv	5.4951	0.2958	0.7383	0.0220
IlliteJF - 20.csv	6.1977	0.3320	0.7420	0.0212
IlliteJF - 20.csv	6.1475	0.2853	0.7416	0.0217
IlliteJF - 21.csv	6.5100	0.2466	0.7516	0.0200
IlliteJF - 22.csv	6.7751	0.2929	0.7320	0.0176
IlliteJF - 23.csv	4.2361	0.1686	0.7263	0.0183
IlliteJF - 23.csv	4.2779	0.1821	0.7103	0.0223
IlliteJF - 24.csv	6.2196	0.3280	0.7508	0.0242
IlliteJF - 24.csv	6.0646	0.2673	0.7472	0.0208
IlliteJF - 25.csv	6.2106	0.3949	0.7590	0.0324
IlliteJF - 25.csv	6.2492	0.2887	0.7185	0.0243
IlliteJF - 26.csv	4.8047	0.2235	0.7332	0.0188
IlliteJF - 27.csv	5.0793	0.2028	0.7242	0.0170
IlliteJF - 27.csv	6.1098	0.2462	0.7390	0.0280
IlliteJF - 28.csv	2.8092	0.1831	0.7194	0.0171
IlliteJF - 28.csv	5.5015	0.3319	0.7298	0.0187
IlliteJF - 28.csv	3.7701	0.1600	0.7274	0.0259
IlliteJF - 29.csv	6.2776	0.2311	0.7407	0.0247
IlliteJF - 3.csv	6.3300	0.2810	0.7257	0.0195
IlliteJF - 30.csv	5.1016	0.2422	0.7396	0.0192
IlliteJF - 30.csv	7.0077	0.2779	0.7372	0.0194
IlliteJF - 31.csv	7.1889	0.2838	0.7448	0.0245
IlliteJF - 32.csv	3.5284	0.2006	0.7303	0.0348
IlliteJF - 32.csv	5.4447	0.2407	0.7421	0.0196
IlliteJF - 33.csv	6.4102	0.2315	0.7280	0.0179
IlliteJF - 34.csv	6.8137	0.2540	0.7383	0.0206
IlliteJF - 35.csv	5.5027	0.2424	0.7488	0.0286
IlliteJF - 35.csv	6.6528	0.2555	0.7381	0.0182
IlliteJF - 36.csv	2.6244	0.1057	0.7207	0.0169
IlliteJF - 36.csv	3.7374	0.1748	0.7243	0.0216
IlliteJF - 37.csv	3.1399	0.1270	0.7241	0.0171
IlliteJF - 37.csv	2.2594	0.1334	0.7355	0.0189
IlliteJF - 38.csv	2.4668	0.1057	0.7173	0.0157
IlliteJF - 38.csv	3.1573	0.1377	0.7225	0.0193

IlliteJF - 39.csv	3.8937	0.1504	0.7266	0.0171
IlliteJF - 4.csv	5.2150	0.2842	0.7195	0.0165
IlliteJF - 40.csv	4.9665	0.1979	0.7439	0.0188
IlliteJF - 41.csv	6.3256	0.2711	0.7201	0.0182
IlliteJF - 42.csv	5.3524	0.2009	0.7405	0.0164
IlliteJF - 43.csv	7.0198	0.3115	0.7345	0.0296
IlliteJF - 44.csv	3.1976	0.1457	0.7180	0.0221
IlliteJF - 44.csv	5.2297	0.2955	0.7371	0.0210
IlliteJF - 45.csv	3.6450	0.2540	0.7240	0.0174
IlliteJF - 46.csv	4.9252	0.2259	0.7349	0.0186
IlliteJF - 47.csv	5.2174	0.2467	0.7403	0.0168
IlliteJF - 48.csv	4.2260	0.2194	0.7312	0.0167
IlliteJF - 49.csv	6.7729	0.2430	0.7409	0.0188
IlliteJF - 5.csv	6.9869	0.3122	0.7510	0.0189
IlliteJF - 50.csv	1.2011	0.0924	0.7171	0.0144
IlliteJF - 51.csv	5.9497	0.2652	0.7413	0.0180
IlliteJF - 52.csv	4.9289	0.2541	0.7327	0.0180
IlliteJF - 53.csv	6.2665	0.2618	0.7418	0.0176
IlliteJF - 54.csv	5.0848	0.2301	0.7306	0.0172
IlliteJF - 55.csv	3.4876	0.2866	0.7303	0.0169
IlliteJF - 56.csv	3.9731	0.2715	0.7299	0.0160
IlliteJF - 57.csv	6.4215	0.3127	0.7394	0.0165
IlliteJF - 58.csv	5.2557	0.2534	0.7337	0.0193
IlliteJF - 59.csv	6.5040	0.2613	0.7312	0.0176
IlliteJF - 6.csv	8.4503	0.3476	0.7460	0.0198
IlliteJF - 60.csv	8.9257	0.4294	0.7436	0.0201
IlliteJF - 61.csv	6.3686	0.2212	0.7311	0.0164
IlliteJF - 62.csv	7.6369	0.2973	0.7478	0.0184
IlliteJF - 63.csv	5.2740	0.2021	0.7276	0.0175
IlliteJF - 64.csv	5.2898	0.2510	0.7374	0.0190
IlliteJF - 65.csv	3.9187	0.3212	0.7231	0.0163
IlliteJF - 66.csv	3.5071	0.2083	0.7221	0.0155
IlliteJF - 67.csv	6.7440	0.2917	0.7368	0.0227
IlliteJF - 68.csv	6.0048	0.3201	0.7462	0.0203
IlliteJF - 69.csv	6.0798	0.2524	0.7319	0.0175
IlliteJF - 7.csv	7.0296	0.2562	0.7449	0.0211
IlliteJF - 70.csv	6.4952	0.2742	0.7356	0.0211
IlliteJF - 71.csv	8.9787	0.5085	0.7659	0.0191
IlliteJF - 72.csv	3.3179	0.2600	0.7342	0.0224
IlliteJF - 73.csv	6.8353	0.2628	0.7362	0.0174
IlliteJF - 74.csv	6.3457	0.2942	0.7365	0.0176
IlliteJF - 75.csv	5.5988	0.4109	0.7513	0.0272
IlliteJF - 76.csv	7.4983	0.3241	0.7475	0.0189
IlliteJF - 77.csv	6.6560	0.3876	0.7351	0.0214
IlliteJF - 78.csv	6.7550	0.2546	0.7428	0.0174

llliteJF - 79.csv		2.8931		0.1723		0.7262		0.0319
llliteJF - 8.csv		4.7688		0.1994		0.7391		0.0208
llliteJF - 8.csv		6.2147		0.2724		0.7535		0.0306
llliteJF - 80.csv		4.5709		0.2776		0.7259		0.0188
llliteJF - 9.csv		3.7774		0.1917		0.7193		0.0175
llliteJF - 9.csv		4.3434		0.1589		0.7249		0.0175

**Table S.2.1.** Laser data of standards used in Chapter 2.

u6-269-3 -	u6-269-3 -	u6-269-3 -	u6-269-3 -	u6-269-3 -	u6-269-3 -	u6-269-3 -	u6-269-3 -	u6-269-3 -	u6-269-3 -	u6-269-3 -	u6-269-3 -	u6-269-3 -	u6-269-3 -	u6-269-3 -	u6-269-3 -	u6-269-3 -	u6-269-3 -	u6-269-3 -	u6-269-3 -
551010.00	638137.00	508031.00	471219.00	347994.00	419340.00	439022.00	356929.00	493037.00	La CPS										
24306.60	25205.00	17436.50	25103.30	25562.40	15557.70	33530.50	25863.50	26355.10	La CPS 2SE										
1122710.00	1315250.00	1012920.00	952364.00	689609.00	865563.00	926671.00	680455.00	1020850.00	Ce CPS										
58348.80	64262.20	33303.90	47987.20	47622.70	34944.50	80421.60	36473.60	73379.00	Ce CPS 2SE										
148581.00	170357.00	137386.00	127500.00	91260.90	114850.00	119326.00	94123.30	141976.00	Pr CPS										
6733.27	6800.30	5134.59	6392.89	6279.64	5091.35	8987.68	5912.35	9813.65	Pr CPS 2SE										
93318.50	106957.00	85404.90	82777.30	59356.20	73842.00	72893.00	59583.50	92411.20	Nd CPS										
4663.10	4501.96	3462.27	4721.48	4398.16	3487.65	5361.30	3398.64	6865.94	Nd CPS 2SE										
14944.20	16483.80	13477.00	12357.60	8836.18	11459.20	11675.40	10487.10	15027.40	Sm CPS										
881.09	686.12	649.03	800.60	671.13	597.01	1138.08	700.53	1216.53	Sm CPS 2SE										
8615.08	9813.03	8172.11	6980.89	5439.79	7060.21	6318.04	6940.16	8082.21	Eu CPS										
508.30	487.63	396.01	444.68	430.59	424.89	451.25	453.11	463.00	Eu CPS 2SE										
9605.71	11529.60	9645.06	7009.20	5639.67	7896.88	7049.96	8437.94	8660.99	Gd Cps										
581.84	747.35	523.21	438.01	380.31	525.40	527.59	532.04	410.03	Gd CPS 2SE										
9479.10	11165.60	10629.00	6096.01	5382.78	7854.76	6879.20	9705.37	8023.04	Tb CPS										
526.73	958.24	684.95	393.23	385.85	594.42	400.39	789.39	369.22	Tb CPS 2SE										
14577.20	16388.30	16145.30	9048.05	8240.47	11784.50	10794.30	15349.80	11480.50	Dy CPS										
816.23	1380.13	1256.61	549.63	553.97	913.88	607.88	1168.64	560.74	Dy CPS 2SE										
10920.80	12604.40	12725.20	7061.68	6374.82	9682.66	8292.92	12306.80	8793.40	Ho CPS										
619.52	1091.28	971.31	451.32	458.41	870.49	454.53	950.13	453.55	Ho CPS 2SE										
11869.90	13555.30	13991.20	7241.54	7142.73	9454.67	8421.01	12612.50	9473.77	Er CPS										
705.30	1249.60	1116.01	437.62	560.89	814.97	482.28	1011.95	564.03	Er CPS 2SE										
8251.90	8265.25	8382.94	4819.48	4832.70	6501.25	5783.21	8540.74	5988.98	Yb CPS										
516.38	651.15	588.15	308.11	359.23	526.23	365.64	667.82	361.31	Yb CPS 2SE										
5784.30	6142.28	5897.31	3440.46	3560.59	4560.42	4292.43	6182.13	4365.38	Lu CPS										
405.12	497.23	429.10	246.69	307.04	438.33	284.79	512.13	244.36	Lu CPS 2SE										
7.30	7.45	9.27	8.51	10.07	9.91	9.61	9.52	9.52	Rb87/Sr86										
0.19	0.17	0.21	0.25	0.36	0.30	0.17	0.23	0.23	Rb87/Sr86 2S										
0.87	0.87	0.91	0.90	0.93	0.92	0.92	0.92	0.91	Sr87/Sr86										
0.01	0.01	0.01	0.01	0.01	0.01	0.01	0.01	0.01	Sr87/Sr86 2S										

u6-269-3 -	u6-269-3 -	u6-269-3 -	u6-269-3 -	u6-269-3 -	u6-269-3 -	u6-269-3 -	u6-269-3 -	u6-269-3 -	u6-269-3 -	u6-269-3 -	u6-269-3 -	u6-269-3 -	u6-269-3 -	u6-269-3 -	u6-269-3 -	u6-269-3 -	u6-269-3 -
575037.00	413170.00	543336.00	607377.00	697739.00	905533.00	507433.00	389312.00	323263.00	295066.00	365443.00	1065760.00						
52801.90	10454.20	20218.50	25419.50	108475.00	113344.00	30079.20	20863.60	18081.90	14937.70	12642.90	122793.00						
1225550.00	833852.00	1067820.00	1245750.00	1540970.00	1846650.00	1011420.00	804483.00	648029.00	595852.00	740730.00	2197450.00						
119103.00	23991.00	34304.40	59453.40	265542.00	237887.00	61953.50	46157.60	34805.30	29789.00	22078.60	255345.00						
159857.00	107965.00	144141.00	165780.00	198867.00	232488.00	136071.00	111093.00	91666.90	80285.40	94607.50	260559.00						
14068.70	3223.94	5094.00	7306.36	33317.60	26818.90	7622.92	6472.92	5847.52	4396.11	2538.67	27468.80						
105718.00	66515.70	90736.10	103015.00	132865.00	145968.00	85850.90	71359.50	57802.10	49903.30	60313.20	161046.00						
9551.92	1516.90	3374.21	5019.73	23205.60	17578.30	5532.25	4175.05	3653.30	3078.91	1760.41	16031.70						
20211.80	9842.40	13792.00	15666.90	20245.30	21148.60	13769.60	11746.30	9768.71	8360.39	9434.99	23599.70						
2499.85	357.26	576.69	914.78	3728.36	2453.62	916.87	745.18	674.23	563.90	400.96	2358.44						
15597.30	5890.49	7896.03	8754.67	10445.80	11064.50	8267.02	7020.23	5942.47	4757.36	5568.11	12461.10						
2695.42	264.89	366.38	527.96	1751.05	1058.76	454.48	373.51	499.51	377.12	322.05	1218.26						
33005.30	6524.15	8779.82	8797.22	9730.54	10516.00	10415.70	8135.27	6566.94	4939.01	6236.51	12562.50						
8580.02	321.44	381.26	475.66	1340.12	871.78	531.67	472.42	543.46	353.41	332.82	922.57						
47547.30	6299.87	8623.62	7624.54	6860.66	8600.54	10351.90	8601.20	6633.75	4518.51	5988.28	10542.20						
13914.80	268.79	420.15	405.88	541.65	488.90	556.01	693.06	655.33	334.97	402.09	608.56						
72135.30	9552.86	12977.00	11699.40	8265.56	12171.80	16063.10	13316.10	9960.23	6679.69	9735.65	15735.10						
22066.40	372.16	580.01	608.06	494.18	514.39	928.68	925.42	1025.34	495.18	726.24	944.85						
57221.90	7362.15	9963.93	9133.11	6323.20	9126.46	12414.20	9931.87	8052.73	5473.13	7400.29	11565.90						
17158.10	361.32	467.52	504.52	387.20	348.85	690.29	622.86	865.46	452.54	488.08	657.68						
50359.30	7717.60	10117.50	9379.76	6236.61	9715.64	12269.40	10864.40	8399.84	5335.63	7839.88	11425.20						
14810.30	372.01	462.28	546.93	275.14	429.91	593.24	817.37	952.68	351.38	488.98	524.94						
27511.70	5209.96	6331.88	6238.32	4513.13	6566.59	7602.01	7156.39	5709.29	3622.95	5234.51	7798.57						
6840.29	282.01	345.92	338.13	325.14	359.67	427.52	517.11	589.08	290.08	385.86	359.63						
19879.30	3624.51	4550.75	4730.88	3256.77	4635.12	5420.16	5292.09	4972.05	2616.30	3875.93	5413.05						
4757.50	181.44	255.29	302.08	219.07	246.09	295.27	433.51	695.73	210.57	281.12	259.39						
8.67	9.42	8.73	7.76	9.79	8.52	8.98	11.10	11.52	11.05	9.53	6.81						
0.46	0.15	0.18	0.17	0.48	0.24	0.27	0.38	0.35	0.26	0.23	0.16						
0.90	0.91	0.90	0.87	0.93	0.90	0.90	0.95	0.97	0.95	0.93	0.86						
0.01	0.01	0.01	0.01	0.01	0.01	0.01	0.01	0.01	0.01	0.01	0.01						

u6-269-3 -	u6-269-3 -	u6-269-3 -	u6-269-3 -	u6-269-3 -	u6-269-3 -	u6-269-3 -	u6-269-3 -	u6-269-3 -	u6-269-3 -	u6-269-3 -	u6-269-3 -	u6-269-3 -	u6-269-3 -	u6-269-3 -
386885.00	454502.00	356615.00	562408.00	507372.00	579161.00	650790.00	577695.00	339174.00	558211.00	628155.00	695977.00			
18166.80	24112.60	21657.90	29345.80	34041.50	16925.80	31557.40	22314.80	10897.60	20604.00	26754.10	34799.90			
798906.00	938137.00	730441.00	1173290.00	1033260.00	1192270.00	1402690.00	1176430.00	678445.00	1113230.00	1325360.00	1481480.00			
35797.90	54534.90	48140.40	68557.80	71168.00	38446.40	87828.10	45307.10	21757.80	38431.90	69773.20	94877.50			
108674.00	127052.00	101992.00	151865.00	134299.00	156229.00	186905.00	153128.00	88527.60	150123.00	174734.00	194880.00			
4609.66	7673.00	8088.83	8108.05	8752.31	5223.29	12462.30	6006.23	3036.75	5989.72	8034.64	11731.20			
68510.40	81059.30	65025.60	96226.20	83374.00	97967.00	122393.00	96472.20	57120.90	91858.50	111831.00	126408.00			
2826.69	5265.19	5073.76	5458.72	5227.88	3106.37	8804.15	3796.63	2050.32	3144.83	5430.49	8882.15			
10921.20	12465.60	10518.00	14463.30	12695.80	15322.10	18872.00	14153.40	9031.51	14500.10	17696.80	19043.50			
519.30	846.60	1001.98	818.67	812.84	602.83	1524.94	689.25	432.59	546.47	1029.80	1441.12			
6189.37	7294.83	6099.61	8249.13	7071.04	8701.51	11022.90	8315.87	5581.35	8557.46	9697.74	10917.90			
299.66	476.58	586.60	474.16	515.79	396.83	915.24	419.40	276.49	427.47	545.19	855.44			
6632.27	8040.77	6987.38	10090.90	7707.78	9405.77	11842.60	9041.41	6159.48	10189.90	11816.90	12201.30			
300.03	486.81	671.87	548.19	527.71	443.62	953.21	491.58	268.49	525.67	720.08	1021.39			
6113.23	7964.37	6440.02	9699.95	7418.24	8798.87	11263.90	8749.78	6652.89	10289.20	11956.50	11504.20			
317.75	493.19	590.13	556.92	560.81	420.90	1028.37	597.95	365.96	617.84	910.00	1103.59			
9290.61	11798.80	9835.17	14789.40	11139.40	13362.50	16914.40	13757.60	10466.70	15362.60	17813.40	17870.50			
584.76	635.59	988.19	925.28	923.75	633.59	1610.03	1066.11	605.57	842.94	1314.95	1886.19			
6843.80	9187.11	7701.84	11746.80	8921.21	10611.00	13354.30	11431.80	8573.61	12192.90	14039.40	13155.10			
387.29	552.86	814.68	721.59	673.24	577.74	1386.35	1095.82	493.45	750.78	959.42	1247.91			
7251.72	9231.00	7879.03	12025.10	8686.98	11257.50	13765.10	11828.80	8518.27	13674.00	14295.90	14461.30			
438.72	464.65	718.15	746.37	667.28	582.66	1332.00	1183.96	459.04	1009.47	944.61	1685.76			
5067.81	6108.59	5078.96	7764.06	5969.70	7512.99	8298.88	7441.43	5856.01	8779.82	9039.52	9138.99			
328.44	349.69	441.94	529.37	415.26	446.16	699.36	632.67	349.73	625.34	510.56	871.40			
3698.37	4466.04	3430.75	5856.75	4056.27	5623.23	5781.42	5307.90	4302.07	6133.27	6286.67	6943.45			
245.52	274.53	292.77	458.26	295.37	380.73	429.66	387.69	284.46	461.75	365.69	675.36			
9.29	9.52	11.19	8.41	8.80	8.16	8.03	8.34	12.83	8.51	8.47	7.74			
0.25	0.27	0.19	0.39	0.27	0.17	0.26	0.11	0.34	0.12	0.21	0.20			
0.91	0.91	0.96	0.89	0.90	0.89	0.88	0.89	0.98	0.89	0.88	0.87			
0.01	0.01	0.01	0.01	0.01	0.01	0.01	0.01	0.01	0.01	0.01	0.01			

u6-269-3 -	u6-269-3 -	u6-269-3 -	u6-269-3 -	u6-269-3 -	u6-269-3 -	u6-269-3 -	u6-269-3 -	u6-269-3 -	u6-269-3 -	u6-269-3 -	u6-269-3 -	u6-269-3 -	u6-269-3 -	u6-269-3 -	u6-269-3 -	u6-269-3 -	u6-269-3 -	u6-269-3 -
280159.00	451968.00	439324.00	595188.00	520400.00	530911.00	475309.00	240045.00	309562.00	734828.00	588037.00	291405.00							
20265.40	37279.80	28346.60	32664.30	31100.30	23577.20	26728.90	10234.50	18806.70	91075.30	21345.70	14064.30							
608419.00	877174.00	877081.00	1225810.00	1078480.00	1070710.00	974781.00	503782.00	662060.00	1453830.00	1161530.00	588368.00							
47106.50	65872.50	55090.40	75835.80	75377.60	50575.40	57002.60	20687.50	42203.90	164081.00	38129.10	25242.00							
77606.90	120586.00	119079.00	162187.00	149591.00	143008.00	128308.00	67615.40	89035.60	187264.00	151941.00	77217.60							
6171.05	9231.31	7964.50	10019.20	11445.00	6470.54	7880.76	3072.52	6326.40	18467.50	5104.62	3497.45							
48897.40	79997.50	73741.60	103214.00	96649.80	90215.20	80884.30	43287.40	55410.70	111423.00	92853.70	48153.60							
3796.03	6505.78	4779.27	6590.94	7698.16	4242.49	5311.64	2199.10	3831.80	10509.90	2852.79	2404.55							
7701.48	12850.70	13097.70	16040.30	15699.50	13862.50	12194.50	6750.96	8804.92	16308.30	13620.90	7602.19							
554.91	1210.99	1076.93	1074.68	1476.28	649.64	831.02	366.96	678.09	1458.87	482.86	366.26							
4957.39	7255.72	8979.03	9511.44	8824.57	8203.68	7246.90	4069.67	5291.27	8661.54	7693.90	4416.54							
362.52	610.98	1246.43	678.30	784.89	479.15	522.57	241.88	421.35	635.20	326.72	208.65							
6349.92	8281.91	12097.70	10664.00	8791.27	9721.43	8024.97	4775.80	5966.63	9116.34	8431.73	4909.18							
460.99	762.58	2776.24	814.51	567.11	871.33	607.78	282.00	456.56	614.50	330.59	248.06							
6957.20	7618.31	15184.20	10157.10	7702.29	10147.40	7367.97	4862.21	6091.37	7304.42	8078.43	5286.64							
643.82	764.27	4299.67	739.26	372.47	1014.56	592.91	316.23	444.44	423.66	356.61	378.60							
11731.30	11491.20	26028.00	15045.70	11220.90	15399.10	11860.60	7359.67	9542.48	10687.20	12589.70	8519.09							
1321.59	1233.81	7950.55	1151.18	458.49	1572.89	1035.62	472.70	660.39	721.46	663.87	650.32							
9190.01	9014.48	17644.20	11764.10	8526.69	12217.60	9041.11	5753.42	7492.42	8140.92	9668.46	6675.59							
1218.76	981.30	4910.94	938.37	439.99	1365.17	855.94	383.03	503.58	575.85	567.29	528.13							
9609.75	9143.65	15653.30	12067.10	8907.83	12809.60	9216.55	6070.02	8041.27	8526.00	9689.23	7026.35							
1160.89	1014.13	4038.67	835.42	408.09	1364.00	896.55	452.55	528.36	647.88	531.83	546.06							
6134.16	6078.31	8565.60	7514.67	5924.85	8036.95	6298.03	4057.66	5274.23	5534.53	6235.06	4526.52							
714.50	716.75	1667.32	488.55	349.82	677.91	598.90	271.18	366.89	413.08	329.26	339.83							
4277.92	4282.11	5762.87	5614.94	4294.58	5865.70	4534.28	2811.25	3877.63	4333.74	4478.44	3412.92							
422.60	519.27	1034.73	370.25	234.81	390.05	410.45	201.33	291.69	331.74	218.11	264.88							
11.71	9.50	7.99	8.42	8.09	8.70	8.94	12.91	13.51	9.54	9.15	12.98							
0.18	0.53	0.34	0.13	0.34	0.16	0.34	0.35	0.43	0.27	0.21	0.29							
0.96	0.91	0.89	0.89	0.89	0.90	0.89	0.98	1.01	0.91	0.91	0.98							
0.01	0.01	0.01	0.01	0.01	0.01	0.01	0.01	0.01	0.01	0.01	0.01							



u6-269-3 -	u6-269-3 -	u6-269-3 -	u6-269-3 -	u6-269-3 -	u6-269-3 -	u6-269-3 -	u6-269-3 -	u6-269-3 -	u6-269-3 -	u6-269-3 -	u6-269-3 -	u6-269-3 -	u6-269-3 -	u6-269-3 -	u6-269-3 -	u6-269-3 -	
331207.00	245263.00	1067410.00	540267.00	568291.00	808291.00	516448.00	756745.00	746409.00	458381.00	473435.00	312089.00						
17069.60	11869.20	195045.00	33445.60	28017.60	50282.20	20539.40	42388.60	118074.00	20913.80	20137.90	36253.70						
682796.00	517185.00	2247360.00	1140190.00	1196850.00	1765440.00	1101180.00	1634490.00	1623760.00	913472.00	981163.00	597106.00						
33482.60	241136.90	408939.00	78959.40	66880.70	148418.00	60139.20	100913.00	259383.00	41718.90	49973.20	46992.50						
91576.60	70051.50	294459.00	153536.00	156207.00	210086.00	145875.00	209777.00	203041.00	125399.00	130837.00	81841.80						
4804.77	3885.11	50635.30	9783.10	8373.66	15552.00	7606.82	12162.40	31047.60	5718.09	6382.54	7141.77						
57170.70	44853.00	194773.00	104242.00	98196.50	130307.00	94288.20	133381.00	127242.00	78128.30	81503.30	52075.80						
2876.10	2468.00	34088.90	8418.09	5076.14	10151.10	5131.59	7934.89	19109.90	3506.36	3745.83	4433.26						
9328.01	8773.78	28270.00	15680.10	15261.60	20084.90	14163.50	19228.20	18236.80	12671.90	12741.00	8660.49						
472.53	771.31	4717.36	1214.80	904.00	1822.84	849.24	1021.09	2552.35	716.61	648.72	807.46						
5950.45	6094.54	14940.60	8509.98	9233.81	11035.70	8830.71	10154.30	9366.78	8205.60	7272.24	5058.31						
327.79	733.21	2288.34	577.39	554.30	940.37	605.10	457.24	1297.08	624.40	429.88	380.76						
7239.72	10188.70	13737.50	9144.39	9980.48	12217.60	10521.50	10463.80	8837.89	10410.20	8361.00	5179.78						
432.03	1942.16	1871.45	577.46	653.74	1110.68	974.72	451.94	1085.35	1131.95	631.02	311.98						
8908.32	13129.90	9111.72	8109.21	9754.13	12226.50	10449.40	9267.44	6408.04	11073.00	7948.28	5143.03						
570.16	2853.29	813.58	381.48	917.03	1085.61	1263.20	469.30	609.41	1539.40	788.83	271.96						
15703.80	24321.40	12046.40	11470.20	15639.50	18280.40	15814.90	13402.40	8561.65	16786.50	13548.40	8011.08						
1293.35	5846.89	697.65	574.07	1549.44	1653.28	1861.04	710.08	783.30	2150.72	1633.73	453.36						
11917.80	16639.90	8764.34	9252.89	11932.10	14052.10	12497.30	10452.20	6446.85	12757.20	9862.64	6111.48						
994.94	3874.40	460.38	454.21	1140.11	1273.64	1605.77	567.21	520.71	1574.75	1069.54	373.66						
12627.90	16611.00	9035.65	9201.70	12872.50	14629.50	11806.10	10934.10	6552.68	14110.20	10913.50	6574.28						
978.84	3736.03	446.00	433.91	1222.63	1312.26	1212.00	627.15	493.67	1874.72	1316.62	431.63						
7689.16	9724.24	6093.18	6074.64	7944.04	9570.59	7704.55	7107.77	4618.90	9362.24	6892.84	4517.04						
596.19	1939.80	296.92	349.46	672.13	905.54	722.06	365.09	410.27	1239.60	714.73	331.69						
5259.89	5514.31	4276.06	4244.52	5779.86	6783.93	5281.01	5160.12	3117.66	6561.80	4639.76	3244.83						
417.05	890.82	232.62	246.53	579.22	615.08	458.99	267.27	282.91	802.34	415.21	242.63						
12.24	13.86	8.45	9.97	9.23	6.85	8.45	6.87	8.44	8.55	9.63	11.77						
0.41	0.29	0.42	0.58	0.23	0.17	0.13	0.25	0.76	0.13	0.21	0.21						
0.98	1.01	0.89	0.93	0.90	0.85	0.89	0.86	0.90	0.90	0.92	0.96						
0.01	0.01	0.01	0.01	0.01	0.01	0.01	0.01	0.02	0.01	0.01	0.01						

u5-139-95 -		u6-269-3 -	u6-269-3 -	u6-269-3 -	u6-269-3 -	u6-269-3 -	u6-269-3 -	u6-269-3 -	u6-269-3 -	u6-269-3 -	u6-269-3 -	u6-269-3 -
24193.40	La CPS	454822.00	507561.00	514768.00	439370.00	469782.00	528972.00	640958.00	620492.00	255841.00	460052.00	
4364.55	La CPS 25E	18304.70	55651.90	50825.10	12041.90	21615.10	26695.40	45072.40	25926.90	9672.34	10773.90	
55578.40	Ce CPS	918296.00	1127370.00	1132740.00	905389.00	909344.00	1090000.00	1304920.00	1251150.00	527600.00	922399.00	
8414.19	Ce CPS 25E	36654.70	152504.00	137404.00	29942.50	363550.90	61135.20	92166.30	52339.40	17608.00	21187.90	
9204.04	Pr CPS	123236.00	143102.00	147799.00	123368.00	123575.00	145370.00	176998.00	167707.00	69645.50	122864.00	
1436.89	Pr CPS 25E	4985.67	17463.30	17207.40	4814.44	4914.02	7938.33	12813.70	6600.25	2583.31	2893.88	
7718.51	Nd CPS	78976.90	94857.00	92978.70	78101.30	76672.40	95436.00	117488.00	105391.00	43491.10	80103.10	
1107.25	Nd CPS 25E	3555.89	11838.20	10763.60	3096.78	3078.96	5814.68	8783.68	4007.60	1571.30	2073.80	
2516.23	Sm CPS	13119.60	15188.80	16209.30	12701.40	12053.00	13873.10	18448.10	16672.10	6987.23	12289.70	
248.73	Sm CPS 25E	1058.98	1638.54	2295.14	841.69	558.86	851.02	1497.36	697.85	335.71	385.46	
2214.59	Eu CPS	8952.74	8533.76	8176.96	7981.48	7490.38	7649.05	10178.00	9701.04	4141.03	7250.04	
201.11	Eu CPS 25E	1098.12	936.46	1055.13	710.52	490.28	455.44	715.32	454.96	250.81	338.12	
3784.07	Gd CPS	13328.10	11278.30	9002.45	9342.05	8317.11	7506.88	11560.10	11790.90	4932.49	8857.51	
338.81	Gd CPS 25E	3047.49	1986.19	1068.71	1116.53	535.48	420.60	922.89	575.27	315.66	488.51	
6275.82	Tb CPS	20587.90	11486.90	8189.35	9541.97	8525.90	6336.11	9545.76	12272.90	4739.37	10728.00	
554.84	Tb CPS 25E	6700.00	2985.87	714.27	1563.66	639.66	284.06	801.08	822.15	339.03	1063.09	
11355.20	Dy CPS	30996.10	15700.60	13177.40	14634.90	13773.80	9045.43	13372.00	18112.90	7268.13	16718.10	
858.07	Dy CPS 25E	9692.45	4296.49	1253.85	2464.38	1175.81	358.18	1430.67	1229.57	521.68	1665.66	
8733.89	Ho CPS mea	27948.00	9214.00	10153.30	13103.30	10808.90	7152.13	9953.27	13598.20	5974.58	12276.80	
715.58	Ho CPS 25E	8807.43	1492.99	981.62	2785.06	882.76	262.63	1049.06	919.97	521.74	1249.54	
8644.81	Er CPS	19196.80	8898.63	9840.42	13445.40	10817.60	7590.34	10269.20	13775.40	6165.55	12368.60	
665.78	Er CPS 25E	4817.11	1471.94	811.65	2594.00	863.80	277.45	912.32	977.76	533.80	1036.96	
5123.25	Yb CPS	10897.00	5393.15	6515.63	7898.54	7239.06	4858.45	6763.45	9020.30	3921.51	8226.88	
412.49	Yb CPS 25E	2249.77	552.14	542.44	1453.37	606.70	193.64	498.54	705.57	291.05	665.61	
3609.31	Lu CPS	8404.46	3802.50	4292.73	5904.69	4953.76	3596.81	4538.25	5965.54	2980.90	5383.54	
284.37	Lu CPS 25E	1717.54	402.60	285.68	1118.28	458.85	165.12	320.60	436.73	244.37	404.64	
34.81	Rb87Sr86	9.73	9.11	8.96	8.88	9.91	8.32	8.29	8.46	19.03	9.63	
0.37	Rb87Sr86 2S	0.21	0.17	0.18	0.15	0.16	0.29	0.36	0.33	0.85	0.15	
1.35	Sr87 Sr86	0.93	0.91	0.91	0.91	0.92	0.90	0.89	0.89	1.14	0.92	
0.01	Sr87 Sr86 2S	0.01	0.01	0.01	0.01	0.01	0.01	0.01	0.01	0.02	0.01	

u5-139-95 -	u5-139-95 -	u5-139-95 -	u5-139-95 -	u5-139-95 -	u5-139-95 -	u5-139-95 -	u5-139-95 -	u5-139-95 -	u5-139-95 -	u5-139-95 -	u5-139-95 -	u5-139-95 -	u5-139-95 -
31749.70	69046.40	32392.40	35436.40	40651.90	42571.50	28848.60	36401.50	127528.00	41422.40	76391.20	41422.40	56749.10	56749.10
5354.74	18073.90	7543.50	5984.01	6376.43	5055.39	2415.67	5195.24	41955.30	7762.63	17190.20	7762.63	10702.10	10702.10
78519.70	145733.00	71701.40	84731.20	99376.00	102639.00	71053.90	87159.10	315316.00	91828.20	158800.00	91828.20	131942.00	131942.00
11850.00	36428.30	13479.80	14194.40	14429.50	11639.00	5465.58	12276.60	107626.00	14629.80	31169.40	14629.80	25083.20	25083.20
11829.10	21220.40	11173.90	13720.50	15630.50	16917.60	11164.60	13977.40	46626.20	13937.80	23302.50	13937.80	22922.10	22922.10
1837.34	5150.53	2137.81	2215.85	2265.55	2051.76	856.21	1925.40	15140.70	2176.67	4395.18	2176.67	4712.91	4712.91
9064.80	15258.10	8650.94	10342.20	11729.80	12725.30	8755.68	10296.10	37008.30	10486.60	17356.20	10486.60	13878.30	13878.30
1220.64	3508.13	1584.61	1563.27	1481.97	1430.92	596.79	1279.20	12033.00	1489.16	2968.07	1489.16	2424.78	2424.78
2533.19	3221.27	2326.71	3022.39	3096.25	3320.54	2906.89	2803.54	9363.15	2804.29	4088.50	2804.29	3518.89	3518.89
247.84	550.35	310.14	298.45	278.52	241.60	213.37	225.66	2788.93	205.55	460.37	205.55	447.49	447.49
2244.43	2623.83	1789.01	2740.66	2535.46	2974.17	2518.12	2687.59	6417.06	2571.93	3198.05	2571.93	2950.26	2950.26
190.12	346.88	191.29	206.74	169.88	224.44	193.10	212.99	1671.77	149.75	245.29	149.75	277.46	277.46
3475.94	3523.08	2921.17	4596.74	4337.31	4630.47	4340.84	4406.66	7330.91	3983.83	5053.61	3983.83	4281.83	4281.83
213.55	333.52	207.16	350.74	374.28	305.96	414.64	323.20	1238.76	218.76	308.35	218.76	293.00	293.00
5492.35	5103.46	4692.78	7823.79	6847.33	7493.20	7190.53	7089.54	9457.02	6736.75	7938.47	6736.75	6473.97	6473.97
278.25	315.51	244.28	504.11	563.76	502.75	705.58	538.60	828.65	297.69	441.87	297.69	334.71	334.71
9442.31	9016.96	8093.45	13701.70	12395.70	12830.70	13779.90	12857.90	15399.80	12191.00	13755.50	12191.00	11793.70	11793.70
437.42	529.10	347.04	806.01	916.01	828.27	1567.66	861.24	847.12	470.76	786.64	470.76	503.27	503.27
7570.63	6863.54	6794.38	10926.60	9708.39	10171.40	11006.70	10350.50	11517.60	9605.62	10878.00	9605.62	8903.76	8903.76
355.44	435.99	294.39	658.01	719.88	658.20	1359.85	728.05	590.43	408.45	772.66	408.45	413.49	413.49
7455.19	6916.14	6525.43	10715.40	9897.38	10015.30	11228.00	10092.60	11272.80	9627.94	10547.00	9627.94	9292.74	9292.74
365.81	448.14	294.46	723.00	822.30	601.15	1424.55	681.09	533.08	365.68	608.29	365.68	391.14	391.14
4404.63	4187.25	4102.33	6430.28	5909.32	6294.23	6402.68	5955.86	6852.26	5689.14	6119.12	5689.14	5575.46	5575.46
221.80	315.75	238.64	438.64	505.58	439.48	710.70	422.86	327.26	234.14	357.39	234.14	270.43	270.43
3161.51	2925.04	2829.98	4641.22	4129.36	4316.56	4717.64	4118.97	4619.24	4044.64	4497.11	4044.64	3844.25	3844.25
204.75	231.36	174.45	324.07	334.27	277.60	538.17	268.54	263.80	203.58	263.01	203.58	211.28	211.28
33.19	32.82	42.60	34.45	33.56	35.16	36.86	34.67	40.60	35.65	34.17	35.65	33.75	33.75
0.51	0.72	2.30	0.47	0.64	0.52	0.37	0.37	1.10	0.76	0.65	0.76	0.82	0.82
1.34	1.32	1.57	1.36	1.34	1.37	1.41	1.37	1.49	1.38	1.35	1.38	1.35	1.35
0.02	0.02	0.05	0.01	0.02	0.02	0.01	0.02	0.03	0.02	0.02	0.02	0.02	0.02



u5-139-95 -	u5-139-95 -	u5-139-95 -	u5-139-95 -	u5-139-95 -	u5-139-95 -	u5-139-95 -	u5-139-95 -	u5-139-95 -	u5-139-95 -	u5-139-95 -	u5-139-95 -	u5-139-95 -	u5-139-95 -	u5-139-95 -	u5-139-95 -	u5-139-95 -	u5-139-95 -	u5-139-95 -	u5-139-95 -
51524.50	18236.10	23989.60	30828.20	36571.30	37824.70	52363.90	22006.80	42871.80	116169.00	46065.20	45334.80								
10455.60	1591.25	5132.42	5006.49	5586.05	4231.94	15327.30	2430.23	4337.23	44534.10	7256.67	10971.00								
113595.00	47051.00	59942.20	76699.40	81089.50	93419.80	133626.00	52245.00	116173.00	267701.00	102943.00	91856.70								
22079.80	3810.87	13069.10	12645.50	12225.80	10020.20	36600.00	5515.05	10138.10	104447.00	15119.30	18987.70								
16261.40	6980.97	8814.96	13085.10	11486.80	13980.10	20577.60	9115.99	17966.80	38452.40	15395.40	14559.60								
2996.67	638.45	1855.78	2314.08	1615.39	1437.33	5560.76	1070.80	1739.11	13977.00	2178.60	3015.30								
12144.70	5617.54	6705.02	10102.70	9499.18	10581.30	13300.30	7329.38	13466.20	27342.60	11431.50	10572.10								
2244.24	448.85	1351.71	1741.83	1424.37	1028.29	3286.26	897.93	1206.97	9977.00	1514.36	2076.43								
2515.48	1904.30	1871.63	3102.87	2384.19	2873.27	3389.19	2364.51	3178.13	5295.13	2792.04	3103.94								
344.33	141.64	265.48	404.87	264.33	216.64	529.77	219.51	217.58	1317.72	310.58	358.97								
2143.59	1838.48	1748.97	2700.17	2157.91	2467.89	2610.51	2252.68	2559.41	4505.43	2402.06	3120.75								
196.39	135.33	168.72	247.51	155.68	156.45	322.15	160.42	165.97	940.35	238.72	376.84								
3095.95	3099.99	2578.59	4806.41	3297.77	3732.96	4365.61	3615.48	3808.56	5550.59	3808.68	4647.30								
259.93	242.22	196.21	368.28	200.61	242.95	416.64	217.35	229.57	837.17	368.82	508.15								
4797.58	5136.78	4191.84	7652.93	5509.79	6264.78	6141.26	5726.16	5911.06	8634.67	5564.09	7179.16								
355.99	266.77	233.31	439.04	279.10	405.25	460.29	335.47	363.89	841.04	476.94	821.16								
8802.03	9473.54	7529.42	13578.60	9608.85	10959.20	10188.40	10146.60	10471.40	14471.60	9814.73	12784.00								
632.34	437.48	361.14	747.54	429.99	656.58	654.60	568.64	668.18	1169.86	753.80	1429.88								
6805.80	7235.66	5897.31	10970.00	7639.60	8719.12	7970.04	8324.35	7957.55	11332.90	7646.59	10964.40								
492.62	374.26	269.68	654.99	339.33	547.24	489.99	506.67	543.02	1022.13	615.03	1530.90								
6749.44	7239.12	5999.07	10650.90	7664.91	8518.36	7768.87	8248.71	8193.70	10561.00	7255.54	10989.40								
494.81	366.01	297.03	566.97	353.39	524.17	600.18	460.44	564.66	748.95	548.96	1361.11								
4223.29	4705.34	3652.04	6715.27	4404.08	5233.91	4720.91	4905.83	4819.43	5992.94	4454.26	6893.83								
334.48	320.07	199.09	381.14	210.76	356.37	406.44	329.53	341.65	446.17	326.17	1138.67								
2745.03	3061.94	2532.66	4687.93	3166.60	3477.47	3416.32	3247.92	3590.92	4268.26	3164.18	5375.32								
228.85	180.41	155.72	265.59	163.95	240.27	316.14	212.48	273.98	308.79	247.03	972.28								
32.87	34.15	34.10	36.57	36.28	35.92	33.11	36.10	33.90	32.41	35.89	33.35								
0.31	0.58	1.00	0.35	0.57	0.50	0.89	0.50	0.48	0.86	0.55	0.35								
1.34	1.34	1.40	1.40	1.40	1.39	1.35	1.41	1.36	1.33	1.40	1.34								
0.01	0.02	0.03	0.01	0.02	0.02	0.02	0.01	0.01	0.02	0.02	0.01								

u5-139-95 -	u5-139-95 -	u5-139-95 -	u5-139-95 -	u5-139-95 -	u5-139-95 -	u5-139-95 -	u5-139-95 -	u5-139-95 -	u5-139-95 -	u5-139-95 -	u5-139-95 -	u5-139-95 -	u5-139-95 -
38697.90	33965.80	1418190.00	60753.60	28980.60	19047.50	25700.80	58959.20	50864.40	55766.20	22370.70	132887.00	55766.20	22370.70
4098.93	5269.86	376138.00	9861.77	2865.91	2198.59	2840.47	6985.43	11762.90	21316.70	1884.75	29174.00	21316.70	1884.75
92525.70	80864.70	2789420.00	124387.00	71106.50	48060.40	63807.10	142154.00	134891.00	119058.00	52758.20	268542.00	119058.00	52758.20
9167.16	12601.00	724889.00	16858.70	7949.51	6060.56	6793.55	14677.70	28741.80	42345.70	4346.76	56586.90	42345.70	4346.76
14222.80	12100.80	344359.00	19003.20	11222.60	7318.68	9466.11	22329.80	20938.70	16569.00	7688.90	35763.50	16569.00	7688.90
1603.09	1816.05	89588.50	2516.00	1438.93	757.36	1063.51	2431.20	4533.65	5591.67	550.59	7807.07	5591.67	550.59
10768.20	9509.48	231524.00	13226.40	8064.50	6046.23	7214.14	16382.70	16482.30	13105.70	6205.08	21406.50	13105.70	6205.08
1118.11	1433.24	59898.80	1635.57	904.04	674.57	787.92	1787.20	3515.96	4196.60	425.90	4507.51	4196.60	425.90
2720.07	2428.47	32546.30	2918.42	2210.81	1992.43	1989.80	3741.08	3596.18	3435.80	1938.58	4266.57	3435.80	1938.58
214.48	229.78	8118.86	289.42	187.48	200.04	191.77	320.03	562.35	693.01	150.58	750.65	693.01	150.58
2366.62	2203.20	17536.20	2434.75	1979.52	1892.68	1716.17	2759.73	3082.87	2777.92	2054.76	2965.68	2777.92	2054.76
154.94	188.17	4217.27	193.34	131.93	172.91	172.56	206.77	381.16	311.92	138.20	436.35	311.92	138.20
3777.60	3405.76	16915.50	3462.02	3125.35	3318.99	2621.00	3917.06	4464.44	4437.85	3247.13	3885.87	4437.85	3247.13
227.95	271.18	3758.33	217.12	173.91	288.98	242.10	232.81	372.97	425.07	229.25	420.86	425.07	229.25
5882.96	5474.91	13019.80	5283.19	5122.52	5301.92	4129.14	5965.37	6460.46	6846.23	5446.07	5194.26	6846.23	5446.07
296.93	448.81	2198.10	271.24	241.82	388.46	435.56	254.57	434.44	375.19	355.65	284.28	375.19	355.65
10221.90	9243.62	16002.10	9076.00	8876.16	9823.06	7645.69	10179.80	10998.50	11712.20	9892.38	9162.02	11712.20	9892.38
411.23	704.84	1867.41	407.94	368.86	723.98	906.57	392.43	617.54	462.52	563.41	446.35	462.52	563.41
7986.50	7738.78	9978.20	7176.68	7045.54	7477.28	6002.59	8222.29	8490.57	9308.97	7817.66	7055.58	9308.97	7817.66
373.03	665.08	901.84	351.25	314.40	565.44	605.31	309.62	474.82	408.55	498.43	356.25	408.55	498.43
7901.31	7447.01	9145.97	7296.26	7075.07	7895.46	6000.30	8096.69	8172.59	9093.41	7730.85	6803.45	9093.41	7730.85
351.69	561.15	634.70	312.17	328.82	512.89	741.87	383.15	441.33	390.91	455.18	336.14	390.91	455.18
4883.02	4295.54	5034.57	4381.20	4514.43	4580.35	3376.85	5058.77	4728.17	5269.61	4691.54	4180.51	5269.61	4691.54
253.44	341.37	296.01	223.40	243.66	344.94	304.70	241.26	297.10	288.03	281.82	240.15	288.03	281.82
3375.36	3151.89	3428.52	3151.48	3250.72	3331.01	2506.40	3548.50	3431.92	3863.81	3325.37	2765.58	3863.81	3325.37
165.46	262.78	226.34	180.06	185.62	292.29	244.84	181.71	224.99	196.98	243.36	190.13	196.98	243.36
34.66	34.31	36.28	33.58	30.65	34.68	30.77	32.98	36.41	33.64	36.46	24.99	33.64	36.46
0.41	0.44	0.63	0.29	0.51	0.40	0.69	0.81	0.33	0.80	0.76	0.53	0.80	0.76
1.37	1.39	1.39	1.35	1.33	1.39	1.30	1.33	1.40	1.36	1.43	1.19	1.36	1.43
0.01	0.01	0.02	0.01	0.02	0.02	0.02	0.02	0.01	0.02	0.02	0.02	0.02	0.02

u5-139-95 -	u5-139-95 -	u5-139-95 -	u5-139-95 -	u5-139-95 -	u5-139-95 -	u5-139-95 -	u5-139-95 -	u5-139-95 -	u5-139-95 -	u5-139-95 -	u5-139-95 -	u5-139-95 -	u5-139-95 -
37998.50	17968.10	195751.00	60992.10	66419.50	61818.90	51958.50	36979.30	80829.30	18953.70	17477.70	39408.50		
5794.54	1955.90	47640.60	12967.00	20101.70	17255.80	6900.53	9433.17	21694.60	1888.63	1485.13	6202.64		
99654.40	47538.20	383695.00	136020.00	149107.00	142339.00	125335.00	91342.60	154435.00	47275.20	51946.20	77711.00		
14312.20	5136.43	86303.30	27678.60	42626.30	40396.10	16403.00	23157.70	37630.00	4780.36	4712.28	10265.20		
15178.20	7128.86	51498.20	20307.20	22663.80	22412.50	18145.30	13421.00	22395.90	8202.22	9962.55	11085.80		
1942.21	783.01	11257.70	4075.66	6150.54	6484.33	2469.14	3528.84	5261.60	886.11	1331.08	1327.81		
10771.90	5947.38	34511.60	13968.50	16918.40	16744.10	13710.70	10330.90	15690.60	6586.30	10917.70	8614.07		
1260.25	571.50	7203.06	2646.34	4164.69	4841.19	1862.82	2511.08	3546.43	736.77	2278.71	888.64		
3132.41	2045.66	5909.76	2879.48	4712.06	3579.88	2814.06	2364.77	3320.20	2632.71	5926.93	2843.23		
388.78	183.33	1045.89	366.68	753.22	779.59	311.20	395.17	448.88	386.51	1754.67	222.66		
2761.56	1928.50	3770.69	2297.53	4283.21	2638.76	2246.55	2122.30	2796.23	2612.54	5783.91	2656.26		
314.01	159.89	564.91	206.13	687.51	415.89	208.04	253.72	343.87	386.54	1557.34	177.19		
4377.49	3498.78	4975.23	3371.92	6233.16	3678.57	2677.63	2993.06	4451.87	4415.70	14602.80	4819.39		
603.73	343.33	694.75	216.54	1092.47	438.96	196.78	247.24	415.57	781.20	4582.84	301.56		
6965.35	5952.06	5910.67	5403.78	10644.50	5410.04	3731.65	4722.36	6519.38	8649.33	21581.90	7932.62		
929.96	525.78	508.65	251.20	2327.57	305.62	225.58	275.72	566.67	1775.09	6733.50	461.55		
12464.10	10718.10	9990.20	9217.92	15564.00	8643.92	6535.04	8447.57	11738.30	14245.10	40795.70	14167.50		
1976.16	913.92	713.35	420.06	2801.46	406.15	279.83	340.30	1153.26	2646.68	13856.90	890.22		
10267.00	8304.29	7352.51	7505.88	12901.50	6821.97	5020.58	6711.63	9056.58	10780.00	29220.20	10981.00		
1561.89	639.37	529.12	368.53	2521.05	258.52	194.65	281.11	869.37	1831.38	9160.81	688.78		
9112.14	8292.73	7563.42	7203.57	12087.30	6759.18	4768.18	6617.99	9406.74	10041.90	29245.20	10676.80		
1095.93	660.17	677.59	387.33	2056.49	267.26	201.57	297.43	896.58	1596.93	9495.83	605.06		
5435.10	5119.53	4333.02	4306.31	7509.14	4048.48	2850.48	3988.52	5713.74	7341.31	18829.50	6400.71		
642.78	483.26	358.82	238.17	1328.44	176.87	151.74	216.82	607.75	1343.26	6099.70	387.59		
4125.68	3657.12	3017.87	3060.29	5045.19	3030.88	2023.23	2735.10	3919.60	5045.57	14920.70	4604.21		
558.13	397.51	246.40	189.03	802.46	153.27	124.96	162.67	416.40	930.99	4771.59	323.11		
30.81	35.80	35.99	32.15	32.75	31.46	34.10	29.95	34.00	33.84	32.06	32.48		
0.49	1.70	0.62	0.45	0.82	0.57	1.00	0.98	1.00	0.50	0.47	0.79		
1.31	1.39	1.41	1.35	1.34	1.31	1.37	1.31	1.36	1.35	1.30	1.35		
0.01	0.05	0.02	0.01	0.02	0.02	0.02	0.02	0.02	0.01	0.02	0.02		

u5-229-6 -	u5-229-6 -	u5-229-6 -	u5-229-6 -	u5-229-6 -	u5-229-6 -	u5-229-6 -	u5-229-6 -	u5-229-6 -	u5-229-6 -	u5-229-6 -	u5-229-6 -	u5-139-95 -
41310.30	38474.90	13456.90	48478.90	19386.60	21557.80	166191.00	45845.10	17363.30	306382.00	La CPS	29019.40	
11542.00	8892.93	2942.88	6377.80	2949.52	1887.41	52765.50	6585.02	2355.82	61520.10	La CPS 2SE	3031.90	
108146.00	77753.70	29367.20	95893.60	42064.30	45925.30	383952.00	119606.00	34778.50	756992.00	Ce CPS	73383.40	
29417.80	15267.00	5713.85	11055.70	5658.33	3590.14	121552.00	15894.00	3964.05	167699.00	Ce CPS 2SE	7736.87	
12499.80	9537.79	4257.95	13527.90	6110.96	6032.15	37269.20	16199.50	4606.28	93879.80	Pr CPS	11560.30	
3208.56	1854.38	951.28	1453.20	786.69	412.92	11077.00	2377.58	460.39	19951.60	Pr CPS 2SE	1141.77	
8682.19	6585.73	3768.34	9609.42	4789.03	4042.33	28226.30	11598.70	3477.39	61614.50	Nd CPS	9395.35	
1989.40	1096.67	722.61	971.10	513.73	277.76	8141.64	1712.17	303.19	13450.70	Nd CPS 2SE	939.18	
2399.46	2040.02	1258.20	2669.01	1889.33	1266.87	3890.08	2636.12	1337.98	11157.70	Sm CPS	2539.07	
345.11	276.53	191.15	206.43	152.54	107.10	840.47	302.37	99.24	2473.78	Sm CPS 2SE	203.34	
2582.21	2495.49	1306.74	2859.64	2067.91	1813.05	3150.43	2961.51	1636.42	11526.90	Eu CPS	2234.04	
310.26	353.11	163.39	147.39	144.58	141.06	406.57	206.82	118.15	2707.00	Eu CPS 2SE	158.98	
3831.81	4273.73	2185.93	4599.85	3678.19	2524.45	3184.41	3103.81	2643.72	8767.93	Gd CPS	3582.78	
366.35	977.96	236.00	202.67	207.74	181.29	304.95	249.07	161.77	1586.84	Gd CPS 2SE	209.21	
5586.09	5784.69	2947.80	6865.11	5914.25	3787.15	3875.69	3736.91	3963.66	8701.90	Tb CPS	5614.59	
358.42	1358.45	248.13	268.47	287.44	236.09	236.27	312.06	210.97	1142.55	Tb CPS 2SE	335.89	
9158.37	9343.45	4875.29	11159.00	9882.77	6227.74	5740.13	6034.53	6787.24	12357.70	Dy CPS	10426.20	
577.73	1933.67	384.83	325.22	473.14	405.54	299.98	710.97	259.01	1293.13	Dy CPS 2SE	535.90	
7247.11	6467.43	3701.49	8715.09	7646.86	4670.21	4261.29	4267.35	5276.83	8482.66	Ho CPS mea	8159.45	
466.74	1246.04	313.42	271.08	374.42	300.66	243.68	436.13	250.25	719.31	Ho CPS 2SE	425.93	
7293.99	6412.08	4022.75	8601.92	8073.77	4952.62	4488.19	4311.32	5214.45	7714.82	Er CPS	7643.98	
431.65	1136.79	335.58	272.86	417.20	334.04	211.11	462.76	231.23	557.60	Er CPS 2SE	456.55	
4801.98	3492.07	2762.08	5825.47	5200.89	3168.05	2822.63	2641.01	3509.84	4604.42	Yb CPS	4865.53	
304.44	410.34	268.40	240.13	283.48	238.24	199.38	306.40	171.87	292.91	Yb CPS 2SE	323.35	
3433.54	2154.41	1847.78	4169.47	3634.31	2102.52	1952.82	1841.80	2572.48	3078.62	Lu CPS	3390.07	
266.63	230.03	168.67	227.73	188.95	161.75	164.98	196.32	177.37	223.21	Lu CPS 2SE	240.93	
38.10	31.00	42.96	57.40	60.96	46.30	26.20	25.90	44.40	38.60	Rb87/Sr86	21.80	
0.60	1.70	0.86	2.30	0.99	2.60	1.10	1.10	1.10	1.30	Rb87/Sr86 2S	1.60	
1.44	1.30	1.53	1.78	1.84	1.57	1.21	1.23	1.52	1.43	Sr87 /Sr86	1.13	
0.02	0.03	0.02	0.05	0.03	0.05	0.03	0.03	0.03	0.03	Sr87 /Sr86 2S	0.03	



u5-229-6 -	u5-229-6 -	u5-229-6 -	u5-229-6 -	u5-229-6 -	u5-229-6 -	u5-229-6 -	u5-229-6 -	u5-229-6 -	u5-229-6 -	u5-229-6 -	u5-229-6 -	u5-229-6 -	u5-229-6 -	u5-229-6 -
28916.10	58621.30	24364.30	30490.00	28398.70	28779.00	22625.30	253967.00	153506.00	64016.70	21864.00				
5789.46	15333.70	2451.37	4475.46	3337.61	3518.02	6432.89	79967.20	28612.00	19808.50	2878.36				
76344.50	110324.00	48654.30	69591.30	65803.90	62794.40	44647.60	441426.00	284893.00	132074.00	48630.90				
14128.10	28947.80	37566.40	10403.70	6666.34	7093.09	11957.40	142584.00	48660.40	35696.90	6612.06				
9620.44	14799.90	6579.08	9827.51	9775.82	8382.89	7058.70	51936.00	39396.10	19080.30	6845.44				
1881.56	3715.84	2645.47	1441.24	985.56	948.03	1655.28	15644.00	6828.30	5289.77	835.24				
6012.82	9978.06	5909.75	7004.36	6833.23	5931.57	4435.13	33214.60	25984.50	11113.90	5010.93				
985.51	2489.38	1757.61	1048.64	653.02	570.02	917.44	9845.27	4244.38	2761.35	607.45				
1683.69	2266.69	1850.68	1600.38	2269.29	1650.16	1247.33	4755.34	4946.03	3153.04	1727.28				
229.74	371.54	283.70	189.58	258.10	134.22	156.69	1064.27	615.55	597.19	217.41				
2013.16	2520.43	2758.29	1556.11	2819.05	2094.91	1872.23	3046.42	3496.48	2552.85	2423.99				
299.21	305.92	345.81	156.22	306.74	146.47	162.95	379.32	299.13	310.24	162.96				
2546.39	3422.79	3576.33	2323.28	4483.74	2523.11	2317.41	3585.29	4436.82	4228.48	2821.28				
225.32	371.12	408.46	186.58	600.19	200.78	194.83	345.17	368.28	443.15	238.37				
3490.05	4788.22	5531.57	3041.31	6643.31	3805.74	3231.49	4050.19	5112.11	5763.65	4329.44				
265.09	418.75	539.64	255.19	888.07	296.29	241.83	255.03	417.29	549.45	457.83				
5964.52	8063.75	8971.27	4993.49	11109.90	6319.75	5186.11	6108.18	7869.58	9618.30	7123.31				
349.59	695.69	863.27	418.56	1723.69	531.54	301.42	388.47	616.27	863.26	719.40				
4486.75	6188.40	7127.71	3945.22	8652.83	4887.35	4053.27	4951.10	6001.00	7113.92	5579.75				
335.71	467.95	674.74	317.84	1437.21	421.72	253.22	354.78	467.51	546.55	566.70				
4465.70	6253.63	7225.58	3800.20	8402.19	4798.00	4003.79	4872.15	5926.91	7352.36	5904.65				
290.06	592.20	688.42	349.31	1230.95	414.57	247.04	351.58	425.49	551.97	612.84				
2972.39	3911.31	4625.26	2421.06	5606.29	3125.53	2613.34	3229.17	3855.76	4652.94	3924.68				
213.33	312.41	423.02	224.77	786.95	278.75	188.05	270.46	306.59	382.38	437.40				
2036.05	2806.49	3430.10	2498.47	3775.38	2261.48	2107.23	2308.74	2603.67	3298.12	2878.59				
162.05	260.37	342.14	165.56	453.31	237.53	185.74	191.76	241.19	249.11	332.60				
55.60	43.40	50.60	49.60	41.60	34.60	25.40	10.32	100.50	56.00	16.08				
1.60	1.10	1.50	1.00	2.00	1.40	1.00	0.28	6.00	1.10	0.28				
1.76	1.55	1.66	1.45	1.45	1.40	1.22	0.91	2.69	1.74	1.02				
0.03	0.02	0.03	0.02	0.03	0.03	0.02	0.01	0.12	0.03	0.01				

u5-229-6 -	u5-229-6 -	u5-229-6 -	u5-229-6 -	u5-229-6 -	u5-229-6 -	u5-229-6 -	u5-229-6 -	u5-229-6 -	u5-229-6 -	u5-229-6 -	u5-229-6 -	u5-229-6 -	u5-229-6 -	u5-229-6 -
39066.20	30896.00	14676.90	27148.20	78424.30	108030.00	16806.50	166919.00	22094.20	22117.70	17143.60	10035.60			
11410.60	6142.10	1755.92	6015.24	22089.10	40990.70	2275.84	35658.70	4587.88	5629.62	2215.49	2020.45			
79991.00	64330.00	31899.80	55344.10	178563.00	208073.00	39812.10	374981.00	46318.00	45501.40	42810.80	20619.10			
23132.60	10985.10	3859.65	9813.46	50524.00	71255.30	4530.75	72927.80	9925.57	9341.32	4917.31	3408.41			
11899.70	9442.40	4885.89	8074.51	22886.90	26704.90	5866.87	54485.00	5960.51	6702.03	5696.87	3275.64			
3527.47	1541.91	615.01	1769.21	6054.66	8871.45	781.66	10762.70	1168.72	1307.89	637.51	451.96			
9844.96	6729.12	3543.30	5917.90	16698.80	18357.70	4417.95	36591.50	4869.31	4799.39	4404.04	3273.85			
2840.39	936.93	389.81	992.65	4404.59	5477.32	492.85	7250.58	865.22	732.82	488.76	335.14			
2486.14	2352.10	1671.91	2024.84	3216.54	3723.00	1830.73	6281.76	1266.73	1942.65	1844.42	1953.07			
517.87	189.89	156.17	251.38	606.35	690.41	148.95	1120.99	174.06	203.96	143.05	132.56			
3111.94	2689.74	1950.12	2481.84	2577.85	3665.23	2139.29	4603.17	1523.33	2225.41	2210.37	2542.75			
642.17	168.61	154.73	226.53	257.43	247.38	165.23	615.12	121.48	161.62	152.82	163.24			
3482.28	4483.85	3452.83	4332.55	3927.14	5372.27	3763.72	5039.40	2407.70	3505.84	3423.75	4598.06			
486.29	251.63	217.80	320.59	255.10	480.38	239.01	592.79	171.28	243.54	176.34	253.50			
3990.07	6334.20	5334.91	6289.81	5288.36	7723.71	5845.38	5131.23	3652.23	5669.38	4998.11	7245.89			
437.47	262.20	320.51	368.20	257.40	478.54	372.93	407.28	213.35	282.97	301.22	338.16			
6376.63	10781.80	8933.07	10527.10	8270.03	12608.30	10043.90	7239.40	5492.54	9175.99	8208.41	12368.60			
622.64	414.21	428.72	663.40	318.44	645.69	567.97	484.79	301.91	480.27	434.47	481.03			
4950.43	8456.28	7144.55	8223.87	6579.36	9684.26	7893.84	5077.35	4564.35	7286.12	6615.45	9322.18			
510.61	435.39	393.60	424.83	299.60	454.11	479.53	328.02	234.35	391.18	358.48	388.75			
5096.28	8509.22	7336.93	8530.58	6754.32	9732.56	7816.83	5269.45	4480.84	7719.72	6591.73	9725.47			
571.86	459.92	420.18	500.48	309.82	521.52	453.88	320.90	264.23	448.63	367.88	424.85			
3577.41	5511.55	4853.79	5504.60	4376.86	6412.96	5427.31	3143.20	3064.34	4964.14	4482.81	6270.45			
410.26	260.68	270.07	348.07	253.73	341.98	349.65	236.04	188.54	275.26	268.68	313.83			
2916.36	4072.98	3388.68	3676.29	2968.42	4663.45	3761.42	2214.12	2029.92	3531.21	3078.97	4442.95			
292.58	221.71	215.33	253.82	173.80	318.02	271.22	165.84	131.62	215.61	221.11	230.68			
24.60	57.31	56.90	45.76	56.00	45.50	37.30	23.20	38.82	49.40	48.30	62.30			
1.10	0.60	1.90	0.87	1.10	2.30	1.90	1.40	0.94	1.50	0.93	2.70			
1.18	1.76	1.75	1.54	1.75	1.57	1.40	1.16	1.42	1.64	1.60	1.84			
0.03	0.02	0.04	0.02	0.02	0.04	0.04	0.03	0.02	0.03	0.02	0.06			

u5-229-6 -	u5-229-6 -	u5-229-6 -	u5-229-6 -	u5-229-6 -	u5-229-6 -	u5-229-6 -	u5-229-6 -	u5-229-6 -	u5-229-6 -	u5-229-6 -	u5-229-6 -	u5-229-6 -	u5-229-6 -
13687.50	9619.09	23914.60	29340.60	19815.40	72139.10	13057.80	22621.00	37571.50	19290.40	74726.30	81646.10		
3303.73	2351.43	3673.76	4458.99	2075.57	15689.30	2298.03	4899.60	7512.55	1682.57	12489.10	20959.50		
38753.50	26848.70	52751.40	62929.30	54237.90	150375.00	25774.20	47697.40	88490.90	45188.80	200190.00	210183.00		
8915.90	6070.88	6640.03	8910.76	6162.79	29604.40	4019.97	10286.50	15266.70	3846.11	30493.10	44427.90		
5326.81	3185.06	7525.37	8102.16	7721.56	20931.10	3424.43	6994.34	12128.20	6406.32	27174.30	29144.40		
1190.77	654.91	1109.29	1028.10	701.99	4132.57	537.21	1499.61	2183.95	555.11	3907.66	5821.54		
4324.84	2397.64	4771.16	5968.39	5437.09	14788.20	2660.68	5190.42	8213.03	4874.28	18847.40	18478.70		
981.57	328.09	689.69	561.07	477.69	2689.46	436.52	1024.65	1228.44	333.98	2766.24	3379.11		
1250.76	1071.38	1381.82	2178.55	2189.95	2723.41	1222.37	1532.60	2240.20	1946.42	4554.18	4028.34		
259.55	131.14	133.52	160.17	190.45	307.16	111.46	210.38	216.55	150.86	465.17	503.91		
1524.90	1662.70	1447.43	2742.09	2735.75	2554.97	2253.19	1587.19	2602.52	2373.67	3913.70	3399.02		
268.27	129.47	130.80	161.37	202.15	249.69	208.65	180.52	196.87	171.23	333.35	285.49		
2187.28	2384.09	2473.09	4503.45	4450.28	3421.02	2534.41	2480.67	3928.97	4448.58	5977.83	3757.36		
383.31	217.43	184.69	243.63	338.01	270.01	159.09	233.61	278.44	255.52	452.37	262.39		
3317.70	4018.01	3600.72	7012.35	6659.03	4259.90	3923.74	3667.54	6010.01	6624.74	7343.55	4781.50		
517.86	349.70	220.23	282.80	497.03	295.77	200.46	334.21	326.47	322.89	487.60	353.65		
5643.90	6264.12	5576.69	11418.10	11298.20	7075.19	6860.92	6163.86	9515.15	11389.20	12432.80	7249.41		
820.66	532.09	263.24	464.15	824.18	548.50	271.08	516.66	496.08	594.67	1088.94	506.30		
4235.94	4901.45	4472.17	9197.06	8710.40	5033.44	5067.70	4503.48	7550.94	8522.50	8932.93	5318.11		
602.34	384.36	241.66	385.61	555.38	397.23	231.00	338.24	330.53	473.69	597.45	466.22		
4378.90	5020.05	4537.02	9100.07	8898.65	5319.16	5412.20	4680.50	7710.16	9127.46	8691.56	5499.15		
650.02	403.35	269.06	387.65	650.99	450.32	231.92	349.39	351.87	437.76	711.76	432.62		
2596.68	3346.28	2816.58	5995.23	5719.70	3640.14	3611.43	3091.21	5263.40	5897.44	6124.51	3601.90		
387.79	314.05	149.16	252.26	432.36	291.01	187.39	262.41	299.19	364.56	564.51	329.49		
2149.35	2407.47	2077.66	4404.86	4091.35	2457.53	2585.35	2279.03	3604.37	4214.24	4347.77	2307.54		
339.96	213.26	140.30	177.24	349.81	237.32	156.57	191.22	231.24	269.75	381.95	249.02		
55.40	44.20	44.67	49.90	40.93	33.70	40.40	23.02	42.30	46.20	21.30	40.34		
1.10	1.10	0.65	1.80	0.87	1.30	1.20	0.43	1.20	1.70	1.10	0.87		
1.76	1.52	1.54	1.62	1.51	1.37	1.50	1.16	1.52	1.57	1.11	1.47		
0.03	0.03	0.02	0.04	0.02	0.02	0.02	0.01	0.03	0.03	0.02	0.03		

u5-229-6 -	u5-229-6 -	u5-229-6 -	u5-229-6 -	u5-229-6 -	u5-229-6 -	u5-229-6 -	u5-229-6 -	u5-229-6 -	u5-229-6 -	u5-229-6 -	u5-229-6 -	u5-229-6 -	u5-229-6 -	u5-229-6 -	u5-229-6 -
15246.40	464334.00	48924.40	15324.10	143370.00	48029.00	10575.10	48781.40	24772.20	246070.00	227042.00	263889.00				
1712.01	144638.00	11649.30	1619.18	54112.60	12096.80	3687.92	11468.90	1901.67	86838.30	45494.60	85453.20				
33332.30	913211.00	103864.00	34367.90	256420.00	125920.00	20280.30	112700.00	68941.80	690157.00	492823.00	610336.00				
4029.55	277851.00	24361.00	3115.03	83393.40	31588.90	6160.30	21959.90	5006.30	256561.00	104445.00	186851.00				
4360.17	107450.00	17136.20	5141.33	30470.10	17849.60	3149.98	15075.00	9626.45	94315.50	69117.10	69688.40				
557.92	32108.10	4350.05	404.70	9912.43	4393.39	1027.94	2808.97	633.17	34139.60	14542.80	19741.80				
3025.28	65581.30	10676.60	3917.09	16463.50	11866.10	2513.56	9977.58	6500.29	66585.70	47104.60	43016.40				
445.67	19689.20	2440.94	310.77	4988.33	2707.93	539.58	1639.63	388.14	24341.40	10165.30	11549.90				
1056.99	10790.90	2654.38	1721.01	2586.70	2651.41	1385.24	2955.07	2291.41	11609.20	7199.62	6128.14				
129.26	2869.40	487.70	130.16	421.72	451.86	176.62	324.32	159.35	3888.59	1352.97	1234.45				
1698.29	5508.12	2628.93	2181.94	2199.98	2309.55	1744.14	3440.54	2575.84	8159.08	4209.79	5136.87				
135.08	983.45	279.91	144.23	261.55	315.47	171.35	305.36	209.24	2301.25	626.66	790.48				
2011.96	7060.07	3635.69	4156.52	3165.94	3233.10	2728.00	5279.97	4192.40	10175.20	4469.41	4764.92				
196.44	894.13	369.49	271.01	259.32	362.39	249.67	342.41	300.89	2367.52	434.28	425.05				
2884.99	7835.77	4462.86	6237.70	4299.98	4473.27	4093.62	7833.05	6048.91	8890.73	4437.00	5200.29				
223.90	465.84	345.21	319.57	198.39	415.02	381.81	489.48	415.85	1059.64	261.60	291.15				
4946.72	12135.60	6806.63	10665.80	6825.93	7715.72	6660.18	13498.50	10398.30	12526.40	7070.00	7838.62				
398.10	631.11	491.85	611.87	269.05	659.38	490.49	873.94	697.04	816.37	328.55	437.85				
3914.63	9160.62	5189.81	8123.80	5292.19	5843.15	5186.87	9991.77	7759.57	9138.29	5164.40	5949.62				
333.20	534.65	397.19	401.34	212.32	485.45	371.47	651.16	577.52	422.22	252.52	388.78				
3824.38	9313.13	5447.53	8383.36	5419.01	6136.35	5299.83	10981.30	8045.93	8726.84	5242.92	5690.58				
327.20	514.89	446.47	434.55	245.94	499.73	398.47	704.75	573.37	366.70	263.05	414.31				
2589.07	6189.25	3747.09	5485.57	3440.79	4380.03	3444.37	7078.72	5411.28	5372.36	3504.22	3863.02				
219.21	356.62	342.11	309.44	161.65	411.04	262.63	504.53	441.22	306.50	206.10	331.70				
1807.04	4369.37	2605.21	3752.15	2460.47	2932.62	2499.32	5070.55	3730.62	3830.23	2439.76	2666.76				
179.31	248.76	278.96	206.62	155.44	279.35	253.42	336.07	281.77	215.51	151.43	231.47				
26.40	39.75	30.40	56.00	51.70	42.80	67.20	61.60	46.88	48.70	55.40	47.70				
1.10	0.92	2.00	1.50	1.10	2.20	2.50	3.30	0.58	1.40	1.30	1.30				
1.23	1.46	1.30	1.71	1.65	1.53	2.00	1.86	1.55	1.61	1.78	1.62				
0.02	0.02	0.04	0.03	0.02	0.05	0.05	0.07	0.01	0.03	0.03	0.03				

u5-578 - 13.d	u5-578 - 12.d	u5-578 - 11.d	u5-578 -	u5-578 -	u5-578 -	u5-578 -	u5-578 -	u5-578 - 10.d	u5-578 - 1.d		u5-229-6 -	u5-229-6 -
372.108.00	365262.00	260928.00	220553.00	234673.00	327331.00	331556.00	272369.00	262356.00	La CPS	La CPS	79586.10	20576.40
54553.40	37409.20	26317.30	17332.40	14305.70	23293.30	28014.50	21535.10	18894.00	La CPS 25E	La CPS 25E	17726.10	4049.91
768891.00	719360.00	485817.00	436993.00	441871.00	636376.00	644491.00	518128.00	511530.00	Ce CPS	Ce CPS	167281.00	41479.20
133924.00	68696.90	47179.90	34521.40	26656.70	45250.80	53795.20	38927.00	30010.80	Ce CPS 25E	Ce CPS 25E	32738.50	7540.55
98391.20	88614.90	59081.40	51306.60	53729.40	80577.90	82136.40	64432.20	68872.90	Pr CPS	Pr CPS	22786.20	5823.63
17794.00	7836.46	5419.72	3850.52	3319.74	5788.49	7136.89	5180.85	3887.02	Pr CPS 25E	Pr CPS 25E	4263.02	984.68
64375.90	53732.60	33434.50	30918.90	32677.40	48224.30	49820.00	38776.30	43784.50	Nd CPS	Nd CPS	16021.10	4266.12
13125.70	4410.69	2883.84	2560.08	2039.39	3528.67	4099.51	2786.29	2456.43	Nd CPS 25E	Nd CPS 25E	3352.80	617.85
8883.52	8567.32	4453.38	4644.49	5080.97	7237.07	7352.07	5631.75	6555.06	Sm CPS	Sm CPS	3028.61	1536.55
1549.07	854.00	370.52	449.14	395.47	486.00	477.75	412.04	439.56	Sm CPS 25E	Sm CPS 25E	485.85	173.61
5549.67	5440.43	2900.67	3092.90	3911.18	4834.15	4656.33	3866.25	4055.19	Eu CPS	Eu CPS	2912.50	1910.07
820.59	630.87	203.48	290.30	369.68	324.95	287.65	301.13	261.71	Eu CPS 25E	Eu CPS 25E	350.62	174.42
6212.84	7208.66	3490.20	3396.52	4989.16	5461.55	5570.14	4481.16	4513.68	Gd CPS	Gd CPS	4210.93	3035.06
719.82	1295.59	216.56	283.40	499.21	337.34	374.82	363.94	258.61	Gd CPS 25E	Gd CPS 25E	451.40	276.52
6495.67	8924.58	4293.00	3827.70	5803.66	5552.55	6245.97	5257.90	4845.18	Tb CPS	Tb CPS	6346.74	4909.59
535.03	1826.30	252.85	262.08	611.09	318.72	543.06	405.35	300.38	Tb CPS 25E	Tb CPS 25E	633.16	388.79
9282.39	16397.00	6990.34	6278.91	9834.23	8820.38	10598.70	8670.81	7152.96	Dy CPS	Dy CPS	10464.30	7880.59
582.59	3733.07	324.91	415.05	967.80	524.03	948.80	610.18	374.17	Dy CPS 25E	Dy CPS 25E	1045.87	617.96
6666.26	13364.60	5876.09	4977.21	8091.23	6938.28	8340.66	7099.33	5748.52	Ho CPS mea	Ho CPS mea	8073.90	6413.34
354.69	3159.02	313.77	380.00	765.60	353.91	770.99	599.29	352.88	Ho CPS 25E	Ho CPS 25E	820.03	536.06
6754.58	13450.10	5858.07	5144.31	8097.95	6805.12	8485.90	6966.85	5711.21	Er CPS	Er CPS	8352.93	6322.44
365.88	3200.00	277.93	326.83	743.35	379.39	788.15	508.44	313.22	Er CPS 25E	Er CPS 25E	876.43	493.46
4271.52	9062.29	3964.44	3311.98	4687.48	4141.01	5468.27	4409.73	3482.02	Yb CPS	Yb CPS	5356.73	4292.27
275.63	2236.04	240.70	242.08	422.04	242.57	553.52	351.29	238.57	Yb CPS 25E	Yb CPS 25E	567.56	338.31
2962.74	6329.31	2713.72	2386.83	3356.53	2934.31	3927.61	3277.42	2470.39	Lu CPS	Lu CPS	4021.17	2845.80
215.62	1642.18	175.13	164.61	311.84	184.62	432.09	258.87	188.28	Lu CPS 25E	Lu CPS 25E	444.68	272.54
16.88	17.61	21.30	21.81	20.54	21.70	25.18	17.81	22.00	Rb87Sr86	Rb87Sr86	71.90	54.80
0.90	0.60	1.10	0.75	0.61	0.97	0.95	0.69	1.10	Rb87Sr86 2S	Rb87Sr86 2S	2.30	2.20
1.05	1.06	1.15	1.15	1.12	1.16	1.21	1.06	1.15	Sr87 Sr86	Sr87 Sr86	2.11	1.73
0.02	0.02	0.02	0.02	0.02	0.02	0.03	0.02	0.02	Sr87 Sr86 2S	Sr87 Sr86 2S	0.06	0.04

u5-578 - 41.d	u5-578 - 39.d	u5-578 - 37.d	u5-578 - 36.d	u5-578 - 35.d	u5-578 - 32.d	u5-578 - 31.d	u5-578 - 3.d	u5-578 - 25.d	u5-578 - 22.d	u5-578 - 19.d	u5-578 - 18.d
279747.00	284933.00	314339.00	200631.00	327580.00	324331.00	219973.00	362992.00	238603.00	289607.00	238653.00	249767.00
29505.90	22062.60	28713.20	17309.00	27343.50	24149.90	10532.90	22414.70	13486.30	17731.10	15636.20	10554.20
525582.00	557260.00	609009.00	395113.00	625627.00	602075.00	408303.00	702244.00	448673.00	551667.00	452762.00	475401.00
499566.60	49587.90	53163.80	36095.80	49542.70	43231.10	19975.50	43224.40	24083.40	34145.70	28433.90	21667.10
62387.60	65630.90	72961.80	49452.00	80021.30	72999.20	50324.90	87439.20	54565.00	68376.20	57338.70	59646.10
55444.93	5291.41	6192.66	5232.08	6750.14	5229.12	2615.62	5470.16	2821.03	4986.78	3634.40	3131.34
36946.40	39585.00	43673.70	32629.20	46776.30	43414.60	30219.90	53146.80	32905.40	37825.90	34099.50	36612.90
3032.24	3334.33	3337.00	4912.90	3856.32	3122.23	1519.44	3081.71	1665.01	2438.39	1946.60	1974.20
5157.69	5327.12	6284.30	5961.53	5883.96	5912.95	4248.47	8633.02	4333.70	5854.48	5745.00	5710.00
361.27	403.75	429.81	1379.95	485.59	372.71	306.48	563.57	258.76	600.84	372.42	508.16
3262.63	3910.26	4044.13	4108.03	3596.72	3894.54	2809.95	6016.21	3045.88	3926.00	3802.05	3903.05
201.74	308.22	265.06	953.09	284.14	261.55	186.21	348.58	193.59	368.44	226.61	341.16
4103.40	4317.60	4336.00	4566.87	4164.65	4563.56	3461.90	6827.50	3219.09	4623.55	5079.26	4792.37
245.91	294.98	285.24	1034.68	335.03	248.32	261.25	441.13	177.56	345.23	279.61	421.99
4475.32	4933.12	5235.05	4673.69	4114.87	5102.75	4375.89	7391.05	3915.69	5456.84	5995.97	5306.53
257.15	304.47	314.51	859.02	250.14	179.72	298.81	439.91	188.96	342.51	368.94	438.63
7274.05	8096.68	8282.84	6916.47	6764.99	8080.29	7460.41	11271.70	6503.48	9010.01	9912.56	8491.57
337.08	481.89	486.05	852.98	360.27	330.48	517.03	593.11	294.38	511.55	583.65	548.17
5529.24	6589.28	6544.94	4961.92	5191.80	6565.85	6089.75	8605.61	5128.56	7312.98	8043.22	6794.49
253.69	391.37	445.33	480.16	317.17	294.37	387.08	441.06	263.33	388.38	466.60	449.77
5633.06	6580.65	6707.27	4921.39	5289.80	6700.41	6172.56	8852.85	5304.97	7209.62	7850.43	6947.36
261.07	354.37	435.79	386.40	295.54	307.81	394.59	418.92	252.32	393.32	485.69	431.96
3747.79	4127.53	4093.00	2883.58	3502.25	4035.01	3808.70	5416.26	3244.72	4599.53	5052.13	4156.95
206.58	253.39	303.58	162.20	208.40	236.64	263.60	306.63	202.05	248.85	320.91	294.11
2662.39	3071.04	3012.83	2143.50	2585.99	2896.17	2592.64	3787.95	2386.24	3300.61	3571.20	3129.87
153.89	199.28	213.91	152.07	176.62	204.37	174.19	237.61	156.23	222.20	223.97	224.75
38.00	29.02	30.24	22.82	21.77	19.43	28.80	22.60	18.74	23.34	22.10	25.10
1.20	0.69	0.57	0.86	0.69	0.71	1.30	0.85	0.98	0.96	1.30	1.00
1.46	1.28	1.31	1.16	1.15	1.11	1.28	1.16	1.08	1.17	1.15	1.19
0.03	0.02	0.02	0.02	0.02	0.02	0.03	0.02	0.02	0.02	0.03	0.02

u5-578 - 58.d	u5-578 - 57.d	u5-578 - 56.d	u5-578 - 52.d	u5-578 - 51.d	u5-578 - 50.d	u5-578 - 49.d	u5-578 - 48.d	u5-578 - 46.d	u5-578 - 45.d	u5-578 - 44.d	u5-578 - 43.d
299082.00	347526.00	246363.00	250864.00	283736.00	425155.00	270607.00	255305.00	258409.00	252744.00	332642.00	289231.00
18166.60	41481.40	15890.80	14415.00	27479.70	29515.80	12003.10	15550.30	17669.10	17357.30	23961.60	24916.40
581704.00	661375.00	463270.00	500252.00	578253.00	805373.00	537970.00	495959.00	487644.00	477951.00	643258.00	571072.00
36179.00	76540.20	27589.90	27574.50	55866.40	55642.40	24359.10	29864.30	32652.00	30513.90	42849.50	49345.50
69207.40	80149.20	56740.80	62458.70	70298.10	99294.10	65702.10	61573.40	59488.50	59188.30	80594.90	72966.70
3928.96	8958.95	3259.07	3648.56	6392.45	7838.23	2932.76	3633.60	4360.48	4091.49	5434.84	6720.00
41040.30	50700.80	32781.10	38083.50	42066.60	57766.60	40376.40	37782.80	34918.70	37806.10	49775.60	45004.10
2485.45	5927.96	1836.81	2295.13	4163.42	4737.10	1819.26	2345.83	2728.72	3386.67	3596.25	4234.03
5776.14	6876.42	4402.44	6183.34	5512.50	7027.03	6479.92	5872.71	4380.11	5706.84	6942.66	6577.62
383.67	522.83	250.94	467.64	451.44	670.14	403.21	422.35	379.76	648.67	598.43	610.62
3763.70	4370.78	2886.93	4592.19	3518.35	4218.25	4318.54	4228.32	3006.26	3900.49	4074.78	4082.54
243.65	282.88	187.31	528.88	237.65	367.78	333.65	335.23	271.51	315.53	280.19	343.89
4464.79	5375.20	3546.51	4847.19	4147.48	4878.82	5591.85	4856.66	3712.60	4724.65	4670.19	4577.35
297.90	337.91	239.38	364.38	293.07	445.22	472.32	365.75	325.56	370.31	357.25	324.27
4691.36	6233.26	4199.39	5304.51	4723.74	5484.33	6202.96	5064.42	4214.95	5075.88	5045.36	4645.31
296.78	383.51	242.66	391.32	335.58	425.13	455.48	455.60	386.16	313.81	299.01	295.62
7551.57	10236.80	7022.17	9206.49	7527.82	8861.48	9938.65	8428.33	7037.01	8316.53	8068.57	7261.47
428.96	595.95	318.98	753.96	641.42	579.00	868.39	654.45	562.41	501.54	480.81	402.30
6064.82	8266.96	5859.13	7095.54	5963.03	7054.30	8187.88	6726.59	5815.65	6556.62	6301.98	5969.52
406.50	544.39	292.94	585.99	474.38	415.84	740.14	654.01	466.14	434.13	375.83	362.74
6037.68	8742.87	5810.25	7461.58	6264.11	7481.92	8096.29	6833.63	6526.25	6897.79	6050.12	5988.62
353.40	652.89	293.05	696.09	564.39	464.58	608.68	751.98	625.32	442.94	368.37	341.03
3834.78	5264.77	3824.48	4688.29	3781.66	4314.27	5144.65	4082.27	4162.28	4145.64	3788.06	3809.30
244.48	341.58	246.32	413.07	339.04	220.53	499.76	441.25	470.52	284.65	254.54	291.51
2804.37	3750.04	2680.16	3564.01	2705.45	3240.53	3454.50	3035.25	3234.26	3080.55	2790.14	2755.17
224.77	282.21	172.45	376.10	264.50	204.92	251.50	329.41	463.07	217.30	221.42	210.13
15.83	23.59	16.45	27.03	20.54	30.36	21.80	17.71	22.81	15.20	25.43	29.70
0.34	0.98	0.62	0.70	0.70	0.97	1.10	0.39	0.85	0.47	0.94	1.20
1.03	1.18	1.04	1.24	1.11	1.31	1.15	1.08	1.17	1.03	1.24	1.28
0.01	0.02	0.02	0.02	0.02	0.02	0.02	0.01	0.02	0.02	0.02	0.03

u5-578 - 81.d	u5-578 - 78.d	u5-578 - 77.d	u5-578 - 75.d	u5-578 - 72.d	u5-578 - 71.d	u5-578 - 7.d	u5-578 - 69.d	u5-578 - 66.d	u5-578 - 65.d	u5-578 - 64.d	u5-578 - 59.d
260563.00	498881.00	255677.00	208021.00	362147.00	314658.00	331886.00	262848.00	690456.00	317066.00	295733.00	296817.00
19620.00	60074.70	15441.50	11030.70	14536.60	17377.30	17000.50	23194.90	119842.00	23967.40	22677.10	20112.90
507634.00	996481.00	505576.00	414534.00	697172.00	649786.00	648451.00	523465.00	1261130.00	652695.00	552725.00	586238.00
34685.30	132204.00	27029.40	21602.90	29068.70	39748.70	34572.90	48090.80	215239.00	64355.50	38467.00	40396.70
63355.40	108735.00	63095.30	51097.90	84332.60	83768.80	83906.40	66730.50	134539.00	84515.00	66588.20	71202.80
4175.30	11948.10	4648.52	3019.68	3693.62	6301.35	5641.46	6643.55	20465.20	9050.25	4467.18	5006.53
37357.10	63533.00	36928.70	32089.00	49191.30	50849.00	51627.10	40896.30	76363.50	53552.10	40234.30	40495.00
2594.68	7112.32	2437.06	2235.03	2080.47	3969.40	3981.67	4345.88	11453.80	6511.22	2782.96	2482.03
5510.43	7404.27	5401.34	5223.22	7239.53	8072.30	7688.46	6504.34	7922.16	8184.93	5676.03	5232.19
420.62	642.57	359.50	614.93	425.92	590.28	731.81	787.16	856.15	995.14	307.95	309.18
3562.97	4626.64	3417.46	3655.69	5167.68	5393.75	4811.66	3964.18	4488.57	5306.44	3820.43	3398.41
246.51	337.73	229.64	404.09	325.75	328.22	428.34	343.52	377.39	652.71	213.80	208.27
4516.17	5425.36	3676.23	4290.48	5878.36	6269.30	5128.97	4499.32	5378.36	6434.89	4683.47	3872.38
336.81	476.48	246.10	523.33	335.35	351.74	463.48	344.34	342.77	827.49	263.76	204.47
5047.69	5899.77	4403.00	4794.95	6871.08	6572.75	5181.90	4679.09	5896.35	6535.60	5998.24	4805.38
360.41	527.05	212.96	500.91	453.79	347.58	365.71	284.99	412.39	679.60	367.24	275.78
7823.93	9819.35	7296.18	7716.34	11232.80	10314.50	7839.29	7221.26	10042.70	10322.60	10260.70	8008.96
590.23	781.14	422.66	687.83	728.72	428.71	461.61	422.03	708.61	1100.51	615.97	324.96
6133.26	7555.71	5761.14	5843.88	8880.16	8128.53	6046.35	5652.83	7966.24	8052.93	8256.33	6365.67
464.23	550.75	293.69	488.91	601.93	361.31	387.12	330.03	555.83	943.28	476.19	349.37
6378.86	7202.98	5939.80	5741.65	9097.91	8097.46	5895.76	5705.36	8388.23	8575.35	8205.32	6754.75
433.57	524.32	270.12	413.88	600.10	353.96	312.34	354.12	624.67	952.28	446.03	318.46
3932.91	4566.17	3713.97	3692.38	5377.97	5555.70	3873.13	3561.97	5396.16	5197.13	5267.04	4242.22
266.87	308.66	201.37	289.23	372.38	315.81	254.88	231.28	410.14	581.35	320.07	198.25
2803.95	3163.47	2710.91	2653.71	3938.00	3968.08	2773.93	2523.60	3850.34	3553.36	3809.86	3125.13
226.82	202.32	181.82	197.06	267.35	240.81	193.29	193.44	304.87	328.25	210.17	186.29
24.60	18.62	25.40	29.20	22.25	27.41	26.08	13.02	20.03	22.79	18.62	26.37
1.60	0.71	1.10	1.20	0.64	0.81	0.84	0.44	0.90	0.66	0.87	0.75
1.19	1.09	1.24	1.30	1.16	1.27	1.21	0.98	1.12	1.15	1.08	1.22
0.03	0.02	0.03	0.03	0.02	0.02	0.02	0.01	0.02	0.02	0.02	0.02



u5-578 - 99.d	u5-578 - 97.d	u5-578 - 95.d	u5-578 - 93.d	u5-578 - 91.d	u5-578 - 89.d	u5-578 - 85.d	u5-578 - 84.d	u5-578 - 83.d	u5-578 - 82.d
225619.00	343479.00	312961.00	265489.00	267574.00	535949.00	341820.00	1421800.00	469634.00	356292.00
11492.30	24764.00	26598.80	9174.50	20805.20	103833.00	17560.70	450995.00	53007.90	32092.30
473912.00	672888.00	617507.00	543624.00	532180.00	1046810.00	637429.00	2685530.00	850737.00	687842.00
29106.20	44325.90	51761.20	20469.40	38872.30	204782.00	30242.20	845150.00	90386.40	56928.80
56406.50	83827.90	75516.60	68499.30	66686.00	139500.00	78229.80	286914.00	100953.00	89325.50
3191.19	5770.62	6435.72	2892.08	4662.51	28444.60	4270.71	90990.00	9870.11	8024.24
35019.30	49676.00	50168.10	45895.20	40811.00	89306.40	43455.50	165549.00	58814.90	55370.80
2062.00	3121.07	4776.66	2456.24	2652.80	20396.50	2008.25	49971.30	5635.63	5035.47
5275.41	7137.21	8253.98	8434.50	6115.05	13853.80	5997.32	16250.60	7108.67	8311.73
432.86	435.04	889.04	661.51	384.10	3201.18	340.39	3734.95	504.66	773.18
3594.56	4881.79	6022.06	5545.50	4295.23	8929.77	3776.64	7725.99	4455.36	5575.00
253.63	328.17	784.77	456.47	263.96	2023.01	264.98	1202.81	357.07	527.59
4148.74	5382.81	6651.78	6964.59	4939.79	9406.96	4817.09	7508.55	5451.13	6023.75
315.65	384.79	707.38	550.60	332.72	1893.35	296.27	817.81	405.86	526.60
4577.33	5508.97	7456.11	6889.38	5920.29	8092.26	5589.76	7124.15	6165.52	6505.82
289.94	340.68	1001.77	436.88	409.31	930.15	308.11	431.64	569.53	498.95
7436.08	8461.61	12162.90	9915.57	9463.59	11006.80	9013.12	10402.90	9627.33	10182.60
386.67	498.91	1600.72	491.62	527.16	680.03	435.10	580.42	701.27	734.02
6120.59	6643.33	9773.90	7604.17	7454.69	8450.65	7014.83	7818.64	8037.29	8246.09
303.72	345.46	1407.08	332.79	432.61	437.63	403.34	349.86	633.54	615.02
6055.53	6791.45	10751.50	7126.21	7936.05	8270.32	7197.37	7826.15	8284.23	8645.33
323.00	375.77	1735.00	280.79	597.15	367.88	349.30	337.97	685.09	773.42
3711.93	4328.99	6770.81	4482.07	4383.59	5148.41	4643.83	4639.73	5588.07	6026.49
201.78	285.61	1073.93	229.23	268.79	292.27	265.27	252.44	548.87	578.54
2504.33	3016.84	5240.34	3004.95	3317.37	3745.31	3185.69	3228.11	4273.15	4430.08
164.57	216.95	870.35	171.65	247.79	234.99	212.68	188.73	545.20	431.92
33.00	22.37	26.30	27.86	21.71	27.42	24.81	20.80	29.30	22.00
1.70	0.73	1.10	0.65	0.32	0.75	0.48	1.10	1.20	1.10
1.37	1.17	1.23	1.26	1.16	1.23	1.20	1.13	1.28	1.15
0.04	0.02	0.03	0.02	0.02	0.02	0.02	0.02	0.03	0.02

Table S.2.2. Laser data of samples in Chapter 2.

### Additional information for Chapter 3

Samples were comprehensively characterized by scanning electron microscope (SEM) energy dispersive X-ray spectroscopy (EDS) for mineral liberation analysis (MLA) in conjunction with bulk XRD data to confirm phase identifications. Backscatter electron (BSE) images and MLA maps were obtained with a Hitachi SU3800 Automated Mineralogy Scanning Electron Microscope at Adelaide Microscopy. Classification of individual spectra

was done using the Advanced Mineral Identification and Characterization System (AMICS) software. AMICS deconvolves mixed spectra and assigns up minerals per analysed in a single spot. Mineral concentrations (reported as wt. %) in the mapped areas are determined by converting the mineral area % to wt. % using published densities for all identified sample constituents, with accuracy and precision comparable to quantitative XRD analysis. Bulk XRD analyses (Cox et al., 2016; NTGS, 2012) were used as an independent crystallography based mineral identification of samples to confirm the phases characterized by AMICS micro-imaging.

Laser analyses on samples and standards were carried out at Adelaide Microscopy, University of Adelaide using a laser ablation (RESOLUTION-LR ArF 193nm excimer laser) inductively couple-mass spectrometer (Agilent 8900x ICP-MS/MS) with the analytical parameters and tuning conditions following Redaa et al. (2021) and summarised in Table S.3.1. One spot analysis consisted of 20 seconds of gas background collected while the laser was not firing followed by 40 seconds of ablated signal. Strontium isotopes were measured in the oxidised molecule SrO. Strontium is oxidised with N<sub>2</sub>O gas in the reaction chamber (e.g. <sup>87</sup>Sr<sup>16</sup>O formed from <sup>87</sup>Sr at 103 amu) whilst the unreactive <sup>85</sup>Rb was measured on-mass. Dwell times for each Sr isotope were 50ms, 10ms for Rb and 5ms for all other masses totalling to 0.31 seconds.

<i>Laser Parameters</i>	<i>Value</i>	<i>Unit</i>
<i>Ar carrier gas</i>	1050	ml/min
<i>Fluence</i>	3.5	J/cm <sup>2</sup>
<i>He carrier gas</i>	350	ml/min
<i>N<sub>2</sub> addition</i>	3.5	ml/min
<i>Repetition rate</i>	10	Hz
<i>Spot size</i>	74	µm
<i>ICP-MS/MS Plasma Parameters</i>	<i>Value</i>	<i>Unit</i>
<i>RF plasma power</i>	1350	W
<i>ICP-MS/MS Lens Parameters</i>	<i>Value</i>	<i>Unit</i>
<i>Lens extract 1</i>	-2.0	V
<i>Lens extract 2</i>	-150	V
<i>Omega bias</i>	75	V
<i>Omega lens</i>	7.0	V
<i>Q1 entrance</i>	2.0	V
<i>Q1 exit</i>	-1.0	V
<i>Cell focus</i>	-2.0	V

<i>Cell entrance</i>	-100	V
<i>Cell exit</i>	-150	V
<i>Deflect</i>	-10	V
<i>Plate bias</i>	-80	V
<b>ICP-MS/MS Q1 Parameters</b>	<b>Value</b>	<b>Unit</b>
<i>Q1 bias</i>	-2.0	V
<i>Q1 prefilter bias</i>	-9.0	V
<i>Q1 postfilter bias</i>	-10	V
<b>ICP-MS/MS Cell Parameters</b>	<b>Value</b>	<b>Unit</b>
<i>N<sub>2</sub>O flow rate</i>	0.37	mL/min
<i>OctP bias</i>	-23	V
<i>Axial acceleration</i>	2.0	V
<i>OctP RF</i>	180	V
<i>Energy discrimination</i>	-10	V
<b>ICP-MS/MS Q2 Parameters</b>	<b>Value</b>	<b>Unit</b>
<i>Q2 bias</i>	-33	V

**Table S.3.1.** LA-ICP-MS/MS instrumental parameters following Redaa et al. (2021).

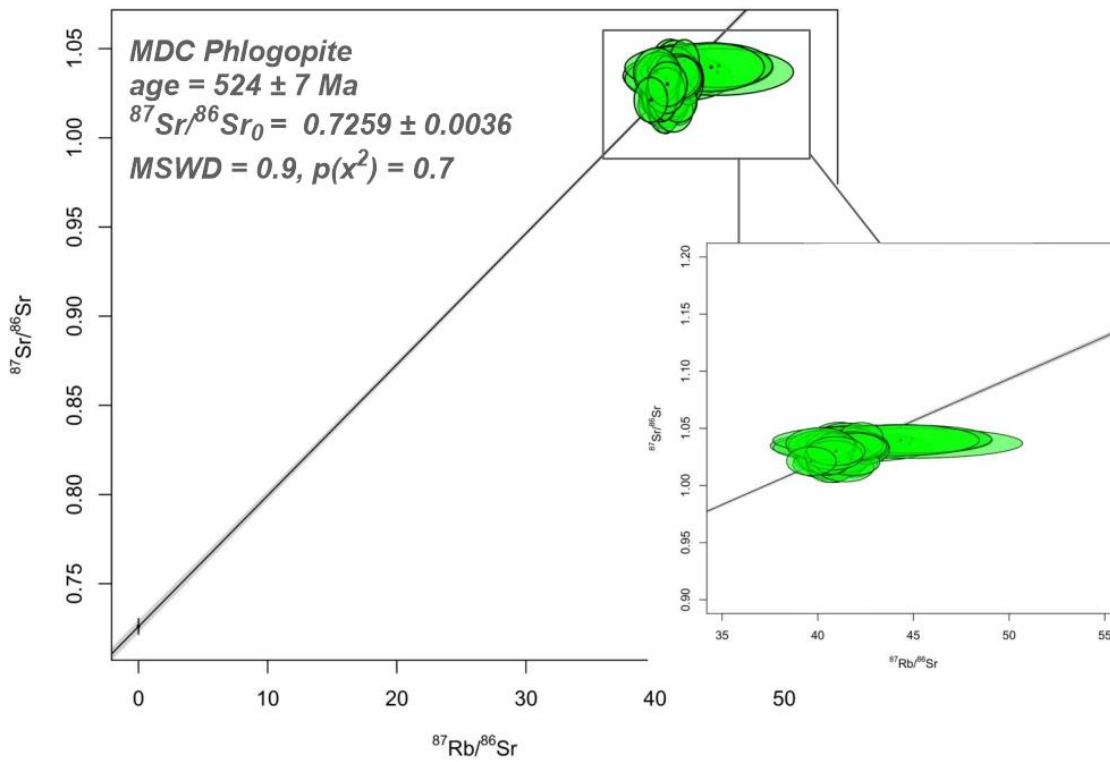
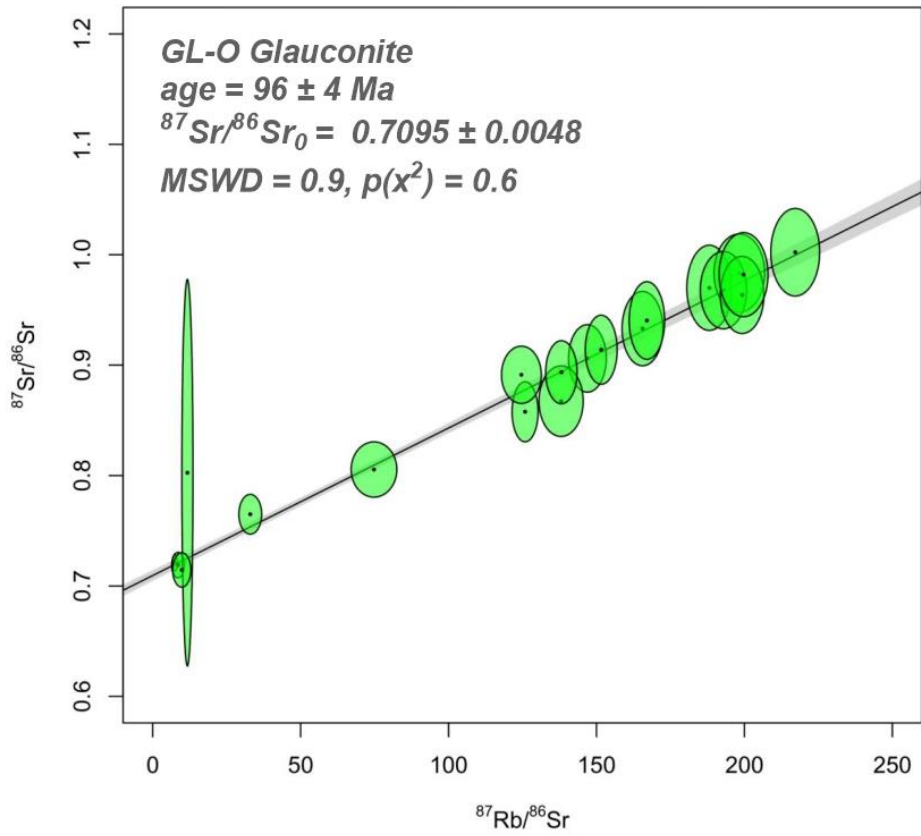


**Figure S.3.1.** Summary of geochronological data from standards GL-O glauconite (Charbit et al., 1998; Derkowski et al., 2009) and MDC phlogopite (Hogmalm et al., 2017) used in this study agrees with published values.

## Petrography and Mineralogy

The MLA images for the samples analysed here cannot be inserted into the thesis as the file is too large but can be found in <https://doi.org/10.25909/6315ea488cc5f>. High resolution SEM-EDS MLA mapping and bulk XRD analysis showed that quartz was the most abundant mineral phase in all samples selected for in situ laser ablation investigation in this study. They are the main detrital component, with grain sizes ranging from < 10 µm and up to 50 µm. They are commonly sub-angular in coarser layers and more sub-rounded in finer interbeds. Quartz has negligible Rb and Sr, so does not influence our results.

All Upper and Middle Velkerri Formation had similar mineral assemblages based on bulk XRD and SEM-EDS mineral mapping. The sample derived from 415 m and 520 m depth were matrix-supported siltstones (Figure S.3.2A-B), with illite being the second most dominant mineral phase (ca. 35 wt. %). These samples still preserve its primary sedimentary structures, with well-defined interbedded siltstones and very fine sands. Illite here is mottled and commonly intergrown with authigenic quartz. Some phases can be seen forming thin elongated interconnected slivers. Furthermore, illite in these samples are dispersed throughout the matrix, filling in pore spaces. These illite domains are commonly randomly oriented with respect to bedding. Some matrices are so fine that individual flakes could not be distinguished. This can be similarly found in the Velkerri Formation shale from 696 m (Figure S.3.2C). However, Velkerri Formation shale from 696 m was more dominated by detrital quartz and had less illite phases within the sample. Some larger flakes of illite can be found are likely physical weathering products of biotite. Another less common occurrence of illite morphology is the alteration of feldspar. Nevertheless, the matrix supported nature of samples and the presence of illite compacted concretions are found in other Roper Group shales and suggest that they originate through reverse weathering processes (Rafiei and Kennedy, 2019; Subarkah et al., 2021). These are the dominant mineralogy in each sample. Therefore, we conclude that the Rb–Sr data collected from each spot analysis are derived predominantly from cogenetic K-hosting (and therefore Rb-bearing) illites.

The Lower Velkerri Formation shales consisted of similar mineral assemblages compared to samples from the Upper and Middle Velkerri Formation. However, these samples did not preserve primary sedimentary textures as the previous subset. The sample sourced from 938 m depth had illite matrices which looked fissile, with a prominent foliated fabric (Figure S.3.2D). This is not commonly found in clay morphologies originating from authigenic or early diagenetic processes and is instead likely induced by a later-stage secondary reaction. Pyrite present in this sample filled cavities and overprint earlier illite and chlorite phases. In addition, apatite in this sample has two main morphologies. This included phosphates that either grew in framboidal structures or as alteration products of clay minerals. On the other hand, the Lower Velkerri Formation shale from 1220 m depth is comparatively more crystalline (Figure S3.2E). Only a minor amount of detrital quartz has evident, and they are consistently up to 100 µm in size. However, illite grain morphologies in this sample do not look detrital. Instead, they form interlocking grain fabrics and seemed to be products from recrystallisation of a finer-grained clay matrix. Moreover, fine-grained clays can also be seen replaced by large chlorite domains larger than 100 µm in size. Overall, the petrography of

the Lower Velkerri Formation shales suggest that they have experienced post-depositional secondary fluid-rock interactions.

### One-Dimensional Thermal Modelling

One-dimensional thermal modelling of the Atree 2 well was conducted using the MATLAB code SILLi 1.0, as produced by Iyer et al. (2018). As the simulation aims to model thermal conditions following emplacement of a Derim Derim Dolerite sill at ca. 1300 Ma, the modelled sedimentary column is different to that preserved currently in the Atree 2 well. Post-Mesoproterozoic sedimentary rocks have been removed for this simulation, and an additional 1.5 km of upper Roper Group sedimentary rocks have been added to satisfy the maximum Palaeotemperatures predicted by  $T_{\max}$  values preserved in the upper and middle Velkerri Formation. Physical properties for lithologies are from the global geochemical dataset of Gard et al. (2019), apart from average density and TOC values, which are taken from Atree 2 well logs. A typical geothermal gradient of 25 °C/km has been used for the simulation, with a surface temperature of 25 °C. Input model formation top ages are not true representations of the Mesoproterozoic strata but are instead designed to deposit required sedimentary rocks over a reasonable time period and allow the geothermal gradient to achieve equilibrium prior to sill emplacement at a model time of 10 Ma. Full sedimentary rock physical properties and model deposition times are provided in Table S.3.2, and sill physical properties and emplacement characteristics are provided in Table S.3.3.

<i>Lithology</i>	<i>Top Depth (m)</i>	<i>Top Age (Ma)</i>	<i>Density (kg m<sup>-3</sup>)</i>	<i>Heat Capacity (J kg<sup>-1</sup> C<sup>-1</sup>)</i>	<i>Thermal Conductivity (W m<sup>-1</sup> K<sup>-1</sup>)</i>	<i>TOC (wt. %)</i>
Upper Roper Group	0	20	2550	731	2.79	0
Moroak Sandstone	1500	40	2450	780	3.76	0
Upper Velkerri Formation	1572	60	2625	731	2.79	0.55
Upper Velkerri Formation	1800	63	2550	731	2.79	2.74
Middle Velkerri Formation	1852	65	2550	731	2.79	5.41
Middle Velkerri Formation	1980	67	2450	731	2.79	3.51
Lower Velkerri Formation	2128	69	2550	731	2.79	0.12
Lower Velkerri Formation	2135	70	2100	731	2.79	0.07
Lower Velkerri Formation	2140	71	2550	731	2.79	0.58
Lower Velkerri Formation	2307	73	2450	734	3.77	3.12
Lower Velkerri Formation	2310	74	2650	731	2.79	0.78
Bessie Creek Sandstone	2410	106	2750	780	3.76	0
Bessie Creek Sandstone	2415	108	2500	780	3.76	0
Corcoran Formation	2827	120	2625	780	3.76	0
Corcoran Formation	2980	122	2625	731	2.79	0

**Table S.3.2.** Lithospheric and stratigraphic parameters used for one-dimensional modelling with SILLi 1.0.

<i>Top Depth (m)</i>	2868
<i>Thickness (m)</i>	75
<i>Emplacement Time (Ma)</i>	10
<i>Emplacement Temp (°C)</i>	1150
<i>Density melt (kg m<sup>-3</sup>)</i>	2550
<i>Heat Capacity melt (J kg<sup>-1</sup> K<sup>-1</sup>)</i>	850
<i>Density solid (kg m<sup>-3</sup>)</i>	3000
<i>Heat Capacity solid (J kg<sup>-1</sup> K<sup>-1</sup>)</i>	820
<i>Thermal Conductivity (W m<sup>-1</sup> K<sup>-1</sup>)</i>	2.1
<i>Solidus T (°C)</i>	950
<i>Liquidus T (°C)</i>	1150
<i>Latent Heat of Crystallization (kJ kg<sup>-1</sup>)</i>	320

**Table S.3.3.** Thermal properties and emplacement conditions for Derim Derim Dolerite sill used in one-dimensional modelling with SILLI 1.0.

### Analytical Data

Strat. Height (m)	Member	S1	S2	S3	T <sub>max</sub>	HI*	OI*	TOC*	TPI	Estimated R0	Min Palaeo T Estimate	Palaeo T Median	Max Palaeo T Estimate
394.10	Upper	0.0	0.3	0.1	427.0	75.0	27.0	0.3	0.0	0.5	69.1	90.6	112.1
396.48	Upper	0.0	0.3	0.1	426.0	69.0	31.0	0.4	0.1	0.5	67.7	89.6	111.5
401.20	Upper	0.0	0.4	0.1	430.0	98.0	37.0	0.4	0.0	0.6	73.0	93.5	114.0
405.90	Upper	0.0	0.3	0.2	431.0	95.0	76.0	0.3	0.0	0.6	74.3	94.5	114.6
410.55	Upper	0.0	0.3	3.0	438.0	39.0	437.0	0.7	0.0	0.7	83.0	101.0	119.1

447.95	443.27	438.53	433.88	430.20	430.20	429.27	424.61	419.86	415.15	411.60	411.60
Upper	Upper	Upper	Upper	Upper	Upper	Upper	Upper	Upper	Upper	Upper	Upper
0.0	0.0	0.0	0.1	0.1	0.1	0.0	0.0	0.0	0.0	0.0	0.0
0.4	0.4	0.7	0.4	0.4	0.4	0.4	0.2	0.3	0.5	0.4	0.4
0.2	0.3	0.8	0.3	0.2	0.2	0.2	0.5	0.1	0.4	1.0	1.0
430.0	426.0	432.0	430.0	429.0	429.0	428.0	428.0	427.0	434.0	430.0	430.0
94.0	75.0	155.0	99.0	91.9	91.9	97.0	63.0	58.0	128.0	87.7	87.7
54.0	56.0	175.0	61.0	36.3	36.3	53.0	133.0	29.0	91.0	217.1	217.1
0.4	0.5	0.5	0.5	0.5	0.5	0.4	0.3	0.5	0.4	0.5	0.5
0.1	0.1	0.0	0.1	0.1	0.1	0.0	0.0	0.0	0.0	0.1	0.1
0.6	0.5	0.6	0.6	0.6	0.6	0.5	0.5	0.5	0.7	0.6	0.6
73.0	67.7	75.6	73.0	71.7	71.7	70.4	70.4	69.1	78.1	73.0	73.0
93.5	89.6	95.4	93.5	92.5	92.5	91.6	91.6	90.6	97.3	93.5	93.5
114.0	111.5	115.3	114.0	113.4	113.4	112.7	112.7	112.1	116.5	114.0	114.0



497.50	494.77	490.14	485.45	480.65	475.91	471.24	469.00	459.85	459.85	457.06	452.64
Upper	Upper	Upper	Upper	Upper	Upper	Upper	Upper	Upper	Upper	Upper	Upper
0.2	0.2	0.0	0.1	0.0	0.9	1.4	0.3	0.1	0.1	0.0	0.1
0.6	0.7	0.2	0.4	0.2	1.3	4.3	1.1	0.4	0.4	0.3	1.5
0.3	0.1	0.2	0.3	2.4	0.2	0.2	0.3	0.6	0.6	0.2	0.6
425.0	425.0	427.0	428.0	436.0	410.0	408.0	430.0	428.0	428.0	430.0	431.0
103.4	114.0	45.0	78.0	52.0	151.0	381.0	158.0	107.4	107.4	83.0	214.0
55.9	24.0	35.0	54.0	610.0	24.0	20.0	37.0	162.5	162.5	45.0	86.0
0.6	0.6	0.5	0.5	0.4	0.9	1.1	0.7	0.4	0.4	0.4	0.7
0.2	0.3	0.1	0.2	0.0	0.4	0.3	0.2	0.2	0.1	0.1	0.1
0.5	0.5	0.5	0.5	0.7	0.2	0.2	0.6	0.5	0.5	0.6	0.6
66.3	66.3	69.1	70.4	80.6	43.9	40.6	73.0	70.4	70.4	73.0	74.3
88.6	88.6	90.6	91.6	99.2	72.6	70.4	93.5	91.6	91.6	93.5	94.5
110.8	110.8	112.1	112.7	117.8	101.3	100.1	114.0	112.7	112.7	114.0	114.6

555.24	Upper	550.72	545.98	541.46	536.75	532.01	527.37	522.75	518.05	509.16	504.35	499.49
	Upper	Upper	Upper	Upper	Upper	Upper	Upper	Upper	Upper	Upper	Upper	Upper
0.1	0.1	0.1	0.1	0.1	0.1	0.1	0.2	0.0	0.1	0.1	0.0	0.0
0.9	0.3	0.3	0.9	0.5	0.4	0.7	0.5	0.4	0.4	0.4	0.3	0.3
0.8	0.3	0.3	0.3	0.2	0.2	0.4	0.1	0.1	0.2	0.4	0.1	0.2
436.0	423.0	433.0	433.0	427.0	424.0	433.0	426.0	425.0	422.0	421.0	424.0	426.0
142.0	64.0	117.0	117.0	74.0	65.0	125.0	79.0	66.0	86.0	79.0	62.0	70.0
126.0	62.0	33.0	33.0	23.0	29.0	72.0	23.0	22.0	37.0	79.0	33.0	37.0
0.6	0.5	0.8	0.8	0.6	0.6	0.5	0.6	0.6	0.5	0.6	0.4	0.5
0.1	0.1	0.1	0.1	0.1	0.2	0.1	0.3	0.1	0.1	0.1	0.1	0.1
0.7	0.5	0.6	0.6	0.5	0.5	0.6	0.5	0.5	0.4	0.4	0.5	0.5
80.6	63.6	76.9	76.9	69.1	65.0	76.9	67.7	66.3	62.2	60.7	65.0	67.7
99.2	86.6	96.4	96.4	90.6	87.6	96.4	89.6	88.6	85.5	84.5	87.6	89.6
117.8	109.6	115.9	115.9	112.1	110.2	115.9	111.5	110.8	108.9	108.3	110.2	111.5

610.00	607.60	602.77	597.91	593.09	588.25	583.49	579.02	574.40	569.51	564.75	559.99
Upper	Upper	Upper	Upper	Upper	Upper	Upper	Upper	Upper	Upper	Upper	Upper
0.3	0.2	0.1	0.1	0.1	0.1	0.1	0.1	0.1	0.1	0.0	0.1
1.1	1.2	0.8	0.3	0.7	0.6	0.5	0.7	1.0	1.0	0.5	0.5
0.5	0.5	0.6	0.1	0.7	0.2	0.6	0.7	0.6	0.5	0.3	0.4
429.0	434.0	433.0	426.0	436.0	424.0	433.0	427.0	434.0	431.0	427.0	433.0
186.7	161.0	144.0	58.0	121.0	74.0	97.0	116.0	140.0	178.0	57.0	93.0
80.0	71.0	116.0	20.0	116.0	23.0	97.0	107.0	87.0	87.0	30.0	76.0
0.6	0.8	0.5	0.6	0.6	0.8	0.6	0.6	0.7	0.6	0.9	0.6
0.2	0.2	0.1	0.1	0.1	0.2	0.1	0.1	0.1	0.1	0.1	0.1
0.6	0.7	0.6	0.5	0.7	0.5	0.6	0.5	0.7	0.6	0.5	0.6
71.7	78.1	76.9	67.7	80.6	65.0	76.9	69.1	78.1	74.3	69.1	76.9
92.5	97.3	96.4	89.6	99.2	87.6	96.4	90.6	97.3	94.5	90.6	96.4
113.4	116.5	115.9	111.5	117.8	110.2	115.9	112.1	116.5	114.6	112.1	115.9

664.69	661.98	655.27	650.50	645.75	640.98	636.12	631.30	626.56	621.84	617.12	612.34
Upper	Upper	Upper	Upper	Upper	Upper	Upper	Upper	Upper	Upper	Upper	Upper
1.7	2.5	0.7	2.4	0.9	0.7	0.7	0.4	1.2	1.5	0.2	0.1
8.4	15.4	3.3	9.6	4.6	4.8	2.8	1.4	4.1	10.3	0.6	0.8
0.4	0.2	0.4	0.2	0.3	0.3	0.3	0.2	0.2	0.2	0.2	0.7
428.0	433.0	426.0	433.0	427.0	428.0	430.0	428.0	427.0	428.0	427.0	434.0
319.0	348.0	142.0	313.0	184.0	185.0	181.0	109.0	195.0	290.0	86.0	140.0
15.0	5.0	15.0	7.0	11.0	12.0	19.0	13.0	11.0	7.0	36.0	134.0
2.6	4.4	2.3	3.1	2.5	2.6	1.6	1.2	2.1	3.5	0.7	0.6
0.2	0.1	0.2	0.2	0.2	0.1	0.2	0.2	0.2	0.1	0.2	0.1
0.5	0.6	0.5	0.6	0.5	0.5	0.6	0.5	0.5	0.5	0.5	0.7
70.4	76.9	67.7	76.9	69.1	70.4	73.0	70.4	69.1	70.4	69.1	78.1
91.6	96.4	89.6	96.4	90.6	91.6	93.5	91.6	90.6	91.6	90.6	97.3
112.7	115.9	111.5	115.9	112.1	112.7	114.0	112.7	112.1	112.7	112.1	116.5

731.54	722.05	707.31	700.45	697.90	695.35	688.61	682.07	682.07	679.11	674.32	669.51
Middle	Middle	Middle	Middle	Middle	Middle	Middle	Middle	Middle	Middle	Middle	Upper
1.8	1.9	2.0	4.3	2.4	3.9	3.0	3.6	3.6	2.0	2.5	1.9
5.7	17.3	21.0	28.5	20.6	22.6	27.2	28.5	28.5	12.8	18.0	15.3
0.1	0.2	0.3	0.5	0.3	0.5	0.2	0.6	0.6	0.2	0.2	0.4
429.0	429.0	430.0	435.0	434.0	431.0	433.0	431.0	431.0	432.0	431.0	430.0
314.0	280.0	306.0	365.4	341.0	335.5	365.0	480.6	480.6	370.0	344.0	370.0
8.0	4.0	4.0	6.7	5.0	7.6	2.0	9.6	9.6	7.0	4.0	9.0
1.8	6.2	6.9	7.8	6.1	6.7	7.4	5.9	5.9	3.5	5.2	4.1
0.2	0.1	0.1	0.1	0.1	0.1	0.1	0.1	0.1	0.1	0.1	0.1
0.6	0.6	0.6	0.7	0.7	0.6	0.6	0.6	0.6	0.6	0.6	0.6
71.7	71.7	73.0	79.4	78.1	74.3	76.9	74.3	74.3	75.6	74.3	73.0
92.5	92.5	93.5	98.3	97.3	94.5	96.4	94.5	94.5	95.4	94.5	93.5
113.4	113.4	114.0	117.2	116.5	114.6	115.9	114.6	114.6	115.3	114.6	114.0

802.74	793.37	783.81	769.64	765.29	760.33	754.96	750.28	746.50	746.50	746.02	736.33
Middle	Middle	Middle	Middle	Middle	Middle	Middle	Middle	Middle	Middle	Middle	Middle
2.4	2.2	1.9	1.8	1.6	1.6	0.3	0.6	2.1	2.1	1.3	2.3
16.4	15.7	12.1	9.6	8.9	10.0	0.5	1.2	16.3	16.3	9.7	21.4
0.3	0.3	0.2	0.3	0.3	0.3	0.2	0.3	0.5	0.5	0.3	0.3
432.0	432.0	430.0	429.0	428.0	430.0	435.0	435.0	431.0	431.0	427.0	433.0
263.0	206.0	204.0	169.0	180.0	192.0	107.0	138.0	280.0	280.0	191.0	265.0
4.0	4.0	4.0	5.0	5.0	6.0	31.0	36.0	8.9	8.9	6.0	4.0
6.2	7.6	5.9	5.7	4.9	5.2	0.5	0.8	5.8	5.8	5.1	8.1
0.1	0.1	0.1	0.2	0.2	0.1	0.4	0.3	0.1	0.1	0.1	0.1
0.6	0.6	0.6	0.6	0.5	0.6	0.7	0.7	0.6	0.6	0.5	0.6
75.6	75.6	73.0	71.7	70.4	73.0	79.4	79.4	74.3	74.3	69.1	76.9
95.4	95.4	93.5	92.5	91.6	93.5	98.3	98.3	94.5	94.5	90.6	96.4
115.3	115.3	114.0	113.4	112.7	114.0	117.2	117.2	114.6	114.6	112.1	115.9

850.00	850.00	850.00	845.48	831.63	831.63	831.21	824.20	821.78	820.70	814.40	812.11
Middle	Middle	Middle	Middle	Middle	Middle	Middle	Middle	Middle	Middle	Middle	Middle
2.2	2.2	0.7	3.4	2.8	2.8	2.1	3.6	2.2	3.6	4.3	2.3
5.4	5.4	1.6	10.0	7.0	7.0	10.1	19.7	16.0	18.4	23.6	17.5
0.4	0.4	0.8	0.2	0.5	0.5	0.3	0.8	0.3	0.7	0.6	0.3
430.0	430.0	442.0	433.0	425.0	425.0	436.0	433.0	438.0	437.0	439.0	437.0
157.1	157.1	159.0	281.0	192.1	192.1	264.0	290.8	279.0	285.0	298.0	295.0
12.2	12.2	79.0	5.0	12.4	12.4	9.0	11.7	6.0	11.0	8.0	4.0
3.4	3.4	1.0	3.5	3.6	3.6	3.8	6.8	5.7	6.4	7.9	6.0
0.3	0.3	0.3	0.3	0.3	0.3	0.2	0.2	0.1	0.2	0.2	0.1
0.6	0.6	0.8	0.6	0.5	0.5	0.7	0.6	0.7	0.7	0.7	0.7
73.0	73.0	87.7	76.9	66.3	66.3	80.6	76.9	83.0	81.8	84.2	81.8
93.5	93.5	104.7	96.4	88.6	88.6	99.2	96.4	101.0	100.1	101.9	100.1
114.0	114.0	121.6	115.9	110.8	110.8	117.8	115.9	119.1	118.4	119.7	118.4

918.77	912.37	898.25	883.63	879.90	879.90	879.90	876.25	873.77	864.50	863.60	854.93
Middle	Middle	Middle	Middle	Middle	Middle	Middle	Middle	Middle	Middle	Middle	Middle
0.4	3.5	1.3	1.8	3.1	3.1	3.1	3.2	1.6	2.5	3.2	3.3
0.3	7.3	4.0	6.0	5.5	5.5	5.5	6.5	3.6	10.8	8.3	9.1
0.3	0.2	0.7	0.2	0.5	0.5	0.5	0.5	0.2	0.2	0.7	0.2
408.0	407.0	429.0	429.0	438.0	438.0	438.0	435.0	435.0	433.0	428.0	433.0
82.8	305.0	232.0	187.0	226.6	226.6	226.6	243.7	184.0	253.0	274.0	220.0
112.6	8.0	41.0	6.0	18.6	18.6	18.6	18.3	9.0	5.0	21.0	5.0
0.3	2.4	1.7	3.2	2.4	2.4	2.4	2.7	2.0	4.3	3.0	4.2
0.6	0.3	0.2	0.2	0.4	0.4	0.4	0.3	0.3	0.2	0.3	0.3
0.2	0.2	0.6	0.6	0.7	0.7	0.7	0.7	0.7	0.6	0.5	0.6
40.6	38.9	71.7	71.7	83.0	83.0	83.0	79.4	79.4	76.9	70.4	76.9
70.4	69.2	92.5	92.5	101.0	101.0	101.0	98.3	98.3	96.4	91.6	96.4
100.1	99.4	113.4	113.4	119.1	119.1	119.1	117.2	117.2	115.9	112.7	115.9



945.50	945.50	940.69	935.60	935.60	935.60	931.53	926.59	926.50	924.90	922.05	918.77
Middle	Middle	Middle	Middle	Middle	Middle	Middle	Middle	Middle	Middle	Middle	Middle
1.7	1.7	2.8	3.1	3.1	2.6	1.4	2.1	2.1	2.5	2.7	0.4
2.7	2.7	8.0	5.9	5.9	11.3	3.8	5.5	5.5	6.1	10.9	0.3
0.5	0.5	0.2	0.7	0.7	0.3	0.3	0.7	0.7	0.6	0.3	0.3
425.0	425.0	436.0	434.0	434.0	434.0	422.0	435.0	435.0	428.0	437.0	408.0
77.6	77.6	182.0	152.5	152.5	193.0	95.0	162.2	162.2	157.0	197.0	82.8
13.6	13.6	5.0	18.0	18.0	5.0	7.0	21.6	21.6	14.7	5.0	112.6
3.5	3.5	4.4	3.8	3.8	5.9	4.0	3.4	3.4	3.9	5.5	0.3
0.4	0.4	0.3	0.4	0.3	0.2	0.3	0.3	0.3	0.3	0.2	0.6
0.5	0.5	0.7	0.7	0.7	0.7	0.4	0.7	0.7	0.5	0.7	0.2
66.3	66.3	80.6	78.1	78.1	78.1	62.2	79.4	79.4	70.4	81.8	40.6
88.6	88.6	99.2	97.3	97.3	97.3	85.5	98.3	98.3	91.6	100.1	70.4
110.8	110.8	117.8	116.5	116.5	116.5	108.9	117.2	117.2	112.7	118.4	100.1

1141.42	1131.74	1127.10	1122.40	1117.48	1088.21	1055.15	1040.86	1002.46	983.38	957.65	950.64
Lower	Lower	Lower	Lower	Lower	Lower	Lower	Lower	Lower	Lower	Lower	Lower
0.0	1.0	1.5	0.0	0.0	0.0	1.2	0.0	0.0	0.0	0.0	0.0
0.1	2.7	4.0	0.1	0.2	0.1	3.5	0.0	0.1	0.1	0.1	0.1
0.0	0.2	0.1	0.1	0.1	0.1	0.3	0.1	0.1	0.1	0.1	0.1
436.0	449.0	446.0	502.0	461.0	447.0	451.0	490.0	454.0	452.0	442.0	456.0
79.0	80.0	127.0	78.0	52.0	92.0	93.0	42.0	108.0	102.0	101.0	65.0
32.0	5.0	3.0	48.0	19.0	47.0	7.0	104.0	51.0	108.0	89.0	57.0
0.1	3.4	3.1	0.1	0.3	0.2	3.8	0.1	0.1	0.1	0.1	0.1
0.1	0.3	0.3	0.0	0.1	0.1	0.3	0.0	0.0	0.0	0.0	0.1
0.7	0.9	0.9	1.9	1.1	0.9	1.0	1.7	1.0	1.0	0.8	1.0
80.6	95.6	92.3	143.3	108.1	93.4	97.8	133.9	100.9	98.8	87.7	103.0
99.2	110.8	108.2	151.4	120.8	109.1	112.5	142.9	115.1	113.4	104.7	116.7
117.8	126.0	124.1	159.5	133.6	124.7	127.3	152.0	129.2	127.9	121.6	130.4

1122.4	983.38	957.65	950.64	1220.65	1208.10	1203.28	1193.68	1174.62	1164.90	1155.43	1150.63
Lower	Lower	Lower	Lower	Lower	Lower	Lower	Lower	Lower	Lower	Lower	Lower
0.9	0.0	0.0	0.0	0.0	0.0	0.9	0.0	0.0	0.0	0.0	0.0
2.9	0.1	0.1	0.1	0.0	0.0	1.9	0.0	0.0	0.0	0.1	0.0
0.3	0.2	0.1	0.1	0.0	0.1	0.2	0.1	0.1	0.0	0.0	0.1
451.9	447.8	447.4	456.6	485.0	496.0	461.0	481.0	482.0	493.0	465.0	481.0
66.4	47.8	64.3	43.8	27.0	28.0	53.0	35.0	24.0	67.0	44.0	31.0
6.2	73.9	78.6	31.3	21.0	56.0	4.0	55.0	43.0	80.0	24.0	139.0
4.3	0.2	0.1	0.2	0.2	0.1	3.5	0.1	0.1	0.1	0.2	0.0
0.2	0.2	0.2	0.1	0.1	0.2	0.3	0.1	0.0	0.0	0.1	0.0
1.0	0.9	0.9	1.1	1.6	1.8	1.1	1.5	1.5	1.7	1.2	1.5
98.7	94.3	93.8	103.6	129.8	138.7	108.1	126.4	127.3	136.3	112.0	126.4
113.3	109.8	109.4	117.2	139.3	147.2	120.8	136.4	137.1	145.1	124.0	136.4
127.8	125.3	125.0	130.8	148.8	155.7	133.6	146.3	146.9	153.9	136.1	146.3

1220.65	1193.68	1174.62	1155.43	1150.63	1040.86	1141.42
Lower	Lower	Lower	Lower	Lower	Lower	Lower
0.0	0.0	0.0	0.0	0.0	0.0	0.1
0.1	0.1	0.1	0.1	0.1	0.1	0.2
0.1	0.1	0.1	0.1	0.1	0.1	0.2
501.8	497.1	494.3	476.7	489.5	485.5	473.6
27.3	43.5	28.6	27.6	30.0	50.0	34.0
27.3	43.5	33.3	20.7	35.0	57.1	38.3
0.3	0.2	0.2	0.3	0.2	0.1	0.5
0.2	0.2	0.1	0.2	0.3	0.2	0.2
1.9	1.8	1.7	1.4	1.7	1.6	1.4
143.1	139.5	137.4	122.7	133.5	130.2	119.9
151.3	148.0	146.0	133.1	142.6	139.7	130.8
159.4	156.4	154.7	143.5	151.6	149.1	141.6

Table S.3.4. Source-rock analytical data for samples in Chapter 3.

Strat. Height (m)	Member	La	Ce	Pr	Nd	Sm	Eu	Gd	Tb	Dy	Y	Ho	Er	Yb	Lu
401.20	Upper	53.70	119.00	12.20	43.70	7.20	1.30	5.40	0.90	5.70	32.00	1.20	3.40	3.50	0.50
396.48	Upper	56.00	119.00	12.80	45.00	7.80	1.40	6.50	1.10	6.40	38.00	1.30	3.90	4.00	0.63
394.10	Upper	57.00	122.00	13.30	51.60	11.60	2.00	9.40	1.40	8.10	46.00	1.60	4.30	4.10	0.62

457.06		452.64	447.95	443.27	438.53	433.88	429.27	424.61	419.86	415.15	410.55	405.90
Upper	Upper	Upper	Upper	Upper	Upper	Upper	Upper	Upper	Upper	Upper	Upper	Upper
58.60	88.40	59.60	55.60	57.20	57.90	63.30	56.60	63.60	58.20	41.40	54.60	
125.00	185.00	125.00	123.00	125.00	122.00	139.00	121.00	134.00	123.00	85.90	113.00	
13.60	19.90	13.30	12.60	13.00	13.10	14.80	13.00	14.50	13.40	9.70	12.80	
49.90	71.10	47.00	44.90	46.70	46.60	52.30	47.00	52.30	48.40	35.60	46.30	
9.00	12.10	7.90	7.90	8.50	7.90	8.80	8.50	8.90	8.80	6.60	8.50	
1.50	2.20	1.50	1.30	1.60	1.50	1.50	1.50	1.70	1.60	1.20	1.80	
7.00	8.60	6.70	5.60	6.70	6.60	7.00	6.40	6.60	6.70	5.70	7.60	
1.10	1.40	1.10	0.80	1.10	1.10	1.10	1.00	1.10	1.10	1.00	1.60	
7.00	7.90	6.60	5.30	6.70	6.70	6.50	6.20	6.30	6.40	7.20	8.00	
34.00	38.00	35.00	30.00	36.00	34.00	40.00	34.00	34.00	36.00	43.00	41.00	
1.30	1.60	1.40	1.00	1.40	1.30	1.30	1.20	1.20	1.30	1.70	1.80	
4.20	4.80	3.90	3.00	4.00	4.00	3.70	3.80	3.60	3.80	5.90	5.10	
4.20	4.90	4.10	3.10	4.40	4.20	3.40	4.00	3.60	3.70	7.50	5.00	
0.62	0.87	0.64	0.45	0.63	0.64	0.53	0.57	0.50	0.59	1.23	1.07	

522.75	518.05	509.16	504.35	499.49	494.77	490.14	485.45	480.65	475.91	471.24	469.00
Upper	Upper	Upper	Upper	Upper	Upper	Upper	Upper	Upper	Upper	Upper	Upper
73.40	54.70	71.80	54.10	55.20	56.40	68.10	51.50	27.90	49.50	57.30	78.30
153.00	127.00	160.00	152.00	157.00	120.00	143.00	108.00	59.90	104.00	120.00	162.00
16.80	13.50	17.40	15.00	15.00	12.90	15.90	12.40	6.40	11.50	13.70	17.80
61.90	49.90	63.30	55.20	55.40	46.70	57.40	44.60	23.30	41.60	51.00	63.40
10.40	9.00	11.30	10.20	9.70	8.10	9.50	8.30	4.00	7.20	10.40	11.20
2.00	1.70	2.20	1.90	1.70	1.40	1.70	1.50	0.80	1.40	1.70	2.10
8.40	7.30	9.50	8.30	7.60	6.80	7.70	7.10	4.20	6.80	9.50	9.00
1.30	1.10	1.50	1.20	1.10	1.10	1.20	1.10	0.80	1.00	1.60	1.40
7.80	7.00	8.50	7.70	7.20	6.80	7.50	7.00	5.50	6.20	10.00	8.60
37.00	38.00	41.00	40.00	38.00	34.00	32.00	34.00	34.00	33.00	50.00	39.00
1.60	1.40	1.70	1.50	1.40	1.30	1.40	1.40	1.40	1.20	2.00	1.70
4.30	3.80	4.80	4.20	4.00	3.80	4.30	4.00	4.70	3.50	6.10	5.00
4.20	3.80	4.60	4.00	4.00	3.90	4.30	4.00	6.00	3.50	5.80	5.30
0.61	0.60	0.68	0.55	0.63	0.55	0.63	0.59	0.99	0.55	0.95	0.80

579.02		574.40	569.51	564.75	559.99	555.24	550.72	545.98	541.46	536.75	532.01	527.37
Upper	Upper	Upper	Upper	Upper	Upper	Upper	Upper	Upper	Upper	Upper	Upper	Upper
73.00	83.60	62.60	73.90	65.90	66.70	73.60	67.60	61.40	70.90	73.20	77.00	
156.00	178.00	136.00	154.00	143.00	141.00	152.00	143.00	127.00	150.00	155.00	162.00	
17.30	19.50	14.80	17.00	15.60	15.60	17.00	16.00	14.10	16.40	17.10	17.90	
64.20	71.80	54.80	61.40	58.00	57.20	62.30	58.20	50.50	60.20	62.50	64.90	
11.80	12.70	9.80	11.30	10.30	11.00	10.90	11.40	9.00	10.80	11.00	11.70	
2.10	2.30	1.80	2.00	2.00	1.80	2.00	2.00	1.70	2.00	2.10	2.10	
9.50	10.40	8.40	8.60	8.70	8.90	9.00	9.00	7.80	8.40	9.00	10.20	
1.50	1.60	1.40	1.40	1.40	1.40	1.40	1.40	1.20	1.30	1.40	1.60	
9.10	10.40	8.60	8.00	8.40	8.60	8.60	8.70	7.10	8.00	8.40	9.50	
44.00	50.00	39.00	39.00	42.00	41.00	38.00	43.00	35.00	38.00	42.00	46.00	
1.80	2.00	1.60	1.50	1.60	1.70	1.60	1.70	1.40	1.60	1.70	1.90	
5.40	5.80	4.80	4.60	5.00	5.00	4.60	5.00	4.10	4.60	5.00	5.40	
5.70	5.70	4.90	4.50	5.00	5.20	4.70	5.00	3.90	4.50	4.90	5.50	
0.86	0.86	0.72	0.70	0.74	0.75	0.71	0.74	0.52	0.67	0.77	0.82	

636.12		631.30	626.56	621.84	617.12	612.34	607.60	602.77	597.91	593.09	588.25	583.49
Upper	Upper	Upper	Upper	Upper	Upper	Upper	Upper	Upper	Upper	Upper	Upper	Upper
61.80	63.40	46.80	48.40	78.50	59.50	63.80	69.00	70.40	66.90	88.70	75.50	
128.00	134.00	94.30	97.60	163.00	127.00	138.00	146.00	151.00	151.00	185.00	159.00	
14.70	15.30	12.40	12.40	18.60	14.00	15.80	16.20	16.70	16.20	20.40	17.90	
55.70	57.40	48.00	46.90	68.10	51.80	57.50	58.40	61.10	60.90	72.70	63.40	
11.70	10.80	9.50	10.00	12.10	9.70	10.50	10.10	11.10	11.00	12.20	11.50	
2.10	2.00	1.80	1.90	2.30	1.90	2.00	2.00	1.80	2.00	2.30	2.10	
10.40	9.00	9.40	9.20	10.20	8.40	9.30	8.50	9.40	8.40	10.20	9.60	
1.70	1.40	1.60	1.50	1.60	1.30	1.50	1.40	1.60	1.40	1.60	1.50	
10.00	8.40	9.50	8.80	10.00	8.50	8.60	8.70	9.60	8.60	9.80	8.90	
44.00	41.00	53.00	49.00	40.00	39.00	40.00	41.00	43.00	44.00	46.00	47.00	
1.90	1.60	2.00	1.70	2.00	1.60	1.70	1.60	1.90	1.70	1.90	1.80	
5.50	4.60	6.00	5.00	6.10	5.00	4.90	4.90	5.40	5.30	5.50	5.30	
5.00	4.60	5.90	4.80	6.20	5.30	4.90	4.70	5.20	5.40	5.50	5.50	
0.73	0.67	0.88	0.74	0.92	0.79	0.70	0.71	0.78	0.78	0.80	0.80	





802.74		793.37	783.81	769.64	765.29	760.33	754.96	750.28	746.02	736.33	731.54	722.05
Middle	Middle	Middle	Middle	Middle	Middle	Middle	Middle	Middle	Middle	Middle	Middle	Middle
50.20	59.70	58.40	45.30	45.30	51.20	50.30	45.20	38.60	47.60	43.60	46.80	44.70
87.80	107.00	104.00	86.80	86.80	96.70	96.90	92.40	86.60	92.00	95.30	94.40	77.70
12.90	15.30	14.90	11.90	11.90	12.50	13.00	11.00	9.80	12.10	13.10	11.40	11.00
51.90	63.10	61.40	48.40	48.40	49.90	51.90	40.80	35.20	48.00	57.30	43.30	42.80
10.90	13.30	13.60	10.80	10.80	9.80	11.60	6.70	6.20	9.70	16.30	8.10	7.90
2.00	2.60	2.60	2.20	2.20	2.10	2.30	1.20	1.20	2.10	3.50	1.60	1.70
11.60	13.60	14.40	10.70	10.70	10.10	11.50	5.20	4.80	9.80	18.80	7.10	8.40
1.90	2.00	2.10	1.60	1.60	1.50	1.70	0.90	0.70	1.50	2.70	1.10	1.30
12.40	12.80	12.70	10.00	10.00	9.40	9.80	5.70	5.00	9.20	14.80	6.80	8.40
81.00	83.00	76.00	55.00	55.00	55.00	54.00	35.00	34.00	54.00	69.00	39.00	55.00
2.60	2.70	2.60	2.10	2.10	1.90	2.00	1.20	1.00	1.80	2.70	1.40	1.90
8.20	8.30	7.70	6.00	6.00	5.40	5.60	3.50	2.90	5.40	6.90	4.10	5.50
8.20	7.60	7.10	5.60	5.60	5.30	5.10	3.40	2.70	5.20	5.70	4.20	5.40
1.27	1.19	1.11	0.80	0.80	0.86	0.77	0.53	0.38	0.76	0.82	0.65	0.83

926.59		922.05	912.37	898.25	883.63	873.77	864.50	854.93	845.48	831.21	821.78	812.11
Middle	Middle	Middle	Middle	Middle	Middle	Middle	Middle	Middle	Middle	Middle	Middle	Middle
35.30	35.80	32.90	32.90	31.50	39.00	37.90	45.40	36.10	33.20	47.40	46.10	42.60
65.20	66.40	63.00	63.00	63.40	71.20	70.90	83.60	66.60	58.20	91.50	89.00	79.40
8.30	8.30	9.00	9.00	8.30	9.30	9.20	11.80	8.90	8.50	12.20	12.00	10.70
32.10	32.00	36.90	36.90	33.30	36.60	35.90	47.90	36.60	33.90	47.80	48.30	43.30
6.20	6.30	7.60	7.60	6.40	7.50	7.20	9.80	7.50	7.30	9.50	10.10	8.50
1.50	1.50	1.50	1.50	1.60	1.60	1.40	2.00	1.60	1.50	1.90	1.90	1.70
6.70	6.70	8.10	8.10	7.40	7.50	7.30	10.30	7.90	7.50	9.40	9.70	9.00
1.10	1.10	1.20	1.20	1.20	1.20	1.20	1.70	1.30	1.20	1.40	1.50	1.40
7.30	7.00	7.60	7.60	7.50	7.90	7.50	10.10	8.30	7.40	9.70	9.80	9.10
43.00	47.00	50.00	50.00	48.00	50.00	47.00	65.00	54.00	49.00	61.00	63.00	62.00
1.50	1.50	1.50	1.50	1.50	1.70	1.50	2.20	1.70	1.60	1.90	2.00	2.00
4.70	4.70	4.20	4.20	4.30	5.10	4.80	6.30	5.20	4.60	5.80	6.20	5.80
4.90	4.50	4.00	4.00	4.20	5.20	4.60	6.30	4.90	4.50	5.70	6.10	5.80
0.74	0.73	0.64	0.64	0.64	0.83	0.69	0.95	0.82	0.68	0.83	0.95	0.88

1122.40		1117.48	1088.21	1055.15	1040.86	1019.75	1002.46	983.38	957.65	950.64	940.69	931.53
	Lower	Lower	Lower	Lower	Lower	Lower	Lower	Lower	Lower	Lower	Middle	Middle
37.00	76.00	92.40	41.90	26.90	30.80	35.40	37.80	33.30	37.50	37.50	28.10	40.30
88.90	162.00	208.00	92.70	60.40	79.60	89.90	95.70	76.00	80.80	80.80	53.70	77.00
9.60	18.80	23.10	10.90	6.90	8.50	9.80	9.90	9.20	9.20	9.20	6.70	10.50
37.10	70.40	83.70	41.80	28.30	34.00	38.20	37.30	37.50	33.80	33.80	25.90	44.40
7.40	12.00	12.30	9.80	6.60	8.00	7.40	6.10	8.70	6.00	6.00	4.70	8.80
1.50	2.00	2.10	1.70	1.30	1.70	1.40	1.20	1.70	0.90	0.90	1.20	2.00
6.00	8.80	9.90	9.20	5.80	7.70	5.90	5.40	7.90	4.90	4.90	5.40	10.00
1.00	1.40	1.70	1.50	0.90	1.20	1.00	0.90	1.20	0.80	0.80	0.90	1.60
5.70	8.70	10.90	9.10	5.10	7.30	5.90	5.40	6.70	5.30	5.30	6.10	10.30
29.00	44.00	56.00	44.00	30.00	34.00	31.00	29.00	34.00	30.00	30.00	37.00	69.00
1.10	1.70	2.20	1.80	0.90	1.40	1.20	1.10	1.20	1.10	1.10	1.30	2.20
3.20	5.10	6.60	5.70	3.00	3.90	3.40	3.30	3.60	3.40	3.40	3.90	6.50
3.30	5.70	6.90	5.90	3.00	4.00	3.70	3.50	3.60	3.50	3.50	4.10	6.30
0.49	0.79	1.07	0.87	0.48	0.60	0.55	0.50	0.57	0.52	0.52	0.59	0.95

1220.65		1208.10	1193.68	1174.62	1164.90	1155.43	1150.63	1141.42	1131.74	1127.10
Lower	Lower	Lower	Lower	Lower	Lower	Lower	Lower	Lower	Lower	Lower
35.80	37.40	48.70	55.90	50.00	32.70	61.50	36.80	76.70	47.90	39.80
82.80	80.90	102.00	117.00	104.00	70.00	162.00	87.50	169.00	110.00	90.00
8.70	8.80	12.40	14.00	12.10	8.10	17.10	9.30	18.80	12.60	10.00
32.30	32.70	47.90	52.20	45.30	32.00	63.00	36.50	69.70	48.60	37.60
6.40	6.40	9.90	8.60	8.90	5.80	10.50	7.30	12.20	9.00	7.10
1.10	1.20	1.90	1.80	1.70	1.30	1.70	1.30	2.10	1.50	1.30
4.80	5.40	9.20	7.20	9.00	5.70	7.20	6.00	8.90	7.10	6.30
0.80	0.80	1.40	1.10	1.40	1.00	1.10	0.90	1.40	1.20	1.00
4.70	4.80	9.10	7.10	9.10	6.10	7.40	5.40	9.10	7.30	6.50
21.00	24.70	43.00	39.00	43.00	35.00	39.00	26.00	50.00	40.00	32.00
0.90	0.90	1.80	1.50	1.80	1.30	1.50	1.10	1.80	1.60	1.40
2.70	2.70	5.00	4.40	4.80	3.90	4.60	3.20	5.80	5.10	4.20
2.80	2.70	5.10	4.70	4.90	3.70	4.90	3.30	5.90	5.60	4.40
0.41	0.41	0.82	0.65	0.73	0.55	0.74	0.49	0.88	0.81	0.64

Table S.3.5. Geochemical data for samples in Chapter 3.

Sample Depth	Width	Scale	Kubler Index 2 Theta	Reference
504.00	4.53	0.19	0.87	Capogreco2017
573.60	2.30	0.29	0.67	CSR0181
596.10	1.98	0.30	0.60	CSR0181
665.00	3.51	0.18	0.64	Capogreco2017
688.00	2.70	0.20	0.54	NTGSRec2021
710.00	5.77	0.08	0.47	CSR0181
735.80	5.55	0.08	0.43	CSR0181
800.00	2.20	0.19	0.42	NTGSRec2021
822.00	2.00	0.19	0.38	NTGSRec2021
863.00	2.55	0.18	0.46	Capogreco2017
1110.00	2.20	0.20	0.43	Capogreco2017
1121.10	4.20	0.09	0.36	CSR0181

**Table S.3.6.** Illite crystallinity data for samples in Chapter 3.

Depth (m)	Amount extracted (g)	Sats mg	Arom mg	sats/arom	mgsats/gTOC	mgaroms/g TOC	mg HC/gTOC	TOC	MPDFI	VRC(MPDFJ)	VRC(MPR)L	MPRK	DBT/PM	Temp(MPD F)	Temp(MPR)
410.55	11.14	0.40	0.20	2.00	5.28	2.64	7.92	0.68	0.31	0.54	0.69	0.57	0.00	70.09	80.73
452.64	10.88	0.80	0.20	4.00	10.81	2.70	13.52	0.68	0.31	0.54	0.79	0.70	0.11	70.09	87.35
471.24	10.62	5.00	0.40	12.50	41.66	3.33	45.00	1.13	0.36	0.64	0.84	0.79	0.15	77.28	90.54
527.37	8.13	3.60	0.20	18.00	72.59	4.03	76.62	0.61	0.33	0.56	0.75	0.64	0.06	71.56	84.74
569.51	8.51	22.80	2.00	11.40	461.93	40.52	502.45	0.58	0.32	0.54	0.83	0.78	0.51	70.09	89.91
669.51	14.59	13.20	6.60	2.00	29.47	14.74	44.21	3.07	0.30	0.51	0.73	0.61	0.63	67.86	83.42
688.61	17.96	17.60	11.00	1.60	23.73	14.83	38.56	4.13	0.32	0.55	0.79	0.70	0.64	70.83	87.35

1203.28	1122.40	940.69	912.37	812.11	793.37	750.28	
8.41	14.77	4.65	11.78	8.16	13.42	20.33	
0.20	13.40	36.60	29.40	8.80	20.80	10.80	
5.20	1.60	5.00	17.20	3.00	10.80	3.60	
0.04	8.38	7.32	1.71	2.93	1.93	3.00	
4.32	146.33	1405.53	509.34	158.59	20.31	7.76	
112.42	17.47	192.01	297.98	54.07	10.55	2.59	
116.74	163.80	1597.54	807.32	212.66	30.86	10.34	
0.55	0.62	0.56	0.49	0.68	7.63	6.85	
0.64	0.59	0.44	0.47	0.39	0.39	0.38	
1.27	1.16	0.82	0.89	0.70	0.70	0.69	
1.29	1.29	0.89	1.05	0.98	0.95	0.91	
2.26	2.24	0.88	1.30	1.09	1.03	0.94	
0.18	0.20	0.81	0.79	0.35	0.55	0.75	
115.11	109.26	89.28	93.65	81.40	81.40	80.73	
116.15	116.15	93.65	103.13	99.07	97.29	94.88	
Well ID	Depth from (m)	Bitumen (VRE value)					PalaeoT
		Mean	Stdev.	Minimum	Maximum	Number	
Altree 2	559	0.52	0.08	0.39	0.73	18.00	68.61
Altree 2	574	0.48	0.15	0.35	0.65	4.00	65.58
Altree 2	625	0.55	0.15	0.41	0.79	4.00	70.83
Altree 2	676	0.34	0.06	0.25	0.42	5.00	54.38
Altree 2	682	0.46	0.07	0.33	0.56	9.00	64.04
Altree 2	712	0.41	0.06	0.27	0.50	25.00	60.10
Altree 2	801	0.61	0.06	0.51	0.70	10.00	75.16
Altree 2	821	0.68	0.12	0.48	0.86	25.00	80.04
Altree 2	863	0.84	0.09	0.70	0.95	5.00	90.54
Altree 2	922	0.90	0.09	0.67	1.10	25.00	94.27
Altree 2	1060	1.33	0.18	1.04	1.81	24.00	118.19
Altree 2	1126	1.19	0.50	0.72	3.07	33.00	110.88

Table S.3.7. Aromatic hydrocarbon date compiled for samples in Chapter 3.

Sample	87Rb/ 86Sr	87Rb/86Sr 2 SE Error	87Sr/8 6Sr	87Sr/86Sr 2SE Error	Error Correlation	Single Spot Ages	Single Spot Age Standard Error
Altree 2 - 415 m	4.17	0.11	0.79	0.01	0.25	1450	6
Altree 2 - 415 m	5.10	0.25	0.81	0.01	0.42	1446	8
Altree 2 - 415 m	6.68	0.15	0.84	0.01	0.34	1451	6
Altree 2 - 415 m	3.88	0.10	0.78	0.01	0.45	1447	6
Altree 2 - 415 m	4.18	0.13	0.79	0.01	0.30	1449	6
Altree 2 - 415 m	3.29	0.22	0.77	0.01	0.61	1451	8
Altree 2 - 415 m	5.75	0.21	0.82	0.01	0.51	1442	8
Altree 2 - 415 m	3.30	0.12	0.78	0.01	0.24	1460	7
Altree 2 - 415 m	4.26	0.15	0.79	0.01	0.33	1444	8
Altree 2 - 415 m	3.25	0.17	0.77	0.01	0.32	1449	7
Altree 2 - 415 m	3.78	0.15	0.78	0.01	0.25	1455	8
Altree 2 - 415 m	4.33	0.10	0.80	0.01	0.23	1462	7
Altree 2 - 415 m	4.33	0.14	0.79	0.01	0.38	1445	8
Altree 2 - 415 m	4.71	0.16	0.80	0.01	0.09	1444	7
Altree 2 - 415 m	3.79	0.13	0.78	0.01	0.13	1438	7
Altree 2 - 415 m	4.48	0.13	0.79	0.01	0.26	1442	6
Altree 2 - 415 m	4.94	0.15	0.80	0.01	0.27	1450	7
Altree 2 - 415 m	4.63	0.19	0.80	0.01	0.35	1452	8
Altree 2 - 415 m	3.73	0.16	0.77	0.01	0.13	1437	8
Altree 2 - 415 m	3.09	0.14	0.76	0.01	0.08	1444	7
Altree 2 - 415 m	3.82	0.14	0.77	0.01	0.44	1433	8
Altree 2 - 415 m	3.17	0.21	0.77	0.01	0.58	1443	9
Altree 2 - 415 m	4.07	0.15	0.79	0.01	0.23	1451	7
Altree 2 - 415 m	3.10	0.17	0.77	0.01	0.51	1453	8
Altree 2 - 415 m	4.36	0.17	0.79	0.01	0.55	1437	7
Altree 2 - 415 m	3.82	0.17	0.78	0.01	0.24	1452	8
Altree 2 - 415 m	3.94	0.14	0.78	0.01	0.29	1438	7
Altree 2 - 415 m	3.70	0.11	0.78	0.01	0.33	1445	7
Altree 2 - 415 m	4.40	0.20	0.79	0.01	0.45	1450	8
Altree 2 - 415 m	4.97	0.16	0.80	0.01	0.35	1443	6



Altree 2 - 415 m	8.27	0.35	0.88	0.01	0.67	1453	7
Altree 2 - 415 m	3.49	0.13	0.77	0.01	-0.07	1448	7
Altree 2 - 415 m	3.87	0.18	0.78	0.01	0.44	1443	7
Altree 2 - 415 m	3.59	0.16	0.78	0.01	0.33	1453	8
Altree 2 - 415 m	3.42	0.14	0.77	0.01	0.46	1444	7
Altree 2 - 415 m	3.31	0.13	0.77	0.01	0.33	1445	6
Altree 2 - 415 m	3.16	0.13	0.77	0.01	0.32	1447	6
Altree 2 - 415 m	4.38	0.19	0.80	0.01	0.34	1463	8
Altree 2 - 415 m	4.53	0.36	0.80	0.01	0.74	1458	8
Altree 2 - 415 m	2.81	0.24	0.76	0.01	0.76	1453	7
Altree 2 - 415 m	5.96	0.22	0.82	0.01	0.43	1447	8
Altree 2 - 415 m	5.06	0.29	0.81	0.01	0.55	1454	7
Altree 2 - 415 m	3.91	0.16	0.78	0.01	0.43	1443	7
Altree 2 - 415 m	3.49	0.22	0.78	0.01	0.46	1453	8
Altree 2 - 415 m	4.10	0.15	0.79	0.01	0.50	1456	7
Altree 2 - 415 m	4.29	0.17	0.79	0.01	0.51	1441	6
Altree 2 - 415 m	2.85	0.18	0.76	0.01	0.52	1451	7
Altree 2 - 415 m	3.77	0.11	0.78	0.01	0.14	1455	10
Altree 2 - 415 m	4.27	0.14	0.79	0.01	0.39	1446	8
Altree 2 - 415 m	3.93	0.17	0.78	0.01	0.50	1449	6
Altree 2 - 415 m	3.86	0.11	0.79	0.01	0.45	1459	7
Altree 2 - 415 m	3.05	0.16	0.77	0.01	0.36	1447	6
Altree 2 - 415 m	3.90	0.12	0.78	0.01	0.24	1447	8
Altree 2 - 415 m	4.91	0.16	0.81	0.01	0.52	1460	6
Altree 2 - 415 m	2.91	0.11	0.77	0.01	0.34	1466	8
Altree 2 - 520 m	7.44	0.56	0.85	0.02	0.73	1417	12
Altree 2 - 520 m	15.93	0.74	1.05	0.02	0.67	1447	12
Altree 2 - 520 m	11.65	0.32	0.95	0.01	0.34	1435	9
Altree 2 - 520 m	5.02	0.15	0.83	0.01	0.25	1454	10
Altree 2 - 520 m	14.14	0.79	0.99	0.02	0.79	1414	9
Altree 2 - 520 m	4.06	0.37	0.81	0.02	0.71	1448	14

Altree 2 - 520 m	21.27	1.35	1.17	0.03	0.86	1458	10
Altree 2 - 520 m	36.74	1.94	1.44	0.05	0.75	1419	15
Altree 2 - 520 m	17.68	0.79	1.09	0.02	0.74	1462	11
Altree 2 - 520 m	21.70	0.86	1.16	0.03	0.83	1436	11
Altree 2 - 520 m	10.11	0.56	0.92	0.02	0.68	1429	11
Altree 2 - 520 m	22.61	0.78	1.18	0.02	0.65	1443	11
Altree 2 - 520 m	13.37	0.50	1.00	0.02	0.47	1451	12
Altree 2 - 520 m	12.19	0.59	0.98	0.03	0.32	1460	20
Altree 2 - 520 m	6.28	0.73	0.82	0.02	0.78	1402	12
Altree 2 - 520 m	11.82	0.47	0.96	0.02	0.22	1446	12
Altree 2 - 520 m	11.82	0.40	0.96	0.01	0.55	1444	8
Altree 2 - 520 m	1.34	0.09	0.74	0.01	0.38	1426	7
Altree 2 - 520 m	29.39	2.27	1.30	0.05	0.92	1425	11
Altree 2 - 520 m	10.47	0.54	0.93	0.02	0.54	1435	10
Altree 2 - 520 m	16.02	0.94	1.03	0.02	0.81	1426	10
Altree 2 - 520 m	13.05	0.67	0.98	0.02	0.74	1436	10
Altree 2 - 520 m	14.81	0.89	1.01	0.02	0.70	1423	12
Altree 2 - 520 m	10.58	0.57	0.93	0.02	0.61	1430	10
Altree 2 - 520 m	10.46	0.54	0.91	0.02	0.55	1409	12
Altree 2 - 520 m	6.49	0.52	0.84	0.02	0.82	1430	9
Altree 2 - 520 m	9.53	0.45	0.92	0.03	0.42	1447	19
Altree 2 - 520 m	9.98	1.20	0.92	0.03	0.90	1439	12
Altree 2 - 520 m	12.49	0.63	0.96	0.02	0.64	1420	9
Altree 2 - 520 m	7.11	0.97	0.85	0.03	0.75	1426	15
Altree 2 - 520 m	19.64	1.02	1.13	0.02	0.73	1454	10
Altree 2 - 520 m	18.16	0.86	1.08	0.03	0.53	1436	16
Altree 2 - 520 m	5.31	0.37	0.83	0.01	0.62	1453	10
Altree 2 - 520 m	24.06	1.02	1.20	0.03	0.86	1428	8
Altree 2 - 520 m	14.96	0.71	1.01	0.02	0.63	1425	10
Altree 2 - 520 m	13.05	0.65	0.96	0.02	0.64	1401	10
Altree 2 - 520 m	6.54	0.47	0.85	0.01	0.57	1437	10

Altree 2 - 520 m	18.88	0.89	1.11	0.02	0.61	1446	11
Altree 2 - 520 m	13.69	0.89	0.97	0.02	0.75	1408	10
Altree 2 - 520 m	23.24	1.05	1.18	0.02	0.59	1429	11
Altree 2 - 520 m	18.10	0.90	1.09	0.02	0.16	1447	14
Altree 2 - 520 m	17.89	0.85	1.07	0.02	0.68	1428	10
Altree 2 - 520 m	9.85	0.44	0.92	0.01	0.24	1445	11
Altree 2 - 520 m	39.06	2.45	1.52	0.06	0.62	1450	23
Altree 2 - 520 m	7.64	1.28	0.88	0.05	0.84	1454	23
Altree 2 - 520 m	15.31	1.79	1.04	0.04	0.92	1454	12
Altree 2 - 520 m	10.01	0.55	0.92	0.02	0.54	1436	14
Altree 2 - 520 m	12.46	0.52	0.97	0.01	0.49	1433	9
Altree 2 - 520 m	11.38	0.42	0.94	0.02	0.39	1420	11
Altree 2 - 520 m	33.04	1.26	1.37	0.04	0.81	1421	11
Altree 2 - 520 m	4.50	0.30	0.80	0.01	0.43	1425	11
Altree 2 - 520 m	24.80	1.19	1.23	0.02	0.62	1448	12
Altree 2 - 520 m	12.48	0.72	0.97	0.02	0.62	1436	11
Altree 2 - 520 m	10.56	0.54	0.92	0.02	0.62	1421	13
Altree 2 - 520 m	4.55	0.34	0.80	0.02	0.34	1415	15
Altree 2 - 520 m	11.90	0.74	0.96	0.02	0.72	1433	11
Altree 2 - 520 m	7.02	0.56	0.86	0.02	0.67	1434	11
Altree 2 - 520 m	4.70	0.23	0.83	0.02	0.25	1462	15
Altree 2 - 520 m	42.20	1.39	1.55	0.04	0.73	1419	11
Altree 2 - 520 m	5.99	0.34	0.84	0.01	0.49	1444	11
Altree 2 - 520 m	11.04	0.62	0.92	0.02	0.50	1411	13
Altree 2 - 696 m	3.09	0.29	0.77	0.01	0.47	1408	10
Altree 2 - 696 m	4.06	0.24	0.80	0.02	0.50	1429	12
Altree 2 - 696 m	4.02	0.27	0.78	0.01	0.46	1396	9
Altree 2 - 696 m	3.71	0.21	0.78	0.01	0.23	1408	11
Altree 2 - 696 m	4.58	0.26	0.80	0.01	0.22	1407	10
Altree 2 - 696 m	5.67	0.33	0.83	0.01	0.32	1423	11
Altree 2 - 696 m	3.73	0.22	0.78	0.01	0.42	1412	9

Altree 2 - 696 m	1.55	0.15	0.73	0.01	0.31	1392	11
Altree 2 - 696 m	3.05	0.18	0.76	0.01	0.14	1402	11
Altree 2 - 696 m	3.44	0.23	0.77	0.01	0.43	1410	11
Altree 2 - 696 m	3.75	0.21	0.77	0.01	0.39	1388	9
Altree 2 - 696 m	3.89	0.30	0.78	0.01	0.49	1401	9
Altree 2 - 696 m	1.81	0.17	0.74	0.01	0.36	1399	11
Altree 2 - 696 m	4.02	0.25	0.80	0.01	0.35	1427	10
Altree 2 - 696 m	4.37	0.26	0.78	0.01	0.16	1391	11
Altree 2 - 696 m	4.36	0.27	0.79	0.01	0.36	1408	8
Altree 2 - 696 m	3.43	0.23	0.78	0.01	0.27	1410	9
Altree 2 - 696 m	3.38	0.29	0.77	0.01	0.51	1410	8
Altree 2 - 696 m	3.04	0.20	0.76	0.01	0.39	1401	12
Altree 2 - 696 m	4.06	0.27	0.79	0.01	0.44	1413	10
Altree 2 - 696 m	4.48	0.17	0.80	0.01	0.32	1421	9
Altree 2 - 696 m	3.57	0.12	0.77	0.01	0.35	1389	10
Altree 2 - 696 m	3.59	0.11	0.78	0.01	0.45	1410	8
Altree 2 - 696 m	2.89	0.17	0.76	0.01	0.35	1399	9
Altree 2 - 696 m	3.79	0.14	0.78	0.01	0.45	1403	9
Altree 2 - 696 m	3.43	0.13	0.77	0.01	0.39	1396	10
Altree 2 - 696 m	3.11	0.10	0.77	0.01	0.43	1416	8
Altree 2 - 696 m	4.41	0.18	0.80	0.01	0.36	1411	10
Altree 2 - 696 m	3.57	0.11	0.78	0.01	0.16	1409	8
Altree 2 - 696 m	3.21	0.12	0.78	0.01	0.12	1422	11
Altree 2 - 696 m	2.84	0.12	0.76	0.01	0.03	1401	8
Altree 2 - 696 m	3.67	0.15	0.77	0.01	0.22	1400	10
Altree 2 - 696 m	3.33	0.17	0.77	0.01	0.24	1409	9
Altree 2 - 696 m	3.36	0.11	0.78	0.01	0.54	1422	8
Altree 2 - 696 m	3.30	0.14	0.77	0.01	0.37	1409	9
Altree 2 - 696 m	3.56	0.14	0.77	0.01	0.34	1404	9
Altree 2 - 696 m	2.29	0.26	0.75	0.01	0.43	1400	12
Altree 2 - 696 m	4.06	0.15	0.78	0.01	0.34	1404	10

Altree 2 - 696 m	3.83	0.17	0.77	0.01	0.42	1389	10
Altree 2 - 696 m	3.68	0.14	0.77	0.01	0.33	1399	8
Altree 2 - 696 m	3.78	0.23	0.79	0.01	0.41	1419	8
Altree 2 - 696 m	3.62	0.17	0.77	0.01	0.32	1391	12
Altree 2 - 696 m	2.72	0.17	0.76	0.01	0.24	1407	9
Altree 2 - 696 m	2.57	0.17	0.76	0.01	0.06	1420	12
Altree 2 - 696 m	3.91	0.16	0.78	0.01	0.21	1395	9
Altree 2 - 696 m	3.78	0.26	0.78	0.01	0.52	1401	8
Altree 2 - 696 m	3.14	0.16	0.77	0.01	0.43	1408	9
Altree 2 - 696 m	4.06	0.17	0.79	0.01	0.14	1422	11
Altree 2 - 696 m	3.99	0.28	0.79	0.01	0.33	1415	10
Altree 2 - 696 m	3.35	0.09	0.77	0.01	0.28	1404	9
Altree 2 - 696 m	4.76	0.19	0.81	0.01	0.14	1418	11
Altree 2 - 696 m	4.33	0.15	0.79	0.01	0.36	1409	7
Altree 2 - 696 m	3.32	0.24	0.76	0.01	0.35	1394	12
Altree 2 - 696 m	3.33	0.15	0.78	0.01	0.03	1416	9
Altree 2 - 696 m	2.78	0.09	0.77	0.01	0.18	1417	8
Altree 2 - 696 m	2.92	0.12	0.77	0.01	0.12	1414	10
Altree 2 - 696 m	3.29	0.18	0.78	0.01	0.20	1415	10
Altree 2 - 696 m	3.50	0.11	0.77	0.01	0.10	1395	10
Altree 2 - 696 m	2.93	0.15	0.77	0.01	0.30	1421	10
Altree 2 - 696 m	3.12	0.15	0.76	0.01	0.10	1391	9
Altree 2 - 696 m	3.19	0.14	0.77	0.01	0.38	1410	10
Altree 2 - 696 m	3.43	0.22	0.78	0.01	0.42	1419	9
Altree 2 - 696 m	4.56	0.17	0.79	0.01	0.30	1397	9
Altree 2 - 696 m	3.88	0.14	0.78	0.01	0.36	1400	8
Altree 2 - 696 m	4.50	0.17	0.79	0.01	0.25	1392	9
Altree 2 - 696 m	3.93	0.15	0.78	0.01	0.33	1400	8
Altree 2 - 696 m	4.39	0.16	0.78	0.01	0.46	1392	9
Altree 2 - 696 m	4.36	0.18	0.78	0.01	0.46	1395	9
Altree 2 - 696 m	3.16	0.20	0.77	0.01	0.28	1414	12

Altree 2 - 938 m	5.31	0.22	0.81	0.01	0.48	1329	10
Altree 2 - 938 m	5.22	0.19	0.80	0.01	0.44	1321	10
Altree 2 - 938 m	5.45	0.19	0.81	0.01	0.48	1319	9
Altree 2 - 938 m	7.17	0.30	0.85	0.02	0.63	1326	10
Altree 2 - 938 m	1.86	0.11	0.74	0.01	0.25	1322	8
Altree 2 - 938 m	5.26	0.20	0.80	0.01	0.29	1318	8
Altree 2 - 938 m	4.08	0.16	0.78	0.01	0.63	1319	7
Altree 2 - 938 m	3.28	0.12	0.77	0.01	0.47	1319	6
Altree 2 - 938 m	4.06	0.22	0.78	0.01	0.43	1312	8
Altree 2 - 938 m	3.05	0.10	0.77	0.01	0.44	1325	7
Altree 2 - 938 m	3.81	0.17	0.77	0.01	0.36	1311	8
Altree 2 - 938 m	5.01	0.17	0.80	0.01	0.35	1319	8
Altree 2 - 938 m	4.07	0.12	0.78	0.01	0.40	1310	7
Altree 2 - 938 m	6.19	0.20	0.82	0.01	0.42	1317	9
Altree 2 - 938 m	4.86	0.17	0.80	0.01	0.05	1327	9
Altree 2 - 938 m	3.73	0.12	0.78	0.01	0.31	1324	8
Altree 2 - 938 m	4.73	0.16	0.79	0.01	0.28	1317	9
Altree 2 - 938 m	4.27	0.13	0.79	0.01	0.34	1320	8
Altree 2 - 938 m	5.10	0.21	0.80	0.01	0.38	1311	8
Altree 2 - 938 m	4.56	0.23	0.79	0.01	0.51	1310	7
Altree 2 - 938 m	4.96	0.15	0.80	0.01	0.46	1315	7
Altree 2 - 938 m	4.50	0.20	0.79	0.01	0.33	1323	9
Altree 2 - 938 m	5.57	0.19	0.81	0.01	0.33	1320	9
Altree 2 - 938 m	5.08	0.16	0.79	0.01	0.04	1308	9
Altree 2 - 938 m	6.17	0.18	0.82	0.01	0.60	1321	7
Altree 2 - 938 m	4.78	0.19	0.80	0.01	0.44	1319	7
Altree 2 - 938 m	4.85	0.13	0.80	0.01	0.48	1329	7
Altree 2 - 938 m	3.78	0.15	0.78	0.01	0.29	1315	10
Altree 2 - 938 m	4.05	0.17	0.79	0.01	0.23	1327	9
Altree 2 - 938 m	4.83	0.27	0.79	0.01	0.49	1314	9
Altree 2 - 938 m	2.40	0.11	0.75	0.01	0.04	1321	7

Altree 2 - 938 m	4.03	0.13	0.78	0.01	0.48	1323	8
Altree 2 - 938 m	3.28	0.18	0.77	0.01	0.51	1319	7
Altree 2 - 938 m	4.42	0.18	0.79	0.01	0.39	1312	8
Altree 2 - 938 m	7.46	0.31	0.84	0.01	0.37	1313	9
Altree 2 - 938 m	4.28	0.22	0.79	0.01	0.65	1318	5
Altree 2 - 938 m	4.57	0.19	0.79	0.01	0.30	1319	8
Altree 2 - 938 m	5.47	0.22	0.81	0.01	0.27	1316	9
Altree 2 - 938 m	6.51	0.24	0.83	0.01	0.24	1325	9
Altree 2 - 938 m	5.18	0.23	0.80	0.01	0.30	1314	9
Altree 2 - 938 m	6.39	0.30	0.83	0.01	0.44	1327	9
Altree 2 - 1220 m	11.04	0.56	0.92	0.01	0.70	1345	7
Altree 2 - 1220 m	10.62	0.45	0.91	0.01	0.56	1332	7
Altree 2 - 1220 m	10.51	0.49	0.91	0.01	0.59	1342	8
Altree 2 - 1220 m	11.34	0.52	0.91	0.01	0.66	1317	8
Altree 2 - 1220 m	11.44	0.51	0.93	0.02	0.64	1341	8
Altree 2 - 1220 m	12.36	0.46	0.94	0.01	0.14	1330	11
Altree 2 - 1220 m	12.54	0.44	0.95	0.01	0.61	1347	7
Altree 2 - 1220 m	11.53	0.47	0.93	0.01	0.62	1340	7
Altree 2 - 1220 m	11.59	0.48	0.92	0.01	0.66	1327	7
Altree 2 - 1220 m	11.40	0.47	0.92	0.01	0.60	1324	8
Altree 2 - 1220 m	11.13	0.59	0.92	0.02	0.68	1340	8
Altree 2 - 1220 m	11.72	0.49	0.92	0.01	0.45	1314	9
Altree 2 - 1220 m	5.89	0.46	0.83	0.01	0.56	1343	9
Altree 2 - 1220 m	8.90	0.60	0.87	0.02	0.78	1331	8
Altree 2 - 1220 m	9.51	0.54	0.89	0.02	0.73	1342	8
Altree 2 - 1220 m	6.88	0.36	0.84	0.01	0.65	1343	7
Altree 2 - 1220 m	12.00	0.55	0.94	0.01	0.68	1339	7
Altree 2 - 1220 m	10.10	0.53	0.90	0.01	0.67	1343	7
Altree 2 - 1220 m	8.04	0.58	0.85	0.02	0.83	1325	7
Altree 2 - 1220 m	12.41	0.54	0.94	0.01	0.55	1334	8
Altree 2 - 1220 m	10.16	0.56	0.90	0.01	0.64	1333	8

Altree 2 - 1220 m	3.43	0.45	0.78	0.02	0.79	1339	10
Altree 2 - 1220 m	3.69	0.37	0.77	0.02	0.71	1327	12
Altree 2 - 1220 m	11.82	0.54	0.95	0.02	0.40	1357	11
Altree 2 - 1220 m	10.86	0.54	0.91	0.02	0.40	1334	11
Altree 2 - 1220 m	10.71	0.51	0.91	0.01	0.59	1334	8
Altree 2 - 1220 m	11.16	0.59	0.93	0.01	0.71	1348	7
Altree 2 - 1220 m	11.58	0.54	0.92	0.02	0.65	1326	8
Altree 2 - 1220 m	8.82	0.47	0.89	0.01	0.47	1351	9
Altree 2 - 1220 m	9.29	0.47	0.89	0.01	0.68	1347	7
Altree 2 - 1220 m	10.50	0.48	0.92	0.01	0.44	1350	8
Altree 2 - 1220 m	10.06	0.57	0.90	0.02	0.69	1336	8
Altree 2 - 1220 m	11.30	0.55	0.92	0.01	0.67	1337	8
Altree 2 - 1220 m	7.60	0.52	0.85	0.01	0.73	1335	7
Altree 2 - 1220 m	9.04	0.44	0.88	0.01	0.71	1341	6
Altree 2 - 1220 m	9.27	0.57	0.89	0.02	0.80	1339	8
Altree 2 - 1220 m	8.22	0.62	0.87	0.02	0.77	1338	8
Altree 2 - 1220 m	12.17	0.61	0.95	0.01	0.57	1346	9
Altree 2 - 1220 m	10.47	0.45	0.91	0.01	0.55	1336	6
Altree 2 - 1220 m	10.76	0.48	0.91	0.01	0.51	1333	8
Altree 2 - 1220 m	7.21	0.51	0.84	0.01	0.68	1332	8
Altree 2 - 1220 m	7.61	0.59	0.86	0.02	0.84	1342	8
Altree 2 - 1220 m	10.96	0.56	0.91	0.01	0.70	1331	8
Altree 2 - 1220 m	12.96	0.85	0.96	0.02	0.83	1349	8
Altree 2 - 1220 m	2.60	0.27	0.76	0.02	0.86	1337	13
Altree 2 - 1220 m	10.28	0.53	0.91	0.01	0.64	1344	7
Altree 2 - 1220 m	10.99	0.48	0.93	0.01	0.44	1349	9
Altree 2 - 1220 m	9.69	0.74	0.89	0.02	0.89	1337	7
Altree 2 - 1220 m	11.66	0.67	0.92	0.02	0.75	1330	8
Altree 2 - 1220 m	5.02	0.52	0.81	0.02	0.85	1342	8
Altree 2 - 1220 m	8.74	0.62	0.88	0.02	0.80	1340	8
Altree 2 - 1220 m	11.54	0.50	0.93	0.01	0.43	1336	9



Altree 2 - 1220 m	9.76	0.47	0.88	0.01	0.47	1319	8
Altree 2 - 1220 m	7.89	0.64	0.86	0.02	0.18	1335	13
Altree 2 - 1220 m	11.43	0.53	0.92	0.01	0.67	1326	7
Altree 2 - 1220 m	11.57	0.49	0.92	0.02	0.70	1327	8
Altree 2 - 1220 m	7.82	0.61	0.86	0.02	0.84	1334	7
Altree 2 - 1220 m	9.77	0.52	0.89	0.01	0.69	1338	8
Altree 2 - 1220 m	11.63	0.49	0.93	0.01	0.53	1341	8
Altree 2 - 1220 m	11.17	0.44	0.92	0.01	0.59	1337	7
Altree 2 - 1220 m	9.08	0.63	0.89	0.02	0.84	1350	8
Altree 2 - 1220 m	11.67	0.57	0.92	0.01	0.69	1317	7
Altree 2 - 1220 m	9.03	0.52	0.88	0.01	0.80	1342	6
Altree 2 - 1220 m	12.08	0.54	0.95	0.02	0.62	1358	8
Altree 2 - 1220 m	11.42	0.48	0.93	0.01	0.58	1348	8
Altree 2 - 1220 m	11.44	0.54	0.93	0.01	0.67	1337	8
Altree 2 - 1220 m	10.62	0.39	0.91	0.01	0.64	1331	7
Altree 2 - 1220 m	12.96	0.52	0.96	0.01	0.68	1345	7
Altree 2 - 1220 m	13.27	0.67	0.96	0.02	0.69	1335	9
Altree 2 - 1220 m	5.14	0.53	0.81	0.02	0.85	1339	7
Altree 2 - 1220 m	11.29	0.43	0.93	0.01	0.61	1353	7
GL-O Glauconite	125.87	3.60	0.86	0.02			
GL-O Glauconite	217.18	6.75	1.00	0.03			
GL-O Glauconite	188.14	6.21	0.97	0.03			
GL-O Glauconite	124.61	5.50	0.89	0.02			
GL-O Glauconite	146.93	5.22	0.91	0.03			
GL-O Glauconite	165.56	5.65	0.93	0.03			
GL-O Glauconite	198.29	7.01	0.98	0.03			
GL-O Glauconite	192.91	6.40	0.97	0.03			
GL-O Glauconite	199.23	6.02	0.96	0.03			
GL-O Glauconite	199.71	6.75	0.98	0.03			
GL-O Glauconite	138.03	6.12	0.87	0.03			
GL-O Glauconite	151.60	4.40	0.91	0.03			

GL-O Glauconite	7.48	0.70	0.72	0.01			
GL-O Glauconite	8.58	1.78	0.72	0.01			
GL-O Glauconite	11.73	1.54	0.80	0.14			
GL-O Glauconite	138.14	4.35	0.89	0.02			
GL-O Glauconite	9.84	2.51	0.71	0.01			
GL-O Glauconite	32.98	3.15	0.76	0.01			
GL-O Glauconite	74.79	6.32	0.81	0.02			
GL-O Glauconite	167.04	4.90	0.94	0.03			
MDC Phlogopite	41.80	1.10	1.02	0.01			
MDC Phlogopite	41.58	1.12	1.03	0.01			
MDC Phlogopite	40.99	1.08	1.03	0.01			
MDC Phlogopite	41.17	1.08	1.03	0.01			
MDC Phlogopite	40.71	1.09	1.02	0.01			
MDC Phlogopite	40.98	1.07	1.03	0.01			
MDC Phlogopite	40.75	1.07	1.03	0.01			
MDC Phlogopite	40.90	1.02	1.03	0.01			
MDC Phlogopite	40.80	1.06	1.02	0.01			
MDC Phlogopite	41.05	1.08	1.02	0.01			
MDC Phlogopite	41.28	1.03	1.03	0.01			
MDC Phlogopite	41.39	1.09	1.03	0.01			
MDC Phlogopite	41.59	1.06	1.03	0.01			
MDC Phlogopite	41.15	1.07	1.02	0.01			
MDC Phlogopite	41.33	1.09	1.03	0.01			
MDC Phlogopite	40.58	1.06	1.02	0.01			
MDC Phlogopite	41.33	1.11	1.04	0.01			
MDC Phlogopite	41.31	1.11	1.02	0.01			
MDC Phlogopite	41.47	1.15	1.03	0.01			
MDC Phlogopite	41.61	1.08	1.03	0.01			
MDC Phlogopite	42.16	1.24	1.03	0.01			
MDC Phlogopite	40.09	1.09	1.02	0.01			
MDC Phlogopite	40.67	1.25	1.03	0.01			

MDC Phlogopite	41.11	1.30	1.03	0.01			
MDC Phlogopite	40.36	1.55	1.03	0.01			
MDC Phlogopite	40.63	1.58	1.02	0.01			
MDC Phlogopite	41.01	1.13	1.02	0.01			
MDC Phlogopite	41.44	1.17	1.03	0.01			
MDC Phlogopite	40.87	0.75	1.03	0.01			
MDC Phlogopite	40.80	0.78	1.01	0.01			
MDC Phlogopite	40.70	0.96	1.01	0.01			
MDC Phlogopite	41.43	1.20	1.03	0.01			
MDC Phlogopite	41.36	0.96	1.02	0.01			
MDC Phlogopite	41.67	0.89	1.04	0.01			
MDC Phlogopite	41.45	0.94	1.02	0.01			
MDC Phlogopite	40.70	0.93	1.03	0.01			
MDC Phlogopite	40.90	0.87	1.03	0.01			
MDC Phlogopite	40.82	1.23	1.03	0.01			
MDC Phlogopite	40.94	1.24	1.04	0.01			
MDC Phlogopite	41.16	1.17	1.04	0.01			
MDC Phlogopite	41.40	1.21	1.04	0.01			
MDC Phlogopite	42.00	1.19	1.03	0.01			
MDC Phlogopite	40.93	1.57	1.02	0.01			
MDC Phlogopite	41.45	1.20	1.02	0.01			
MDC Phlogopite	41.58	1.34	1.03	0.01			
MDC Phlogopite	41.51	1.32	1.04	0.01			
MDC Phlogopite	41.68	3.41	1.03	0.01			
MDC Phlogopite	41.84	3.41	1.03	0.01			
MDC Phlogopite	43.39	4.69	1.04	0.01			
MDC Phlogopite	44.81	4.83	1.04	0.01			
MDC Phlogopite	44.91	3.42	1.04	0.01			
MDC Phlogopite	44.33	3.36	1.04	0.01			
MDC Phlogopite	42.56	0.97	1.03	0.01			
MDC Phlogopite	41.29	1.57	1.04	0.01			

MDC Phlogopite	42.26	0.93	1.04	0.01			
MDC Phlogopite	42.27	1.15	1.03	0.01			
MDC Phlogopite	41.81	1.17	1.02	0.01			
MDC Phlogopite	41.83	1.29	1.04	0.01			
MDC Phlogopite	41.98	1.31	1.03	0.01			
MDC Phlogopite	40.26	1.09	1.02	0.01			
MDC Phlogopite	40.69	1.09	1.03	0.01			
MDC Phlogopite	40.42	0.72	1.02	0.01			
MDC Phlogopite	40.97	0.73	1.03	0.01			
MDC Phlogopite	40.51	0.87	1.03	0.01			
MDC Phlogopite	40.26	1.45	1.04	0.01			
MDC Phlogopite	40.50	0.91	1.02	0.01			
MDC Phlogopite	40.80	0.87	1.03	0.01			
MDC Phlogopite	40.50	0.87	1.02	0.01			
MDC Phlogopite	40.76	0.78	1.02	0.01			
MDC Phlogopite	40.85	0.76	1.03	0.01			
MDC Phlogopite	40.13	1.47	1.04	0.01			
MDC Phlogopite	40.82	1.24	1.03	0.01			
MDC Phlogopite	40.95	1.25	1.03	0.01			
MDC Phlogopite	39.67	1.06	1.02	0.01			
Mica-MG Phlogopite	161.26	8.03	1.85	0.03			
Mica-MG Phlogopite	156.34	3.96	1.86	0.02			
Mica-MG Phlogopite	154.84	3.92	1.86	0.02			
Mica-MG Phlogopite	152.36	3.86	1.87	0.02			
Mica-MG Phlogopite	157.38	3.37	1.84	0.02			
Mica-MG Phlogopite	153.12	3.27	1.83	0.02			
Mica-MG Phlogopite	153.23	3.28	1.85	0.02			
Mica-MG Phlogopite	153.59	1.76	1.85	0.02			
Mica-MG Phlogopite	154.99	1.77	1.87	0.02			
Mica-MG Phlogopite	155.33	1.78	1.86	0.02			
Mica-MG Phlogopite	153.36	3.38	1.84	0.02			

Mica-MG Phlogopite	150.58	7.50	1.84	0.03			
Mica-MG Phlogopite	155.34	3.42	1.87	0.02			
Mica-MG Phlogopite	155.02	3.41	1.85	0.02			
Mica-MG Phlogopite	157.16	3.27	1.87	0.02			
Mica-MG Phlogopite	153.92	3.20	1.87	0.02			
Mica-MG Phlogopite	152.56	3.18	1.88	0.02			
Mica-MG Phlogopite	155.72	2.60	1.86	0.02			
Mica-MG Phlogopite	153.66	2.56	1.83	0.03			
Mica-MG Phlogopite	154.46	2.58	1.84	0.02			
Mica-MG Phlogopite	153.65	5.01	1.85	0.02			
Mica-MG Phlogopite	153.37	5.00	1.87	0.02			
Mica-MG Phlogopite	151.45	7.54	1.85	0.03			
Mica-MG Phlogopite	156.68	5.11	1.86	0.02			
Mica-MG Phlogopite	158.56	4.61	1.87	0.02			
Mica-MG Phlogopite	152.97	4.45	1.85	0.02			
Mica-MG Phlogopite	152.07	4.43	1.84	0.02			
Mica-MG Phlogopite	155.05	1.92	1.86	0.02			
Mica-MG Phlogopite	153.98	1.91	1.88	0.02			
Mica-MG Phlogopite	154.71	1.91	1.85	0.02			
Mica-MG Phlogopite	155.12	3.50	1.88	0.02			
Mica-MG Phlogopite	155.58	3.51	1.86	0.02			
Mica-MG Phlogopite	152.91	3.45	1.84	0.02			
Mica-MG Phlogopite	156.05	1.85	1.89	0.03			
Mica-MG Phlogopite	157.02	3.34	1.86	0.02			
Mica-MG Phlogopite	154.20	3.28	1.83	0.02			
Mica-MG Phlogopite	152.43	3.24	1.86	0.02			
Mica-MG Phlogopite	155.69	1.68	1.85	0.02			
Mica-MG Phlogopite	153.39	1.65	1.86	0.02			
Mica-MG Phlogopite	154.71	1.66	1.85	0.02			
Mica-MG Phlogopite	154.09	1.92	1.86	0.02			
Mica-MG Phlogopite	155.22	1.94	1.84	0.03			

Mica-MG Phlogopite	154.50	1.93	1.86	0.02			
Mica-MG Phlogopite	155.31	2.24	1.86	0.02			
Mica-MG Phlogopite	153.30	1.81	1.85	0.02			
Mica-MG Phlogopite	152.95	2.21	1.83	0.02			
Mica-MG Phlogopite	155.48	2.24	1.87	0.02			
Mica-MG Phlogopite	155.77	2.83	1.86	0.02			
Mica-MG Phlogopite	154.52	2.81	1.86	0.02			
Mica-MG Phlogopite	153.53	2.79	1.87	0.02			
Mica-MG Phlogopite	154.05	3.04	1.86	0.02			
Mica-MG Phlogopite	153.12	3.02	1.85	0.02			
Mica-MG Phlogopite	156.76	3.09	1.87	0.02			
Mica-MG Phlogopite	152.87	3.01	1.84	0.02			
Mica-MG Phlogopite	155.75	3.07	1.86	0.02			
Mica-MG Phlogopite	154.38	1.83	1.88	0.03			
Mica-MG Phlogopite	155.18	3.06	1.86	0.02			
Mica-MG Phlogopite	154.44	2.72	1.86	0.02			
Mica-MG Phlogopite	155.00	2.73	1.85	0.02			
Mica-MG Phlogopite	154.20	2.72	1.83	0.02			
Mica-MG Phlogopite	152.33	4.10	1.85	0.02			
Mica-MG Phlogopite	153.75	4.27	1.85	0.02			
Mica-MG Phlogopite	153.51	4.27	1.84	0.02			
Mica-MG Phlogopite	156.42	4.35	1.85	0.02			
Mica-MG Phlogopite	157.56	3.54	1.87	0.02			
Mica-MG Phlogopite	153.52	3.45	1.86	0.02			
Mica-MG Phlogopite	152.58	3.43	1.83	0.02			
Mica-MG Phlogopite	154.49	4.25	1.85	0.02			
Mica-MG Phlogopite	154.29	4.24	1.85	0.02			
Mica-MG Phlogopite	155.20	4.27	1.85	0.02			
Mica-MG Phlogopite	150.75	5.40	1.85	0.02			
Mica-MG Phlogopite	157.04	4.23	1.87	0.02			
Mica-MG Phlogopite	157.50	5.64	1.88	0.02			

Mica-MG Phlogopite	155.55	5.57	1.86	0.02			
Mica-MG Phlogopite	157.74	3.73	1.85	0.02			
Mica-MG Phlogopite	153.69	3.64	1.85	0.02			
Mica-MG Phlogopite	152.16	3.60	1.84	0.02			
Mica-MG Phlogopite	154.69	1.96	1.86	0.02			
Mica-MG Phlogopite	154.33	1.96	1.85	0.02			
Mica-MG Phlogopite	154.67	1.96	1.84	0.02			
Mica-MG Phlogopite	155.75	2.88	1.87	0.02			
Mica-MG Phlogopite	154.95	2.86	1.85	0.02			
Mica-MG Phlogopite	154.97	4.17	1.83	0.02			
Mica-MG Phlogopite	152.88	2.82	1.86	0.02			
Mica-MG Phlogopite	156.04	2.64	1.85	0.02			
Mica-MG Phlogopite	155.00	2.62	1.86	0.02			
Mica-MG Phlogopite	152.56	2.58	1.84	0.02			
Mica-MG Phlogopite	155.79	2.74	1.85	0.02			
Mica-MG Phlogopite	154.37	2.71	1.84	0.02			
Mica-MG Phlogopite	153.64	2.70	1.84	0.02			
Mica-MG Phlogopite	152.53	4.14	1.85	0.02			
Mica-MG Phlogopite	156.39	4.25	1.87	0.02			
Mica-MG Phlogopite	154.79	4.20	1.84	0.02			
Mica-MG Phlogopite	154.80	5.67	1.87	0.02			
Mica-MG Phlogopite	157.73	4.10	1.85	0.02			
Mica-MG Phlogopite	153.33	3.99	1.84	0.03			
Mica-MG Phlogopite	152.61	3.97	1.84	0.02			
Mica-MG Phlogopite	153.07	3.92	1.85	0.02			
Mica-MG Phlogopite	156.16	4.00	1.85	0.02			
Mica-MG Phlogopite	154.53	3.96	1.86	0.02			
Mica-MG Phlogopite	154.29	4.37	1.86	0.02			
Mica-MG Phlogopite	157.34	4.46	1.87	0.02			
Mica-MG Phlogopite	151.97	4.31	1.86	0.02			
Mica-MG Phlogopite	156.91	12.63	1.86	0.02			

Mica-MG Phlogopite	152.18	5.57	1.83	0.02			
Mica-MG Phlogopite	153.07	12.32	1.85	0.02			
Mica-MG Phlogopite	153.65	12.37	1.85	0.02			
Mica-MG Phlogopite	160.64	17.20	1.84	0.02			
Mica-MG Phlogopite	143.33	15.35	1.85	0.02			
Mica-MG Phlogopite	159.22	17.05	1.85	0.02			
Mica-MG Phlogopite	160.25	12.02	1.85	0.02			
Mica-MG Phlogopite	159.07	11.93	1.85	0.02			
Mica-MG Phlogopite	143.93	10.80	1.84	0.02			
Mica-MG Phlogopite	153.75	2.76	1.85	0.02			
Mica-MG Phlogopite	155.82	2.80	1.88	0.02			
Mica-MG Phlogopite	156.63	5.74	1.85	0.02			
Mica-MG Phlogopite	154.27	2.77	1.85	0.02			
Mica-MG Phlogopite	155.51	3.81	1.85	0.02			
Mica-MG Phlogopite	152.47	3.73	1.84	0.02			
Mica-MG Phlogopite	156.00	3.82	1.86	0.02			
Mica-MG Phlogopite	152.81	4.27	1.87	0.02			
Mica-MG Phlogopite	154.24	4.31	1.85	0.02			
Mica-MG Phlogopite	157.09	4.39	1.85	0.02			
Mica-MG Phlogopite	151.66	3.61	1.85	0.02			
Mica-MG Phlogopite	155.23	3.69	1.87	0.02			
Mica-MG Phlogopite	157.06	3.73	1.88	0.03			
Mica-MG Phlogopite	158.86	5.41	1.86	0.02			
Mica-MG Phlogopite	154.80	1.93	1.87	0.02			
Mica-MG Phlogopite	155.47	1.94	1.87	0.02			
Mica-MG Phlogopite	153.55	1.92	1.84	0.02			
Mica-MG Phlogopite	154.09	2.79	1.85	0.02			
Mica-MG Phlogopite	153.77	2.78	1.86	0.02			
Mica-MG Phlogopite	156.01	2.82	1.86	0.02			
Mica-MG Phlogopite	153.56	2.65	1.86	0.02			
Mica-MG Phlogopite	156.68	2.70	1.88	0.03			



Mica-MG Phlogopite	153.41	2.64	1.84	0.02			
Mica-MG Phlogopite	155.10	1.96	1.86	0.02			
Mica-MG Phlogopite	152.68	5.20	1.85	0.02			
Mica-MG Phlogopite	155.22	1.96	1.86	0.02			
Mica-MG Phlogopite	153.48	1.94	1.85	0.02			
Mica-MG Phlogopite	152.13	5.18	1.85	0.02			

**Table S.3.8.** Geochronological data for samples in Chapter 3.

### Additional information for Chapter 4

Carbonate samples were leached to ensure minimum incorporation of non-carbonate phases (Cao et al., 2020; Halverson et al., 2010; Tostevin et al., 2016). Rock chips were micro-drilled along laminae to target the carbonate matrix, making sure to avoid veining, clasts and weathered surface. The rock powder were then reacted with 1M ammonium acetate to remove any loose cations on the surface. This was then followed by a second and third leach with 0.2 M acetic acid to extract the carbonate phase. Between each step, the solution was sonicated and centrifuged for 20 and 10 minutes respectively. The final supernatant was set aside for solution inductively coupled plasma mass spectrometer (ICP-MS) analysis at Adelaide Microscopy using an Agilent 8900x mass spectrometer instrument. This was then digested with 2% nitric acid and split into aliquots of 1:10000 and 1:1000 dilutions for major and trace element analysis. Calibration solutions were prepared from a multi-element stock standard solution and diluted with 2% nitric acid as well. Primary standard JDo-1 was used for all analytical runs (IMAI et al., 1996).

For sample introduction, the ICP-MS was equipped with a Miramist nebuliser and a quartz spray chamber, into which samples were introduced by a peristaltic pump at a flow rate of 1.0mL/min. An internal standard, Indium, was mixed online with the samples to compensate for matrix effects. All element concentrations were determined against certified multi-element calibration standards (Choice Analytical, Australia) and blanks were interspersed throughout the analysis session, as well as measurement of the 200ppb calibration solution to check the instrument stability. The instrument was operated with an RF power of 1500W, a carrier gas flow of 0.89 L/min and a make-up gas flow of 0.19 L/min. Sample uptake rate was 1.0 mL/min and the dwell times ranged between 10ms to 1s. Three replicates were obtained for each sample. The data was processed using Agilent Mass-Hunter Data Analysis.

### Carbonate Isotopic Analysis

A fraction of the solution prepared for elemental geochemistry in carbonates were measured for isotopic analyses. Coupled  $^{87}\text{Sr}/^{86}\text{Sr}$  and  $\delta^{88/86}\text{Sr}$  analyses were undertaken using a Phoenix Isotopx thermal ionisation mass spectrometry (TIMS) following the extensive methodology described by (Shao et al., 2018; Shao et al., 2021). Two aliquots each containing around 500 ng of Sr were taken from the sample solution, with one being spiked with an  $^{87}\text{Sr}$ - $^{84}\text{Sr}$  double spike solution and consequently giving a spike to sample ratio  $^{84}\text{Sr}_{\text{sp}}/^{84}\text{Sr}_{\text{sa}}$  between 10-50. The  $^{87}\text{Sr}$ - $^{84}\text{Sr}$  double spike solution was prepared at GEOMAR (Kiel, Germany) with a total Sr concentration of 0.0090mg/g, and its respective Sr isotope

composition as determined by TIMS at University of Adelaide is provided in Shao et al. (2021) .

Procedural Sr blanks prepared for analyses consisted of a drop of deionized water, a drop of 0.1 M phosphoric acid and an additional drop of  $^{84}\text{Sr}$ -enriched single spike in a Teflon vial. Next, the Sr fraction of all samples and standers along with the blanks used were purified using a 600  $\mu\text{L}$  Micro Bio-Spin separation columns filled with Sr-specific resin (Eichrom Sr-SPS). They were then loaded onto single degassed Re filaments to be prepared for  $^{87}\text{Sr}/^{86}\text{Sr}$  and  $\delta^{88/86}\text{Sr}$  data collected.

$^{87}\text{Sr}/^{86}\text{Sr}$  isotopic ratios of carbonate samples were analysed through the conventional 'dynamic' analytical method for better accuracy (Shao et al., 2018). On the other hand  $\delta^{88/86}\text{Sr}$  data were collected using a 'static' analytical method and corrected for instrumental and procedural fractionation effects via the double spike technique (Krabbenhöft et al., 2010). To apply this method, a separate analyses with an 'un-spiked' aliquot for each sample also needed to be analysed concurrently (Krabbenhöft et al., 2010). As such, each analytical session contained both spiked and un-spiked samples ran parallel with NIST SRM 987 (Krabbenhöft et al., 2009) and JCP-1 (Inoue et al., 2004) standards. Both spiked and unspiked samples were analysed by TIMS using a static multicollection routine. During analysis, an  $^{88}\text{Sr}$  beam with a magnitude of about 5–6 V was attained, and  $^{84}\text{Sr}$ ,  $^{85}\text{Rb}$ ,  $^{86}\text{Sr}$ ,  $^{87}\text{Sr}$ , and  $^{88}\text{Sr}$  isotope beams were collected over 200 cycles (10 cycles for 20 blocks, with 30 s baseline and 8 s peak integrations). From these collected data, the following isotope ratios were calculated:  $^{88}\text{Sr}/^{84}\text{Sr}$ ,  $^{86}\text{Sr}/^{84}\text{Sr}$ ,  $^{87}\text{Sr}/^{84}\text{Sr}$  and  $^{88}\text{Sr}/^{86}\text{Sr}$ . This is then used to determine the 'double-spike corrected'  $^{88}\text{Sr}/^{86}\text{Sr}$  ratios. Isotopic fractionation effects due to the procedure or instrument applied were corrected using a modified  $^{87}\text{Sr}$ - $^{84}\text{Sr}$  double spike correction algorithm (Shao et al., 2021) modified from Heuser et al. (2002) and Samanta et al. (2016).

Stable Sr isotopic data of all samples is normalised relative to SRM 987 standard following the equation:

$$\delta^{88/86}\text{Sr} = [({}^{88}\text{Sr}/{}^{86}\text{Sr})_{\text{sample}} / ({}^{88}\text{Sr}/{}^{86}\text{Sr})_{\text{SRM 987}} - 1] * 1000$$

$\delta^{88/86}\text{Sr}$  values of unknown samples as well as the JCP-1 standards were normalised to the average of the SRM987 standards analysed in the same analytical session. This approach was used to correct any session-to-session drifts, which were quantified by monitoring SRM 987 like previously done in other high-precision Sr isotope studies (Andrews and Jacobson, 2017; Andrews et al., 2016; Krabbenhöft et al., 2010; Ohno et al., 2008; Shalev et al., 2017; Shao et al., 2021; Vollstaedt et al., 2014).

High precision  $^{87}\text{Sr}/^{86}\text{Sr}$  isotopic results were collected by re-running the TIMS on unspiked samples using the 'dynamic' method. With this analysis, a typical  $^{88}\text{Sr}$  beam of 5–6 V was attained, and the following isotope ratios were collected:  $^{87}\text{Sr}/^{86}\text{Sr}$ ,  $^{86}\text{Sr}/^{88}\text{Sr}$  and  $^{84}\text{Sr}/^{86}\text{Sr}$ , using a method consisting of 100 cycles (20 cycles for 5 blocks). Mass dependent fractionation due to the instrument or procedural effects were corrected using an internal

normalisation assuming the  $^{86}\text{Sr}/^{88}\text{Sr}$  ratio of 0.1194 (Nier, 1938). Sr isotopic results from secondary standard JCP-1 and NIST SRM 987 are summarised in Supplementary Figure 1 and compared with their published values (Balcaen et al., 2005; Inoue et al., 2004; Krabbenhöft et al., 2009).

Approximately 100 mg of carbonate powder were micro-drilled for each sample to prepare for analysis of  $\delta^{13}\text{C}_{\text{carb}}$  and  $\delta^{18}\text{O}$  values. Analysis were undertaken using a dual inlet Isotope Ratio Mass Spectrometry (IRMS) Fision Optima with combined Isocarb Carbonate Preparation System at the University of Adelaide following Falster et al. (2018). Powders were purged with 1M phosphoric acid to dissolve the carbonate and injected with helium. The resultant fumes were then measured to produce  $\delta^{13}\text{C}_{\text{carb}}$  and  $\delta^{18}\text{O}$  values. An in-house standard ANU-P3 (Australian National University- carbonate), UAC-1 and IAEA CO-8 was used during analysis which all have been calibrated against international standards. The analytical errors (2SD) for  $\delta^{13}\text{C}_{\text{carb}}$  and  $\delta^{18}\text{O}$  values are on the order of 0.05 per mil (‰) or better. Carbonate and Oxygen isotopic ratios were recorded in conventional delta notation with respect to values of Pee Dee Belemnite (VPDB) as follows:

$$\delta^{13}\text{C} = [({}^{13}\text{C}/{}^{12}\text{C})_{\text{sample}}/({}^{13}\text{C}/{}^{12}\text{C})_{\text{standard}} - 1] * 1000$$

$$\delta^{18}\text{O} = [({}^{18}\text{O}/{}^{16}\text{O})_{\text{sample}}/({}^{18}\text{O}/{}^{16}\text{O})_{\text{standard}} - 1] * 1000$$

### Shale Geochemical Analysis

Black, organic-rich shale intervals were crushed into a fine powder using a tungsten carbide mill for their elemental and pyrolysis analysis. Major and trace element concentrations were done using an Agilent 8900 quadrupole ICP-MS with Octopole Reaction System from a multi-acid dissolution of individual shale powdered samples following Cox et al. (2016) and Yang et al. (2020) at Adelaide Microscopy. Integrated sample introduction was tuned daily to optimise plasma conditions and sensitivity. Calibration was carried out using standards prepared from two multi-element stock standard solutions in the range 0.3  $\mu\text{g}/\text{L}$  to 300  $\mu\text{g}/\text{L}$ . A single solution prepared from an independent set of stock standards was analysed as an 'unknown' to determine the accuracy of the calibration standards. The data was processed using Agilent Mass-Hunter Data Analysis. An internal standard solution containing  $^{61}\text{Ni}$ ,  $^{115}\text{In}$ ,  $^{147}\text{Sm}$ ,  $^{169}\text{Tm}$  and  $^{205}\text{Tl}$  was mixed in-line with the sample stream ahead of aspiration.

Organic geochemical pyrolysis measurements were done using a Weatherfords Source Rock Analyser and Rock-Eval 6 Turbo at the University of Adelaide. Shale powders were loaded onto the carousel and heated under inert helium in the pyrolysis and oxidation modes to obtain S1-4 peaks as well as  $T_{\text{max}}$ . The pyrolysis oven was first held at 300°C for 5 minutes and ramped at 25°C per minute from 300°C to 650°C. Subsequently the oven was reduced to 220°C and held for 5 minutes with the carrier gas converted to inert air (CO & CO<sub>2</sub> free) and purged, ramped at maximum heating to 580°C and held for 20 minutes. The flame ionisation detector (FID) was calibrated by running Weatherford Laboratories Instruments Division Standard 533. The IR Analysers were calibrated against standard gas with known concentration of CO<sub>2</sub> and CO. An analysis blank was run as 'blank' mode with the sample

batch and the blank data was automatically subtracted from all analyses. An external check standard was also run first with each batch to ensure the instrument status with additional check standards every 10 samples. The results were processed where peak areas and geochemical indices including Total organic carbon (TOC), Oxygen Index (OI), Hydrogen Index (HI) and Production Index (PI) are automatically calculated. Rock-Eval pyrolysis data was screened using quality control criteria defined by Hall et al. (2016).

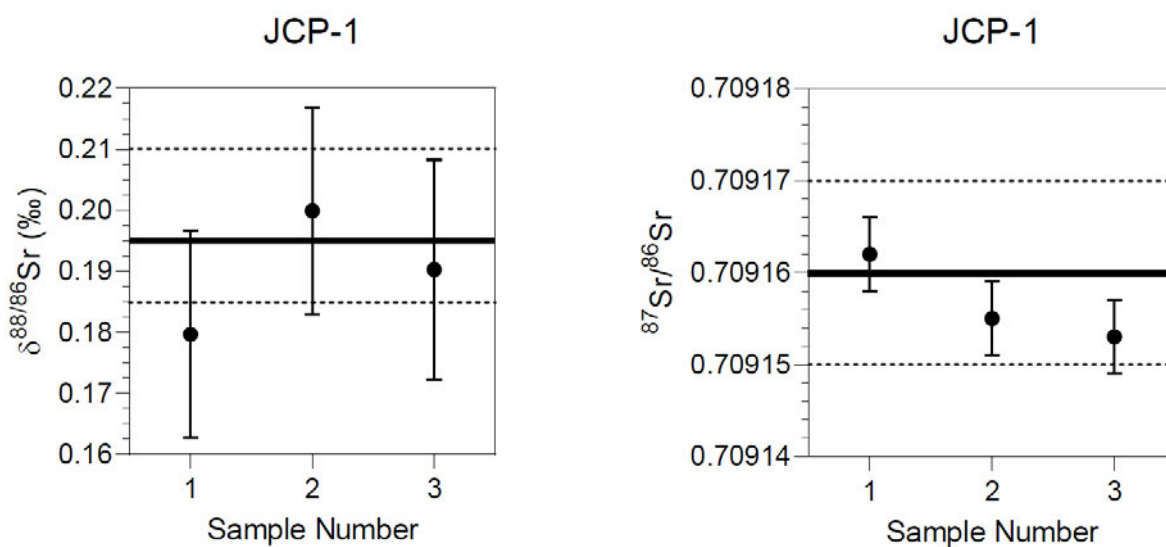


Figure S.4.1. Sr isotopic values of standard JCP-1 and NIST SRM 987 in relation to published data (Balcaen et al., 2005; Inoue et al., 2004; Krabbenhöft et al., 2009).

### Analytical Data

IDENT	MCDD0005 Shale 1	MCDD0005 Shale 2	MCDD0005 Shale 3	MCDD0005 Shale 4
Depth	165.2	166.3	167.3	167.9
Formation	Mallapunyah	Mallapunyah	Mallapunyah	Mallapunyah
Mo/Al	0.17	0.13	#VALUE!	#VALUE!
U/Al	0.23	0.25	0.40	0.50
V/Al	16.20	22.53	12.80	12.02
Al	8.64	7.99	6.25	4.99
Ba	220.00	140.00	200.00	220.00
Mo	1.50	1.00	<0.5	<0.5
P	0.07	0.04	0.07	0.05
V	140.00	180.00	80.00	60.00
Zr	103.00	100.00	109.00	80.00
La	23.90	27.40	40.40	20.00
Ce	45.70	49.40	76.80	40.70
Pr	5.60	5.60	9.10	5.10
Nd	20.60	18.30	31.80	19.20
Sm	4.10	2.95	5.35	4.10
Eu	0.85	0.60	1.10	0.80
Gd	3.80	2.60	5.00	3.80
Tb	0.54	0.38	0.68	0.52
Dy	3.30	2.35	3.90	3.25
Ho	0.64	0.50	0.74	0.64
Er	1.90	1.60	2.30	1.90
Tm	0.30	0.25	0.35	0.30
Yb	1.85	1.65	2.15	1.75
Lu	0.30	0.26	0.34	0.26

MCDD0005 Shale 16	182.8	MCDD0005 Shale 15	181.6	MCDD0005 Shale 14	180.6	MCDD0005 Shale 13	179.1	MCDD0005 Shale 12	177.5	MCDD0005 Shale 11	176.3	MCDD0005 Shale 10	175.3	MCDD0005 Shale 9	173.9	MCDD0005 Shale 8	172.8	MCDD0005 Shale 7	171.8	MCDD0005 Shale 6	170.7	MCDD0005 Shale 5	169.9
Mallapunya		Mallapunya	Mallapunya	Mallapunya	Mallapunya	Mallapunya	Mallapunya	Mallapunya	Mallapunya	Mallapunya	Mallapunya	Mallapunya	Mallapunya	Mallapunya	Mallapunya	Mallapunya	Mallapunya	Mallapunya	Mallapunya	Mallapunya	Mallapunya	Mallapunya	Mallapunya
0.18	0.19	#VALUE!	0.13	0.13	0.26	0.13	0.13	0.13	0.13	0.13	0.13	#VALUE!	#VALUE!	#VALUE!	#VALUE!	#VALUE!	#VALUE!	#VALUE!	#VALUE!	0.13	0.13	#VALUE!	#VALUE!
0.71	0.56	0.20	0.26	0.26	0.26	0.26	0.26	0.26	0.26	0.26	0.27	0.33	0.33	0.33	0.26	0.33	0.33	0.33	0.79	0.26	0.26	0.28	
14.13	22.50	24.00	28.13	25.54	18.67	18.67	26.32	26.32	18.35	16.72	16.72	12.66	12.66	21.08	21.08	21.08	21.08	21.08	21.08	21.08	21.08	21.08	16.93
5.66	8.00	7.50	7.82	7.83	7.50	7.50	7.60	7.60	7.63	5.98	5.98	6.32	6.32	7.59	7.59	7.59	7.59	7.59	7.59	7.59	7.59	7.59	7.09
220.00	760.00	560.00	180.00	140.00	180.00	180.00	140.00	140.00	200.00	160.00	160.00	220.00	220.00	160.00	160.00	160.00	160.00	160.00	220.00	160.00	160.00	200.00	200.00
1.00	1.50	<0.5	1.00	1.00	1.00	1.00	<0.5	<0.5	<0.5	1.00	1.00	<0.5	<0.5	<0.5	<0.5	<0.5	<0.5	<0.5	<0.5	1.00	1.00	<0.5	<0.5
0.07	0.06	0.03	0.07	0.06	0.08	0.08	0.11	0.11	0.07	0.08	0.08	0.07	0.07	0.08	0.07	0.08	0.08	0.07	0.07	0.08	0.08	0.09	0.09
80.00	180.00	180.00	220.00	200.00	140.00	140.00	200.00	200.00	140.00	100.00	100.00	80.00	80.00	160.00	160.00	160.00	160.00	160.00	80.00	160.00	160.00	120.00	120.00
100.00	120.00	92.00	99.00	102.00	99.00	99.00	91.00	91.00	96.00	96.00	96.00	111.00	111.00	100.00	100.00	100.00	100.00	100.00	111.00	100.00	100.00	100.00	100.00
27.70	20.50	21.00	25.20	22.10	28.10	28.10	19.20	19.20	31.80	25.80	25.80	27.90	27.90	24.60	24.60	24.60	24.60	24.60	27.90	24.60	24.60	26.90	26.90
49.70	34.90	38.10	49.40	43.40	55.30	55.30	39.60	39.60	58.20	47.30	47.30	56.60	56.60	45.10	45.10	45.10	45.10	45.10	56.60	45.10	45.10	51.00	51.00
5.35	3.60	4.60	6.15	5.35	6.65	6.65	5.35	5.35	6.70	5.80	5.80	7.15	7.15	5.20	5.20	5.20	5.20	5.20	7.15	5.20	5.20	6.05	6.05
18.00	12.40	16.10	22.60	18.80	23.60	23.60	21.30	21.30	23.30	21.90	21.90	26.50	26.50	18.90	18.90	18.90	18.90	18.90	26.50	18.90	18.90	22.10	22.10
3.05	2.55	2.45	4.50	3.35	4.30	4.30	4.85	4.85	4.30	4.55	4.55	5.00	5.00	3.25	3.25	3.25	3.25	3.25	5.00	3.25	3.25	4.05	4.05
0.60	0.60	0.55	1.00	0.75	0.95	0.95	1.10	1.10	0.90	1.00	1.00	0.95	0.95	0.60	0.60	0.60	0.60	0.60	0.95	0.60	0.60	0.85	0.85
2.80	2.80	2.00	4.20	3.20	4.20	4.20	4.60	4.60	4.00	4.40	4.40	4.60	4.60	2.80	2.80	2.80	2.80	2.80	4.60	2.80	2.80	3.80	3.80
0.38	0.36	0.34	0.62	0.48	0.58	0.58	0.62	0.62	0.54	0.62	0.62	0.62	0.62	0.42	0.42	0.42	0.42	0.42	0.62	0.42	0.42	0.50	0.50
2.35	2.30	2.35	3.70	3.05	3.45	3.45	3.50	3.50	3.10	3.55	3.55	3.35	3.35	2.70	2.70	2.70	2.70	2.70	3.35	2.70	2.70	3.10	3.10
0.46	0.48	0.52	0.78	0.60	0.66	0.66	0.66	0.66	0.60	0.68	0.68	0.64	0.64	0.50	0.50	0.50	0.50	0.50	0.64	0.50	0.50	0.62	0.62
1.55	1.65	1.65	2.05	1.90	1.95	1.95	1.90	1.90	1.80	2.00	2.00	1.90	1.90	1.65	1.65	1.65	1.65	1.65	1.90	1.65	1.65	1.90	1.90
0.25	0.25	0.25	0.30	0.30	0.30	0.30	0.30	0.30	0.30	0.30	0.30	0.30	0.30	0.30	0.30	0.30	0.30	0.30	0.30	0.30	0.30	0.30	0.30
1.50	1.60	1.65	2.05	1.90	1.85	1.85	1.70	1.70	1.80	1.85	1.85	1.80	1.80	1.55	1.55	1.55	1.55	1.55	1.80	1.55	1.55	1.90	1.90
0.24	0.28	0.26	0.30	0.30	0.30	0.30	0.28	0.28	0.30	0.30	0.30	0.28	0.28	0.24	0.24	0.24	0.24	0.24	0.28	0.24	0.24	0.30	0.30

MCDD0005 Shale 197.6	MCDD0005 Shale 196.3	MCDD0005 Shale 195	MCDD0005 Shale 194	MCDD0005 Shale 192.3	MCDD0005 Shale 190.8	MCDD0005 Shale 189.6	MCDD0005 Shale 188	MCDD0005 Shale 187.2	MCDD0005 Shale 185.9	MCDD0005 Shale 185.1	MCDD0005 Shale 184.2
Mallapunya	Mallapunya	Mallapunya	Mallapunya	Mallapunya	Mallapunya	Mallapunya	Mallapunya	Mallapunya	Mallapunya	Mallapunya	Mallapunya
0.15	0.23	0.43	0.28	0.28	0.34	#VALUE!	0.81	0.30	0.22	0.20	0.40
0.54	0.54	0.54	0.71	0.55	0.43	0.55	0.63	0.99	0.65	0.50	0.64
9.20	12.44	12.93	11.30	11.07	13.65	8.81	14.44	12.20	12.93	11.95	9.66
6.52	6.43	4.64	3.54	5.42	5.86	4.54	5.54	6.56	4.64	5.02	6.21
560.00	340.00	360.00	420.00	840.00	360.00	900.00	260.00	740.00	320.00	300.00	260.00
1.00	1.50	2.00	1.00	1.50	2.00	<0.5	4.50	2.00	1.00	1.00	2.50
0.05	0.05	0.06	0.07	0.05	0.06	0.05	0.06	0.14	0.08	0.05	0.07
60.00	80.00	60.00	40.00	60.00	80.00	40.00	80.00	80.00	60.00	60.00	60.00
150.00	142.00	92.00	74.00	153.00	104.00	121.00	110.00	135.00	96.00	114.00	183.00
40.00	35.00	24.90	17.60	32.30	33.50	21.90	31.00	26.80	23.80	27.60	34.00
91.00	68.90	54.50	36.80	61.90	65.10	41.90	63.90	50.50	48.80	52.30	67.30
11.60	8.20	6.65	4.55	7.45	7.80	4.95	7.65	5.95	5.95	6.15	8.25
42.70	29.10	24.20	17.60	25.70	27.30	18.10	28.30	21.50	22.40	21.30	30.30
6.60	4.90	4.55	3.70	4.70	4.85	3.55	5.10	4.05	4.40	3.90	5.40
1.10	0.85	0.85	0.75	0.90	0.90	0.70	0.90	0.80	0.80	1.05	1.05
5.20	4.20	4.20	3.60	4.20	4.40	3.20	4.40	4.00	4.00	3.60	5.20
0.74	0.60	0.58	0.48	0.60	0.58	0.44	0.58	0.52	0.56	0.50	0.78
4.45	3.55	3.50	2.75	3.60	3.55	2.90	3.50	3.10	3.10	3.00	4.90
0.86	0.70	0.68	0.48	0.74	0.70	0.54	0.66	0.62	0.60	0.60	0.96
2.70	2.10	2.10	1.45	2.15	2.05	1.70	2.00	1.90	1.80	1.90	2.85
0.40	0.35	0.30	0.20	0.35	0.30	0.25	0.30	0.30	0.25	0.30	0.45
2.60	2.15	1.90	1.40	2.10	1.90	1.60	2.00	1.95	1.75	1.85	2.70
0.42	0.34	0.30	0.22	0.34	0.32	0.24	0.32	0.32	0.26	0.30	0.44

MCDD0005 Shale 40	MCDD0005 Shale 39	MCDD0005 Shale 38	MCDD0005 Shale 37	MCDD0005 Shale 36	MCDD0005 Shale 35	MCDD0005 Shale 34	MCDD0005 Shale 33	MCDD0005 Shale 32	MCDD0005 Shale 31	MCDD0005 Shale 30	MCDD0005 Shale 29
211.4	210.5	209.3	207.9	206.6	204.9	203.9	202.8	201.6	200.9	199.5	198.4
Mallapunya	Mallapunya	Mallapunya	Mallapunya	Mallapunya	Mallapunya	Mallapunya	Mallapunya	Mallapunya	Mallapunya	Mallapunya	Mallapunya
#VALUE!	#VALUE!	#VALUE!	#VALUE!	#VALUE!	#VALUE!	#VALUE!	0.18	0.21	0.19	0.18	0.17
0.35	0.48	0.53	0.64	0.46	0.53	0.42	0.45	0.62	0.37	0.53	0.67
7.09	6.40	10.58	7.26	10.99	7.05	6.66	10.87	8.23	7.45	10.60	10.12
5.64	6.25	5.67	5.51	5.46	5.67	6.01	5.52	4.86	5.37	5.66	5.93
420.00	700.00	480.00	2280.00	440.00	400.00	520.00	220.00	300.00	680.00	480.00	420.00
<0.5	<0.5	<0.5	<0.5	<0.5	<0.5	<0.5	1.00	1.00	1.00	1.00	1.00
0.03	0.04	0.04	0.03	0.04	0.05	0.04	0.05	0.04	0.06	0.05	0.05
40.00	40.00	60.00	40.00	60.00	40.00	40.00	60.00	40.00	40.00	60.00	60.00
109.00	116.00	142.00	116.00	104.00	143.00	131.00	121.00	158.00	137.00	138.00	146.00
27.10	30.90	38.30	28.50	26.00	37.40	34.60	31.70	31.90	31.90	41.40	38.40
53.40	58.90	66.80	64.00	55.40	69.80	67.90	65.00	62.90	63.90	77.70	77.10
6.30	6.85	7.20	8.10	7.00	8.15	8.10	7.85	7.45	7.55	8.65	9.30
21.80	23.50	24.60	29.80	25.60	28.10	29.20	28.00	25.90	26.20	29.50	32.50
4.15	4.25	4.65	5.20	4.55	5.25	5.20	4.80	5.10	4.65	5.05	5.55
0.80	0.85	0.85	0.85	0.80	0.90	0.95	0.85	0.90	0.85	0.85	0.95
3.80	4.00	4.60	4.60	4.00	4.80	4.60	4.20	4.80	4.00	4.40	4.80
0.54	0.56	0.62	0.62	0.54	0.66	0.64	0.56	0.66	0.56	0.62	0.68
3.25	3.35	3.70	3.65	3.10	3.95	3.85	3.30	4.00	3.45	4.05	4.30
0.62	0.64	0.70	0.74	0.60	0.74	0.74	0.62	0.74	0.66	0.72	0.84
1.90	1.95	2.00	2.20	1.85	2.65	2.20	1.90	2.30	2.00	2.20	2.60
0.30	0.30	0.30	0.35	0.30	0.35	0.35	0.30	0.35	0.30	0.35	0.40
1.85	2.00	1.95	2.20	1.75	2.15	2.20	1.85	2.15	1.95	2.05	2.55
0.28	0.30	0.30	0.34	0.28	0.36	0.34	0.28	0.34	0.32	0.34	0.40

MCDD0005 Shale 52	MCDD0005 Shale 51	MCDD0005 Shale 50	MCDD0005 Shale 49	MCDD0005 Shale 48	MCDD0005 Shale 47	MCDD0005 Shale 46	MCDD0005 Shale 45	MCDD0005 Shale 44	MCDD0005 Shale 43	MCDD0005 Shale 42	MCDD0005 Shale 41
225.5	224.9	224	222.9	221.9	220.7	218.8	217	216	214.9	213.9	212.6
Mallapunya	Mallapunya	Mallapunya	Mallapunya	Mallapunya	Mallapunya	Mallapunya	Mallapunya	Mallapunya	Mallapunya	Mallapunya	Mallapunya
3.37	#VALUE!	#VALUE!	3.03	#VALUE!	0.15	#VALUE!	#VALUE!	0.16	#VALUE!	#VALUE!	#VALUE!
7.87	8.70	1.06	16.67	2.47	1.04	0.75	0.65	0.47	0.49	0.41	0.34
#VALUE!	#VALUE!	#VALUE!	#VALUE!	#VALUE!	5.97	7.53	7.39	9.48	9.87	9.72	6.72
0.45	0.12	1.89	0.33	0.41	6.70	5.31	5.41	6.33	6.08	6.17	5.95
160.00	17400.00	60.00	1480.00	4900.00	760.00	680.00	380.00	480.00	340.00	540.00	480.00
1.50	<0.5	<0.5	1.00	<0.5	1.00	<0.5	<0.5	1.00	<0.5	<0.5	<0.5
0.03	0.01	0.02	0.02	0.02	0.06	0.05	0.04	0.03	0.05	0.04	0.03
<20	<20	<20	<20	<20	40.00	40.00	40.00	60.00	60.00	60.00	40.00
7.00	3.00	28.00	4.00	10.00	105.00	96.00	101.00	80.00	104.00	102.00	96.00
3.20	2.10	13.60	2.70	2.50	27.60	26.20	27.00	30.40	31.90	28.20	28.50
7.20	6.10	31.50	7.20	6.20	47.20	54.30	53.00	61.90	58.70	56.90	56.50
0.90	0.85	3.85	1.10	0.80	5.00	6.65	6.45	7.60	6.95	6.85	6.70
3.60	3.35	13.80	4.35	2.95	16.70	23.70	23.20	28.10	24.50	25.20	24.20
0.70	0.80	2.10	1.05	0.60	3.05	3.70	4.25	4.70	4.45	4.55	4.35
0.15	0.20	0.40	0.20	0.15	0.55	0.65	0.75	0.85	0.80	0.85	0.85
0.60	0.80	1.60	1.00	0.60	3.00	3.20	3.80	4.00	4.00	3.80	4.00
0.10	0.10	0.22	0.14	0.08	0.36	0.42	0.54	0.52	0.54	0.54	0.54
0.55	0.60	1.40	0.80	0.45	2.15	2.60	3.15	3.10	3.30	3.10	3.25
0.10	0.12	0.26	0.14	0.08	0.44	0.52	0.62	0.60	0.64	0.60	0.62
0.25	0.25	0.80	0.40	0.20	1.50	1.70	1.90	1.90	1.90	1.85	1.90
<0.05	<0.05	0.10	<0.05	<0.05	0.25	0.25	0.30	0.30	0.30	0.25	0.30
0.20	0.30	0.80	0.30	0.20	1.60	1.55	1.80	1.70	1.85	1.75	1.85
0.04	0.06	0.12	0.04	0.04	0.26	0.26	0.30	0.28	0.30	0.28	0.28



MCDD0005 Shale 64	243.1	MCDD0005 Shale .63	242.2	MCDD0005 Shale 62	240	MCDD0005 Shale .61	238.8	MCDD0005 Shale 60	237.3	MCDD0005 Shale 59	236.1	MCDD0005 Shale 58	233.7	MCDD0005 Shale 57	232.6	MCDD0005 Shale 56	232	MCDD0005 Shale 55	229.9	MCDD0005 Shale 54	229.1	MCDD0005 Shale 53	227.8
Mallapunya	#VALUE!	Mallapunya	Mallapunya	Mallapunya	Mallapunya	Mallapunya	Mallapunya	Mallapunya	Mallapunya	Mallapunya	Mallapunya	Mallapunya	Mallapunya	Mallapunya	Mallapunya	Mallapunya	Mallapunya	Mallapunya	Mallapunya	Mallapunya	Mallapunya	Mallapunya	Mallapunya
	0.43	0.37	#VALUE!	0.60	0.51	0.64	0.72	#VALUE!	0.88	6.98	4.65	#VALUE!	0.76	#VALUE!	8.77	#VALUE!	0.02	0.01	0.02	0.02	0.02	0.02	0.02
	8.62	7.49	#VALUE!	4.81	8.21	#VALUE!	8.11	#VALUE!	8.11	#VALUE!	#VALUE!	#VALUE!	#VALUE!	#VALUE!	#VALUE!	#VALUE!	#VALUE!	#VALUE!	#VALUE!	#VALUE!	#VALUE!	#VALUE!	#VALUE!
	4.64	5.34	0.08	4.16	3.13	3.13	4.87	0.10	7.40	0.22	1.97	0.29	0.29	0.29	0.29	0.29	0.29	0.29	0.29	0.29	0.29	0.29	0.29
	260.00	240.00	980.00	160.00	80.00	3000.00	320.00	340.00	200.00	300.00	120.00	120.00	120.00	120.00	120.00	120.00	120.00	120.00	120.00	120.00	120.00	120.00	120.00
	<0.5	<0.5	1.00	<0.5	<0.5	<0.5	<0.5	<0.5	<0.5	<0.5	<0.5	<0.5	<0.5	<0.5	<0.5	<0.5	<0.5	<0.5	<0.5	<0.5	<0.5	<0.5	<0.5
	0.05	0.04	0.02	0.04	0.03	0.03	0.03	0.01	0.05	0.01	0.01	0.01	0.01	0.01	0.01	0.01	0.01	0.01	0.01	0.01	0.01	0.01	0.01
	40.00	40.00	<20	20.00	<20	<20	40.00	<20	60.00	<20	<20	<20	<20	<20	<20	<20	<20	<20	<20	<20	<20	<20	<20
	78.00	105.00	2.00	101.00	131.00	96.00	138.00	3.00	135.00	4.00	32.00	5.00	32.00	10.00	10.00	32.00	10.00	10.00	10.00	10.00	10.00	10.00	10.00
	19.40	27.80	2.10	33.40	3.70	21.10	35.00	2.10	34.10	2.10	10.00	2.50	10.00	10.00	10.00	10.00	10.00	10.00	10.00	10.00	10.00	10.00	10.00
	39.00	55.50	4.20	62.70	8.50	42.90	68.40	6.80	54.70	5.30	19.10	6.20	19.10	19.10	19.10	19.10	19.10	19.10	19.10	19.10	19.10	19.10	19.10
	4.65	6.60	0.70	7.30	1.20	5.15	8.00	0.95	5.80	0.70	2.20	0.80	2.20	2.20	2.20	2.20	2.20	2.20	2.20	2.20	2.20	2.20	2.20
	17.30	23.80	1.80	25.90	5.25	19.10	28.80	3.65	20.00	2.80	7.90	3.35	7.90	7.90	7.90	7.90	7.90	7.90	7.90	7.90	7.90	7.90	7.90
	3.40	4.00	0.35	4.70	1.75	3.80	5.20	0.85	3.60	0.60	1.45	0.60	1.45	1.45	1.45	1.45	1.45	1.45	1.45	1.45	1.45	1.45	1.45
	0.65	0.75	0.10	0.90	0.40	0.75	1.00	0.20	0.65	0.15	0.10	0.10	0.10	0.10	0.10	0.10	0.10	0.10	0.10	0.10	0.10	0.10	0.10
	3.40	3.40	0.40	4.20	2.60	3.60	4.60	0.80	3.40	0.60	1.20	0.60	1.20	1.20	1.20	1.20	1.20	1.20	1.20	1.20	1.20	1.20	1.20
	0.44	0.46	0.04	0.56	0.46	0.48	0.64	0.12	0.48	0.08	0.18	0.08	0.18	0.18	0.18	0.18	0.18	0.18	0.18	0.18	0.18	0.18	0.18
	2.60	3.00	0.25	3.50	3.10	2.75	3.90	0.65	3.15	0.50	1.05	0.45	1.05	1.05	1.05	1.05	1.05	1.05	1.05	1.05	1.05	1.05	1.05
	0.50	0.54	0.04	0.66	0.64	0.50	0.74	0.12	0.74	0.08	0.20	0.08	0.20	0.20	0.20	0.20	0.20	0.20	0.20	0.20	0.20	0.20	0.20
	1.55	1.70	0.10	1.90	1.95	1.50	2.30	0.30	2.30	0.25	0.60	0.25	0.60	0.60	0.60	0.60	0.60	0.60	0.60	0.60	0.60	0.60	0.60
	0.25	0.25	<0.05	0.30	0.30	0.20	0.35	<0.05	0.35	<0.05	0.10	<0.05	0.10	<0.05	<0.05	<0.05	<0.05	<0.05	<0.05	<0.05	<0.05	<0.05	<0.05
	1.50	1.65	0.10	1.85	2.00	1.45	2.25	0.20	2.40	0.20	0.60	0.20	0.60	0.60	0.60	0.60	0.60	0.60	0.60	0.60	0.60	0.60	0.60
	0.24	0.26	<0.02	0.28	0.34	0.22	0.36	0.04	0.38	0.02	0.10	0.02	0.10	0.10	0.10	0.10	0.10	0.10	0.10	0.10	0.10	0.10	0.10

MCDD0005 Shale 76	258.3	MCDD0005 Shale 75	256.8	MCDD0005 Shale 74	255.5	MCDD0005 Shale 73	254.5	MCDD0005 Shale 72	252.5	MCDD0005 Shale 71	251.5	MCDD0005 Shale 70	249.7	MCDD0005 Shale 69	248.6	MCDD0005 Shale 68	247.5	MCDD0005 Shale 67	246.9	MCDD0005 Shale 66	245.8	MCDD0005 Shale 65	244.5
Mallapunya	#VALUE!	Mallapunya	Mallapunya	Mallapunya	Mallapunya	Mallapunya	Mallapunya	Mallapunya	Mallapunya	Mallapunya	Mallapunya	Mallapunya	Mallapunya	Mallapunya	Mallapunya	Mallapunya	Mallapunya	Mallapunya	Mallapunya	Mallapunya	Mallapunya	Mallapunya	Mallapunya
	0.69	1.27	0.50	0.53	0.83	0.89	0.76	0.47	0.43	0.59	0.46	0.29											
	11.90	#VALUE!	7.92	8.55	8.33	9.76	7.60	9.43	8.58	7.86	9.24	5.90											
	5.04	0.79	5.05	4.68	4.80	6.15	5.26	4.24	4.66	5.09	4.33	6.78											
	640.00	200.00	220.00	580.00	640.00	600.00	260.00	180.00	200.00	200.00	140.00	280.00											
	<0.5	<0.5	<0.5	<0.5	<0.5	<0.5	<0.5	<0.5	<0.5	<0.5	<0.5	<0.5											
	0.08	0.03	0.06	0.06	0.06	0.07	0.07	0.07	0.05	0.06	0.05	0.10											
	60.00	<20	40.00	40.00	40.00	60.00	40.00	40.00	40.00	40.00	40.00	40.00											
	121.00	23.00	67.00	66.00	118.00	102.00	150.00	97.00	83.00	92.00	87.00	112.00											
	22.30	12.30	27.60	24.00	25.20	19.70	28.90	22.30	23.10	27.40	19.50	39.70											
	43.90	29.40	56.00	48.20	49.80	35.60	56.80	45.70	45.70	53.90	39.50	82.00											
	5.15	3.30	6.40	5.65	5.90	4.15	6.60	5.20	5.25	6.25	4.75	9.85											
	19.30	12.30	23.00	20.70	22.20	15.40	23.90	18.60	18.60	22.20	17.50	36.60											
	3.65	2.35	3.85	3.85	4.05	3.15	3.85	3.15	2.85	3.75	3.15	6.50											
	0.70	0.50	0.70	0.75	0.70	0.60	0.70	0.60	0.50	0.65	0.55	1.05											
	3.40	2.40	3.20	3.40	3.60	3.00	3.20	2.80	2.40	3.20	2.80	5.20											
	0.44	0.30	0.42	0.48	0.50	0.42	0.44	0.36	0.34	0.42	0.40	0.70											
	2.75	1.80	2.65	3.00	3.00	2.60	2.75	2.35	2.10	2.50	2.35	4.10											
	0.54	0.36	0.48	0.56	0.58	0.50	0.52	0.44	0.42	0.48	0.48	0.74											
	1.70	0.95	1.60	1.70	1.85	1.55	1.65	1.35	1.30	1.50	1.45	2.25											
	0.25	0.15	0.20	0.25	0.25	0.25	0.25	0.20	0.20	0.25	0.20	0.35											
	1.65	0.75	1.45	1.65	1.75	1.50	1.65	1.35	1.30	1.50	1.40	2.10											
	0.28	0.12	0.24	0.26	0.28	0.24	0.26	0.22	0.20	0.24	0.22	0.34											

MCDD0005 Shale .88	277.3	MCDD0005 Shale .87	276.2	MCDD0005 Shale .86	274.6	MCDD0005 Shale .85	273.4	MCDD0005 Shale .84	271.7	MCDD0005 Shale .83	269.7	MCDD0005 Shale .82	268.5	MCDD0005 Shale .81	266.8	MCDD0005 Shale .80	264.2	MCDD0005 Shale .79	262.6	MCDD0005 Shale .78	261.6	MCDD0005 Shale .77	259.8
Mallapunya	Mallapunya	Mallapunya	Mallapunya	Mallapunya	Mallapunya	Mallapunya	Mallapunya	Mallapunya	Mallapunya	Mallapunya	Mallapunya	Mallapunya	Mallapunya	Mallapunya	Mallapunya	Mallapunya	Mallapunya	Mallapunya	Mallapunya	Mallapunya	Mallapunya	Mallapunya	Mallapunya
#VALUE!	#VALUE!	#VALUE!	#VALUE!	#VALUE!	#VALUE!	#VALUE!	#VALUE!	#VALUE!	#VALUE!	#VALUE!	#VALUE!	#VALUE!	#VALUE!	#VALUE!	#VALUE!	#VALUE!	#VALUE!	#VALUE!	#VALUE!	#VALUE!	#VALUE!	#VALUE!	#VALUE!
0.50	0.43	0.59	1.92	0.74	0.44	0.40	0.43	0.40	0.40	0.44	0.44	0.43	0.40	0.43	0.43	0.43	0.58	0.78	0.78	0.77	0.77	0.41	
3.98	6.93	7.87	102.30	7.38	10.47	9.62	10.26	9.62	9.62	10.47	10.47	10.26	9.62	10.26	10.26	9.24	7.78	7.78	10.20	10.20	8.23	8.23	
5.02	5.77	5.08	3.91	5.42	5.73	6.24	5.85	6.24	6.24	5.73	5.73	5.85	6.24	5.85	5.85	4.33	5.14	5.14	3.92	3.92	4.86	4.86	
380.00	200.00	180.00	520.00	220.00	240.00	360.00	740.00	360.00	360.00	240.00	240.00	740.00	360.00	740.00	740.00	1240.00	200.00	200.00	460.00	460.00	220.00	220.00	
<0.5	<0.5	<0.5	<0.5	<0.5	<0.5	<0.5	<0.5	<0.5	<0.5	<0.5	<0.5	<0.5	<0.5	<0.5	<0.5	<0.5	<0.5	<0.5	<0.5	<0.5	<0.5	<0.5	
0.04	0.03	0.05	0.03	0.04	0.04	0.05	0.04	0.05	0.05	0.04	0.04	0.04	0.05	0.04	0.04	0.03	0.06	0.06	0.07	0.07	0.09	0.09	
20.00	40.00	40.00	400.00	40.00	60.00	60.00	60.00	60.00	60.00	60.00	60.00	60.00	60.00	60.00	60.00	40.00	40.00	40.00	40.00	40.00	40.00	40.00	
116.00	106.00	88.00	110.00	100.00	104.00	96.00	123.00	96.00	96.00	104.00	104.00	123.00	96.00	123.00	123.00	96.00	111.00	111.00	71.00	71.00	77.00	77.00	
29.00	36.10	27.60	24.10	33.20	32.40	29.40	27.20	29.40	29.40	32.40	32.40	27.20	29.40	27.20	27.20	22.00	25.00	25.00	15.30	15.30	25.30	25.30	
61.90	73.80	59.00	45.90	64.20	61.80	53.20	55.40	53.20	53.20	61.80	61.80	55.40	53.20	55.40	55.40	43.70	50.40	50.40	31.80	31.80	52.60	52.60	
7.20	8.40	6.90	5.45	7.55	7.25	6.20	6.35	6.20	6.20	7.25	7.25	6.35	6.20	6.35	6.35	5.20	5.65	5.65	3.75	3.75	6.05	6.05	
27.60	30.70	25.90	20.60	27.90	26.30	22.00	23.80	22.00	22.00	26.30	26.30	23.80	22.00	23.80	23.80	19.50	20.60	20.60	14.10	14.10	22.50	22.50	
5.05	5.45	4.80	4.10	5.05	4.80	4.15	4.50	4.15	4.15	4.80	4.80	4.50	4.15	4.50	4.50	3.65	3.65	3.65	2.75	2.75	3.60	3.60	
1.00	1.00	0.85	0.85	1.00	0.95	0.80	0.85	0.80	0.80	0.95	0.95	0.85	0.80	0.85	0.85	0.70	0.60	0.60	0.55	0.55	0.60	0.60	
4.80	4.60	4.20	4.00	4.60	4.40	3.80	4.60	3.80	3.80	4.40	4.40	4.60	3.80	4.60	4.60	3.40	3.00	3.00	2.60	2.60	3.00	3.00	
0.68	0.62	0.56	0.58	0.64	0.62	0.54	0.72	0.54	0.54	0.62	0.62	0.72	0.54	0.72	0.72	0.48	0.42	0.42	0.34	0.34	0.38	0.38	
4.15	3.80	3.40	3.70	3.90	3.60	3.10	4.45	3.10	3.10	3.60	3.60	4.45	3.10	4.45	4.45	2.85	2.75	2.75	2.05	2.05	2.30	2.30	
0.82	0.74	0.64	0.70	0.76	0.70	0.60	0.84	0.60	0.60	0.70	0.70	0.84	0.60	0.84	0.84	0.54	0.54	0.54	0.40	0.40	0.44	0.44	
2.50	2.20	1.90	2.15	2.40	2.05	1.90	2.65	1.90	1.90	2.05	2.05	2.65	1.90	2.65	2.65	1.65	1.75	1.75	1.20	1.20	1.40	1.40	
0.35	0.35	0.30	0.30	0.35	0.30	0.25	0.40	0.25	0.25	0.30	0.30	0.40	0.25	0.40	0.40	0.25	0.30	0.30	0.20	0.20	0.20	0.20	
2.15	2.15	1.75	1.95	2.15	1.90	1.65	2.50	1.65	1.65	1.90	1.90	2.50	1.65	2.50	2.50	1.50	1.80	1.80	1.15	1.15	1.35	1.35	
0.36	0.34	0.28	0.30	0.34	0.30	0.28	0.40	0.28	0.28	0.30	0.30	0.40	0.28	0.40	0.40	0.26	0.28	0.28	0.18	0.18	0.22	0.22	

MCDD0005 Shale 100	MCDD0005 Shale 99	MCDD0005 Shale 98	MCDD0005 Shale 97	MCDD0005 Shale 96	MCDD0005 Shale 95	MCDD0005 Shale 94	MCDD0005 Shale 93	MCDD0005 Shale 92	MCDD0005 Shale 91	MCDD0005 Shale 90	MCDD0005 Shale 89
Mallapunya	Mallapunya	Mallapunya	Mallapunya	Mallapunya	Mallapunya	Mallapunya	Mallapunya	Mallapunya	Mallapunya	Mallapunya	Mallapunya
#VALUE!	#VALUE!	#VALUE!	#VALUE!	#VALUE!	#VALUE!	#VALUE!	#VALUE!	#VALUE!	#VALUE!	#VALUE!	#VALUE!
0.76	0.66	0.65	0.67	0.72	0.55	0.69	0.50	0.70	0.65	0.78	1.35
6.06	5.26	5.18	4.47	12.35	13.19	9.20	5.04	9.28	8.66	7.84	8.32
3.30	3.80	3.86	4.47	4.86	4.55	4.35	3.97	4.31	4.62	5.10	4.81
340.00	220.00	1900.00	220.00	240.00	240.00	420.00	1160.00	260.00	260.00	220.00	260.00
<0.5	<0.5	<0.5	<0.5	<0.5	<0.5	<0.5	<0.5	<0.5	<0.5	<0.5	<0.5
0.04	0.04	0.03	0.03	0.04	0.05	0.03	0.03	0.03	0.04	0.04	0.05
20.00	20.00	20.00	20.00	60.00	60.00	40.00	20.00	40.00	40.00	40.00	40.00
140.00	106.00	123.00	141.00	126.00	106.00	129.00	75.00	127.00	146.00	149.00	138.00
30.80	26.80	26.30	34.40	36.10	26.60	25.50	22.80	26.50	29.20	37.90	33.80
61.60	55.00	52.70	69.60	73.30	58.30	53.40	56.10	49.90	58.80	63.40	58.20
7.40	6.50	6.25	8.20	8.45	6.90	6.15	6.95	5.95	6.90	7.35	6.85
27.60	24.20	22.90	30.40	30.70	26.70	23.30	26.50	22.10	25.50	25.80	24.50
5.00	4.55	4.60	5.10	5.25	5.35	4.50	4.80	4.30	4.80	4.70	4.50
0.90	0.85	0.90	0.95	0.95	1.00	0.85	0.85	0.80	0.90	0.90	0.85
4.60	4.00	4.20	4.60	4.60	4.60	4.20	3.80	4.00	4.40	4.60	4.20
0.66	0.54	0.60	0.62	0.64	0.64	0.64	0.50	0.58	0.62	0.66	0.60
3.70	3.25	3.70	3.85	3.80	3.90	3.80	2.95	3.35	3.65	4.10	3.50
0.74	0.64	0.72	0.72	0.72	0.74	0.74	0.54	0.66	0.70	0.78	0.70
2.10	1.85	2.20	2.30	2.15	2.25	2.25	1.65	1.95	2.10	2.40	2.10
0.30	0.30	0.30	0.35	0.35	0.35	0.35	0.25	0.30	0.30	0.35	0.30
2.00	1.75	2.00	2.15	2.05	2.10	2.10	1.50	1.90	2.05	2.25	2.00
0.32	0.28	0.34	0.34	0.34	0.34	0.34	0.24	0.30	0.32	0.36	0.32

MCDD0005 Shale 112	312.8	MCDD0005 Shale 111	311.2	MCDD0005 Shale 110	310.4	MCDD0005 Shale 108	308.9	MCDD0005 Shale 108	307.4	MCDD0005 Shale 107	306.2	MCDD0005 Shale 106	304.9	MCDD0005 Shale 105	302.7	MCDD0005 Shale 104	301.4	MCDD0005 Shale 103	299.5	MCDD0005 Shale 102	297.9	MCDD0005 Shale 101	296.2
Mallapunya	#VALUE!	Mallapunya	Mallapunya	Mallapunya	Mallapunya	Mallapunya	Mallapunya	Mallapunya	Mallapunya	Mallapunya	Mallapunya	Mallapunya	Mallapunya	Mallapunya	Mallapunya	Mallapunya	Mallapunya	Mallapunya	Mallapunya	Mallapunya	Mallapunya	Mallapunya	Mallapunya
0.55	0.52	0.63	0.82	0.68	0.63	0.46	0.56	0.46	0.80	0.05	0.04	0.86	0.04	0.05	0.04	0.86	0.64	0.05	0.05	0.04	0.64	0.47	
7.33	6.96	7.16	6.53	6.85	6.32	7.43	6.44	7.43	10.68	40.00	40.00	5.76	7.35	40.00	40.00	5.76	7.35	40.00	40.00	40.00	7.35	6.27	
5.46	5.75	5.59	6.13	5.84	6.33	5.38	6.21	5.38	5.62	760.00	280.00	280.00	6.21	5.38	5.62	6.95	5.44	6.95	5.44	5.44	5.44	6.38	
880.00	500.00	280.00	400.00	320.00	280.00	280.00	280.00	280.00	720.00	760.00	280.00	280.00	280.00	760.00	720.00	300.00	500.00	300.00	300.00	500.00	500.00	300.00	300.00
<0.5	<0.5	<0.5	<0.5	<0.5	<0.5	<0.5	<0.5	<0.5	<0.5	<0.5	<0.5	<0.5	<0.5	<0.5	<0.5	<0.5	<0.5	<0.5	<0.5	<0.5	<0.5	<0.5	
0.04	0.05	0.04	0.05	0.04	0.05	0.04	0.04	0.04	0.04	0.04	0.05	0.04	0.04	0.04	0.04	0.05	0.04	0.05	0.04	0.04	0.04	0.06	
40.00	40.00	40.00	40.00	40.00	40.00	40.00	40.00	40.00	40.00	40.00	40.00	40.00	40.00	40.00	40.00	40.00	40.00	40.00	40.00	40.00	40.00	40.00	
135.00	146.00	150.00	154.00	158.00	116.00	173.00	166.00	173.00	188.00	173.00	116.00	166.00	166.00	173.00	173.00	188.00	178.00	171.00	178.00	178.00	178.00	113.00	
30.20	28.80	30.90	34.70	31.60	30.90	31.80	31.80	29.00	31.50	29.00	30.90	31.80	31.80	29.00	31.50	40.30	30.50	40.30	30.50	30.50	30.50	32.20	
61.00	58.50	63.40	70.80	63.60	63.90	64.60	64.60	59.10	65.00	59.10	63.90	64.60	64.60	59.10	65.00	82.30	61.90	82.30	61.90	61.90	61.90	66.90	
7.40	6.95	7.45	8.30	7.45	7.40	7.55	7.55	7.25	7.70	7.25	7.40	7.55	7.55	7.25	7.70	9.70	7.20	9.70	7.20	7.20	7.20	7.75	
27.40	25.20	27.20	30.80	28.00	27.60	27.60	27.60	27.20	28.90	27.20	27.60	27.60	27.60	27.20	28.90	35.90	26.90	35.90	26.90	26.90	26.90	28.90	
4.95	4.70	5.15	5.70	4.90	5.10	5.30	5.30	5.60	5.40	5.60	5.10	5.30	5.30	5.60	5.40	6.05	4.75	6.05	4.75	4.75	4.75	5.05	
0.95	0.90	1.00	1.05	0.95	0.90	1.05	1.05	1.15	1.05	1.15	0.90	1.05	1.05	1.15	1.05	1.15	0.95	1.15	0.95	0.95	0.95	1.00	
4.40	4.40	4.80	5.20	4.40	4.40	5.00	5.00	5.40	5.00	5.40	4.40	5.00	5.00	5.40	5.00	5.40	4.20	5.40	4.20	4.20	4.20	4.60	
0.62	0.58	0.66	0.70	0.62	0.62	0.70	0.70	0.78	0.68	0.78	0.62	0.70	0.70	0.78	0.68	0.80	0.58	0.80	0.58	0.58	0.58	0.64	
3.80	3.60	4.00	4.30	3.70	3.80	4.35	4.35	4.75	4.15	4.75	3.80	4.35	4.35	4.75	4.15	4.95	3.55	4.95	3.55	3.55	3.55	3.70	
0.72	0.70	0.74	0.82	0.72	0.72	0.82	0.82	0.90	0.78	0.90	0.72	0.82	0.82	0.90	0.78	0.94	0.70	0.94	0.70	0.70	0.70	0.70	
2.20	2.05	2.30	2.50	2.20	2.15	2.50	2.50	2.80	2.45	2.80	2.15	2.50	2.50	2.80	2.45	2.95	2.05	2.95	2.05	2.05	2.05	2.10	
0.30	0.30	0.35	0.35	0.30	0.30	0.40	0.40	0.45	0.40	0.45	0.30	0.40	0.40	0.45	0.40	0.45	0.30	0.45	0.30	0.30	0.30	0.30	
2.05	1.95	2.10	2.35	2.10	2.00	2.35	2.35	2.65	2.30	2.65	2.00	2.35	2.35	2.65	2.30	2.70	2.05	2.70	2.05	2.05	2.05	2.00	
0.32	0.32	0.36	0.36	0.32	0.32	0.38	0.38	0.42	0.38	0.42	0.32	0.38	0.38	0.42	0.38	0.44	0.32	0.44	0.32	0.32	0.32	0.34	

MCDD0005 Shale 124	332.9	MCDD0005 Shale 123	331.7	MCDD0005 Shale 122	330.1	MCDD0005 Shale 121	329.1	MCDD0005 Shale 120	326.7	MCDD0005 Shale 119	325	MCDD0005 Shale 118	323.6	MCDD0005 Shale 117	319.3	MCDD0005 Shale 116	318.5	MCDD0005 Shale 115	317.4	MCDD0005 Shale 114	315.5	MCDD0005 Shale 113	314.3
Mallapunyah #VALUE!	Mallapunyah	Mallapunyah	Mallapunyah	Mallapunyah	Mallapunyah	Mallapunyah	Mallapunyah	Mallapunyah	Mallapunyah	Mallapunyah	Mallapunyah	Mallapunyah	Mallapunyah	Mallapunyah	Mallapunyah	Mallapunyah	Mallapunyah	Mallapunyah	Mallapunyah	Mallapunyah	Mallapunyah	Mallapunyah	Mallapunyah
0.48	0.53	0.49	0.38	0.55	0.54	0.57	0.52	0.52	0.52	0.54	0.54	0.57	0.52	0.52	0.52	0.56	0.56	0.53	0.53	0.56	0.56	0.58	
6.43	10.70	11.76	15.12	15.85	10.75	9.69	6.93	6.93	6.42	6.08	6.08	6.42	6.93	6.93	6.08	6.42	6.08	6.08	6.08	6.08	6.08	7.75	
6.22	5.61	5.10	5.29	6.31	5.58	6.19	5.77	5.77	6.23	6.58	6.58	6.23	5.77	5.77	6.58	6.23	6.58	6.58	6.58	6.58	5.31	5.16	
860.00	500.00	300.00	320.00	300.00	320.00	280.00	280.00	280.00	340.00	340.00	320.00	280.00	280.00	280.00	280.00	340.00	340.00	260.00	260.00	340.00	340.00	420.00	
<0.5	<0.5	1.50	<0.5	<0.5	<0.5	<0.5	<0.5	<0.5	<0.5	<0.5	<0.5	<0.5	<0.5	<0.5	<0.5	<0.5	<0.5	<0.5	<0.5	<0.5	<0.5	<0.5	
0.05	0.05	0.05	0.03	0.05	0.04	0.04	0.05	0.05	0.05	0.04	0.04	0.05	0.05	0.05	0.05	0.05	0.05	0.05	0.05	0.05	0.05	0.04	
40.00	60.00	60.00	80.00	100.00	60.00	60.00	40.00	40.00	40.00	60.00	60.00	40.00	40.00	40.00	40.00	40.00	40.00	40.00	40.00	40.00	40.00	40.00	
151.00	114.00	113.00	89.00	160.00	153.00	170.00	135.00	135.00	172.00	154.00	154.00	172.00	135.00	135.00	154.00	172.00	154.00	154.00	154.00	170.00	170.00	150.00	
31.00	30.70	28.10	21.60	30.50	32.00	33.90	31.20	31.20	32.40	32.30	32.30	32.40	31.20	31.20	32.30	32.40	32.30	32.30	32.30	31.50	31.50	28.30	
62.90	61.70	56.30	45.00	62.20	64.90	68.40	62.80	62.80	66.20	65.70	65.70	66.20	62.80	62.80	65.70	66.20	65.70	65.70	65.70	63.90	63.90	56.90	
7.60	7.40	6.65	5.10	7.30	7.70	8.20	7.45	7.45	7.80	7.85	7.85	7.80	7.45	7.45	7.85	7.80	7.85	7.85	7.85	7.80	7.80	6.90	
28.20	27.30	24.70	18.40	26.60	28.60	29.50	27.60	27.60	29.00	28.80	28.80	29.00	27.60	27.60	28.80	29.00	28.80	28.80	28.80	28.50	28.50	25.80	
5.55	5.05	4.60	3.85	4.95	5.05	5.10	5.10	5.10	5.10	5.05	5.05	5.10	5.10	5.10	5.10	5.10	5.45	5.45	5.45	5.20	5.20	4.90	
1.10	0.95	0.90	0.75	0.95	0.95	0.90	0.95	0.95	0.95	0.95	0.95	0.95	0.95	0.95	0.95	0.95	1.00	1.00	1.00	0.95	0.95	0.95	
5.60	4.60	4.20	3.80	4.40	4.40	4.60	4.60	4.60	4.60	4.40	4.40	4.60	4.60	4.60	4.60	4.60	5.00	5.00	5.00	4.60	4.60	4.40	
0.84	0.62	0.60	0.52	0.64	0.62	0.62	0.62	0.62	0.64	0.62	0.62	0.62	0.62	0.62	0.62	0.64	0.70	0.70	0.70	0.66	0.66	0.62	
5.20	3.70	3.45	3.45	3.80	3.70	3.85	3.85	3.85	3.80	3.70	3.70	3.85	3.85	3.85	3.85	3.90	4.35	4.35	4.35	3.90	3.90	3.70	
1.02	0.70	0.66	0.60	0.72	0.70	0.74	0.74	0.74	0.72	0.70	0.70	0.74	0.74	0.74	0.74	0.74	0.82	0.82	0.82	0.74	0.74	0.72	
3.20	2.15	1.95	1.80	2.20	2.25	2.30	2.15	2.15	2.30	2.30	2.25	2.30	2.30	2.15	2.15	2.30	2.55	2.55	2.55	2.25	2.25	2.30	
0.45	0.30	0.30	0.25	0.35	0.35	0.35	0.30	0.30	0.35	0.35	0.35	0.35	0.35	0.30	0.30	0.35	0.40	0.40	0.40	0.35	0.35	0.35	
3.00	2.05	1.90	1.65	2.10	2.10	2.20	2.05	2.05	2.20	2.10	2.10	2.20	2.20	2.05	2.05	2.20	2.40	2.40	2.40	2.15	2.15	2.00	
0.48	0.32	0.30	0.26	0.34	0.34	0.36	0.34	0.34	0.34	0.34	0.34	0.36	0.34	0.34	0.34	0.34	0.38	0.38	0.38	0.34	0.34	0.32	

MCDD0005 Shale 135	492.8	MCDD0005 Shale 134	491.9	MCDD0005 Shale 132	490.3	MCDD0005 Shale 131	488.8	MCDD0005 Shale 133	390.8	MCDD0005 Shale 126	353.4	MCDD0005 Shale 130	344.9	MCDD0005 Shale 129	341.7	MCDD0005 Shale 128	340.8	MCDD0005 Shale 127	336.8	MCDD0005 Shale 172	335	MCDD0005 Shale 125	334.2
Wologorang		Wologorang	Wologorang	Wologorang	Wologorang	Wologorang	Wologorang	Mallapunya	Mallapunya	Mallapunya	Mallapunya	Mallapunya	Mallapunya	Mallapunya	Mallapunya	Mallapunya	Mallapunya	Mallapunya	Mallapunya	Mallapunya	Mallapunya	Mallapunya	Mallapunya
#VALUE!	0.52	0.52	0.42	0.51	0.57	0.16	0.17	0.16	0.16	0.16	0.16	0.16	0.17	0.16	0.16	0.23	#VALUE!	#VALUE!	#VALUE!	0.31	#VALUE!	#VALUE!	
0.68	1.03	0.90	1.16	1.00	1.00	0.49	0.51	0.55	0.53	0.53	0.55	0.51	0.51	0.55	0.55	0.53	0.53	0.53	0.59	0.77	0.77	0.73	0.73
9.13	11.78	11.13	11.59	11.44	9.72	9.72	10.24	9.51	9.10	9.10	9.51	10.24	10.24	9.51	9.51	9.10	9.10	8.90	8.90	21.67	21.67	7.33	7.33
2.19	6.79	7.19	6.90	6.99	6.17	6.17	5.86	6.31	6.59	6.59	6.31	5.86	5.86	6.31	6.31	6.59	6.59	6.74	6.74	6.46	6.46	5.46	5.46
100.00	10100.00	400.00	2620.00	7860.00	300.00	300.00	260.00	320.00	280.00	280.00	320.00	260.00	260.00	320.00	320.00	280.00	280.00	380.00	380.00	340.00	340.00	360.00	360.00
<0.5	3.50	3.00	3.50	4.00	4.00	1.00	1.00	1.00	1.00	1.00	1.00	1.00	1.00	1.00	1.00	1.50	1.50	<0.5	<0.5	2.00	2.00	<0.5	<0.5
0.02	0.05	0.05	0.05	0.05	0.05	0.05	0.04	0.05	0.06	0.06	0.05	0.04	0.04	0.05	0.05	0.06	0.06	0.05	0.05	0.08	0.08	0.05	0.05
20.00	80.00	80.00	80.00	80.00	80.00	60.00	60.00	60.00	60.00	60.00	60.00	60.00	60.00	60.00	60.00	60.00	60.00	60.00	60.00	140.00	140.00	40.00	40.00
34.00	96.00	104.00	113.00	101.00	101.00	119.00	104.00	123.00	196.00	196.00	123.00	104.00	104.00	123.00	123.00	196.00	196.00	123.00	123.00	76.00	76.00	126.00	126.00
9.90	68.70	61.80	58.30	63.90	31.20	31.20	28.20	34.30	39.60	39.60	34.30	28.20	28.20	34.30	34.30	39.60	39.60	35.20	35.20	31.10	31.10	29.00	29.00
21.60	126.00	123.00	116.00	121.00	63.40	63.40	57.80	72.10	83.00	83.00	72.10	57.80	57.80	72.10	72.10	83.00	83.00	72.90	72.90	54.50	54.50	59.10	59.10
2.95	11.70	11.80	11.10	11.80	7.50	7.50	6.75	8.20	9.50	9.50	8.20	6.75	6.75	8.20	8.20	9.50	9.50	8.45	8.45	6.40	6.40	6.95	6.95
13.10	36.10	36.00	35.90	37.30	27.30	27.30	24.90	29.40	34.30	34.30	29.40	24.90	24.90	29.40	29.40	34.30	34.30	30.20	30.20	24.00	24.00	25.40	25.40
3.40	4.55	4.55	4.65	4.70	4.85	4.85	4.25	4.80	5.35	5.35	4.80	4.25	4.25	4.80	4.80	5.35	5.35	5.40	5.40	4.60	4.60	4.70	4.70
0.80	0.90	0.90	0.95	0.95	0.95	0.90	0.80	0.80	0.90	0.90	0.80	0.80	0.80	0.80	0.80	0.90	0.90	1.00	1.00	0.85	0.85	0.85	0.85
3.60	4.20	3.60	3.60	3.60	3.60	4.40	3.80	4.00	4.40	4.40	4.00	3.80	3.80	4.00	4.00	4.40	4.40	5.20	5.20	4.20	4.20	4.20	4.20
0.50	0.46	0.48	0.50	0.48	0.48	0.62	0.52	0.56	0.64	0.64	0.56	0.52	0.52	0.56	0.56	0.64	0.64	0.72	0.72	0.58	0.58	0.58	0.58
2.90	2.70	3.05	3.10	3.00	3.00	3.75	3.20	3.40	3.95	3.95	3.40	3.20	3.20	3.40	3.40	3.95	3.95	4.35	4.35	3.30	3.30	3.50	3.50
0.52	0.50	0.58	0.58	0.56	0.74	0.74	0.60	0.66	0.76	0.76	0.66	0.60	0.60	0.66	0.66	0.76	0.76	0.82	0.82	0.64	0.64	0.68	0.68
1.50	1.60	1.75	1.85	1.75	2.25	2.25	1.90	2.00	2.45	2.45	2.00	1.90	1.90	2.00	2.00	2.45	2.45	2.50	2.50	1.90	1.90	2.15	2.15
0.20	0.25	0.25	0.30	0.25	0.35	0.35	0.30	0.30	0.35	0.35	0.30	0.30	0.30	0.30	0.30	0.35	0.35	0.40	0.40	0.30	0.30	0.30	0.30
1.25	1.55	1.70	1.70	1.70	2.10	2.10	1.85	1.90	2.30	2.30	1.90	1.85	1.85	1.90	1.90	2.30	2.30	2.30	2.30	1.70	1.70	2.00	2.00
0.18	0.28	0.28	0.28	0.28	0.34	0.34	0.30	0.30	0.36	0.36	0.30	0.30	0.30	0.30	0.30	0.36	0.36	0.38	0.38	0.28	0.28	0.32	0.32

MCDD0005 Shale 148	507.5	Wollogorang	MCDD0005 Shale 147	506.6	Wollogorang	MCDD0005 Shale 146	505.6	Wollogorang	MCDD0005 Shale 145	503.8	Wollogorang	MCDD0005 Shale 143	501.1	Wollogorang	MCDD0005 Shale 142	500.1	Wollogorang	MCDD0005 Shale 141	499	Wollogorang	MCDD0005 Shale 140	498.1	Wollogorang	MCDD0005 Shale 139	496.7	Wollogorang	MCDD0005 Shale 138	495.6	Wollogorang	MCDD0005 Shale 137	495.3	Wollogorang	MCDD0005 Shale 136	493.3	Wollogorang
	0.21			0.23	#VALUE!		#VALUE!			#VALUE!		0.40	0.26	#VALUE!		0.30	0.34		0.30	0.34		0.30	0.34		0.34		1.14	0.62		0.62	0.53		0.53		
	0.50			0.54	0.46		0.46			0.42		0.60	0.64	0.34		0.82	0.93		0.82	0.93		0.82	0.93		0.93		1.54	0.96		0.96	0.53		0.53		
	8.56			12.23	13.23		13.23			10.08		8.05	10.24	#VALUE!		8.93	10.19		8.93	10.19		8.93	10.19		10.19		10.74	8.23		8.23	#VALUE!		#VALUE!		
	7.01			6.54	7.56		7.56			5.95		7.45	7.81	10.40		6.72	5.89		6.72	5.89		6.72	5.89		5.89		7.45	7.29		7.29	1.88		1.88		
	500.00			360.00	2620.00		2620.00			320.00		1040.00	560.00	680.00		360.00	1660.00		360.00	1660.00		360.00	1660.00		1660.00		420.00	420.00		420.00	660.00		660.00		
	1.50			1.50	<0.5		<0.5			<0.5		3.00	2.00	<0.5		2.00	2.00		2.00	2.00		2.00	2.00		2.00		8.50	4.50		4.50	1.00		1.00		
	0.07			0.07	0.07		0.07			0.06		0.08	0.08	0.03		0.08	0.06		0.06	0.06		0.06	0.06		0.06		0.08	0.08		0.08	0.02		0.02		
	60.00			80.00	100.00		100.00			60.00		60.00	80.00	<20		60.00	60.00		60.00	60.00		60.00	60.00		60.00		80.00	60.00		60.00	<20		<20		
	76.00			92.00	90.00		90.00			78.00		96.00	83.00	210.00		90.00	61.00		90.00	61.00		90.00	61.00		61.00		89.00	78.00		78.00	23.00		23.00		
	40.70			18.30	46.80		46.80			40.40		57.70	61.60	8.30		68.40	57.30		68.40	57.30		68.40	57.30		57.30		118.00	71.20		71.20	7.50		7.50		
	78.10			32.40	88.40		88.40			78.70		108.00	128.00	29.40		127.00	88.40		127.00	88.40		127.00	88.40		88.40		188.00	122.00		122.00	18.60		18.60		
	9.35			4.45	9.80		9.80			8.50		12.10	13.00	4.45		12.60	9.85		12.60	9.85		12.60	9.85		9.85		17.00	11.40		11.40	2.70		2.70		
	32.10			19.10	32.90		32.90			28.00		42.30	43.70	19.70		40.10	32.30		40.10	32.30		40.10	32.30		32.30		49.40	35.20		35.20	11.20		11.20		
	4.55			4.20	5.40		5.40			4.55		6.55	6.40	5.15		5.90	4.75		5.90	4.75		5.90	4.75		4.75		5.45	5.15		5.15	2.45		2.45		
	0.85			0.80	0.95		0.95			0.85		1.40	1.25	1.00		1.20	0.95		1.20	0.95		1.20	0.95		0.95		1.05	1.00		1.00	0.55		0.55		
	3.80			4.00	4.80		4.80			4.00		5.20	5.20	5.80		5.00	4.00		5.00	4.00		5.00	4.00		4.00		4.00	4.20		4.20	2.40		2.40		
	0.50			0.54	0.62		0.62			0.56		0.66	0.66	1.00		0.66	0.50		0.66	0.50		0.66	0.50		0.50		0.52	0.52		0.52	0.32		0.32		
	3.00			3.15	3.70		3.70			3.30		3.75	3.65	6.85		3.90	2.70		3.90	2.70		3.90	2.70		2.70		3.00	2.95		2.95	1.75		1.75		
	0.54			0.60	0.68		0.68			0.62		0.70	0.68	1.42		0.70	0.48		0.70	0.48		0.70	0.48		0.48		0.56	0.54		0.54	0.32		0.32		
	1.65			1.85	2.00		2.00			1.95		2.05	2.00	4.55		2.10	1.45		2.10	1.45		2.10	1.45		1.45		1.70	1.70		1.70	0.90		0.90		
	0.25			0.25	0.30		0.30			0.30		0.30	0.30	0.65		0.30	0.20		0.30	0.20		0.30	0.20		0.20		0.25	0.25		0.25	0.15		0.15		
	1.50			1.65	1.70		1.70			1.75		1.85	1.85	4.10		2.00	1.25		2.00	1.25		2.00	1.25		1.25		1.50	1.50		1.50	0.70		0.70		
	0.24			0.28	0.28		0.28			0.28		0.30	0.30	0.64		0.32	0.20		0.32	0.20		0.32	0.20		0.20		0.24	0.24		0.24	0.10		0.10		



MCDD0005 Shale 161	MCDD0005 Shale 160	MCDD0005 Shale 159	MCDD0005 Shale 157	MCDD0005 Shale 156	MCDD0005 Shale 155	MCDD0005 Shale 154	MCDD0005 Shale 153	MCDD0005 Shale 151	MCDD0005 Shale 152	MCDD0005 Shale 150	MCDD0005 Shale 149
523	520.8	519.4	516.9	515.8	514.3	512.9	512	510.7	510.6	509.2	508.6
Wollogorang	Wollogorang	Wollogorang	Wollogorang	Wollogorang	Wollogorang	Wollogorang	Wollogorang	Wollogorang	Wollogorang	Wollogorang	Wollogorang
0.47	0.92	#VALUE!	0.14	#VALUE!	0.32	0.35	0.23	0.14	#VALUE!	0.20	0.16
0.63	0.74	0.68	0.57	2.45	0.64	0.70	0.45	0.48	0.90	0.48	0.48
12.66	14.71	9.11	11.33	13.51	12.82	14.04	13.54	10.96	14.34	10.93	9.57
3.16	2.72	4.39	7.06	5.92	4.68	2.85	4.43	7.30	2.79	7.32	6.27
980.00	3720.00	780.00	1360.00	480.00	340.00	11700.00	800.00	400.00	2740.00	440.00	360.00
1.50	2.50	<0.5	1.00	<0.5	1.50	1.00	1.00	1.00	<0.5	1.50	1.00
0.05	0.04	0.05	0.07	0.06	0.06	0.04	0.06	0.08	0.03	0.06	0.06
40.00	40.00	40.00	80.00	80.00	60.00	40.00	60.00	80.00	40.00	80.00	60.00
73.00	28.00	125.00	132.00	125.00	93.00	135.00	71.00	92.00	151.00	92.00	78.00
19.60	13.20	29.80	46.50	39.10	26.50	17.60	23.70	54.30	14.10	47.20	39.40
38.90	30.80	58.20	78.90	66.40	51.70	40.50	52.60	89.30	31.30	96.30	75.30
4.65	4.05	6.90	8.55	7.50	6.35	5.30	6.35	9.35	4.20	10.20	8.55
17.30	15.90	24.40	28.00	25.60	23.70	20.60	23.50	30.20	16.70	33.50	29.50
3.30	2.90	4.65	4.65	4.55	4.25	4.15	4.15	4.85	3.70	5.20	4.65
0.65	0.55	0.90	0.85	0.85	0.80	0.80	0.80	0.90	0.70	1.00	0.85
3.20	2.80	4.40	4.20	4.20	4.00	4.00	3.80	4.20	3.60	4.40	4.20
0.46	0.36	0.62	0.62	0.62	0.54	0.54	0.50	0.56	0.50	0.58	0.56
2.70	1.90	3.75	3.70	3.85	3.25	3.25	3.05	3.40	3.10	3.50	3.25
0.50	0.36	0.74	0.72	0.74	0.60	0.62	0.56	0.64	0.58	0.68	0.64
1.50	1.05	2.25	2.25	2.40	1.80	1.90	1.75	1.95	1.70	2.00	1.90
0.20	0.15	0.35	0.35	0.35	0.30	0.25	0.25	0.30	0.25	0.30	0.30
1.40	0.90	2.05	2.05	2.20	1.60	1.70	1.55	1.85	1.65	1.90	1.75
0.22	0.14	0.34	0.34	0.36	0.28	0.28	0.26	0.28	0.26	0.30	0.28

MCDD0005 Shale 174	538.1	MCDD0005 Shale 173	537.5	MCDD0005 Shale 171	534.3	MCDD0005 Shale 170	532.8	MCDD0005 Shale 169	531.2	MCDD0005 Shale 168	529.5	MCDD0005 Shale 167	528.6	MCDD0005 Shale 166	527.7	MCDD0005 Shale 165	527	MCDD0005 Shale 164	526.7	MCDD0005 Shale 163	525.2	MCDD0005 Shale 162	524
Wologorang	Wologorang	Wologorang	Wologorang	Wologorang	Wologorang	Wologorang	Wologorang	Wologorang	Wologorang	Wologorang	Wologorang	Wologorang	Wologorang	Wologorang	Wologorang	Wologorang	Wologorang	Wologorang	Wologorang	Wologorang	Wologorang	Wologorang	Wologorang
0.60	0.38	0.46	0.31	0.23	0.27	0.15	0.26	0.14	0.28	0.21	0.16	0.16	0.15	0.26	0.14	0.28	0.21	0.28	0.21	0.21	0.21	0.16	0.16
1.20	1.14	0.99	1.03	1.45	0.54	0.83	0.88	0.78	0.76	0.62	0.63	0.63	0.83	0.88	0.78	0.76	0.62	0.76	0.62	0.62	0.62	0.63	0.63
23.90	27.78	31.79	20.58	9.13	16.30	21.02	10.51	17.02	11.36	12.40	12.54	12.54	21.02	10.51	17.02	11.36	12.40	11.36	12.40	12.40	12.40	12.54	12.54
5.02	7.92	7.55	4.86	6.57	3.68	6.66	5.71	7.05	5.28	4.84	6.38	6.38	6.66	5.71	7.05	5.28	4.84	5.28	4.84	4.84	4.84	6.38	6.38
220.00	360.00	400.00	680.00	260.00	900.00	620.00	240.00	600.00	2900.00	1180.00	300.00	300.00	620.00	240.00	600.00	2900.00	1180.00	2900.00	1180.00	1180.00	1180.00	300.00	300.00
3.00	3.00	3.50	1.50	1.50	1.00	1.00	1.50	1.00	1.00	1.00	1.00	1.00	1.00	1.50	1.00	1.50	1.00	1.50	1.00	1.00	1.00	1.00	1.00
0.05	0.07	0.06	0.06	0.05	0.05	0.04	0.06	0.05	0.05	0.05	0.05	0.05	0.04	0.06	0.05	0.06	0.05	0.06	0.06	0.06	0.06	0.07	0.07
120.00	220.00	240.00	100.00	60.00	60.00	140.00	60.00	120.00	60.00	60.00	60.00	60.00	140.00	60.00	120.00	60.00	60.00	60.00	60.00	60.00	60.00	80.00	80.00
42.00	125.00	125.00	78.00	227.00	55.00	83.00	99.00	121.00	90.00	113.00	121.00	121.00	83.00	99.00	121.00	90.00	113.00	90.00	113.00	113.00	113.00	121.00	121.00
14.60	44.10	36.80	24.90	19.20	19.40	14.90	26.60	19.60	24.40	26.40	27.60	27.60	14.90	26.60	19.60	24.40	26.40	24.40	26.40	26.40	26.40	27.60	27.60
29.80	77.80	55.90	45.60	37.60	36.40	27.00	47.10	29.80	43.40	47.00	47.10	47.10	27.00	47.10	29.80	43.40	47.00	43.40	47.00	47.00	47.00	47.10	47.10
3.80	9.30	6.00	5.45	4.70	4.35	3.20	5.45	3.35	5.20	5.50	5.35	5.35	3.20	5.45	3.35	5.20	5.50	5.20	5.50	5.50	5.50	5.35	5.35
14.30	33.40	21.70	19.70	18.40	16.70	11.60	20.40	12.30	18.60	20.10	19.40	19.40	11.60	20.40	12.30	18.60	20.10	18.60	20.10	20.10	20.10	19.40	19.40
2.75	8.15	3.85	3.75	4.55	3.10	2.35	4.05	2.75	3.65	3.95	3.85	3.85	2.35	4.05	2.75	3.65	3.95	3.65	3.95	3.95	3.95	3.85	3.85
0.50	1.15	0.75	0.75	0.95	0.60	0.50	0.75	0.55	0.70	0.75	0.75	0.75	0.50	0.75	0.55	0.70	0.75	0.70	0.75	0.75	0.75	0.75	0.75
2.40	5.40	3.60	3.60	4.60	3.00	2.40	3.60	3.00	3.40	3.60	3.60	3.60	2.40	3.60	3.00	3.40	3.80	3.40	3.80	3.80	3.80	3.60	3.60
0.32	0.76	0.48	0.48	0.70	0.42	0.34	0.54	0.44	0.48	0.52	0.52	0.52	0.34	0.54	0.44	0.48	0.52	0.48	0.52	0.52	0.52	0.52	0.52
1.80	4.55	3.00	2.70	4.50	2.40	2.10	3.25	2.85	2.95	3.00	3.00	3.00	2.10	3.25	2.85	2.95	3.20	2.95	3.20	3.20	3.20	3.00	3.00
0.32	0.88	0.58	0.50	0.94	0.46	0.44	0.64	0.58	0.58	0.62	0.60	0.60	0.44	0.64	0.58	0.58	0.62	0.58	0.62	0.62	0.62	0.60	0.60
0.90	2.70	1.85	1.60	3.05	1.45	1.35	1.95	1.85	1.85	1.90	1.90	1.90	1.35	1.95	1.85	1.85	1.90	1.85	1.90	1.90	1.90	1.90	1.90
0.15	0.40	0.30	0.25	0.50	0.20	0.20	0.30	0.30	0.30	0.30	0.30	0.30	0.20	0.30	0.30	0.30	0.30	0.30	0.30	0.30	0.30	0.30	0.30
0.80	2.45	1.85	1.45	3.25	1.25	1.30	1.85	1.85	1.85	1.85	1.85	1.85	1.30	1.85	1.85	1.85	1.85	1.70	1.85	1.85	1.85	1.90	1.90
0.14	0.40	0.30	0.24	0.52	0.20	0.22	0.30	0.28	0.30	0.28	0.28	0.28	0.22	0.30	0.28	0.28	0.30	0.28	0.30	0.30	0.30	0.30	0.30

MCDD0005 Shale 186	MCDD0005 Shale 185	MCDD0005 Shale 184	MCDD0005 Shale 183	MCDD0005 Shale 182	MCDD0005 Shale 181	MCDD0005 Shale 180	MCDD0005 Shale 179	MCDD0005 Shale 178	MCDD0005 Shale 177	MCDD0005 Shale 176	MCDD0005 Shale 175
551.1	550.9	550.5	549.7	548.9	547.9	546.8	544.8	544.5	541.5	540.7	539.1
Wollogorang	Wollogorang	Wollogorang	Wollogorang	Wollogorang	Wollogorang	Wollogorang	Wollogorang	Wollogorang	Wollogorang	Wollogorang	Wollogorang
3.66	4.79	2.32	4.29	3.32	4.61	2.08	2.43	4.16	3.63	2.81	3.24
1.94	2.31	1.98	2.56	1.52	1.71	1.92	1.83	2.18	4.50	1.00	1.27
30.17	41.10	19.07	36.30	11.66	27.30	19.17	16.23	24.95	61.58	8.02	27.45
4.64	5.84	7.34	6.06	8.58	2.93	3.13	4.93	4.81	8.12	7.48	5.10
300.00	380.00	420.00	400.00	440.00	200.00	200.00	300.00	360.00	520.00	220.00	240.00
17.00	28.00	17.00	26.00	28.50	13.50	6.50	12.00	20.00	29.50	21.00	16.50
0.02	0.04	0.08	0.04	0.07	0.02	0.05	0.12	0.07	0.07	0.08	0.04
140.00	240.00	140.00	220.00	100.00	80.00	60.00	80.00	120.00	500.00	60.00	140.00
54.00	83.00	90.00	85.00	188.00	45.00	42.00	77.00	80.00	346.00	55.00	48.00
21.70	22.10	101.00	19.20	41.90	38.40	16.20	22.10	16.60	17.10	16.90	17.00
37.70	36.30	219.00	30.50	79.90	75.90	35.00	44.40	33.00	33.90	33.30	32.20
4.30	4.05	22.20	3.40	9.20	8.40	4.55	5.70	4.15	4.60	4.45	4.00
15.20	15.70	73.60	12.10	32.50	27.00	18.10	22.00	15.40	19.40	18.40	15.30
2.55	2.75	9.70	2.45	5.90	3.80	3.85	4.35	3.05	5.90	3.85	2.80
0.50	0.50	1.20	0.50	1.00	0.50	0.65	0.70	0.55	1.30	0.70	0.50
2.40	2.60	6.00	2.40	5.20	2.60	3.60	3.80	2.80	6.60	3.60	2.60
0.26	0.34	0.66	0.34	0.76	0.32	0.48	0.46	0.34	0.98	0.44	0.34
1.45	2.00	3.65	2.00	4.95	1.85	2.80	2.45	2.05	6.40	2.40	1.90
0.28	0.40	0.64	0.40	1.06	0.34	0.48	0.44	0.40	1.36	0.44	0.38
0.80	1.15	1.80	1.20	3.70	1.05	1.25	1.30	1.15	4.70	1.20	1.10
0.15	0.20	0.25	0.20	0.60	0.15	0.20	0.20	0.15	0.80	0.15	0.15
0.80	1.25	1.55	1.30	3.95	1.00	1.00	1.05	1.00	4.95	1.00	1.00
0.14	0.20	0.24	0.20	0.64	0.16	0.16	0.18	0.16	0.82	0.16	0.16

UNITS	MCDD0005 Shale 181	MCDD0005 Shale 190	MCDD0005 Shale 189	MCDD0005 Shale 188	MCDD0005 Shale 187
M	554.4	554.6	554.3	553.4	551.7
	Wollogorang	Wollogorang	Wollogorang	Wollogorang	Wollogorang
	4.55	3.22	2.87	3.21	3.40
	1.61	1.64	1.63	1.73	2.36
	18.98	17.03	18.63	20.80	26.42
%	5.27	8.22	6.44	5.77	5.30
ppm	320.00	420.00	380.00	400.00	340.00
ppm	24.00	26.50	18.50	18.50	18.00
%	0.05	0.04	0.06	0.02	0.04
ppm	100.00	140.00	120.00	120.00	140.00
ppm	54.00	104.00	81.00	74.00	65.00
ppm	26.40	34.30	28.30	25.10	27.80
ppm	46.30	47.00	51.00	46.10	47.90
ppm	5.10	4.70	5.85	5.25	5.60
ppm	17.60	15.70	21.00	18.30	20.50
ppm	2.65	2.80	3.70	3.05	3.30
ppm	0.50	0.55	0.65	0.60	0.65
ppm	2.00	2.60	3.20	2.60	3.00
ppm	0.26	0.36	0.40	0.32	0.32
ppm	1.40	2.30	2.45	1.75	1.80
ppm	0.28	0.48	0.46	0.34	0.32
ppm	0.95	1.60	1.50	1.10	0.95
ppm	0.15	0.25	0.25	0.15	0.15
ppm	0.90	1.75	1.50	1.10	0.90
ppm	0.14	0.28	0.24	0.18	0.16

Table S.4.1. Shale geochemical analyses for samples from MCDD005 in this study.

4	3	2	1	Sample
167.9	167.3	166.3	165.2	Depth (m)
Mallapunyah	Mallapunyah	Mallapunyah	Mallapunyah	Formation
0.40	0.25	0.23	0.45	SRA TOC
0.04	0.01	0.01	0.03	S1
0.07	0.02	0.03	0.04	S2
0.32	0.17	0.11	0.32	S3
308.82	345.90	N/A	359.03	Tmax (°C)
				Calc. % Ro
17.50	8.00	13.04	8.89	HI
80.00	68.00	47.83	71.11	OI
0.22	0.12	0.27	0.13	S2/S3
10.00	4.00	4.35	6.67	S1/TOC *100
0.36	0.33	0.25	0.43	PI

79		69	59	49	39	29	19	9	8	7	6	5
262.6	248.6	236.1	222.9	210.5	198.4	185.9	173.9	172.8	171.8	170.7	169.9	
Mallapunyah	Mallapunyah	Mallapunyah	Mallapunyah	Mallapunyah	Mallapunyah	Mallapunyah	Mallapunyah	Mallapunyah	Mallapunyah	Mallapunyah	Mallapunyah	Mallapunyah
0.17	0.20	0.22	0.42	0.20	0.19	0.38	0.05	0.06	0.12	0.21	0.74	
0.00	0.01	0.00	0.00	0.00	0.00	0.01	0.00	0.00	0.00	0.01	0.02	
0.00	0.01	0.00	0.01	0.02	0.00	0.04	0.00	0.00	0.02	0.03	0.09	
0.14	0.19	0.41	0.41	0.17	0.16	0.25	0.00	0.02	0.08	0.10	0.22	
549.67	369.17	342.04	431.87	606.39	609.23	314.49	389.58	335.52	337.65	552.66	333.53	
2.73			0.61	3.75	3.81					2.79		
0.00	5.00	0.00	2.38	10.00	0.00	10.53	0.00	0.00	16.67	14.29	12.16	
82.35	95.00	186.36	97.62	85.00	84.21	65.79	0.00	33.33	66.67	47.62	29.73	
0.00	0.05	0.00	0.02	0.12	0.00	0.16	0.00	0.00	0.25	0.30	0.41	
0.00	5.00	0.00	0.00	0.00	0.00	2.63	0.00	0.00	0.00	4.76	2.70	
#DIV/0!	0.50	#DIV/0!	0.00	0.00	#DIV/0!	0.20	#DIV/0!	#DIV/0!	0.00	0.25	0.18	

177	176	175	169	159	149	139	129	119	109	99	89
541.45	540.7	539.1	531.17	519.36	508.6	496.66	341.7	325	308.9	293.9	279.1
Wologorang	Wologorang	Wologorang	Wologorang	Wologorang	Wologorang	Wologorang	Mallapunya	Mallapunya	Mallapunya	Mallapunya	Mallapunya
0.94	0.71	0.61	0.43	0.29	0.29	0.21	0.58	0.17	0.15	0.20	0.22
0.13	0.13	0.09	0.00	0.01	0.03	0.00	0.01	0.01	0.00	0.01	0.01
0.49	0.39	0.22	0.06	0.03	0.12	0.03	0.02	0.02	0.00	0.02	0.05
0.28	0.28	0.31	0.22	0.47	0.36	0.30	0.32	0.10	0.15	0.24	0.23
438.33	450.79	439.85	357.79	308.37	322.53	363.80	335.71	367.99	575.55	318.52	333.48
0.73	0.95	0.76							3.20		
52.13	54.93	36.07	13.95	10.34	41.38	14.29	3.45	11.76	0.00	10.00	22.73
29.79	39.44	50.82	51.16	162.07	124.14	142.86	55.17	58.82	100.00	120.00	104.55
1.75	1.39	0.71	0.27	0.06	0.33	0.10	0.06	0.20	0.00	0.08	0.22
13.83	18.31	14.75	0.00	3.45	10.34	0.00	1.72	5.88	0.00	5.00	4.55
0.21	0.25	0.29	0.00	0.25	0.20	0.00	0.33	0.33	#DIV/0!	0.33	0.17

189		188	187	186	185	184	183	182	181	180	179	178
554.25	553.38	551.72	551.1	550.9	549.67	548.9	547.9	546.8	544.8	544.5		
Wologorang	Wologorang	Wologorang	Wologorang	Wologorang	Wologorang	Wologorang	Wologorang	Wologorang	Wologorang	Wologorang	Wologorang	Wologorang
2.30	2.23	2.32	2.52	2.47	2.36	2.63	1.54	1.80	2.79	3.52	3.74	
0.72	0.79	0.88	1.20	1.02	0.80	1.03	0.33	0.95	1.04	1.50	1.37	
2.02	2.90	3.82	5.02	4.12	1.83	3.50	0.97	4.57	3.42	5.38	5.53	
0.09	0.08	0.07	0.09	0.04	0.04	0.04	0.08	0.20	0.35	0.08	0.29	
436.73	423.50	416.33	417.55	418.32	438.09	424.13	440.23	422.49	435.76	430.42	432.88	
0.70	0.46	0.33	0.36	0.37	0.73	0.47	0.76	0.44	0.68	0.59	0.63	
87.83	130.04	164.66	199.21	166.80	77.54	133.08	62.99	253.89	122.58	152.84	147.86	
3.91	3.59	3.02	3.57	1.62	1.69	1.52	5.19	11.11	12.54	2.27	7.75	
22.44	36.25	54.57	55.78	103.00	45.75	87.50	12.13	22.85	9.77	67.25	19.07	
31.30	35.43	37.93	47.62	41.30	33.90	39.16	21.43	52.78	37.28	42.61	36.63	
0.26	0.21	0.19	0.19	0.20	0.30	0.23	0.25	0.17	0.23	0.22	0.20	

191	190
555.39	554.63
Wologorang	Wologorang
1.81	1.48
0.72	0.38
2.97	0.89
0.09	0.01
415.78	438.09
0.32	0.73
164.09	60.14
4.97	0.68
33.00	89.00
39.78	25.68
0.20	0.30

**Table S.4.2.** Shale Source-Rock analyses for samples from MCDD005 in this study.

MCDD0003	MCDD0003	MCDD0003	MCDD0003	MCDD0003	MCDD0003	DETECTION	SCHEME	UNITS	IDENT
12.7	11.55	10.68	9.35	8.67					Depth
Wologorang	Wologorang	Wologorang	Wologorang	Wologorang					Formation
0.29	0.40	0.35	1.06	0.38	Mo/Al				
0.98	0.81	0.66	0.67	0.75	U/Al				
11.53	16.13	13.89	14.18	15.09	V/Al				
3.47	2.48	2.88	2.82	2.65	0.005	LB101	%	Al	
300.00	120.00	500.00	140.00	180.00	20	LB101	ppm	Ba	
1.00	1.00	1.00	3.00	1.00	0.5	MA102	ppm	Mo	
0.05	0.04	0.05	0.04	0.03	0.005	LB101	%	P	
3.40	2.00	1.90	1.90	2.00	0.1	MA102	ppm	U	
40.00	40.00	40.00	40.00	40.00	20	LB101	ppm	V	
21.70	16.10	16.00	13.30	16.90	0.1	MA102	ppm	La	
45.10	33.70	33.30	28.60	37.50	0.1	MA102	ppm	Ce	
5.35	4.05	4.05	3.60	4.65	0.05	MA102	ppm	Pr	
19.80	15.20	15.30	14.10	18.50	0.05	MA102	ppm	Nd	
3.85	3.05	2.80	3.05	3.80	0.05	MA102	ppm	Sm	
0.70	0.60	0.60	0.60	0.75	0.05	MA102	ppm	Eu	
3.80	3.00	2.80	2.80	3.60	0.2	MA102	ppm	Gd	
0.52	0.38	0.38	0.38	0.50	0.02	MA102	ppm	Tb	
3.10	2.35	2.30	2.10	3.10	0.05	MA102	ppm	Dy	
0.60	0.42	0.46	0.42	0.60	0.02	MA102	ppm	Ho	
1.85	1.25	1.25	1.15	1.80	0.05	MA102	ppm	Er	
0.25	0.15	0.20	0.15	0.25	0.05	MA102	ppm	Tm	
1.75	1.20	1.20	1.00	1.65	0.05	MA102	ppm	Yb	
0.26	0.16	0.16	0.14	0.26	0.02	MA102	ppm	Lu	





MCDD0003	MCDD0003	MCDD0003	MCDD0003	MCDD0003	MCDD0003	MCDD0003	MCDD0003	MCDD0003	MCDD0003	MCDD0003	MCDD0003	MCDD0003	MCDD0003	MCDD0003
41.75	40.65	39.35	38.4	36.4	35.6	34.12	33.21	32.15	31.1	30.18	30.18	30.18	30.18	29
Wologorang	Wologorang	Wologorang	Wologorang	Wologorang	Wologorang	Wologorang	Wologorang	Wologorang	Wologorang	Wologorang	Wologorang	Wologorang	Wologorang	Wologorang
3.37	3.02	3.15	3.46	5.08	0.22	0.72	5.75	6.65	3.14	6.98	6.98	6.98	6.98	0.71
2.27	2.36	1.92	2.02	1.35	0.87	0.66	3.22	1.87	1.43	2.11	2.11	2.11	2.11	1.07
17.98	25.13	17.48	20.24	19.92	35.87	17.34	43.33	26.22	40.00	32.04	32.04	32.04	32.04	28.21
4.45	3.98	5.72	5.93	5.02	4.46	3.46	6.00	5.34	7.00	4.37	4.37	4.37	4.37	7.09
260.00	460.00	340.00	340.00	280.00	240.00	160.00	340.00	260.00	340.00	200.00	200.00	200.00	200.00	280.00
15.00	12.00	18.00	20.50	25.50	1.00	2.50	34.50	35.50	22.00	30.50	30.50	30.50	30.50	5.00
0.08	0.09	0.06	0.18	0.05	0.04	0.03	0.05	0.11	0.06	0.09	0.09	0.09	0.09	0.08
10.10	9.40	11.00	12.00	6.80	3.90	2.30	19.30	10.00	10.00	9.20	9.20	9.20	9.20	7.60
80.00	100.00	100.00	120.00	100.00	160.00	60.00	260.00	140.00	280.00	140.00	140.00	140.00	140.00	200.00
15.10	20.40	22.90	22.60	15.50	27.90	21.00	29.70	33.30	37.90	25.60	25.60	25.60	25.60	33.60
30.90	38.90	41.40	51.10	30.20	45.20	41.60	49.00	65.80	58.30	52.90	52.90	52.90	52.90	62.80
4.05	4.90	4.70	6.80	3.50	4.75	4.85	5.50	8.25	6.15	6.90	6.90	6.90	6.90	7.60
15.70	19.80	16.80	27.60	12.90	16.30	16.30	22.20	31.40	20.60	27.00	27.00	27.00	27.00	28.60
3.55	4.20	2.80	5.25	2.35	2.55	2.50	3.80	6.10	3.80	5.35	5.35	5.35	5.35	5.35
0.60	0.70	0.50	0.90	0.50	0.50	0.50	0.70	1.10	0.75	0.90	0.90	0.90	0.90	1.05
3.60	4.40	2.40	4.60	2.00	2.20	2.20	3.40	5.20	3.60	4.40	4.40	4.40	4.40	4.80
0.44	0.54	0.34	0.52	0.28	0.32	0.30	0.46	0.64	0.48	0.56	0.56	0.56	0.56	0.64
2.60	3.30	2.20	2.90	1.80	2.00	1.85	2.65	3.60	2.85	3.20	3.20	3.20	3.20	3.85
0.46	0.50	0.44	0.52	0.36	0.40	0.38	0.52	0.66	0.52	0.56	0.56	0.56	0.56	0.74
1.25	1.30	1.40	1.40	1.05	1.15	1.05	1.60	1.80	1.50	1.55	1.55	1.55	1.55	2.15
0.15	0.15	0.20	0.15	0.15	0.15	0.15	0.20	0.25	0.20	0.20	0.20	0.20	0.20	0.30
1.15	1.15	1.30	1.20	1.15	1.20	0.95	1.45	1.55	1.50	1.35	1.35	1.35	1.35	2.10
0.16	0.16	0.18	0.16	0.16	0.18	0.16	0.22	0.24	0.24	0.18	0.18	0.18	0.18	0.30

MCDD0003	MCDD0003	MCDD0003	MCDD0003	MCDD0003	MCDD0003	MCDD0003	MCDD0003	MCDD0003	MCDD0003	MCDD0003	MCDD0003	MCDD0003	MCDD0003	MCDD0003	MCDD0003	MCDD0003	MCDD0003	MCDD0003	MCDD0003		
54.55	53.42	52.45	51.62	49.73	48.52	47.75	46.65	45.85	44.76	43.7	42.69	41.6	40.5	39.4	38.3	37.2	36.1	35.0	33.9	32.8	
Wologorang	Wologorang	Wologorang	Wologorang	Wologorang	Wologorang	Wologorang	Wologorang	Wologorang	Wologorang	Wologorang	Wologorang	Wologorang	Wologorang	Wologorang	Wologorang	Wologorang	Wologorang	Wologorang	Wologorang	Wologorang	Wologorang
2.34	2.33	4.27	4.05	4.55	4.48	3.63	5.17	2.97	4.08	3.26	4.10	3.1	2.1	1.1	0.1	0.1	0.1	0.1	0.1	0.1	0.1
2.32	2.27	2.21	1.63	1.36	1.56	1.56	1.82	1.60	1.78	2.06	1.79	1.7	0.7	0.7	0.7	0.7	0.7	0.7	0.7	0.7	0.7
16.13	17.44	26.05	20.92	26.52	22.01	25.28	27.78	36.24	34.76	21.05	21.64	20.5	10.5	10.5	10.5	10.5	10.5	10.5	10.5	10.5	10.5
6.20	3.44	6.91	7.65	5.28	6.36	6.33	6.48	6.07	7.48	4.75	6.47	5.4	4.4	4.4	4.4	4.4	4.4	4.4	4.4	4.4	4.4
360.00	200.00	400.00	420.00	300.00	380.00	400.00	300.00	260.00	400.00	280.00	360.00	350	350	350	350	350	350	350	350	350	350
14.50	8.00	29.50	31.00	24.00	28.50	23.00	33.50	18.00	30.50	15.50	26.50	25.0	25.0	25.0	25.0	25.0	25.0	25.0	25.0	25.0	25.0
0.15	0.06	0.13	0.05	0.04	0.05	0.04	0.05	0.06	0.09	0.03	0.05	0.04	0.04	0.04	0.04	0.04	0.04	0.04	0.04	0.04	0.04
14.40	7.80	15.30	12.50	7.20	9.90	9.90	11.80	9.70	13.30	9.80	11.60	10.5	10.5	10.5	10.5	10.5	10.5	10.5	10.5	10.5	10.5
100.00	60.00	180.00	160.00	140.00	140.00	160.00	180.00	220.00	260.00	100.00	140.00	130	130	130	130	130	130	130	130	130	130
25.60	11.30	34.80	32.00	37.00	32.20	35.60	44.10	39.30	40.80	14.60	24.70	23.0	23.0	23.0	23.0	23.0	23.0	23.0	23.0	23.0	23.0
5.170	21.70	60.30	45.30	59.90	57.50	62.60	66.20	60.90	64.60	27.00	38.30	37.0	37.0	37.0	37.0	37.0	37.0	37.0	37.0	37.0	37.0
6.30	2.65	7.00	4.60	6.45	6.50	6.85	6.65	6.50	7.15	3.10	4.05	3.0	3.0	3.0	3.0	3.0	3.0	3.0	3.0	3.0	3.0
23.00	10.10	25.90	15.60	21.30	21.20	22.90	22.20	22.20	26.00	11.20	13.90	12.0	12.0	12.0	12.0	12.0	12.0	12.0	12.0	12.0	12.0
4.50	2.15	4.95	3.25	3.50	3.30	3.45	3.80	4.05	5.00	2.10	2.60	2.0	2.0	2.0	2.0	2.0	2.0	2.0	2.0	2.0	2.0
0.85	0.45	0.95	0.70	0.70	0.60	0.65	0.75	0.75	0.95	0.40	0.50	0.5	0.5	0.5	0.5	0.5	0.5	0.5	0.5	0.5	0.5
4.40	2.00	4.40	3.00	3.20	2.60	2.80	3.60	4.00	4.40	1.80	2.20	2.0	2.0	2.0	2.0	2.0	2.0	2.0	2.0	2.0	2.0
0.56	0.28	0.56	0.42	0.44	0.34	0.38	0.48	0.52	0.52	0.28	0.30	0.3	0.3	0.3	0.3	0.3	0.3	0.3	0.3	0.3	0.3
3.55	1.55	3.35	2.45	2.70	2.15	2.45	3.15	3.05	2.90	1.75	1.85	1.5	1.5	1.5	1.5	1.5	1.5	1.5	1.5	1.5	1.5
0.64	0.30	0.60	0.50	0.52	0.42	0.48	0.60	0.54	0.52	0.34	0.34	0.3	0.3	0.3	0.3	0.3	0.3	0.3	0.3	0.3	0.3
1.95	0.95	1.75	1.50	1.50	1.30	1.55	1.85	1.60	1.50	1.05	1.15	1.0	1.0	1.0	1.0	1.0	1.0	1.0	1.0	1.0	1.0
0.30	0.10	0.25	0.25	0.20	0.20	0.25	0.25	0.20	0.20	0.10	0.15	0.1	0.1	0.1	0.1	0.1	0.1	0.1	0.1	0.1	0.1
2.20	0.85	1.70	1.70	1.45	1.45	1.60	1.70	1.50	1.45	0.95	1.20	1.0	1.0	1.0	1.0	1.0	1.0	1.0	1.0	1.0	1.0
0.30	0.14	0.22	0.24	0.20	0.22	0.24	0.22	0.22	0.20	0.14	0.16	0.1	0.1	0.1	0.1	0.1	0.1	0.1	0.1	0.1	0.1

MCDD0003	MCDD0003	MCDD0003	MCDD0003	MCDD0003	MCDD0003	MCDD0003	MCDD0003	MCDD0003	MCDD0003	MCDD0003	MCDD0003	MCDD0003	MCDD0003	MCDD0003	MCDD0003	MCDD0003	MCDD0003	MCDD0003	MCDD0003	
65.99	65.05	64.72	63.65	62.33	61.03	60.2	59.63	58.55	57.44	56.3	55.7									
Wologorang	Wologorang	Wologorang	Wologorang	Wologorang	Wologorang	Wologorang	Wologorang	Wologorang	Wologorang	Wologorang	Wologorang	Wologorang	Wologorang	Wologorang	Wologorang	Wologorang	Wologorang	Wologorang	Wologorang	Wologorang
0.58	0.43	0.11	#VALUE!	5.53	4.10	2.59	2.51	3.04	6.32	5.79	4.91									
0.64	0.74	0.93	0.55	2.21	1.94	2.76	2.43	2.04	3.50	3.12	2.27									
23.26	17.32	10.87	#VALUE!	53.48	19.77	22.99	17.06	19.09	26.16	22.07	14.18									
1.72	2.31	9.20	2.37	5.61	7.08	5.22	9.38	8.38	6.88	7.25	8.46									
80.00	100.00	400.00	60.00	380.00	360.00	280.00	460.00	500.00	460.00	460.00	460.00									
1.00	1.00	1.00	<0.5	31.00	29.00	13.50	23.50	25.50	43.50	42.00	41.50									
0.05	0.05	0.14	0.06	0.05	0.09	0.10	0.11	0.14	0.30	0.20	0.14									
1.10	1.70	8.60	1.30	12.40	13.70	14.40	22.80	17.10	24.10	22.60	19.20									
40.00	40.00	100.00	<20	300.00	140.00	120.00	160.00	160.00	180.00	160.00	120.00									
9.80	8.00	17.00	9.10	24.80	15.20	15.10	42.40	49.60	35.40	32.90	31.80									
26.10	18.70	26.30	21.10	44.50	32.40	33.00	56.10	73.00	76.80	58.70	56.30									
3.40	2.45	3.10	2.70	4.85	3.95	4.15	5.70	7.80	9.75	7.05	6.55									
13.80	9.30	12.30	10.60	16.00	13.70	15.60	19.80	27.30	37.30	27.00	23.30									
2.50	1.80	2.75	2.10	2.75	2.65	3.05	3.80	5.50	7.45	5.50	4.40									
0.45	0.35	0.55	0.40	0.50	0.50	0.55	0.75	1.10	1.55	1.00	0.75									
2.20	1.80	3.00	2.00	2.20	2.40	3.00	4.00	5.40	7.20	5.40	4.20									
0.30	0.22	0.44	0.28	0.30	0.40	0.40	0.52	0.74	0.88	0.66	0.52									
1.60	1.30	2.65	1.55	1.90	2.30	2.35	3.35	4.85	5.30	4.35	3.25									
0.30	0.26	0.58	0.28	0.42	0.50	0.48	0.66	0.94	0.94	0.82	0.64									
0.85	0.65	1.75	0.85	1.20	1.55	1.45	2.05	3.00	2.60	2.40	2.05									
0.10	0.10	0.30	0.10	0.20	0.25	0.20	0.30	0.45	0.30	0.30	0.30									
0.75	0.65	1.75	0.70	1.35	1.60	1.45	2.20	3.05	2.30	2.20	2.20									
0.10	0.10	0.26	0.08	0.20	0.24	0.22	0.32	0.44	0.34	0.30	0.32									



MCDD0003	MCDD0003	MCDD0003	MCDD0003	MCDD0003	MCDD0003	MCDD0003	MCDD0003	MCDD0003	MCDD0003	MCDD0003	MCDD0003	MCDD0003	MCDD0003
93.46	92.29	91.6	91.01	89.22	86.79	86.31	85.21	84.16	83.59	82.61	82.01	82.01	82.01
Wologorang	Wologorang	Wologorang	Wologorang	Wologorang	Wologorang	Wologorang	Wologorang	Wologorang	Wologorang	Wologorang	Wologorang	Wologorang	Wologorang
#VALUE!	#VALUE!	0.20	0.13	#VALUE!	0.14	#VALUE!	0.22	0.25	0.27	0.26	0.27	0.27	0.27
0.59	0.49	0.72	0.76	0.81	0.85	0.96	0.80	0.93	0.87	0.76	0.76	0.76	0.76
11.55	10.67	13.14	12.87	11.98	10.99	12.80	13.02	13.49	14.18	14.11	10.60	10.60	10.60
8.66	7.50	7.61	7.77	6.68	7.28	7.81	4.61	5.93	5.64	5.67	5.66	5.66	5.66
260.00	200.00	240.00	180.00	180.00	160.00	220.00	100.00	360.00	140.00	160.00	140.00	140.00	140.00
<0.5	<0.5	1.50	1.00	<0.5	1.00	<0.5	1.00	1.50	1.50	1.50	1.50	1.50	1.50
0.08	0.07	0.07	0.08	0.05	0.07	0.08	0.05	0.06	0.06	0.07	0.06	0.06	0.06
5.10	3.70	5.50	5.90	5.40	6.20	7.50	3.70	5.50	4.90	4.30	4.30	4.30	4.30
100.00	80.00	100.00	100.00	80.00	80.00	100.00	60.00	80.00	80.00	80.00	60.00	60.00	60.00
83.70	37.30	36.80	29.00	20.50	45.50	49.10	28.70	44.60	41.70	37.60	35.10	35.10	35.10
181.00	74.30	74.00	58.60	49.60	84.40	89.40	55.20	82.00	77.40	70.10	65.90	65.90	65.90
17.90	8.70	8.70	6.85	6.55	9.60	9.75	6.25	9.15	8.80	8.20	7.65	7.65	7.65
62.80	31.50	32.10	24.80	26.30	34.20	32.00	22.00	30.40	30.10	28.70	26.30	26.30	26.30
9.50	5.75	5.90	4.75	5.15	6.10	5.05	4.35	4.90	4.90	4.85	4.30	4.30	4.30
2.10	1.35	1.50	1.20	1.10	1.35	1.20	1.10	1.15	1.15	1.15	1.10	1.10	1.10
7.20	5.40	5.60	4.60	4.40	5.20	4.60	4.20	4.40	4.40	4.60	4.20	4.20	4.20
0.80	0.72	0.70	0.58	0.52	0.64	0.62	0.56	0.58	0.56	0.58	0.54	0.54	0.54
4.30	4.65	4.30	3.50	3.35	4.00	3.75	3.40	3.45	3.45	3.55	3.30	3.30	3.30
0.80	0.86	0.80	0.64	0.62	0.76	0.74	0.66	0.66	0.66	0.66	0.60	0.60	0.60
2.20	2.50	2.25	1.80	1.80	2.25	2.05	1.80	1.80	1.85	1.85	1.75	1.75	1.75
0.30	0.30	0.30	0.20	0.25	0.30	0.30	0.25	0.25	0.25	0.25	0.25	0.25	0.25
2.15	2.30	2.00	1.55	1.60	2.20	1.95	1.60	1.75	1.75	1.70	1.55	1.55	1.55
0.34	0.30	0.28	0.22	0.22	0.28	0.28	0.22	0.24	0.26	0.26	0.22	0.22	0.22



MCDD0003	MCDD0003	MCDD0003	MCDD0003	MCDD0003	MCDD0003	MCDD0003	MCDD0003	MCDD0003	MCDD0003	MCDD0003	MCDD0003	MCDD0003	MCDD0003	MCDD0003	MCDD0003
268.35	266.75	265.9	264.91	263.05	262.13	260.9	259.83	257.69	255.9	235.1	227.95	Wuraliwunty	Wuraliwunty	Wuraliwunty	Wuraliwunty
0.36	3.32	0.10	0.11	0.19	0.08	0.31	0.42	0.42	0.67	0.65	1.05	Wuraliwunty	Wuraliwunty	Wuraliwunty	Wuraliwunty
0.62	2.65	0.53	0.48	0.53	0.52	0.63	0.62	0.58	0.57	0.42	0.58	Wuraliwunty	Wuraliwunty	Wuraliwunty	Wuraliwunty
14.41	19.67	17.48	15.61	19.05	13.22	17.86	16.82	18.33	16.04	15.07	16.81	Wuraliwunty	Wuraliwunty	Wuraliwunty	Wuraliwunty
11.10	12.20	10.30	8.97	10.50	12.10	11.20	10.70	12.00	7.48	9.29	11.90	Wuraliwunty	Wuraliwunty	Wuraliwunty	Wuraliwunty
420.00	460.00	440.00	420.00	480.00	480.00	480.00	440.00	500.00	280.00	380.00	400.00	Wuraliwunty	Wuraliwunty	Wuraliwunty	Wuraliwunty
4.00	40.50	1.00	1.00	2.00	1.00	3.50	4.50	5.00	5.00	6.00	12.50	Wuraliwunty	Wuraliwunty	Wuraliwunty	Wuraliwunty
0.08	0.08	0.08	0.07	0.07	0.06	0.06	0.08	0.04	0.05	0.06	0.05	Wuraliwunty	Wuraliwunty	Wuraliwunty	Wuraliwunty
6.90	32.30	5.50	4.30	5.60	6.30	7.00	6.60	6.90	4.30	3.90	6.90	Wuraliwunty	Wuraliwunty	Wuraliwunty	Wuraliwunty
160.00	240.00	180.00	140.00	200.00	160.00	200.00	180.00	220.00	120.00	140.00	200.00	Wuraliwunty	Wuraliwunty	Wuraliwunty	Wuraliwunty
63.20	71.30	66.20	50.20	71.40	64.50	89.50	64.40	35.80	42.20	35.60	82.10	Wuraliwunty	Wuraliwunty	Wuraliwunty	Wuraliwunty
126.00	144.00	131.00	101.00	140.00	127.00	194.00	122.00	66.30	83.20	68.40	169.00	Wuraliwunty	Wuraliwunty	Wuraliwunty	Wuraliwunty
14.90	16.80	15.60	11.90	16.00	14.70	20.50	13.90	7.35	9.75	7.70	16.90	Wuraliwunty	Wuraliwunty	Wuraliwunty	Wuraliwunty
52.90	61.50	55.80	43.30	56.30	52.50	72.60	48.40	24.90	33.90	28.00	56.80	Wuraliwunty	Wuraliwunty	Wuraliwunty	Wuraliwunty
9.20	10.30	9.50	7.25	8.75	8.85	11.00	7.55	5.00	6.10	5.45	8.20	Wuraliwunty	Wuraliwunty	Wuraliwunty	Wuraliwunty
1.70	1.85	1.75	1.40	1.50	1.70	1.90	1.45	1.10	1.20	1.20	1.45	Wuraliwunty	Wuraliwunty	Wuraliwunty	Wuraliwunty
7.60	8.00	7.00	5.80	6.00	8.20	7.20	5.60	5.40	5.00	5.80	4.80	Wuraliwunty	Wuraliwunty	Wuraliwunty	Wuraliwunty
0.94	1.08	0.92	0.80	0.76	1.12	0.94	0.92	0.84	0.80	0.78	0.58	Wuraliwunty	Wuraliwunty	Wuraliwunty	Wuraliwunty
6.00	6.75	6.10	5.00	4.80	8.10	5.95	5.20	5.70	4.70	5.15	3.70	Wuraliwunty	Wuraliwunty	Wuraliwunty	Wuraliwunty
1.12	1.28	1.10	0.98	0.96	1.48	1.16	1.02	1.12	1.02	0.98	0.78	Wuraliwunty	Wuraliwunty	Wuraliwunty	Wuraliwunty
3.40	3.95	3.35	2.80	2.95	4.45	3.75	3.20	3.45	2.85	3.05	2.45	Wuraliwunty	Wuraliwunty	Wuraliwunty	Wuraliwunty
0.45	0.50	0.45	0.40	0.45	0.60	0.50	0.45	0.50	0.50	0.40	0.35	Wuraliwunty	Wuraliwunty	Wuraliwunty	Wuraliwunty
3.25	3.65	3.35	2.75	3.05	4.20	3.95	3.30	3.75	2.95	3.00	2.75	Wuraliwunty	Wuraliwunty	Wuraliwunty	Wuraliwunty
0.46	0.56	0.50	0.42	0.46	0.66	0.62	0.48	0.58	0.50	0.44	0.42	Wuraliwunty	Wuraliwunty	Wuraliwunty	Wuraliwunty



MCDD0003	MCDD0003	MCDD0003	MCDD0003	MCDD0003	MCDD0003	MCDD0003	MCDD0003	MCDD0003	MCDD0003	MCDD0003	MCDD0003	MCDD0003	MCDD0003	MCDD0003	MCDD0003	MCDD0003	MCDD0003	MCDD0003	MCDD0003		
299.1	298.33	297.57	294.5	290.71	284.25	281.91	276	274.54	272.37	271.21	269.78	Wuraliwunty	Wuraliwunty	Wuraliwunty	Wuraliwunty	Wuraliwunty	Wuraliwunty	Wuraliwunty	Wuraliwunty	Wuraliwunty	
Wuraliwunty	Wuraliwunty	Wuraliwunty	Wuraliwunty	Wuraliwunty	Wuraliwunty	Wuraliwunty	Wuraliwunty	Wuraliwunty	Wuraliwunty	Wuraliwunty	Wuraliwunty	Wuraliwunty	Wuraliwunty	Wuraliwunty	Wuraliwunty	Wuraliwunty	Wuraliwunty	Wuraliwunty	Wuraliwunty	Wuraliwunty	Wuraliwunty
#VALUE!	0.85	0.29	#VALUE!	0.19	0.09	#VALUE!	#VALUE!	#VALUE!	#VALUE!	#VALUE!	#VALUE!	#VALUE!	#VALUE!	#VALUE!	#VALUE!	#VALUE!	#VALUE!	#VALUE!	#VALUE!	#VALUE!	#VALUE!
0.79	0.48	0.61	0.55	0.47	0.57	0.64	0.63	0.59	0.52	0.50	0.59	0.59	0.52	0.50	0.59	0.52	0.50	0.59	0.52	0.50	0.59
13.08	15.95	15.27	16.26	13.33	14.04	14.81	16.16	14.37	12.25	14.71	14.68	16.16	14.37	12.25	14.71	12.25	14.71	14.68	12.25	14.71	14.68
10.70	8.78	5.24	12.30	10.50	11.40	10.80	9.90	9.74	6.53	13.60	6.81	9.90	9.74	6.53	13.60	6.53	13.60	6.81	6.53	13.60	6.81
320.00	380.00	260.00	520.00	420.00	500.00	480.00	420.00	420.00	320.00	440.00	520.00	420.00	420.00	320.00	440.00	320.00	440.00	520.00	320.00	440.00	520.00
<0.5	7.50	1.50	<0.5	2.00	1.00	<0.5	<0.5	<0.5	1.00	1.00	1.00	<0.5	<0.5	1.00	1.00	1.00	1.00	1.00	1.00	1.00	1.00
0.08	0.08	0.06	0.08	0.08	0.08	0.07	0.07	0.08	0.06	0.04	0.06	0.07	0.08	0.06	0.04	0.06	0.04	0.06	0.06	0.04	0.06
8.50	4.20	3.20	6.80	4.90	6.50	6.90	6.20	5.70	3.40	6.80	4.00	6.20	5.70	3.40	6.80	3.40	6.80	4.00	3.40	6.80	4.00
140.00	140.00	80.00	200.00	140.00	160.00	160.00	160.00	140.00	80.00	200.00	100.00	160.00	140.00	80.00	200.00	80.00	200.00	100.00	80.00	200.00	100.00
47.60	51.70	30.80	95.90	62.60	82.10	68.80	67.90	55.20	41.20	80.90	41.40	67.90	55.20	41.20	80.90	41.20	80.90	41.40	41.20	80.90	41.40
98.00	103.00	62.00	216.00	126.00	180.00	136.00	134.00	110.00	83.20	167.00	82.80	134.00	110.00	83.20	167.00	83.20	167.00	82.80	83.20	167.00	82.80
12.00	12.20	7.50	23.10	14.90	19.20	15.80	15.60	13.30	10.10	19.00	10.00	15.60	13.30	10.10	19.00	10.10	19.00	10.00	10.10	19.00	10.00
45.00	44.20	27.30	85.10	54.30	68.40	57.00	54.90	48.60	36.20	68.80	37.50	54.90	48.60	36.20	68.80	36.20	68.80	37.50	36.20	68.80	37.50
9.40	7.70	5.30	13.20	9.20	11.20	9.60	8.85	8.50	7.00	11.00	7.25	8.85	8.50	7.00	11.00	7.00	11.00	7.25	7.00	11.00	7.25
1.85	1.40	1.00	2.25	1.60	1.95	1.75	1.55	1.55	1.25	1.80	1.55	1.55	1.55	1.25	1.80	1.25	1.80	1.55	1.25	1.80	1.55
9.00	6.20	5.00	9.20	7.20	9.00	7.60	7.00	7.20	6.20	7.00	8.00	7.00	7.20	6.20	7.00	6.20	7.00	8.00	6.20	7.00	8.00
1.20	0.80	0.68	1.18	0.92	1.14	0.98	0.86	0.90	0.86	0.88	0.84	0.86	0.90	0.86	0.88	0.86	0.88	0.84	0.86	0.88	0.84
7.75	5.10	4.25	8.15	5.95	7.25	6.55	5.35	5.65	5.60	6.25	5.15	5.35	5.65	5.60	6.25	5.60	6.25	5.15	5.60	6.25	5.15
1.46	0.94	0.88	1.36	1.12	1.36	1.24	1.02	1.04	0.98	1.16	0.92	1.02	1.04	0.98	1.16	0.98	1.16	0.92	0.98	1.16	0.92
4.35	2.75	2.30	4.20	3.35	4.05	3.70	3.10	3.10	2.85	3.40	2.70	3.10	3.10	2.85	3.40	2.85	3.40	2.70	2.85	3.40	2.70
0.60	0.35	0.30	0.55	0.45	0.55	0.50	0.45	0.45	0.40	0.50	0.35	0.45	0.45	0.40	0.50	0.40	0.50	0.35	0.40	0.50	0.35
4.50	2.70	2.20	4.10	3.20	3.95	3.45	3.00	2.90	2.50	3.60	2.60	3.00	2.90	2.50	3.60	2.50	3.60	2.60	2.50	3.60	2.60
0.66	0.38	0.32	0.60	0.44	0.56	0.52	0.44	0.42	0.40	0.52	0.38	0.44	0.42	0.40	0.52	0.40	0.52	0.38	0.40	0.52	0.38

MCDD0003	MCDD0003	MCDD0003	MCDD0003	MCDD0003	MCDD0003	MCDD0003	MCDD0003	MCDD0003	MCDD0003	MCDD0003	MCDD0003	MCDD0003	MCDD0003	MCDD0003
339.94	339.08	337.9	335.96	335.16	311.17	310.79	309.25	306.53	304.9	303.11	301.34	Wuraliwunty	Wuraliwunty	Wuraliwunty
0.11	0.10	0.11	0.33	0.18	0.59	0.77	0.43	0.15	0.11	0.10	0.09	0.46	0.47	0.61
12.94	14.33	14.89	11.43	12.28	15.84	16.43	17.00	14.00	12.93	13.86	15.79	9.27	9.41	10.10
400.00	400.00	400.00	400.00	420.00	380.00	380.00	400.00	420.00	400.00	420.00	480.00	1.00	1.00	1.00
0.07	0.08	0.07	0.08	0.10	0.09	0.08	0.09	0.08	0.06	0.07	1.00	4.50	4.40	6.90
120.00	140.00	140.00	120.00	140.00	160.00	160.00	160.00	140.00	120.00	140.00	180.00	51.30	53.00	88.60
101.00	152.00	99.90	93.70	108.00	121.00	110.00	98.90	108.00	106.00	113.00	194.00	12.20	12.60	21.20
44.40	71.00	43.00	40.80	47.10	50.90	46.20	43.00	47.30	46.50	50.00	78.30	8.05	8.50	13.20
1.50	2.00	1.45	1.35	1.70	1.80	1.50	1.50	1.75	1.60	1.70	2.45	7.20	7.40	11.00
0.94	0.98	0.92	0.92	1.06	1.00	0.86	0.94	1.06	0.94	0.96	1.28	5.90	5.95	7.70
1.12	1.12	1.06	1.10	1.32	1.16	1.04	1.00	1.14	1.12	1.12	1.40	3.25	3.35	4.20
0.45	0.45	0.40	0.45	0.55	0.45	0.40	0.35	0.45	0.45	0.45	0.55	3.10	3.10	3.95
0.44	0.44	0.42	0.44	0.54	0.46	0.42	0.42	0.44	0.44	0.50	0.56	0.44	0.44	0.56

MCDD0003	MCDD0003	MCDD0003	MCDD0003	MCDD0003	MCDD0003	MCDD0003	MCDD0003	MCDD0003	MCDD0003	MCDD0003	MCDD0003	MCDD0003	MCDD0003	MCDD0003	MCDD0003	MCDD0003	MCDD0003	MCDD0003	MCDD0003	
357.29	355.11	353.46	352.71	350.91	350.1	348.62	347.81	345.4	344.25	343.18	341.56									
Wuraliwunty	Wuraliwunty	Wuraliwunty	Wuraliwunty	Wuraliwunty	Wuraliwunty	Wuraliwunty	Wuraliwunty	Wuraliwunty	Wuraliwunty	Wuraliwunty	Wuraliwunty	Wuraliwunty	Wuraliwunty	Wuraliwunty	Wuraliwunty	Wuraliwunty	Wuraliwunty	Wuraliwunty	Wuraliwunty	Wuraliwunty
1.33	0.78	0.77	0.32	0.20	0.16	#VALUE!	0.12	0.10	0.10	0.10	0.14									
0.39	0.40	0.68	0.44	0.44	0.44	1.38	0.46	0.47	0.48	0.49	0.54									
12.84	13.73	16.76	11.11	14.34	14.97	15.38	13.94	12.54	15.38	18.00	15.38									
10.90	10.20	7.16	10.80	9.76	9.35	10.40	8.61	9.57	10.40	10.00	10.40									
460.00	660.00	360.00	440.00	440.00	400.00	420.00	400.00	440.00	440.00	420.00	380.00									
14.50	8.00	5.50	3.50	2.00	1.50	<0.5	1.00	1.00	1.00	1.00	1.50									
0.07	0.06	0.06	0.07	0.07	0.07	0.07	0.07	0.09	0.09	0.08	0.11									
4.30	4.10	4.90	4.80	4.30	4.10	14.40	4.00	4.50	5.00	4.90	5.60									
140.00	140.00	120.00	120.00	140.00	140.00	160.00	120.00	120.00	160.00	180.00	160.00									
46.10	56.60	43.00	67.40	71.20	64.40	60.00	43.90	56.10	67.50	60.40	71.10									
91.00	112.00	81.80	141.00	141.00	127.00	118.00	87.70	111.00	133.00	119.00	141.00									
10.70	13.40	9.65	17.40	17.20	15.60	13.90	10.30	13.50	15.80	14.20	16.90									
38.10	48.80	34.40	65.80	62.50	57.80	50.70	37.50	49.00	56.30	51.50	62.00									
7.15	8.60	6.25	11.70	10.30	9.60	8.65	6.80	8.60	9.30	8.90	10.70									
1.40	1.65	1.35	2.05	1.80	1.70	1.65	1.25	1.55	1.70	1.60	1.95									
5.80	6.80	6.00	9.00	7.40	7.00	7.60	6.40	7.20	7.40	7.20	8.60									
0.84	0.92	0.92	1.20	0.94	0.90	1.02	0.80	0.90	0.92	0.92	1.02									
5.15	5.55	5.05	6.75	5.65	5.50	6.65	5.30	5.85	5.50	5.70	6.50									
1.04	1.12	1.00	1.36	1.12	1.02	1.28	1.00	1.08	1.06	1.06	1.20									
3.15	3.15	2.90	3.85	3.25	3.15	3.85	3.00	3.35	3.15	3.35	3.60									
0.50	0.50	0.45	0.55	0.45	0.40	0.50	0.60	0.65	0.50	0.45	0.50									
3.05	3.00	2.80	3.65	2.90	2.80	3.60	2.90	3.15	3.00	3.05	3.50									
0.52	0.48	0.48	0.60	0.48	0.40	0.50	0.42	0.48	0.44	0.44	0.52									

Table S.4.3. Shale geochemical analyses for samples from MCDD003 in this study.

28	39.35	23	13	8	7	6	5	4	3	2	1	Sample
		33.21	22.55	16.35	15.05	13.7	12.7	11.55	10.68	9.35	8.67	Depth (m)
												Formation
												SRA TOC
												S1
												S2
												S3
												Tmax (°C)
												Calc. % Ro
												HI
												OI
												S2/S3
												S1/TOC *100
												PI



53		52	51	50	49	48	47	46	45	44	43	42
65.05	64.72	63.65	62.33	61.03	60.2	59.63	58.55	57.44	56.3	55.7	54.55	
Wologorang	Wologorang	Wologorang	Wologorang	Wologorang	Wologorang	Wologorang	Wologorang	Wologorang	Wologorang	Wologorang	Wologorang	Wologorang
0.39	0.45	0.39	3.07	4.58	7.81	4.01	4.47	8.31	4.71	3.53	4	
0.00	0.02	0.01	0.20	0.43	0.53	0.23	0.30	0.58	0.36	0.20	0.47	
0.01	0.11	0.01	3.46	2.99	7.88	2.50	2.95	8.52	3.63	2.29	3.12	
0.68	0.25	1.24	0.14	0.15	0.14	0.14	0.20	0.08	0.19	0.11	0.09	
535.46	404.30	553.33	425.67	439.69	447.09	446.55	443.58	447.77	439.20	445.98	440.43	
2.48	0.12	2.80	0.50	0.75	0.89	0.88	0.82	0.90	0.75	0.87	0.77	
2.56	24.44	2.56	112.70	65.28	100.90	62.34	66.00	102.53	77.07	64.87	78.00	
174.36	55.56	317.95	4.56	3.28	1.79	3.49	4.47	0.96	4.03	3.12	2.25	
0.01	0.44	0.01	24.71	19.93	56.29	17.86	14.75	106.50	19.11	20.82	34.67	
0.00	4.44	2.56	6.51	9.39	6.79	5.74	6.71	6.98	7.64	5.67	11.75	
0.00	0.15	0.50	0.05	0.13	0.06	0.08	0.09	0.06	0.09	0.08	0.13	

65	78.95	78.11	77.2	76.21	74.79	73.01	71.65	70.6	69.75	68.68	66.93	65.99
	0.31	0.36	0.28	0.27	0.28	0.35	0.42	0.35	0.47	0.69	0.68	0.75
	0.01	0.01	0.01	0.01	0.01	0.01	0.00	0.01	0.03	0.07	0.05	0.10
	0.03	0.02	0.03	0.03	0.02	0.03	0.01	0.04	0.07	0.36	0.30	0.32
	0.23	0.12	0.23	0.17	0.72	0.34	0.11	0.13	0.17	0.52	0.62	0.67
	454.19	404.40	N/A	337.62	501.29	443.73	393.52	449.31	430.08	439.32	436.31	439.64
	1.02	0.12			1.86	0.83		0.93	0.58	0.75	0.69	0.75
	9.68	5.56	10.71	11.11	7.14	8.57	2.38	11.43	14.89	52.17	44.12	42.67
	74.19	33.33	82.14	62.96	257.14	97.14	26.19	37.14	36.17	75.36	91.18	89.33
	0.13	0.17	0.13	0.18	0.03	0.09	0.09	0.31	0.41	0.69	0.48	0.48
	3.23	2.78	3.57	3.70	3.57	2.86	0.00	2.86	6.38	10.14	7.35	13.33
	0.25	0.33	0.25	0.25	0.33	0.25	0.00	0.20	0.30	0.16	0.14	0.24

77		76	75	74	73	72	71	70	69	68	67	66
92.29	91.6	91.01	89.22	86.79	86.31	85.21	84.16	83.59	82.61	82.01	81.12	
Wologorang	Wologorang	Wologorang	Wologorang	Wologorang	Wologorang	Wologorang	Wologorang	Wologorang	Wologorang	Wologorang	Wologorang	Wologorang
0.15	0.13	0.13	0.12	0.81	0.2	0.27	0.35	0.35	0.35	0.29	0.26	
0.00	0.00	0.00	0.00	0.01	0.00	0.04	0.01	0.04	0.00	0.02	0.01	
0.01	0.00	0.01	0.01	0.03	0.00	0.02	0.01	0.04	0.02	0.04	0.02	
0.09	0.08	0.05	0.08	0.19	0.10	0.24	0.68	0.07	0.86	0.11	0.10	
306.17	559.53	564.52	566.30	558.47	565.11	301.56	597.91	306.98	427.19	320.24	451.01	
	2.91	3.00	3.03	2.89	3.01		3.60		0.53		0.96	
6.67	0.00	7.69	8.33	3.70	0.00	7.41	2.86	11.43	5.71	13.79	7.69	
60.00	61.54	38.46	66.67	23.46	50.00	88.89	194.29	20.00	245.71	37.93	38.46	
0.11	0.00	0.20	0.13	0.16	0.00	0.08	0.01	0.57	0.02	0.36	0.20	
0.00	0.00	0.00	0.00	1.23	0.00	14.81	2.86	11.43	0.00	6.90	3.85	
0.00	#DIV/0!	0.00	0.00	0.25	#DIV/0!	0.67	0.50	0.50	0.00	0.33	0.33	







119	299.1	298.33	297.57	294.5	290.71	284.25	281.91	276	274.54	272.37	271.21	269.78
Wuraliwuntya	Wuraliwuntya	Wuraliwuntya	Wuraliwuntya	Wuraliwuntya	Wuraliwuntya	Wuraliwuntya	Wuraliwuntya	Wuraliwuntya	Wuraliwuntya	Wuraliwuntya	Wuraliwuntya	Wuraliwuntya
0.06	0.05	0.09	0.06	0.07	0.06	0.07	0.07	0.05	0.08	0.06	0.05	0.03
0.02	0.03	0.28	0.01	0.01	0.01	0.01	0.22	0.05	0.00	0.00	0.00	0.00
0.02	0.02	0.10	0.01	0.02	0.04	0.03	0.03	0.06	0.01	0.02	0.00	0.00
0.07	0.06	0.23	0.07	0.16	0.03	0.10	0.10	0.07	0.18	0.13	0.19	0.17
347.05	N/A	N/A	339.47	387.72	369.58	387.39	332.95	306.66	489.79	341.26	330.78	
33.33	40.00	111.11	16.67	28.57	66.67	42.86	120.00	12.50	33.33	0.00	0.00	0.00
116.67	120.00	255.56	116.67	228.57	50.00	142.86	140.00	225.00	216.67	380.00	566.67	
0.29	0.33	0.43	0.14	0.13	1.33	0.30	0.86	0.06	0.15	0.00	0.00	0.00
33.33	60.00	311.11	16.67	14.29	16.67	314.29	100.00	0.00	0.00	0.00	0.00	0.00
0.50	0.60	0.74	0.50	0.33	0.20	0.88	0.45	0.00	0.00	0.00	#DIV/0!	#DIV/0!



140	352.71	Wuraliwuntya	0.23	0.02	0.05	0.14	323.97		21.74	60.87	0.36	8.70	0.29
141	353.46	Wuraliwuntya	0.19	0.20	0.11	0.06	N/A		57.89	31.58	1.83	105.26	0.65
142	355.11	Wuraliwuntya	0.14	0.03	0.06	0.09	322.19		42.86	64.29	0.67	21.43	0.33
143	357.29	Wuraliwuntya	0.15	0.02	0.03	0.19	334.58		20.00	126.67	0.16	13.33	0.40

**Table S.4.3.** Shale source-rock analyses for samples from MCDD003 in this study.

Depth (m)	Formation	sample	d13C	d13Cerr	d18O	d18Oerr
10.81	Amelia Dolostone	1	-2.398970	0.031659	-5.374013	0.053277
12.24	Amelia Dolostone	2	-1.274315	0.040261	-5.526674	0.043990
13.71	Amelia Dolostone	3	-0.718041	0.035811	-5.224763	0.036778
14.41	Amelia Dolostone	4	-1.147850	0.113790	-6.790252	0.220442
15.27	Amelia Dolostone	5	-2.251638	0.036053	-6.339857	0.025851
17.51	Amelia Dolostone	6	-0.940106	0.074980	-7.410890	0.031654
21.41	Amelia Dolostone	7	-1.197905	0.041406	-8.210515	0.065914
19.15	Amelia Dolostone	8	0.212951	0.034605	-4.938652	0.067023
23.54	Amelia Dolostone	9	-0.638427	0.064318	-6.012907	0.174699
25.57	Amelia Dolostone	10	-0.962066	0.028253	-8.157862	0.015137
28.02	Amelia Dolostone	11	-0.377927	0.060294	-6.460999	0.101976
29.21	Amelia Dolostone	12	-0.717159	0.043821	-7.567618	0.059202
30.49	Amelia Dolostone	13	-3.098524	0.007111	-2.336324	0.332805
32.72	Amelia Dolostone	14	-0.459038	0.042653	-6.918053	0.035361
33.95	Amelia Dolostone	15	0.470137	0.015821	-8.453661	0.002327
36	Amelia Dolostone	16	-0.756995	0.010319	-7.019091	0.026159
37.54	Amelia Dolostone	17	-0.533133	0.047227	-6.977563	0.141550
38.9	Amelia Dolostone	18	-0.645826	0.063326	-7.016022	0.034816
40.15	Amelia Dolostone	19	-0.540667	0.039928	-6.576114	0.103089
41.5	Amelia Dolostone	20	-0.647701	0.015252	-7.079955	0.070882
43.27	Amelia Dolostone	21	-0.763606	0.063623	-7.604246	0.040792
44	Amelia Dolostone	22	-1.495700	0.027957	-6.790622	0.047746
45.84	Amelia Dolostone	23	-0.697735	0.030755	-7.403886	0.030716
46.9	Amelia Dolostone	24	-1.539568	0.010342	-9.573553	0.037145
48.4	Amelia Dolostone	25	-0.626076	0.046156	-6.883077	0.048768
52.03	Amelia Dolostone	26	-0.534994	0.053474	-6.702204	0.077485
53.93	Amelia Dolostone	27	-0.955263	0.049186	-6.286727	0.025585

55.37	Amelia Dolostone	28	-0.666314	0.086289	-6.344555	0.122489
55.87	Amelia Dolostone	29	-0.745616	0.053126	-6.371771	0.068029
58.8	Amelia Dolostone	30	-0.654938	0.031740	-7.016979	0.046543
60.2	Amelia Dolostone	31	-1.023972	0.020227	-6.330264	0.033463
63.13	Amelia Dolostone	32	-1.465470	0.126380	-7.579400	0.125464
66.69	Amelia Dolostone	33	-1.134553	0.039450	-7.313834	0.056481
68.29	Amelia Dolostone	34	-1.074093	0.101841	-7.132421	0.072265
71.7	Amelia Dolostone	35	-1.354385	0.051313	-7.446143	0.048098
73.35	Amelia Dolostone	36	-1.157086	0.024274	-6.988373	0.042867
75.75	Amelia Dolostone	37	-1.066574	0.024465	-7.618044	0.072680
76.7	Amelia Dolostone	38	-0.742998	0.016421	-6.758903	0.057212
78.57	Amelia Dolostone	39	-1.584950	0.062453	-7.349883	0.186801
80.95	Amelia Dolostone	40	-1.302740	0.015980	-7.150315	0.009418
83.35	Amelia Dolostone	41	-1.301973	0.018517	-7.262446	0.020493
85.6	Amelia Dolostone	42	-1.170228	0.009801	-7.278213	0.062191
85.75	Amelia Dolostone	43	-0.582949	0.019610	-6.090272	0.026643
87.5	Amelia Dolostone	44	-0.454295	0.041568	-6.154548	0.039179
89.42	Amelia Dolostone	45	-0.073442	0.040244	-6.454008	0.074794
91.23	Amelia Dolostone	46	-1.464980	0.028090	-6.291133	0.015921
92.86	Amelia Dolostone	47	-1.490382	0.021199	-5.549547	0.030874
93.2	Amelia Dolostone	48	-1.220126	0.027790	-6.676234	0.059277
95.19	Amelia Dolostone	49	-1.335579	0.017037	-6.615158	0.152904
97.97	Amelia Dolostone	50	-1.386273	0.031891	-5.811961	0.047309
99.5	Amelia Dolostone	51	-1.180000	0.070000	-6.880000	0.120000
101.9	Amelia Dolostone	52	-0.696959	0.046312	-7.516729	0.038389
103.63	Amelia Dolostone	53	-1.224725	0.040000	-7.384319	0.059345
104.83	Amelia Dolostone	54	-1.195199	0.028799	-6.610597	0.074071
107.07	Amelia Dolostone	55	-1.566950	0.075442	-6.839387	0.093922
108.3	Amelia Dolostone	56	-1.360922	0.026014	-7.075101	0.063481
110.75	Amelia Dolostone	57	-1.304523	0.081089	-6.668348	0.053904
113.05	Amelia Dolostone	58	-1.218348	0.041445	-6.425728	0.092084
114	Amelia Dolostone	59	-1.420000	0.040000	-6.960000	0.070000
115.9	Amelia Dolostone	60	-0.764387	0.042105	-6.278177	0.026267
116.77	Amelia Dolostone	61	-0.726178	0.020306	-6.897331	0.086429
119.77	Amelia Dolostone	62	-0.755148	0.022751	-7.017006	0.065175
121.03	Amelia Dolostone	63	-0.680625	0.012091	-6.531241	0.030317
122.86	Amelia Dolostone	64	-0.542646	0.008097	-7.008203	0.022881
124.4	Amelia Dolostone	63	-0.850000	0.020000	-6.610000	0.060000
125.83	Amelia Dolostone	66	-0.482534	0.058876	-6.174672	0.042174
127.71	Amelia Dolostone	67	-0.655271	0.029882	-7.551517	0.049198
129.35	Amelia Dolostone	68	-0.545503	0.033447	-7.372217	0.068670
130.63	Amelia Dolostone	69	-0.526153	0.017907	-6.661308	0.021203
133.09	Amelia Dolostone	70	-0.312890	0.028696	-6.831642	0.012442
135.55	Amelia Dolostone	71	-0.310000	0.040000	-6.960000	0.040000
136.62	Amelia Dolostone	72	-0.481153	0.048861	-8.016830	0.075656

140.1	Amelia Dolostone	73	-1.252713	0.051046	-7.553162	0.044543
142.52	Amelia Dolostone	74	-0.357656	0.031027	-6.942287	0.043431
144.55	Amelia Dolostone	75	-0.546138	0.018583	-7.204997	0.013954
147.07	Amelia Dolostone	76	-0.285600	0.017288	-6.800399	0.037332
148.15	Amelia Dolostone	77	-0.403701	0.047867	-6.674544	0.028547
150.96	Amelia Dolostone	78	-0.883250	0.045709	-7.689497	0.104248
156.42	Amelia Dolostone	80	-0.680000	0.050000	-7.510000	0.060000
158.38	Amelia Dolostone	81	-0.850000	0.020000	-9.600000	0.080000
159.73	Amelia Dolostone	82	-0.930000	0.040000	-7.860000	0.080000
161.98	Amelia Dolostone	83	-0.511710	0.043728	-4.727490	0.068866

Depth (m)	Radiogenic Sr		Stable Sr	
	$^{87}\text{Sr}/^{86}\text{Sr}$	Err	$\delta^{88}/^{86}\text{Sr}$	Err
12.24	0.7395840	0.0000034	0.353	0.02
32.72	0.7382500	0.0000036	0.042	0.02
32.72	0.7382510	0.0000034	0.042	0.02
52.03	0.7187510	0.0000033	0.406	0.01
60.2	0.7249230	0.0000033	0.074	0.01
60.2	0.7249270	0.0000040	0.074	0.01
80.95	0.7145260	0.0000036	0.169	0.01
80.95	0.7145300	0.0000033	0.169	0.01
103.63	0.7118190	0.0000056	0.381	0.01
103.63	0.7118190	0.0000056	0.381	0.01
114	0.7145300	0.0000033	0.389	0.02
136.62	0.7098840	0.0000046	0.339	0.02
159.73	0.7139160	0.0000020	0.485	0.02

**Table S.4.4.** Carbonate isotopic analyses for samples from the Amelia Dolostone.

## Additional information for Chapter 5

Laser analyses on samples and standards were carried out at Adelaide Microscopy, University of Adelaide using a laser ablation (RESOLUTION-LR ArF 193nm excimer laser) inductively couple-mass spectrometer (Agilent 8900x ICP-MS/MS) with the analytical parameters and tuning conditions following Redaa et al. (2021). One spot analysis consisted of 20 seconds of gas background collected while the laser was not firing followed by 40 seconds of ablated signal. Strontium isotopes were measured in the oxidised molecule SrO. Strontium is oxidised with N<sub>2</sub>O gas in the reaction chamber (e.g.  $^{87}\text{Sr}^{16}\text{O}$  formed from  $^{87}\text{Sr}$  at 103 amu) whilst the unreactive  $^{85}\text{Rb}$  was measured on-mass. Dwell times for each Sr isotope were 50ms, 10ms for Rb and 5ms for all other masses totalling to 0.31 seconds. The mass spectrometer and laser analytical parameters as well as tuning conditions used in this study are summarised in Table S.5.1.

*In situ* Rb–Sr dating of CRPG reference material Mica-MG (Govindaraju et al., 1994) prepared as a nano-powder pellet and a phlogopite mineral sample MDC sourced from the same quarry in Bekily, Madagascar were assumed to be of the same age (Armistead et al., 2020; Högalm et al., 2017; Li et al., 2020; Redaa et al., 2021; Tamblyn et al., 2020) were

used as primary and secondary standards respectively (Fig. S.5.1). A glauconite grain mount sample GL-O of known Cretaceous age from Bagnols-sur-Cèze, France was also analysed (Fig. S.5.1) as an independent secondary standard (Rousset et al., 2004). Glass standards NIST-610 and BCR-2G (Jochum et al., 2016; Wilson, 1997) were also analysed for element quantification. Isochron ages were calculated using IsoplotR software (Vermeesch, 2018). The mineral standard MDC was anchored to  $^{87}\text{Rb}/^{86}\text{Sr} = 0.00001 \pm 0.000001$  and  $^{87}\text{Sr}/^{86}\text{Sr} = 0.72607 \pm 0.00363$  initial ratios as reported by Hogmalm et al. (2017) yielding an age of  $529 \pm 6$  Ma (Fig. S.5.1). This is within error of the Mica-MG age from the same analysis of  $523 \pm 4$  Ma (Fig. S.5.1) as well as the mean age of the standard ( $519.4 \pm 6.5$  Ma) published by Hogmalm et al. (2017). Furthermore, the glauconite grain GL-O (Fig. S.5.1) also gave an age ( $94 \pm 3$  Ma) within the error of its published value ( $98 \pm 4$  Ma) published by Rousset et al. (2004). Elemental analyses of standards and their subsequent QAQC are reported in and cross-referenced with their respective published values (Fig. S.5.2). Average values of major and rare earth element in BCR2-G are within error and positively covaries with their published data (Jochum et al., 2016).

<b>Laser Parameters</b>	<b>Value</b>	<b>Unit</b>
<i>Ar carrier gas</i>	1050	ml/min
<i>Fluence</i>	3.5	J/cm <sup>2</sup>
<i>He carrier gas</i>	350	ml/min
<i>N<sub>2</sub> addition</i>	3.5	ml/min
<i>Repetition rate</i>	10	Hz
<i>Spot size</i>	74	µm
<b>ICP-MS/MS Plasma Parameters</b>	<b>Value</b>	<b>Unit</b>
<i>RF plasma power</i>	1350	W
<b>ICP-MS/MS Lens Parameters</b>	<b>Value</b>	<b>Unit</b>
<i>Lens extract 1</i>	-2.0	V
<i>Lens extract 2</i>	-150	V
<i>Omega bias</i>	75	V
<i>Omega lens</i>	7.0	V
<i>Q1 entrance</i>	2.0	V
<i>Q1 exit</i>	-1.0	V
<i>Cell focus</i>	-2.0	V
<i>Cell entrance</i>	-100	V
<i>Cell exit</i>	-150	V



<i>Deflect</i>	-10	V
<i>Plate bias</i>	-80	V
<b>ICP-MS/MS Q1 Parameters</b>	<b>Value</b>	<b>Unit</b>
<i>Q1 bias</i>	-2.0	V
<i>Q1 prefilter bias</i>	-9.0	V
<i>Q1 postfilter bias</i>	-10	V
<b>ICP-MS/MS Cell Parameters</b>	<b>Value</b>	<b>Unit</b>
<i>N<sub>2</sub>O flow rate</i>	0.37	mL/min
<i>OctP bias</i>	-23	V
<i>Axial acceleration</i>	2.0	V
<i>OctP RF</i>	180	V
<i>Energy discrimination</i>	-10	V
<b>ICP-MS/MS Q2 Parameters</b>	<b>Value</b>	<b>Unit</b>
<i>Q2 bias</i>	-33	V

**Table S.5.1.** Summary of LA-ICP-MS/MS instrumental parameters.

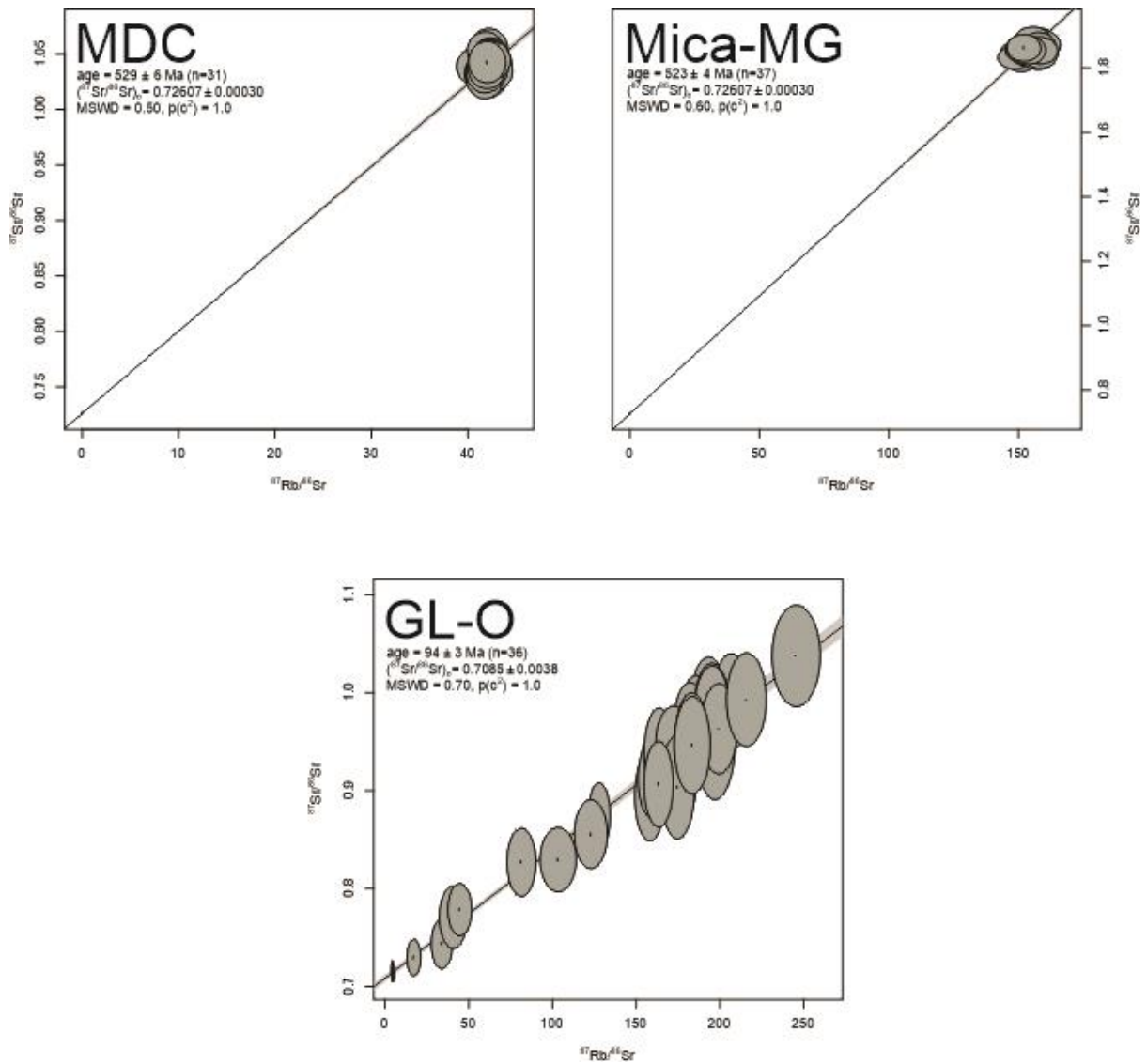


**Figure S.5.1.** Results for primary and secondary standards for in situ Rb–Sr dating shows that they overlap with previously published data (Hogmalm et al., 2017; Rousset et al., 2004).

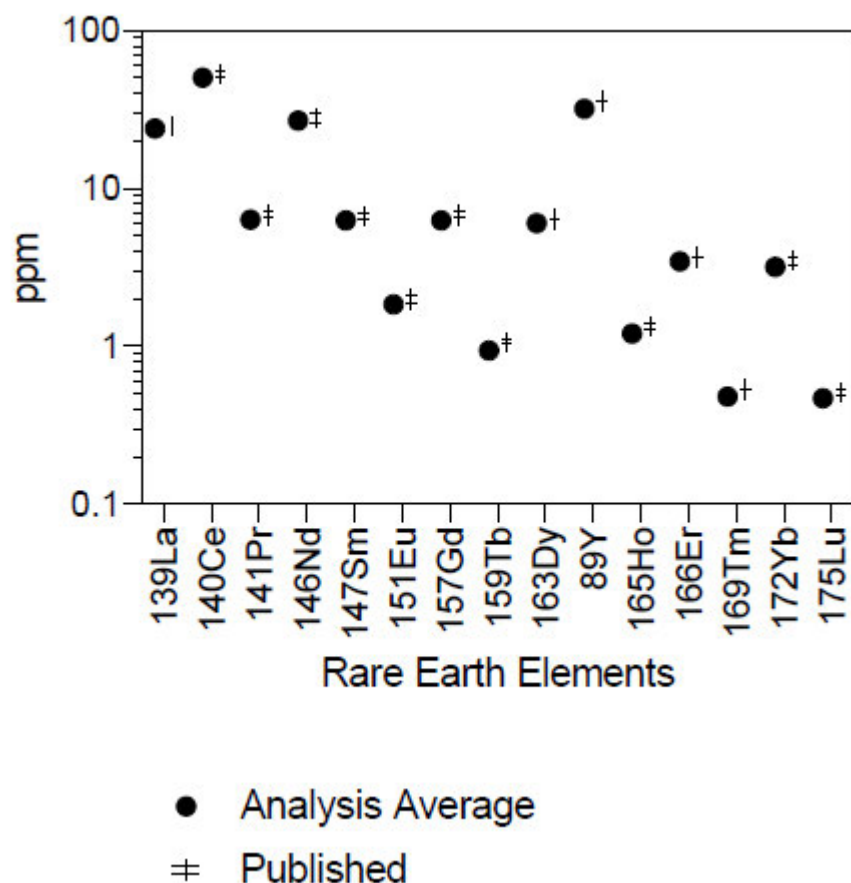


**Figure S.5.2.** Rare earth element values of BCR-2G from *in situ* analyses in comparison with certified data (Jochum et al., 2016).

### Carbonate Elemental Analysis

Carbonate samples were leached to ensure minimum incorporation of non-carbonate phases (Cao et al., 2020; Halverson et al., 2010; Tostevin et al., 2016). Rock chips were micro-drilled along laminae to target the carbonate matrix, making sure to avoid veining, clasts and weathered surface. The rock powder were then reacted with 1M ammonium acetate to remove any loose cations on the surface. This was then followed by a second and third leach with 0.2 M acetic acid to extract the carbonate phase. Between each step, the solution was sonicated and centrifuged for 20 and 10 minutes respectively. The final supernatant was set aside for solution inductively coupled plasma mass spectrometer (ICP-MS) analysis at Adelaide Microscopy using an Agilent 8900x mass spectrometer instrument. This was then digested with 2% nitric acid and split into aliquots of 1:10000 and 1:1000 dilutions for major and trace element analysis. Calibration solutions were prepared from a multi-element stock standard solution and diluted with 2% nitric acid as well. Primary standard JDo-1 was used for all analytical runs (IMAI et al., 1996).

For sample introduction, the ICP-MS was equipped with a Miramist nebuliser and a quartz spray chamber, into which samples were introduced by a peristaltic pump at a flow rate of 1.0mL/min. An internal standard, Indium, was mixed online with the samples to compensate for matrix effects. All element concentrations were determined against certified multi-

element calibration standards (Choice Analytical, Australia) and blanks were interspersed throughout the analysis session, as well as measurement of the 200ppb calibration solution to check the instrument stability. The instrument was operated with an RF power of 1500W, a carrier gas flow of 0.89 L/min and a make-up gas flow of 0.19 L/min. Sample uptake rate was 1.0 mL/min and the dwell times ranged between 10ms to 1s. Three replicates were obtained for each sample. The data was processed using Agilent Mass-Hunter Data Analysis.

### Carbonate Isotopic Analysis

A fraction of the solution prepared for elemental geochemistry in carbonates were measured for isotopic analyses. Coupled  $^{87}\text{Sr}/^{86}\text{Sr}$  and  $\delta^{88/86}\text{Sr}$  analyses were undertaken using a Phoenix Isotopx thermal ionisation mass spectrometry (TIMS) following the extensive methodology described by (Shao et al., 2018; Shao et al., 2021). Two aliquots each containing around 500 ng of Sr were taken from the sample solution, with one being spiked with a  $^{87}\text{Sr}$ - $^{84}\text{Sr}$  double spike solution and consequently giving a spike to sample ratio  $^{84}\text{Sr}_{\text{sp}}/^{84}\text{Sr}_{\text{sa}}$  between 10-50. The  $^{87}\text{Sr}$ - $^{84}\text{Sr}$  double spike solution was prepared at GEOMAR (Kiel, Germany) with a total Sr concentration of 0.0090mg/g, and its respective Sr isotope composition as determined by TIMS at University of Adelaide is provided in Shao et al. (2021) .

Procedural Sr blanks prepared for analyses consisted of a drop of deionized water, a drop of 0.1 M phosphoric acid and an additional drop of  $^{84}\text{Sr}$ -enriched single spike in a Teflon vial. Next, the Sr fraction of all samples and standers along with the blanks used were purified using a 600  $\mu\text{L}$  Micro Bio-Spin separation columns filled with Sr-specific resin (Eichrom Sr-SPS). They were then loaded onto single degassed Re filaments to be prepared for  $^{87}\text{Sr}/^{86}\text{Sr}$  and  $\delta^{88/86}\text{Sr}$  data collected.

$^{87}\text{Sr}/^{86}\text{Sr}$  isotopic ratios of carbonate samples were analysed through the conventional 'dynamic' analytical method for better accuracy (Shao et al., 2018). On the other hand  $\delta^{88/86}\text{Sr}$  data were collected using a 'static' analytical method and corrected for instrumental and procedural fractionation effects via the double spike technique (Krabbenhöft et al., 2010). To apply this method, a separate analyses with an 'un-spiked' aliquot for each sample also needed to be analysed concurrently (Krabbenhöft et al., 2010). As such, each analytical session contained both spiked and un-spiked samples ran parallel with NIST SRM 987 (Krabbenhöft et al., 2009) and JCP-1 (Inoue et al., 2004) standards. Both spiked and unspiked samples were analysed by TIMS using a static multicollection routine. During analysis, an  $^{88}\text{Sr}$  beam with a magnitude of about 5–6 V was attained, and  $^{84}\text{Sr}$ ,  $^{85}\text{Rb}$ ,  $^{86}\text{Sr}$ ,  $^{87}\text{Sr}$ , and  $^{88}\text{Sr}$  isotope beams were collected over 200 cycles (10 cycles for 20 blocks, with 30 s baseline and 8 s peak integrations). From these collected data, the following isotope ratios were calculated:  $^{88}\text{Sr}/^{84}\text{Sr}$ ,  $^{86}\text{Sr}/^{84}\text{Sr}$ ,  $^{87}\text{Sr}/^{84}\text{Sr}$  and  $^{88}\text{Sr}/^{86}\text{Sr}$ . This is then used to determine the 'double-spike corrected'  $^{88}\text{Sr}/^{86}\text{Sr}$  ratios. Isotopic fractionation effects due to the procedure or instrument applied were corrected using a modified  $^{87}\text{Sr}$ - $^{84}\text{Sr}$  double spike correction algorithm (Shao et al., 2021) modified from Heuser et al. (2002) and Samanta et al. (2016).

Stable Sr isotopic data of all samples is normalised relative to SRM 987 standard following the equation:

$$\delta^{88/86}\text{Sr} = [({}^{88}\text{Sr}/{}^{86}\text{Sr})_{\text{sample}} / ({}^{88}\text{Sr}/{}^{86}\text{Sr})_{\text{SRM 987}} - 1] * 1000$$

$\delta^{88/86}\text{Sr}$  values of unknown samples as well as the JCP-1 standards were normalised to the average of the SRM987 standards analysed in the same analytical session. This approach was used to correct any session-to-session drifts, which were quantified by monitoring SRM 987 like previously done in other high-precision Sr isotope studies (Andrews and Jacobson, 2017; Andrews et al., 2016; Krabbenhöft et al., 2010; Ohno et al., 2008; Shalev et al., 2017; Shao et al., 2021; Vollstaedt et al., 2014).

High precision  ${}^{87}\text{Sr}/{}^{86}\text{Sr}$  isotopic results were collected by re-running the TIMS on unspiked samples using the ‘dynamic’ method. With this analysis, a typical  ${}^{88}\text{Sr}$  beam of 5–6 V was attained, and the following isotope ratios were collected:  ${}^{87}\text{Sr}/{}^{86}\text{Sr}$ ,  ${}^{86}\text{Sr}/{}^{88}\text{Sr}$  and  ${}^{84}\text{Sr}/{}^{86}\text{Sr}$ , using a method consisting of 100 cycles (20 cycles for 5 blocks). Mass dependent fractionation due to the instrument or procedural effects were corrected using an internal normalisation assuming the  ${}^{86}\text{Sr}/{}^{88}\text{Sr}$  ratio of 0.1194 (Nier, 1938). Sr isotopic results from secondary standard JCP-1 and NIST SRM 987 are summarised in Fig. S.5.3 and compared with their published values (Balcaen et al., 2005; Inoue et al., 2004; Krabbenhöft et al., 2009).

Approximately 100 mg of carbonate powder were micro-drilled for each sample to prepare for analysis of  $\delta^{13}\text{C}_{\text{carb}}$  and  $\delta^{18}\text{O}$  values. Analysis were undertaken using a dual inlet Isotope Ratio Mass Spectrometry (IRMS) Fision Optima with combined Isocarb Carbonate Preparation System at the University of Adelaide following Falster et al. (2018). Powders were purged with 1M phosphoric acid to dissolve the carbonate and injected with helium. The resultant fumes were then measured to produce  $\delta^{13}\text{C}_{\text{carb}}$  and  $\delta^{18}\text{O}$  values. An in-house standard ANU-P3 (Australian National University- carbonate), UAC-1 and IAEA CO-8 was used during analysis which all have been calibrated against international standards. The analytical errors (2SD) for  $\delta^{13}\text{C}_{\text{carb}}$  and  $\delta^{18}\text{O}$  values are on the order of 0.05 per mil (‰) or better. Carbonate and Oxygen isotopic ratios were recorded in conventional delta notation with respect to values of Pee Dee Belemnite (VPDB) as follows:

$$\delta^{13}\text{C} = [({}^{13}\text{C}/{}^{12}\text{C})_{\text{sample}} / ({}^{13}\text{C}/{}^{12}\text{C})_{\text{standard}} - 1] * 1000$$

$$\delta^{18}\text{O} = [({}^{18}\text{O}/{}^{16}\text{O})_{\text{sample}} / ({}^{18}\text{O}/{}^{16}\text{O})_{\text{standard}} - 1] * 1000$$

### Shale Geochemical Analysis

Black, organic-rich shale intervals were crushed into a fine powder using a tungsten carbide mill for their elemental and pyrolysis analysis. Major and trace element concentrations were done using an Agilent 8900 quadrupole ICP-MS with Octopole Reaction System from a multi-acid dissolution of individual shale powdered samples following Cox et al. (2016) and Yang et al. (2020) at Adelaide Microscopy. Integrated sample introduction was tuned daily to optimise plasma conditions and sensitivity. Calibration was carried out using standards

prepared from two multi-element stock standard solutions in the range 0.3 µg/L to 300 µg/L. A single solution prepared from an independent set of stock standards was analysed as an 'unknown' to determine the accuracy of the calibration standards. The data was processed using Agilent Mass-Hunter Data Analysis. An internal standard solution containing  $^{61}\text{Ni}$ ,  $^{115}\text{In}$ ,  $^{147}\text{Sm}$ ,  $^{169}\text{Tm}$  and  $^{205}\text{Tl}$  was mixed in-line with the sample stream ahead of aspiration.

Organic geochemical pyrolysis measurements were done using a Weatherfords Source Rock Analyser and Rock-Eval 6 Turbo at the University of Adelaide. Shale powders were loaded onto the carousel and heated under inert helium in the pyrolysis and oxidation modes to obtain S1-4 peaks as well as  $T_{\text{max}}$ . The pyrolysis oven was first held at 300°C for 5 minutes and ramped at 25°C per minute from 300°C to 650°C. Subsequently the oven was reduced to 220°C and held for 5 minutes with the carrier gas converted to inert air (CO & CO<sub>2</sub> free) and purged, ramped at maximum heating to 580°C and held for 20 minutes. The flame ionisation detector (FID) was calibrated by running Weatherford Laboratories Instruments Division Standard 533. The IR Analysers were calibrated against standard gas with known concentration of CO<sub>2</sub> and CO. An analysis blank was run as 'blank' mode with the sample batch and the blank data was automatically subtracted from all analyses. An external check standard was also run first with each batch to ensure the instrument status with additional check standards every 10 samples. The results were processed where peak areas and geochemical indices including Total organic carbon (TOC), Oxygen Index (OI), Hydrogen Index (HI) and Production Index (PI) are automatically calculated. Rock-Eval pyrolysis data was screened using quality control criteria defined by Hall et al. (2016).

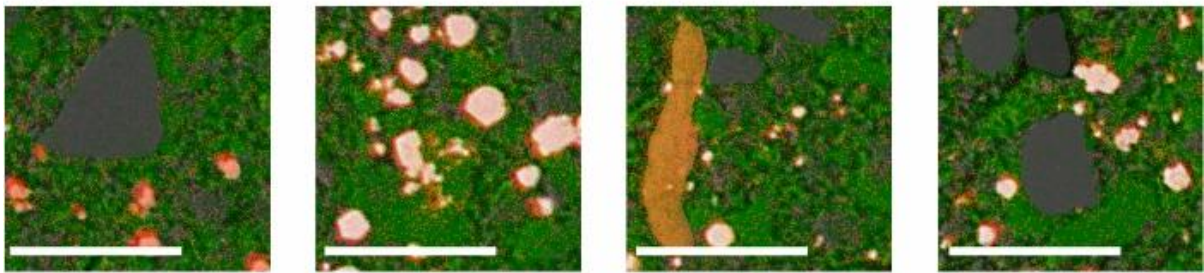
### **High resolution Scanning Electron Microscope mapping of shale samples**

Shale samples investigated for *in situ* Rb–Sr dating and trace element analysis were also mapped to determine their petrographic textures and elemental compositions. This is done to avoid the non-authigenic component of each sample, which can negatively impact the precision and accuracy of the geochronological results and potentially yield mixed ages (Field and Råheim, 1979). Back scatter electron (BSE) and elemental maps of shale samples were obtained using an FEI Quanta 450 Scanning Electron Microscope (SEM) with attached Oxford Ultima Max Large Area SDD EDS detector at Adelaide Microscopy following Subarkah et al. (2021).

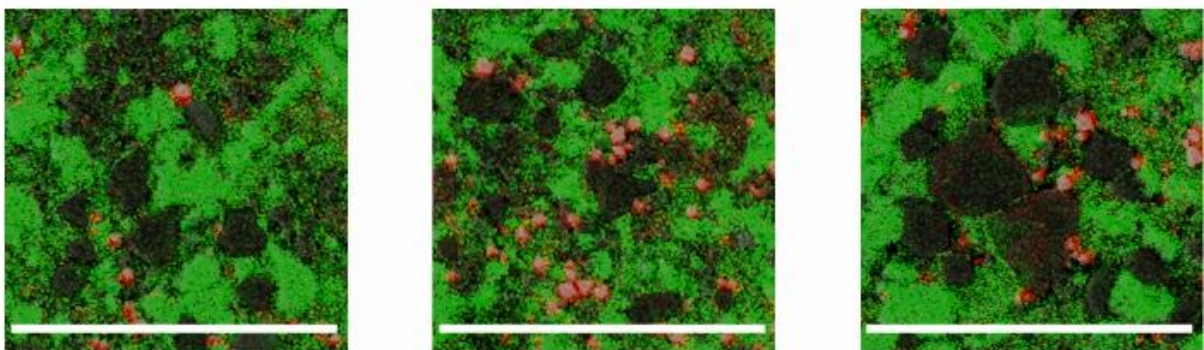
Images of samples in this study show that they have not experienced any extensive, late-stage alteration event (Fig. S.5.4A-D). Samples selected for this study do not look crystalline or fissile. Furthermore, they also do not show evidence of veining or foliation (Fig. S.5.4A-D). In addition, large, sub-rounded or sheet-like detrital grains are still preserved, along with primary sedimentary structures. These detrital grains largely consisted of quartz (Si-bearing, shown in black), micas or clays (K and Fe-bearing, shown in orange) and were circumvented during analysis. Authigenic K-bearing minerals are shown in green and look mottled and mossy, lacking distinct grain boundaries (Fig. S.5.4A-D). They can also be seen wrapping around resistant sedimentary grains, recording the compaction process as these rocks were deposited (Deepak et al., 2022; Rafiei and Kennedy, 2019; Rafiei et al., 2020; Subarkah et al., 2022). Another authigenic phase found in the samples bears Fe and S and are interpreted as

sulphides. These microcrystalline, framboidal crystals were interpreted to have formed syngenetically in the water column or possibly during early diagenesis in the top few centimetres of seafloor muds (Raiswell and Plant, 1980; Wilkin et al., 1996). They are consistently smaller than 100  $\mu\text{m}$  in nature, which further supports their early origin as opposed to forming during late diagenesis or metamorphism (Large et al., 2007; Large et al., 2017). As such, the petrographic evidence found in these samples indicate that they have not been affected by a secondary event after they were deposited. Consequently, the authigenic K-bearing (and therefore Rb-bearing) phases were targeted for *in situ* Rb–Sr dating, as they would have the best potential for recording the primary burial history of these samples.

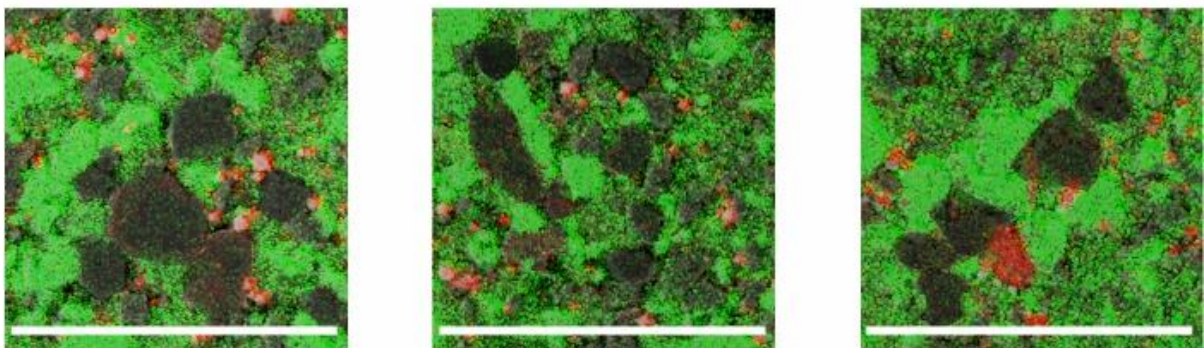
a)



b)



c)





d)

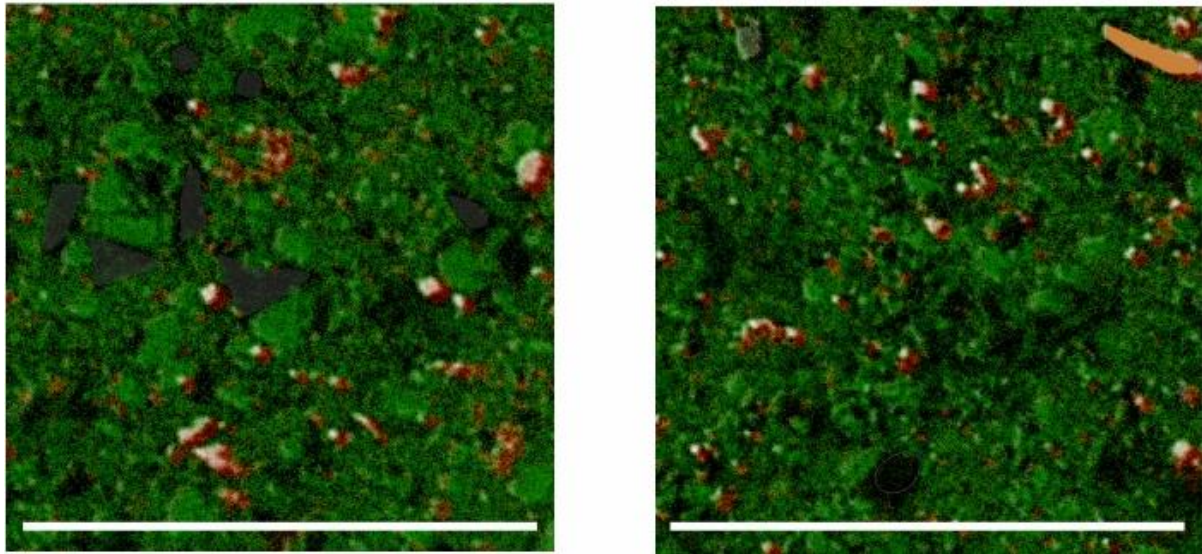


**Figure S.5.A-D.** BSE images overlain with elemental maps of the shale samples selected for in situ laser ablation analysis in this study. Samples a) and b) are from LV09001 at depths 463.60 m and 469.50 m. The Manbulloo S1 well was sampled at depths 785.24 m and 868.75 m, denoted as c) and d). White line = 100  $\mu$ m. Black = Si component, Green = K component, Red = Fe and S components, Orange = Fe and K components.

### Analytical Data

Source	Formation	Depth (m)	S1	S2	S3	Tmax	TO C	HI	OI	Production Index [S1/(s1+s2)]
PR2016-W005	Reward Dolostone	501	0.2 6	1.3 2	0.2 7	473.0 0	1.4 9	89.00	18.00	0.16
PR2016-W005	Reward Dolostone	503.3	0.6 1	1.7 1	0.1 3	459.0 0	2.0 8	82.00	6.00	0.26
PR2016-W005	Reward Dolostone	504.9	0.4 5	0.9 9	0.1 9	450.0 0	1.0 8	92.00	18.00	0.31
PR2016-W005	Reward Dolostone	507.9	0.8 1	2.3 5	0.2 3	440.0 0	1.7 7	133.0 0	13.00	0.26
PR2016-W005	Reward Dolostone	508.2	0.3 9	1.1 3	0.1 3	464.0 0	1.5 3	74.00	8.00	0.26
PR2016-W005	Fraynes Formation	710.6	0.2 1	1.5 6	0.4 5	437.0 0	1.1 3	138.0 0	40.00	0.12
PR2016-W005	Fraynes Formation	713.2	0.4 2	0.5 6	0.2 1	458.0 0	1.6 6	34.00	13.00	0.43
PR2016-W005	Fraynes Formation	714.4	0.3 6	0.6 0	0.1 0	451.0 0	1.5 2	39.00	7.00	0.38
PR2016-W005	Fraynes Formation	716.5	0.0 8	0.1 9	0.1 1	455.0 0	0.2 9	66.00	38.00	0.30
PR2016-W005	Fraynes Formation	720.5	0.0 7	0.1 5	0.3 9	438.0 0	0.3 2	47.00	123.0 0	0.32
CSR0477	Fraynes Formation	720.96	0.0 1	0.0 4	0.7 8	446.0 0	0.1 1	37.00	683.0 0	0.20
CSR0477	Fraynes Formation	721.26	0.0 4	0.7 1	0.4 2	475.0 0	1.8 4	39.00	23.00	0.05
Bullen	Fraynes Formation	721.36	0.2 8	2.0 3	0.2 1	451.0 0	3.4 9	58.00	6.00	0.12
Bullen	Fraynes Formation	721.49	0.4 6	7.2 3	0.2 2	446.0 0	8.3 9	86.00	3.00	0.06
Bullen	Fraynes Formation	721.49	0.3 0	7.0 3	0.2 3	449.2 3	8.1 0			0.04
Bullen	Fraynes Formation	721.69	0.2 7	3.2 3	0.0 2	448.7 7	4.4 1	73.24	0.45	0.08
Bullen	Fraynes Formation	721.93	0.4 2	2.3 8	0.0 7	479.0 0	0.0 0	1.46	0.00	0.15



Bullen	Fraynes Formation	722.07	0.5 9	2.3 0	0.0 4	473.0 0	6.4 2	36.00	1.00	0.20
Bullen	Fraynes Formation	722.07	0.6 7	2.2 0	0.0 7	471.1 7	5.6 0			0.23
Bullen	Fraynes Formation	722.18	0.5 1	1.8 5	0.0 0	467.4 2	6.1 4	30.13	0.00	0.22
Bullen	Fraynes Formation	722.37	0.6 0	1.4 1	0.3 1	458.3 6	5.9 3	23.78	5.23	0.30
Bullen	Fraynes Formation	722.55	0.4 4	1.0 8	0.3 4	466.0 0	3.0 6	35.00	11.00	0.29
PR2016- W005	Fraynes Formation	722.6	0.5 4	0.9 0	0.4 1	472.0 0	2.5 9	35.00	16.00	0.38
Bullen	Fraynes Formation	722.79	0.2 8	0.9 0	0.4 6	458.0 0	2.1 7	41.00	21.00	0.24
Bullen	Fraynes Formation	722.79	0.1 9	0.6 2	0.3 3	457.5 1	1.9 0			0.23
Bullen	Fraynes Formation	722.99	0.3 7	1.1 9	0.3 0	468.0 0	2.9 3	41.00	10.00	0.24
Bullen	Fraynes Formation	723.15	0.4 0	1.3 1	0.1 6	453.0 0	3.4 6	38.00	5.00	0.23
Bullen	Fraynes Formation	723.36	0.3 5	0.9 8	0.2 4	444.0 0	2.9 2	34.00	8.00	0.26
Bullen	Fraynes Formation	723.36	0.3 0	0.7 4	0.2 6	447.1 5	2.6 0			0.29
Bullen	Fraynes Formation	723.57	0.2 4	0.6 0	0.0 7	445.5 7	1.8 5	32.43	3.78	0.29
PR2016- W005	Fraynes Formation	725.5	0.2 1	0.2 8	0.4 9	448.0 0	1.0 7	26.00	46.00	0.43
CSR0477	Fraynes Formation	735.29	0.0 5	0.1 4	0.6 5	439.0 0	0.6 1	23.00	105.0 0	0.27
PR2016- W005	Fraynes Formation	743.5	0.8 5	2.1 8	0.2 0	469.0 0	4.9 8	44.00	4.00	0.28
PR2016- W005	Fraynes Formation	757.5	0.1 1	0.1 8	0.4 8	427.0 0	0.2 6	70.00	188.0 0	0.38
PR2016- W005	Fraynes Formation	759.4	0.1 0	0.1 8	0.4 9	434.0 0	0.2 8	65.00	176.0 0	0.36
PR2016- W005	Fraynes Formation	761.5	0.2 7	0.3 7	0.3 6	432.0 0	0.8 2	45.00	44.00	0.42
PR2016- W005	Fraynes Formation	763.6	0.3 1	0.4 1	0.3 1	444.0 0	0.3 5	117.0 0	89.00	0.43
PR2016- W005	Fraynes Formation	765.5	0.1 7	0.2 9	0.4 1	433.0 0	0.0 4	763.0 0	1079. 00	0.37
PR2016- W005	Fraynes Formation	767.4	0.1 6	0.3 0	0.2 1	435.0 0	0.3 3	91.00	64.00	0.35
CSR0477	Fraynes Formation	767.72	0.0 8	0.1 7	0.4 4	430.0 0	0.6 6	26.00	67.00	0.32
PR2016- W005	Fraynes Formation	769.5	0.2 4	0.4 3	0.3 6	427.0 0	1.0 6	41.00	34.00	0.36
PR2016- W005	Fraynes Formation	771.5	0.2 2	0.3 5	0.3 0	427.0 0	1.1 0	32.00	27.00	0.39
PR2016- W005	Fraynes Formation	773.4	0.2 1	0.2 6	0.3 9	431.0 0	0.8 3	31.00	47.00	0.45
PR2016- W005	Fraynes Formation	776.5	0.1 9	0.3 6	0.4 3	426.0 0	0.8 1	44.00	53.00	0.35
PR2016- W005	Fraynes Formation	778.4	0.3 0	0.5 4	0.3 0	434.0 0	1.2 5	43.00	24.00	0.36
CSR0477	Fraynes Formation	780	0.1 9	0.4 1	0.2 9	427.0 0	1.0 7	38.00	28.00	0.32
PR2016- W005	Fraynes Formation	780.6	0.2 6	0.4 4	0.1 9	420.0 0	1.2 2	36.00	16.00	0.37
Bullen	Fraynes Formation	780.77	0.2 5	0.6 4	0.2 8	430.7 8	1.1 9	53.78	23.53	0.28
Bullen	Fraynes Formation	781.7	0.4 3	0.8 7	0.3 8	436.2 0	1.5 3	56.86	24.84	0.33
PR2016- W005	Fraynes Formation	782.4	0.2 7	0.4 9	0.1 9	424.0 0	1.3 3	37.00	14.00	0.36
Bullen	Fraynes Formation	782.58	0.3 0	0.8 1	0.3 9	432.0 0	1.5 6	52.00	25.00	0.27

Bullen	Fraynes Formation	782.58	0.2 5	0.4 7	0.2 9	432.7 0	1.4 0				0.35
Bullen	Fraynes Formation	783.54	0.2 6	0.7 6	0.1 2	427.0 0	1.7 5	43.00	7.00		0.25
Bullen	Fraynes Formation	783.54	0.2 7	0.5 2	0.0 8	436.5 2	1.6 0				0.34
PR2016- W005	Fraynes Formation	784.4	0.6 6	0.6 9	0.1 7	435.0 0	2.5 1	27.00	7.00		0.49
Bullen	Fraynes Formation	784.65	0.4 0	1.1 1	0.1 2	440.0 0	3.4 3	32.00	3.00		0.26
Bullen	Fraynes Formation	784.65	0.4 4	0.9 7	0.1 3	442.3 8	3.3 0				0.31
Bullen	Fraynes Formation	785.07	0.7 3	1.6 0	0.0 3	454.0 6	5.0 9	31.43	0.59		0.31
Bullen	Fraynes Formation	785.24	0.8 0	2.2 0	0.1 2	451.0 0	6.2 5	35.00	2.00		0.27
Bullen	Fraynes Formation	785.46	0.5 4	1.5 5	0.1 3	450.0 0	5.0 3	31.00	3.00		0.26
Bullen	Fraynes Formation	785.46	0.5 8	1.2 9	0.0 9	453.3 3	4.6 0				0.31
Bullen	Fraynes Formation	786.05	0.6 4	1.5 2	0.0 3	466.6 8	5.0 6	30.04	0.59		0.30
Bullen	Fraynes Formation	786.26	0.3 3	0.4 8	0.0 4	451.5 6	2.5 9	18.53	1.54		0.41
PR2016- W005	Fraynes Formation	786.5	0.9 2	0.9 4	0.1 6	441.0 0	4.0 5	23.00	4.00		0.49
Bullen	Fraynes Formation	786.54	0.5 6	1.4 2	0.1 2	444.0 0	4.9 7	29.00	2.00		0.28
Bullen	Fraynes Formation	786.54	0.5 9	1.1 8	0.1 3	447.0 4	4.6 0				0.33
Bullen	Fraynes Formation	786.91	0.6 2	1.3 2	0.0 6	452.1 1	5.0 0	26.40	1.20		0.32
Bullen	Fraynes Formation	787.31	0.5 1	1.4 8	0.1 4	460.0 0	4.3 1	34.00	3.00		0.26
Bullen	Fraynes Formation	787.31	0.5 4	1.1 7	0.1 0	469.4 2	3.8 0				0.32
Bullen	Fraynes Formation	787.81	0.3 6	0.9 5	0.1 9	435.0 0	2.8 4	33.00	7.00		0.27
Bullen	Fraynes Formation	788.31	0.2 3	0.6 4	0.1 6	424.0 0	1.8 3	35.00	9.00		0.26
Bullen	Fraynes Formation	788.31	0.1 8	0.3 2	0.1 7	439.2 6	1.6 0				0.36
Bullen	Fraynes Formation	788.71	0.2 3	0.7 3	0.1 1	432.0 0	2.0 7	35.00	5.00		0.24
Bullen	Fraynes Formation	789.12	0.2 3	0.6 2	0.1 7	434.0 0	2.0 9	30.00	8.00		0.27
Bullen	Fraynes Formation	789.12	0.2 0	0.4 3	0.1 8	443.0 6	1.8 0				0.32
PR2016- W005	Fraynes Formation	789.4	0.2 8	0.3 1	0.2 6	439.0 0	0.0 4	795.0 0	667.0 0		0.47
Bullen	Fraynes Formation	789.46	0.1 9	0.6 5	0.1 3	420.0 0	1.7 9	36.00	7.00		0.23
PR2016- W005	Fraynes Formation	800.5	0.1 3	0.2 4	0.3 0	493.0 0	0.5 7	42.00	52.00		0.35
PR2016- W005	Fraynes Formation	804.4	0.1 7	0.2 7	0.1 1	492.0 0	0.9 0	30.00	12.00		0.39
PR2016- W005	Fraynes Formation	818.5	0.1 0	0.1 5	0.1 4	464.0 0	0.6 2	24.00	23.00		0.40
CSR0477	Fraynes Formation	822.8	0.0 0	0.0 3	0.1 1	517.0 0	0.1 1	32.00	107.0 0		0.12
PR2016- W005	Fraynes Formation	845.5	0.0 9	0.1 4	0.1 5	302.0 0	0.5 6	25.00	27.00		0.39
PR2016- W005	Fraynes Formation	847.5	0.0 7	0.1 3	0.0 9	302.0 0	0.3 4	38.00	26.00		0.35
PR2016- W005	Fraynes Formation	849.5	0.0 7	0.1 3	0.2 2	445.0 0	0.2 6	50.00	85.00		0.35
PR2016- W005	Fraynes Formation	851.4	0.0 9	0.1 4	0.0 7	305.0 0	0.3 6	39.00	19.00		0.39

CSR0477	Fraynes Formation	852.4	0.0 1	0.0 5	0.1 2	467.0 0	0.3 7	13.00	32.00	0.12
PR2016- W005	Fraynes Formation	853.5	0.1 1	0.1 5	0.0 7	311.0 0	0.3 8	40.00	19.00	0.42
PRMB1-205	Fraynes Formation	855.5	0.1 2	0.1 4	0.0 9	411.0 0	0.3 9	36.00	23.00	0.46
PR2016- W005	Fraynes Formation	857.5	0.3 6	0.2 3	0.0 5	439.0 0	1.7 0	14.00	3.00	0.61
PR2016- W005	Fraynes Formation	859.5	0.1 2	0.1 5	0.0 3	422.0 0	0.6 0	25.00	5.00	0.44
PR2016- W005	Fraynes Formation	861.4	0.1 3	0.1 5	0.0 3	425.0 0	0.7 0	21.00	4.00	0.46
PR2016- W005	Fraynes Formation	863.5	0.1 4	0.1 5	0.0 3	420.0 0	0.9 1	16.00	3.00	0.48
CSR0477	Fraynes Formation	863.75	0.0 1	0.0 4	0.9 7	437.0 0	0.9 2	4.00	105.0 0	0.22
CSR0477	Fraynes Formation	863.85	0.0 6	0.3 0	0.0 4	456.0 0	2.7 2	11.00	1.00	0.17
Bullen	Fraynes Formation	864.7	0.1 2	0.2 3	0.2 9	414.0 0	0.8 4	27.00	35.00	0.34
Bullen	Fraynes Formation	864.7	0.0 4	0.0 9	0.3 1	447.1 1	0.1 0			0.31
PR2016- W005	Fraynes Formation	865.7	0.5 2	0.3 2	0.0 5	432.0 0	2.1 1	15.00	2.00	0.62
Bullen	Fraynes Formation	865.8	0.0 8	0.3 5	0.0 1	481.0 0	1.6 1	22.00	1.00	0.19
Bullen	Fraynes Formation	865.8	0.0 5	0.2 3	0.0 3	492.6 9	1.3 0			0.18
Bullen	Fraynes Formation	867.2	0.0 7	0.4 1	0.0 3	433.0 0	1.0 5	39.00	3.00	0.15
Bullen	Fraynes Formation	867.2	0.0 3	0.1 2	0.0 4	467.7 0	0.8 0			0.20
Bullen	Fraynes Formation	867.5	0.1 1	0.4 3	0.0 0	506.9 5	2.2 0	19.55	0.00	0.20
PR2016- W005	Fraynes Formation	867.6	0.5 7	0.3 9	0.0 4	436.0 0	2.2 8	17.00	2.00	0.59
Bullen	Fraynes Formation	867.9	0.1 0	0.3 7	0.0 0	470.8 3	2.3 3	15.88	0.00	0.21
Bullen	Fraynes Formation	868.15	0.1 1	0.5 8	0.0 2	436.0 0	2.4 5	24.00	1.00	0.16
Bullen	Fraynes Formation	868.15	0.0 7	0.3 6	0.0 5	497.9 0	2.2 0			0.16
Bullen	Fraynes Formation	868.49	0.1 3	0.2 6	0.0 0	471.7 2	1.6 6	15.66	0.00	0.33
Bullen	Fraynes Formation	868.66	0.1 3	0.3 7	0.0 0	463.0 4	2.0 1	18.41	0.00	0.26
Bullen	Fraynes Formation	868.75	0.0 9	0.4 3	0.0 2	482.0 0	1.8 5	23.00	1.00	0.17
Bullen	Fraynes Formation	868.75	0.0 5	0.2 9	0.0 5	494.3 9	1.6 0			0.15
Bullen	Fraynes Formation	868.9	0.0 9	0.3 1	0.0 0	492.1 9	1.8 9	16.40	0.00	0.23
Bullen	Fraynes Formation	869.3	0.1 0	0.4 0	0.0 2	475.0 0	1.7 8	22.00	1.00	0.20
PR2016- W005	Fraynes Formation	869.4	0.2 1	0.2 2	0.0 5	448.0 0	0.1 8	125.0 0	28.00	0.49
Bullen	Fraynes Formation	869.58	0.1 0	0.4 5	0.0 5	501.0 0	1.9 0	24.00	3.00	0.18
Bullen	Fraynes Formation	869.58	0.0 6	0.3 0	0.0 8	501.2 0	1.7 0			0.17
Bullen	Fraynes Formation	869.77	0.0 7	0.2 8	0.0 0	501.8 0	1.5 6	17.95	0.00	0.20
Bullen	Campbell Springs Dolomite	870.1	0.1 1	0.4 6	0.0 2	372.0 0	1.7 9	26.00	1.00	0.19
Bullen	Campbell Springs Dolomite	870.53	0.0 8	0.2 3	0.3 4	423.0 0	0.8 4	27.00	40.00	0.26
Bullen	Campbell Springs Dolomite	870.53	0.0 3	0.0 6	0.2 3	484.1 3	0.3 0			0.33

Bullen	Campbell Springs Dolomite	871.22	0.1 2	0.5 3	0.0 7	428.0 0	1.9 5	27.00	4.00	0.18
PR2016-W005	Campbell Springs Dolomite	871.4	0.3 4	0.3 7	0.0 7	462.0 0	2.6 3	14.00	3.00	0.80
Bullen	Campbell Springs Dolomite	871.48	0.1 4	0.5 6	0.0 2	461.0 0	2.3 6	24.00	1.00	0.20
Bullen	Campbell Springs Dolomite	871.48	0.0 6	0.3 0	0.0 4	494.8 3	2.3 0			0.17
Bullen	Campbell Springs Dolomite	872.93	0.0 7	0.3 9	0.0 0	508.8 2	1.6 5	23.64	0.00	0.15
CSR0477	Campbell Springs Dolomite	873.2	0.0 3	0.4 8	0.0 8	516.0 0	2.1 4	22.00	4.00	0.06
CSR0477	Campbell Springs Dolomite	873.25	0.0 1	0.1 4	0.4 8	493.0 0	0.5 9	25.00	82.00	0.08
PR2016-W005	Campbell Springs Dolomite	953.5	0.0 7	0.1 3	0.0 7	558.0 0	0.1 9	68.00	37.00	0.35
PR2016-W005	Blue Hole Formation	1086.7	0.0 7	0.0 9	0.0 6	362.0 0	0.2 1	42.00	28.00	0.44
PR2016-W005	Kunja Siltstone	1101.4	0.0 6	0.0 8	0.0 4	327.0 0	0.2 5	32.00	16.00	0.43
PR2016-W005	Kunja Siltstone	1118.5	0.0 6	0.0 8	0.0 3	316.0 0	0.1 6	49.00	19.00	0.43
PR2016-W005	Kunja Siltstone	1133.4	0.0 5	0.0 7	0.1 1	389.0 0	0.2 1	33.00	53.00	0.42
PR2016-W005	Kunja Siltstone	1146.6	0.0 9	0.0 5	0.0 5	390.0 0	0.3 6	14.00	14.00	0.64
PR2016-W005	Kunja Siltstone	1158.5	0.1 1	0.0 7	0.0 4	313.0 0	0.4 7	15.00	9.00	0.61
PR2016-W005	Kunja Siltstone	1170.5	0.0 8	0.0 7	0.0 3	310.0 0	0.3 5	20.00	9.00	0.53
PR2016-W005	Kunja Siltstone	1172.5	0.1 0	0.0 9	0.1 0	410.0 0	0.4 2	22.00	24.00	0.53
PR2016-W005	Mallabah Dolostone	1199.6	0.0 9	0.0 8	0.0 5	412.0 0	0.3 3	25.00	15.00	0.53

Table S.5.2. Shale source-rock analysis for samples from Manbulloo S1.

Formation	Depth	P (ppm)	V (ppm)	Mo (ppm)	Fe (ppm)	Al (ppm)	Cr (ppm)	Ti (ppm)	Al wt. %	P/Al	V/Al	Mo/Al	Cr/Al	V/Mo
Upper McArthur	485.75	9.09			3074.17	58.62	14.51		0.01	0.16	0.00	0.00		#DIV/0!
Reward Dolomite	527.40	13.72			5341.87	130.10	0.52		0.01	0.11	0.00	0.00	39.71	#DIV/0!
Reward Dolomite	558.75	4.43			3671.82	58.65	1.43		0.01	0.08	0.00	0.00	244.03	#DIV/0!
Reward Dolomite	585.35	4.55			3678.34	133.67			0.01	0.03	0.00	0.00	0.00	#DIV/0!

Fraynes Formation	Fraynes Formation	Fraynes Formation	Fraynes Formation	Fraynes Formation	Reward Dolomite	Reward Dolomite	Reward Dolomite	Reward Dolomite	Reward Dolomite	Reward Dolomite	Reward Dolomite	Reward Dolomite	Reward Dolomite
721.69	721.49	721.36	708.40	707.20	704.40	679.50	666.70	642.70	619.10	613.90	612.40		
950.00	470.00	650.00	10.45	9.91	10.88	3.12	5.71	7.48	8.46	161.70	4.13		
95.00	60.00	90.00											
6.00	101.00	14.00											
1675.35	1116.90	1116.90	4280.30	4884.28	9161.39	3195.25	2356.51	4042.22	2257.68	734.85	2691.61		
7830.00	7020.00	6480.00	932.05	241.77	535.79	76.93	141.55	121.63	107.66	193.31	110.44		
30.00	40.00	30.00	2.00	0.80	2.17		1.00	2.23	0.60				
1768.08	2517.27	1678.18											
0.78	0.70	0.65	0.09	0.02	0.05	0.01	0.01	0.01	0.01	0.02	0.01		
0.12	0.07	0.10	0.01	0.04	0.02	0.04	0.04	0.06	0.08	0.84	0.04		
121.33	85.47	138.89	0.00	0.00	0.00	0.00	0.00	0.00	0.00	0.00	0.00		
7.66	143.87	21.60	0.00	0.00	0.00	0.00	0.00	0.00	0.00	0.00	0.00		
38.31	56.98	46.30	21.44	33.14	40.43	0.00	70.40	183.28	55.28	0.00	0.00		
15.83	0.59	6.43	#DIV/0!	#DIV/0!	#DIV/0!	#DIV/0!	#DIV/0!	#DIV/0!	#DIV/0!	#DIV/0!	#DIV/0!		

Fraynes Formation	Fraynes Formation	Fraynes Formation	Fraynes Formation	Fraynes Formation	Fraynes Formation	Fraynes Formation	Fraynes Formation	Fraynes Formation	Fraynes Formation	Fraynes Formation	Fraynes Formation	Fraynes Formation	Fraynes Formation	Fraynes Formation	Fraynes Formation	Fraynes Formation	Fraynes Formation	Fraynes Formation
780.77	755.60	729.90	723.57	723.36	723.15	722.99	722.79	722.55	722.37	722.18	722.07							
1000.00	8.56	17.94	1200.00	1360.00	2000.00	900.00	550.00	250.00	7600.00	1050.00	690.00							
165.00			90.00	120.00	150.00	75.00	40.00	30.00	55.00	70.00	60.00							
2.50			13.00	13.50	17.00	8.50	7.00	1.00	9.50	6.00	10.00							
2233.80	2876.92	7597.60	1675.35	1675.35	2233.80	1116.90	1116.90	1675.35	5026.05	5026.05	3909.15							
4320.00	330.95	789.78	8640.00	7020.00	7020.00	3510.00	4860.00	2970.00	5400.00	5670.00	5670.00							
30.00	0.58	2.73		40.00	50.00					50.00	40.00							
2067.75			1768.08	3296.42	1947.88	988.93	1857.98	749.19	1378.50	1498.37	2637.14							
0.43	0.03	0.08	0.86	0.70	0.70	0.35	0.49	0.30	0.54	0.57	0.57							
0.23	0.03	0.02	0.14	0.19	0.28	0.26	0.11	0.08	1.41	0.19	0.12							
381.94	0.00	0.00	104.17	170.94	213.68	213.68	82.30	101.01	101.85	123.46	105.82							
5.79	0.00	0.00	15.05	19.23	24.22	24.22	14.40	3.37	17.59	10.58	17.64							
69.44	17.59	34.57	0.00	56.98	71.23	0.00	0.00	0.00	0.00	88.18	70.55							
66.00	#DIV/0!	#DIV/0!	6.92	8.89	8.82	8.82	5.71	30.00	5.79	11.67	6.00							

787.31	786.91	786.54	786.26	786.05	785.46	785.24	785.07	784.65	783.54	782.58	781.70
1580.00	2800.00	2050.00	1300.00	2400.00	1180.00	2000.00	1600.00	1940.00	1330.00	1200.00	850.00
240.00	235.00	210.00	125.00	250.00	150.00	240.00	210.00	120.00	190.00	210.00	130.00
27.00	31.50	28.00	19.50	30.00	41.00	51.00	29.50	14.50	11.50	5.00	7.00
3909.15	3350.70	2792.25	22896.45	3909.15	4467.60	3350.70	3350.70	2233.80	2792.25	2233.80	2233.80
7290.00	6750.00	6480.00	3780.00	7020.00	7290.00	6750.00	6480.00	7020.00	7830.00	6210.00	4860.00
40.00	60.00	70.00	50.00	50.00	60.00	60.00	60.00	60.00	60.00	40.00	50.00
3116.61	1947.88	3416.29	1288.60	2007.82	3056.68	2157.66	1977.85	3356.35	3715.96	3596.09	2127.69
0.73	0.68	0.65	0.38	0.70	0.73	0.68	0.65	0.70	0.78	0.62	0.49
0.22	0.41	0.32	0.34	0.34	0.16	0.30	0.25	0.28	0.17	0.19	0.17
329.22	348.15	324.07	330.69	356.13	205.76	355.56	324.07	170.94	242.66	338.16	267.49
37.04	46.67	43.21	51.59	42.74	56.24	75.56	45.52	20.66	14.69	8.05	14.40
54.87	88.89	108.02	132.28	71.23	0.00	88.89	92.59	85.47	0.00	64.41	102.88
8.89	7.46	7.50	6.41	8.33	3.66	4.71	7.12	8.28	16.52	42.00	18.57

Campbell Springs Dolomite	868.49	868.15	867.90	867.50	867.20	865.80	801.10	789.46	789.12	788.71	788.31	787.81
	200.00	260.00	300.00	250.00	270.00	300.00	11.45	1900.00	2690.00	3000.00	2110.00	1200.00
	90.00	60.00	90.00	90.00	50.00	60.00		190.00	210.00	215.00	170.00	225.00
	0.50	1.00	0.50	0.50	2.00	1.00		9.50	12.50	13.00	8.00	15.50
	2233.80	1675.35	2233.80	2233.80	1675.35	1675.35	4866.97	2792.25	2233.80	2792.25	2792.25	2792.25
	9450.00	9450.00	9450.00	9450.00	10260.00	9990.00	257.15	6750.00	6750.00	7290.00	6750.00	5940.00
	80.00	60.00	60.00	60.00	70.00		0.83	60.00	70.00	60.00	60.00	50.00
	2517.27	3656.03	2427.36	2337.46	3596.09	3955.70		1887.95	3116.61	2157.66	3416.29	1768.08
	0.95	0.95	0.95	0.95	1.03	1.00	0.03	0.68	0.68	0.73	0.68	0.59
	0.02	0.03	0.03	0.03	0.03	0.03	0.04	0.28	0.40	0.41	0.31	0.20
	95.24	63.49	95.24	95.24	48.73	60.06	0.00	281.48	311.11	294.92	251.85	378.79
	0.53	1.06	0.53	0.53	1.95	1.00	0.00	14.07	18.52	17.83	11.85	26.09
	84.66	63.49	63.49	63.49	68.23	0.00	32.28	88.89	103.70	82.30	88.89	84.18
	180.00	60.00	180.00	180.00	25.00	60.00	#DIV/0!	20.00	16.80	16.54	21.25	14.52



Campbell Springs Dolomite	Campbell Springs Dolomite	Campbell Springs Dolomite	Campbell Springs Dolomite	Campbell Springs Dolomite	Campbell Springs Dolomite	Campbell Springs Dolomite	Campbell Springs Dolomite	Campbell Springs Dolomite	Campbell Springs Dolomite	Campbell Springs Dolomite	Campbell Springs Dolomite	Campbell Springs Dolomite	Campbell Springs Dolomite	Campbell Springs Dolomite	Campbell Springs Dolomite	Campbell Springs Dolomite	Campbell Springs Dolomite	Campbell Springs Dolomite	Campbell Springs Dolomite
883.70	880.80	872.93	871.48	871.22	870.53	870.10	869.77	869.58	869.30	868.90	868.75								
45.95	16.42	250.00	250.00	300.00	110.00	250.00	250.00	270.00	300.00	250.00	270.00								
		90.00	70.00	70.00	10.00	80.00	90.00	50.00	90.00	90.00	70.00								
		2.00	3.50	2.00	7.00	0.50	0.50	1.00	2.50	0.50	1.00								
6687.65	4105.15	1675.35	1675.35	1675.35	1675.35	1675.35	1675.35	1675.35	2233.80	2233.80	1675.35								
357.00	204.44	8910.00	8100.00	9180.00	3240.00	9180.00	9450.00	7020.00	9180.00	9180.00	9720.00								
2.97		60.00	60.00	50.00		50.00	50.00	50.00	50.00	60.00	60.00								
		2517.27	3296.42	1917.92	1378.50	2157.66	2367.43	3116.61	2307.49	2367.43	3895.77								
0.04	0.02	0.89	0.81	0.92	0.32	0.92	0.95	0.70	0.92	0.92	0.97								
0.13	0.08	0.03	0.03	0.03	0.03	0.03	0.03	0.04	0.03	0.03	0.03								
0.00	0.00	101.01	86.42	76.25	30.86	87.15	95.24	71.23	98.04	98.04	72.02								
0.00	0.00	2.24	4.32	2.18	21.60	0.54	0.53	1.42	2.72	0.54	1.03								
83.28	0.00	67.34	74.07	54.47	0.00	54.47	52.91	71.23	54.47	65.36	61.73								
#DIV/0!	#DIV/0!	45.00	20.00	35.00	1.43	160.00	180.00	50.00	36.00	180.00	70.00								

Blue Hole Formation	Blue Hole Formation	Blue Hole Formation	Blue Hole Formation	Campbell Springs Dolomite	Campbell Springs Dolomite	Campbell Springs Dolomite	Campbell Springs Dolomite	Campbell Springs Dolomite
1052.50	1040.60	1003.90	977.70	950.60	932.50	899.30		
10.19	7.97	44.17	16.73	12.71	14.67	16.27		
4395.28	13983.66	7412.55	5444.39	4982.46	3619.75	4111.10		
953.38	553.75	707.84	355.38	429.26	588.19	349.33		
1.18	1.09	3.63	1.60	2.15	1.08	0.80		
0.10	0.06	0.07	0.04	0.04	0.06	0.03		
0.01	0.01	0.06	0.05	0.03	0.02	0.05		
0.00	0.00	0.00	0.00	0.00	0.00	0.00		
0.00	0.00	0.00	0.00	0.00	0.00	0.00		
12.33	19.61	51.30	45.02	50.04	18.31	22.85		
#DIV/0!	#DIV/0!	#DIV/0!	#DIV/0!	#DIV/0!	#DIV/0!	#DIV/0!		#DIV/0!

Table S.5.3. Shale and calcareous siltstone whole-rock analysis for samples from Manbulloo S1.

Reward	Reward	Upper	Formation
558.75	527.4	485.75	Depth (m)
102143.36	115188.89	124591.26	24 -> 24 Mg
58.65	130.10	58.62	27 -> 27 Al
4.43	13.72	9.09	31 -> 47 P
16.33	13.01	22.54	39 -> 39 K
29518.07	32747.24	35629.20	43 -> 43 Ca
1.43	0.52	14.51	52 -> 52 Cr
2337.64	1758.43	2179.78	55 -> 55 Mn
3622.41	5251.71	3020.83	57 -> 73 Fe
2.48	0.15	0.86	63 -> 63 Cu
15.30	12.34	37.07	66 -> 66 Zn
			85 -> 85 Rb
17.38	26.04	23.22	88 -> 88 Sr
1.25	3.96	0.68	137 -> 137
0.26	0.98	1.44	139 -> 139 La
1.06	3.70	3.37	140 -> 140
0.09	0.48	0.35	141 -> 141 Pr
0.73	2.25	1.49	146 -> 146
0.39	0.86	0.28	147 -> 147
	0.18		153 -> 153
0.86	1.67	0.39	157 -> 157
	0.10		159 -> 159
0.38	0.56	0.16	163 -> 163
			165 -> 165
	0.14		166 -> 166 Er
			169 -> 169
			172 -> 172

Fraynes	Fraynes	Fraynes	Reward	Reward	Reward	Reward	Reward	Reward	Reward	Reward	Reward	Reward	Reward	Reward	Reward	Reward	Reward	Reward	Reward	Reward
755.6	729.9	708.4	707.2	704.4	679.5	666.7	642.7	619.1	613.9	612.4	585.35									
14260.64	55810.01	56383.00	71340.57	191087.57	81971.98	92902.01	106657.44	107589.19	4133.16	124337.65	103171.58									
330.95	789.78	932.05	241.77	535.79	76.93	141.55	121.63	107.66	193.31	110.44	133.67									
8.56	17.94	10.45	9.91	10.88	3.12	5.71	7.48	8.46	161.70	4.13	4.55									
91.02	180.59	305.01	47.47	110.79	11.84	10.01	18.23	25.96	142.62	6.47	23.81									
14055.16	39382.33	16198.76	20046.71	51913.50	23903.07	27187.07	28778.78	29208.94	50135.98	35186.23	27941.31									
0.58	2.73	2.00	0.80	2.17		1.00	2.23	0.60												
542.70	667.79	873.33	1030.04	2548.16	1235.99	1711.88	1947.47	2598.35	1860.18	2598.91	2121.11									
2855.75	7513.69	4232.18	4810.09	9518.57	3136.73	2298.47	3996.96	2208.45	754.78	2643.51	3618.45									
0.09	0.70	0.53	0.31	1.51	1.47	0.95	0.99	1.80	73.26	1.85	9.63									
	5.97	1.69	4.77	17.59	16.21	41.63	18.31	21.01	55.55	15.67	11.88									
0.13	0.41	0.40																		
20.33	52.14	7.85	6.76	19.13	8.27	10.66	12.25	16.33	59.24	19.79	16.99									
1.60	4.68	3.35	0.82	2.67	0.72	0.67	2.01	4.30	4.03	0.99	0.97									
5.21	20.60	1.64	0.91	2.07	0.42	0.33	0.30	0.28	4.72	0.38	0.30									
11.97	43.86	4.31	2.19	4.71	1.05	0.93	0.91	0.98	14.96	1.21	1.09									
1.18	4.82	0.48	0.21	0.49					1.67	0.11	0.09									
4.31	16.38	1.95	0.97	2.03	0.45	0.39	0.48	0.58	8.57	0.81	0.67									
0.65	2.45	0.33		0.30					2.20	0.35										
	0.28																			
0.50	1.91	0.30	0.13	0.39	0.10	0.14	0.35	0.56	2.81	0.86	0.84									
	0.18																			
0.38	1.29	0.28	0.09	0.22	0.03	0.03	0.10	0.20	1.31	0.32	0.28									
	0.17																			
0.15	0.63	0.12		0.07																
0.11	0.49	0.13																		

Blue Hole	Blue Hole	Blue Hole	Blue Hole	Campbell	Campbell	Campbell	Campbell	Campbell	Campbell	Campbell	Campbell	Campbell	Campbell
1052.5	1040.6	1003.9	977.7	950.6	932.5	899.3	883.7	880.8	801.1				
110268.88	86427.28	102518.60	99489.67	118191.13	105592.22	119025.94	108335.05	108144.79	35467.55				
953.38	553.75	707.84	353.38	429.26	588.19	349.33	357.00	204.44	257.15				
10.19	7.97	44.17	16.73	12.71	14.67	16.27	45.95	16.42	11.45				
144.75	104.62	102.94					5.21		73.73				
29470.81	25184.55	27807.31	27526.93	32365.22	28300.63	34684.12	32260.48	30647.58	11636.82				
1.18	1.09	3.63	1.60	2.15	1.08	0.80	2.97		0.83				
3571.48	1472.90	1311.25	1219.18	2513.39	1345.89	1108.64	671.22	1644.40	290.45				
4309.81	14391.94	7336.53	5378.75	4948.08	3562.81	4053.44	6590.37	4063.53	4846.79				
1.41	0.19	0.83	0.40	0.80	0.34	0.14	0.55	0.32					
66.05	6.24	22.59	17.30	33.22	41.68	10.95	7.49	30.33	2.33				
0.39	0.35	0.27											
26.22	18.35	50.87	33.92	34.14	37.58	66.66	61.46	46.00	4.48				
4.96	3.71	16.80	2.86	0.76	10.12	6.71	6.77	2.07	1.51				
3.75	6.77	2.15	2.22	0.89	1.60	1.30	1.47	0.94	2.49				
14.76	18.13	8.92	6.63	3.08	4.45	3.63	3.25	2.88	6.80				
2.35	2.38	1.43	0.84	0.36	0.50	0.40	0.33	0.38	1.04				
10.43	9.25	7.40	3.58	2.04	2.17	1.85	1.48	1.92	4.67				
2.33	1.71	2.54	0.85	0.63	0.53	0.45		0.61	0.84				
0.36	0.23	0.53	0.13										
2.40	1.61	2.93	1.02	0.82	0.70	0.60	0.29	0.80	0.65				
0.25	0.17	0.41	0.07										
1.70	1.22	2.62	0.59	0.68	0.45	0.31	0.15	0.58	0.38				
0.24	0.18	0.37											
0.79	0.56	1.03	0.22	0.26	0.15			0.25	0.14				
0.54	0.35	0.63	0.09	0.20				0.22					

Table S.5.4. Carbonate geochemical data for samples from Manbulloo S1.

sample		Depth	d18Oavg	std	d13Cavg	std	87/86 Sr	2se for 87/86 Sr
1	Reward Dolomite Equiv.	429.2	-6.432653911	0.272995055	0.743686318	0.171256087		
2	Reward Dolomite Equiv.	444.9	-6.080056671	0.172720159	0.242768957	0.047768361		
5	Reward Dolomite Equiv.	465.85	-7.095421456	0.115870749	0.054201331	0.081173444		
7	Reward Dolomite Equiv.	481.26	-7.523975637	0.062681278	0.239729811	0.044288666		
8	Reward Dolomite Equiv.	485.75	-7.958547742	0.031538798	0.192321641	0.068354799	0.707043	0.000012

10	Reward Dolomite Equiv.	500.95	-8.346268453	0.175501286	-1.021275026	0.139644442		
15	Reward Dolomite Equiv.	524.45	-9.875162363	0.145151114	0.394386359	0.024589872	0.706071	0.000018
18	Reward Dolomite Equiv.	558.75	-9.879151521	0.053097854	0.444878246	0.003522209	0.707111	0.000005
20	Reward Dolomite Equiv.	568	-10.60312225	0.060720079	-0.125008105	0.063575879		
26	Reward Dolomite Equiv.	585.35	-11.73437518	0.041195753	-0.164043029	0.096298945		
28	Reward Dolomite Equiv.	595.7	-11.63185519	0.135775863	0.059750486	0.119107998	0.707292	0.000005
36	Reward Dolomite Equiv.	630.4	-8.861603481	0.150596528	0.198280852	0.061127185		
37	Reward Dolomite Equiv.	636.5	-10.12908996	0.079557018	-0.013943703	0.039231291		
38	Reward Dolomite Equiv.	642.7	-9.913260668	0.090368955	0.159955283	0.050601799		
40	Reward Dolomite Equiv.	651.5	-10.36041751	0.106829555	0.426551725	0.018176584	0.708052	0.000012
42	Reward Dolomite Equiv.	661.85	-11.23868874	0.150984636	0.127541353	0.071812339		
43	Reward Dolomite Equiv.	666.7	-9.440722212	0.187402475	0.670877668	0.056778371		
43	Reward Dolomite Equiv.	666.7	-9.439276353	0.175936364	0.457322991	0.135899185		
44	Reward Dolomite Equiv.	673.15	-11.43252333	0.122688898	0.276926591	0.016719458	0.707402	0.000006
45	Reward Dolomite Equiv.	679.5	-9.58573367	0.084305268	0.642135268	0.06775063		
46	Reward Dolomite Equiv.	686.05	-9.389797557	0.002897521	0.740228009	0.044717986		
47	Reward Dolomite Equiv.	694.55	-9.202956039	0.045727377	0.409683863	0.045124469	0.707545	0.000018
48	Reward Dolomite Equiv.	697.3	-7.483310067	0.215823935	0.778684602	0.152475418	0.707545	0.000018
49	Reward Dolomite Equiv.	699.7	-7.90478559	0.128323761	0.784910335	0.03413425		
50	Reward Dolomite Equiv.	700.5	-7.770240373	0.003068282	0.763136783	0.029011737	0.706608	0.000008
51	Reward Dolomite Equiv.	701.8	-8.507567033	0.146451422	0.456607925	0.042125258		
52	Reward Dolomite Equiv.	703.2	-7.787621917	0.160123072	0.461664627	0.133950035		
53	Reward Dolomite Equiv.	704.4	-7.642983453	0.209531019	0.947963841	0.056381034		
54	Reward Dolomite Equiv.	705.9	-7.403029815	0.168332336	0.60884545	0.043605898		
54	Reward Dolomite Equiv.	705.9	-7.373456375	0.184421953	0.491145094	0.136893321		
55	Reward Dolomite Equiv.	707.2	-7.344042307	0.191480366	0.71761229	0.089353682		
56	Fraynes Formation (Barney)	708.4	-7.682622587	0.149559126	0.163758591	0.057961365		
59	Fraynes Formation (Barney)	710	-7.868978406	0.079718562	-0.518853999	0.030921446	0.709495	0.000014
61	Fraynes Formation (Barney)	711.1	-8.728420113	0.084351968	-1.271790215	0.031768229	0.707841	0.000007
61	Fraynes Formation (Barney)	711.1	-8.785628852	0.032265758	-1.187831369	0.110501578	0.707841	0.000007
62	Fraynes Formation (Barney)	713	-7.446701998	0.043059671	-0.210739318	0.189345208	0.709342	0.000006
63	Fraynes Formation (Barney)	714.1	-7.719427843	0.163577135	-0.22795477	0.049123738	0.721634	0.000007
66	Fraynes Formation (Barney)	715.5	-7.514724527	0.087763232	-0.298717259	0.06945973		
67	Fraynes Formation (Barney)	716	-6.43461882	0.046917115	-0.400990996	0.06298746		
68	Fraynes Formation (Barney)	716.95	-8.606748603	0.228729747	-0.818651655	0.107034716		
72	Fraynes Formation (Barney)	721.1	-8.993758443	0.039267535	-0.409330037	0.143495682		
79	Fraynes Formation (Barney)	722.37	-6.951564163	0.345935464	-0.535991203	0.232431741		
88	Fraynes Formation (Barney)	727.1	-7.422197548	0.200446449	-1.34169538	0.06866483		
89	Fraynes Formation (Barney)	729.9	-9.619753099	0.185467948	-1.051861024	0.104600464		
89	Fraynes Formation (Barney)	729.9	-9.65974904	0.230315548	-1.171759875	0.142289011		
91	Fraynes Formation (Barney)	738.4	-9.202979864	0.262165765	-0.536535977	0.133834041		
92	Fraynes Formation (Barney)	740.8	-7.125267908	0.357034	0.108375594	0.176334327		
93	Fraynes Formation (Barney)	744.7	-7.175117474	0.205555881	-0.626290269	0.204711479		
94	Fraynes Formation (Barney)	745.3	-9.784422676	0.160560125	-1.108821221	0.087030613	0.71113	0.000004
96	Fraynes Formation (Barney)	747.3	-8.994889677	0.170962706	-0.625061108	0.081388352		

97	Fraynes Formation (Barney)	750.4	-10.31699989	0.021642683	-1.385530431	0.073638154		
99	Fraynes Formation (Barney)	755.6	-10.00167357	0.049490782	-1.634307684	0.094528017		
100	Fraynes Formation (Barney)	757.2	-9.534772083	0.032021263	-1.4136435	0.029347052		
104	Fraynes Formation (Barney)	771.2	-8.380812534	0.265324195	-1.169682746	0.116492908		
105	Fraynes Formation (Barney)	775.1	-9.423275354	0.158245894	-1.408359797	0.279459799		
106	Fraynes Formation (Barney)	779.9	-9.037724306	0.322588592	-1.048084734	0.121914318		
116	Fraynes Formation (Barney)	786.26	-7.762632922	1.103525695	-1.304749043	0.223576271	0.710993	0.000004
125	Fraynes Formation (Barney)	790.4	-8.135723537	0.170671732	-1.021435488	0.00892786		
126	Fraynes Formation (Barney)	796.97	-9.093279908	0.077226145	-1.167734615	0.017667273		
128	Fraynes Formation (Barney)	801.1	-8.391785761	0.207973975	-1.115853124	0.07739064		
129	Fraynes Formation (Barney)	805.7	-8.683056492	0.126725253	-1.084020783	0.014777902		
131	Fraynes Formation (Barney)	813.25	-10.01917953	0.26643004	-1.000295625	0.137264069		
132	Fraynes Formation (Barney)	819.6	-9.308435952	4.593873111	-1.086435127	1.092600974		
133	Fraynes Formation (Barney)	830.17	-8.915891427	0.051673961	-1.023004425	0.017891081		
149	Fraynes Formation (Barney)	869.58	-7.72225343	0.101033735	-1.212916686	0.413675635	0.720968	0.000011
156	Campbell Springs Dolomite	873.8	-6.127150786	0.288817956	-1.358200825	0.126236725		
156	Campbell Springs Dolomite	873.8	-6.443893526	0.158051953	-1.701345727	0.103743509		
157	Campbell Springs Dolomite	875.32	-7.204084384	0.179735704	-1.444035714	0.034835943		
158	Campbell Springs Dolomite	876.6	-8.020555857	0.024339763	-1.264676026	0.017355459		
159	Campbell Springs Dolomite	877.9	-7.144816688	0.019775664	-1.119665299	0.077798706		
160	Campbell Springs Dolomite	878.9	-9.034843414	0.060340853	-1.146130328	0.050394652		
161	Campbell Springs Dolomite	880.2	-6.448886977	0.080497354	-1.448361342	0.109707926		
162	Campbell Springs Dolomite	880.8	-6.256537694	0.173110138	-1.224203505	0.078652532		
163	Campbell Springs Dolomite	881.9	-7.570992692	0.267997648	-1.516496046	0.0633498		
163	Campbell Springs Dolomite	881.9	-7.202489968	0.269668085	-1.571253546	0.037543653		
164	Campbell Springs Dolomite	882.9	-7.052973139	0.152078004	-1.222164471	0.024597033		
165	Campbell Springs Dolomite	883.7	-6.60591858	0.261878697	-1.681201862	0.043100751	0.705446	0.000005
166	Campbell Springs Dolomite	885.6	-7.739000151	0.109699224	-1.455029878	0.038545317		
167	Campbell Springs Dolomite	887.9	-8.959616736	0.165840226	-1.411238993	0.154670892		
169	Campbell Springs Dolomite	893.1	-9.050599083	0.179875772	-1.568772991	0.045110893		
170	Campbell Springs Dolomite	895.6	-7.628602285	0.205511232	-1.653902216	0.051220314		
171	Campbell Springs Dolomite	899.3	-7.203974223	0.202968932	-1.617180904	0.201845672	0.705383	0.000004
173	Campbell Springs Dolomite	905.9	-8.360660813	0.150120177	-1.564712961	0.110574499		
173	Campbell Springs Dolomite	905.9	-8.209730133	0.249296417	-1.762057923	0.051108144		
174	Campbell Springs Dolomite	913.1	-7.093527987	0.132597731	-0.873099443	0.076194355		
176	Campbell Springs Dolomite	920	-8.958863526	0.342955097	-1.257082125	0.041773447		
178	Campbell Springs Dolomite	924	-7.701530036	0.235086493	-0.84582866	0.086432896		
180	Campbell Springs Dolomite	932.5	-7.878787651	0.085571836	-0.966594735	0.028150476	0.705161	0.000003
181	Campbell Springs Dolomite	938.6	-7.014628699	0.178418893	-0.767453327	0.093851511		
182	Campbell Springs Dolomite	946.2	-7.809634514	0.146747832	-1.386915553	0.03563036		
183	Campbell Springs Dolomite	950.6	-7.977988103	0.091344501	-1.344188594	0.136920268		
185	Campbell Springs Dolomite	977.7	-8.27691938	0.198376232	-1.596143455	0.099716545		
185	Campbell Springs Dolomite	977.7	-8.471298933	0.141091322	-1.24677519	0.678987836		
186	Campbell Springs Dolomite	980.9	-9.306438129	0.127041064	-1.814334974	0.137879469	0.705161	0.000003
187	Campbell Springs Dolomite	986.2	-7.772599013	0.175233839	-2.382521776	0.076193158		

188	Campbell Springs Dolomite	990.13	-7.58464654	0.377152113	-2.302274992	0.124433806		
190	Blue Hole Formation	999.6	-7.12988226	0.201856248	-2.585487553	0.085599999	0.706197	0.000004
191	Blue Hole Formation	1003.9	-6.873559753	0.076575181	-2.359024386	0.038362493	0.706434	0.000007
193	Blue Hole Formation	1012.1	-7.50882389	0.542833325	-1.703211797	0.015152985	0.706434	0.000007
194	Blue Hole Formation	1020.2	-5.960965559	0.047395218	-1.799657108	0.135866655		
195	Blue Hole Formation	1029.8	-9.759442005	0.101548852	-1.807537658	0.136420477		
196	Blue Hole Formation	1040.6	-9.742040376	0.311895001	-1.905532763	0.087231238		
197	Blue Hole Formation	1048.3	-11.00081618	0.191203861	-1.87116586	0.09182609		
198	Blue Hole Formation	1052.5	-9.314933139	0.13628194	-1.504524821	0.025919291	0.708386	0.000005
200	Blue Hole Formation	1059.1						
203	Kunja Silts	1069.1						
204	Kunja Silts	1075.9						
205	Kunja Silts	1084.7	-9.148889189	0.264086693	-1.515082575	0.044548567	0.713059	0.000006
206	Kunja Silts	1094.7						
207	Kunja Silts	1110.2						
209	Kunja Silts	1125.8						
210	Kunja Silts	1141.7						
211	Kunja Silts	1152.5						
212	Kunja Silts	1166.3						
213	Mallabah Dolostone?	1185.9						
214	Mallabah Dolostone?	1192.5	-11.03184002	0.221081565	-1.899206199	0.100639481	0.714958	0.000009
215	Mallabah Dolostone?	1199.4						
216	Mallabah Dolostone?	1233.5						

**Table S.5.5.** Carbonate isotopic data for samples from Manbulloo S1.

Drillcore	Sample ID	Formation	Depth (m)	TOC	S1	S2	S3	Tmax (°C)	Rc (%)	HI	OI	S1/TOC*100	PI
LV09	18G014i	Hot Spring Mbr	279.35	0.25	0.04	0.44	0.04	430.00	0.58	176.00	16.00	16.00	0.08
LV09	18G015i	Hot Spring Mbr	289.85	0.13	0.00	0.11	0.16	436.00	0.69	85.00	123.00	0.00	0.03
LV09	18G001i	Barney Creek	393.70	0.11	0.01	0.03	0.16	437.00	0.71	27.00	145.00	9.09	0.14
LV09	18G002i	Barney Creek	402.40	1.09	0.15	3.80	0.12	435.00	0.67	349.00	11.00	13.76	0.04
LV09	18G003i	Barney Creek	406.70	0.88	0.48	3.83	0.14	423.00	0.45	435.00	16.00	54.55	0.11
LV09	18G004i	Barney Creek	414.75	1.12	0.36	3.85	0.18	430.00	0.58	344.00	16.00	32.14	0.09
LV09	18G005i	Barney Creek	429.70	1.57	0.78	7.32	0.14	433.00	0.63	466.00	9.00	49.68	0.10
LV09	18G008i	Barney Creek	443.70	2.30	1.09	9.88	0.18	430.00	0.58	430.00	8.00	47.39	0.10
LV09	17G002i	Barney Creek	450.00	2.26	1.32	10.73	0.11	435.00	0.67	475.00	5.00	58.41	0.11
LV09	18G009i	Barney Creek	461.83	2.23	1.02	9.30	0.15	431.00	0.60	417.00	7.00	45.74	0.10
LV09	17G007i	Barney Creek	470.70	0.87	0.38	3.46	0.32	424.00	0.47	398.00	37.00	43.68	0.10
LV09	17G008i	Barney Creek	477.00	4.36	2.69	22.35	0.03	434.00	0.65	513.00	1.00	61.70	0.11
LV09	17G009i	Barney Creek	478.20	0.60	0.14	1.61	0.29	431.00	0.60	268.00	48.00	23.33	0.08
LV09	17G001i	Barney Creek	485.00	4.71	2.50	24.24	0.09	438.00	0.72	515.00	2.00	53.08	0.09
LV09	17G010i	Barney Creek	489.00	3.78	1.82	17.00	0.17	435.00	0.67	450.00	4.00	48.15	0.10
LV09	18G007i light	Barney Creek	494.50	0.45	0.06	0.73	0.23	436.00	0.69	162.00	51.00	13.33	0.08
LV09	18G006i dark	Barney Creek	494.60	3.26	1.56	13.26	0.14	433.00	0.63	407.00	4.00	47.85	0.11
LV09	18G010i	Barney Creek	498.88	3.38	1.88	12.12	0.15	427.00	0.53	359.00	4.00	55.62	0.13
LV09	18G016i	Barney Creek	522.68	2.52	1.23	12.77	0.05	420.00	0.40	507.00	2.00	48.81	0.09

LV09	18G017i	Barney Creek	527.32	0.60	0.30	2.62	0.19	422.00	0.44	437.00	32.00	50.00	0.10
LV09	18G018i	Barney Creek	542.61	1.25	0.78	5.64	0.22	421.00	0.42	451.00	18.00	62.40	0.12
LV09	18G019i	Teena Dolomite	552.62	0.42	0.07	0.84	0.20	432.00	0.62	200.00	48.00	16.67	0.08
LV09	18G020i	Teena Dolomite	561.50	0.14	0.01	0.09	0.19	442.00	0.80	64.00	136.00	7.14	0.14
LV09	17G005i	Teena Dolomite	577.00	5.01	1.55	23.00	0.12	439.00	0.74	459.00	2.00	30.94	0.06

**Table S.5.6.** Shale source-rock analysis for samples from LV09001.

Drill core	Sample ID	Formation	Depth (m)	K (wt.%)	Al (wt.%)	P (wt.%)	Mn (wt.%)	V (wt.%)	Cr (wt.%)	Ni (wt.%)	Cu (wt.%)	Th (wt.%)	U (wt.%)	Mo (wt.%)
LV09	18G014i	Lynott Formation	279.3	5.73	4.52	0.03	0.05	0.00	0.00	0.00	0.00	0.00	0.00	0.00
9			5	128	496	077	431	266	292	067	065	160	019	005
LV09	18G015i	Lynott Formation	289.8	2.66	2.24	0.01	0.09	0.00	0.00	0.00	0.00	0.00	0.00	0.00
9	5	050	475	996	208	259	285	103	097	056	013	005	005	
LV09	19G001i	Reward	313.4	2.69	2.43	0.01	0.15	0.00	0.00	0.00	0.00	0.00	0.00	0.00
9			3	485	399	448	480	263	372	083	065	050	008	003
LV09	19G002i	Reward	330.4	2.06	1.61	0.01	0.13	0.00	0.00	0.00	0.00	0.00	0.00	0.00
9			206	257	761	757	272	540	112	045	033	008	010	
LV09	19G003i	Reward	338.8	2.12	2.01	0.01	0.03	0.00	0.00	0.00	0.00	0.00	0.00	0.00
9			962	459	068	160	254	084	059	057	023	007	012	
LV09	19G004i	Reward	341.1	1.33	1.03	0.01	0.24	0.00	0.00	0.00	0.00	0.00	0.00	0.00
9			891	313	715	334	261	333	079	018	031	005	003	
LV09	19G005i	Barney Creek	365.2	4.81	4.20	0.03	0.05	0.00	0.00	0.00	0.00	0.00	0.00	0.00
9			328	566	571	961	317	325	170	113	104	018	020	
LV09	19G006i	Barney Creek	371.7	3.13	2.69	0.05	0.05	0.00	0.00	0.00	0.00	0.00	0.00	0.00
9			6	876	593	622	459	295	324	155	087	068	022	020
LV09	19G007i	Barney Creek	376.4	1.69	1.39	0.01	0.14	0.00	0.00	0.00	0.00	0.00	0.00	0.00
9			010	616	628	343	268	544	164	032	039	008	005	
LV09	18G001i	Barney Creek	393.7	1.48	1.33	0.01	0.11	0.00	0.00	0.00	0.00	0.00	0.00	0.00
9			446	416	135	322	246	270	030	039	021	005	012	
LV09	18G002i	Barney Creek	402.4	3.80	3.33	0.05	0.10	0.00	0.00	0.00	0.00	0.00	0.00	0.00
9			829	559	952	479	254	278	090	104	067	015	007	
LV09	18G003i	Barney Creek	406.7	3.75	3.02	0.02	0.11	0.00	0.00	0.00	0.00	0.00	0.00	0.00
9			887	883	883	468	249	273	057	064	049	010	005	
LV09	18G004i	Barney Creek	414.7	4.07	3.49	0.09	0.07	0.00	0.00	0.00	0.00	0.00	0.00	0.00
9			5	463	373	683	239	267	279	085	106	095	017	007
LV09	18G005i	Barney Creek	429.7	4.84	4.01	0.03	0.06	0.00	0.00	0.00	0.00	0.00	0.00	0.00
9			292	669	882	086	270	273	093	104	093	018	005	
LV09	18G008i	Barney Creek	443.7	6.32	5.43	0.05	0.02	0.00	0.00	0.00	0.00	0.00	0.00	0.00
9			479	485	424	676	352	287	132	198	111	024	008	
LV09	17G002i	Barney Creek	450	4.93	4.41	0.04	0.05	0.00	0.00	0.00	0.00	0.00	0.00	0.00
9			302	881	823	613	432	286	187	201	093	027	019	
LV09	19G008i	Barney Creek	452.1	5.98	5.27	0.12	0.02	0.00	0.00	0.00	0.00	0.00	0.00	0.00
9			868	124	724	250	429	289	138	149	148	026	012	
LV09	19G009i	Barney Creek	457.2	6.14	5.72	0.07	0.02	0.00	0.00	0.00	0.00	0.00	0.00	0.00
9			286	569	186	740	455	331	193	252	124	032	012	
LV09	18G009i	Barney Creek	461.8	7.03	5.56	0.07	0.06	0.00	0.00	0.00	0.00	0.00	0.00	0.00
9			3	643	680	722	807	283	311	125	170	097	025	013
LV09	19G010i	Barney Creek	465.3	3.47	3.17	0.04	0.16	0.00	0.00	0.00	0.00	0.00	0.00	0.00
9			536	256	786	961	249	458	171	082	085	012	005	
LV09	17G007i	Barney Creek	470.7	2.69	2.33	0.02	0.23	0.00	0.00	0.00	0.00	0.00	0.00	0.00
9			018	711	688	702	250	363	109	079	048	009	006	
LV09	19G011i	Barney Creek	474.4	4.10	3.77	0.09	0.12	0.00	0.00	0.00	0.00	0.00	0.00	0.00
9			024	105	498	838	356	324	185	200	092	030	015	
LV09	17G008i	Barney Creek	477	4.62	3.97	0.22	0.11	0.00	0.00	0.00	0.00	0.00	0.00	0.00
9			066	195	774	096	391	091	203	266	151	041	031	
LV09	17G009i	Barney Creek	478.2	0.99	0.89	0.02	0.63	0.00	0.00	0.00	0.00	0.00	0.00	0.00
9			277	143	273	974	255	280	056	038	029	005	003	
LV09	17G001i	Barney Creek	485	5.00	4.27	0.19	0.09	0.00	0.00	0.00	0.00	0.00	0.00	0.00
9			261	309	880	979	470	082	203	196	119	047	082	
LV09	17G010i	Barney Creek	489	4.55	3.86	0.21	0.13	0.00	0.00	0.00	0.00	0.00	0.00	0.00
9			360	490	420	286	511	271	169	158	135	057	064	
LV09	18G007i light	Barney Creek	494.5	3.54	3.36	0.02	0.32	0.00	0.00	0.00	0.00	0.00	0.00	0.00
9			508	624	629	007	349	500	163	082	075	016	009	
LV09	18G006i dark	Barney Creek	494.6	4.22	3.92	0.02	0.07	0.00	0.00	0.00	0.00	0.00	0.00	0.00
9			479	048	542	789	304	085	327	322	072	025	083	
LV09	18G010i	Barney Creek	498.8	4.05	3.90	0.02	0.03	0.00	0.00	0.00	0.00	0.00	0.00	0.00
9			8	599	825	354	808	421	093	319	267	094	026	065



LVO 9	19G012i	Barney Creek	506	5.48	4.83	0.03	0.03	0.00	0.00	0.00	0.00	0.00	0.00	0.00	0.00
LVO 9	19G013i	Barney Creek	515.35	4.52	3.96	0.05	0.04	0.00	0.00	0.00	0.00	0.00	0.00	0.00	0.00
LVO 9	18G016i	Barney Creek	522.68	7.14	5.68	0.03	0.00	0.00	0.00	0.00	0.00	0.00	0.00	0.00	0.00
LVO 9	18G017i	Barney Creek	527.32	1.34	1.13	0.02	0.12	0.00	0.00	0.00	0.00	0.00	0.00	0.00	0.00
LVO 9	18G018i	Barney Creek	542.61	1.46	1.22	0.12	0.10	0.00	0.00	0.00	0.00	0.00	0.00	0.00	0.00
LVO 9	18G019i	Teena Dolomite	552.62	0.96	0.82	0.04	0.09	0.00	0.00	0.00	0.00	0.00	0.00	0.00	0.00
LVO 9	19G014i	Teena Dolomite	558.9	0.25	0.21	0.01	0.07	0.00	0.00	0.00	0.00	0.00	0.00	0.00	0.00
LVO 9	18G020i	Teena Dolomite	561.5	1.65	1.30	0.02	0.12	0.00	0.00	0.00	0.00	0.00	0.00	0.00	0.00
LVO 9	17G005i	Teena Dolomite	577	5.91	4.75	0.28	0.02	0.00	0.00	0.00	0.00	0.00	0.00	0.00	0.00
LVO 9	19G015i	Teena Dolomite	578.5	4.72	3.99	0.66	0.05	0.00	0.00	0.00	0.00	0.00	0.00	0.00	0.00

**Table S.5.7.** Shale and calcareous siltstone whole-rock geochemical analysis for samples from LV09001.

	313.43	294.3	279.35	252.55	235.4	210	172.3	Depth
Reward	14583.71	4690.34	9123.79	14280.66	15924.33	13255.63	5537.80	Formation
	6.06	78.89	1101.78	33.35	1842.07	218.72	3.02	24 -> 40 Mg
	<0.612	0.83	111.68	<0.612	74.72	36.32	<0.612	27 -> 27 Al
	20291.31	6867.79	12879.42	19987.86	21225.29	18016.84	7246.86	31 -> 47 P
	24144.75	8250.49	15289.36	23875.67	25248.80	21881.97	8785.21	43 -> 59 Ca
	<664.021	<664.021	145380.39	43962.88	125777.13	14976.13	<664.021	44 -> 60 Ca
	0.04	0.15	<0.007	0.05	<0.007	0.43	<0.007	47 -> 79 Ti
	<5.596	<5.596	<5.596	<5.596	<5.596	<5.596	<5.596	51 -> 83 V
	176.27	165.39	339.36	334.80	424.40	460.68	81.67	52 -> 68 Cr
	310.81	290.20	1572.69	920.33	1678.45	725.72	2.82	55 -> 71 Mn
	302.95	282.57	1530.69	893.57	1635.91	711.93	<5.098	56 -> 72 Fe
	13.99	9.44	0.29	14.85	0.45	11.03	0.05	57 -> 73 Fe
	13.60	9.12	0.28	14.58	0.44	10.34	0.05	59 -> 59 Co
	0.29	<0.202	57.15	0.82	13.51	<0.202	4.96	59 -> 75 Co
	0.46	<0.366	64.83	1.03	15.25	<0.366	5.67	60 -> 60 Ni
	<0.020	0.46	0.30	0.04	0.99	0.17	<0.020	60 -> 76 Ni
	<0.635	<0.635	0.80	0.71	5.44	<0.635	<0.635	63 -> 63 Cu
	0.47	0.31	2.88	1.00	3.63	0.82	1.47	66 -> 66 Zn
	9.72	6.79	18.13	19.37	28.19	35.73	9.12	85 -> 85 Rb
	0.04	0.43	2.00	1.06	2.24	1.32	0.00	88 -> 104 Sr
	<0.018	<0.018	0.09	0.02	0.12	0.02	<0.018	89 -> 105 Y
	0.05	<0.019	<0.019	<0.019	0.05	<0.019	<0.019	90 -> 122 Zr
	7.43	2.74	23.44	15.50	30.51	23.27	7.33	95 -> 95 Mo
								137 -> 153

568.28	567.5	543	534.25	490.7	490.7	452.1	445	419.66	393.7	373.85	341.1
Teena	Teena	Barney Creek	Barney Creek	Barney Creek	Barney Creek	Barney Creek	Barney Creek	Barney Creek	Barney Creek	Barney Creek	Reward
4074.23	5530.75	8146.14	4398.30	6276.26	3623.05	1873.37	4895.27	6583.20	14317.29	9953.98	7035.70
9.05	<1.262	1.35	<1.262	92.42	21.73	191.26	111.21	1108.05	23.57	6.58	<1.262
<0.612	<0.612	<0.612	<0.612	408.89	7.42	164.77	20.00	150.29	<0.612	4.69	<0.612
6122.56	7868.18	11443.94	5831.22	11923.05	6338.36	3020.95	7026.82	9589.77	19850.41	13522.24	9738.25
7177.82	9317.46	13617.76	6944.83	12708.77	6786.28	3542.09	8300.18	11300.84	23526.34	16234.49	11784.16
<664.021	<664.021	<664.021	<664.021	0.43	0.10	12377.20	1827.99	<664.021	<664.021	<664.021	<664.021
0.01	<0.007	0.03	<0.007	0.95	0.33	0.59	0.70	2.44	0.13	0.06	<0.007
<5.596	<5.596	<5.596	<5.596	0.57	0.26	<5.596	<5.596	<5.596	<5.596	<5.596	<5.596
55.70	49.33	111.81	34.46	240.57	146.60	32.36	109.55	81.92	322.46	162.83	100.57
55.37	56.95	81.59	17.34	581.83	278.54	259.32	494.52	1134.66	336.24	373.21	132.55
47.78	57.82	87.23	17.02	582.92	279.14	255.09	484.44	1108.62	327.99	361.19	129.37
1.42	0.18	2.11	0.13	2.81	0.33	3.49	3.89	17.35	0.16	10.02	5.15
1.42	0.18	2.02	0.13	2.76	0.32	3.43	3.77	16.96	0.14	9.82	4.95
<0.202	2.15	<0.202	19.12	0.62	<0.130	0.35	<0.202	1.92	5.43	<0.202	<0.202
<0.366	2.52	<0.366	21.07	0.68	<0.424	0.54	<0.366	2.37	5.48	<0.366	<0.366
<0.020	<0.020	<0.020	<0.020	0.38	0.07	0.89	0.36	4.63	0.06	<0.020	<0.020
<0.635	<0.635	0.78	<0.635	1.16	0.37	0.74	<0.635	2.83	1.32	1.28	<0.635
<0.030	0.17	0.06	0.52	0.22	0.08	0.67	0.29	2.84	0.53	0.21	0.19
2.15	3.15	4.66	2.14	7.06	3.28	2.87	3.79	8.28	6.42	6.62	2.72
0.05	<0.002	0.05	<0.002	2.46	0.26	1.59	0.64	1.88	0.31	0.31	0.05
<0.018	<0.018	<0.018	<0.018	0.05	<0.010	0.05	<0.018	0.18	<0.018	<0.018	<0.018
<0.019	0.02	<0.019	<0.019	0.03	<0.023	<0.019	<0.019	0.03	<0.019	<0.019	<0.019
0.62	2.18	2.44	3.13	5.88	3.77	3.21	4.39	14.51	7.39	5.91	3.68

603.83	601.7
Mitchell Yard	Mitchell Yard
8998.78	9934.19
2.03	<1.262
<0.612	4.97
12534.62	13947.04
14586.71	16436.86
<664.021	<664.021
0.04	0.05
<5.596	<5.596
47.99	69.01
118.05	191.65
107.34	186.59
0.03	7.06
0.03	6.92
4.49	<0.202
5.02	<0.366
<0.020	<0.020
<0.635	<0.635
0.05	0.09
5.12	6.00
0.02	0.02
<0.018	<0.018
<0.019	0.06
1.29	2.57

**Table S.5.8.** Carbonate geochemical analysis for samples from LV09001.

313.43	294.3	279.35	252.55	235.4	210	172.3	Depth
Reward Dolostone	Lynott Formation	Lynott Formation	Lynott Formation	Lynott Formation	Lynott Formation	Yalco Formation	Formation
0.01577	0.09081	2.57031	0.32941	0.78248	0.25451	0.00461	La
0.00803	0.10828	2.46912	0.31533	0.80833	0.27306	0.00351	Ce
0.00712	0.13118	2.47677	0.35396	0.88444	0.30960	0.00349	Pr
0.00812	0.15511	2.36235	0.41145	0.95627	0.35113	0.00340	Nd
0.00667	0.23800	1.89218	0.50294	1.19493	0.46370	0.00276	Sm
0.00578	0.19790	1.27780	0.42239	1.12250	0.42254	0.00221	Eu
0.01154	0.29425	1.45324	0.63321	1.34951	0.54339	0.00507	Gd
0.00603	0.27256	1.11135	0.46952	1.22449	0.47925	PAAS	Tb
0.00612	0.26781	1.06139	0.42787	1.22524	0.50176	0.00266	Dy
0.01347	0.24039	0.89350	0.43277	1.08628	0.49044	0.00352	Y
0.00612	0.23140	0.91687	0.37306	1.05551	0.45880	0.00292	Ho
0.00583	0.21369	0.88957	0.32427	1.02600	0.43627	0.00221	Er
0.00314	0.18145	0.76364	0.22774	0.86440	0.33221	0.00139	Tm
0.00292	0.20798	0.89014	0.23360	1.00632	0.35322	0.00174	Yb
0.00339	0.17981	0.75192	0.19909	0.84119	0.28268	PAAS	Lu

568.28	Teena Dolostone	567.5	Teena Dolostone	543	Cooley Dolostone	534.25	Cooley Dolostone	490.7	Barney Creek Formation	490.7	Barney Creek Formation	445	Barney Creek Formation	419.66	Barney Creek Formation	393.7	Barney Creek Formation	373.85	Barney Creek Formation	341.1	Reward Dolostone
0.01805		0.00129	0.02576	0.00035	0.13047	0.83522	0.35715	0.46055	0.69856	0.21181	0.12421	0.02842									
0.02014		0.00128	0.01791	0.00041	0.13529	1.08090	0.42171	0.48484	0.81686	0.17341	0.12152	0.01891									
0.02337		0.00156	0.01762	0.00047	0.14884	1.54121	0.56818	0.57534	0.99270	0.17072	0.14833	0.01773									
0.02464		0.00157	0.02068	0.00050	0.15837	1.94726	0.73361	0.64664	1.16836	0.16949	0.18351	0.01779									
0.02511		0.00150	0.01619	0.00057	0.18918	2.44190	1.04145	0.80762	1.55597	0.15642	0.20945	0.01427									
0.01903			0.01444		0.17120	2.18075	0.92480	0.62708	1.21501	0.13061	0.17442	0.01197									
0.02551			0.02306		0.19670	2.59658	1.18627	0.81253	1.76007	0.17850	0.25873	0.02116									
0.02078			0.01210		0.18262	2.05500	0.97200	0.68224	1.51111	0.14819	0.18255	0.01277									
0.01925		0.00149	0.01214	0.00061	0.18304	1.78888	0.84135	0.66177	1.49888	0.15292	0.16141	0.01179									
0.01877		0.00155	0.02090	0.00046	0.15564	1.24764	0.56691	0.51779	1.19063	0.17194	0.16609	0.02159									
0.01651		0.00115	0.01218	0.00047	0.16350	1.31857	0.59893	0.54048	1.23708	0.15342	0.13405	0.01159									
0.01590		0.00119	0.00928	0.00041	0.15573	0.91893	0.41487	0.46097	1.14325	0.14177	0.11032	0.00949									
0.01005		0.00140	0.00607		0.12952	0.51972	0.23775	0.34013	0.86147	0.10847	0.07354	0.00577									
0.01119		0.00119	0.00570		0.14427	0.42519	0.20431	0.35681	0.92059	0.12041	0.06687	0.00599									
0.00978			0.00594		0.12353	0.30460	0.14072	0.27693	0.73032	0.10864	0.05850	0.00596									

601.7	Mitchell Yard Dolostone	0.01872	0.00830	0.00706	0.00912	0.00482	0.00469	0.00924		0.00357	0.00838	0.00338	0.00433	0.00198	0.00177	
603.83	Mitchell Yard Dolostone	0.01383	0.00696	0.00613	0.00669	0.00505	0.00420	0.00826	0.00557	0.00549	0.00857	0.00493	0.00501	0.00340	0.00332	0.00314

**Table S.5.9.** Carbonate trace element analysis for samples from LV09001 normalised to PAAS values.

START DEPTH	d13C	d18O	87Sr/86Sr	Unit
164.19	-1.801509	-4.956969	0.725734	Yalco Formation
164.19	-1.831424	-5.223954		Yalco Formation
172.3	-1.206708	-4.116768	0.729247	Lynnot Formation - Hot Spring Member
184.2	-0.969966	-3.881790		Lynnot Formation - Hot Spring Member
184.2	-1.045371	-3.915205		Lynnot Formation - Hot Spring Member
198.2	-0.789540	-4.793098	0.717997	Lynnot Formation - Hot Spring Member
210	-0.992684	-3.804090	0.724628	Lynnot Formation - Caranbini Member
210	-1.077434	-3.671258		Lynnot Formation - Caranbini Member
219.5	-0.931721	-3.724854		Lynnot Formation - Caranbini Member
235.4	-1.130066	-5.046417		Lynnot Formation - Caranbini Member
247.42				Lynnot Formation - Caranbini Member
252.55	-1.047899	-6.016794	0.728764	Lynnot Formation - Caranbini Member
269.5				Lynnot Formation - Caranbini Member
279.35	-1.581221	-5.642431		Lynnot Formation - Caranbini Member
279.35	-1.536948	-6.279951		Lynnot Formation - Caranbini Member
289.85	-1.214245	-6.162059		Lynnot Formation - Caranbini Member
294.3	-1.243717	-6.243239	0.715212	Lynnot Formation - Caranbini Member
301.05	-1.419788	-5.952328		Lynnot Formation - Caranbini Member
313.43	-0.632576	-5.095633	0.715385	Lynnot Formation - Caranbini Member
313.43	-0.593514	-5.015474		Lynnot Formation - Caranbini Member
318.6	-0.864692	-3.776618		Lynnot Formation - Caranbini Member
330.4	-0.704220	-7.211333		Lynnot Formation - Caranbini Member
330.4	-0.690534	-6.559809		Lynnot Formation - Caranbini Member
341.1	-0.253666	-4.510567	0.707034	Lynnot Formation - Caranbini Member
350.9	-0.521836	-6.923510		Reward Dolomite
360.2	-0.497738	-7.624523		Reward Dolomite
360.2	-0.395495	-7.669571		Reward Dolomite
369.81	-0.673470	-7.382166		Reward Dolomite
373.85	-0.344512	-6.091043	0.708152	Reward Dolomite
376.4	-0.503976	-7.011256		Reward Dolomite
380.7	-0.609003	-6.346741		Reward Dolomite
386.9	-0.795824	-7.023159		Reward Dolomite
393.7	-0.908154	-5.761151		Barney Creek Formation
393.7	-0.938417	-6.240174	0.715223	Barney Creek Formation
399.5	-0.729606	-6.866277		Barney Creek Formation

402.4				Barney Creek Formation	
412.88	-1.023825	-6.980935	0.725687	Barney Creek Formation	
412.88	-1.011888	-6.669173		Barney Creek Formation	
419.66	-1.499962	-6.414311	0.735999	Barney Creek Formation	
432.54	-1.483660	-6.300373		Barney Creek Formation	
445	-1.665964	-6.887958	0.722096	Barney Creek Formation	
452.1	-2.078809	-5.620285		Barney Creek Formation	
463.6	-1.866627	-6.441648		Barney Creek Formation	
463.6	-1.979906	-5.987803	0.722673	Barney Creek Formation	
469.5	-1.511676	-6.798791		Barney Creek Formation	
490.7	-1.314865	-6.009110	0.723685	Barney Creek Formation	
502.5				Barney Creek Formation	
502.5	-2.275550	-7.280505	0.733737	Barney Creek Formation	
508.1	-1.784832	-5.426080		Barney Creek Formation	
515	-1.944196	-6.469908		Barney Creek Formation	
530	-1.182552	-7.258971		Barney Creek Formation	
534.25	-1.080101	-7.819741	0.716904	Barney Creek Formation	
534.25	-1.228204	-8.248849		Barney Creek Formation	
540.02	-1.023493	-8.186062		Barney Creek Formation	
543	-0.860849	-8.360600		Barney Creek Formation	
543	-0.706241	-8.602881		Barney Creek Formation	
547.61	-0.805497	-8.290154		Barney Creek Formation	
553.9	-0.600414	-8.385159		Teena Dolomite	
553.9	-0.791564	-8.978096		Teena Dolomite	
554.1	-0.726887	-8.300575		Teena Dolomite	
565.7	-0.905882	-8.924030		Teena Dolomite	
567.5	-0.806220	-8.140486	0.709379	Teena Dolomite	
568.28	-0.628899	-8.498774		Teena Dolomite	
568.28	-0.590944	-7.912189		Teena Dolomite	
573.16	-0.618841	-7.437707		Teena Dolomite	
592.48	-0.749515	-9.091326		Mitchell Yard Dolomite Member	
601.7	-0.518458	-7.897046	0.707078	Mara Dolomite Member	
603.83	-0.550232	-7.320854	0.706190	Mara Dolomite Member	
Depth (m)	Unit	87Sr/86Sr DYN	2SE	δ88/86Sr (‰) Normalised to 987-Batch Average	2SE
210	Hot Sping Member	0.717997	0.000004	0.481183	0.02
252.55	Caranbini Member	0.728764	0.000003	0.523270	0.01
294.3	Caranbini Member	0.715212	0.000003	0.342705	0.03
373.85	Reward Dolomite	0.708152	0.000005	0.652602	0.43
393.7	Barney Creek Formation	0.715223	0.000004	0.377312	0.01
445	Barney Creek Formation	0.734105	0.000003	0.582497	0.01
490.7	Barney Creek Formation	0.715906	0.000002	0.398130	0.02
567.5	Teena Dolomite	0.714633	0.000003	0.416580	0.01
601.7	Mara Dolomite Member	0.707738	0.000003	0.350562	0.02
601.7	Mara Dolomite Member	0.707738	0.000003	0.372114	0.02

**Table S.5.10.** Carbonate isotopic analysis for samples from LV09001.

Source Filename	87Rb/86Sr	87Rb/86Sr	87Sr/86Sr	87Sr/86Sr
GLO - 1.csv	161.285	7.381	0.913	0.041
GLO - 10.csv	171.822	7.429	0.914	0.032
GLO - 11.csv	158.171	7.171	0.894	0.036
GLO - 12.csv	33.994	5.016	0.744	0.020
GLO - 13.csv	180.826	7.629	0.934	0.032
GLO - 14.csv	184.138	7.800	0.954	0.034
GLO - 15.csv	171.952	7.221	0.944	0.033
GLO - 16.csv	159.985	7.039	0.912	0.032
GLO - 17.csv	193.275	8.649	0.988	0.039
GLO - 18.csv	4.799	0.603	0.713	0.007
GLO - 19.csv	175.274	8.660	0.912	0.038
GLO - 2.csv	197.086	9.860	0.955	0.052
GLO - 20.csv	180.703	8.160	0.953	0.035
GLO - 21.csv	103.427	8.633	0.830	0.026
GLO - 22.csv	17.296	3.286	0.729	0.015
GLO - 23.csv	186.007	7.912	0.974	0.035
GLO - 24.csv	4.532	0.616	0.717	0.007
GLO - 25.csv	127.927	5.212	0.874	0.027
GLO - 26.csv	4.401	0.385	0.714	0.006
GLO - 27.csv	122.970	7.861	0.856	0.028
GLO - 28.csv	206.824	9.090	0.991	0.039
GLO - 29.csv	182.071	8.071	0.961	0.040
GLO - 3.csv	163.768	7.225	0.938	0.037
GLO - 30.csv	195.233	8.212	0.988	0.034
GLO - 31.csv	195.297	8.406	0.982	0.037
GLO - 32.csv	199.402	8.690	0.963	0.037
GLO - 33.csv	215.813	9.510	0.993	0.038
GLO - 34.csv	245.518	11.528	1.038	0.042
GLO - 35.csv	172.265	8.461	0.947	0.031
GLO - 36.csv	183.184	7.824	0.955	0.036
GLO - 4.csv	174.667	8.170	0.904	0.043
GLO - 5.csv	81.453	6.861	0.827	0.028
GLO - 6.csv	183.473	8.622	0.946	0.040
GLO - 7.csv	163.434	6.983	0.906	0.035
GLO - 8.csv	40.791	6.620	0.771	0.025
GLO - 9.csv	44.702	5.673	0.779	0.021
MDC - 1.csv	42.568	1.561	1.039	0.014
MDC - 10.csv	41.900	1.531	1.038	0.014
MDC - 11.csv	41.640	1.520	1.035	0.014
MDC - 12.csv	42.076	1.556	1.028	0.014
MDC - 13.csv	42.212	1.536	1.055	0.014
MDC - 14.csv	42.258	1.535	1.034	0.014
MDC - 15.csv	42.285	1.563	1.042	0.014

MDC - 16.csv	42.245	1.561	1.034	0.013
MDC - 17.csv	42.004	1.539	1.038	0.014
MDC - 18.csv	42.250	1.574	1.042	0.013
MDC - 19.csv	41.879	1.560	1.030	0.013
MDC - 2.csv	42.152	1.537	1.035	0.014
MDC - 20.csv	42.130	1.551	1.040	0.013
MDC - 21.csv	40.733	1.507	1.039	0.013
MDC - 22.csv	41.872	1.543	1.053	0.013
MDC - 23.csv	42.376	1.563	1.047	0.014
MDC - 24.csv	42.600	1.561	1.041	0.014
MDC - 25.csv	42.445	1.558	1.034	0.014
MDC - 26.csv	41.860	1.522	1.039	0.014
MDC - 27.csv	41.600	1.538	1.033	0.013
MDC - 28.csv	41.791	1.526	1.036	0.014
MDC - 29.csv	42.701	1.553	1.034	0.014
MDC - 3.csv	42.335	1.557	1.046	0.014
MDC - 30.csv	42.225	1.535	1.036	0.014
MDC - 4.csv	41.629	1.509	1.032	0.014
MDC - 5.csv	41.749	1.540	1.028	0.015
MDC - 6.csv	41.790	1.521	1.032	0.014
MDC - 7.csv	41.987	1.536	1.036	0.014
MDC - 8.csv	42.488	1.542	1.044	0.014
MDC - 9.csv	42.015	1.545	1.043	0.015
MicaMg - 1.csv	152.560	5.228	1.855	0.042
MicaMg - 10.csv	151.010	5.175	1.835	0.030
MicaMg - 11.csv	151.134	5.179	1.826	0.030
MicaMg - 12.csv	149.277	5.116	1.844	0.031
MicaMg - 13.csv	148.442	5.087	1.832	0.029
MicaMg - 14.csv	154.471	5.294	1.879	0.030
MicaMg - 15.csv	156.074	5.349	1.855	0.031
MicaMg - 16.csv	154.249	5.286	1.875	0.030
MicaMg - 17.csv	153.311	5.254	1.845	0.030
MicaMg - 18.csv	154.434	5.292	1.869	0.030
MicaMg - 19.csv	158.703	5.439	1.868	0.033
MicaMg - 2.csv	157.515	5.398	1.841	0.037
MicaMg - 20.csv	156.161	5.352	1.847	0.030
MicaMg - 21.csv	156.959	5.379	1.887	0.031
MicaMg - 22.csv	154.156	5.283	1.871	0.032
MicaMg - 23.csv	155.169	5.318	1.871	0.034
MicaMg - 24.csv	152.099	5.212	1.866	0.030
MicaMg - 25.csv	151.328	5.186	1.856	0.029
MicaMg - 26.csv	153.455	5.259	1.864	0.034
MicaMg - 27.csv	155.387	5.325	1.856	0.031
MicaMg - 28.csv	155.377	5.325	1.872	0.032
MicaMg - 29.csv	155.782	5.339	1.883	0.030



MicaMg - 3.csv	159.367	5.461	1.873	0.036
MicaMg - 30.csv	154.796	5.305	1.862	0.029
MicaMg - 31.csv	153.164	5.249	1.862	0.029
MicaMg - 32.csv	155.541	5.330	1.890	0.029
MicaMg - 33.csv	157.073	5.383	1.848	0.029
MicaMg - 34.csv	157.630	5.402	1.849	0.029
MicaMg - 35.csv	153.815	5.271	1.855	0.029
MicaMg - 36.csv	154.397	5.291	1.862	0.029
MicaMg - 4.csv	157.733	5.405	1.864	0.037
MicaMg - 5.csv	158.393	5.428	1.844	0.036
MicaMg - 6.csv	158.308	5.425	1.854	0.033
MicaMg - 7.csv	152.338	5.221	1.853	0.032
MicaMg - 8.csv	153.911	5.275	1.856	0.035
MicaMg - 9.csv	152.082	5.212	1.863	0.033

**Table S.5.11.** Geochronological standards analysed for Chapter 5.

Source Filename	$^{87}\text{Rb}/^{86}\text{Sr}$	$^{87}\text{Rb}/^{86}\text{Sr}$	$^{87}\text{Sr}/^{86}\text{Sr}$	$^{87}\text{Sr}/^{86}\text{Sr}$	EC (Rho)
LV19 - 1.csv	9.5842	0.3959	0.9199	0.0182	0.4851
LV19 - 10.csv	11.4169	0.4450	0.9628	0.0172	0.4484
LV19 - 11.csv	8.2755	0.3799	0.8980	0.0163	0.4685
LV19 - 12.csv	11.4454	0.5598	0.9665	0.0174	0.5506
LV19 - 13.csv	10.5236	0.4759	0.9496	0.0172	0.4791
LV19 - 14.csv	9.6418	0.5999	0.9314	0.0166	0.6470
LV19 - 15.csv	8.9965	0.4105	0.9108	0.0140	0.5077
LV19 - 16.csv	10.7086	0.5394	0.9496	0.0185	0.5939
LV19 - 17.csv	7.4789	0.2937	0.8735	0.0137	0.3469
LV19 - 19.csv	10.1451	0.4194	0.9358	0.0144	0.4099
LV19 - 2.csv	9.1472	0.3700	0.9217	0.0136	0.4326
LV19 - 20.csv	9.7485	0.4047	0.9275	0.0160	0.4795
LV19 - 21.csv	8.7506	0.3834	0.9182	0.0157	0.4761
LV19 - 22.csv	11.8681	0.5356	0.9910	0.0165	0.4931
LV19 - 23.csv	10.8408	0.4125	0.9655	0.0161	0.3754
LV19 - 24.csv	10.0033	0.4203	0.9452	0.0206	0.4681
LV19 - 25.csv	6.3437	0.2709	0.8505	0.0139	0.4334
LV19 - 26.csv	9.7273	0.3878	0.9388	0.0130	0.4088
LV19 - 27.csv	10.7770	0.6078	0.9529	0.0172	0.6299
LV19 - 28.csv	11.7410	0.6271	0.9741	0.0190	0.6858
LV19 - 3.csv	9.8051	0.4177	0.9268	0.0183	0.5144
LV19 - 30.csv	7.9416	0.4407	0.8827	0.0190	0.6436
LV19 - 31.csv	7.3450	0.4364	0.8669	0.0216	0.5863
LV19 - 32.csv	9.8422	0.4330	0.9396	0.0161	0.4215
LV19 - 33.csv	9.7008	0.4793	0.9305	0.0163	0.5007
LV19 - 35.csv	8.7380	0.3573	0.9014	0.0146	0.4543
LV19 - 36.csv	14.8293	0.9954	1.0504	0.0264	0.7358
LV19 - 37.csv	8.9836	0.4652	0.9143	0.0156	0.5924

LV19 - 38.csv	8.1974	0.3359	0.9042	0.0123	0.3374
LV19 - 4.csv	8.4818	0.3352	0.8950	0.0131	0.3883
LV19 - 41.csv	11.3932	0.5113	0.9785	0.0171	0.5774
LV19 - 42.csv	8.6826	0.3971	0.9018	0.0169	0.4776
LV19 - 43.csv	8.1990	0.3143	0.8953	0.0137	0.3996
LV19 - 46.csv	9.6377	0.4079	0.9362	0.0163	0.5073
LV19 - 48.csv	7.8291	0.3776	0.8818	0.0153	0.4680
LV19 - 49.csv	7.6207	0.3253	0.8879	0.0134	0.4421
LV19 - 5.csv	22.0445	1.1490	1.2000	0.0245	0.6209
LV19 - 50.csv	10.9698	0.5537	0.9608	0.0175	0.5810
LV19 - 51.csv	12.4298	0.6013	0.9906	0.0171	0.5916
LV19 - 52.csv	11.0254	0.4165	0.9623	0.0145	0.4250
LV19 - 53.csv	10.1634	0.4955	0.9484	0.0166	0.5312
LV19 - 54.csv	9.3681	0.4794	0.9128	0.0172	0.5893
LV19 - 55.csv	9.6831	0.3858	0.9298	0.0143	0.4603
LV19 - 56.csv	9.4968	0.5477	0.9275	0.0190	0.7275
LV19 - 57.csv	9.9197	0.3862	0.9325	0.0158	0.3860
LV19 - 58.csv	10.4392	0.4542	0.9514	0.0166	0.4354
LV19 - 59.csv	9.2538	0.3597	0.9078	0.0156	0.4197
LV19 - 6.csv	11.1587	0.6008	0.9578	0.0197	0.6235
LV19 - 60.csv	10.1181	0.3916	0.9508	0.0170	0.3529
LV19 - 8.csv	9.9567	0.4465	0.9228	0.0155	0.5026
LV19 - 9.csv	10.2496	0.4356	0.9466	0.0148	0.4671
LV20 - 1.csv	3.9808	0.2413	0.7861	0.0139	0.5019
LV20 - 10.csv	7.5444	0.4995	0.8747	0.0161	0.5709
LV20 - 11.csv	10.0029	0.4204	0.9192	0.0157	0.4618
LV20 - 12.csv	7.6715	0.3399	0.8772	0.0133	0.5536
LV20 - 13.csv	6.1469	0.2321	0.8459	0.0128	0.3813
LV20 - 14.csv	5.3217	0.2195	0.8254	0.0108	0.3539
LV20 - 15.csv	5.7226	0.2337	0.8322	0.0111	0.3200
LV20 - 16.csv	7.0553	0.2757	0.8690	0.0137	0.3739
LV20 - 17.csv	6.8494	0.2795	0.8586	0.0132	0.4091
LV20 - 18.csv	8.7739	0.3896	0.9069	0.0123	0.4099
LV20 - 19.csv	4.3634	0.1948	0.8019	0.0149	0.3855
LV20 - 2.csv	9.0641	0.5168	0.9151	0.0183	0.5389
LV20 - 20.csv	4.7834	0.2181	0.8058	0.0129	0.4555
LV20 - 21.csv	3.7334	0.1570	0.7912	0.0147	0.3963
LV20 - 22.csv	10.1223	0.5811	0.9417	0.0185	0.6278
LV20 - 23.csv	11.9955	0.6590	0.9709	0.0189	0.6345
LV20 - 24.csv	5.0695	0.2093	0.8247	0.0131	0.3983
LV20 - 25.csv	7.2984	0.2887	0.8675	0.0143	0.4051
LV20 - 28.csv	6.8591	0.3209	0.8543	0.0110	0.3838
LV20 - 29.csv	5.6362	0.2431	0.8398	0.0108	0.4421
LV20 - 30.csv	3.9195	0.1849	0.7944	0.0096	0.2849
LV20 - 32.csv	7.1859	0.3214	0.8602	0.0130	0.5278

LV20 - 33.csv	6.3847	0.2607	0.8480	0.0124	0.4401
LV20 - 35.csv	5.7679	0.3139	0.8420	0.0142	0.6212
LV20 - 37.csv	7.0350	0.2790	0.8748	0.0134	0.3284
LV20 - 39.csv	4.1293	0.1641	0.7992	0.0102	0.3758
LV20 - 4.csv	10.6817	0.6221	0.9378	0.0189	0.7430
LV20 - 40.csv	4.3311	0.1864	0.7903	0.0129	0.3194
LV20 - 43.csv	9.4342	0.7060	0.9160	0.0199	0.6691
LV20 - 45.csv	4.6523	0.1940	0.8066	0.0113	0.3653
LV20 - 46.csv	4.4954	0.1861	0.8074	0.0115	0.4302
LV20 - 47.csv	6.6543	0.2894	0.8578	0.0132	0.4414
LV20 - 48.csv	3.8164	0.2224	0.7920	0.0116	0.6087
LV20 - 49.csv	8.9445	0.4775	0.9177	0.0151	0.5328
LV20 - 5.csv	10.2354	0.3995	0.9501	0.0136	0.3973
LV20 - 50.csv	5.0622	0.2308	0.8119	0.0126	0.5457
LV20 - 51.csv	6.0857	0.2395	0.8507	0.0137	0.4084
LV20 - 52.csv	5.0139	0.2078	0.8211	0.0128	0.2927
LV20 - 53.csv	4.4705	0.2140	0.8058	0.0111	0.4802
LV20 - 55.csv	7.2828	0.3127	0.8775	0.0138	0.4216
LV20 - 56.csv	6.6550	0.3481	0.8691	0.0149	0.5173
LV20 - 57.csv	4.1013	0.2008	0.7878	0.0109	0.4820
LV20 - 58.csv	4.2569	0.1947	0.8022	0.0110	0.4264
LV20 - 59.csv	5.6128	0.3047	0.8283	0.0137	0.6015
LV20 - 61.csv	4.7959	0.2002	0.8038	0.0115	0.3932
LV20 - 62.csv	6.6794	0.2560	0.8579	0.0123	0.3788
LV20 - 64.csv	7.0099	0.4408	0.8598	0.0155	0.5805
LV20 - 65.csv	4.3841	0.1894	0.8032	0.0116	0.4355
LV20 - 9.csv	10.4031	0.4692	0.9335	0.0154	0.4596
MBS1785 - 1.csv	19.3206	0.9685	1.1388	0.0277	0.6712
MBS1785 - 10.csv	14.6484	0.6418	1.0156	0.0194	0.5852
MBS1785 - 11.csv	23.0131	1.0868	1.2048	0.0262	0.5337
MBS1785 - 12.csv	11.0053	0.8466	0.9562	0.0259	0.7916
MBS1785 - 13.csv	12.8342	1.1358	0.9973	0.0288	0.8092
MBS1785 - 14.csv	17.6109	0.9307	1.0810	0.0239	0.6184
MBS1785 - 15.csv	19.0993	0.9614	1.1384	0.0269	0.6511
MBS1785 - 16.csv	21.3884	1.2079	1.1838	0.0300	0.7165
MBS1785 - 17.csv	13.7968	0.5945	1.0069	0.0208	0.4592
MBS1785 - 18.csv	16.9114	0.9766	1.0667	0.0260	0.7653
MBS1785 - 19.csv	18.2894	0.7874	1.0982	0.0207	0.5080
MBS1785 - 20.csv	7.8227	0.5813	0.8689	0.0223	0.7554
MBS1785 - 21.csv	18.5817	0.8490	1.1204	0.0243	0.5531
MBS1785 - 22.csv	19.2950	0.8913	1.1455	0.0245	0.4970
MBS1785 - 23.csv	13.6406	1.0932	1.0181	0.0318	0.8446
MBS1785 - 24.csv	16.1473	0.8512	1.0562	0.0214	0.5983
MBS1785 - 25.csv	17.5450	0.6966	1.1048	0.0231	0.4422
MBS1785 - 26.csv	16.3211	0.8169	1.0661	0.0241	0.5926

MBS1785 - 27.csv	17.6796	0.7720	1.0972	0.0221	0.5536
MBS1785 - 28.csv	20.1361	0.7948	1.1751	0.0202	0.4368
MBS1785 - 29.csv	17.5398	0.7272	1.0950	0.0209	0.4928
MBS1785 - 3.csv	17.1694	0.7737	1.0655	0.0228	0.5041
MBS1785 - 30.csv	17.6121	0.8636	1.0814	0.0254	0.6335
MBS1785 - 32.csv	22.7881	0.9313	1.2078	0.0235	0.5150
MBS1785 - 33.csv	27.0396	1.1998	1.3037	0.0330	0.6082
MBS1785 - 34.csv	20.9052	1.0604	1.1916	0.0279	0.5956
MBS1785 - 35.csv	15.9340	0.7721	1.0813	0.0259	0.6047
MBS1785 - 36.csv	15.7010	0.7576	1.0740	0.0214	0.5977
MBS1785 - 37.csv	23.8645	1.1187	1.2436	0.0255	0.5226
MBS1785 - 38.csv	17.4876	0.8397	1.0886	0.0230	0.5229
MBS1785 - 39.csv	10.5805	1.0078	0.9290	0.0311	0.6576
MBS1785 - 40.csv	14.9216	0.9377	1.0410	0.0237	0.7176
MBS1785 - 42.csv	22.0098	1.3400	1.2070	0.0344	0.7521
MBS1785 - 44.csv	22.5606	0.9369	1.2135	0.0243	0.4999
MBS1785 - 45.csv	15.2242	0.7746	1.0466	0.0241	0.6078
MBS1785 - 46.csv	13.3477	0.7153	1.0007	0.0211	0.6556
MBS1785 - 47.csv	17.1470	1.1466	1.0845	0.0288	0.7436
MBS1785 - 48.csv	8.8079	0.7505	0.8943	0.0273	0.7602
MBS1785 - 49.csv	19.1894	0.8163	1.1471	0.0230	0.5804
MBS1785 - 50.csv	15.4242	0.6750	1.0346	0.0188	0.4541
MBS1785 - 51.csv	13.6142	0.6049	1.0133	0.0175	0.5338
MBS1785 - 52.csv	12.7820	0.6006	0.9973	0.0184	0.5944
MBS1785 - 53.csv	19.8485	1.0393	1.1643	0.0310	0.6705
MBS1785 - 54.csv	13.9687	0.5921	1.0163	0.0158	0.4788
MBS1785 - 56.csv	14.2737	0.6793	1.0309	0.0214	0.5521
MBS1785 - 58.csv	13.2955	0.6201	1.0030	0.0175	0.5302
MBS1785 - 59.csv	13.1221	0.7978	0.9910	0.0226	0.7265
MBS1785 - 6.csv	21.0868	1.0417	1.1830	0.0249	0.6258
MBS1785 - 60.csv	19.2824	0.9545	1.1425	0.0269	0.6705
MBS1785 - 61.csv	16.7458	0.8681	1.0874	0.0230	0.5833
MBS1785 - 62.csv	14.6056	0.6077	1.0362	0.0193	0.4543
MBS1785 - 64.csv	18.9379	1.0719	1.1617	0.0285	0.6895
MBS1785 - 65.csv	18.2850	0.7443	1.1411	0.0203	0.4699
MBS1785 - 8.csv	21.4122	1.0319	1.1833	0.0257	0.6066
MBS1785 - 9.csv	26.1251	1.1950	1.2891	0.0316	0.5455
MBS1868 - 1.csv	5.0639	0.2028	0.8081	0.0140	0.3633
MBS1868 - 10.csv	20.5258	1.2673	1.1895	0.0363	0.6378
MBS1868 - 11.csv	19.5476	0.9462	1.1202	0.0219	0.5106
MBS1868 - 12.csv	12.3364	0.5043	0.9728	0.0225	0.4695
MBS1868 - 13.csv	25.4309	1.4453	1.2603	0.0376	0.6855
MBS1868 - 14.csv	21.5560	1.5417	1.1768	0.0508	0.7181
MBS1868 - 15.csv	20.3310	1.4075	1.1586	0.0426	0.8393
MBS1868 - 16.csv	27.3089	1.9482	1.3137	0.0487	0.7528

MBS1868 - 17.csv	16.7858	1.1669	1.0757	0.0367	0.6412
MBS1868 - 18.csv	19.3163	1.0003	1.1490	0.0295	0.5982
MBS1868 - 2.csv	16.6540	0.9055	1.0531	0.0269	0.5362
MBS1868 - 21.csv	18.1245	1.1958	1.0941	0.0315	0.7428
MBS1868 - 22.csv	4.2249	0.9056	0.7854	0.0289	0.7923
MBS1868 - 26.csv	8.0285	0.6617	0.8698	0.0264	0.6838
MBS1868 - 27.csv	13.4587	0.6693	0.9922	0.0223	0.5882
MBS1868 - 29.csv	17.5982	1.1381	1.1026	0.0290	0.6654
MBS1868 - 3.csv	25.7399	1.4895	1.2795	0.0354	0.7180
MBS1868 - 30.csv	23.3381	1.2302	1.2255	0.0325	0.6306
MBS1868 - 31.csv	17.2513	1.0326	1.0789	0.0369	0.5964
MBS1868 - 32.csv	21.2322	1.4793	1.1768	0.0443	0.7812
MBS1868 - 33.csv	15.5165	1.0230	1.0499	0.0337	0.7201
MBS1868 - 38.csv	16.1155	0.8112	1.0749	0.0309	0.5865
MBS1868 - 4.csv	21.7427	0.8623	1.1756	0.0250	0.3432
MBS1868 - 40.csv	17.3523	0.8696	1.0703	0.0352	0.5322
MBS1868 - 41.csv	24.5870	1.1431	1.2343	0.0341	0.5955
MBS1868 - 42.csv	17.0536	0.7264	1.0750	0.0253	0.4179
MBS1868 - 43.csv	18.7637	0.9066	1.1470	0.0249	0.5700
MBS1868 - 45.csv	17.1344	0.7943	1.0994	0.0245	0.5510
MBS1868 - 46.csv	15.0267	0.6867	1.0437	0.0222	0.5539
MBS1868 - 48.csv	20.6697	0.9049	1.1604	0.0360	0.5518
MBS1868 - 49.csv	21.6471	1.0142	1.2151	0.0269	0.5417
MBS1868 - 5.csv	20.9872	1.0374	1.1523	0.0329	0.5769
MBS1868 - 50.csv	21.4788	1.1556	1.1943	0.0328	0.5991
MBS1868 - 53.csv	26.7901	1.3046	1.3139	0.0281	0.6264
MBS1868 - 56.csv	19.8129	0.9510	1.1781	0.0308	0.4932
MBS1868 - 6.csv	23.3194	1.0528	1.2275	0.0256	0.6019
MBS1868 - 62.csv	18.4495	0.8437	1.1253	0.0329	0.5976
MBS1868 - 64.csv	19.2676	0.9028	1.1319	0.0252	0.4907
MBS1868 - 65.csv	20.4573	0.9211	1.1688	0.0257	0.5864
MBS1868 - 7.csv	23.6372	0.9672	1.2221	0.0282	0.4106
MBS1868 - 9.csv	10.9824	0.8929	0.9319	0.0353	0.7263

**Table S.5.12.** Geochronological samples analysed for Chapter 5.